Ariel Lipson
Stephen G. Lipson
and Henry Lipson

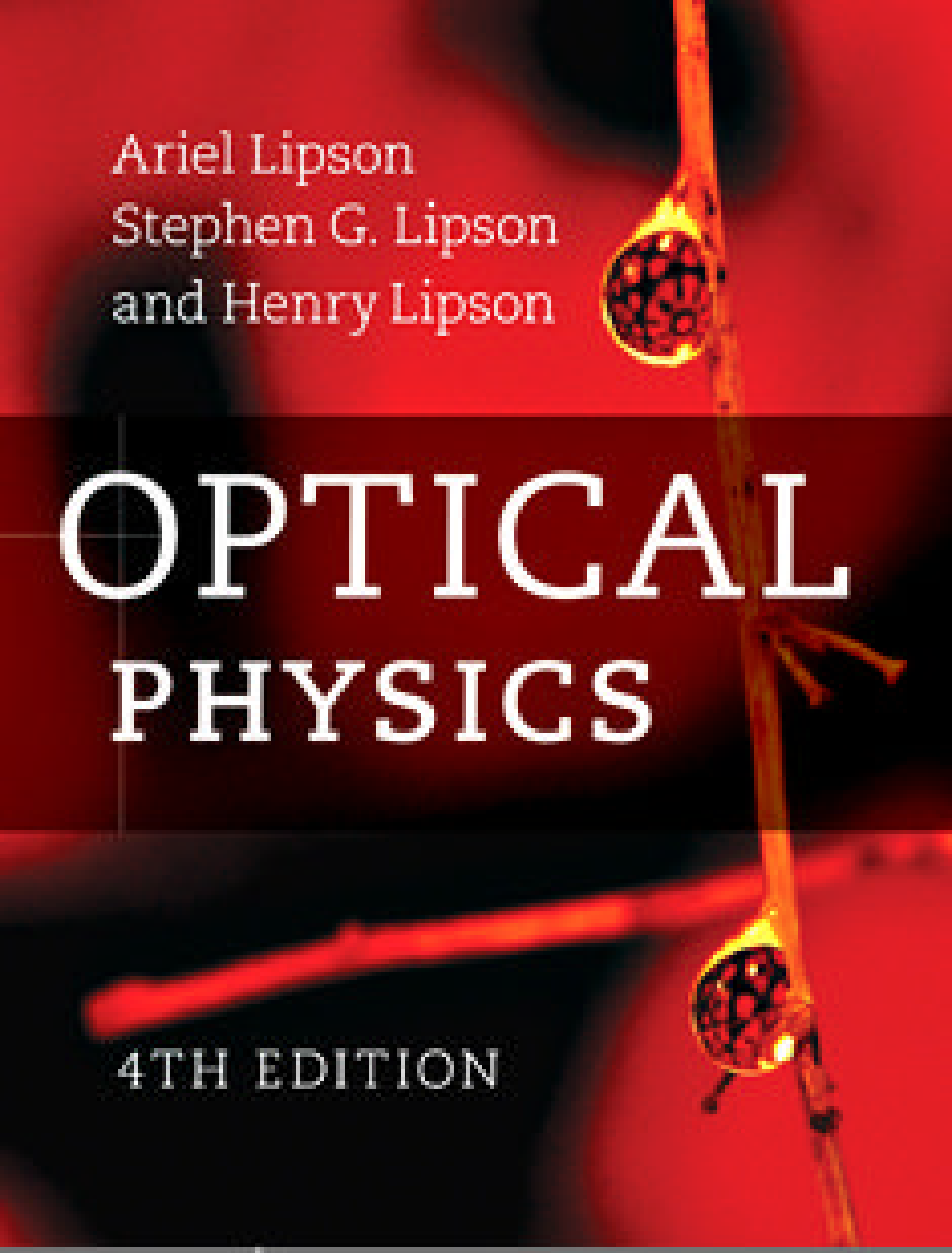

OPTICAL PHYSICS

4TH EDITION

CAMBRIDGE www.cambridge.org/9780521493451

This page intentionally left blank

Optical Physics
Fourth Edition

This fourth edition of a well-established textbook takes students from fundamental ideas to the most modern developments in optics. Illustrated with 400 figures, it contains numerous practical examples, many from student laboratory experiments and lecture demonstrations. Aimed at undergraduate and advanced courses on modern optics, it is ideal for scientists and engineers.

The book covers the principles of geometrical and physical optics, leading into quantum optics, using mainly Fourier transforms and linear algebra. Chapters are supplemented with advanced topics and up-to-date applications, exposing readers to key research themes, including negative refractive index, surface plasmon resonance, phase retrieval in crystal diffraction and the Hubble telescope, photonic crystals, super-resolved imaging in biology, electromagnetically induced transparency, slow light and superluminal propagation, entangled photons and solar energy collectors. Solutions to the problems, simulation programs, key figures and further discussions of several topics are available at www.cambridge.org/Lipson.

Ariel Lipson is Senior Physicist at BrightView Systems Ltd, Israel. He received his Ph.D. from Imperial College, London, and has contributed to three successful start-up companies in optics, which have influenced several of the topics discussed in this book.

Stephen G. Lipson is Professor of Physics and Electro-optics in the Physics Department of the Technion – Israel Institute of Technology, Israel. He holds the El-Op Chair of Electro-optics at Technion, where he has taught courses in optics at both elementary and advanced levels.

Henry Lipson was Professor of Physics at the University of Manchester Institute of Science and Technology, UK. He was a pioneer in the development of optical Fourier transform methods for solving problems in X-ray crystallography.

Optical Physics

Fourth Edition

A. LIPSON
BrightView Systems Ltd, Israel

S. G. LIPSON
Technion – Israel Institute of Technology

H. LIPSON, FRS
Late Professor of Physics
University of Manchester Institute of Science and Technology

CAMBRIDGE
UNIVERSITY PRESS

CAMBRIDGE UNIVERSITY PRESS
Cambridge, New York, Melbourne, Madrid, Cape Town, Singapore,
São Paulo, Delhi, Dubai, Tokyo

Cambridge University Press
The Edinburgh Building, Cambridge CB2 8RU, UK

Published in the United States of America by Cambridge University Press, New York

www.cambridge.org
Information on this title: www.cambridge.org/9780521493451

First published in print format 2010

ISBN-13 978-0-521-49345-1 Hardback

Dedicated to the memory of our parents and grandparents,
Jane Lipson (1910–2009) and Henry Lipson (1910–1991)

Contents

Preface to the fourth edition

We use optics overwhelmingly in our everyday life: in art and sciences, in modern communications and medical technology, to name just a few fields. This is because 90% of the information we receive is visual. The main purpose of this book is to communicate our enthusiasm for optics, as a subject both practical and aesthetic, and standing on a solid theoretical basis.

We were very pleased to be invited by the publishers to update *Optical Physics* for a fourth edition. The first edition appeared in 1969, a decade after the construction of the first lasers, which created a renaissance in optics that is still continuing. That edition was strongly influenced by the work of Henry Lipson (1910–1991), based on the analogy between X-ray crystallography and optical Fraunhofer diffraction in the Fourier transform relationship realized by Max von Laue in the 1930s. The text was illustrated with many photographs taken with the optical diffractometers that Henry and his colleagues built as 'analogue computers' for solving crystallographic problems. Henry wrote much of the first and second editions, and was involved in planning the third edition, but did not live to see its publication. In the later editions, we have continued the tradition of illustrating the principles of physical optics with photographs taken in the laboratory, both by ourselves and by our students, and hope that readers will be encouraged to carry out and further develop these experiments themselves.

We have made every effort to bring this edition up to date, both in terms of its layout and its scientific content. We have introduced several new features. First, starting with Chapter 2, each chapter has a short introduction defining the material that will be covered, with maybe a pictorial example of a significant application, as well as a summary of the main points at the end. In addition there are boxes that describe topics and examples related to the text. Furthermore, we have taken advantage of the margins to include some peripheral notes related to the text, and short remarks to direct the reader to related topics.

For several decades we have used this text for two courses. The first one is a basic second-year course on geometrical and physical optics, given to students who already have an elementary knowledge of electromagnetic theory and an introduction to calculus and linear algebra, which are generally taught in the first year of an undergraduate degree. This first course includes much of Chapters 3 (Geometrical optics), 4 (Fourier theory), 7 (Scalar-wave and Fresnel diffraction), 8 (Fraunhofer diffraction), 11 (Coherence) and 12 (Imaging), with parts of 9 (Interferometry) and 14 (Quantum optics and lasers).

A second advanced course has been built out of Chapters 6 (Crystal optics), 9 (Interferometry), 10 (Optical fibres and multilayers), 13 (Dispersion) and 14 (Quantum optics and lasers), with the more advanced parts of Chapters 8, 11 and 12 and research references. We have included in all the chapters short and not too technical descriptions of many recent developments in the field, either in the boxes or the more extended 'Advanced topic' sections, and hope that lecturers will use these to enliven their presentations and show that optics is a very broad and living subject. The remaining chapters, 1 (History), 2 (Wave propagation), 4 (Fourier theory) and 5 (Electromagnetic waves) contain introductory material, which may or may not have been covered in the prerequisite courses, together with examples of up-to-date applications such as gravitational lensing, spiral waves and negative refractive index materials. To assist lecturers, we shall make many of the figures in the book available on-line in an associated website (www.cambridge.org/Lipson).

We are not mathematicians, and have not indulged in elegant or rigorous mathematics unless they are necessary to underpin physical understanding. On the other hand, we have tried to avoid purely qualitative approaches. The main mathematical tools used are Fourier analysis and linear algebra. It is often claimed that Fraunhofer diffraction and wave propagation are the best ways to learn Fourier methods, and for this reason we devote a full chapter (4) to Fourier methods, including the important concepts of convolution and correlation.

In our efforts to bring the book up to date we have necessarily had to remove some older topics from the previous editions, so as to keep the length similar to the previous edition. Some of these topics will be transferred to the website together with other topics that there was no room to include. The website will also include solutions to the 190 problems at the ends of the chapters, and details of some of the computer programs used in topics such as diffraction, wave propagation and phase retrieval.

We are indebted to our colleagues, students and families for considerable help they have given us in many ways. In particular, David Tannhauser, who was co-author of the third edition, left an indelible mark on the book. Among those who have helped us with discussions of various topics during the preparation of this and the previous editions are: John Baldwin, Eberhart Bodenshatz, Sam Braunstein, Netta Cohen, Arnon Dar, Gary Eden, Michael Elbaum, Yoel Fink, Ofer Firstenberg, Baruch Fischer, Stephen Harris, Rainer Heintzmann, Shahar Hirschfeld, Antoine Labeyrie, Peter Nisenson, Meir Orenstein, Kopel Rabinovitch, Erez Ribak, Amiram Ron, Vassilios Sarafis, David Sayre, Mordechai Segev, Israel Senitzky, John Shakeshaft, Joshua Smith, Michael Woolfson and Eric Yeatman. All these people have our sincere thanks. We are also grateful to Carni Lipson for preparing many of the figures, and to the students who carried out the experiments illustrating many of the topics and are mentioned individually in the figure captions.

We must also thank the many researchers who have given us permission to use some of their most up-to-date research results as illustrations of advanced

topics, and are mentioned in the text. In addition we thank the following publishers and organizations for permission to use copyrighted material:

American Association for the Advancement of Science: Figs. 13.16, 13.17;
American Chemical Society: Fig. 12.39;
American Society for Cell Biology: Fig. 7.17;
Elsevier B.V.: Fig. 10.1;
NASA: Figs. 2.1, 8.35, 8.38;
Nature Publishing Group: Figs. 10.22, 12.1;
U.S. National Academy of Sciences: Figs. 8.39, 12.44;

We are also grateful to John Fowler and Sophie Bulbrook of Cambridge University Press for assistance and advice about the structure and planning of the book.

S.G.L. is indebted to the Materials Science and Engineering Department of the Massachusetts Institute of Technology for hospitality during 2008–9, where much of the work of revision of the book was carried out.

We hope that you will enjoy reading the text as much as we have enjoyed writing it!

Ariel Lipson, Tel Aviv
Stephen G. Lipson, Haifa

Preface from the original edition

There are two sorts of textbooks. On the one hand, there are works of reference to which students can turn for the clarification of some obscure point or for the intimate details of some important experiment. On the other hand, there are explanatory books which deal mainly with principles and which help in the understanding of the first type.

We have tried to produce a textbook of the second sort. It deals essentially with the principles of optics, but wherever possible we have emphasized the relevance of these principles to other branches of physics – hence the rather unusual title. We have omitted descriptions of many of the classical experiments in optics – such as Foucault's determination of the velocity of light – because they are now dealt with excellently in most school textbooks. In addition, we have tried not to duplicate approaches, and since we think that the graphical approach to Fraunhofer interference and diffraction problems is entirely covered by the complex-wave approach, we have not introduced the former.

For these reasons, it will be seen that the book will not serve as an introductory textbook, but we hope that it will be useful to university students at all levels. The earlier chapters are reasonably elementary, and it is hoped that by the time those chapters which involve a knowledge of vector calculus and complex-number theory are reached, the student will have acquired the necessary mathematics.

The use of Fourier series is emphasized; in particular, the Fourier transform – which plays such an important part in so many branches of physics – is treated in considerable detail. In addition, we have given some prominence – both theoretical and experimental – to the operation of convolution, with which we think that every physicist should be conversant.

We would like to thank the considerable number of people who have helped to put this book into shape. Professor C. A. Taylor and Professor A. B. Pippard had considerable influence upon its final shape – perhaps more than they realize. Dr I. G. Edmunds and Mr T. Ashworth have read through the complete text, and it is thanks to them that the inconsistencies are not more numerous than they are. (We cannot believe that they are zero!) Dr G. L. Squires and Mr T. Blaney have given us some helpful advice about particular parts of the book. Mr F. Kirkman and his assistants – Mr A. Pennington and Mr R. McQuade – have shown exemplary patience in producing some of our more exacting photographic illustrations, and in providing beautifully finished

prints for the press. Mr L. Spero gave us considerable help in putting the finishing touches to our manuscript.

And finally we should like to thank the three ladies who produced the final manuscript for the press – Miss M. Allen, Mrs E. Midgley and Mrs K. Beanland. They have shown extreme forbearance in tolerating our last-minute changes, and their ready help has done much to lighten our work.

S. G. L.
H. L.

1 History of ideas

Why should a textbook on physics begin with history? Why not start with what is known now and refrain from all the distractions of out-of-date material? These questions would be justifiable if physics were a complete and finished subject; only the final state would then matter and the process of arrival at this state would be irrelevant. But physics is not such a subject, and optics in particular is very much alive and constantly changing. It is important for the student to study the past as a guide to the future. Much insight into the great minds of the era of classical physics can be found in books by Magie (1935) and Segré (1984).

By studying the past we can sometimes gain some insight – however slight – into the minds and methods of the great physicists. No textbook can, of course, reconstruct completely the workings of these minds, but even to glimpse some of the difficulties that they overcame is worthwhile. What seemed great problems to them may seem trivial to us merely because we now have generations of experience to guide us; or, more likely, we have hidden them by cloaking them with words. For example, to the end of his life Newton found the idea of 'action at a distance' repugnant in spite of the great use that he made of it; we now accept it as natural, but have we come any nearer than Newton to understanding it? It is interesting that the question of 'action at a distance' resurfaced in a different way in 1935 with the concept of 'entangled photons', which will be mentioned in §1.7.2 and discussed further in §14.3.3.

The history of optics is summarized in Fig. 1.1, which shows many of the important discoveries and their interactions, most of which are discussed in the chapters that follow. First, there was the problem of understanding the nature of light; originally the question was whether light consisted of massive corpuscles obeying Newtonian mechanics, or was it a wave motion, and if so in what medium? As the wave nature became clearer, the question of the medium became more urgent, finally to be resolved by Maxwell's electromagnetic theory and Einstein's theory of relativity. But the quantum nature of physics re-aroused the wave–particle controversy in a new form, and today many basic questions are still being asked about the interplay between particle and wave representations of light.

We shall touch on some of these questions, which have been addressed by some very thought-provoking experiments, in Chapter 14.

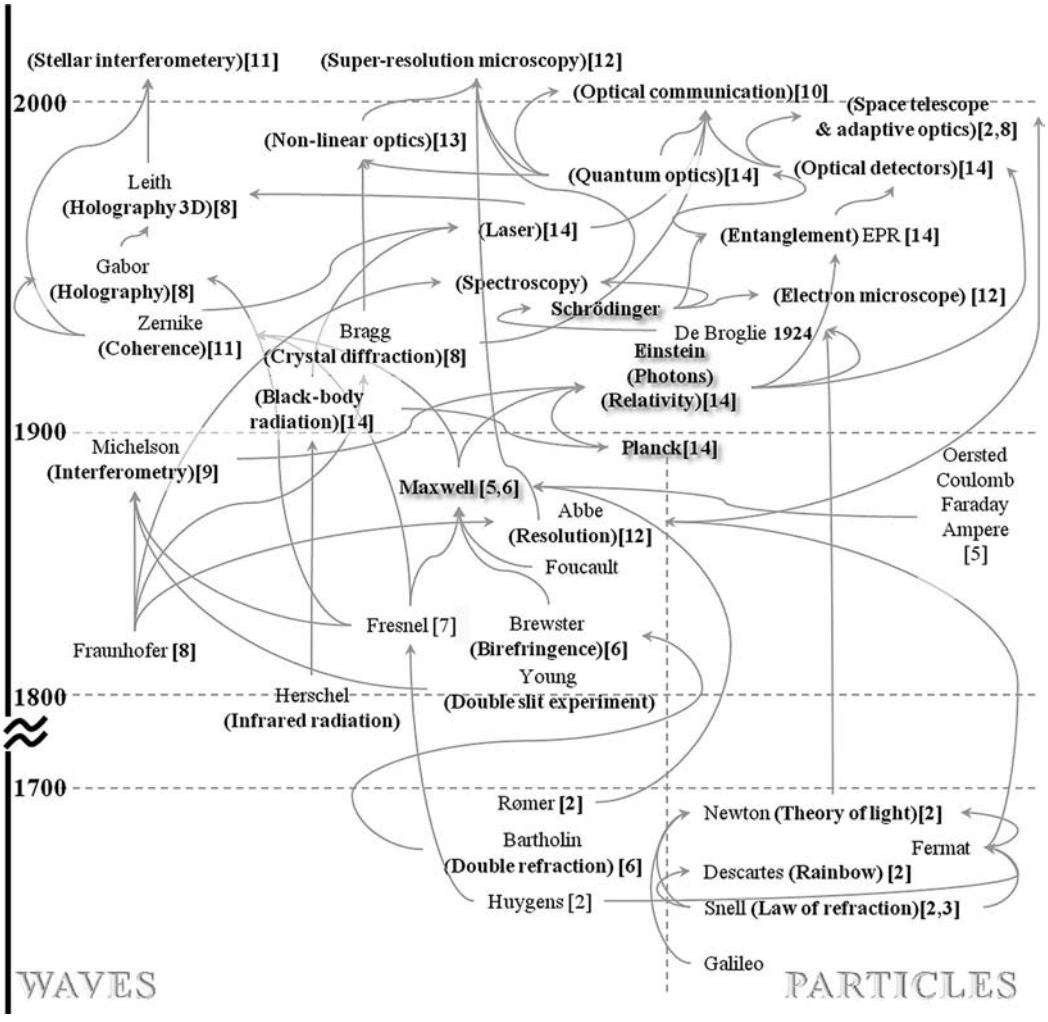

Figure 1.1 The development of optics, showing many of the interactions. Notice that there was little development in the eighteenth century, mainly because of Newton's erroneous idea of light particles. The numbers in square brackets indicate the chapters where the topics are discussed.

A complementary trail follows the applications of optics. Starting with simple refractive imaging devices, well explained by corpuscular considerations, the wave theory became more and more relevant as the design of these instruments improved, and it became clear that bounds to their performance existed. But even the wave theory is not quite adequate to deal with the sensitivity of optical instruments, which is eventually limited by quantum theory. A fuller understanding of this is leading us today towards more sensitive and more accurate measurement and imaging techniques.

1.1 The nature of light

1.1.1 The basic facts

Let us go back to the time of Galileo (1564–1642). What was known about light in the seventeenth century? First of all, it travelled in straight lines and Galileo, who originated the idea of testing theories by experiment, tried unsuccessfully to measure its speed. Second, it was reflected off smooth surfaces and the laws of reflection were known. Third, it changed direction when it passed from one medium to another (refraction, §2.6.2); the laws for this phenomenon were not so obvious, but they were established by Snell (1591–1626) and were later confirmed by Descartes (1596–1650). Fourth, what we now call Fresnel diffraction (§7.2) had been discovered by Grimaldi (1618–63) and by Hooke (1635–1703). Finally, double refraction (§6.5) had been discovered by Bartholinus (1625–98). It was on the basis of these phenomena that a theory of light had to be constructed.

The last two facts were particularly puzzling. Why did shadows reach a limiting sharpness as the size of the source became small, and why did fringes appear on the light side of the shadow of a sharp edge? And why did light passing through a crystal of calcite (see Fig. 1.4) produce two images while light passing through most other transparent materials produced only one?

1.1.2 The wave–corpuscle controversy

Two explanations were put forward: corpuscules and waves, and an acrimonious controversy resulted. Newton (1642–1727) threw his authority behind the theory that light is corpuscular, mainly because his first law of motion said that if no force acts on a particle it will travel in a straight line; he assumed that the velocity of the corpuscles was large enough that gravitational bending would be negligible. Double refraction he explained by some asymmetry in the corpuscles, so that their directions depended upon whether they passed through the crystal forwards or sideways. He envisaged the corpuscles as resembling magnets and the word ‘polarization’ is still used even though this explanation has long been discarded.

Newton did consider gravitational bending of light. He obtained a value a factor of two smaller than later predicted by relativity, but this was not discovered till 1919 (§2.8)!

Diffraction, however, was difficult. Newton realized its importance and was aware of what are now known as Newton’s rings (§9.1.2), and he saw that the fringes formed in red light were separated more than those formed in blue light. He was also puzzled by the fact that light was partly transmitted and partly reflected by a glass surface; how could his corpuscles sometimes go through and sometimes be reflected? He answered this question by propounding the

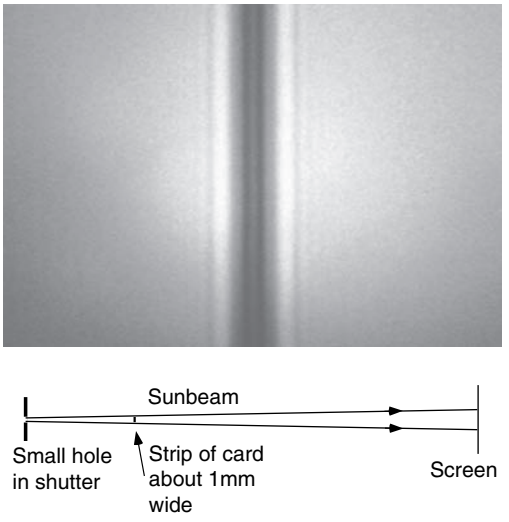

Figure 1.2
Young's interference experiment. In a narrow beam of sunlight he placed a narrow strip of card, about 1 mm in width, to create two separate beams, and then observed on a screen that there were fringes in the region where the two beams overlapped.

idea that they had internal vibrations that caused 'fits of reflexion' and 'fits of transmission'; in a train of corpuscles some would go one way and some the other. He even worked out the lengths of these 'fits' (which came close to what we now know as half the wavelength). But the idea was very cumbersome and was not really satisfying.

His contemporary Huygens (1629–95) was a supporter of the wave theory. With it he could account for diffraction and for the behaviour of two sets of waves in a crystal, without explaining *how* the two sets arose. Both he and Newton thought that light waves, if they existed, must be like sound waves, which are longitudinal. It is surprising that two of the greatest minds in science should have had this blind spot; if they had thought of transverse waves, the difficulties of explaining double refraction would have disappeared.

1.1.3 Triumph of the wave theory

Newton's authority kept the corpuscular theory going until the end of the eighteenth century, but by then ideas were coming forward that could not be suppressed. In 1801 Young (1773–1829) demonstrated interference fringes between waves from two sources (Fig. 1.2) – an experiment so simple to carry out and interpret that the results were incontrovertible. In 1815 Fresnel (1788–1827) worked out the theory of the Grimaldi–Hooke fringes (§7.1) and in 1821 Fraunhofer (1787–1826) invented the diffraction grating and produced diffraction patterns in parallel light for which the theory was much simpler (§9.2). These three men laid the foundation of the wave theory that is still the basis of what is now called physical optics.

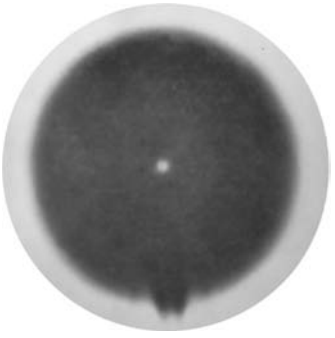

Figure 1.3
Fresnel and Arago's experiment: the bright spot at the centre of the shadow of a disc. The experimental arrangement was similar to that of Young, shown in Fig. 1.2.

The defeat of the corpuscular theory, at least until the days of quantum ideas, came in 1818. In that year, Fresnel wrote a prize essay on the diffraction of light for the French Académie des Sciences on the basis of which Poisson (1781–1840), one of the judges, produced an argument that seemed to invalidate the wave theory by *reductio ad absurdum*. Suppose that a shadow of a perfectly round object is cast by a point source; at the periphery all the waves will be in phase, and therefore the waves should also be in phase at the centre of the shadow, and there should therefore be a bright spot at this point. Absurd! Then Fresnel and Arago (1786–1853) carried out the experiment and found that there really was a bright spot at the centre (Fig. 1.3). The triumph of the wave theory seemed complete.

The Fresnel–Arago experiment is discussed in detail in §7.2.4.

1.2 Speed of light

The methods that Galileo employed to measure the speed of light were far too crude to be successful. In 1678 Römer (1644–1710) realized that an anomaly in the times of successive eclipses of the moons of Jupiter could be accounted for by a finite speed of light, and deduced that it must be about 3×10^8 m s^{-1}. In 1726 Bradley (1693–1762) made the same deduction from observations of the small ellipses that the stars describe in the heavens; since these ellipses have a period of one year they must be associated with the movement of the Earth.

It was not, however, until 1850 that direct measurements were made, by Fizeau (1819–96) and Foucault (1819–68), confirming the estimates obtained by Römer and Bradley. Knowledge of the exact value was an important confirmation of Maxwell's (1831–79) theory of electromagnetic waves (§5.1), which allowed the wave velocity to be calculated from the results of laboratory experiments on static and current electricity. In the hands of Michelson (1852–1931) their methods achieved a high degree of accuracy – about 0.03 per cent. Subsequently much more accurate determinations have been made, and the velocity of light in vacuum has now become one of the fundamental constants of physics, replacing the standard metre.

1.2.1 Refractive index

The idea that refraction occurs because the velocity of light is dependent on the medium dates back to Huygens and Newton. According to the corpuscular theory, the speed of light should be greater in a denser medium than in air because the corpuscles must be attracted towards the denser medium to account for the changed direction of the refracted light. According to the wave theory, the waves must travel more slowly in the medium and 'slew' round to give the new direction (Fig. 2.9). Foucault's method of measurement only required a relatively short path, and the speed of light could therefore be measured directly in media other than air – water, for example. Although the wave theory was by then completely accepted, Foucault provided welcome confirmation that the velocity was indeed smaller in water. A variation on the experiment performed by Fizeau provided a method of investigating the effects of motion of the medium on the velocity of light, because it was possible to carry out the measurements when the water was flowing through the apparatus (§9.4.1). The results could not be explained on the basis of nineteenth century physics of course, but preempted the theory of relativity.

1.3 The nature of light waves: Transverse or longitudinal?

The distinction between transverse and longitudinal waves had been appreciated early in the history of physics; sound waves were found to be longitudinal and water waves were obviously transverse. In the case of light waves, the phenomenon that enabled a decision to be made was that of double refraction in calcite. As we mentioned before, Huygens had pointed out that this property, which is illustrated in Fig. 1.4, means that the orientation of the crystal must somehow be related to some direction in the wave, but he had failed to appreciate the connection with transversality of the waves.

The greatest step towards understanding the waves came from a completely different direction – the theoretical study of magnetism and electricity.

In the first half of the nineteenth century the relationship between magnetism and electricity had been worked out fairly thoroughly, by men such as Oersted (1777–1851), Ampère (1775–1836) and Faraday (1791–1867). In order to visualize his experimental results, Faraday invented around 1851 the concept of 'lines of force', which described the 'action at a distance' that had so worried his predecessors in magnetism, electricity and gravitation. In 1865, Maxwell was inspired to combine his predecessors' observations in mathematical form by describing the region of influence around electric charges and magnets as an

The concept of a 'field', which is widely used today in all areas of physics, was originated by Faraday in this work.

Figure 1.4
Double refraction in a calcite crystal.

'electromagnetic field' and expressing the observations in terms of differential equations. In manipulating these equations he found that they could assume the form of a transverse wave equation (§2.1.1), a result that had already been guessed by Faraday in 1846. The velocity of the wave could be derived from the known magnetic and electric constants, and was found to be equal to the measured velocity of light; thus light was established as an electromagnetic disturbance. A key to Maxwell's success was his invention of the concept of a 'field', which is a continuous function of space and time representing the mutual influence of one body on another, a prolific idea that has dominated the progress of physics ever since then. This began one of the most brilliant episodes in physics, during which different fields and ideas were brought together and related to one another.

1.4 Quantum theory

With the marriage of geometrical optics and wave theory (physical optics) it seemed, up to the end of the nineteenth century, that no further rules about the behaviour of light were necessary. Nevertheless there remained some basic problems, as the study of the light emitted by hot bodies indicated. Why do such bodies become red-hot at about 600 °C and become whiter as the temperature increases? The great physicists such as Kelvin (1824–1907) were well aware of this problem, but it was not until 1900 that Planck (1858–1947) put forward, very tentatively, an ad hoc solution, now known as the quantum theory.

Planck had a hard time defending his doctoral dissertation, in which the idea of quantization was proposed!

Planck's idea (§14.1.1) was that wave energy is divided into packets (quanta), now called photons, whose energy content is proportional to the frequency. The lower frequencies, such as those of red light, are then more easily produced than higher frequencies. The idea was not liked – even Planck himself was

hesitant in proposing it – but gradually scepticism was overcome as more and more experimental evidence in its favour was produced. By about 1920 it was generally accepted, largely on the basis of Einstein's (1879–1955) study of the photo-electric effect (1905) and of Compton's (1892–1962) understanding of energy and momentum conservation in the scattering of X-rays by electrons (1923); even though, in retrospect, neither of these experiments conclusively shows that an electromagnetic wave itself is quantized, but only that it interacts with a material in a quantized way, which might be a property of the material itself. The real proof had to wait for the advent of non-linear optics (§1.7.2).

1.4.1 Wave–particle duality

So it seems that light has both corpuscular properties and wave-like features at the same time. This duality is still difficult to appreciate to those of us who like intuitive physical pictures. The energy of a wave is distributed through space; the energy of a particle would seem to be concentrated in space. A way of understanding duality questions in linear optics is to appreciate that the wave intensity tells us the probability of finding a photon at any given point. The corpuscular features only arise when the wave interacts with a medium, such as a detector, and gives up its energy to it. Thus, any given problem should be solved in terms of wave theory right until the bitter end, where the outcome is detected. However, this interpretation is not sufficient when non-linear phenomena are involved; curious correlations between different photons then arise, defying attempts to make simple interpretations (§14.3).

1.4.2 Corpuscular waves

As usual in physics one idea leads to another, and in 1924 a new idea occurred to de Broglie (1892–1987), based upon the principle of symmetry. Faraday had used this principle in his discovery of electromagnetism; if electricity produces magnetism, does magnetism produce electricity? De Broglie asked, 'If waves are corpuscles, are corpuscles waves?' Within three years his question had been answered. Davisson (1881–1958) and Germer (1896–1971) by ionization methods and G. P. Thomson (1892–1975) by photographic methods, showed that fast-moving electrons could be diffracted by matter similarly to X-rays. Since then other particles such as neutrons, protons and atoms have also been diffracted. Based on these experiments, Schrödinger (1887–1961) in 1928 produced a general wave theory of matter, which has stood the test of time down to atomic dimensions at least.

1.5 Optical instruments

1.5.1 The telescope

Newton apparently did not realize that different types of glass had different degrees of dispersion, so he did not think that an achromatic doublet could be made.

Although single lenses had been known from time immemorial, it was not until the beginning of the seventeenth century that optical instruments as we know them came into being. Lippershey (d. 1619) discovered in 1608, probably accidentally, that two separated lenses, an objective and an eye lens, could produce a clear enlarged image of a distant object (§3.3.2). Galileo seized upon the discovery, made his own telescope, and began to make a series of discoveries – such as Jupiter's moons and Saturn's rings – that completely altered the subject of astronomy. Newton, dissatisfied with the colour defects in the image, invented the reflecting telescope (Fig. 1.5).

Modern telescopes have retained the basic elements of these original designs, but many additional features have made them much more powerful and accurate. In about 1900, Lord Rayleigh (1842–1919) showed that the angular resolution of a telescope is limited by diffraction at its aperture (§12.2.1), so that bigger and bigger telescopes were built in order to produce brighter images and, hopefully, to improve the resolution too. But it appeared that resolution was limited by atmospheric turbulence effects once the aperture diameter exceeded about 15 cm. Both Rayleigh's resolution limit and the atmospheric limitation were first circumvented by Michelson in 1921, who used interference between a pair of small telescope apertures (15 cm diameter) separated by several metres, to achieve resolution equivalent to the separation, and not the telescope aperture (§11.8.1). Later, in 1972, Labeyrie showed how to overcome the atmospheric limitations of a single large-aperture telescope, and for the first time achieved diffraction-limited resolution from the Palomar 2.5 m ground-based telescope by using an image-combination technique called 'speckle interferometry' (§12.7).

The story of how the Hubble telescope was launched with a serious aberration in the primary mirror, and how this was analyzed and corrected *in situ*, is told in §8.9.

Since 1994, superb astronomical images with almost diffraction-limited resolution are being routinely obtained with the Hubble Space Telescope, which has an aperture of 2.4 m and is of course not limited by atmospheric turbulence or transmission. But more recently, ground-based telescopes with apertures up to 10 m diameter use real-time atmospheric correction at infra-red and visible wavelengths, called 'adaptive optics', to produce stellar images that rival those from the space telescope in brightness and resolution.

1.5.2 The microscope

The story of the microscope is different. Its origin is uncertain; many people contributed to its early development. The microscope originated from the

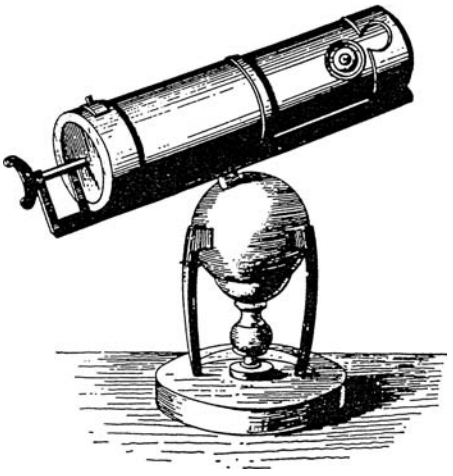

Figure 1.5
Newton's reflecting telescope.

Figure 1.6
Hooke's microscope, from his *Micrographia*.

We suggest you try making your own 'Hooke microscope' using a drop of honey or better, corn syrup, and relive some of Hooke's discoveries.

magnifying glass. In the sixteenth and seventeenth centuries considerable ingenuity was exercised in making high-powered lenses; a drop of water or honey could produce wonderful results in the hands of an enthusiast. Hooke (1635–1703) played perhaps the greatest part in developing the compound microscope which consisted, like the telescope, of an objective and an eye lens (§3.4). Some of his instruments (Fig. 1.6) already showed signs of future trends in design. One can imagine the delight of such an able experimenter in having the privilege of developing a new instrument and of using it to examine for the first time the world of the very small, depicted in his *Micrographia* (1665). Microscope technology improved continuously throughout the years, producing ever clearer images of absorbing objects, but an invention by Zernike (1888–1966)

changed the direction of development. Zernike's invention, the phase-contrast microscope (§12.4.2), for which he received the Nobel prize in 1953, made refractive index variations visible and this allowed in vivo biological observation by eliminating the need for staining. Zernike's invention was the first of a multitude of methods now known as 'spatial filtering' (§12.4) which have made the modern optical microscope a most versatile instrument.

1.5.3 Resolution limit

In order to put the design of optical instruments on a sound basis, the discipline of geometrical optics was founded, based entirely on the concept of rays of light, which trace straight lines in uniform media and are refracted according to Snell's law at boundaries. Based on these concepts, rules were formulated to improve the performance of lenses and mirrors, in particular by skilful figuring of surfaces and by finding ways in which inevitable aberrations would cancel one another.

But the view that progress in optical instruments depended only upon the skill of their makers was suddenly brought to an end by Abbe (1840–1905) in 1873. He showed that the geometrical optical theory – useful though it was in developing optical instruments – was incomplete in that it took no account of the wave properties of light. Geometrically, the main condition that is necessary to produce a perfect image is that the rays from any point in the object should be so refracted that they meet together at a point on the image. Abbe showed that this condition is necessarily only approximate; waves spread because of diffraction and so cannot intersect in a point.

He put forward another interpretation of image formation – that an image is formed by two processes of diffraction (§12.2). As a result, one cannot resolve detail less than about half a wavelength, even with a perfectly corrected instrument. This simple result was greeted by microscopists with disbelief; many of them had already observed detail less than this with good rigidly mounted instruments. Abbe's theory, however, proves that such detail is erroneous; it is a function of the instrument rather than of the object. Improving lenses further is not the only thing needed to improve microscopes.

But in recent decades, Abbe's limit has been significantly superceded, and it appears that the resolution is only limited by the amount of light available (§12.6).

1.5.4 Resolving-power challenge: ultra-violet, soft X-ray and electron microscopy

Any fundamental limitation of this sort should be regarded as a challenge. Until difficulties are clearly exposed no real progress is possible. Now that

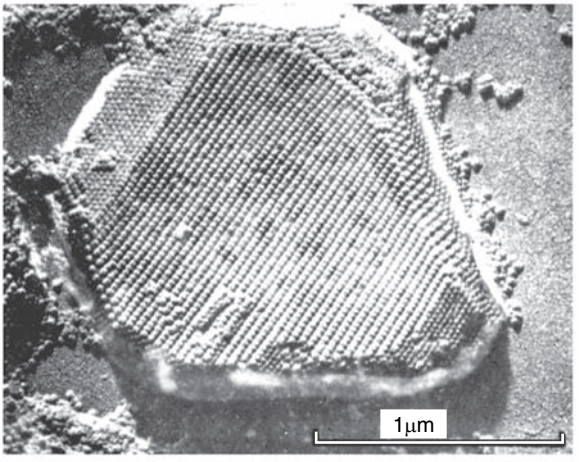

Figure 1.7
Electron microscope image of a virus crystal, magnified 3×10^4, showing resolution of individual molecules. (Courtesy of R. W. G. Wyckoff)

it was known where the limitations of optical instruments lay, it was possible to concentrate upon *them* rather than upon lens design. One obvious way of approaching the problem is to consider new radiations with shorter wavelengths. Ultra-violet light is an obvious choice, and is now widely used in photolithography. Other radiations that have been effective are electron waves and X-rays; these have wavelengths about 10^{-4} of those of visible light and have produced revolutionary results.

The realization that moving particles also have wave properties (§1.4.2) heralded new imaging possibilities. If such particles are charged they can be deflected electrostatically or magnetically, and so refraction can be simulated. It was found that suitably shaped fields could act as lenses so that image formation was possible. Electrons have been used with great success for this work, and electron microscopes with magnetic (or more rarely electrostatic) 'lenses' are available for producing images with very high magnifications. By using accelerating voltages of the order of 10^6 V, wavelengths of less than 0.1 Å can be produced, and thus a comparable limit of resolution should be obtainable. In practice, however, electron lenses are rather crude by optical standards and thus only small apertures are possible, which degrade the resolution. But today, with improvements in electron lenses, images showing atomic and molecular resolution are available, and these have revolutionized fields such as solid-state physics and biology (Fig. 1.7).

Even today, the largest numerical aperture (§12.2) of electron lenses is about 0.04.

1.5.5 X-ray microscopy and diffraction

X-rays were discovered in 1895, but for 17 years no one knew whether they were particles or waves. Then, in 1912, a brilliant idea of von Laue (1879–1960) solved the problem; he envisaged the possibility of using a crystal as

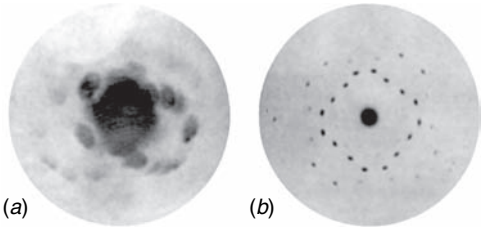

Figure 1.8
X-ray diffraction patterns produced by a crystal. (*a*) Original results obtained by Friedrich and Knipping; (*b*) a clearer picture taken with modern equipment, showing the symmetry of the diffraction pattern. (Ewald (1962))

a (three-dimensional) diffraction grating and the experiment of passing a fine beam of X-rays onto a crystal of copper sulphate (Fig. 1.8) showed definite indications of diffraction, indicating wave-like properties.

The problem in constructing an X-ray microscope is that lenses are not available; the refractive index of all materials in this region of the spectrum is less than unity, but only by an amount of the order of 10^{-5}. However, the wave properties can be used directly, by diffraction, to produce images using a Fresnel zone plate, and this type of microscope has recently been developed (§7.5). But long before such zone-plate 'lenses' became available, a new subject – X-ray crystallography – was born (§8.6). This relies on Abbe's observation that imaging is essentially a double diffraction process. The experiments on crystals showed that the results of the first diffraction process could be recorded on film; the question was, could the second diffraction process be carried out mathematically in order to create the image? The problem that arose was that the film used to record the diffraction pattern only recorded part of the information in the diffracted waves – the intensity. The phase of the waves was lacking. Nothing daunted, generations of physicists and chemists sought ways of solving this problem, and today methods of 'phase retrieval' (§8.8), for which Hauptman and Karle received the Nobel prize in 1985, have made X-ray imaging, at least of crystals, a relatively straightforward process.

1.5.6 Super-resolution

Another approach to the resolution problem was to ask whether there exist ways of getting around the Abbe limit. The first positive answer to this question was given by G. Toraldo di Francia in 1952, who showed that masking the aperture of a microscope lens in a particular manner could, theoretically, result in resolution as high as one could want – at a price: the intensity of the image (§12.6). Although the method he suggested has not been significantly used, it inspired attempts to find other ways around the Abbe limit. Today, several techniques achieve resolutions considerably better than half a wavelength; for example, the near-field optical microscope (NSOM – §12.6.3) and stochastic optical reconstruction microscopy (STORM – §12.6.5) can resolve detail smaller than one-tenth of a wavelength.

1.6 Coherence, holography and aperture synthesis

In 1938 Zernike developed and quantified the idea of coherence, an important concept that related light waves from real sources to the ideal sinusoidal waves of theory (§11.3). The concept of coherence had widespread implications. It could be applied not only to light waves, but also to other types of wave propagation, such as electron waves in metals and superconductors. One of the results was an attempt to improve the resolution of electron microscopy by Gabor, who in 1948 invented an interference technique that he called 'holography', which employed wave coherence to record images without the use of lenses (§12.5.1). The technique could not at the time be implemented in electron microscopy for technical reasons, but implanted an idea that blossomed with the invention of the laser in the 1960s. Gabor was awarded the Nobel prize for holography in 1971. It took till 1980 for holography eventually to be applied to electron microscopy by Tonamura, when sufficiently coherent electron sources became available, albeit not for the original purpose for which Gabor invented it, since in the meantime electron lenses had been sufficiently improved to make it unnecessary for improving resolution.

Electron holography is used today for investigating magnetic structures, which are invisible to electromagnetic waves.

The way in which the idea of coherence inspired further developments illustrates the influence that an elegant theoretical concept can have. It can make a subject so clear that its implications become almost obvious. Michelson's 1921 experiments to measure the diameters of stars by using interference were reinterpreted in terms of Zernike's coherence function and inspired Ryle and Hewish in 1958 to develop 'aperture synthesis' in radio astronomy, where groups of radio telescopes could be connected coherently to give images with angular resolution equivalent to that of a single telescope the size of the greatest distance between them (§11.8). In recent years, aperture synthesis has been extended to the infra-red and visible regions of the spectrum, and several observatories now use groups of separated telescopes, with variable separations up to hundreds of metres, to create images with very high angular resolution (§11.8.4).

1.7 Lasers

In 1960 the laser was invented, and this brought optics back into the limelight after quarter of a century of relative obscurity. Stimulated emission, the basic physical concept that led to the laser, was originally discussed by Einstein as early as 1917, but the idea lay dormant until Purcell and Pound created population inversion in an atomic system in 1950. This achievement independently inspired Townes in the USA and Basov and Prokhorov in the USSR (who

jointly received the Nobel prize in 1964) to suggest a microwave amplifier based on stimulated emission, and led to the first maser, using ammonia (NH_3) gas, which was constructed by Townes in 1954. The extension to light waves took several years, the first ruby laser being constructed by Maiman in 1960. The laser, a non-equilibrium source of radiation, could produce highly coherent radiation with power densities greatly exceeding the limitations that Planck's quantum thermodynamics placed on the brightness of a light source (§14.5). Within an incredibly short period, many brilliant experiments were performed with the new light sources, which allowed things to be done in the laboratory that could previously only be imagined. Prominent amongst these is non-linear optics, pioneered by Bloembergen (§13.6). This is the result of being able to focus high light power into a very small volume of a material, thus creating an electric field comparable with that inside an atom. In the non-linear regime, where the refractive index is a function of light intensity, new types of wave propagation appear; waves can be mixed, new frequencies created and one wave used to control another.

Non-linear frequency doubling is today used in some commonly available items such as green laser-pointers.

1.7.1 Optical communications

The invention of the laser has had enormous technical implications, many of which affect our everyday life and may be the reason that you are reading this book. Married to optical fibres (§10.2), lasers have spawned the field of optical communications, and today modulated light waves carry data streams across the world with very high fidelity at rates in excess of giga-bits per second. At similar rates, tiny semiconductor lasers can write and read data on temporary and permanent storage materials such as hard-discs and CDs.

For realizing that optical fibres could be used for long-distance data transmission, C. Kao received the Nobel prize in 2009.

1.7.2 Non-linear optics and photons

Non-linear processes allow photons to be handled almost individually. This is a field where there are still many open questions, which are still being actively investigated (§14.3). Noteworthy is the concept of 'entangled' photons, which had its origin in a paper by Einstein, Podolsky and Rosen (1935). In single photon processes, measuring the properties of a photon (e.g. its energy or its polarization) is possible only by destroying it. But if two photons are emitted simultaneously by a non-linear process, their properties are correlated; for example the sum of their energies is known, but not their individual values, and the photons must have the same polarization, but its orientation is unknown. Measuring the properties of one photon therefore allows those of the other one to be deduced, while destroying only one of them. Clearly, here we have

an intriguing non-local situation in which two photons are represented by one wave, and the photons may be a long way apart at the time of the measurement of one of them; does this bring us back to Newton's concern about 'action at a distance'? Such thinking is playing a great part in present-day research, and has led to many challenging situations that bode well for the future of optics.

References

Einstein, A., Podolsky, B. and Rosen, N. (1935), Can a quantum-mechanical description of physical reality be considered complete?, *Phys. Rev*. **47**, 777.

Ewald, P. P. (1962), *Fifty Years of X-ray Diffraction*, Utrecht: Oosthoek.

Magie, F. W. (1935), *A Source Book in Physics*, New York: McGraw-Hill.

Segré, E. (1984), *From Falling Bodies to Radio Waves: Classical Physicists and their Discoveries*, New York: Freeman.

2 Waves

Optics is the study of wave propagation and its quantum implications, the latter now being generally called 'photonics'. Traditionally, optics has centred around visible light waves, but the concepts that have developed over the years have been found increasingly useful when applied to many other types of wave, both inside and outside the electromagnetic spectrum. This chapter will first introduce the general concepts of classical wave propagation, and describe how waves are treated mathematically.

However, since there are many examples of wave propagation that are difficult to analyze exactly, several concepts have evolved that allow wave propagation problems to be solved at a more intuitive level. The latter half of the chapter will be devoted to describing these methods, due to Huygens and Fermat, and will be illustrated by examples of their application to wave propagation in scenarios where analytical solutions are very hard to come by. One example, the propagation of light waves passing near a heavy massive body, called 'gravitational lensing' is shown in Fig. 2.1; the figure shows two images of distant sources distorted by such gravitational lenses, taken by the Hubble Space Telescope, compared with experimental laboratory simulations. Although analytical methods do exist for these situations, Huygens' construction makes their solution much easier (§2.8).

A wave is essentially a temporary disturbance in a medium in stable equilibrium. Following the disturbance, the medium returns to equilibrium, and the energy of the disturbance is dissipated in a dynamic manner. The behaviour can be described mathematically in terms of a **wave equation**, which is a differential equation relating the dynamics and statics of small displacements of the medium, and whose solution is a propagating disturbance. The first half of the chapter will be concerned with such equations and their solutions. The term 'displacements of the medium' is not, of course, restricted to mechanical displacement but can be taken to include any field quantity (continuous function of $\mathbf{r}$ and t) that can be used to measure a departure from equilibrium, and the equilibrium state itself may be nothing more than the vacuum – in electromagnetic waves, for example.

The energy of a disturbance may not always be dissipated in what looks like a 'wave-like' manner, but such behaviour can still be derived as the solution of a wave equation.

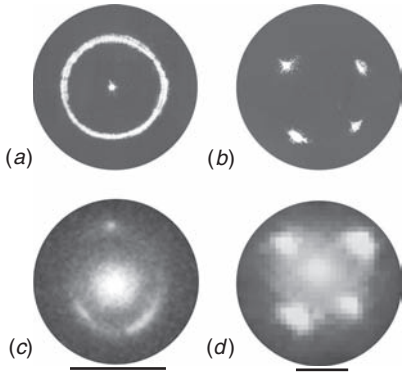

Figure 2.1 **Images formed after light from a point source passes through a gravitational lens: (*a*) imaged in the laboratory through the lens of Fig. 2.14(*d*) on axis, showing the Einstein ring; (*b*) as (*a*), but off-axis (a fifth point, near the centre, is too weak to be seen in the photograph); (*c*) image of the source B1938+666 showing an Einstein ring, diameter 0.95 arcsec, taken with the near infra-red NICMOS camera on the Hubble Space Telescope (King *et al.* (1998)); (*d*) image of the source Q2237+0305, obtained in the near infra-red by the JPL wide-field telescope, showing five distinct images with the same red-shift, 1.695 (Huchra *et al.* (1985); Paczyński and Wambsganss (1993)). The scale bars under (*c*) and (*d*) indicate 1 arcsec. (Telescope photographs courtesy of NASA)**

In this chapter we shall learn:

- what a wave equation is, and how to find its solutions;
- about non-dispersive waves, like electromagnetic waves in vacuum;
- about wave equations leading to dispersive wave solutions;
- what is meant by complex wavenumber, frequency and velocity;
- the difference between phase and group velocities;
- about wave propagation in two and three dimensions;
- some methods for dealing with wave propagation in inhomogeneous media, due to Huygens and Fermat;
- how waves propagate in a dispersive medium, leading to distortion and chirping;
- about gravitational lensing in the cosmos, as an example of Huygens' principle.

2.1 The non-dispersive wave equation in one dimension

Once an equation describing the dynamics of a system has been set up, to call it a wave equation we require it to have propagating solutions. This means

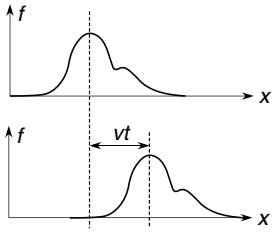

Figure 2.2

An arbitrary disturbance moves at a constant velocity.

that if we supply initial conditions in the form of a disturbance that is centred around some given position at time zero, then we shall find a disturbance of similar type centred around a new position at a later time. The term we used: 'centred around' is sufficiently loose that it does not require the disturbance to be unchanged, but only refers to the position of its centre of gravity. We simply ask for some definition of a centre that can be applied similarly to the initial and later stages, and that shows propagation. This way we can include many interesting phenomena in our definition, and benefit from the generality. But first we shall consider the simplest case, in which the propagating disturbance is indeed unchanged with time.

2.1.1 Differential equation for a non-dispersive wave

The most important elementary wave equation in one dimension can be derived from the requirement that any solution:

1. propagates in either direction ($\pm x$) at a constant velocity v,
2. does not change with time, when referred to a centre which is moving at this velocity. This invariance of the solution with time is what is meant by 'non-dispersive'.

The term 'non-dispersive' also means that the wave velocity is independent of its frequency, as we shall see later.

These are restrictive conditions, but, just the same, they apply to a very large and diverse group of physical phenomena. The resulting wave equation is called the **non-dispersive wave equation**.

We start with the requirement that a solution $f(x,t)$ of the equation must be unchanged if we move the origin a distance $x = \pm vt$ in time t (Fig. 2.2). This gives two equations:

$$f(x,t) = f(x - vt, 0), \tag{2.1}$$

$$f(x,t) = f(x + vt, 0), \tag{2.2}$$

where f can be any continuous function which can be differentiated twice. The argument

$$(x \pm vt) \equiv \phi_{\pm} \tag{2.3}$$

is called the **phase** of the wave.

Differentiating (2.1) by x and t respectively, we have

$$\frac{\partial f}{\partial x} = \frac{\mathrm{d}f}{\mathrm{d}\phi_-}, \quad \frac{\partial f}{\partial t} = -v\frac{\mathrm{d}f}{\mathrm{d}\phi_-} \tag{2.4}$$

and for (2.2)

$$\frac{\partial f}{\partial x} = \frac{\mathrm{d}f}{\mathrm{d}\phi_+}, \quad \frac{\partial f}{\partial t} = v\frac{\mathrm{d}f}{\mathrm{d}\phi_+}. \tag{2.5}$$

Equations (2.4) and (2.5) can be reconciled to a single equation by a second similar differentiation followed by eliminating $\mathrm{d}^2f/\mathrm{d}\phi^2$ between the pairs; either equation gives

$$\frac{\partial^2 f}{\partial x^2} = \frac{\mathrm{d}^2 f}{\mathrm{d}\phi^2}, \quad \frac{\partial^2 f}{\partial t^2} = v^2 \frac{\mathrm{d}^2 f}{\mathrm{d}\phi^2},$$

whence

$$\frac{\partial^2 f}{\partial x^2} = \frac{1}{v^2}\frac{\partial^2 f}{\partial t^2}, \tag{2.6}$$

of which (2.1) and (2.2) are the most general solutions. Equation (2.6) is known as the **non-dispersive wave equation**.

The displacement or wave field f has been assumed above to be a scalar function, but in a three-dimensional world it can also be the component of a vector, and therefore have a direction in space. The direction is called the **polarization** of the wave. Important cases are **longitudinal waves** where f represents a field parallel to the direction of propagation x (e.g. the velocity field in a sound wave) and **transverse waves** where f represents a field normal to the direction of propagation, y or z (e.g. electric and magnetic fields in electromagnetic waves). Often, the displacement includes more than one component, such as surface waves on water or seismic waves (see Box 2.2).

Although (2.6) has general solutions (2.1) and (2.2), there is a particular solution to it that is more important because it satisfies a larger class of equations known generally as **wave equations**. This solution is a **simple-harmonic wave** of **amplitude** a, which we write in its complex exponential form:

$$f(x,t) = a\exp\left[2\pi \mathrm{i}\left(\frac{x}{\lambda} - \nu t\right)\right],$$

where ν is the **frequency** in cycles per unit time and λ is the wavelength. A tidier expression can be written in terms of

$$\text{the } \textbf{spatial frequency} \text{ or } \textbf{wavenumber} \quad k = 2\pi/\lambda,$$
$$\text{the } \textbf{angular frequency} \quad \omega = 2\pi\nu.$$

The latter is just the frequency expressed in units of radians per second, and we shall generally refer to it simply as 'frequency'. These give

$$f(x,t) = a\exp[\mathrm{i}(kx - \omega t)]. \tag{2.7}$$

It is easy to verify that this function satisfies (2.6), and that the velocity is given by

$$v = \omega/k; \tag{2.8}$$

this is known as the **phase velocity** or **wave velocity**.

2.1.2 Harmonic waves and their superposition

In Chapter 4, we shall see how Fourier analysis allows us to calculate the values of a_j for a particular wave.

One particular value of using simple-harmonic waves is that, as we shall see in Chapter 4, any other wave-form can be built up out of these by superposition. Now *if the wave equation is linear in f*, the propagation of a number of simple-harmonic waves superposed can easily be studied by considering the propagation of each of the components separately, and then recombining. In the case of the non-dispersive wave equation this is easy.

Consider an elementary wave with wavenumber k, for which $\omega = kv$:

$$f(x,t) = a\exp[\mathrm{i}(kx - \omega t)] = a\exp(\mathrm{i}\phi). \tag{2.9}$$

Take an initial ($t = 0$) superposition of such waves:

$$g(x,0) = \sum_j f_j(x,0) = \sum_j a_j \exp(\mathrm{i}k_j x). \tag{2.10}$$

At time t, each of the elementary waves has evolved as in (2.9) so:

$$g(x,t) = \sum_j a_j \exp[\mathrm{i}(k_j x - \omega_j t)] \tag{2.11}$$

$$= \sum_j a_j \exp[\mathrm{i}k_j(x - vt)] \tag{2.12}$$

$$= g(x - vt, 0). \tag{2.13}$$

In words, the initial function $g(x,0)$ has propagated with no change at velocity v; (2.13) is equivalent to (2.1). It is important to realize that this simple result arose because of the substitution of kv for ω in (2.11). If different frequencies travel at different velocities (a **dispersive** wave) our conclusions will be modified (§2.7).

2.1.3 Example of a non-dispersive wave

Sound waves in air are compressional waves, for which the value of K is proportional to the air pressure.

To illustrate the non-dispersive one-dimensional wave equation we shall consider a compressional wave in a continuous medium, a fluid. If the fluid has compressibility K and density ρ, the equilibrium-state equation is Hooke's law:

$$P = K\frac{\partial \eta}{\partial x}, \tag{2.14}$$

where P is the local pressure, i.e. the stress, and η the local displacement from equilibrium. The differential $\partial\eta/\partial x$ is thus the strain. A dynamic equation

relates the deviation from the equilibrium state (uniform and constant P) to the local acceleration:

$$\rho \frac{\partial^2 \eta}{\partial t^2} = \frac{\partial P}{\partial x}. \tag{2.15}$$

Equations (2.14) and (2.15) lead to a wave equation

$$\frac{\partial^2 \eta}{\partial x^2} = \frac{\rho}{K} \frac{\partial^2 \eta}{\partial t^2}. \tag{2.16}$$

Thus the waves are non-dispersive, with wave velocity

$$v = \left(\frac{K}{\rho} \right)^{\frac{1}{2}}. \tag{2.17}$$

The wave equation (2.16) is valid provided that the stress–strain relationship (2.14) remains linear, i.e. for small stress. It would not describe shock waves, for example, for which the stress exceeds the elastic limit. Another example of a non-dispersive wave equation is that derived by Maxwell for electromagnetic waves, which will be discussed in depth in Chapter 5.

2.1.4 Energy density in a wave

Since a wave represents a deviation from the equilibrium state, it must add an additional energy to the system. This can usually be best represented as an energy density, which is energy per unit length, area or volume, depending on the dimensionality of the system. In the compressional wave discussed above, the energy is partly kinetic and partly potential, and at any particular point oscillates between the two. The kinetic energy per unit volume is $\frac{1}{2}\rho(\partial\eta/\partial t)^2$ and the potential energy per unit volume is stress times strain which is $\frac{1}{2}K(\partial\eta/\partial x)^2$. For the sinusoidal wave $\eta = a\exp[\mathrm{i}\omega(t - x/v)]$ it immediately follows that the average kinetic and potential energy densities are equal, and their sum is $a^2\omega^2\rho$. This illustrates a general principle that the **energy density is proportional to the squares of the amplitude and frequency**. The energy density multiplied by the wave velocity is then the rate at which the wave transfers energy, or loosely, its **intensity**.

2.2 Dispersive waves in a linear medium: The dispersion equation

In general, wave equations are not restricted to second derivatives in x and t. Provided that the equation remains linear in f, derivatives of other orders can occur; in all such cases, a solution of the form $f = a\exp[\mathrm{i}(kx - \omega t)]$ is found.

Box 2.1 Waves on a guitar string: example of a non-dispersive wave

Like the compression wave of §2.1.3, transverse waves on a guitar string also obey a non-dispersive wave equation. The transverse string displacement $f(x,t)$ has to satisfy boundary conditions $f(0,t) = f(L,t) = 0$ at the two ends, $x = 0$ and $x = L$. The waves that satisfy these conditions are the **harmonics**, $f_m(x,t) = a_m \sin(m\pi x/L)\exp(\mathrm{i}m\omega_1 t)$, which are all solutions of the non-dispersive wave equation (2.6). These waves are called **standing waves**, and each one is the sum of two identical travelling waves with the same frequency, going in opposite directions (2.2). But when a guitar string is plucked, in the centre, for example, the wave-form is not sinusoidal, but rather a triangular wave (Fig. 2.3). This can be expressed, as in §4.1.2, as the sum of harmonics; the amplitudes of the various harmonics, which are necessary to express this shape, are what gives the guitar its characteristic tone.

Naively, one might expect that the triangular wave would retain its shape and oscillate to and fro, but in fact the result is quite different; it goes through a series of trapezoidal shapes, which are shown in the figure and are confirmed by flash photography. This happens because, since the wave equation for the guitar string is non-dispersive, not only do sinusoidal waves propagate unchanged but so does *any wave-form* – in particular, the triangular wave itself. Then we can express the initial triangular deformation at $t = 0$ as the sum of two triangular waves propagating at the phase velocity, each having half the amplitude, one in the $+x$ direction and one in the $-x$ direction. Their sum at $x = 0$ and $x = L$ is zero at all times, and it is easy to see that at non-zero time they together form a trapezoidal wave just like that observed in the experiments (Fig. 2.3). Of course, the same result can be obtained by harmonic analysis; this is left as a problem (2.9).

For such a wave one can replace $\partial f/\partial t$ by $-\mathrm{i}\,\omega f$ and $\partial f/\partial x$ by $\mathrm{i}\,kf$, so that if the wave equation can be written

$$p\left(\frac{\partial}{\partial x}, \frac{\partial}{\partial t}\right) f = 0, \tag{2.18}$$

where p is a polynomial function of $\partial/\partial x$ and $\partial/\partial t$, which operates on f, the result will be an equation

$$p(\mathrm{i}k, -\mathrm{i}\omega) = 0, \tag{2.19}$$

which is called the **dispersion equation**.

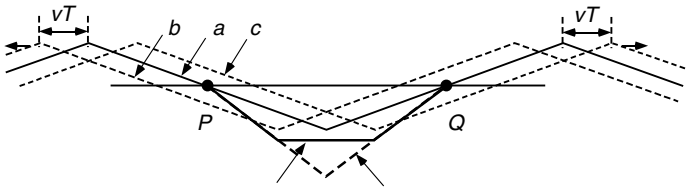

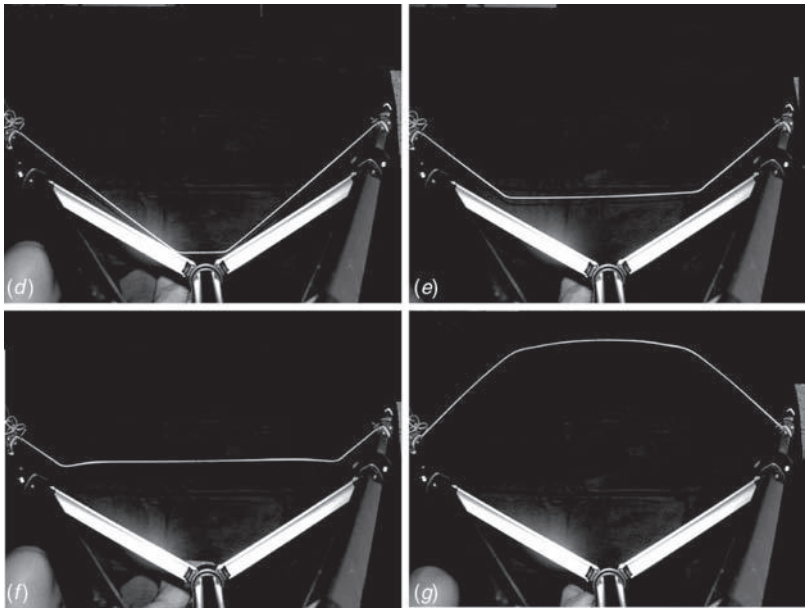

Figure 2.3

Profile of an oscillating guitar string, plucked in the centre. Above, the initial wave-form is represented as the sum of two triangular waves (*a*), travelling in opposite directions (*b*, *c*). After time *T*, their sum is shown as the unbroken line. Note that the sum is always zero at *P* and *Q*. (*d*–*g*) Flash photographs in an experiment confirming the trapezoidal evolution of the wave-form. (Courtesy of E. Raz, Israel Physics Olympiad)

For example, we shall first return to the non-dispersive equation (2.6) and see it in this light. We had

$$\frac{\partial^2 f}{\partial x^2} = \frac{1}{v^2}\frac{\partial^2 f}{\partial t^2}, \tag{2.20}$$

which can be written

$$\left[\left(\frac{\partial}{\partial x}\right)^2 - \frac{1}{v^2}\left(\frac{\partial}{\partial t}\right)^2\right] f = 0. \tag{2.21}$$

Thus, from (2.18) and (2.19):

$$(\mathrm{i}k)^2 - \frac{1}{v^2}(-\mathrm{i}\omega)^2 = 0 = \frac{\omega^2}{v^2} - k^2, \tag{2.22}$$

implying

$$\omega/k = \pm v. \tag{2.23}$$

Box 2.2 Seismic waves as examples of transverse and longitudinal waves

Seismic waves are a nice example of several types of waves travelling through the same medium with different wave and group velocities. There are two types of body waves, which travel in the bulk of the Earth with different polarizations, and another two surface waves, which travel on the interface between the Earth and the atmosphere. The bulk waves are longitudinal (P) or transverse (S), the former travelling at about 5 km/s depending on the constitution of the Earth's crust and the latter at about half this speed.

The two surface waves are called Rayleigh and Love waves. They are transverse and dispersive; Rayleigh waves being normal to the surface and Love waves parallel to it. They are much lower in frequency than the bulk waves and have less damping, and Rayleigh waves in particular have large amplitudes and create substantial damage. Modern seismographs use the fact that the waves have different velocities. The P wave can be used as a warning that the destructive Rayleigh wave is on its way, and comparison of the arrival times determines the epicentre of the earthquake. Since the Earth's constitution is not uniform, propagation of the P and S waves has to be solved using Huygens' principle. This has provided much information about the Earth's inner structure, such as the fact that it has liquid and solid cores. Seismic waves caused by man-made explosions are used to map the Earth accurately, mainly for mineral and oil exploration.

2.2.1 Example of a dispersive wave equation: Schrödinger's equation

Schrödinger originally suggested that this equation would represent particle motion because its dispersion relation corresponds to Newtonian mechanics when the experimentally demonstrated wave–particle equivalence is assumed.

A dispersive wave equation that rivals Maxwell's electromagnetic wave equation in its importance is Schrödinger's wave equation for a non-relativistic particle of mass m, moving in a potential field V, which we quote here in its one-dimensional form:

$$\mathrm{i}\hbar\frac{\partial\psi}{\partial t} = \frac{-\hbar^2}{2m}\cdot\frac{\partial^2\psi}{\partial x^2} + V(x)\psi. \tag{2.24}$$

Here $|\psi|^2\delta x$ is the probability of finding the particle in the region between x and $x+\delta x$, and ψ is called the **probability amplitude** or simply **wave-function**. Using (2.18) and (2.19) we can immediately write down the dispersion equation as

$$\mathrm{i}\hbar(-\mathrm{i}\omega) = \frac{-\hbar^2}{2m}\cdot(\mathrm{i}k)^2 + V(x), \tag{2.25}$$

$$\hbar\omega = \frac{(\hbar k)^2}{2m} + V(x). \tag{2.26}$$

We identify $\hbar\omega$ as the total energy E of the particle (Planck: $\hbar\omega = h\nu$) and $\hbar k$ as its momentum, $p = mv$ (de Broglie: $\hbar k = h/\lambda$). Thus, (2.26) becomes

$$E = \frac{p^2}{2m} + V(x) = \frac{1}{2}mv^2 + V(x) \tag{2.27}$$

or total energy = kinetic energy + potential energy. In this case the dispersion equation expresses the Newtonian mechanics, while the wave equation is the quantum-mechanical equivalent.

2.3 Complex wavenumber, frequency and velocity

Solution of a dispersion equation such as (2.26) may give rise to complex values for k or ω, and it is important to give a physical interpretation to such cases. The velocity ω/k may also be complex as a result.

Complex wavenumbers are important in optics when discussing propagation in absorbing media, such as metals.

2.3.1 Complex wavenumber: attenuated waves

Suppose that the frequency ω is real, but the dispersion relation then leads us to a complex value of $k \equiv k_1 + \mathrm{i}k_2$. We then have

$$\begin{aligned} f &= a\exp[\mathrm{i}(k_1 + \mathrm{i}k_2)x - \mathrm{i}\omega t] \\ &= a\exp(-k_2 x)\exp[\mathrm{i}(k_1 x - \omega t)]. \end{aligned} \tag{2.28}$$

This describes a propagating wave, with velocity $v = \omega/k_1$, attenuated progressively by the factor $\exp(-k_2 x)$. Thus its amplitude decays by a factor e^{-1} in every **characteristic decay distance** of length k_2^{-1} (Fig. 2.4).

2.3.2 Imaginary velocity: evanescent waves

Sometimes the wavenumber turns out to be purely imaginary ($k_1 = 0$). Now, in (2.28) the wave clearly has no harmonic space dependence at all; it is a purely exponential function of x, but still oscillates in time with frequency ω (Fig. 2.5). It is then called an **evanescent wave**. We shall meet evanescent electromagnetic waves in §5.5.

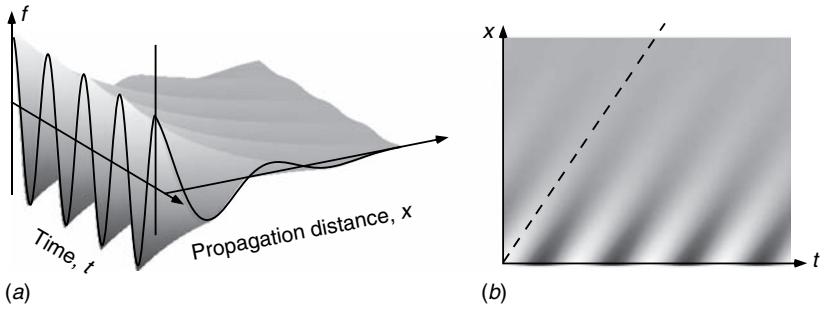

Figure 2.4

(*a*) An attenuated harmonic wave exhibited as a function of *x* and *t*; (*b*) shows the projection on the *x*, *t* plane. The broken line emphasizes a wave crest; it travels at the phase velocity, which is the gradient of this line, x/t.

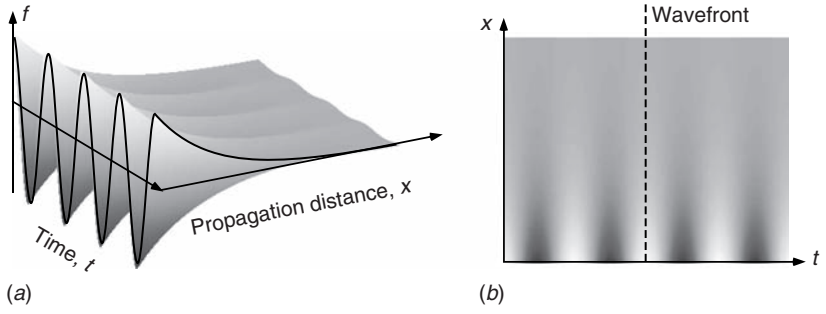

Figure 2.5

(*a*) An evanescent wave exhibited as a function of *x* and *t*; (*b*) shows the projection on the *x*, *t* plane. Comparing this with Fig. 2.4 shows the phase velocity to be infinite! This topic will be expanded in §13.5.2.

2.3.3 Example: attenuated and evanescent wave solutions of the diffusion equation

It was solving this equation for arbitrary boundary conditions that led to the invention of what are now known as 'Fourier series' (Chapter 4). Fourier methods are the foundation of much of the optics discussed in this book.

The diffusion equation can be considered as a wave equation, although it has many commonly known solutions that are not wave-like. This wave equation in one dimension arises from the heat conduction equation along, for example, a bar with negligible heat losses from its surfaces,

$$q = -\kappa\ \partial\theta/\partial x, \tag{2.29}$$

which relates heat flux q per unit area to temperature θ in a medium with thermal conductivity κ and specific heat s per unit volume. Conservation of heat then requires

$$s\ \partial\theta/\partial t = -\partial q/\partial x, \tag{2.30}$$

whence we have the **diffusion equation**

$$\frac{\partial\theta}{\partial t} = D\frac{\partial^2\theta}{\partial x^2}, \tag{2.31}$$

where the diffusion constant $D = \kappa/s$. The dispersion relation (2.19) is thus

$$\mathrm{i}\omega = -Dk^2, \tag{2.32}$$

giving, for real ω,

$$k = \left(\frac{\omega}{2D}\right)^{\frac{1}{2}} (1 + \mathrm{i}). \tag{2.33}$$

If one end of the bar is subjected to alternating heating and cooling so that its temperature rise above ambient θ can be written as

$$\theta(0, t) = \theta_0 \exp(-\mathrm{i}\omega t), \tag{2.34}$$

the wave is propagated along the bar in the form

$$\begin{aligned}\theta(x, t) &= \theta_0 \exp\left\{\mathrm{i}\left[\left(\frac{\omega}{2D}\right)^{\frac{1}{2}} (1 + \mathrm{i})x - \omega t\right]\right\} \\ &= \theta_0 \exp\left[-\left(\frac{\omega}{2D}\right)^{\frac{1}{2}} x\right] \exp\left\{\mathrm{i}\left[\left(\frac{\omega}{2D}\right)^{\frac{1}{2}} x - \omega t\right]\right\}.\end{aligned} \tag{2.35}$$

This wave is attenuated along the bar with characteristic decay distance $(2D/\omega)^{\frac{1}{2}}$. The propagated disturbance is still a wave, however; the phase of oscillation progresses regularly with x.

Now suppose that the same bar has an initial temperature distribution

$$\theta = \theta_0 \exp(\mathrm{i}kx) \quad (k \text{ real}) \tag{2.36}$$

impressed upon it at time $t = 0$, and the temperature distribution is left to its own devices. From (2.35), we write the subsequent temperature distribution

$$\begin{aligned}\theta(x, t) &= \theta_0 \exp[\mathrm{i}(kx - \omega t)] \\ &= \theta_0 \exp[-(Dk^2 t)] \exp(\mathrm{i}kx).\end{aligned} \tag{2.37}$$

There is no oscillatory time dependence; the spatial dependence $\exp(\mathrm{i}kx)$ remains unchanged, but its amplitude decays to zero with time-constant $(Dk^2)^{-1}$. This is a wave evanescent in time. Thus the heat-diffusion equation illustrates both types of behaviour; **it supports a wave attenuated in distance for a real frequency, or evanescent in time for a real wavelength**.

2.4 Group velocity

Details of the analysis of a wave-group into sinusoidal components are given in §4.7, but are not needed to follow the argument here.

The non-dispersive wave equation (2.6) has the property that disturbances of all frequencies travel with the same velocity. The result, according to §2.1.2, is that a wave of any form propagates undistorted. On the other hand, in many **dispersive** media we find that:

- Waves of different frequencies propagate with different velocities.
- The form of the wave becomes distorted as it progresses.

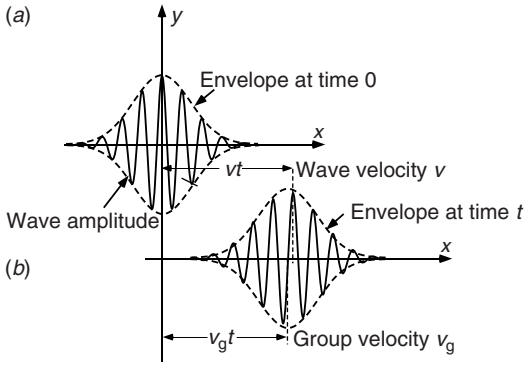

Figure 2.6

A wave-group. The wave amplitude can be described as a sinusoidal wave with its amplitude modulated by an envelope function. To illustrate wave and group velocity, the group is shown above at time $t = 0$ and below at time t. During the time t, the sinusoidal wave peak has travelled distance vt and the envelope has travelled $v_g t$.

Let us suppose that we have a **wave-group**, which is a wave of given ω_0 and k_0 whose amplitude is modulated so that it is limited to a restricted region of space at time $t = 0$ (Fig. 2.6(a)).

It is clear that all the energy associated with the wave is concentrated in the region where its amplitude is non-zero. Such a wave can be built up by superposition of many component waves whose frequencies are approximately ω_0 and spatial frequencies approximately k_0. Methods for calculating their amplitudes will be discussed in Chapter 4; we do not need them explicitly here. At a given time, the maximum value of the wave-group envelope occurs at the point where all the component waves have approximately the same phase, and thus reinforce one another. We shall now show that this point travels at the **group velocity**, a well-defined but different velocity from that of the individual waves themselves; this is also the velocity at which energy is transported by the wave.

The maximum of the envelope must correspond to the point at which the phases of the largest components are equal; then

$$\frac{\mathrm{d}\phi}{\mathrm{d}k} = \frac{\mathrm{d}}{\mathrm{d}k}(kx - \omega t) = x - t\frac{\mathrm{d}\omega}{\mathrm{d}k} = 0 \tag{2.38}$$

at that point. The velocity at which the maximum moves is then given by

$$v_\mathrm{g} = \frac{x}{t} = \frac{\mathrm{d}\omega}{\mathrm{d}k}, \tag{2.39}$$

which is the basic expression for the group velocity. It can be reformulated in several ways in terms of $\lambda = 2\pi/k$, $\omega/k = v$ and $\nu = \omega/2\pi$, such as

$$v_\mathrm{g} = v - \lambda\ \mathrm{d}v/\mathrm{d}\lambda. \tag{2.40}$$

In general, of course, $\mathrm{d}\omega/\mathrm{d}k$ is not a constant. Since the wave-group consists of components around k_0, the value of $\mathrm{d}\omega/\mathrm{d}k$ or $\mathrm{d}v/\mathrm{d}\lambda$ evaluated at k_0 is

There has recently been a lot of interest in **slow light** (§13.5), which is an example where the group and wave velocity differ by many orders of magnitude.

implied. To a first approximation the envelope of the wave-group propagates at this velocity with little change if the wave-group is not too short. But when the phase velocity v is not equal to v_g, the individual waves can be seen to move relative to the envelope in either a forward or backward direction (Fig. 2.6(b)). Such a behaviour can easily be observed in water waves (Problem 2.4), since these waves have quite strong dispersion.

The wave-form is usually distorted with propagation. In §2.7 we shall analyze an illustrative example of this. Very strong dispersion makes the subject quite complicated and can lead to apparently paradoxical situations in which v_g is greater than the velocity of light (§13.5; Brillouin (1960)).

2.5 Waves in three dimensions

The reader might consider it a trivial exercise to repeat in three dimensions the analysis in §2.1.1 in which we derived the non-dispersive wave equation in one dimension; but it is not! The reason is that, even in a non-dispersive medium, a three-dimensional wave in general changes its profile as it propagates. Consider, for example, the spherical acoustic waves emanating from a source in air (which is a good non-dispersive acoustic medium at audible frequencies). As we go further from the source the sound intensity weakens as r^{-2}, so the amplitude of the disturbance is obviously changing with distance.

There is, however, one important type of wave that can propagate in three dimensions without change. This is the **plane wave**.

2.5.1 Plane waves

Plane waves are the basic building-blocks for almost all types of wave propagation, such as diffraction (Chapter 8).

A plane wave that propagates at velocity v in a direction described by the unit vector $\hat{\mathbf{n}}$ has the general form equivalent to (2.1):

$$f(\mathbf{r},t) = f(\mathbf{r}\cdot\hat{\mathbf{n}} - vt, 0). \tag{2.41}$$

As in (2.3), the phase ϕ is then

$$\phi = \mathbf{r}\cdot\hat{\mathbf{n}} - vt = xn_x + yn_y + zn_z - vt. \tag{2.42}$$

This is a constant on any plane satisfying $\mathbf{r}\cdot\hat{\mathbf{n}} - vt = \text{const}$. Such a plane is called a **wavefront** and is a plane of constant phase normal to the direction of propagation $\hat{\mathbf{n}}$ (Fig. 2.7).

2.5.2 Wave equation in three dimensions

On this basis we can derive the wave equation. We have (2.41)

$$f(\mathbf{r},t) = f(\mathbf{r}\cdot\hat{\mathbf{n}} - vt, 0) = f(\phi). \tag{2.43}$$

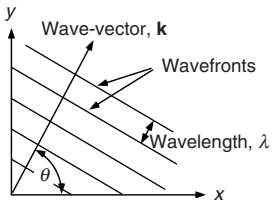

Figure 2.7

A plane wave with wave-vector k normal to the wavefronts.

For this function, the time and spatial derivatives are

$$\partial/\partial t = -v\,\mathrm{d}/\mathrm{d}\phi, \tag{2.44}$$

$$\nabla \equiv \left(\frac{\partial}{\partial x}, \frac{\partial}{\partial y}, \frac{\partial}{\partial z}\right) = \left(\frac{\partial \phi}{\partial x}, \frac{\partial \phi}{\partial y}, \frac{\partial \phi}{\partial z}\right)\frac{\mathrm{d}}{\mathrm{d}\phi} = \hat{\mathbf{n}}\frac{\mathrm{d}}{\mathrm{d}\phi}, \tag{2.45}$$

where (2.42) has been used to calculate $\partial\phi/\partial x$ etc. Thus, from (2.43)

$$\frac{\partial^2 f}{\partial t^2} = v^2\frac{\mathrm{d}^2 f}{\mathrm{d}\phi^2} \tag{2.46}$$

and from (2.45)

$$\nabla \cdot (\nabla f) = (\hat{\mathbf{n}} \cdot \hat{\mathbf{n}})\frac{\mathrm{d}^2 f}{\mathrm{d}\phi^2} = \frac{\mathrm{d}^2 f}{\mathrm{d}\phi^2}, \tag{2.47}$$

whence

$$\nabla \cdot \nabla f \equiv \nabla^2 f = \frac{\partial^2 f}{\partial x^2} + \frac{\partial^2 f}{\partial y^2} + \frac{\partial^2 f}{\partial z^2} = \frac{1}{v^2}\frac{\partial^2 f}{\partial t^2}. \tag{2.48}$$

So far, f has been considered as a scalar, but the same analysis can be repeated for each component of a vector field, giving

$$\nabla^2 \mathbf{f} = \frac{1}{v^2}\frac{\partial^2 \mathbf{f}}{\partial t^2}. \tag{2.49}$$

This is the **three-dimensional non-dispersive wave equation**.

Following (2.7), a harmonic plane wave can be constructed by replacing **f** by $\mathbf{a}\exp[\mathrm{i}(\mathbf{k}\cdot\mathbf{r} - \omega t)]$. The phase is

$$\phi = \mathbf{k}\cdot\mathbf{r} - \omega t = k\left(\frac{\mathbf{k}}{k}\cdot\mathbf{r} - \frac{\omega}{k}t\right) = k\left(\frac{\mathbf{k}}{k}\cdot\mathbf{r} - vt\right), \tag{2.50}$$

from which it follows, using (2.42), that $\hat{\mathbf{n}} = \mathbf{k}/k$, which is the unit vector in the direction **k**. The wavefront is therefore **normal to the direction of propagation k**. The magnitude of **k** is $k = 2\pi/\lambda$, as in (2.7). Because of this relationship, λ is not a vector, even though it has both magnitude and direction, because its components do not combine in the prescribed manner.

Dispersion equations in three dimensions are derived in a similar manner to those in one dimension, by using the substitutions $\nabla = \mathrm{i}\mathbf{k}$, $\partial/\partial t = -\mathrm{i}\omega$. This will give, in general, a vector equation of the form $p(\mathrm{i}\mathbf{k}, -\mathrm{i}\omega) = 0$ (compare to (2.19)).

2.5.3 Spherical and cylindrical waves

Other possible waves in three dimensions are the **spherical wave**, for which the wavefronts are spheres, and the **cylindrical wave**, for which the wavefronts are cylinders. These are very intuitive wave-forms, because they are typical of surface waves on water. A converging spherical wave also represents a wave

being focused to a point. Unfortunately, purely spherical and cylindrical waves are exact solutions of a wave equation only in the limit $r \to \infty$.

For the spherical wave radiated by a source at $r = 0$, we postulate a scalar amplitude:

$$f(\mathbf{r}, t) = A(\mathbf{r}) \exp[\mathrm{i}(kr - \omega t)]. \tag{2.51}$$

Here we will assume that $A \equiv A(r)$ is a function of the radius r alone; problems where A is also a function of the angle will be discussed in §5.3, radiation, and §7.3, Gaussian beams. The total power transmitted by the wave is the energy density multiplied by the velocity, and integrated over the whole wavefront. The latter is a sphere with radius r and area $4\pi r^2$, and so from §2.1.4, the power is $4\pi r^2 A^2(r)\omega^2 \rho v$. For energy to be conserved, this must be a constant, and so

$$A(r) = a_0/r, \tag{2.52}$$

Note that if $A(r) = a_0/r$, the wave phase should jump by π on going through the origin (a focus). This is the 'Gouy effect'; see §7.3.

where a_0 indicates the amplitude of the source. The radial dependence of the intensity $A^2 \sim r^{-2}$ is known as the **inverse square law**. This is true only at large distances $r \gg \lambda$, since there is obviously a singularity at $r = 0$. In this book, the scalar spherical wave will be an important starting point in our discussion of diffraction, §7.1.

The treatment of a cylindrical wave, emanating isotropically from a line source, is similar. Then

$$f(\mathbf{r}, t) = A(r) \exp\left\{\mathrm{i}\left[k(x^2 + y^2)^{\frac{1}{2}} - \omega t\right]\right\}. \tag{2.53}$$

Energy conservation then requires $A(r) = a_0/\sqrt{r}$ and $A^2 \sim r^{-1}$.

2.6 Waves in inhomogeneous media

Propagation of a simple-harmonic wave in a homogeneous medium is a relatively straightforward matter, but when the medium is inhomogeneous, problems arise that often defy analytical treatment. Two important principles, developed by Huygens and Fermat, go a long way to simplifying the physics of such situations. Although we shall illustrate these principles using optical examples, they are equally applicable to any type of wave propagation.

2.6.1 Huygens' construction

As we have seen, Huygens was a staunch advocate of the wave theory and introduced several ideas that have stood the test of time. One of these was the wavefront, which we have already described as a surface of constant phase (§2.5.1). Huygens considered the wave more as a transient phenomenon, which

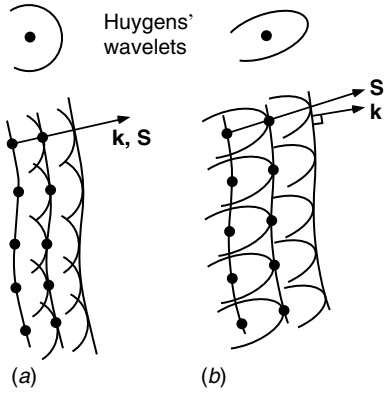

Figure 2.8
Huygens' construction: (*a*) in an isotropic medium, (*b*) in an anisotropic medium. At the top we see the individual wavelet emanating from a point source, and below, the way in which an arbitrary wavefront develops. The wave-vector k is normal to the local wavefront, and the ray vector S is the direction of energy flow (§5.1). In (*b*), the two are not necessarily parallel.

was emitted from a point at a certain instant. Then the wavefront is defined as the surface that the wave disturbance has reached at a given time. In principle, a wavefront can have almost any shape, but only plane, cylindrical, spherical or occasionally ellipsoidal wavefronts have any analytical importance.

Huygens pointed out that if one knows the wavefront at a certain moment, the wavefront at a later time can be deduced by considering each point on the first one as the source of a new disturbance. The new disturbance is a spherical wave, propagating in the forward direction. At the later time, the spherical waves will have grown to a certain radius, and the new wavefront is the envelope of all the new disturbances (Fig. 2.8(*a*)).

In an anisotropic medium, the spherical wavelets become ellipsoids (§6.3.1).

The idea was later justified mathematically by Kirchhoff, and his analysis will be detailed in an appendix to Chapter 7. The new disturbances are known as **Huygens' wavelets**. On the basis of this principle, one can easily see that spherical, plane and cylindrical waves will retain their shapes, but other shapes can become distorted. Huygens' construction is most useful in getting a physical picture of wave propagation under conditions where an exact calculation defeats us; an illustration follows in §2.8.

The construction can be applied to anisotropic materials (§6.3.1) by realizing that, if the wave velocity is a function of direction, the wavelets are ellipsoids and not spheres. An important corollary then follows when we consider the progress of a wavefront of limited spatial extent. The direction of energy flow (**S**, the **ray direction**), is given by joining the origin of each wavelet to the point at which it touches the envelope, and this direction does not always coincide with that of the wave-vector **k** (Fig. 2.8(*b*)).

Another way of deriving Snell's law from Huygens' principle is to minimize the distance between two fixed points on opposite sides of a boundary; see Problem 2.5.

2.6.2 Huygens' principle used to derive Snell's law of refraction

The fact that wavefronts are separated by equal intervals of time allows us to derive **Snell's law of refraction**, when a wave goes from one medium to

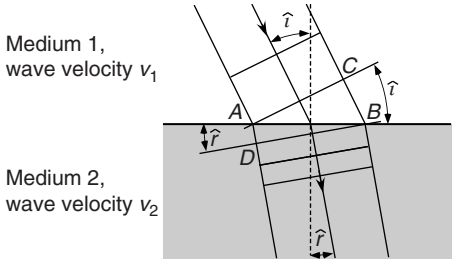

Figure 2.9
Snell's law derived from Huygens' principle.

another. This is one of many ways to prove Snell's law (see also §5.4). We consider a plane wave incident on an interface at angle $\hat{\imath}$ and refracted at angle $\hat{r}$ (Fig. 2.9). The velocity of the wave in the first medium is v_1, where a typical wavefront is AC, normal to the direction of propagation; in the second the velocity is v_2, and a typical wavefront is DB. Then, since B and D are generated by wavelets emitted simultaneously from C and A, the time from A to D must be equal to that from C to B:

$$\begin{aligned} CB/v_1 &= AD/v_2, \\ AB\sin\hat{\imath}/v_1 &= AB\sin\hat{r}/v_2, \\ (c/v_1)\sin\hat{\imath} &= (c/v_2)\sin\hat{r}. \end{aligned} \tag{2.54}$$

This would be true for any type of wave, where c is a constant. In the case of light waves, when c is the velocity in free space and $n = c/v$ is the **refractive index**, (2.54) gives us **Snell's law of refraction**:

$$n_1\sin\hat{\imath} = n_2\sin\hat{r}. \tag{2.55}$$

2.6.3 Fermat's principle

Suppose that a light wave is emitted from a point source in an inhomogeneous medium, and can 'choose' between several possible routes to an observer. Which one will it take? Fermat originally stated that it will choose that which takes the minimum time, thus illustrating Nature's concern with economy! The law of rectilinear propagation in a homogeneous medium is an obvious result, and the laws of reflection and refraction can also be deduced. The time taken from A to B is

$$t = \int_A^B \frac{1}{v(s)}\mathrm{d}s, \tag{2.56}$$

where $v(s)$ is the velocity at the point a distance s along the route. In optics, the refractive index n is the ratio c/v (§2.6.2), so that ct then defines the

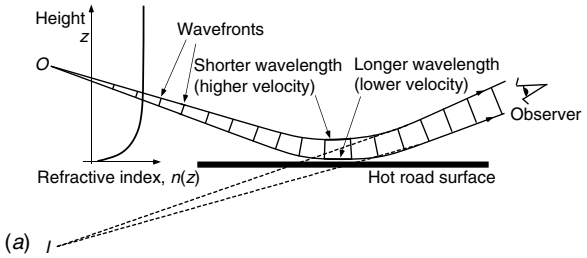

(b)

Figure 2.10

The mirage: (*a*) Huygens' principle applied to the mirage; a point object *O* in the sky appears reflected at *I*. (*b*) A typical driver's mirage on a desert road. (Photograph by Shahar Hirshfeld)

Box 2.3 The mirage, as explained by Huygens' construction

The velocity of light depends on the refractive index of the medium, $v = c/n$ (§5.1.2). In air, as in most materials, the refractive index falls as the temperature rises, roughly: $n(T) = 1.000291 - 1.0 \times 10^{-6}T$, where T is the temperature in degrees Celsius. The mirage, which we often see when motoring along an asphalt road in the heat of a summer's day, is an apparent reflection of sky light by a distant layer of overheated air in contact with the road, which might have reached 70 °C or more. It looks as if the road is wet, and there are many stories about mirages masquerading as oases before the eyes of thirsty desert-travellers.

The important point here is to consider the light that is propagating almost parallel to the road (Fig. 2.10). Then the upper part of the wave is in a region cooler than the lower part, and therefore has larger n and a shorter wavelength. Using Huygens' construction, the wavefronts, being separated by one wavelength, are therefore not quite parallel; this results in an upward curvature in the wave-vector, the normal to the wavefronts. The effect is negligible except where the wave is travelling close to the ground and parallel to it, so the mirage is always seen a long way off! Now this is a continuous form of reflection, not an abrupt one like from a mirror, so it is interesting to see if the geometrical aspects are different. For example, is the image upright or inverted? Can you estimate how far away the mirage is seen, given the temperature difference between the air in contact with the road and far from it?

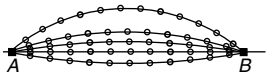

Figure 2.11

Illustrating Fermat's principle. The circles along the rays indicate units of one wavelength. The waves arrive in phase only when they are close to the shortest route, the straight line from *A* to *B*.

optical path $\overline{AB}$:

$$\overline{AB} = \int_A^B n(s)\mathrm{d}s. \tag{2.57}$$

Fermat's principle can only be understood properly in terms of interference, but the concepts needed are elementary. Supposing that light waves propagate from A to B by *all possible* routes AB_j, unrestricted initially by rules of geometrical or physical optics (those rules will emerge). The various optical paths $\overline{AB_j}$ will vary by amounts greatly in excess of one wavelength, and so the waves arriving at B will have a large range of phases and will tend to interfere destructively. But if there is a shortest route $\overline{AB_0}$, and the optical path varies *smoothly* through it, then a considerable number of neighbouring routes close to $\overline{AB_0}$ will have optical paths differing from $\overline{AB_0}$ by second-order amounts only, $< \lambda$, and will therefore interfere constructively. Waves along and close to this shortest route will thus dominate (Fig. 2.11) and AB_0 will be the route along which the light is seen to travel. The same argument also shows that a possible route is that when $\overline{AB_j}$ is *maximum*. Sometimes profligate Nature takes the *longest* path! A good example of this behaviour is the graded-index optical fibre described in §10.2.2, where the light propagates along the axis where the refractive index is maximum; this has the longest optical path.

2.6.4 Fermat's principle applied to imaging by a lens

Fermat's principle corresponds mathematically to Huygens' propagation evaluated by using stationary phase integration.

Fermat's principle can be used to explain simply why lenses have spherical or parabolic surfaces. If the routes from A to B all have the **same** optical path, the waves travelling by them will interfere constructively at B. Then no particular route for the light is chosen. A and B are then **conjugate points**, the term used for **object** and **image**. Let us see how Fermat's principle, stated this way, leads us directly to a lens with parabolic or spherical surfaces.

We can describe the imaging action of a lens by looking at the way that the varying thickness of the lens compensates the optical length of rays leaving the object O in different directions, so that all the optical path lengths from object to image I are equalized. The total optical path length $\overline{OI}$ from O to I via P, which is required to be constant, is to a good approximation (Fig. 2.12(a))

$$\overline{OI} = \text{constant} = \sqrt{u^2 + r^2} + \sqrt{v^2 + r^2} + (n-1)t(r) + t(0) \tag{2.58}$$

$$\approx u + v + \frac{1}{2}r^2\left[\frac{1}{u} + \frac{1}{v}\right] + (n-1)t(r) + t(0), \tag{2.59}$$

when expanded by the binomial theorem to first order. It follows that, for this to be true, $t(r)$ has the parabolic form

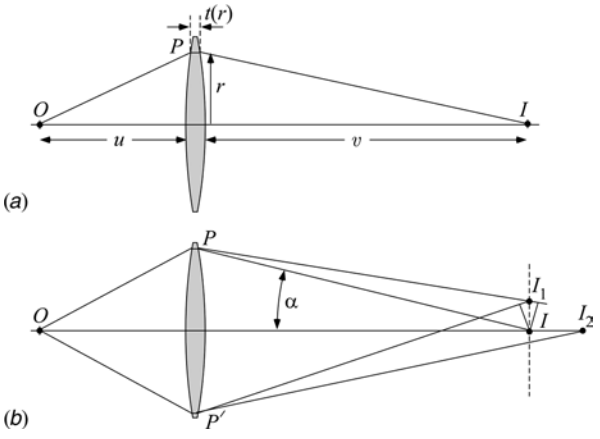

Figure 2.12
Using Fermat's principle to illustrate imaging by a lens. (*a*) Conjugate points; (*b*) lateral and axial deviations from the image points.

$$t(r) = t(0) - \frac{1}{2(n-1)} r^2 \left[\frac{1}{u} + \frac{1}{v}\right]. \tag{2.60}$$

This explains simply why lens surfaces are parabolic or spherical, and why higher refractive index n leads to thinner and lighter lenses. We shall discuss lenses and lens systems more thoroughly (though, in fact, no more accurately) in Chapter 3. Box 2.4 shows how the argument above leads to a basic understanding of imaging resolution and depth of focus. The same ideas will be applied to understanding gradient index lenses in the next chapter.

2.7 Advanced topic: Propagation and distortion of a wave-group in a dispersive medium

In §2.1.2 we considered the propagation of the superposition of a number of elementary waves of the form

$$F(x,t) \equiv \sum_j f_{k_j}(x,t) = \sum_j a_{k_j} \exp[\mathrm{i}(k_j x - \omega_j t)]. \tag{2.61}$$

Let us replace the summation by an integral

$$F(x,t) = \int_{-\infty}^{\infty} f(k,x,t)\mathrm{d}k = \int_{-\infty}^{\infty} a(k) \exp[\mathrm{i}(kx - \omega t)]\mathrm{d}k, \tag{2.62}$$

where $\omega(k)$ is defined. Now we take the particular case of a **Gaussian wave-group** (§4.4.3 and Box 4.3) in which $a(k)$ is the Gaussian function

$$a(k) = \left(\frac{2\pi}{\sigma}\right)^{-\frac{1}{2}} \exp\left(\frac{-(k-k_0)^2\sigma^2}{2}\right), \tag{2.63}$$

centred on $k = k_0$ and having variance σ^{-1}.

Box 2.4 Resolution and depth of focus, by Fermat's principle

In §2.6.4 we showed how Fermat's principle describes imaging by a simple lens. Now we can ask a subsidiary question: if we move to a new point in the image space, how much error do we introduce into the equality of the path lengths? If the total inequality is less than half a wavelength, the different rays will still interfere constructively; this way the size of the image, both in the lateral and axial directions, can be deduced. Let's do this just for the extreme rays, to get the general picture (Fig. 2.12(*b*)).

To estimate the spatial resolution we consider an off-axis image point I_1, in the same plane as I. The marginal ray, when P is situated at the edge of the lens, has been shortened by about $II_1 \sin\alpha$, where α is the angular aperture of the lens at the image. The marginal ray from the diametrically opposite point P' has been lengthened by the same amount. If these two adjustments in the optical lengths are less than $\lambda/2$, they will still not cause destructive interference and so the image of the point source O is extended this far. The resulting image radius II_1 is equal to about $\lambda/2\sin\alpha$. This is also the resolution limit, because two images separated by less than this will not be observed as separated. We shall get the same result in Chapter 12.

The depth of focus refers to the axial extent of the image of a point object. At a point I_2 on the axis, the marginal rays are lengthened by $II_2\cos\alpha$, and the axial ray by II_2. The difference is thus $II_2(\cos\alpha - 1) \approx II_2(\alpha^2/2)$. Putting this difference between path lengths again equal to $\lambda/2$, we find that the axial extent of the image is about $II_2 = \lambda/\alpha^2$. This is a useful result (again, it agrees with more exact methods) for estimating the depth of focus of a camera in terms of the aperture of the lens.

To translate these results into object space, just perform the same calculations with a fixed image point and variable object points; then the (now small) angle α is the lens semi-aperture divided by the object distance. So for a lens with aperture radius 20 mm, at a distance of 10 m and wavelength 0.5 μm, the depth of field is $0.5/(2\times10^{-3})^2 = 10^5\ \mu\text{m} = 0.1\ \text{m}$.

The integral (2.62) can be performed for $t=0$ (§4.4.3) and the result (Fig. 2.13(*a*)) is

$$F(x,0) = \exp(-x^2/2\sigma^2)\ \exp(\mathrm{i}k_0x). \tag{2.64}$$

The envelope $\exp(-x^2/2\sigma^2)$ of this wave-group peaks at $x=0$ and has half-peak-width (§4.4.6) $w = 2.36\sigma$.

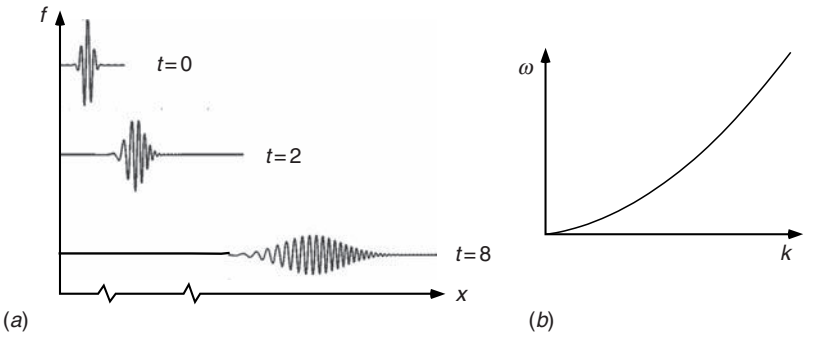

Figure 2.13

(*a*) A Gaussian wave-group at $t = 0$ and its evolution at two later times computed using the quadratic dispersion relationship shown in (*b*).

Now let us consider the propagation of this wave-group in three media:

- a non-dispersive medium, for which $\omega = vk$;
- a linearly dispersive medium, for which $\omega = v_g k + \alpha$ (the phase velocity is not constant in this example);
- a quadratic dispersive medium, for which $\omega = v_g k + \alpha + \beta(k - k_0)^2$.

In the first case, as we saw in §2.1.2, we write $x' = x - vt$ and immediately find $F(x, t) = F(x', 0) = F(x - vt, 0)$: the wave-group propagates unchanged at velocity v.

In the second case, substitution for ω in (2.62) gives us

$$F(x,t) = \int_{-\infty}^{\infty} a(k) \exp\{\mathrm{i}[kx - t(v_g k + \alpha)]\}\mathrm{d}k. \tag{2.65}$$

Substituting x' for $x - v_g t$ gives, as above,

$$F(x,t) = \mathrm{e}^{-\mathrm{i}\alpha t} F(x', 0) = \mathrm{e}^{-\mathrm{i}\alpha t} F(x - v_g t, 0). \tag{2.66}$$

Thus the wave-group propagates with unchanged envelope at velocity v_g ($= \mathrm{d}\omega/\mathrm{d}k$, the group velocity), but the phase of the wave changes with propagation; this is the process of 'individual waves moving through the envelope' remarked in §2.4.

Neither of the above examples invoked explicitly the form of $a(k)$, and the results would be true for any form of wave-group. This is because $\mathrm{d}\omega/\mathrm{d}k$ is not a function of k. But in the third example, the way in which the wave envelope behaves depends on its initial form. Equation (2.61) becomes

$$\begin{aligned} F(x,t) &= (2\pi/\sigma)^{-\frac{1}{2}} \int_{-\infty}^{\infty} \exp\left[\frac{-(k_0 - k)^2\sigma^2}{2}\right] \\ &\quad \times \exp\{\mathrm{i}[kx - (v_g k + \alpha + \beta(k + k_0)^2)t]\}\mathrm{d}k \\ &= (2\pi/\sigma)^{-\frac{1}{2}} \mathrm{e}^{-\mathrm{i}\alpha t} \int_{-\infty}^{\infty} \exp\left[-(k - k_0)^2 \left(\frac{\sigma^2}{2} + \mathrm{i}\beta t\right)\right] \exp(\mathrm{i}kx')\mathrm{d}k. \end{aligned} \tag{2.67}$$

Formidable as it may look, the integral can be evaluated just like any other Gaussian integral (§4.4.3) and gives

$$F(x',t) = (1+4\beta^2\sigma^{-4}t^2)^{-\frac{1}{4}} \exp\left(\frac{-x'^2}{2(\sigma^2+4\beta^2t^2\sigma^{-2})}\right) e^{i\psi(t)}. \qquad (2.68)$$

The phenomenon of chirping is really rather intuitive. If the medium is dispersive the wave velocity depends on frequency, and the low frequencies will arrive before the higher ones or vice versa, depending on the sign of the dispersion.

The form is not complicated. The envelope is centred on the point $x' = (x - v_g t) = 0$, so that once again we see the peak propagating at the group velocity. But the half-width and amplitude of the envelope have changed. The half-peak-width is now $2.36(\sigma^2 + 4\beta^4t^2\sigma^{-2})^{\frac{1}{2}}$, which is always greater than the initial $w = 2.36\sigma$, and continues to grow with time. In concert with this, the amplitude falls so that total energy is conserved. Notice that the narrower the original pulse (smaller σ) the faster the pulse broadens; for a given time of travel, there is a particular initial pulse-width that gives the narrowest final pulse. The phase factor $\psi(t)$ is complicated and is best calculated numerically. It contains the factor αt, which occurred in the linear dispersive media, and also extra factors; it shows **chirping**, a variation of local k with distance. A numerically calculated example is shown in Fig. 2.13. Study of the propagation of pulses in dispersive media is very important in designing optical communication systems (§10.2.4) and this calculation is only a modest beginning.

2.8 Advanced topic: Gravitational lenses

Some recent astronomical observations show multiple images that all have the same spectra and whose intensity fluctuations (e.g. bursts) are identical, although there may be time delays between them. They must therefore have originated from the same stellar object. These images are considered to have arisen as the result of gravitational lensing, which means that the light from the star has been deviated by the gravitational field of a massive dark object that lies close to the line of sight. Understanding the way in which such multiple images arise is a nice exercise in the use of Fermat's and Huygens' principles, which shows that the gravitational field around a compact body can act like a rather strange converging lens.

The idea that a massive body can deflect a light wave is not new; Newton thought of it as a result of the mass of his assumed light corpuscles (Problem 2.10), but today it is considered as arising from the distortion of space-time near a massive body as described by general relativity. Einstein's prediction of the size of the effect, which was twice that of classical theory, was first confirmed in 1919 by Eddington's observations of the apparent deflection of star positions near to the direction of the Sun at the time of a complete eclipse. This was an important proof of general relativity, and the story of how the

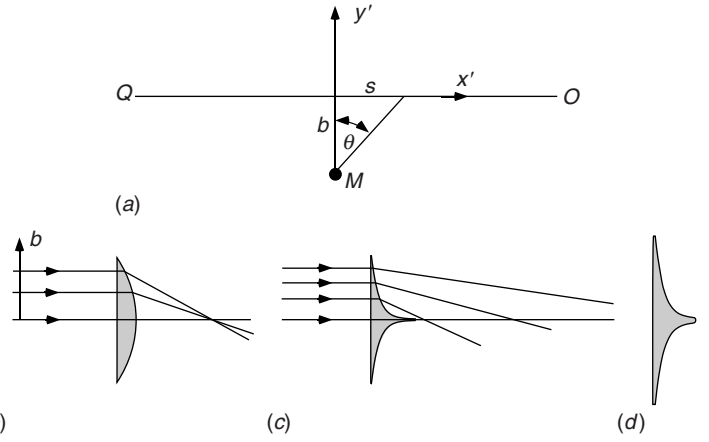

Figure 2.14 **Gravitational lensing. (*a*) Light from the source *Q* to the observer *O* passes close to a lensing mass *M*; the distance of closest approach, or impact parameter, is *b*. (*b*) A normal lens deviates an incident ray by an angle proportional to *b*. (*c*) The lens that simulates gravitational lensing by a point mass has profile $\sim \log b$ and deviates the incident ray by an angle proportional to $1/b$. (*d*) Profile of a plastic lens used to simulate gravitational lensing in the laboratory (Fig. 2.1(*a*,*b*)); the singularity at $b = 0$ is rounded off and simulates a finite-sized lensing mass.**

observations were made and interpreted is told in the book *The Big Bang* by Singh (2004).

Bending of a light ray by a gravitational field can be understood in the following way. Suppose an observer is situated in a lift, together with a laser that shines a beam horizontally from one side to the other. The observer marks the point at which the beam strikes the far wall. If the lift moves at constant linear velocity, this will not make any difference since both the laser and the far wall are moving at the same velocity. But if the lift falls freely with acceleration g, its velocity changes by gt during the beam's time of flight t and the point of arrival will move by an amount $\frac{1}{2}gt^2$, which is the additional amount by which the lift has fallen since the light beam was emitted. Let the beam's route in the inertial frame be $y = 0, x = ct$; then in the freely falling frame it will be $y' = \frac{1}{2}gt'^2, x' = ct'$.

Now we can apply this idea to the astronomical situation. According to the principle of equivalence in relativity, the effect of a gravitational field is indistinguishable from that of the equivalent acceleration field. To a very good approximation the optical path from a quasar Q to the observer O is a straight line whose closest approach to the lensing mass M is a distance b. This distance is usually called, in deference to nuclear physics, the **impact parameter** (Fig. 2.14(*a*)). In a uniform gravitational field g normal to the optical path, the small angular deviation from the straight line of the inertial frame is then

$$\alpha = \frac{\mathrm{d}y'}{\mathrm{d}x'} = gx'/c^2. \tag{2.69}$$

Now we consider the non-uniform gravitational field around the lensing mass. The change in the direction of propagation α in a distance ds along the x' axis is

$$\mathrm{d}\alpha = g(s)\mathrm{d}s/c^2. \tag{2.70}$$

From the figure, when $x' = s$ the gravitational acceleration is directed at angle θ to the y'-axis and has value $GM/(s^2 + b^2) = GM\cos^2\theta/b^2$. Thus the y'-component, $g'_y(s) = GM\cos^3\theta/b^2$. It follows that

$$\mathrm{d}\alpha = [GM/c^2b^2]\cos^3\theta\,\mathrm{d}s \tag{2.71}$$

and since $s = b\tan\theta$, $\mathrm{d}s = b\sec^2\theta\,\mathrm{d}\theta$ from which

$$\mathrm{d}\alpha = \frac{GM}{bc^2}\cos\theta\,\mathrm{d}\theta, \tag{2.72}$$

$$\alpha = \frac{GM}{bc^2}\int_{-\pi/2}^{\pi/2}\cos\theta\,\mathrm{d}\theta = \frac{2GM}{bc^2}. \tag{2.73}$$

This is the classical result which can also be obtained from Newtonian mechanics. General relativity predicts that the result should be *twice* this value, i.e. $\alpha = 4GM/bc^2$. This basically results from the fact that in space-time x, y and ct behave in exactly the same way, so that taking into account the difference between t and t', which we assumed to be equal in the above argument, results in a doubling of the value of α:

$$\alpha = \frac{4GM}{bc^2}. \tag{2.74}$$

The unusual fact about this gravitational lens is that **the deviation α is proportional to $1/b$ and not to b like a normal lens** (Fig. 2.14(*b*)). While a normal lens has a spherical profile, the gravitational deviation would result from a lens with logarithmic profile, its thickness d being equal to $-(n-1)\log b$. (Remember that $\log b$ is negative for small b.) Then the deviation of a ray at radius b, from Fermat's principle, is $(n-1)\mathrm{d}d/\mathrm{d}b = -(n-1)/b$ (Fig. 2.14(*c*)). This lens profile diverges at $b = 0$, but this can be excused since the source was assumed to be a point mass, and if it is replaced by a finite massive body, the singularity is rounded out as shown in the lens of Fig. 2.14(*d*).

Now let us get a qualitative picture of the lensing that occurs when the Earth, a distant quasar and a massive dark lensing galaxy at intermediate distance lie very close to a straight line, so that b is very small. Astronomers assure us that there is a reasonable chance for such an occurrence. We consider a plane wave incident from Q on the lensing mass and use Huygens' construction to continue the propagation of the wavefront W (Fig. 2.15). Because of the increased optical thickness in the region of the lensing mass, the wavefront W_1 leaving it acquires a dimple in that region. Continuing the evolution of the wavefront, we find that

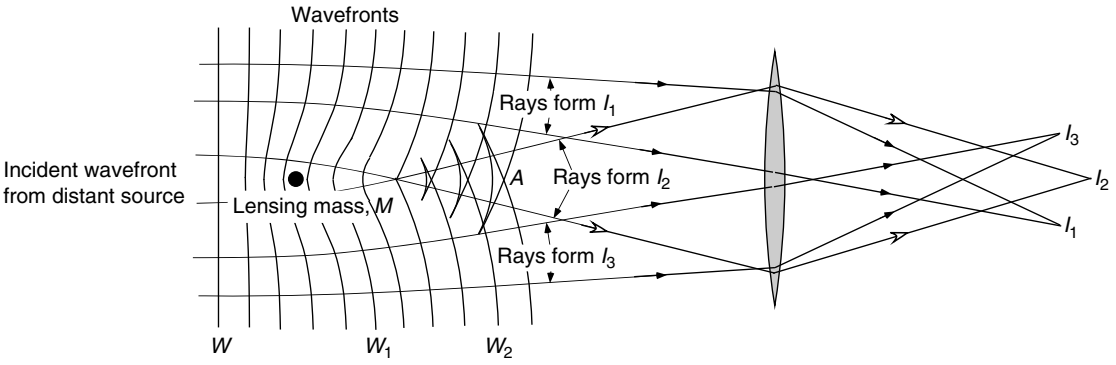

Figure 2.15 **Huygens' construction used to show the development of wavefronts in the gravitationally modified region. An incident plane wavefront *W* develops a dimple in the region of the lensing mass *M* due to the gravitational field in its locality. Light rays, which travel normal to the wavefronts, are also shown. Development of *W* into W_1, W_2 etc. shows the formation of three distinct images, I_1, I_2 and I_3.**

the wavefront at W_2 has quite a complicated structure. The propagation we see in this figure is just the Huygens picture of the free-space development of the wavefront that emerged from the lensing-mass region, in the complete absence of any further distortion. One sees that at sufficient distance from the mass a region occurs in which the wavefront is multi-valued. The margins of this region are a **caustic**, which is a pair of lines of cusps. Clearly an observer within the caustic observes three different wavefronts simultaneously, each with a different shape, and therefore sees three separate images. Notice also that the three wavefronts passing through A may not be at the same optical distance from the source – hence the relative time delays observed. The above argument has been developed in two dimensions. Had the observer, the lensing galaxy and the source been in a straight line, it is clear from the resultant axial symmetry that the image observed would be a central point surrounded by a ring of light. This is called an 'Einstein ring'. If the lens is not spherically symmetrical, or the system not coaxial, a three-dimensional argument, similar to the one above, gives five point images. Several gravitationally lensed images have been observed with the aid of the Hubble Space Telescope since its launching. Figure 2.1 (at the beginning of the chapter) shows two observed images that appear to be gravitationally distorted by a galaxy close to the line of sight, compared with laboratory photographs of a point source as seen through a plastic lens constructed with the profile of Fig. 2.14(*c*).

2.8.1 Gravitational micro-lensing

Since the lensing mass is, by astronomical standards, fairly close to us, we can sometimes observe its apparent motion relative to the source; this is known as

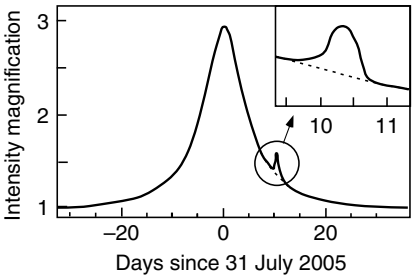

Figure 2.16 Representative sketch of gravitational micro-lensing data. This graph shows intensity of a distant source as a function of time, as measured by six independent telescopes around the world. It shows two peaks which are explained as resulting from an invisible lensing star and an associated planet passing close to the line of sight. (After Beaulieu *et al.* (2006))

'parallax'. Then, as one of the cusps crosses the line of sight, there is a peak in the observed intensity, which can be looked at as a merging of two of the sub-images, which then suddenly disappear into another one. Alternatively, this can be understood as an intensity propagation anomaly (Problem 2.8). This type of intensity fluctuation can be seen even by a telescope that is too small to resolve the angular structure of the image, and is called **gravitational micro-lensing**. Many small astronomical telescopes are today being used on a long-term basis to monitor likely sources for such events. In particular, when the lensing mass is a star with a planetary system, there might be subsidiary peaks in intensity due to a planet. An example of data is shown in Fig. 2.16.

Chapter summary

This chapter was devoted to a discussion of how waves – not necessarily light waves – propagate in linear media. We studied:

- The concept of a wave equation, and how it can be solved using harmonic waves;
- Some examples of non-dispersive waves, whose velocity is independent of frequency, a topic which will be expanded in Chapter 5 for the case of electromagnetic waves;
- Dispersive waves, whose velocity is frequency dependent, and how the dispersion equation for a medium is derived;
- Plane waves and other solutions of a homogeneous wave equation;
- Ways to solve wave propagation problems in heterogeneous media, using Huygens' wavelets and Fermat's principle of least time;

- **Propagation of a wave-group in a dispersive medium;**
- **Gravitational lensing as an example of Huygens' wavelets applied to a cosmological scenario.**

Problems

2.1. A chain of masses m are situated on the x-axis at equally spaced points $x = na$. They are connected by springs having spring constant K and are restrained to move only along the x-axis. Show that longitudinal waves can propagate along the chain, and that their dispersion relation is

$$\omega = 2(K/m)^{\frac{1}{2}} \left|\sin \tfrac{1}{2}ka\right|. \tag{2.75}$$

Explain in physical terms why this dispersion relation is periodic. Calculate the phase and group velocities when $\omega \to 0$ and $\omega = 2(K/m)^{\frac{1}{2}}$.

2.2. Flexural waves on a bar have a wave equation of the form

$$\frac{\partial^2 y}{\partial t^2} = -B^2 \frac{\partial^4 y}{\partial x^4}, \tag{2.76}$$

where B is a constant. Find the dispersion relation. Under what conditions are the waves evanescent?

2.3. X-rays in a medium have refractive index $n = (1 - \Omega^2/\omega^2)^{\frac{1}{2}}$ (§13.3.4) Show that the product of group and phase velocities is c^2.

2.4. Waves on the surface of water, with depth h and surface tension σ, have a dispersion relation

$$\omega^2 = (gk + \sigma k^3/\rho)\tanh(kh), \tag{2.77}$$

where g is the gravitational acceleration and ρ is the density. Find the group velocity as a function of k and show that it has a turning point at a certain point related to the depth h. What is a typical value for this group velocity?

2.5. Two media, with wave velocities v_1 and v_2, are separated by a plane boundary. A source point A and an observer B are on opposite sides of the boundary, and not on the same normal. Derive Snell's law from Fermat's principle by finding the minimum time for a wave to propagate from A to B.

2.6. Use Fermat's principle and the properties of conic sections to prove that a point source at one focus of an ellipsoidal or hyperbolic mirror is imaged at the other focus (the most common example is the paraboloid, which has one focus at infinity). The Cassegrain and Gregorian reflecting telescopes use both concave and convex mirrors to obtain high magnification (like a telephoto lens). What profiles of mirror should ideally be used?

2.7. Show that the multiple images caused by a gravitational lensing mass of finite size a correspond to both maximum and minimum optical paths. Use a simplified model consisting of a region of thickness a normal to the propagation direction having refractive index $n(r) = 1 + 2MG/c^2\sqrt{(a^2 + r^2)}$, where r is measured from the observation axis in the plane normal to it. Show that the optical path from source to observer has both maximum and minimum values, which correspond to the images observed. (The different optical paths result in light variations appearing with different delays, which are indeed observed.)

2.8. A non-planar wavefront propagates in the z-direction according to Huygens' principle. The wavefront has radii of curvature R_x in the (x, z) plane and R_y in the (y, z) plane. The intensity in plane $z = \text{const}$ is $I_z(x, y)$. By using conservation of energy for a rectangular region of the wavefront, relate the change in intensity after a further short distance $\delta z \ll |R_1|, |R_2|$ to the radii of curvature. Show that this can be expressed as a **radiative transport equation**

$$\frac{\mathrm{d}I_z}{\mathrm{d}z} = I\kappa = I\nabla^2 w, \tag{2.78}$$

where $w(x, y)$ is an algebraic form for the wavefront, and $\kappa \equiv R_1^{-1} + R_2^{-1}$ is its Gaussian curvature.

2.9. Confirm the demonstration in Box 2.1 using Fourier analysis from Chapter 4. Analyze the triangular wave into Fourier components analytically, and then let each one evolve, as described in §2.1.2. You should get the same result as in the box!

2.10. According to Newton, light particles of mass m passed near to a heavy body of mass M and were deflected due to its gravitational attraction GMm/r^2. Show (for small angles) that the result (2.73) is obtained, independent of m, which can then be taken as zero for a photon!

References

Beaulieu, J.-P., Bennett, D. P., Fouqué, P. *et al.* (2006), Discovery of a cool planet of 5.5 Earth masses through gravitational microlensing, *Nature* **439**, 440.

Brillouin, L. (1960), *Wave Propagation and Group Velocity*, New York: Academic Press.

Huchra, J., Gorenstein, M., Kent, S. *et al*. (1985), *Astron. J.* **90**, 691.

King, L. J., Jackson, N., Blandford, R. D. *et al*. (1998), A complete infrared Einstein ring in the gravitational lensing system B1938+666, *M. Not. R. Astron. Soc.* **295**, L41-44.

Paczyński, B. and Wambsganss, J. (1993), Gravitational microlensing, *Physics World* **6**(5), 26.

Singh, S. (2004), *The Big Bang*, New York: Harper Collins.

3 Geometrical optics

If this book were to follow historical order, the present chapter should have preceded the previous one, since lenses and mirrors were known and studied long before wave theory was understood. However, once we have grasped the elements of wave theory, it is much easier to appreciate the strengths and limitations of geometrical optics, so logically it is quite appropriate to put this chapter here. Essentially, geometrical optics, which considers light waves as rays that propagate along straight lines in uniform media and are related by Snell's law (§2.6.2 and §5.4) at interfaces, has a relationship to wave optics similar to that of classical mechanics to quantum mechanics. For geometrical optics to be strictly true, it is important that the sizes of the elements we are dealing with be large compared with the wavelength λ. Under these conditions we can neglect diffraction, which otherwise prevents the exact simultaneous specification of the positions and directions of rays on which geometrical optics is based.

Analytical solutions of problems in geometrical optics are rare, but fortunately there are approximations, in particular the Gaussian or paraxial approximation, which work quite well under most conditions and will be the basis of the discussion in this chapter. Exact solutions can be found using specialized computer programs, which will not be discussed here. However, from the practical point of view, geometrical optics answers most questions about optical instruments extremely well and in a much simpler way than wave theory could do. For example, we show in Fig. 3.1 the basic idea of a zoom lens (§3.6.4), which today is part of every camera, and is a topic that can be addressed clearly by the methods developed in §3.5. Geometrical optics fails only in that it cannot define the limits of performance such as resolving power, and it does not work well for very small devices such as optical fibres. These will be dealt with by wave theory in Chapters 10 and 12.

In this chapter we shall learn:

- about the classical theory of thin lenses according to the paraxial or Gaussian approximation, which assumes that all ray angles are small;
- how to trace rays geometrically through paraxial optical systems;
- about telescopes and microscopes, as examples of simple optical instruments;
- how the paraxial optical theory can be elegantly reformulated by the use of matrices;

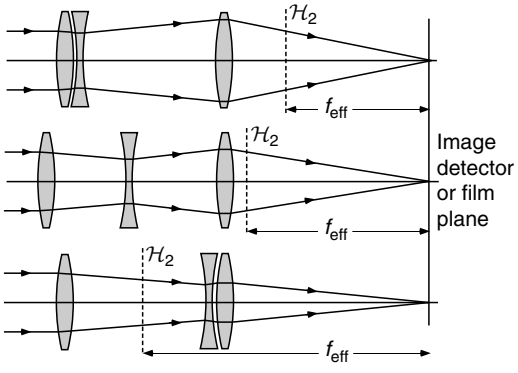

Figure 3.1

A simple zoom lens combination is constructed from three coaxial lenses, two converging and one diverging. The combination behaves like a single lens with focal length f_{eff}, placed in the principal plane $\mathcal{H}_2$. By moving the two lenses on the left, different focal lengths are obtained, while the image remains focused on the image sensor, resulting in different magnifications.

- that an optical system can be represented by its focal, principal and nodal points, which are called cardinal points;
- about telephoto and zoom lenses, as examples of the importance of principal points;
- a little about lens aberrations;
- about aplanatic microscope objectives, which allow the use of large-angle rays without introducing aberrations;
- about the stability of optical resonators, which are used in lasers and advanced interferometers.

This chapter really only skims the surface of geometrical optics, and is limited to image-forming lenses and lens combinations. We shall only mention here that there is also an important field of **non-imaging optics**, which provides solutions for problems in which power efficiency rather than imaging quality is the prime concern, such as illumination design and solar energy collection. See Box 3.5 (Welford and Winston (1989)). Readers interested in a deeper study of geometrical optics and optical system design are referred to the texts by Kingslake (1983) and Smith (2008).

3.1 The basic structure of optical imaging systems

The main elements from which optical systems are built are:

- thin lenses, for example spectacles or magnifying glasses, that converge or diverge bundles of light rays;
- compound lenses that, in addition to the above, are designed to correct various aberrations; examples are achromatic doublets and microscope objectives;

- plane mirrors or prisms that change the direction of the optical path and may be used to invert an image as in binocular field glasses;
- spherical or parabolic mirrors that replace lenses in large telescopes or in instruments working with wavelengths absorbed by common optical materials.

We shall always assume here that an optical system has axial symmetry. The elements are therefore coaxial, which means that an **optical axis** z can be defined such that all plane interfaces between optical materials are normal to it and the centres of curvature of all spherical lens and mirror surfaces lie on it.

We shall limit the treatment in this chapter to lens systems only, although curved mirrors may be preferable when chromatic effects are important or wavelengths are used that can be absorbed by common optical materials. The reason is that curved mirrors behave quite similarly to lenses but introduce minus signs into the equations, which add little to the physics but help to confuse the reader. The way in which mirrors can be treated using lens equivalents is illustrated in §3.9.

Most lenses have spherical surfaces for the purely practical reason that such surfaces are easy to grind and polish. Spherical surfaces have no special optical significance that distinguishes them from paraboloidal, ellipsoidal or other analytical surfaces. All give rise to aberrations, and all are perfect solutions for some special cases that are too rare to be worth mentioning here. An exception is the aplanatic system (§3.8) in which a spherical surface turns out to be a perfect solution that can be applied to many important problems such as the design of microscope objectives.

3.1.1 The philosophy of optical design

Before discussing details and calculations, we shall briefly describe the steps taken when designing a lens-based imaging system. This in fact includes almost all applications of geometrical optics.

1. Decide in general how to solve your problem. Take into account requirements such as overall size, field of view, magnification and resolution, although the latter often includes wavelength-dependent factors which are not discussed in this chapter.
2. Draw a ray diagram for object and image on the axis, using paraxial optics ray-tracing (§3.1.2).
3. Draw a similar paraxial diagram for an off-axis object. This will clarify the magnification of the system and emphasize any problem caused by light rays missing the finite apertures of the optical elements. Such a problem is called **vignetting** (see §3.3.2).

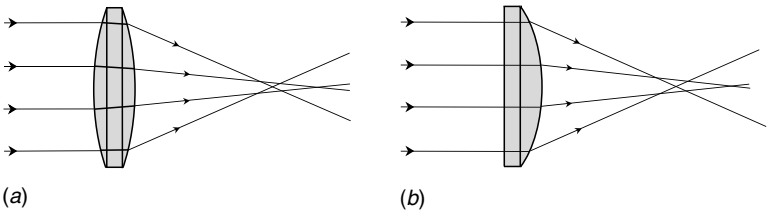

Figure 3.2
Spherical aberration of simple lenses: (*a*) biconvex; (*b*) plano-convex. The two lenses have the same paraxial focal length, but the distance between the paraxial and marginal foci is greater in (*b*).

We emphasize the importance of stages 2 and 3, which will usually fulfil the requirements of all but professional optical designers.

4. Solve the problem in detail using matrix optics (§3.4) or a computer-based optical design program to find the best location of the lenses.
5. Consider the effects of large-angle rays and aberrations.
6. Consider the possible use of aspherical lenses etc.

Stages 5 and 6 involve technical aspects that are outside the scope of this book.

3.1.2 Classical optics in the Gaussian approximation

The small angle or paraxial approximation is often known as **Gaussian optics**. In real life, rays propagating through lenses do not usually make small angles with the optical axis; two typical situations are shown in Fig. 3.2 where we have traced the rays through each lens by using Snell's law. We see that a bundle of rays entering parallel to z does *not* meet at a point on the axis. This is an example of **spherical aberration**, which will be further discussed in §3.7.3. However, in most of this chapter we shall try to avoid the problems created by large angles, and **we shall therefore assume that the angle θ of all rays with respect to z is small enough that** $\theta \approx \sin\theta \approx \tan\theta$. This defines the scope of Gaussian optics, which in practice does an excellent job even under conditions where the approximation is invalid! We also need to linearize Snell's law of refraction, $n_1 \sin\hat{\imath} = n_2 \sin\hat{r}$, to the form $n_1\hat{\imath} = n_2\hat{r}$. This requires $\hat{\imath}$ and $\hat{r}$ to be small too, so that all refracting surfaces must be almost normal to z. It follows that their radii must be large compared to the distance of rays from the optical axis.

The sign convention is that distances to the left of a vertex are negative, and those to the right are positive. It is very important to adhere strictly to this.

3.1.3 Sign conventions

It is helpful to have a consistent convention for the use of positive and negative quantities in optics. In this book, we use a simple Cartesian convention, as

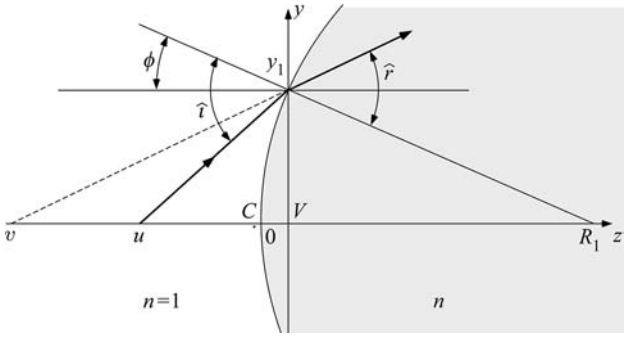

Figure 3.3

Deviation of a ray by a single refracting surface. In the Gaussian approximation, $y_1 \ll R_1$ so that $VC \ll R_1$ and is taken as zero in the theory. According to the sign convention, in this diagram u and v are both negative, R_1 and angles $\hat{\imath}$ and $\hat{r}$ are positive.

shown in Fig. 3.3, together with the rules that surfaces concave to the right have a positive radius and that angles of rays ascending to the right are taken as positive. It is also assumed that light rays go from left to right as long as we limit ourselves to lens systems. Other conventions – based upon whether real or virtual images or objects are involved – lead to difficulties.

When drawing ray diagrams the y-axis has to be scaled by a large factor, otherwise small angles are invisible. Therefore, spherical surfaces will appear in the diagrams to be planar, whatever their radii of curvature.

3.2 Imaging by a single thin lens in air

A **thin lens** is the simplest lens we can imagine, and consists of a piece of glass[1] having refractive index n bounded by two spherical surfaces; the line joining their centres of curvature defines the optical axis of the lens. The thickness of the lens on its axis is assumed to be much smaller than either of the radii. This lens is the basic building block of paraxial geometrical optics. We treat it first by considering the ray optics; later we shall see how much more easily the same calculation can be made by the matrix method (§3.5.1).

We treat first a single refracting spherical surface of radius R_1 located at $z = 0$ as in Fig. 3.3 with $n = 1$ on the left, and consider a ray originating from a point object O located on the axis at $z = u$. In accordance with the sign convention, distances to the left of the vertex V are taken as negative. A ray from O passes through the surface at $y = y_1$. It is refracted from angle $\hat{\imath}$ to angle $\hat{r}$ and consequently seems to have originated from a virtual image I located at $z = v$. We then have

$$\hat{\imath} - \phi = -y_1/u, \quad \hat{r} - \phi = -y_1/v, \quad \phi = y_1/R_1, \tag{3.1}$$

[1] Of course, any other homogeneous transparent material can be used instead of glass.

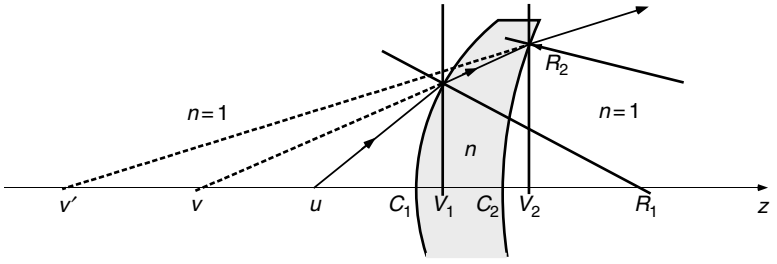

Figure 3.4

Image formation by a thin lens in air. The object at $u < 0$ forms a virtual image at $v' < 0$.

and it follows that

$$\frac{\hat{\imath}}{\hat{r}} = n = \frac{y_1\left(\frac{1}{R_1} - \frac{1}{u}\right)}{y_1\left(\frac{1}{R_1} - \frac{1}{v}\right)}, \tag{3.2}$$

which simplifies to

$$-\frac{n}{v} + \frac{1}{u} = \frac{1}{R_1}(1 - n). \tag{3.3}$$

The n in the first term of (3.3) indicates that v refers to a region of refractive index n.

The position $z = v'$ of the image generated by a thin lens in air can now be derived by using (3.3) for a second surface with radius R_2 and replacing the object position by the v just calculated (Fig. 3.4). This replacement implies that vertices of the two surfaces coincide geometrically, i.e. that the lens is indeed thin compared with v and u. The roles of n and 1 are interchanged and we get

$$-\frac{1}{v'} + \frac{n}{v} = \frac{1}{R_2}(n - 1). \tag{3.4}$$

Make sure you use the Cartesian sign convention when substituting in these equations.

We now find by substitution of n/v from (3.3) that

$$-\frac{1}{v'} + \frac{1}{u} + \frac{1}{R_1}(n - 1) = \frac{1}{R_2}(n - 1). \tag{3.5}$$

Therefore we obtain the well-known formula:

$$-\frac{1}{u} + \frac{1}{v'} = \frac{1}{f}, \tag{3.6}$$

where

$$\frac{1}{f} = (n - 1)\left(\frac{1}{R_1} - \frac{1}{R_2}\right). \tag{3.7}$$

This equation is known as the **lens-maker's equation**.

The object and image distances u and v' are called **conjugates**. When $u \to \infty$, $v' \to f$. This means that all rays entering the lens parallel to the

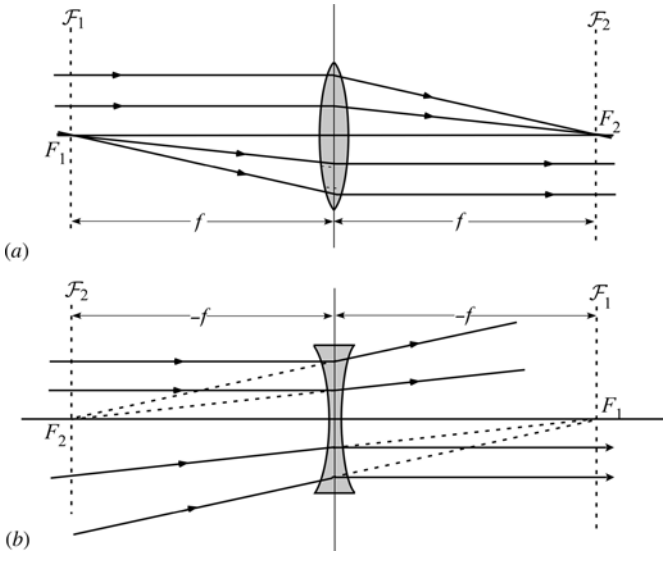

Figure 3.5

Focal planes and focal length of thin lenses in air: (*a*) converging; (*b*) diverging. The paths of various rays are shown.

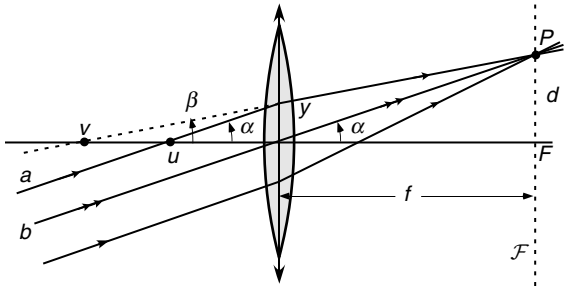

Figure 3.6

All rays at a given angle to the axis converge to a single point in the focal plane.

axis cut the axis at the focus F (Fig. 3.5). The quantity f is called the **focal length** and its reciprocal $1/f$ the **power** of the lens. When f is measured in metres, the unit of power is the **dioptre**. A lens with $f > 0$ is called a **converging** lens and one with $f < 0$ is **diverging**. Only the former can produce a real image of a physical object.

The **focal plane**, $\mathcal{F}$, is defined as the plane through F perpendicular to the optical axis. All rays entering the lens at a given small angle α to the axis will converge on the same point in $\mathcal{F}$. One can see this by reference to Fig. 3.6, which shows a general ray a entering at angle α after intersecting the x-axis at some u. It cuts $\mathcal{F}$ at P, with height d, and v is the conjugate to u. We have

$$y = -u\alpha, \quad d = \beta(f - v) = \frac{y}{v}(v - f) \tag{3.8}$$

and, using (3.6), it follows that $d = f\alpha$ independent of u. The easiest way to find P is to use the undeviated ray b at α through the centre of the lens.

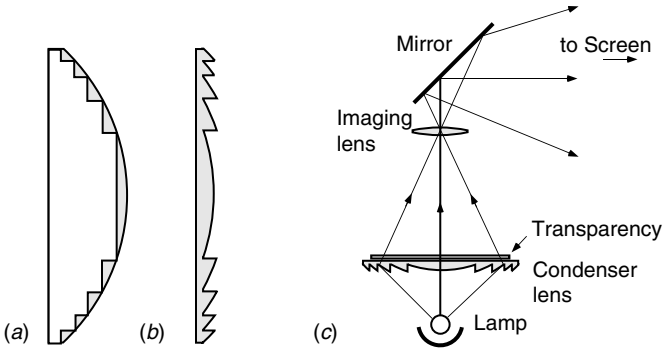

Figure 3.7

Principle and use of a Fresnel lens: (*a*) plano-convex lens with parallel-sided rings marked; (*b*) after removal of the rings and rearrangement; (*c*) use of Fresnel lens as a condenser in an overhead projector.

Box 3.1 Fresnel lenses

Augustin Fresnel, whose brilliant work on diffraction will be described in Chapter 7, was employed as inspector of lighthouses for the French government during a period around 1800. A coastal lighthouse uses a bright incandescent source and one or more large collimating lenses to produce parallel beams of light which can be seen at distances of 30 km or more from the coast. The whole system rotates so as to sweep the horizon, and a boat approaching the shore then sees a periodically modulated light source. The period and form of the modulation give the pilot information on his locality. A major problem in the building of lighthouses was the sheer weight of the lenses, several of which had to be kept rotating around the lamp the whole night long. Assuming a focal length of 1.5 m and a diameter of 1 m (needed to collect a good fraction of the emitted light) it is easy to estimate the mass of a lens as about 200 kg, which would need a considerable mechanism to keep it in rotation. The lens did not need to be of very high quality, since the large source inevitably results in a diverging beam, and Fresnel realized that removing parallel-sided rings of glass would not affect the optical properties. So he devised a much lighter type of lens which could be constructed from cast glass prisms and would have the same optical properties. Mathematically, it would be flat on one side and piecewise spherical on the other side, as shown in Fig. 3.7, and the first one was installed in 1823. Such lenses are now cast from plastics and are widely used for many non-critical imaging tasks, such as car headlights and solar energy collectors, because they can be made to have very large apertures without being bulky. They suffer, of course, from light scattering by the discontinuities, and for this reason are unsuitable for high-resolution tasks. One sees them in overhead projectors, for example, where the light from the lamp has to illuminate all the slide uniformly, and also be focused onto the imaging lens, but scattered light is eliminated by the finite lens aperture (Fig. 3.7(*c*)).

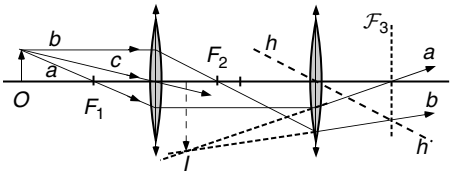

Figure 3.8
Ray-tracing through a pair of lenses.

3.3 Ray-tracing through simple systems

Paraxial ray-tracing is an important tool in optical design, and involves following through the optical system the routes of several paraxial rays leaving an off-axis point object. There are three types of rays that can be traced simply through a thin lens (see Figs. 3.5 and 3.6):

1. all rays through a focal point on one side continue parallel to the axis on the other side and vice versa;
2. any ray passing through the centre of the lens continues in a straight line;
3. all rays of a parallel bundle on one side of a lens go through a single point in the focal plane on the other side, and vice versa; the point can be found by drawing the one ray of the bundle which passes through the centre of the lens, and is therefore undeviated.

Box 3.2 An exercise in ray-tracing in a non-trivial system

This example shows how to deal with ray-tracing when several lenses are involved. We have two converging lenses separated by a distance larger than the sum of their focal lengths, and an object at a finite distance to the left of the first lens (Fig. 3.8). From the object O we follow the usual two rays, one a passing through F_1 of the first lens and one b parallel to the axis. These continue as shown, a parallel to the axis and b through F_2. On reaching the second lens, a continues through F_2 of that lens. How do we find the route of b after the second lens? We have to construct an assistant ray h which is parallel to b before the second lens, but goes through the centre of that lens. This ray continues without deviation, but because it starts parallel to b, it must intersect b in the plane $\mathcal{F}_3$. This gives the direction of b after the second lens. Finally, the intersection between a and b in the image space gives the position and size of the (virtual) image I. Now try to follow a third ray c from the object going through the centre of the first lens, which will need a different assistant ray at the second lens, and show that it leads to the same image.

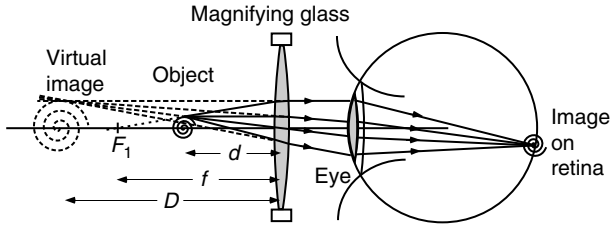

Figure 3.9

Ray diagram for a magnifying glass. The object height is y and that of the image y'. In practice, $D \gg f$ and the object distance would be nearly equal to f.

Using these rays, we can generally get a good picture of the optical properties of a complete system. We shall treat three examples, the magnifying glass, the astronomical telescope and the compound microscope; the last is essentially a combination of the first two. In the second example we shall also introduce the concepts of vignetting and stops.

3.3.1 The magnifying glass

A magnifying glass produces the largest magnification when it is closest to your eye.

The magnifying glass is the simplest optical instrument and its function should be clearly understood. Its main purpose is to create linear magnification of the retinal image of an object, and it does this by allowing us to bring it to a position well within the **near point** (the closest distance at which the eye can produce a sharply focused image, about 25 cm for young people with normal eyesight), while creating a virtual image at or beyond the near point, often at infinity. This is illustrated in Fig. 3.9.

For a magnifying glass, or any optical instrument that forms a virtual image, the **magnifying power** is a more useful quantity than the linear magnification (the ratio of image to object size). It can be defined in two equivalent ways:

1. the ratio between the angle subtended at the eye by the image and the angle that would be subtended at the eye by the object if it were situated at the near point, which is at a distance D from the eye;
2. the ratio between the linear dimensions of the retinal image produced with the instrument and those of the largest clear retinal image that can be produced without it, i.e. when the object is at the near point.

Normally the magnifying lens is close to the eye. The magnifying power is then (Fig. 3.9)

$$M = \frac{y'}{y} = \frac{D}{d}. \tag{3.9}$$

Since $1/d - 1/D = 1/f$, we find that

$$M = 1 + \frac{D}{f}; \tag{3.10}$$

usually $D \gg f$ so that the approximation $M = D/f$ can be used.

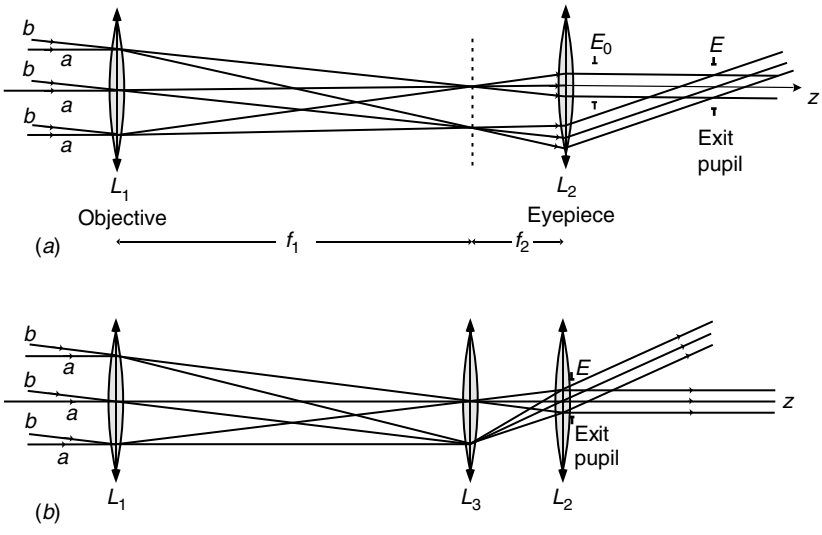

Figure 3.10

Ray-tracing through a telescope with angular magnification 3. (*a*) Simple astronomical telescope; (*b*) with the addition of a field lens. The exit pupil is at *E* in both drawings.

The single lens is used only for informal purposes. When incorporated in an instrument such as a microscope or telescope it becomes part of a compound eyepiece, as described in §3.3.2.

Refractor telescopes are rarely used in astronomy, because big lenses sag under their own weight. For terrestrial use, an additional erector lens has to be added to create an upright image.

3.3.2 The astronomical refractor telescope, and the concept of stops

A telescope converts a bundle of parallel rays making an angle α with the optical axis to a second parallel bundle with angle β. The ratio β/α is called the **angular magnification**; it equals the ratio between the retinal image sizes obtained with and without the telescope. Figure 3.10(*a*) shows a simple telescope based on two lenses, L_1 (objective) and L_2 (eyepiece) with focal lengths f_1 and f_2; the distance between the lenses is $f_1 + f_2$, so that an object at infinity produces a real image in the common focal plane.

One's first instinct is to place the eye at E_0 immediately behind L_2, but we shall see that this may unnecessarily limit the field of view. Let us try to analyze the light throughput by means of the paraxial ray diagram. A bundle of parallel rays (*aaa*) from a distant point on the optical axis enters the objective L_1 parallel to the axis and leaves through the eyepiece L_2, entering the iris of the observer's eye. Now consider a bundle of parallel rays (*bbb*) from a second distant point, not on the axis. We assume, for the moment, that the aperture of L_2 is very large. The rays enter L_1 at an angle to the axis, and may miss the iris E_0 because of its limited size. This is called **vignetting** (§3.1.1). However, it should be clear from the diagram that if we move the eye further back from L_2, so that the iris is now at E, rays from the oblique bundle (*bbb*) will also enter it.

From the figure, one can see that E is in the plane of the image of L_1 formed by L_2; this image is called the **exit pupil**, which will be defined formally below. Positioning the eye in the plane of the exit pupil allows it to receive light from off-axis points and thus maximizes the field of view.

Now we have assumed so far that the aperture of L_2 was very large, and did not limit the light throughput. If L_2 is finite in size, vignetting of the oblique bundle might occur there. To avoid that problem, we need to add another lens L_3, called a **field lens** (Fig. 3.10(*b*)). This is placed in the common focal plane, where it has no effect on the intermediate image, and is designed to create an image of L_1 on L_2. Then, it is easy to see that an oblique bundle of rays entering L_1 must leave through the centre of L_2. The exit pupil has now been moved to coincide with L_2 and so in this case the best place for the eye is indeed close behind L_2. Vignetting can now occur at the field lens, but since this is in the intermediate image plane its aperture simply forms a sharp edge to the image, which limits the angular field of view. This is called a **field stop**, and an actual ring aperture is usually placed there for aesthetic reasons.

In the end, certain practical considerations win, and it is usual to put the exit pupil somewhat behind L_2, for the observer's comfort, and to place the field lens not quite in the intermediate image plane, so that dust on it will not spoil the image and also to allow cross-hairs or a reticle scale to be placed in the field stop itself. Both of these compromises require that the lenses be slightly larger than the absolute minimum requirement.

3.3.3 Stops and pupils

The aperture stop, entrance pupil and exit pupil are in conjugate planes.

It is useful, in discussing optical instruments, to have some additional definitions at our disposal, some of which have already been introduced. The aperture that limits the amount of light passing through an optical instrument from a point on its axis is called the **aperture stop**; in this case it is L_1 (if L_2 is slightly larger than needed), but can in principle be any aperture or lens in the instrument. A complex optical system is usually designed so that the most expensive item, or the one most problematic to design, is the aperture stop, so that it can be fully used.[2] The image of the aperture stop in the optical elements following it is then the exit pupil. Clearly, the eye or a camera lens should be placed at this position. If the aperture stop is not the first element in the system, then the image of the aperture stop in the lenses *preceding* it is called the **entrance pupil**. The theory of stops has many other applications; for example, a camera lens always includes an adjustable aperture stop, which controls the

[2] Two examples: a large-aperture telescope mirror or lens will always be made the aperture stop because of its cost. In optical systems involving mechanical scanners, the scanner is usually the aperture stop so as to minimize its size and hence its moment of inertia.

light intensity in the film plane, and whose position within the compound lens is calculated to give a uniformly bright image at off-axis points. The aperture is often expressed in terms of a dimensionless number, the **f-number** or 'f/#' of the lens, defined as the ratio of focal length f to aperture-stop diameter D (*small* f-number means *large* aperture). In addition, the brightness of the image, which determines the exposure needed in photography, is proportional to the area of the lens aperture divided by the square of the distance to the sensor, i.e. to $(\text{f/\#})^{-2}$.

We should also point out that ray-tracing allows the designer to calculate the optimum sizes for the components. For example, in the case of the telescope, since the size of the pupil of the observer's eye is given anatomically, this in turn determines the sizes of L_1 and L_2 that can be utilized for a given magnification.

The field lens and the eyepiece are often combined in a single unit called a **compound eyepiece**, or simply eyepiece for short. This has several advantages, amongst them the possibility of using the two lenses to correct aberrations, and the inclusion of a field stop which defines the field of view and can often be useful in obstructing stray light reflected or scattered by the various components of a system.

The relationship between f/# and depth of focus is often used by photographers for aesthetic purposes.

3.3.4 Depth of focus

Although the focal or image plane is an exact mathematical plane for an ideal lens in geometrical optics, in reality this is of course not so because of physical optics. The practical accuracy to which the position of this plane can be determined depends on the aperture D of the lens. Then, rays converge on the focus within a cone, whose angle is given by the aperture of the lens and for small angles is $D/f = (\text{f/\#})^{-1}$. At distance δz from the focus, the geometrical diameter of the image spot is then $\delta z\, D/f$. If this diameter is smaller than the diffraction-limited spot diameter $1.22 f\lambda/D$ (§12.2), there will be no significant deterioration of the image compared to the focal plane. Twice the distance at which the geometrical and diffraction-limited diameters are equal (because δz can be either positive or negative) is called the **depth of focus**. From the above, this has the value:

$$\text{depth of focus} \approx \frac{2.4\lambda f^2}{D^2} = 2.4\lambda(\text{f/\#})^2. \tag{3.11}$$

A different approach, giving a similar result, was given in Chapter 2 as an example of Fermat's principle. Of course the size of the image in the focal plane may also be affected by residual aberrations, in which case the depth of focus becomes larger.

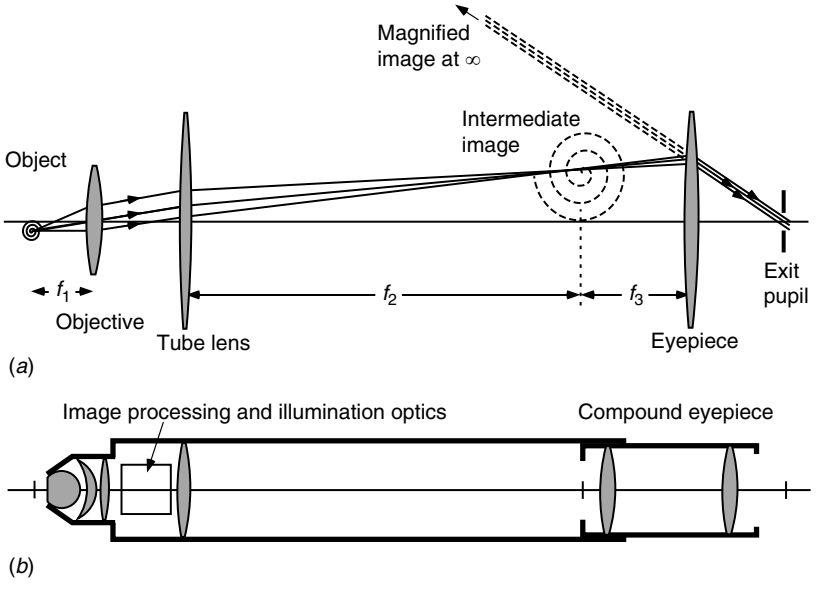

Figure 3.11

(*a*) Ray diagram for a microscope showing position of the exit pupil. (*b*) Basic structure of a microscope for visual observations, showing image-processing optics and a compound eyepiece. When a camera is used, its sensor surface (film or electronic device) is often placed in the field stop position.

3.3.5 The microscope

The essential principle of the microscope is that an objective lens with very short focal length (often a few mm) is used to form a highly magnified real image of the object. Here, the quantity of interest is **linear magnification**, and this number is generally inscribed on the objective lens casing. In practice, today, this magnification is carried out by means of two lenses: the objective lens which creates an image at infinity, and a second weak **tube lens** which then forms a real image in its focal plane. The distance between the two lenses is not important, and the linear magnification is easily seen to be the ratio between the focal lengths of the two lenses. The object is then exactly in the focal plane of the objective. In more primitive microscopes, the pair of lenses was replaced by a single lens, but the two-lens system used today has the advantage that further components such as beamsplitters, polarizers etc. can be placed between the objective and the tube lens; these are used for illumination of the object and various spatial-filtering operations which will be discussed in Chapter 12. Such components do not affect the geometrical principle of the microscope, but their design is simpler if they operate in parallel light. In the focal plane of the tube lens, a photographic film or electronic image sensor can be situated. For visual observation, an eyepiece is used to magnify the image further, and the ray diagram for this case is shown in Fig. 3.11. Clearly, the tube lens and eyepiece together have the structure of a telescope, observing the virtual image of the sample at infinity provided by the objective lens.

A microscope objective is usually labelled with the magnification obtained with a standard tube lens of 160 or 200 mm focal length; this magnification,

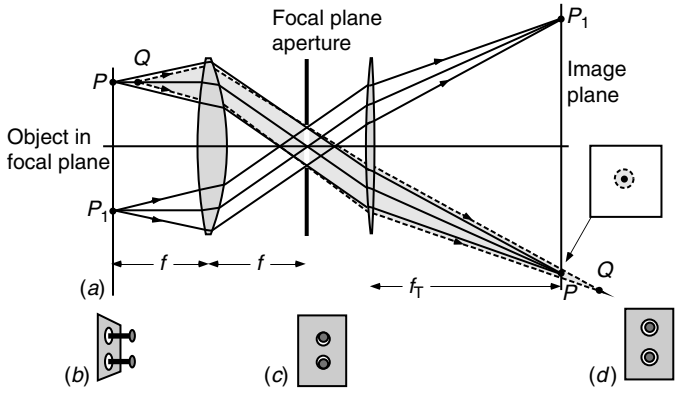

Figure 3.12

Principle of a telecentric metrology imaging system. (*a*) Optical ray diagram, showing imaging of points *P*, P_1 in the focal plane and *Q* out of the focal plane; (*b*) a pair of nails and (*c*) how they are seen by a non-telecentric system; (*d*) the same object as seen by a telecentric system.

which is generally a number up to 100, can then be multiplied by the eyepiece magnification. After the tube lens, the ray diagram is identical to that of a telescope, and the same considerations about field lens and exit pupil apply. Because of its intricate design and the need to use large angles of refraction, the design centres around the objective, which contains the aperture stop within it. It will be seen that the final image is virtual and inverted.

Box 3.3 A telecentric microscope for metrology applications

Metrological optical systems are geared towards measuring the dimensions of three-dimensional objects. This requires both absence of distortion across the field of view and a magnification that is independent of the depth dimension. These can be achieved if we limit the rays forming the image to an identical cone from every point on the object, which we do by putting a small aperture in the back focal plane of the objective lens. Figure 3.12(*a*) shows a ray diagram for such a system, called a telecentric system. Since the axes of the cones of light from all the object points such as *P* and P_1 are parallel, clearly the magnification does not depend on the depth, eliminating perspective effects, which are undesirable in metrology. However, the depth of focus is still given by (3.11) where the aperture stop diameter is that of the aperture in the focal plane. This means the object can be out of focus but retains the correct shape. Then the blurring introduced by the defocus (inset on the right of (*a*)) is symmetrical and field independent, which makes it easier to correct by image processing.

What is the price we pay for having such a system? The light throughput and resolution are poor because of the small aperture, despite the fact that the objective lens has to be as large as the field of view, which, for large objects, is a great disadvantage. Moreover, we have not addressed the issue of distortion, and in practice the design of a good telecentric lens system without distortion and other aberrations is quite complex.

The objects typically observed through a microscope contain detail as small as, or smaller than, the wavelength of light, and so geometrical optics only gives us a very general description of the imaging process. A full picture of the capabilities and limitations of microscope imaging only emerges with the use of wave optics. This will be described in Chapter 12.

3.4 The matrix formalism of the Gaussian optics of axially symmetric refractive systems

It is very cumbersome to extend the algebraic type of analysis we saw in §3.2 to more complicated systems. A much more convenient method, which utilizes the fact that equations (3.2)–(3.10) are linear as a result of the approximation (3.1), uses matrices to make the calculation of the optical properties of even the most complicated systems quite straightforward, and is also particularly convenient for numerical computations (Problem 3.14).

The propagation of a ray through an axially symmetric system of lenses consists of successive refractions and translations. As mentioned earlier, the direction of propagation of a ray through the system will be taken from left to right. We shall treat only rays that lie in a plane containing the optical axis z; we shall ignore what are called **skew rays**, which are defined as rays that are incident in a plane that does not include the optical axis, and that add no new information in the paraxial approximation.[3] Since the system has rotational symmetry around z, a ray at $z = z_0$ is specified if we know its algebraic distance y from the axis and its inclination $\mathrm{d}y/\mathrm{d}z = \theta$; it is therefore sufficient to follow the rays in one (y, z) plane.

We encourage the reader to write a short computer code to study paraxial optics. It helps a lot in following the ideas and solving problems.

3.4.1 The translation and refraction matrices

Let us consider first a ray that propagates in a straight line in a uniform medium of index n (Fig. 3.13(a)). It has height y_1 and inclination θ_1 at $z = z_1$, and y_2 and $\theta_2 = \theta_1$ at $z_2 = z_1 + t$. Then

$$y_2 = y_1 + t\theta_1, \tag{3.12}$$

$$\theta_2 = \theta_1. \tag{3.13}$$

[3] The projection of a skew ray on any plane containing the optical axis is itself a valid ray in the paraxial approximation. This is not true at large angles.

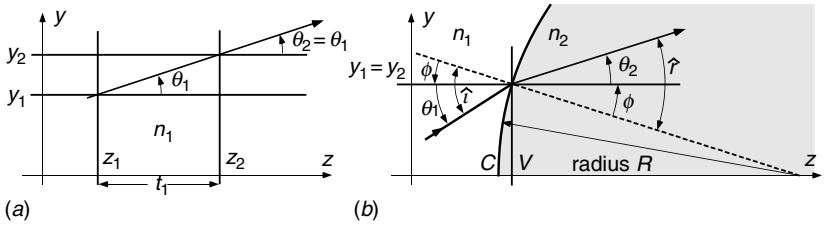

Figure 3.13

(*a*) Paraxial diagram for the translation matrix. (*b*) Paraxial diagram for the refraction matrix; in the spirit of Gaussian optics, where $R \gg h$, points *V* and *C* coincide.

These equations can be described by the matrix equation between vectors $(y, n\theta)$:[4]

$$\begin{pmatrix} y_2 \\ n\theta_2 \end{pmatrix} = \begin{pmatrix} 1 & t/n \\ 0 & 1 \end{pmatrix} \begin{pmatrix} y_1 \\ n\theta_1 \end{pmatrix} = \mathsf{T} \begin{pmatrix} y_1 \\ n\theta_1 \end{pmatrix} \tag{3.14}$$

which defines T, the **translation matrix** from z_1 to z_2.

A second matrix describing the refraction as a ray passes through a surface with radius R from a medium with index n_1 to a medium with index n_2 is derived as follows (see Fig. 3.13(*b*)). Snell's law $n_1 \sin\hat{\imath} = n_2 \sin\hat{r}$ gives

$$n_1 \sin(\phi + \theta_1) = n_2 \sin(\phi + \theta_2), \tag{3.15}$$

which becomes, for small angles,

$$n_1\phi + n_1\theta_1 = n_2\phi + n_2\theta_2. \tag{3.16}$$

With $\phi = y_1/R$ we get

$$n_2\theta_2 = n_1\theta_1 - (n_2 - n_1)y_1/R. \tag{3.17}$$

Note that $\phi > 0$. Since z_1 and z_2 coincide we have $y_1 = y_2$ and so we can define a **refraction matrix** R by the following equation:

$$\begin{pmatrix} y_2 \\ n_2\theta_2 \end{pmatrix} = \begin{pmatrix} 1 & 0 \\ \dfrac{n_1 - n_2}{R} & 1 \end{pmatrix} \begin{pmatrix} y_1 \\ n_1\theta_1 \end{pmatrix} = \mathsf{R} \begin{pmatrix} y_1 \\ n_1\theta_1 \end{pmatrix}. \tag{3.18}$$

A general matrix M_{21} which connects a ray at z_1 with its continuation at z_2 performs the operation

$$\begin{pmatrix} y_2 \\ n_2\theta_2 \end{pmatrix} = \mathsf{M}_{21} \begin{pmatrix} y_1 \\ n_1\theta_1 \end{pmatrix}, \tag{3.19}$$

where M_{21} is a product of T and R matrices. Since $\det\{\mathsf{R}\} = \det\{\mathsf{T}\} = 1$, $\det\{\mathsf{M}_{21}\} = 1$. **We used the combination $n\theta$, and not θ alone, to make these determinants unity**.

[4] We use the product $n\theta$ rather than θ alone for later convenience, since then the determinants of all our matrices will be unity. This convention is not universally used in textbooks.

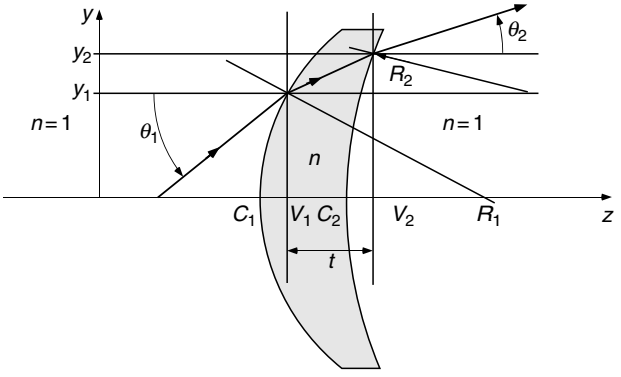

Figure 3.14
Ray diagram for image formation by a thin lens in air with all quantities positive. In the spirit of the Gaussian approximation, V_1 and C_1 coincide, as do V_2 and C_2.

3.4.2 Matrix representation of a simple lens

As we saw in §3.2 a simple lens consists of an optically transparent medium, with refractive index n, bounded by two spherical surfaces (Fig. 3.14). The line joining the centres of the two spheres defines the optical axis z, and the system is symmetric about it. Initially we shall assume that the medium outside the lens has unit refractive index. The vertices of the lens (the points at which the surfaces cut the axis) are z_1 and z_2 where $t = z_2 - z_1$. The matrix M_{21} between $z = z_1$ and $z = z_2$ is derived as follows:

$$\begin{aligned}\begin{pmatrix} y_2 \\ \theta_2 \end{pmatrix} &= \begin{pmatrix} 1 & 0 \\ \dfrac{n-1}{R_2} & 1 \end{pmatrix} \begin{pmatrix} 1 & t/n \\ 0 & 1 \end{pmatrix} \begin{pmatrix} 1 & 0 \\ \dfrac{1-n}{R_1} & 1 \end{pmatrix} \begin{pmatrix} y_1 \\ \theta_1 \end{pmatrix} \\ &= \mathsf{M}_{21} \begin{pmatrix} y_1 \\ \theta_1 \end{pmatrix}, \end{aligned} \tag{3.20}$$

where

$$\mathsf{M}_{21} = \begin{pmatrix} 1 + \dfrac{t(1-n)}{nR_1} & t/n \\ (n-1)\left(\dfrac{1}{R_2} - \dfrac{1}{R_1}\right) - \dfrac{t(1-n)^2}{R_1 R_2 n} & 1 + \dfrac{(n-1)t}{R_2 n} \end{pmatrix}. \tag{3.21}$$

For a thin lens we assume that t is small enough for the second term in the lower left element to be negligible; since $n - 1$ is of the order of 1, this means that $t \ll |R_1 - R_2|$. Then, putting $t = 0$, we have

$$\mathsf{M}_{21} = \begin{pmatrix} 1 & 0 \\ (n-1)\left(\dfrac{1}{R_2} - \dfrac{1}{R_1}\right) & 1 \end{pmatrix} = \begin{pmatrix} 1 & 0 \\ -\dfrac{1}{f} & 1 \end{pmatrix}, \tag{3.22}$$

where the focal length is the same as that defined in (3.7). We emphasize that the matrix M_{21} summarizes what we already expect from a thin lens in air:

1. An incident ray parallel to the axis at height y_1, i.e. $(y_1, 0)$, leaves the lens at the same height, but is tilted downwards, if f is positive, to cut the axis at distance f, and is represented by $(y_1, -y_1/f)$ on exiting the lens.
2. If $R_1 = R_2$, we have a spherical shell. We might expect this to have infinite focal length, but t cannot be neglected (since $R_1 - R_2 = 0$) and the full expression for f from (3.21) must be used (Problem 3.12).
3. If $R_1^{-1} > R_2^{-1}$, as in Fig. 3.14, and $n > 1$, the lens is converging. This relationship means that the lens is thickest in the centre.

If the lens is surrounded by media of refractive indices n_1 on the left and n_2 on the right, it is easy to repeat the calculation and show that, in the case where t is negligible,

$$\begin{pmatrix} y_2 \\ n_2\theta_2 \end{pmatrix} = \mathsf{M}_{21} \begin{pmatrix} y_1 \\ n_1\theta_1 \end{pmatrix}, \tag{3.23}$$

$$\text{where} \quad \mathsf{M}_{21} = \begin{pmatrix} 1 & 0 \\ \dfrac{n - n_2}{R_2} + \dfrac{n_1 - n}{R_1} & 1 \end{pmatrix}. \tag{3.24}$$

We shall return to this situation in §3.6.2.

3.4.3 Object and image space

A system of lenses is limited by its left and right vertices, V_1 and V_2. It is useful to define the **object space** as a space with origin at V_1 and the **image space** with origin at V_2. To the left of V_1 we can put a real object, and we can project a real image onto a screen if it is to the right of V_2. Both spaces also have 'virtual' parts. For instance, a virtual image can be formed to the left of V_2 by a magnifying glass, but one cannot put a screen at the location of this image; similarly, a virtual object can be produced to the right of V_1 by some preceding optics.

3.5 Image formation

The matrix $[AB, CD]$ defined here relates conjugate planes.

The formation of images is the most common task of an optical system, and we shall now see how it is described by the matrices. Consider a general system, extending from z_O to z_I and described by the matrix $\mathsf{M}_{21} = \begin{pmatrix} A & B \\ C & D \end{pmatrix}$. This matrix performs the operation

$$\begin{pmatrix} y_2 \\ n_2\theta_2 \end{pmatrix} = \begin{pmatrix} A & B \\ C & D \end{pmatrix} \begin{pmatrix} y_1 \\ n_1\theta_1 \end{pmatrix}. \tag{3.25}$$

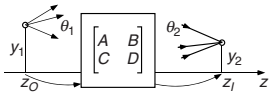

Figure 3.15

Matrix for imaging between conjugate planes z_O and z_I. All rays leaving the object point arrive at the same image point independent of the angle θ_1.

If this system forms at z_I an image of an object at z_O, then the (x,y) planes at z_O and at z_I are called **conjugate planes**. Imaging means that y_2 must be independent of $n_1\theta_1$; in other words, **all rays leaving a point** (y_1, z_O) **in any direction** θ **must arrive at the same point** (y_2, z_I) (Fig. 3.15).

Since the point of arrival is independent of the angle θ_1, B **must be 0**. It then follows, since the determinant of M_{21} is unity, that $AD = 1$. The **linear magnification** produced by the system is

$$m = \frac{y_2}{y_1} = A. \tag{3.26}$$

A ray originating at $(0, z_O)$ with angle θ_1 will pass through $(0, z_I)$ with angle θ_2. The ratio between the ray angles is the **angular magnification**:

$$\frac{\theta_2}{\theta_1} = D\frac{n_1}{n_2} = \frac{1}{m}\frac{n_1}{n_2}. \tag{3.27}$$

Notice that when $n_1 = n_2$, **the angular magnification is the reciprocal of the linear magnification**.

3.5.1 Imaging by a thin lens in air

Now let us return to the thin lens (§3.4.2). We put an object at $z_O = u$ (where u is negative), a thin lens at $z = 0$ and find an image at $z_I = v$. Using (3.22), we write the matrix of the complete system of Fig. 3.14:

$$\begin{pmatrix} A & B \\ C & D \end{pmatrix} = \begin{pmatrix} 1 & v \\ 0 & 1 \end{pmatrix}\begin{pmatrix} 1 & 0 \\ -1/f & 1 \end{pmatrix}\begin{pmatrix} 1 & -u \\ 0 & 1 \end{pmatrix}$$

$$= \begin{pmatrix} 1 - v/f & -u + v + vu/f \\ -1/f & 1 + u/f \end{pmatrix}. \tag{3.28}$$

Since the system is image-forming,

$$B = -u + v + vu/f = 0, \tag{3.29}$$

$$\text{or} \quad -\frac{1}{u} + \frac{1}{v} = \frac{1}{f}. \tag{3.30}$$

We have therefore recovered (3.6). The linear magnification is $m = 1 - v/f = v/u$ while for a ray with $y_1 = 0$ the angular magnification is $1 + u/f = 1/m = u/v$.

Another way of expressing the imaging comes from the fact that if $B = 0$, then $AD = 1$. Therefore we have

$$(1 - v/f)(1 + u/f) = 1, \tag{3.31}$$

$$\text{or} \quad (f - v)(u + f) = f^2, \tag{3.32}$$

which is called **Newton's equation**. Remember that u is negative. This equation is very useful; we shall see that it applies to any lens, not just a thin lens, and

its usefulness derives from the fact that it does not refer to the vertices of the lens, but only involves the image point, object point and foci. We emphasize that (3.30) and (3.32) are not independent, but each can be derived from the other.

Telescopic mirror systems (Cassegrain, Gregorian) are often used because they are achromatic, and also can be applied to UV and IR radiations that are not transmitted by glass.

3.5.2 Telescopic or afocal systems

If $C = 0$, θ_2 does not depend on y_1 and a bundle of parallel rays entering the system will emerge as a bundle of parallel rays, but at a different angle. A system with this property is called **telescopic** or **afocal**. From an object at infinity it creates an image at infinity. Two common telescopic systems are the simple astronomical telescope (§3.3.2) and the Galilean telescope (Problem 3.4).

3.6 The cardinal points and planes

Let us consider an imaging lens system in air that is represented, between its vertices V_1 at z_1 and V_2 at z_2, by the general matrix $\mathsf{M}_{21} = \begin{pmatrix} a & b \\ c & d \end{pmatrix}$, which replaces $\begin{pmatrix} 1 & 0 \\ -1/f & 1 \end{pmatrix}$ of the thin lens in air from §3.5.1 (Fig. 3.16(*a*)). Instead of (3.28) we then have

$$\begin{pmatrix} A & B \\ C & D \end{pmatrix} = \begin{pmatrix} 1 & v \\ 0 & 1 \end{pmatrix} \begin{pmatrix} a & b \\ c & d \end{pmatrix} \begin{pmatrix} 1 & -u \\ 0 & 1 \end{pmatrix}$$

$$= \begin{pmatrix} a + vc & b - au + v(d - cu) \\ c & d - cu \end{pmatrix}, \tag{3.33}$$

where we recall that u and v are measured from V_1 and V_2 respectively in the positive z-direction.

Once again, the imaging condition is represented by $B = 0$, which leads to

$$b - au + vd - vcu = 0. \tag{3.34}$$

If $B = 0$, it follows again that $AD = 1$, which gives

$$(a + vc)(d - cu) = 1. \tag{3.35}$$

The clue to simplification is then given by comparing (3.35) with Newton's equation (3.32) for the thin lens. Clearly the two are similar when we write (3.35)

$$(fa - v)(fd + u) = f^2, \tag{3.36}$$

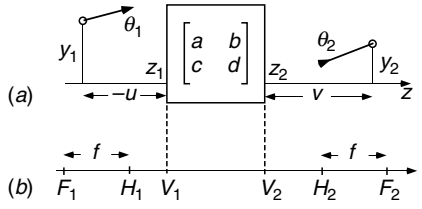

Figure 3.16
(*a*) Matrix for the optical system, between vertices V_1 and V_2. (*b*) The focal (*F*) and principal (*H*) points.

where we define $-1/c$ as the focal length (or the **effective focal length**) f, as it was for the thin lens. By putting $v = \infty$ and $u = -\infty$ respectively, the **focal points** F_1 and F_2 are then found to be at $z_1 + d/c$ and $z_2 - a/c$. Next we write (3.36) in the form

$$\{f - [v - (a-1)f]\}\{f + [u - (1-d)f]\} = f^2, \tag{3.37}$$

and use the definitions

$$u_\mathrm{p} = (d-1)/c, \tag{3.38}$$

$$v_\mathrm{p} = (1-a)/c, \tag{3.39}$$

$$f = -1/c, \tag{3.40}$$

to write this as

$$[f - (v - v_\mathrm{p})][f + (u - u_\mathrm{p})] = f^2. \tag{3.41}$$

This is the same as Newton's equation provided we measure the object and image distances from the **principal points** H_1 at $z = z_1 + u_\mathrm{p}$ and H_2 at $z = z_2 + v_\mathrm{p}$ respectively. Equation (3.37) can then be written (cf. (3.30))

$$-\frac{1}{u - u_\mathrm{p}} + \frac{1}{v - v_\mathrm{p}} = \frac{1}{f}. \tag{3.42}$$

It is easy to show from the above equations that the linear magnification is now $m = A = (v - v_\mathrm{p})/(u - u_\mathrm{p})$ and the angular magnification, as usual, is $1/m$.

The **principal planes** $\mathcal{H}_1$ and $\mathcal{H}_2$, normal to z through H_1 and H_2, are defined in many texts as conjugate planes with unit magnification. On substituting $u = u_\mathrm{p}$, $v = v_\mathrm{p}$ into (3.33) we find immediately:

$$\begin{pmatrix} A & B \\ C & D \end{pmatrix} = \begin{pmatrix} 1 & 0 \\ C & 1 \end{pmatrix}; \tag{3.43}$$

and see that the principal planes are indeed conjugate ($B = 0$) with unit linear and angular magnifications ($A = 1$). We remind the reader that positive unit magnification means that an *upright* image of the same size as the object is formed. There is a situation that might be confused with this where $u - u_\mathrm{p} = -2f$, $v - v_\mathrm{p} = 2f$, but this has magnification -1.

The cardinal points of a lens system describe it completely for paraxial optics, but not for large-angle optics.

The four points H_1, H_2, F_1 and F_2 are four of six **cardinal points** that represent the lens system matrix for ray-tracing purposes (Fig. 3.16(*b*)). The other two (nodal points N_1 and N_2, which coincide with H_1 and H_2 when the object and image spaces have the same refractive index) will be discussed later (§3.6.2). We summarize the positions of the principal and focal points in terms of the matrix elements of the system, emphasizing that it is immersed in a medium of unit refractive index.

- Principal points: H_1 at $z = (d-1)/c + z_1$, H_2 at $z = (1-a)/c + z_2$.
- Focal points: F_1 at $z = d/c + z_1$, F_2 at $z = -a/c + z_2$.

Clearly, $F_1H_1 = H_2F_2 = -1/c = f$, so that each focal point is a distance f from the related principal point.

3.6.1 Geometrical meaning of the focal and principal points

If a bundle of rays parallel to z enters the lens system, we have $u = -\infty$, whence $v - v_p = f$ so that the bundle is focused to F_2. An oblique incident bundle at angle α focuses to $y = \alpha f$ in the **focal plane**, $\mathcal{F}_2$, which is normal to z through F_2. Similarly, any ray passing through F_1 leaves the system parallel to the axis and the focal plane $\mathcal{F}_1$ is normal to z through F_1. These are just like in a thin lens.

For a thin lens, $\mathcal{H}_1$ and $\mathcal{H}_2$ are both in the plane of the lens but in a general lens system they may be somewhere else (see example in §3.6.4). They generally do not coincide. Since F_1 is at a distance f to the left of $\mathcal{H}_1$, $\mathcal{H}_1$ can be interpreted as **the position of the thin lens of focal length f which would focus light from a point source at F_1 to a parallel beam travelling to the right**; similarly, $\mathcal{H}_2$ is the plane of **the same thin lens when it is required to focus a parallel beam incident from the left to F_2**.

For the purposes of ray-tracing through a lens system in air we use the cardinal points as follows (Fig. 3.17(*a*)). Any incident ray (1) passing through F_1 leaves the system parallel to the axis at the height it reaches $\mathcal{H}_1$, as if there were a thin lens in that plane. Likewise, a ray (2) incident from the left and parallel to the axis goes through F_2 as if it had been refracted by a lens in $\mathcal{H}_2$. Any incident ray (3) through the point H_1 exits through H_2 since $\mathcal{H}_1$ and $\mathcal{H}_2$ are conjugate; moreover, the incident and exiting rays are parallel because the angular magnification between the principal planes of a system in air is unity. Thus any ray through the system can be traced by finding its intersection with $\mathcal{H}_1$, and continuing it from $\mathcal{H}_2$ at the same height (unit magnification), using an auxiliary parallel ray through a focus to help find the exit direction.

A convenient way to visualize ray tracing through a complete system in air is carried out by the following steps, shown schematically in Fig. 3.17(*b*). Given the data on the system,

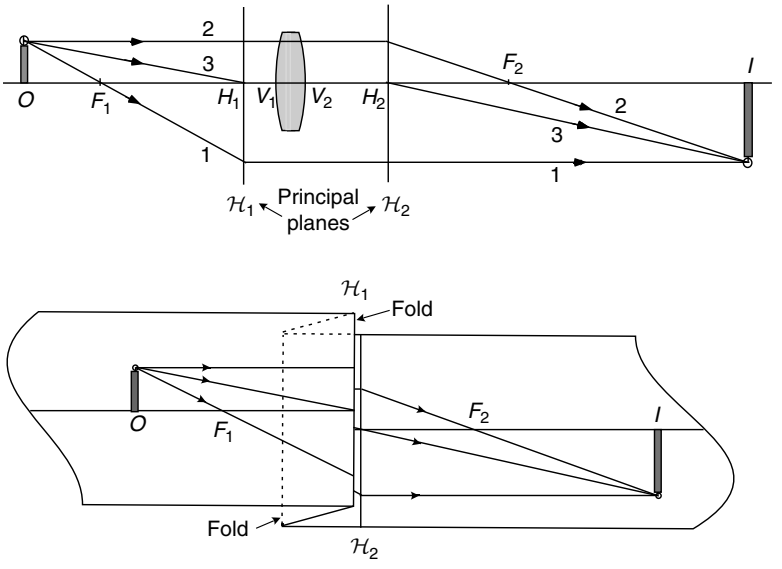

Figure 3.17

(*a*) Tracing rays through a general optical system in air, using the principal and focal points. (*b*) The paper-folding method.

1. find the cardinal points, F_1, F_2, H_1 and H_2, and mark them along the z-axis on a piece of paper, together with V_1 and V_2;
2. fold the paper so that the planes $\mathcal{H}_1$ and $\mathcal{H}_2$ coincide, and the z-axis remains continuous (this needs two parallel folds, one along $\mathcal{H}_1$ and the other along the mid-plane between $\mathcal{H}_1$ and $\mathcal{H}_2$);
3. trace rays as if the (coincidental) principal planes were a thin lens (§3.3);
4. unfold the paper. The rays that are drawn on it represent their paths outside V_1V_2. Within V_1V_2, further information is necessary to complete them (see §3.6.4 for an example).

3.6.2 Lens systems immersed in media: nodal points

Although many optical systems have $n = 1$ in both object and image spaces, this is not a requirement. Indeed, the eye has vitreous fluid ($n = 1.336$) in the image region. The most general system will have $n = n_1$ in its object space and $n = n_2$ in its image space. The thin lens of §3.4.2 then has a matrix (3.24):

$$\mathsf{M}_{21} = \begin{pmatrix} 1 & 0 \\ \frac{n-n_2}{R_2} + \frac{n_1-n}{R_1} & 1 \end{pmatrix}, \tag{3.44}$$

where n is the refractive index of the lens material. Its focal length is f, where

$$-\frac{1}{f} = \frac{n-n_2}{R_2} + \frac{n_1-n}{R_1}. \tag{3.45}$$

Replacing u by u/n_1 and v by v/n_2 in the matrices of (3.28) gives immediately

$$-\frac{n_1}{u}+\frac{n_2}{v}=\frac{1}{f}. \tag{3.46}$$

The focal lengths are then $n_1 f$ and $n_2 f$ on the left and right. For the general system described by (3.33) we use the same replacement and the following results can be derived straightforwardly. Newton's equation (3.32) becomes

$$\left(\frac{-an_2}{c}-v\right)\left(\frac{-dn_1}{c}+u\right)=\frac{n_1n_2}{c^2}=n_2n_1f^2. \tag{3.47}$$

Once again, we have principal planes $\mathcal{H}_1$ and $\mathcal{H}_2$ in the positions of thin lenses equivalent to the system we had in §3.6.1. Now $\mathcal{H}_1$ is at $z=z_1+n_1(d-1)/c$ and $\mathcal{H}_2$ is at $z=z_2+n_2(1-a)/c$. As before the planes $\mathcal{H}_1$ and $\mathcal{H}_2$ are conjugate with unit linear magnification. But the angular magnification between the principal planes is now, from (3.27),

$$Dn_1/n_2=n_1/n_2, \tag{3.48}$$

which is not unity. In order to complete the ray tracing by the method described in §3.6.1, we need to locate a pair of conjugate axial points N_1 and N_2 at z_1+u_N and z_2+v_N (the **nodal points**) related by unit *angular* magnification. This requires $D=1/A=n_2/n_1$, whence

$$A=\frac{n_1}{n_2}=a+\frac{v_Nc}{n_2}\Rightarrow v_N=\frac{n_1-n_2a}{c}, \tag{3.49}$$

$$D=\frac{n_2}{n_1}=d-\frac{u_Nc}{n_1}\Rightarrow u_N=\frac{n_1d-n_2}{c}. \tag{3.50}$$

Simple subtraction gives $H_1N_1=H_2N_2=(n_1-n_2)/c$. We leave the reader to devise a paper-folding method of ray-tracing (§3.6.1) when $n_1\neq n_2$. It involves two separate folding procedures.

3.6.3 Example: A meniscus lens

A simple experiment will show that the principal planes of a meniscus lens, an asymmetrical lens having the centres of curvature of both surfaces on the same side of it, do not coincide with its plane. You can see this by determining the two focal points of a strong, thick, positive spectacle lens (reading glasses) by imaging a bright distant object. It is easy to see that they are not the same distance from the lens. Since the object and image spaces are both in air, this is an indication that the principal planes are not symmetrical.

A numerical example will show that the principal planes are both displaced to one side of the meniscus lens. A lens with radii of curvature 50 and 100 mm (both positive) made from glass with refractive index $n=1.5$, 7.5 mm thick on the axis, has matrix representation

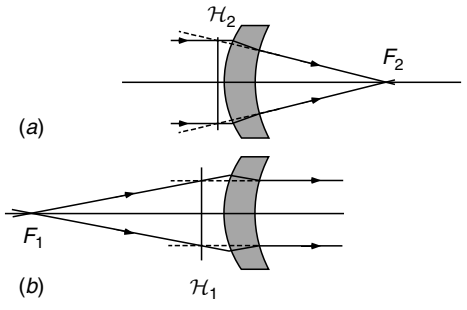

Figure 3.18
A positive meniscus lens. (*a*) Parallel rays entering from the left, showing the principal plane $\mathcal{H}_2$; (*b*) parallel rays exit from the right, showing the principal plane $\mathcal{H}_1$.

$$\begin{pmatrix} 1 & 0 \\ \frac{0.5}{100} & 1 \end{pmatrix} \begin{pmatrix} 1 & \frac{7.5}{1.5} \\ 0 & 1 \end{pmatrix} \begin{pmatrix} 1 & 0 \\ \frac{-0.5}{50} & 1 \end{pmatrix}$$
$$= \begin{pmatrix} 0.95 & 5 \\ -0.00525 & 1.025 \end{pmatrix} = \begin{pmatrix} a & b \\ c & d \end{pmatrix}. \tag{3.51}$$

From the values of a, b, c and d we find that the principal planes are at $z_1 - 5$ mm and at $z_2 - 10$ mm, both of which are to the left of the lens and are separated by 2.5 mm (Fig. 3.18). This displacement is large enough to be appreciated in a qualitative manner.

3.6.4 Example: The telephoto and zoom lens systems, and Cassegrain telescopes

A more dramatic demonstration of the function of the cardinal planes is provided by a telephoto system. This can be defined as a system where the effective focal length $-1/c$ is considerably larger than the physical distance V_1F_2 between the front vertex and the back focal plane. For this reason, it is widely used in cameras to achieve a relatively short lens system with a long focal length, thus creating a highly magnified image on the film or sensor. Usually the positions of the component lenses can be varied mechanically so as to obtain a variable focal length, with the image plane remaining fixed on the sensor, and is called a **zoom lens** (Fig. 3.1). An example of the basic telephoto system is shown in Fig. 3.19. When the lenses are exchanged by curved mirrors, the telephoto system is called a **Cassegrain telescope** (Fig. 3.20). This design is almost invariably used for astronomical telescopes with apertures greater than about 20 cm. Actually, the Cassegrain telescope has no aberrations for an image on the optical axis if the primary mirror has the form of a paraboloid and the secondary a hyperboloid, where the two foci of the hyperboloid are located at the focus of the paraboloid and at the image respectively.[5]

[5] A larger aberration-free field of view is obtained when both mirrors have a hyperboloidal shape, and the configuration is then called a Ritchey–Chrétien telescope, but we do not know of an intuitive way of seeing this. The Hubble Space Telecope has this design.

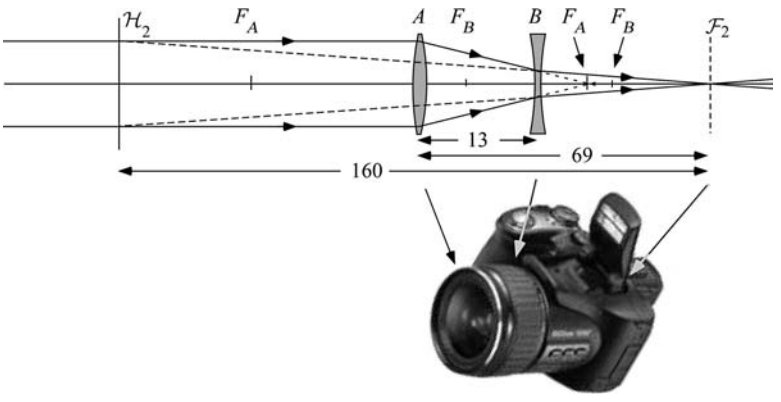

Figure 3.19

A telephoto system with effective focal length 160 mm, made of two lenses *A* and *B* having focal lengths 20 mm and −8 mm respectively, separated by 13 mm. Cardinal planes $\mathcal{H}_2$ and $\mathcal{F}_2$, and ray-trace for an axial object at $u = -\infty$. The equivalent thin lens at $\mathcal{H}_2$ would refract the rays as shown by the broken lines between $\mathcal{H}_2$ and *B*. The dimensions correspond roughly to the camera pictured below.

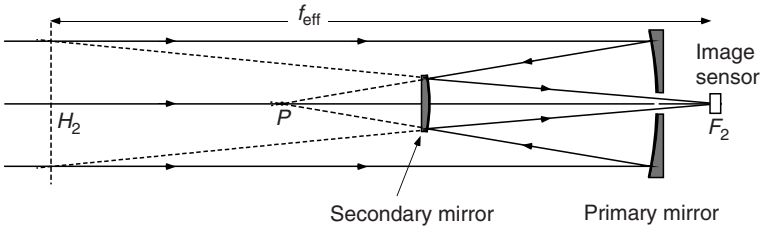

Figure 3.20

Optics of a Cassegrain telescope. The primary mirror has an axial hole. The effective focal length is H_2F_2; to show geometrically the position of H_2, we have had to break the axes. The primary mirror is a paraboloid with focus at *P* and the secondary is one sheet of a hyperboloid-of-two-sheets with foci at *P* and F_2.

The telephoto system consists of a pair of thin lenses A and B, the weaker one being converging ($f_A > 0$) and the stronger one diverging ($f_B < 0$). They are separated by a distance l which is somewhat greater than $f_A + f_B$, and the combination acts as a weak converging lens. Calculation of the positions of H_1 and H_2 shows both of them to be on the same side of the lens, a considerable distance from it. The system matrix in this case is the product of a thin lens matrix, a translation matrix and a second thin lens matrix:

$$\begin{pmatrix} a & b \\ c & d \end{pmatrix} = \begin{pmatrix} 1 & 0 \\ -f_B^{-1} & 1 \end{pmatrix} \begin{pmatrix} 1 & l \\ 0 & 1 \end{pmatrix} \begin{pmatrix} 1 & 0 \\ -f_A^{-1} & 1 \end{pmatrix}$$
$$= \begin{pmatrix} 1 - lf_A^{-1} & l \\ -f_A^{-1} - f_B^{-1} + l(f_A f_B)^{-1} & 1 - lf_B{}^{-1} \end{pmatrix}. \qquad (3.52)$$

From this we see that the effective focal length f_{eff} of the combination is given by:

$$\frac{1}{f_{\text{eff}}} = \frac{1}{f_A} + \frac{1}{f_B} - \frac{l}{f_A f_B} = \frac{f_A + f_B - l}{f_A f_B}. \qquad (3.53)$$

Inserting the fact that $l > f_A + f_B$ shows that the effective focal length is positive when f_A and f_B have opposite signs. The figure shows the positions of the principal planes for a numerical example, where $f_A = 20\,\text{mm}$ and

$f_B = -8$ mm, the lenses being separated by 13 mm. Each point on a distant object is imaged on $\mathcal{F}_2$ and the system behaves as a thin lens situated at H_2 with a focal length $H_2F_2 = 160$ mm, while the physical length of the hardware is $V_1F_2 = 69$ mm.

Essentially the same telephoto system but with a different distance $AB = 12.1$ cm can be used in the diffractometer for classroom demonstration of Fraunhofer diffraction patterns described in Appendix B. Here each group of parallel rays belongs to one order of diffraction from the mask. The telephoto system enables one to project the diffraction pattern with a size determined by f_{eff} (which is 16 m in the example) on a screen at distance V_2F_2, only 6.4 m from the optics. This gives a real image of the diffraction pattern 2.5 times larger than could be obtained using a simple lens with the screen at the same distance.

3.6.5 Experimental determination of cardinal points for a system in air

Determination of the cardinal points for a converging optical system in air involves finding the two focal points F_1 and F_2 and the effective focal length f_{eff}. Then the principal planes are defined. The focal points can be found accurately by focusing light from a distant source onto a plane mirror normal to the axis; when the light returns to the source as a parallel beam, the mirror is situated in the focal plane. The same method can be used to determine one or more pairs of conjugate object–image positions. Then, Newton's equation (3.32) can be used to determine the effective focal length, and then the principal planes can be found. Alternatively, if a laser with known wavelength is used for the experiment, one can measure in the focal plane the spacing between the orders of the Fraunhofer diffraction pattern of a grating with measured period and use this to calculate f_{eff}.

It is a more difficult problem, which will be left to the reader, to devise a method of determining the principal planes of a diverging optical system. This requires addition of an auxiliary lens. Determination of the properties of complex lens systems are generally carried out with the aid of an **autocollimator**, which essentially provides a source projected to $z = -\infty$ on the optical axis and the means to determine when the light returned from an optical system is collimated and parallel to the axis.

3.7 Aberrations

The Gaussian approximation does not, of course, apply to real lenses and mirrors. Unfortunately, the moment we abandon the approximation that

$\sin\hat{\imath} \simeq \tan\hat{\imath} \simeq \hat{\imath}$, the subject of geometrical optics loses its elegant simplicity and becomes very technical. However, since these technicalities are often of great practical importance, we shall skim very superficially over a few examples of lens aberrations and their correction. Much more complete discussions are given by Kingslake (1983) and Welford (1986).

3.7.1 The monochromatic aberrations

No image-forming instrument can produce a perfect image of an extended object, and the best that can be done in practice is to ensure that the aberrations that would be most disturbing in a particular experiment are made as small as possible, sometimes at the expense of making others larger. Although monochromatic aberrations can be discussed on a purely geometrical-optics basis, they are much easier to understand if we look at them as distortions of the wavefront exiting the system, which will be the basis of the discussion here.

The Seidel aberrations correspond to an expansion of the wavefront error in terms of Zernike polynomials, which will not be discussed here.

The classification of aberrations now usually accepted, which makes their practical importance rather clear, was first introduced by von Seidel in about 1860, and therefore predates the diffraction theory of imaging (Chapter 12). Ideally, a perfect lens imaging a luminous point object would create an exactly spherical wavefront converging on a point in the image plane. The position of this point in the plane would be related linearly to that of the point object in its plane by the magnification M. Some of the named aberrations – **spherical aberration, coma, astigmatism** – describe the blurring of the image point. Others describe the deviation of the best image point from its expected position; **curvature of field** tells us how far in front or behind the image plane we shall find it and **distortion** tells us how big are the deviations from a uniform magnification. All these aberrations are functions of the object point position (x, y, z) and also depend on the lens parameters. In general, the severity of all aberrations is a strong function of the aperture of the lens system.

From the point of view of wave theory, the exiting wavefront simply does not coincide exactly with the sphere converging on the 'right' point, as defined by Gaussian optics. If we calculate the deviation of the real wavefront from the expected sphere in the exit pupil, we derive a function Δ that describes the aberrations. The Seidel classification breaks this function down into a linear superposition of radial and angular functions, each one of which corresponds to one of the named aberrations mentioned above (and there are higher-order ones that we did not mention, too). Any one of them that does not introduce a deviation greater than about $\lambda/2$ at the edge of the aperture of the lens is negligible, and will not significantly affect imaging. If there are no significant aberrations, the system is called 'diffraction-limited' because the only reason that the image is not an ideal point is diffractive broadening resulting from the limited aperture (§12.2).

Some examples for axially symmetric lenses, where the coordinates in the exit pupil are denoted by (ρ, θ), are as follows:

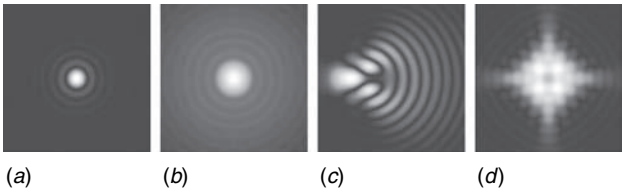

Figure 3.21
Examples of the intensity distribution in images of a point source in the paraxial focal plane: (*a*) diffraction-limited; (*b*) with spherical aberration; (*c*) with coma; (*d*) with astigmatism.

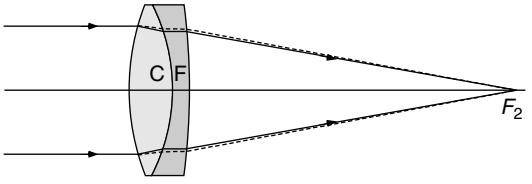

Figure 3.22
Illustrating the principle of an achromatic doublet. After entering the lens, the blue rays are shown as full lines and the red rays broken.

1. **Axial defocus** is a quadratic error of the form $\Delta(\rho,\theta) = A\rho^2$.
2. If the object is on the axis, **spherical aberration** in the paraxial image plane corresponds to the error function $\Delta(\rho,\theta) = B\rho^4$.
3. If the image is at lateral distance x from the axis, there are additional terms dependent on x called **coma** where $\Delta(\rho,\theta) = Cx\rho^3\cos\theta$ and **astigmatism** where $\Delta(\rho,\theta) = Ex^2\rho^2\cos 2\theta$.

Anticipating Chapter 8, this approach can be developed further by considering Δ as a phase error $k_0\Delta$, where $k_0 = 2\pi/\lambda$, and then calculating the form of the distorted image of a point as the Fraunhofer diffraction pattern (§8.2) of the 'phase object' $f(\rho,\theta) = \exp[-ik_0\Delta(\rho,\theta)]$. The above examples are shown in Fig. 3.21 (*b*), (*c*) and (*d*) as images of a distant point source, where they are compared with the ideal diffraction-limited image in (*a*).

3.7.2 Chromatic aberration and its correction

In addition to the monochromatic aberrations, a simple lens system has cardinal points whose positions depend on refractive indices, which are a function of λ. Mirror systems are of course free of such defects. The refractive index $n(\lambda)$ of a transparent medium is always a decreasing function of λ, but varies from material to material (§13.4).

Achromatic triplets can be designed, using three different glasses, to obtain better colour correction than that of a doublet.

For a simple thin lens, the power is given by (3.7): $f^{-1} = (n-1)(R_1^{-1} - R_2^{-1})$. A combination of two or more lenses made from different glasses can then be designed, by a suitable choice of radii of curvature R for each component, to have equal focal lengths at two or more specified wavelengths. The most common implementation has two components with radii of curvature R_1, R_2 and S_1, S_2 respectively; it is called an **achromatic doublet** or **achromat** (Fig. 3.22).

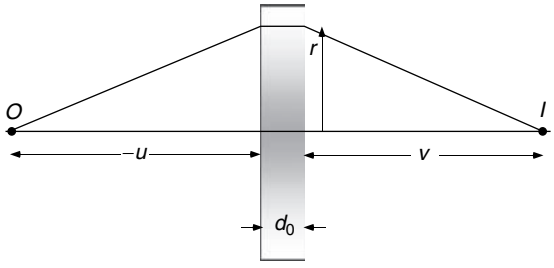

Figure 3.23
Fermat's principle applied to the GRIN lens. The refractive index is a function of radius r.

Box 3.4 Gradient index (GRIN) lenses

Many small lenses used for fibre-optics instrumentation are produced today by using a medium having radial variation in the refractive index $n(r)$ and flat surfaces. They are called **gradient index** or GRIN lenses. In a conventional lens with spherical surfaces, n is a constant and the thickness d varies quadratically with r. In a GRIN lens d is a constant, d_0, and the optical thickness $n(r)d_0$ is then arranged to have the required parabolic profile by designing $n(r)$. The easiest way to see the relationship between the material parameters and the focal length is to use Fermat's principle, as we did in §2.6.3. Remembering that according to the sign convention the real object O in Fig. 3.23 is at distance $-u$ (left of the origin), we calculate the optical path $\overline{OI}$ to image I as

$$\begin{aligned}\overline{OI} &= \sqrt{u^2 + r^2} + \sqrt{v^2 + r^2} + d_0 n(r) \\ &\approx -u - \frac{r^2}{2u} + v + \frac{r^2}{2v} + d_0 n(r),\end{aligned} \tag{3.54}$$

which must be a constant for imaging. It follows that

$$\frac{r^2}{2}\left(\frac{1}{v} - \frac{1}{u}\right) + d_0 n(r) = \frac{r^2}{2f} + d_0 n(r) = \text{const.} \tag{3.55}$$

The profile of $n(r)$ must therefore be quadratic in order that (3.55) be independent of r. It must have the form

$$n(r) = n_0 - \frac{r^2}{2fd_0}. \tag{3.56}$$

The required profile is created by progressive deposition of glasses of varying densities on a cylindrical former, after which a prolonged annealing process allows the layers to merge by diffusion and create a smooth profile. The product can then be stretched to achieve a required diameter, after which it is sliced into lenses and the faces polished flat.

The refractive index variation $n(\lambda)$ of each glass is specified by its **dispersive power**, defined for visible optics systems by the **Abbe number**

$$V = \frac{n_y - 1}{n_b - n_r}, \tag{3.57}$$

where n_b, n_y and n_r are the indices for blue, yellow and red light respectively (usually $\lambda = 486.1$ nm, 587.6 nm and 656.3 nm; for other spectral regions different wavelengths would be appropriate). Refractive indices and Abbe numbers for many materials are listed in glass tables. It is a simple calculation to show that the focal lengths for blue and red light are equal if

$$(n_{bF} - n_{rF})\left(R_1^{-1} - R_2^{-1}\right) + (n_{bC} - n_{rC})\left(S_1^{-1} - S_2^{-1}\right) = 0, \tag{3.58}$$

where the two types of glass are indicated by the second suffices F and C.[6] In terms of the individual focal lengths of the two lenses for yellow light, f_F and f_C, this can be expressed as

$$V_F f_F + V_C f_C = 0, \tag{3.59}$$

and the combined power is of course

$$f^{-1} = f_F^{-1} + f_C^{-1}. \tag{3.60}$$

A cemented doublet has a common interface, $R_2 = S_1$, and so the two equations (3.59) and (3.60) determine three radii of curvature. One degree of freedom therefore remains; we shall see in §3.7.3 how this can be used to correct another aberration. An uncemented doublet, $R_2 \neq S_1$, has two free parameters.

3.7.3 Correction of spherical aberration

Ray diagrams showing spherical aberration were shown in Fig. 3.2. Comparison of (*a*) and (*b*) suggests that some form of compensation for the defect might be achieved by **bending** the lens, which means adding a constant to each of R_1^{-1} and R_2^{-1}; this will not change the focal length, which is determined only by their difference. However, it turns out that bending cannot eliminate the spherical aberration of a single lens completely if the object is at infinity. It *can* do so if the object is closer than the focal length, as will be seen in §3.8 for the aplanatic system (which is a particular form of meniscus lens). When the object is at infinity it turns out, for $n = 1.6$ for example, that the best one can do to reduce spherical aberration is to use a ratio $R_2/R_1 = -12$. The result is close to a plano-convex lens, with the flatter side facing the image (*not* like Fig. 3.2(*b*)!). This tends to divide the refraction more-or-less equally between

[6] The letters F and C stand for flint and crown glass, which are the commonest glasses used for chromatic correction, but of course could just as well represent other materials.

Box 3.5 Solar concentrators

One branch of geometrical optics is not concerned with imaging quality, but with efficient transportation of radiant energy. This is known as **non-imaging optics**. A major application is to the concentration of solar energy. This is important for two reasons. First, because it can be used to create very high temperatures, theoretically up to the temperature of the Sun's surface, were there no atmosphere to intervene. Second, because it allows energy to be concentrated on smaller solar cells, which can then generate electricity more efficiently.

However, it is not obvious that the best way to concentrate energy is to produce a good image of the Sun on the receiver. The important things to ensure are that every ray entering the collector reaches the detector somewhere on its surface and that the detector has the smallest area theoretically allowed. The fact that there exists a smallest area follows from the second law of thermodynamics. When all the collected radiation is concentrated on this smallest area, it reaches radiative equilibrium at the same temperature as the source; if the area were smaller than this, it would be hotter than the source and a heat engine could then be designed to provide perpetual motion.

Optically, this smallest area follows from the Abbe sine rule (§3.7.4). In order not to lose collected energy we require:

1. points on the edge of the Sun's disc are imaged perfectly onto points on the edge of the detector or solar cell;
2. any ray from a point within the Sun's disc that goes through the aperture stop of the optical system reaches some point on the detector.

We denote the Sun's angular radius as $\alpha = r_s/D_s = 0.25°$, where r_s and D_s are its radius and distance respectively, the collector has aperture radius r_c and the detector is circular with radius r_d. The Abbe sine rule, required for perfect imaging, tells us that $r_d \sin\theta_d = r_s \sin\theta_s$, where the θs are the angles of the rays with respect to the optical axis (Fig. 3.24(*a*)). Now the ray with largest angle $\theta_s = r_c/D_s$ must then correspond to the largest θ_d, whose sine cannot be larger than 1. Therefore, we have for this ray

$$r_d \sin\theta_d = r_d = r_s \sin\theta_s = r_s\, r_c/D_s = r_c\, \alpha_s. \tag{3.61}$$

This gives a maximum linear concentration ratio $r_c/r_d = 1/\alpha_s = 230$. If the system has axial symmetry and circular aperture and detector, the power concentration ratio is $\alpha^{-2} = 230^2 = 53\,000$. The challenge is to reach this figure, in a practical system, which also fulfils requirement 2.

An elegant method of achieving this requirement, almost ideally, is the compound parabolic concentrator (CPC), which is designed to achieve an aberration-free image of the edge of the Sun on the detector while ignoring the quality of imaging nearer the axis. This is done using the fact that a

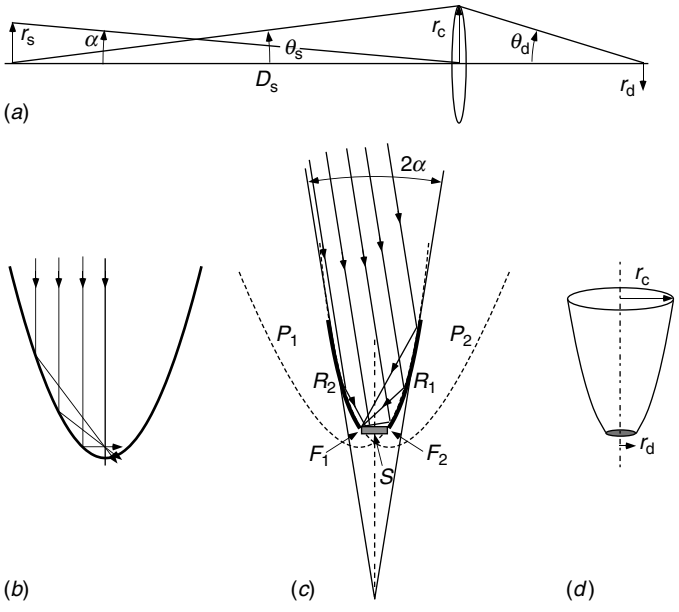

Figure 3.24 **An example of a non-imaging reflecting system, a compound parabolic concentrator (CPC), designed to concentrate sunlight onto a solar cell. The principle is such that any incident ray from within the Sun's angular diameter is reflected to some point on the solar cell, but no actual image is formed. The marginal rays are incident at 90° onto the cell, and so the detector receives at all available angles and is therefore used with ideal efficiency. (*a*) Abbe's sine rule for an imaging ray; (*b*) ideal imaging of a parallel beam by a parabolic reflector; (*c*) the CPC images the edge of the Sun to the edge of the detector, and rays closer to the axis hit the detector closer to its centre; (*d*) sketch of a three-dimensional CPC.**

parabolic mirror concentrates all rays parallel to its axis to a point focus with no spherical aberration (Fig. 3.24(*b*)); then (*c*) shows how the edge of the Sun is imaged onto the edge of the detector by an axially symmetric concave mirror whose section is an arc of a parabola with its axis inclined to the rotation axis by α. You can easily check from the figure that any ray from the Sun in the plane of the diagram strikes the detector after a number (usually zero or 1) of reflections off the mirror. In three dimensions (*d*) the only rays that miss the detector are some skew rays near the extreme angle. The important point is that the rays at the detector fill all angles of incidence θ_d up to $\pi/2$, so that the concentration ratio is as high as theoretically possible.

Some less ideal methods of achieving the same goal, which are easier to manufacture, include specially profiled Fresnel lenses and conical reflectors. It is easy to show that a conical reflector can reach a concentration ratio of one-quarter of the ideal value. Do there exist reflecting surfaces that concentrate solar radiation almost ideally onto a square or rectangular detector?

the two surfaces, which is a good rule of thumb to follow if aplanatic conditions are inappropriate.

When an achromatic doublet is used, the extra degree of freedom (§3.7.2) can be employed to correct spherical aberration. In this case, good correction can be achieved by bending the lens even for an object at infinity, and most refractive telescope objectives are designed this way. It is also common to use cemented achromats even for laboratory experiments using monochromatic light so as to take advantage of their correction for spherical aberration.

3.7.4 Coma and other aberrations

The **Abbe sine rule**, which will be proved in §12.1.2 by diffraction methods,[7] states that if a ray leaves a point object at angle θ_1 and converges on the image at angle θ_2 such that

$$\frac{\sin\theta_1}{\sin\theta_2} = \text{constant}, \tag{3.62}$$

both spherical aberration and coma are absent. The constant is, of course, the angular magnification, which can be seen by making θ very small, when the paraxial equations will apply. The aplanatic system (§3.8) satisfies this condition, but it is easy to see that a thin lens does not, since the ratio between the tangents of the angles is constant.

Distortion, however, is smallest in lens systems that are symmetrical about their central plane. If the magnification is -1, this can be seen (Problem 3.15) as resulting from the reversibility of light rays, but it is found to be approximately true at other magnifications too. The problems facing the lens designer now become clear if one contemplates, for example, correcting distortion (indicating a symmetrical system), spherical aberration and coma (requiring an asymmetrical bent lens) simultaneously. The solution has to be sought with a larger number of component lenses.

3.8 Advanced topic: The aplanatic objective

A system that has no spherical aberration in spite of large-angle rays is the aplanatic spherical lens. Despite its being a particular application of Snell's law with no fundamental significance, it is widely used in optical design, particularly in microscope objectives when a limit of resolution near the theoretical maximum is required.

[7] It can be proved by geometrical optics also, but one proof seems enough!

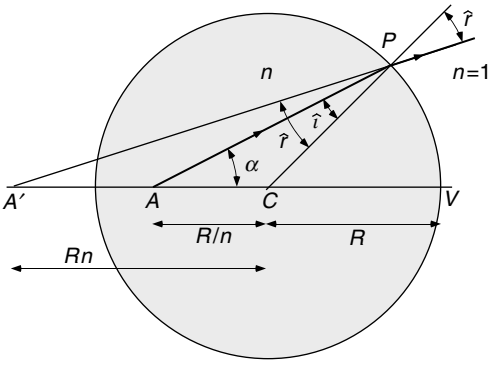

Figure 3.25
Aplanatic points of a sphere of radius R, drawn for $n = 1.50$. Triangles ACP and PCA' are similar.

Consider a sphere of glass with radius R (Fig. 3.25). The object is placed at A, at distance R/n from the centre C. We shall show that in this case an image is formed at A', distant Rn from C, and that this relation holds for all angles.

We apply the geometrical sine law to the triangle ACP and see immediately that $\sin\hat{\imath}/\sin\alpha = 1/n$. By Snell's law, $\sin\hat{\imath}/\sin\hat{r} = 1/n$ and so $\hat{r} = \alpha$. The triangles ACP and PCA' are therefore similar and it follows that

$$A'C/R = R/(R/n) = n; \qquad A'C = nR. \tag{3.63}$$

Therefore rays diverging from a point distant R/n from the centre of a sphere of radius R will, after refraction, appear to be diverging from a point distant nR from the centre. Since no approximations are involved, the result is correct for all angles. For example, if $n = 1.50$ a beam with a semi-angle of 64° ($\sin 64° = 0.90$) will emerge as a beam with a semi-angle of 37° ($\sin 37° = 0.60$).

Since the imaging is perfect for all angles, including small ones, the formal optical properties of the aplanatic sphere can be handled by matrix optics. The optical system consists of one refracting surface and is described by the matrix

$$\begin{pmatrix} 1 & 0 \\ \frac{1-n}{R} & 1 \end{pmatrix} \tag{3.64}$$

(note that the radius of the surface is $-R$!). The principal planes pass through the vertex. The focal lengths are $f_1 = Rn/(n-1)$ and $f_2 = R/(n-1)$. Since $u = -(R+R/n)$ (measured from V) we confirm from (3.46) that $v = -(R+Rn)$. The virtual image formed is n^2 larger than the object.

At first sight it might appear that the aplanatic properties are rather useless, since the object is immersed in the sphere,[8] but they are in fact widely used in two ways.

[8] The magnified virtual image of a small goldfish, swimming in a spherical globe of water at distance R/n from the centre, would be perfect.

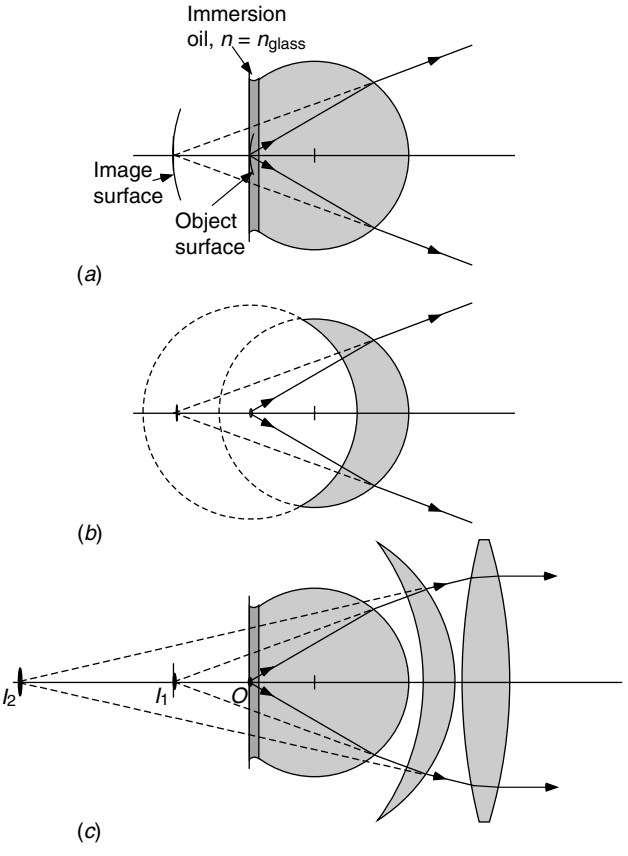

Figure 3.26

Application of the aplanatic points: (*a*) imaging a point immersed in oil; (*b*) imaging an external point; (*c*) a microscope objective using both of the above applications. *O* is the object and I_1 and I_2 images.

First, the sphere can be cut by a section passing through its internal aplanatic point; the specimen is placed near this point and immersed in a liquid (called 'index-matching' oil or gel) of the same refractive index as the glass (Fig. 3.26(*a*)). This has the additional advantage that the wavelength in the medium is smaller than in air, which improves the resolution (§12.2.5). The system is known as **oil-immersion** and is used almost universally for microscopes of the highest resolution.

The second way in which the principle can be used involves putting the object at the centre of curvature of the first concave face of a lens and making this same point the inner aplanatic point of the second surface. All the deviation then occurs at the second surface and the image is formed at the outer aplanatic point (Fig. 3.26(*b*)). It is easy to show that the magnification of such a lens is n. In this case we have corrected spherical aberration by bending the lens (§3.7.3).

The complete microscope objective illustrated in Fig. 3.26(*c*) uses both applications of the aplanatic principle in two successive stages. The semi-angle of the emergent beam that started at 64° is then reduced to 24°. The virtual

image is then re-imaged to infinity by an additional relatively weak converging lens.

The freedom from coma of the aplanatic sphere can be seen from the fact that all points at distance R/n from the centre of the sphere are aplanatic points. Thus, if we ignore the curvature of the surface on which these points lie, we deduce that all points on a plane object will form a plane image that is free from spherical aberration and coma. Correction for curvature of field, which is inherent in the aplanatic system, is more involved.

3.9 Advanced topic: Optical cavity resonators

Most gas laser resonators are constructed from two spherical mirrors, usually concave towards one another, so that the light is 'trapped' between them. The idea is that light travelling at a small angle to the axis will not diverge to larger and larger angles after multiple reflections but will stay within the finite volume of the lasing medium (Fig. 3.27(*a*)). These resonators are derivatives of the Fabry–Perot interferometer, which consists of two parallel mirrors; the physical optics of the Fabry–Perot is discussed in detail in §9.5.1.

Although we have intentionally avoided discussing spherical mirrors in this chapter, this particular problem deserves mention because of its importance in lasers (§14.6.1). We can convert it to an equivalent lens system, and investigate that by using matrices (in fact, most mirror systems are best dealt with this way). A spherical mirror of radius R has focal length $f = R/2$.[9] So when the light is reflected backwards and forwards between the two mirrors of radii R_1 and R_2, separated by L (positive values of R mean concave sides facing one another), this is equivalent to a repeated pair of lenses, with focal lengths $R_1/2$ and $R_2/2$ as in Fig. 3.27(*b*). This is a periodic system, one period of which is represented by the matrix M_P, where

$$\mathsf{M}_\mathrm{P} = \begin{pmatrix} 1 & L \\ 0 & 1 \end{pmatrix} \begin{pmatrix} 1 & 0 \\ -\frac{2}{R_2} & 1 \end{pmatrix} \begin{pmatrix} 1 & L \\ 0 & 1 \end{pmatrix} \begin{pmatrix} 1 & 0 \\ -\frac{2}{R_1} & 1 \end{pmatrix}. \tag{3.65}$$

Multiplying the matrices gives

$$\mathsf{M}_\mathrm{P} = \begin{pmatrix} 1 - \frac{2L}{R_2} - \frac{4L}{R_1} + \frac{4L^2}{R_1 R_2} & 2L - \frac{2L^2}{R_2} \\ -2\left(\frac{1}{R_1} + \frac{1}{R_2}\right) + \frac{4L}{R_1 R_2} & 1 - \frac{2L}{R_2} \end{pmatrix}. \tag{3.66}$$

When light passes through N periods of the system, equivalent to being reflected back and forth N times in the mirror system, we have the matrix M_P^N.

[9] This leads us to the conclusion, for example, that an object at $u = -R = -2f$ is imaged at $v = 2f = R$; taking into account reversal of the direction of the light, the object and image coincide, and the linear magnification is $v/u = -1$.

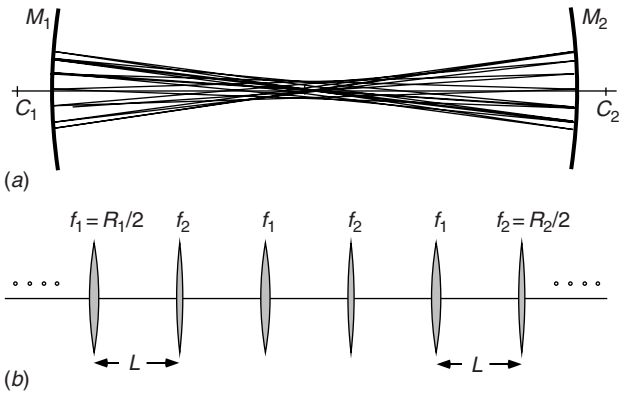

Figure 3.27

(*a*) Tracing a ray through a stable spherical Fabry–Perot resonator; (*b*) the equivalent infinite periodic set of thin lenses.

To see its convergence properties, it is easiest to diagonalize it. This means, essentially, 'rotating' the vector (h, θ) to a new vector $(ah + b\theta, -bh + a\theta)$, where $a^2 + b^2 = 1$, for which the matrix is diagonal. The technique for doing this is described in any text on linear algebra, and consists of solving the secular equation

$$\det\{\mathsf{M}_\mathrm{P} - \lambda \mathrm{I}\} = 0 \tag{3.67}$$

for its two solutions, λ_1 and λ_2. The diagonal matrix is $\mathsf{M}_\mathrm{D} \equiv \begin{pmatrix} \lambda_1 & 0 \\ 0 & \lambda_2 \end{pmatrix}$. Since $\det\{\mathsf{M}_\mathrm{P}\} = 1$, (3.67) is easily shown to give

$$\lambda^2 - \left[4\left(1 - \frac{L}{R_1}\right)\left(1 - \frac{L}{R_2}\right) - 2\right]\lambda + 1 = 0, \tag{3.68}$$

whence λ_1 and λ_2 can be found. Before writing down the solutions, we shall look at their significance. The determinant of M_D is unity, and so $\lambda_1\lambda_2 = 1$. The possible solutions of the quadratic equation (3.68) can be divided into two groups.

1. Real solutions, λ_1 and λ_1^{-1}, for which we shall show that the rays progressively diverge. We define λ_1 to be the larger solution, and exclude $\lambda_1 = \lambda_2 = 1$.
2. Complex solutions, which are of the form $\lambda_1 = \mathrm{e}^{\mathrm{i}\alpha}$, $\lambda_2 = \mathrm{e}^{-\mathrm{i}\alpha}$, including the solution $\alpha = 0$ $(\lambda_1 = \lambda_2 = 1)$. For these values the ray divergence is bounded.

Consider case (1). The matrix M_D^N is then

$$\mathsf{M}_\mathrm{D}^N = \begin{pmatrix} \lambda_1^N & 0 \\ 0 & \lambda_1^{-N} \end{pmatrix}. \tag{3.69}$$

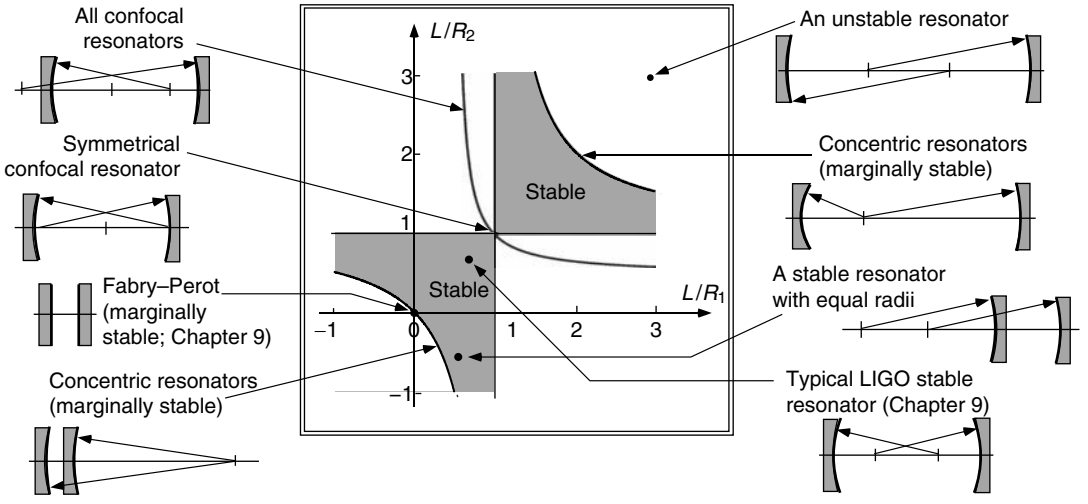

Figure 3.28

Stable and unstable resonators. In the centre, the region of stability (3.73) is shown in the $(L/R_1, L/R_2)$ plane, and around it there are examples illustrating the configurations typical of various regions on the diagram. It is interesting that the most commonly used configurations (symmetrical confocal and Fabry–Perot) are marginally stable. The Fabry–Perot and LIGO resonators will be discussed in Chapter 9.

After a large enough number N of passes, λ_1^{-N} will be small enough to be negligible, and we can write

$$\begin{pmatrix} ah_N + b\theta_N \\ -bh_N + a\theta_N \end{pmatrix} \simeq \begin{pmatrix} \lambda_1^N & 0 \\ 0 & 0 \end{pmatrix} \begin{pmatrix} ah_1 + b\theta_1 \\ -bh_1 + a\theta_1 \end{pmatrix}, \tag{3.70}$$

where h_N and θ_N are the height and angle after N passes. The solution to these equations is clearly that h_N and θ_N are proportional to λ_1^N, and therefore diverge as N increases. The rays therefore get farther and farther from the axis; such a situation is **unstable**.

For case (2), (3.69) becomes

$$\mathsf{M}_{\mathrm{D}}^N = \begin{pmatrix} \mathrm{e}^{Ni\alpha} & 0 \\ 0 & \mathrm{e}^{-Ni\alpha} \end{pmatrix} \tag{3.71}$$

and the solution to (3.70) is periodic, with period $2\pi/\alpha$. This means that h and θ just oscillate periodically about the axis, with finite amplitude, and the solution is **stable**.

The condition for stability is therefore for the solutions of (3.68) to be unity or complex i.e.

$$-1 \le 2\left(1 - \frac{L}{R_1}\right)\left(1 - \frac{L}{R_2}\right) - 1 \le 1, \tag{3.72}$$

$$\text{or, equivalently,} \qquad 0 \le \left(1 - \frac{L}{R_1}\right)\left(1 - \frac{L}{R_2}\right) \le 1. \tag{3.73}$$

The stability region defined by this equation and examples of stable and unstable resonators are shown in Fig. 3.28. The most commonly used stable resonator for gas lasers is called the **confocal resonator**, in which the two mirrors have equal radii and a common focus. It is **marginally stable** ($|\lambda| = 1$), since it lies on the

border between stability and instability, with $R_1 = R_2 = L$. The plane Fabry–Perot interferometer (§9.5.1), consisting of a pair of parallel plane mirrors ($R_1 = R_2 = \infty$), is also marginally stable and is used in solid-state lasers.

We should point out that although from the point of view of geometrical optics it is possible to choose the apertures of the two mirrors of a stable resonator such that no rays ever leak out of it, when diffraction is taken into account there will always be some losses, and in the design of a laser these diffraction losses, as well as those arising from imperfect reflection by the mirrors, have to be offset by the amplification of the active medium (§14.5) before the laser oscillates. On the other hand, if the medium amplifies strongly enough, even mildly unstable resonators can be tolerated.

Chapter summary

In this chapter we studied basic geometrical optics. We learnt:

- **What are the basic optical elements and how they are used to build more complex optical systems;**
- **About Gaussian or paraxial optics, which assumes the angles between all rays and the optical axis to be very small, and their deviations from the axis to be much smaller than typical axial distances between elements;**
- **How to use ray-tracing to get a general idea of the behaviour of an optical system;**
- **About the optical principles of the astronomical telescope and the microscope;**
- **A matrix formulation of paraxial geometrical optics, where axial systems of any degree of complexity can be described by a 2×2 matrix, composed by multiplying the translation and refraction matrices representing each interface;**
- **How to describe any coaxial system in terms of six cardinal points: two focal points, two principal points and two nodal points, whose positions can be derived from the system matrix;**
- **About the application of these principles to telescopes and zoom lens combinations;**
- **The basic principles of lens aberrations, and what they look like;**
- **About the aplanatic system, which is not limited to paraxial conditions, and its application to microscope objectives;**
- **How to quantify the stability of optical resonators, which are used in the construction of lasers and advanced interferometers.**

Problems

3.1. The foci of a mirror in the form of an ellipsoid of revolution are conjugate points (Problem 2.6). What is the magnification produced, in terms of the eccentricity of the ellipsoid? (Tricky.)

3.2. In order to use a microscope to observe an inaccessible specimen, one can introduce a relay lens between the specimen and the objective, so that the microscope looks at a real image of the specimen. Draw a ray diagram of the system, and find the influence of the relay lens on the exit pupil and the field of view.

3.3. Design a periscope having a length of 2 m and a tube diameter of 0.1 m. The field of view must be a cone of semi-angle 30°. The periscope needs several relay and field lenses. Use paraxial optics only.

3.4. A Galilean telescope has an objective lens with a long positive focal length and an eyepiece with a short negative focal length.
(a) What is the distance between the two lenses when the telescope is focused on infinity and the image appears at infinity?
(b) Is the image upright or inverted?
(c) Where is the exit pupil?
(d) What determines the field of view in this type of telescope?
(e) Why are Galilean telescopes rarely used except as toys?

3.5. Two converging lenses are separated by a distance a little greater than the sum of their focal lengths. Show that this combination produces a real image of a distant source, but that the focal length is negative! How can you explain this surprising fact physically?

3.6. A compound lens consists of two positive thin lenses L_1 and L_2, with focal lengths 90 mm and 30 mm and apertures 60 mm and 20 mm respectively. $L_1L_2 = 50$ mm. Between the lenses, in the plane 30 mm from L_1 there is an axial aperture with diameter 10 mm. Where is the aperture stop, for a given axial object 120 mm in front of L_1? Find also the positions of the entrance and exit pupils.

3.7. The following is a useful method of finding the refractive index of a transparent material in the form of a parallel-sided plate with thickness d. A microscope is focused on an object. The plate is inserted between the object and the microscope objective, and the microscope is refocused. The distance that the microscope moves in refocusing is measured.

Find the relationship between this distance, the refractive index and d. Estimate the accuracy of the method (Problem 2.6 may help you).

3.8. A planar object is imaged by a thin lens. The object lies in a plane which is not normal to the optical axis of the lens. Show that the image lies in a plane that is also inclined to the optical axis, and that the object and image planes intersect in the plane of the lens. This is called the **Scheimpflug construction**, and is important in the design of cameras for architectural and aerial photography. Show that the image of a rectangular object is distorted into a trapezoidal shape.

3.9. Within the limitations of Gaussian optics, show that it is possible to replace a glass sphere of any refractive index by a single thin lens. If the thin lens is symmetrical and made of glass with the same refractive index as the sphere, what are its radii of curvature?

3.10. Why do eyes reflect incident light back in the direction of the source (the 'red eye' phenomenon in flash photography)? How are 'cat's eye' reflectors on roads and road signs constructed?

3.11. A zoom lens consists of two thin lenses, one with focal length 100 mm and aperture diameter 50 mm, and the second with focal length −20 mm and diameter 10 mm. Plot a graph showing the effective focal length and f-number of the combination, as a function of the distance between the two lenses.

3.12. A glass shell with refractive index 1.5 has equal radii of curvature on both sides (one is convex, the other concave). The radii are both 100 mm and the thickness is 1.5 mm.
(a) Without carrying out any calculation, decide whether the shell acts as a lens with positive or negative optical power.
(b) Find its focal length and principal planes.

3.13. The glass shell of the previous problem now has two concentric surfaces, the outer one having radius 100 mm. Answer the same questions about the new shell.

3.14. Write a computer program based on the Gaussian matrices to find the cardinal points of any paraxial optical system defined by coaxial spherical interfaces between regions of given refractive indices, and/or thin lenses. Use it to check the results of Problems 3.11–3.13.

3.15. Show that in a symmetrical imaging system with unit paraxial magnification the distortion must be zero.

3.16. Design a lens of the type shown in Fig. 3.26(*b*) with $n = 2$ and $f = \infty$. What is m when O is at the aplanatic point? Explain physically why the lens magnifies, even though its effective focal length is infinite.

3.17. An observer sees an object through a thick glass window. Design a paraxial optical system that can be placed before the window so that the observer sees the object in its actual position, as if the window were not there. (This problem was posed as a challenge to optical designers by the journal *Applied Optics* some decades ago, but is quite easily solved using matrix optics when you decide exactly what you require of the principal points.)

3.18. Can you find a thin lens combination that has positive effective focal length but has the principal point H_1 to the right of H_2?

3.19. A slide projector has a powerful lamp, a condenser lens, a slide-holder and an imaging lens. Draw a ray diagram for rays forming an image of a point on the slide on a distant screen, and determine where are the entrance and exit pupils of this system.

3.20. Discuss the ray optics involved in the formation of a rainbow (both first and second orders) by refraction and reflection of sunlight by spherical water drops. There are also 'supernumerary bows', which occur next to the blue edge of the rainbow, when the raindrops are uniform in size. These can be explained by interference. If the water drops were replaced by an assembly of zinc sulphide spheres ($n = 2.32$), at what angles would the rainbows appear, and how many would there be? (NB This problem cannot be solved analytically, but needs numerical calculations.) With the help of Chapter 5, explain why light from the rainbow is polarized.

3.21. The aplanatic surfaces of a sphere are spherical, and therefore the edges of a circular source can be imaged with no aberrations using a spherical immersion lens. Discuss how this remark could be developed into a design for an ideal solar concentrator, with the addition of a single lens (as in the microscope objective in §3.8). How could you overcome the problem of chromatic dispersion in this system?

References

Kingslake, R. (1983), *Optical System Design*, Orlando, FL: Academic Press.

Smith, W. J. (2008), *Modern Optical Engineering: The Design of Optical Systems*, 4th edn., New York: McGraw-Hill.

Welford, W. T. (1986), *Aberrations of Optical Systems*, Bristol: Adam Hilger.

Welford, W. T. and Winston, R. (1989), *High Collection Nonimaging Optics*, San Diego, CA: Academic Press.

4 Fourier theory

J. B. J. Fourier (1768–1830), applied mathematician and Egyptologist, was one of the great French scientists working at the time of Napoleon. Today, he is best remembered for the **Fourier series** method, which he invented for representation of any periodic function as a sum of discrete sinusoidal harmonics of its fundamental frequency. By extrapolation, his name is also attached to **Fourier transforms** or **Fourier integrals**, which allow almost any function to be represented in terms of an integral of sinusoidal functions over a continuous range of frequencies. Fourier methods have applications in almost every field of science and engineering. Since optics deals with wave phenomena, the use of Fourier series and transforms to analyze them has been particularly fruitful. For this reason, we shall devote this chapter to a discussion of the major points of Fourier theory, hoping to make the main ideas sufficiently clear in order to provide a 'language' in which many of the phenomena in the rest of the book can easily be discussed. More complete discussions, with greater mathematical rigour, can be found in many texts such as Brigham (1988), Walker (1988) and Prestini (2004).

In this chapter we shall learn:

- what is a Fourier series;
- about real and complex representation of the Fourier coefficients, and how they are calculated;
- how the Fourier coefficients are related to the symmetry of the function;
- how to represent the coefficients as a discrete spectrum in reciprocal, or wave-vector, space;
- that non-periodic functions can be represented as a continuous Fourier transform in reciprocal space;
- that the Fourier series can be considered as a special case of the transform;
- about the Dirac δ-function and its applications;
- examples of transforms of simple real and complex functions;
- about two- and three-dimensional Fourier transforms;
- the Fourier inversion theorem, a reciprocal relationship between a function and its transform;
- about the way in which two functions can be combined by convolution, whose transform is a product of the individual transforms;

- that the Fourier transform of a periodic lattice in real space is a reciprocal lattice in reciprocal space.
- about correlation and auto-correlation functions, which are forms of convolution, and their transforms.

4.1 Analysis of periodic functions

Fourier invented his series method in order to solve the heat-diffusion equation (2.31) under specified boundary conditions. This involved expressing the temperature field as the sum of functions that were periodic in both space and time. In this chapter, we shall mainly use the spatial representation, $f(x)$, since later we shall need to extend it to two- and three-dimensional functions. There is no intrinsic difference, of course, between the mathematics of functions of x and of t, provided that we interpret the results correctly, and appreciate the meaning of a spatial frequency, which is simply the inverse of wavelength.

4.1.1 Fourier's theorem

Fourier's theorem states that any periodic function $f(x)$ can be expressed as the sum of a series of sinusoidal functions which have wavelengths that are integral fractions of the wavelength λ of $f(x)$. To make this statement complete, zero is counted as an integer, giving a constant leading term to the series:

$$\begin{aligned} f(x) &= \frac{1}{2}C_0 + C_1 \cos\left(\frac{2\pi x}{\lambda} + \alpha_1\right) + C_2 \cos\left(\frac{2\pi x}{\lambda/2} + \alpha_2\right) + \cdots \\ &\quad + C_n \cos\left(\frac{2\pi x}{\lambda/n} + \alpha_n\right) + \cdots \\ &= \frac{1}{2}C_0 + \sum_{n=1}^{\infty} C_n \cos(nk_0 x + \alpha_n), \end{aligned} \tag{4.1}$$

where $k_0 \equiv 2\pi/\lambda$ is the **fundamental spatial frequency**. The ns are called the **orders** of the terms, which are harmonics. The following argument demonstrates the theorem as reasonable. If we cut off the series after the first term, choice of C_0 allows the equation to be satisfied at a discrete number of points – at least two per wavelength. If we add a second term the number of points of agreement will increase; as we continue adding terms the number of intersections between the synthetic function and the original can be made to increase

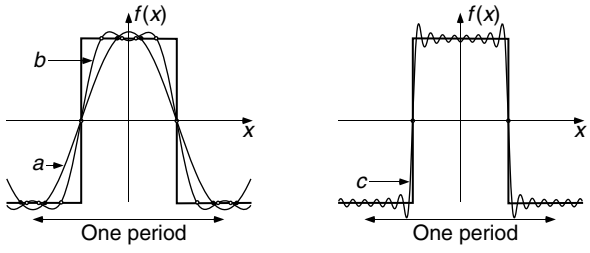

Figure 4.1
Intersections between a square wave and its Fourier series terminated after (*a*) the first, (*b*) the third and (*c*) the fifteenth term.

without limit (Fig. 4.1). This does not prove that the functions *must* be identical when the number of terms becomes infinite; there are examples that do not converge to the required function, but the regions of error must become vanishingly small.

This reasoning would, of course, apply to basic functions other than sinusoidal waves. The sine curve, however, being the solution of all wave equations, is of particular importance in physics, and hence gives Fourier's theorem its fundamental significance.

4.1.2 Fourier coefficients

Each term in the series (4.1) has two **Fourier coefficients**, an **amplitude** C_n and a **phase angle** α_n. The latter quantity provides the degree of freedom necessary for relative displacements of the terms of the series along the x-axis. The determination of these quantities for each term of the series is called **Fourier analysis**.

Another way to express the Fourier coefficients is to write (4.1) as a sum of sine and cosine terms:

$$f(x) = \frac{1}{2}A_0 + \sum_1^\infty A_n \cos nk_0x + \sum_1^\infty B_n \sin nk_0x, \tag{4.2}$$

where $A_n = C_n \cos\alpha_n$, $B_n = -C_n \sin\alpha_n$.

4.1.3 Complex Fourier coefficients

The real functions $\cos\theta$ and $\sin\theta$ can be regarded as real and imaginary parts of the complex exponential $\exp(\mathrm{i}\theta)$. Algebraically, there are many advantages in using the complex exponential, and in this book we shall use it almost without exception. We can write (4.2) in the form

$$f(x) = \frac{1}{2}A_0 + \sum F_n \exp(\mathrm{i}nk_0x), \tag{4.3}$$

where the range of summation is as yet unspecified. Now let us equate (4.3) and (4.2) for a real $f(x)$. We then have

$$\sum F_n[\cos(nk_0x) + \mathrm{i}\sin(nk_0x)] = \sum_1^\infty [A_n\cos(nk_0x) + B_n\sin(nk_0x)]. \tag{4.4}$$

If we assume that the ranges of the summation are identical and then equate equivalent cosine and sine terms independently, we get

$$F_n = A_n; \quad \mathrm{i}F_n = B_n. \tag{4.5}$$

This leads to $\mathrm{i}A_n = B_n$, which cannot be true since A_n and B_n are both real! We have to carry out the complex summation in (4.3) from $n = -\infty$ to $+\infty$ in order to solve the problem. There are then two independent complex coefficients, F_n and F_{-n}, corresponding to the pair A_n, B_n, and we have, on comparing terms in (4.4),

$$F_n + F_{-n} = A_n; \quad \mathrm{i}(F_n - F_{-n}) = B_n, \tag{4.6}$$

whence

$$F_n = \frac{1}{2}(A_n - \mathrm{i}B_n) = \frac{1}{2}C_n\ \exp(\mathrm{i}\alpha_n), \tag{4.7}$$

$$F_{-n} = \frac{1}{2}(A_n + \mathrm{i}B_n) = \frac{1}{2}C_n\ \exp(-\mathrm{i}\alpha_n). \tag{4.8}$$

The Fourier series is therefore written in complex notation as

$$f(x) = \sum_{-\infty}^{\infty} F_n \exp(\mathrm{i}nk_0x), \tag{4.9}$$

where $F_0 = \frac{1}{2}A_0$. So far, the function $f(x)$, and hence A_n and B_n, have been assumed to be **real**. It then follows from (4.7) and (4.8) that F_n and F_{-n} are complex conjugates:

$$F_n = F_{-n}^*. \tag{4.10}$$

In general, however, a **complex function** $f(x)$ can be represented by complex A_n and B_n which bear no such relationship.

4.2 Fourier analysis

The determination of the coefficients F_n, called **Fourier analysis**, can be carried out by a process that depends on an obvious property of a sinusoidal function – that its integral over a complete number of wavelengths is zero. Consequently,

The reasoning here can be applied to any set of functions that are orthogonal, meaning that the integral of the product of two different members is zero.

the integral of the product of two sinusoidal functions with integrally related wavelengths over a complete number of cycles of both functions is also zero with one exception: if the two wavelengths are equal and the two sine functions are not in quadrature, then the integral is non-zero. Therefore, if we integrate the product of $f(x)$ (wavelength λ) with a sine function of wavelength λ/m, the result will be zero for all the Fourier components of $f(x)$ except the mth, which has wavelength λ/m, and the value of the integral will then give the amplitude of the coefficient F_m.

To express this mathematically let us find the mth Fourier coefficient by multiplying the function $f(x)$ by $\exp(-\mathrm{i}mk_0x)$ and integrating over a complete wavelength λ. It is convenient to replace x by the angular variable $\theta = k_0x$ and then to take the integral I_m over the range $-\pi \leq \theta \leq \pi$, which is one wavelength. Then

$$\begin{aligned} I_m &= \int_{-\pi}^{\pi} f(\theta)\ \exp(-\mathrm{i}m\theta)\,\mathrm{d}\theta \\ &= \int_{-\pi}^{\pi} \sum_{-\infty}^{\infty} F_n\ \exp(\mathrm{i}n\theta)\exp(-\mathrm{i}m\theta)\,\mathrm{d}\theta. \end{aligned} \tag{4.11}$$

Every term in the summation is sinusoidal, with wavelength $\lambda/|m-n|$, with the exception of the one for which $n = m$. The sinusoidal terms, being integrated over $|m - n|$ wavelengths, do not contribute; so that

$$I_m = \int_{-\pi}^{\pi} F_m\,\mathrm{d}\theta = 2\pi F_m. \tag{4.12}$$

Thus we have a general expression for the mth Fourier coefficient:

$$F_m = \frac{1}{2\pi}\int_{-\pi}^{\pi} f(\theta)\ \exp(-\mathrm{i}m\theta)\,\mathrm{d}\theta. \tag{4.13}$$

Note that it includes the zero term, the mean value of $f(\theta)$:

$$F_0 = \frac{1}{2\pi}\int_{-\pi}^{\pi} f(\theta)\,\mathrm{d}\theta. \tag{4.14}$$

4.2.1 Symmetry: even and odd functions

Sometimes a function satisfies the relationship $f(\theta) = f(-\theta)$, in which case it is said to be **even** or **symmetric**; likewise, if $f(\theta) = -f(-\theta)$ it is **odd** or **antisymmetric** (see Fig. 4.2). Let us return for a moment to the formulation (4.2) of the Fourier series in terms of the sine and cosine functions. Now a periodic even function must be expressed as a sum of cosine functions only, since the sine terms make contributions of opposite sign at $+\theta$ and $-\theta$.

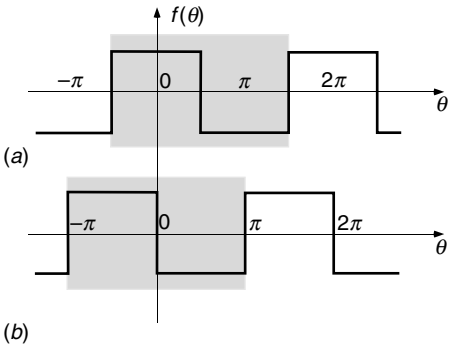

Figure 4.2

A square wave (*a*) as an even function, (*b*) as an odd function. The function is defined in the highlighted region.

Box 4.1 A basic example: Fourier analysis of a square wave

We shall illustrate Fourier analysis by analyzing a **square wave**. This has value 1 over half its period ($-\pi/2$ to $\pi/2$) and -1 over the other half ($\pi/2$ to $3\pi/2$) (Fig. 4.2(*a*)). The function as defined above is **real and even**; F_n is therefore real. If possible, it is usually worthwhile choosing the position of the origin to make a function even, since then we only need to calculate the real part of its transform; alternatively, if we had chosen to make the function equal to 1 from $-\pi$ to 0 and -1 for 0 to π it would have been odd and its coefficients all imaginary (Fig. 4.2(*b*)). This effect – the altering of the phase of all coefficients together by a shift of origin – is often important (§4.3.4); the form of the function determines the relative phases of the coefficients only. For the even function, Fig. 4.2(*a*):

$$f(\theta) = 1 \quad \in (-\pi/2 \le \theta \le \pi/2);\ f(\theta) = -1 \quad \in (\pi/2 \le \theta \le 3\pi/2), \tag{4.15}$$

$$\begin{aligned} F_n &= \frac{1}{2\pi}\int_{-\pi}^{\pi} f(\theta)\ \exp(-\mathrm{i}n\theta)\,\mathrm{d}\theta \\ &= \frac{1}{2\pi}\int_{-\pi/2}^{\pi/2} \exp(-\mathrm{i}n\theta)\,\mathrm{d}\theta - \frac{1}{2\pi}\int_{\pi/2}^{3\pi/2} \exp(-\mathrm{i}n\theta)\,\mathrm{d}\theta \\ &= \frac{1}{n\pi}\sin\frac{n\pi}{2}[1-\exp(-\mathrm{i}n\pi)]. \end{aligned} \tag{4.16}$$

Thus we have, evaluating F_0 from (4.14),

$$F_0 = 0, \quad F_{\pm1} = \frac{2}{\pi}, \quad F_{\pm2} = 0, \quad F_{\pm3} = -\frac{2}{3\pi},$$
$$F_{\pm4} = 0, \quad F_{\pm5} = \frac{2}{5\pi}\ldots$$

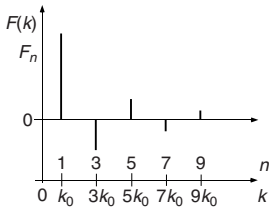

Figure 4.3

Positive half of the functions $F(n)$ and $F(k)$ for a square wave.

Thus $B_n = 0$ and it follows from (4.7) and (4.8) that

$$\text{even function:} \quad F_n = F_{-n}. \tag{4.17}$$

If, in addition, the function is real, so that (4.10) is true, we find

$$\text{real even function:} \quad F_n = F^*_{-n} = F_{-n}, \tag{4.18}$$

implying that F_n is real.

Similarly, for an odd function, we must have coefficients $A_n = 0$ and

$$\text{odd function:} \quad F_n = -F_{-n}, \tag{4.19}$$

$$\text{real odd function:} \quad F_n = F^*_{-n} = -F_{-n}, \tag{4.20}$$

implying that F_n is purely imaginary in the latter case. We see that in all these cases the symmetry of $f(x)$ is also present in F_n.

4.2.2 Reciprocal space in one dimension

Describing a function in wavenumber, or reciprocal, space emphasizes its oscillatory properties. It is like a musical score, which describes music in terms of component frequencies rather than sound amplitude as a function of time.

We can think of the Fourier coefficients F_n as a function $F(n)$ of n. As $F(n)$ is non-zero only for integral values of n, the function can be considered as being defined for non-integral values but as having zero value there; the positive half of the function $F(n)$ which represents the series for a square wave can therefore be drawn as in Fig. 4.3. Given this drawing, we could simply reconstruct the original square wave by summing the series it represents, except that it gives no information about the wavelength λ of the original wave. This defect can be simply remedied. Written in terms of x, the expression for F_n is

$$F_n = \frac{1}{\lambda}\int_0^{\lambda} f(x)\ \exp(-\mathrm{i}nk_0x)\,\mathrm{d}x. \tag{4.21}$$

Information about the wavelength λ is included in (4.21) where $k_0 \equiv 2\pi/\lambda$ and the variable $k = nk_0$ is used rather than n (Fig. 4.3); this corresponds to a harmonic of wavelength λ/n. The variable k is called the **wavenumber** or **spatial frequency**. The function (4.21) becomes

$$F(k) = \frac{1}{\lambda}\int_0^{\lambda} f(x)\ \exp(-\mathrm{i}kx)\,\mathrm{d}x. \tag{4.22}$$

It is useful now to compare the functions $F(k)$ as λ changes. In Fig. 4.4 this comparison is carried out, the scales of k and x being the same in (a), (b), (c). Clearly the abscissa scale of $F(k)$ is inversely proportional to that of $f(x)$. For this reason (k proportional to $1/\lambda$) the space whose coordinates are measured by k is called **reciprocal space**; real space has coordinates measured by x and reciprocal space by x^{-1}. So far, of course, we have discussed a purely one-dimensional space; the extension to two and three dimensions is simple, and will be discussed later.

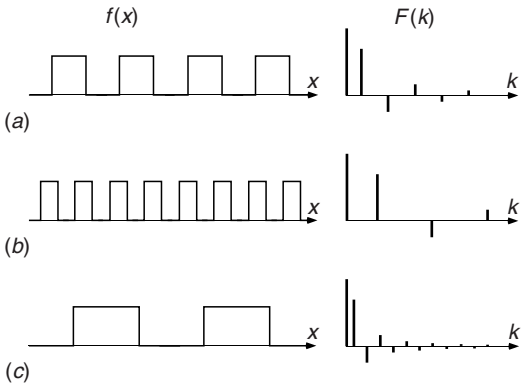

Figure 4.4
Square waves of different scales and their Fourier coefficients $F(k)$. The waves are assumed to continue from $-\infty$ to $+\infty$.

4.3 Non-periodic functions

Although crystals, which have sets of atoms repeating accurately in three dimensions, are almost ideally periodic, matter on the macroscopic scale is usually not so. Natural objects sometimes simulate periodicity in their growth, but this is never precise and most objects that we have to deal with optically (i.e. on a scale greater than the wavelength of light) are completely non-periodic. Since this book is concerned with light and real objects we may therefore ask why Fourier methods are of any importance, since they apply to periodic functions only. The answer is that the theory has an extension, not visualized by Fourier himself, to non-periodic functions. The extension is based upon the concept of the **Fourier transform**.

4.3.1 The Fourier transform

We have seen in §4.1.1 that a periodic function can be analyzed into harmonics of wavelengths ∞, λ, $\lambda/2$, $\lambda/3, \ldots$, and we have shown by Fig. 4.4 how the form of the function $F(k)$ depends on the scale of λ. When our interest turns to non-periodic functions we can proceed as follows. Construct a wave of wavelength λ in which each unit consists of some non-periodic function (Fig. 4.5). We can always make λ so large that an insignificant amount of the function lies outside the one-wavelength unit. Now allow λ to increase without limit, so that the repeats of the non-periodic function separate further and further. What happens to the function $F(k)$? The spikes approach one another as λ increases, but one finds that the envelope of the tips of the spikes remains invariant; it is determined only by the unit, the original non-periodic function. In the limit of $\lambda \to \infty$ the spikes are infinitely close to one another,

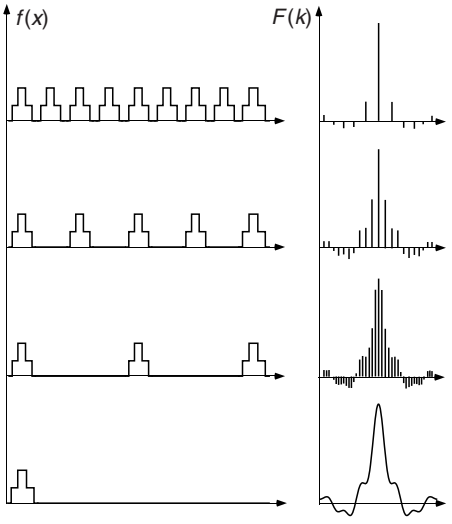

Figure 4.5

Illustrating the progression from Fourier series to transform. In each line, the period has been increased, but the component wave-form remains the same. The spectrum $F(k)$ is therefore sampled at closer and closer intervals.

and the function $F(k)$ has just become the envelope. This envelope is called the **Fourier transform** of the non-periodic function. The limiting process is illustrated in Fig. 4.5.

Admittedly, this suggests that the Fourier series for a non-periodic function is a set of spikes at discrete but infinitesimally spaced frequencies rather than a continuous function. The argument does not show that in the limit $\lambda \to \infty$ the function becomes continuous, although physically the difference may seem rather unimportant. From the mathematical point of view it is better to work in reverse. We now *define* the Fourier transform of a function $f(x)$ as

$$F(k) = \int_{-\infty}^{\infty} f(x) \exp(-\mathrm{i}kx)\mathrm{d}x, \tag{4.23}$$

which is a continuous function of the spatial frequency k. In comparing this with (4.13), notice that the $1/2\pi$ has been dropped; this has no physical significance. Later (§4.7.5), we shall use the concept of convolution to show that if $f(x)$ is periodic the transform $F(k)$ is non-zero at discrete and periodic values of k only.

An important idea illustrated by Fig. 4.5 is that of **sampling**. The set of orders of a periodic function can be regarded as equally spaced ordinates of the Fourier transform of the unit. As the spacing is reduced by increasing the repeat distance λ, the orders sweep through the transform, sampling its value at ever closer intervals. This idea is particularly relevant to digital operations. Numerically, a function (the unit) is defined only within a certain limited region of space. The mathematics 'assumes' that this unit is repeated periodically, and uses (4.13) to calculate the Fourier series. The transform of the unit is therefore sampled

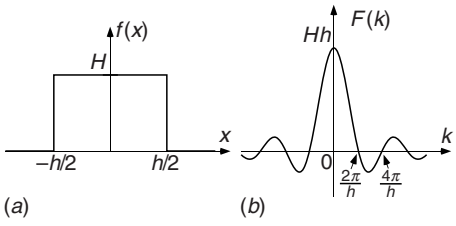

Figure 4.6
(*a*) A square pulse and (*b*) its Fourier transform, a sinc function.

digitally at closely spaced but distinct points, whose spacing is determined by the length of the repeat period.

4.3.2 Fourier transform of a square pulse: the 'sinc' function

Our first illustration of the calculation of a Fourier transform is the equivalent example to that in Box 4.1, a single square pulse. We define it to have height H and width h (Fig. 4.6(*a*)), being zero outside this region,[1] and the integral (4.23) becomes

The square pulse will be used frequently to represent light waves transmitted through slits or holes. It can also create a function limited in space, by multiplying an infinite function.

$$\begin{aligned} F(k) &= \int_{-h/2}^{h/2} H \ \exp(-\mathrm{i}kx)\,\mathrm{d}x \\ &= \frac{H}{-\mathrm{i}k}\left[\exp\left(\frac{-ikh}{2}\right) - \exp\left(\frac{\mathrm{i}kh}{2}\right)\right] \\ &= Hh\,\frac{\sin(kh/2)}{kh/2}. \end{aligned} \tag{4.24}$$

The function $\sin(\theta)/\theta$ appears very frequently in Fourier transform theory, and has therefore been given its own name, 'sinc(θ)'. Equation (4.24) can thus be written:

$$F(k) = Hh\ \mathrm{sinc}\,(kh/2). \tag{4.25}$$

The transform is illustrated in Fig. 4.6(*b*). It has a value Hh (the area under the pulse) at $k = 0$ and decreases as k increases, reaching zero when $kh = 2\pi$. It then alternates between positive and negative values, being zero at $kh = 2n\pi$ where integer ($n \neq 0$). It should be noted that the transform is real: this follows because the function is symmetrical about the origin (see §4.2.1 and §4.5).

In Fig. 4.7 we can see the reciprocal property of the transform discussed in §4.2.2. As h is increased, the value of k at which the transform becomes zero decreases and the interval between successive zeros also decreases; the coarser the function, the finer is the detail of its transform. Conversely, as h decreases

[1] The square pulse with unit height and width is often called 'rect(x)', which has unit value between $x = \pm\frac{1}{2}$ and zero outside.

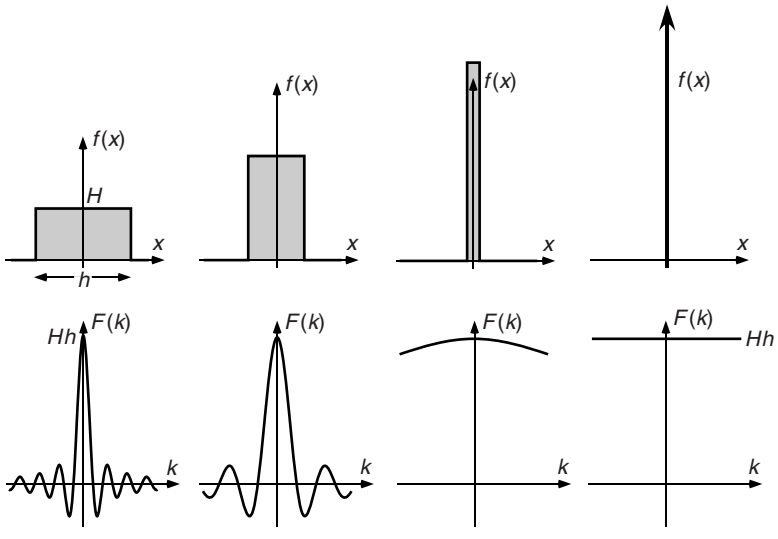

Figure 4.7

Progression from a square pulse to a δ-function, and the corresponding changes in the Fourier transform. The area *Hh* remains constant throughout.

the transform spreads out and when h reaches zero there is no detail at all in the transform, which has become a constant, Hh.

4.3.3 A change in scale

The discussion above allows us to formalize the way in which a change in the scale of a function affects its Fourier transform. We consider the effect of changing the x-scale by factor b. Since we have seen that the scales of a function and its transform are inversely related, we expect that the transform should be scaled by $1/b$. To show that this is indeed correct, we calculate the transform $F_b(k)$ of $f(x/b)$:

$$F_b(k) = \int_{-\infty}^{\infty} f(x/b)\exp(-\mathrm{i}kx)\,\mathrm{d}x \tag{4.26}$$

$$= |b|\int_{-\infty}^{\infty} f(x/b)\exp(-\mathrm{i}kb\,x/b)\,\mathrm{d}(x/b) \tag{4.27}$$

$$= |b|F(kb). \tag{4.28}$$

As well as the inverse change in scale, notice that the amplitude is also scaled.

Sliding a function to the right or left along the x-axis only changes its phase; its amplitude is unaffected.

4.3.4 A shift of origin

When a function is translated along the x-axis, with no other change in its form, only the phase of its Fourier transform is affected. To show this, we

can calculate the transform of the function $f_1(x) = f(x - x_0)$. We write x' for $x - x_0$, and

$$\begin{aligned} F_1(k) &= \int_{-\infty}^{\infty} f(x - x_0) \exp(-\mathrm{i}kx)\, \mathrm{d}x \\ &= \int_{-\infty}^{\infty} f(x') \exp\{-\mathrm{i}k(x' + x_0)\}\, \mathrm{d}x' \\ &= \exp(-\mathrm{i}kx_0) \int_{-\infty}^{\infty} f(x') \exp(-\mathrm{i}kx')\, \mathrm{d}x' \\ &= \exp(-\mathrm{i}kx_0)\, F(k). \end{aligned} \tag{4.29}$$

This differs from $F(k)$ only by the phase factor $\exp(-\mathrm{i}kx_0)$. In particular, the amplitudes $|F_1(k)|$ and $|F(k)|$ are equal.

4.3.5 Fourier transform of the derivative of a function

Suppose we know the Fourier transform of the function $f(x)$, and need the transform of its derivative $\mathrm{d}f/\mathrm{d}x$. This can be found very simply. We write the transform of the derivative

$$\begin{aligned} F^{(1)}(k) &= \int_{-\infty}^{\infty} \frac{\mathrm{d}f}{\mathrm{d}x} \exp(-\mathrm{i}kx)\, \mathrm{d}x \\ &= \int_{-\infty}^{\infty} \exp(-\mathrm{i}kx)\, \mathrm{d}f, \end{aligned} \tag{4.30}$$

which can be integrated by parts, giving

$$F^{(1)}(k) = [f\, \exp(-\mathrm{i}kx)]_{-\infty}^{\infty} + \mathrm{i}k \int_{-\infty}^{\infty} f(x) \exp(-\mathrm{i}kx)\, \mathrm{d}x \tag{4.31}$$

$$= \mathrm{i}k\, F(k). \tag{4.32}$$

The first term in (4.31) is zero because the value of $f(x)$ at $\pm\infty$ must vanish for its transform to exist. Therefore,

$$\frac{\mathrm{d}f}{\mathrm{d}x} \rightarrow \mathrm{i}k\, F(k). \tag{4.33}$$

4.4 The Dirac δ-function

The δ-function is widely used in optics to represent an ideal point source or slit.

The limiting process described in §4.3.2 leads to a new and very useful function, the Dirac δ-function. It is the limit of a square pulse as its width h goes to zero but its enclosed area Hh remains at unity. It is therefore zero everywhere except at $x = 0$, when it has infinite value, $\lim_{h\to 0} 1/h$. The transform of the δ-function

can be found by the limiting process above; we start with a square pulse of width h and height h^{-1}, which has transform

$$F(k) = \mathrm{sinc}(kh/2) \tag{4.34}$$

and see that as $h \to 0$ the transform becomes unity for all values of k. The transform of a δ-function at the origin in one dimension is unity.

A mathematically important property of this function is

$$\int_{-\infty}^{\infty} f(x)\,\delta(x-a)\,\mathrm{d}x = f(a). \tag{4.35}$$

This integral **samples** $f(x)$ at $x = a$.

4.4.1 A pair of δ-functions

An array of δ-functions at various values of x is a function we shall use repeatedly:

$$f(x) = \sum_n \delta(x - x_n). \tag{4.36}$$

From (4.29) its transform is clearly

$$F(k) = \sum_n \exp(-\mathrm{i}kx_n). \tag{4.37}$$

If there are two δ-functions, for example, at $x_n = \pm b/2$ we have a transform

$$F(k) = \exp(\mathrm{i}kb/2) + \exp(-\mathrm{i}kb/2) = 2\cos(kb/2), \tag{4.38}$$

which is real ($f(x)$ is even) and oscillatory (Fig. 4.8). Its importance in discussing the optical experiment of Young's fringes will be evident in §8.5.1.

4.4.2 A regular array of δ-functions

An array of δ-functions can be used in optics to represent a diffraction grating, or in three dimensions, a crystal lattice.

The transform of a regular array of δ-functions at $x = nb$ is particularly important (Fig. 4.9):

$$f(x) = \sum_{n=-\infty}^{\infty} \delta(x - nb). \tag{4.39}$$

This function is often called the 'comb' or 'sha' function, i.e. $f(x) = \mathrm{comb}(x/b)$. It follows from (4.37) that

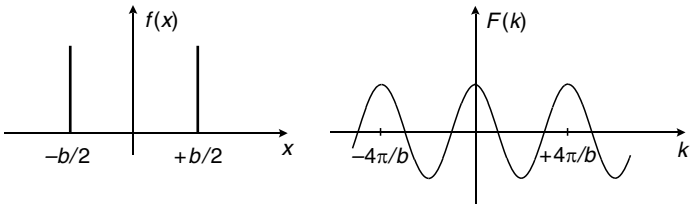

Figure 4.8
(*a*) Two δ-functions at $\pm b/2$ and (*b*) their transform, a cosine function.

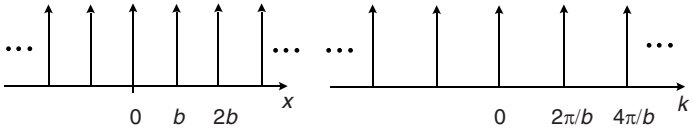

Figure 4.9
Periodic array of δ-functions and its transform, another periodic array.

$$F(k) = \sum_{-\infty}^{\infty} \exp(-\mathrm{i}knb). \tag{4.40}$$

Now the function $f(x)$ extends to infinity in both the positive and negative directions, and its integral is infinite. As a result, from the purely mathematical point of view it does not have a Fourier transform. However, we know that the mathematics only represents a real physical entity, which must itself be finite in extent.

We can evaluate (4.40) by considering it as the limit of a finite series, which can easily be summed. To maintain a real transform, we consider the sum from $-N$ to $+N$, which is symmetric about $x = 0$:

$$F_N(k) = \sum_{n=-N}^{N} \exp(-\mathrm{i}knb), \tag{4.41}$$

which is easily evaluated as a geometrical series to have the value

$$F_N(k) = \frac{\sin\left[\left(N + \frac{1}{2}\right) bk\right]}{\sin\left(\frac{1}{2}bk\right)}. \tag{4.42}$$

This function has periodic peaks, of height $2N + 1$ whenever the denominator is zero, i.e. when $bk = 2m\pi$. For large N each one looks like a sinc function: $\sin(Nbk)/\frac{1}{2}bk \approx 2N\mathrm{sinc}(Nbk)$. In the limit, when $N \to \infty$, each of these peaks becomes a δ-function, with strength $2N \times \pi/Nb = 2\pi/b$. Thus the transform of the infinite array of δ-functions separated by b (4.39) is a new array, in which the δ-functions are separated by $2\pi/b$:

$$f(x) = \sum_{n=-\infty}^{\infty} \delta(x - nb) \Rightarrow F(k) = \frac{2\pi}{b} \sum_{m=-\infty}^{\infty} \delta(k - 2\pi m/b) \tag{4.43}$$

$$\text{or} \qquad \mathrm{comb}(x/b) \Rightarrow \frac{2\pi}{b}\mathrm{comb}(kb/2\pi). \tag{4.44}$$

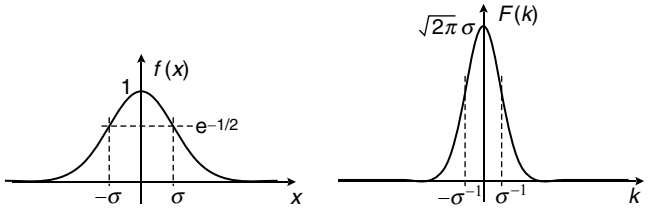

Figure 4.10
Gaussian function and its transform, another Gaussian. The widths are shown at $e^{-\frac{1}{2}} = 0.60$ of the maximum height.

4.4.3 The Gaussian function

Any function that is smoothly distributed and concentrated around a defined origin has a transform similar to that of the Gaussian function.

Another function whose Fourier transform is particularly useful in optics is the **Gaussian** (Fig. 4.10):

$$f(x) = \exp(-x^2/2\sigma^2). \tag{4.45}$$

From the definition of the transform, (4.23), we have

$$F(k) = \int_{-\infty}^{\infty} \exp(-x^2/2\sigma^2)\exp(-\mathrm{i}kx)\,\mathrm{d}x \tag{4.46}$$

$$= \exp\left[-k^2\left(\frac{\sigma^2}{2}\right)\right]\int_{-\infty}^{\infty}\exp\left\{-\left[\frac{x}{(2\sigma^2)^{\frac{1}{2}}} + \mathrm{i}k\left(\frac{\sigma^2}{2}\right)^{\frac{1}{2}}\right]^2\right\}\mathrm{d}x$$

by completing the square in the exponent. The integral is standard and occurs frequently in statistical theory. Its value is independent of k,

$$\int_{-\infty}^{\infty}\exp\frac{-\xi^2}{2\sigma^2}\,\mathrm{d}\xi = (2\pi\sigma^2)^{\frac{1}{2}}, \tag{4.47}$$

and therefore

$$F(k) = (2\pi\sigma^2)^{\frac{1}{2}}\exp\left[-k^2\left(\frac{\sigma^2}{2}\right)\right]. \tag{4.48}$$

When we study Gaussian beam propagation in §7.3, the value of σ will become complex. But the mathematics here is still valid.

The original function (4.45) was a Gaussian with variance σ^2; the transform is also a Gaussian, but with variance σ^{-2}. The **half-peak-width** of the Gaussian (the width of the peak at half its maximum height) can be shown to be equal to 2.36σ. Because the Gaussian transforms into a Gaussian, this example illustrates particularly clearly the reciprocal relationship between the scales of the function and its transform.

4.5 Transforms of complex functions

In §4.2.1 we discussed the relationships between F_n and F_{-n} for periodic functions having various symmetry properties. We included in the discussion the possibility that $f(x)$ was complex, and since complex functions form the backbone of wave optics we must extend our discussion of transforms to include them too. If the function $f(x)$ is complex, and has transform $F(k)$ defined in the usual manner, we can write down the transform of its complex conjugate $f^*(x)$ as

$$\int_{-\infty}^{\infty} f^*(x)\exp(-\mathrm{i}kx)\,\mathrm{d}x = \left[\int_{-\infty}^{\infty} f(x)\exp(\mathrm{i}kx)\,\mathrm{d}x\right]^* = F^*(-k). \quad (4.49)$$

Thus the transform of $f^*(x)$ is $F^*(-k)$. It now follows that if $f(x)$ is real, then $f(x) = f^*(x)$ and so, as in (4.10),

$$\text{real function:} \quad F^*(-k) = F(k). \quad (4.50)$$

By similar manipulations we obtain the following relationships, which can be compared to those derived for Fourier series in (4.17)–(4.20):

$$\text{even function:} \quad F(k) = F(-k), \quad (4.51)$$

$$\text{odd function:} \quad F(k) = -F(-k). \quad (4.52)$$

Combining these with (4.50) for real functions, it follows that a real even function has a real transform, and a real odd function has a pure imaginary transform. For all these cases, the absolute values $|F(k)|^2$ are symmetrical:

$$|F(-k)|^2 = |F(k)|^2. \quad (4.53)$$

4.5.1 The Hilbert transform

The Hilbert transform is important in aperture synthesis (§11.8) where we shall be calculating correlations between experimentally measured signals received from stellar objects.

In later chapters we shall often be using complex functions to represent real physical quantities, for mathematical convenience. The **Hilbert transform** is a formal way of defining a **complex function associated with a given real function**, and it can be easily expressed in terms of their Fourier transforms. If the real function is $f^{\mathrm{R}}(x)$, where

$$f^{\mathrm{R}}(x) = \int_{-\infty}^{\infty} F(k)\exp(-\mathrm{i}kx)\,\mathrm{d}k, \quad (4.54)$$

the **associated complex function** $f(x) = \mathrm{Re}f(x) + \mathrm{i}\mathrm{Im}f(x)$ is

$$f(x) = 2\int_{0}^{\infty} F(k)\exp(-\mathrm{i}kx)\,\mathrm{d}k. \quad (4.55)$$

The Hilbert transform is unambiguous, because the original function was real, and therefore $F^*(-k) = F(k)$. It follows that eliminating the transform for negative k has destroyed no information about the function.

4.5.2 The Fourier transform in two dimensions, and axial symmetry properties

All that has been said so far about Fourier transforms and series in one dimension also applies to higher dimensionalities. In particular, two-dimensional functions (screens) are very important in optics. The transform is defined in terms of two spatial frequency components, k_x and k_y, by a double integral:

$$F(k_x,\ k_y) = \int\int_{-\infty}^{\infty} f(x,\ y) \exp\left[-\mathrm{i}(xk_x + yk_y)\right] \mathrm{d}x\ \mathrm{d}y. \tag{4.56}$$

If the function $f(x, y)$ can be written as the product $f_1(x)f_2(y)$, the integral (4.56) can be factorized into two one-dimensional transforms:

$$\begin{aligned} F(k_x,\ k_y) &= \int_{-\infty}^{\infty} f_1(x) \exp(-\mathrm{i}xk_x)\ \mathrm{d}x \int_{-\infty}^{\infty} f_2(y) \exp(-\mathrm{i}yk_y)\ \mathrm{d}y \\ &= F_1(k_x)\ F_2(k_y). \end{aligned} \tag{4.57}$$

In the same way as the components (x, y) form a vector **r** in direct space, the components (k_x, k_y) form a vector **k** in reciprocal space.

Three-dimensional analogues of (4.56) and (4.57) can be written down with no trouble.

When $f(x, y)$ cannot be expressed as a product in the above way, the integral (4.56) may be difficult to evaluate analytically. An important class of such problems in optics is that for which f has axial symmetry, and can be written in terms of polar coordinates $(r,\ \theta)$:

$$f(r, \theta) = f_1(r) f_2(\theta). \tag{4.58}$$

Examples of such problems are discussed in Appendix A.

In two dimensions, axial symmetry properties become prominent. If $f(x, y)$ is **centrosymmetric**, i.e.

$$f(x, y) = f(-x, -y), \tag{4.59}$$

$$F(k_x, k_y) = F(-k_x, -k_y). \tag{4.60}$$

Similarly for the case

$$f(x, y) = -f(-x, -y) \tag{4.61}$$

$$F(k_x, k_y) = -F(-k_x, -k_y). \tag{4.62}$$

A most important result follows if $f(x, y)$ is real:

$$F(k_x, k_y) = F^*(-k_x, -k_y), \tag{4.63}$$

Box 4.2 Fourier algorithms: fast and discrete Fourier transforms

In general, when $f(x)$ is not a simple analytical function, the Fourier transform has to be evaluated numerically. In order to do this, the function $f(x)$ must be defined in a given finite region of size Na, in which it is sampled at N discrete points $x_n = na$. The Fourier transform is then evaluated in a finite regime in reciprocal space, at say M discrete points. In this way, the function is essentially considered as one period of a periodic function, for which the Fourier coefficients are then calculated using (4.13) in the form of a sum for each of the latter values:

$$F(m) = \frac{1}{2\pi} \sum_{n=1}^{N} f(na) \ \exp\left(-\frac{2\pi \mathrm{i} nm}{NM}\right). \tag{4.64}$$

When N and M are large, this is a very time-consuming calculation to carry out directly. A very efficient algorithm, the **fast Fourier transform** (FFT), which uses matrix factorization methods to simplify the calculation when $M = N$ is an integer power of 2, was proposed by Cooley and Tukey in 1965 (Brigham (1988)) and is now very widely used. If M and N are not powers of 2, the algorithm pads the regions to make them so. However, the fast Fourier transform is not always the ideal tool. There are many cases where, for example, one needs the Fourier transform in a limited region only, or $M \neq N$, or the sampling is not uniform; in these cases, the direct evaluation of (4.64) might be more efficient. This is called a **discrete Fourier transform** (DFT).

implying that $|F(k_x, k_y)|^2$ is centrosymmetric. Equations (4.59) and (4.60) imply that both the function and its transform are invariant on rotation by 180° about the origin. More generally, if the function is invariant on rotation by $360°/n$ (n-fold axial symmetry) its transform behaves likewise. Finally, consider the case of a *real* function with odd n. $|F(k_x, k_y)|^2$ has n-fold symmetry and is also centrosymmetric, implying $2n$-fold symmetry. An example is an equilateral triangle which has a transform with six-fold symmetry. Mirror-plane symmetry or antisymmetry behave similarly; if $f(x,y) = \pm f(-x,y)$ then $F(-k_x, k_y) = \pm F(k_x, k_y)$, and in both cases $|F(k_x, k_y)|^2$ has mirror-plane symmetry.

4.6 The Fourier inversion theorem

One very useful property of Fourier transforms is that the processes of transforming and untransforming are identical. This property is not trivial, and will

The Fourier inversion theorem will be seen to be the mathematical basis of imaging (§12.1) and is the reason why an image is an inverted picture of the object.

be proved below. Another way of stating it is to say that the Fourier transform of the Fourier transform is the original function again, which is true except for some minor details, and is known as the **Fourier inversion theorem**.

If the original function is $f(x)$, the Fourier transform $f_1(x')$ of its Fourier transform can be written down directly as a double integral:

$$f_1(x') = \int \left\{ \int_{-\infty}^{\infty} f(x) \exp(-\mathrm{i}kx)\, \mathrm{d}x \right\} \exp(-\mathrm{i}kx')\, \mathrm{d}k, \tag{4.65}$$

which can be evaluated as follows:

$$\begin{aligned} f_1(x') &= \int \int_{-\infty}^{\infty} f(x) \exp\{-\mathrm{i}k(x+x')\}\, \mathrm{d}x\, \mathrm{d}k \\ &= \int_{-\infty}^{\infty} f(x) \left[\frac{\exp\{-\mathrm{i}k(x+x')\}}{-\mathrm{i}(x+x')} \right]_{k=-\infty}^{k=\infty} \mathrm{d}x. \end{aligned} \tag{4.66}$$

Replacing $(x+x')$ by y, the function with the square brackets can be written as the limit

$$\lim_{k\to\infty} \frac{2 \sin ky}{y} = 2k \lim_{k\to\infty} \operatorname{sinc} ky. \tag{4.67}$$

Clearly, this limit looks like a δ-function; it becomes narrower and higher as $k \to \infty$. The appropriate value of the δ-function can be found by integrating the function $2k \operatorname{sinc} ky$. We quote the known definite integral

$$\int_{-\infty}^{\infty} \frac{\sin ky}{y} \mathrm{d}y = \pi, \tag{4.68}$$

from which we deduce that the transform $f_1(x')$ is

$$f_1(x') = \int_{-\infty}^{\infty} 2\pi \delta(x+x') f(x)\, \mathrm{d}x = 2\pi f(-x'). \tag{4.69}$$

On retransforming the transform we have therefore recovered the original function, intact except for inversion through the origin (x has become $-x$) and multiplied by a factor 2π.[2] In the two-dimensional transform of a function $f(x, y)$ (§4.5.2), the result of retransforming the transform is to invert *both* axes, which is equivalent to a rotation of 180° about the origin.[3]

[2] This factor is compensation for the $1/2\pi$ which we ignored in the definition of the transform, §4.3.1.

[3] It is common to redefine an *inverse Fourier transform* in a way that 'corrects' the above two deficiencies, so that the transform of the transform comes out exactly equal to the original function. One defines the *forward transform*, $f(x)$ to $F(k)$, as before (4.23), and the *inverse transform*, $F(k)$ to $f_1(x')$, as

$$f_1(x') = \frac{1}{2\pi} \int_{-\infty}^{\infty} F(k) \exp(+\mathrm{i}kx')\, \mathrm{d}k.$$

With this convention the inverse transform $f_1(x')$ of the forward transform is identical to the original function $f(x)$. Of course, physical systems are ignorant of such conventions. If we carry out the transform and its inverse experimentally, as in an imaging system (§12.1.3), the image is indeed inverted!

4.6.1 Examples of Fourier inversion

In §4.3.5 we saw that the transform of the derivative $\mathrm{d}f(x)/\mathrm{d}x$ is $\mathrm{i}kF(k)$. Now we can use Fourier inversion to conclude that the integral $\int^x f(x)\,\mathrm{d}x$ has transform $(\mathrm{i}k)^{-1}F(k)$.

The Fourier inversion theorem can be illustrated by any function that can itself be transformed analytically, and whose transform can also be transformed analytically. An obvious example is the Gaussian function (§4.4.3) which transforms into another Gaussian, the product of their widths being unity. Another example from §4.4.1 is the pair of δ-functions. We saw that the function $\delta(x + b/2) + \delta(x - b/2)$ transforms into $2\cos(kb/2)$, (4.38). The inverse transform of the cosine can be evaluated as

$$\begin{aligned} &2\int_{-\infty}^{\infty} \cos\left(\frac{kb}{2}\right) \exp(\mathrm{i}kx)\,\mathrm{d}k \\ &\quad = \int_{-\infty}^{\infty} \left\{ \exp\left[\mathrm{i}k\left(x+\frac{b}{2}\right)\right] + \exp\left[\mathrm{i}k\left(x-\frac{b}{2}\right)\right]\right\} \mathrm{d}k \\ &\quad = 2\pi\left[\delta\left(x+\frac{b}{2}\right) + \delta\left(x-\frac{b}{2}\right)\right], \end{aligned} \tag{4.70}$$

which is the original function multiplied by 2π. In integrating the exponentials above, we used the same limiting process as before in §4.6. The Fourier inversion theorem is particularly useful, of course, when the transform can be carried out analytically in one direction only.

4.7 Convolution

Convolution is a very generalized form of blurring or smudging, where the way in which an individual point is smudged is defined mathematically.

An operation which appears very frequently in optics – and indeed in physics in general – is called **convolution**, or folding. The convolution of two real functions f and g is defined mathematically as

$$h(x) = \int_{-\infty}^{\infty} f(x')g(x - x')\,\mathrm{d}x'. \tag{4.71}$$

The convolution operation will be represented in this book by the symbol $\otimes$ so that (4.71) is written

$$h(x) = f(x) \otimes g(x). \tag{4.72}$$

The symbols $\star$ or * are also commonly used to represent convolution.

This operation is particularly important in Fourier theory since, as we shall see, the Fourier transform of the convolution of two functions is the product of their transforms (§4.7.4).

4.7.1 Convolution with an array of δ-functions

Convolution with a single δ-function is particularly easy to appreciate. Suppose that the function $g(x)$ is a δ-function situated at the point $x = b$, i.e. $g(x) = \delta(x - b)$. Then the convolution integral (4.71) becomes

$$h(x) = \int_{-\infty}^{\infty} f(x')\delta(x - b - x')\,\mathrm{d}x'. \tag{4.73}$$

Using the sampling equation (4.35), which we write for convenience

$$\int_{-\infty}^{\infty} f(x')\delta(a - x')\,\mathrm{d}x' = f(a), \tag{4.74}$$

we see that

$$h(x) = f(x - b). \tag{4.75}$$

The origin of the function has been translated to $x = b$. When $g(x)$ is an array of δ-functions, convolution with $f(x)$ places this function around every one of the δs, in any dimensionality. This is the origin of the importance of convolution in crystallography, where it provides a natural way to describe a periodically repeated atomic arrangement.

Convolution with the periodic array $g(x) = \sum_n \delta(x - nb)$ provides the link between the Fourier transform and Fourier coefficients for a periodic function. If one individual period is described by $f(x)$, convolution then repeats this at intervals b, thus forming the periodically repeating function. We shall see in §4.7.5 that the transform recovers the original Fourier coefficients.

4.7.2 Illustration of convolution by means of a 'pinhole' camera

The convolution function can be well illustrated by the simplest optical instrument, the pinhole camera. Suppose we consider the photograph of a plane object taken with a pinhole camera with a large pinhole. Because of the size of the pinhole, any one bright point on the object will produce a blurred spot in the image plane, centred at the point x' where the image would come if focusing were sharp. In one dimension this blurred spot would be described as a function $g(x - x')$ whose origin is at $x = x'$. The intensity of the blurred spot is proportional to the intensity $f(x')$ that the sharp image would have at x'. The intensity at point x is therefore

$$f(x')g(x - x') \tag{4.76}$$

and for the complete blurred image the total intensity observed at x is the integral

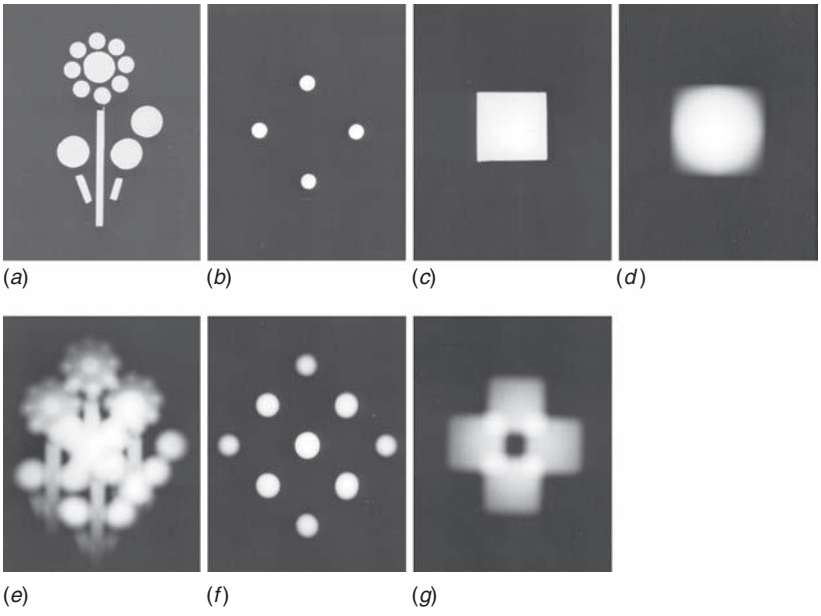

Figure 4.11

Convolution of two-dimensional functions illustrated by the pinhole camera method described in §4.7.2. The objects are shown in (*a*), (*b*) and (*c*); the 'pinholes' used are transparencies identical to (*b*) and (*c*). (*d*) shows the self-convolution $c \otimes c$, (*e*) shows $a \otimes b$, (*f*) shows the self-convolution $b \otimes b$ and (*g*) shows $b \otimes c$. Since (*b*) and (*c*) are centrosymmetric, their self-convolutions and auto-correlations are identical.

$$h(x) = \int_{-\infty}^{\infty} f(x')g(x - x')\,\mathrm{d}x'. \tag{4.77}$$

The above description is illustrated in Fig. 4.11, where two dimensions have been employed and some fancy 'pinholes' have been introduced in order to illustrate various features of convolution. In two dimensions, the convolution function is written

$$h(x,y) = \int\int_{-\infty}^{\infty} f(x',y')g(x - x', y - y')\,\mathrm{d}x'\,\mathrm{d}y'. \tag{4.78}$$

A quantitative analysis of this demonstration is given in Appendix B.

4.7.3 The importance of convolution in optics

We have devoted considerable attention to the convolution operation because it has many applications in optics. Although we are preempting discussions in later chapters, we can briefly mentions three examples of situations that are considerably simplified by the use of convolutions:

1. A diffraction grating (§9.2) can be represented by a slit or other arbitrary line-shape function convoluted with a one-dimensional array of δ-functions.
2. The electron density in a crystal is represented by the density in a single molecular unit convoluted with the three-dimensional lattice of δ-functions representing the crystal lattice (§8.6.1).

3. In a Fraunhofer diffraction experiment, the intensity is all that can be observed directly. The intensity function is the transform of the auto-correlation of the object, which is a form of self-convolution (§4.9.1).

The convolution and multiplication operations are Fourier transforms of one another.

4.7.4 Fourier transform of a convolution

Not only does the convolution operation occur frequently in physics, but its Fourier transform is particularly simple. This fact makes it very attractive. We shall now prove the **convolution theorem**, which states that the **Fourier transform of the convolution of two functions is the product of the transforms of the original functions**.

Consider the convolution $h(x)$ of the functions $f(x)$ and $g(x)$, as defined in (4.71). Its Fourier transform is

$$H(k) = \int_{-\infty}^{\infty} \left[\int_{-\infty}^{\infty} f(x')\, g(x - x')\mathrm{d}x' \right] \exp(-\mathrm{i}kx)\mathrm{d}x$$
$$= \int\int_{-\infty}^{\infty} f(x')\, g(x - x') \exp(-\mathrm{i}kx)\mathrm{d}x'\mathrm{d}x. \tag{4.79}$$

By writing $y = x - x'$, we can rewrite this as

$$H(k) = \int\int_{-\infty}^{\infty} f(x')\, g(y) \exp\{-\mathrm{i}k(x' + y)\}\mathrm{d}x'\mathrm{d}y, \tag{4.80}$$

which separates into two factors:

$$\int_{-\infty}^{\infty} f(x') \exp(-\mathrm{i}kx')\mathrm{d}x' \int_{-\infty}^{\infty} g(y) \exp(-\mathrm{i}ky)\mathrm{d}y = F(k)\, G(k) \tag{4.81}$$

or, simply,

$$H(k) = F(k)\, G(k). \tag{4.82}$$

This is the required result.

We can now invoke the Fourier inversion theorem (§4.6) and deduce immediately that **the Fourier transform of the product of two functions equals the convolution of their individual transforms** (up to the ubiquitous multiplying factor of 2π), which is an alternative statement of the convolution theorem.

4.7.5 Fourier transform of a periodic function: back to Fourier series

The link between the Fourier series and Fourier transform can be reforged using the convolution operation. As we saw in §4.7.1, a periodic function can

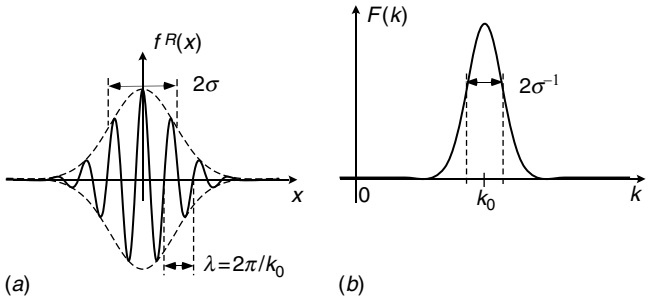

Figure 4.12
(*a*) Real part of the wave-group (4.83); (*b*) its Fourier transform.

Box 4.3 Transform of a wave-group as an example of convolution

There are many examples of functions that can most conveniently be Fourier transformed after they have been broken down into a convolution or a product, and the reader will meet many of them in the succeeding chapters. We shall give one simple example here, which can be employed as a convenient model for more complicated ideas (e.g. in §2.4 and §11.1.2).

A **Gaussian wave-group** has the form $A\exp(\mathrm{i}k_0x)$ modified by a Gaussian envelope (§4.4.3) having variance σ^2 (Fig. 4.12(*a*)). It can be written in the form

$$f(x) = A\exp(\mathrm{i}k_0x)\exp(-x^2/2\sigma^2). \tag{4.83}$$

This function will immediately be recognized as the *product* of the complex exponential $\exp(\mathrm{i}k_0x)$ and the Gaussian (4.45). Its transform is therefore the *convolution* of the transforms of these two functions which are, respectively, $2\pi A\,\delta(k-k_0)$ and (4.48), namely, $(2\pi\sigma^2)^{\frac{1}{2}}\exp(-k^2\sigma^2/2)$. Now the first of these transforms is a δ-function at the point $k = k_0$, and on convolving the latter transform with it, we simply shift the origin of the transform Gaussian to that point, getting

$$F(k) = (2\pi)^{\frac{3}{2}}\sigma A\exp\left[-(k-k_0)^2\sigma^2/2\right], \tag{4.84}$$

as shown in Fig. 4.12(*b*). This result was used in §2.7.

be represented as the convolution of one period $g(x)$ with a one-dimensional periodic array of δ-functions (Fig. 4.13):

$$f(x) = g(x) \otimes \sum_m \delta(x - mb). \tag{4.85}$$

The Fourier transform $F(k)$ is then

$$F(k) = G(k) \cdot \sum_n \delta(k - 2\pi n/b), \tag{4.86}$$

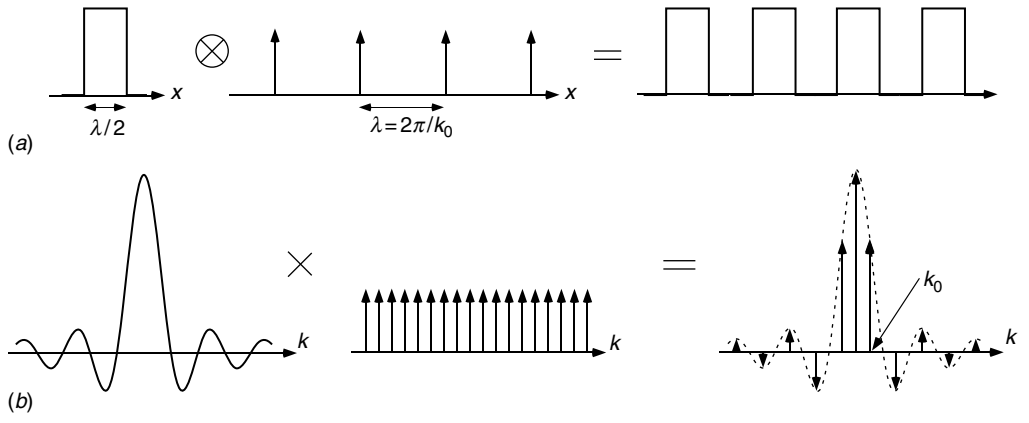

Figure 4.13

A periodic square wave (*a*) represented as the convolution between a square pulse and an array of δ-functions, and (*b*) its Fourier transform, the product of the sinc function and the transformed array of δ-functions.

which samples the transform $G(k)$ at intervals separated by $2\pi/b$ in k. These values can be identified as the Fourier coefficients F_n, i.e. F_n is the strength of the δ-function which appears at $k = 2\pi n/b$.[4]

4.8 Fourier transform of two- and three-dimensional lattices

We have seen above that the concept of a lattice, which is a multi-dimensional array of δ-functions with periodic spacing, is important in describing several physical objects, notably the crystal. In §4.4.2 we calculated the Fourier transform of a one-dimensional lattice, i.e. an infinite array of δ-functions equally spaced by distance b. We showed this to be also an infinite array of δ-functions, with separation $2\pi/b$. In mathematical terms,

$$\sum_{n=-\infty}^{\infty} \delta(x - nb) \quad \overset{FT}{\Longleftrightarrow} \quad \sum_{m=-\infty}^{\infty} \delta(k_x - 2\pi m/b), \tag{4.87}$$

$$\text{or,} \quad \text{comb}(x/b) \quad \overset{FT}{\Longleftrightarrow} \quad \text{comb}(k_x b/2\pi). \tag{4.88}$$

The origin of this method of deriving the transform of a two-dimensional periodic array of points was in a very effective lecture demonstration of the diffraction pattern of two superimposed (multiplied) periodic gratings. See Appendix B.

We can use this result to generate transforms of higher-dimensional lattices. The formal mathematical development for a three-dimensional lattice is given in the appendix to this chapter; here we will limit ourselves to a geometrical two-dimensional derivation which follows directly from the idea of convolution.

[4] It is interesting to note, in passing, that we did not need to stipulate $g(x)$ to be a function limited to a region of length b. Even if it is not so, the Fourier coefficients come out right. There may be several different functions $g(x)$ which give rise to the *same* wave-form; the differences in their transforms $G(k)$ will only be evident at values of $k \neq 2n\pi/b$ which are not sampled! See Problem 2.1.

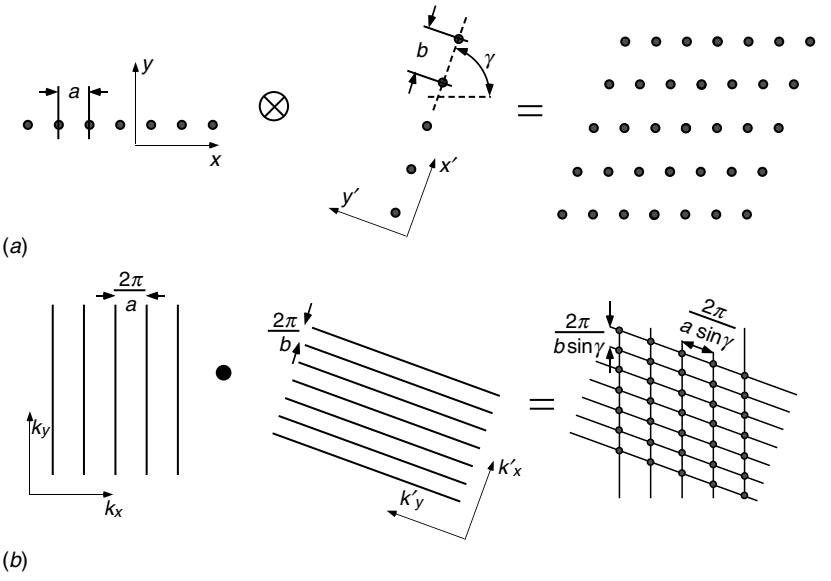

Figure 4.14

Illustrating the Fourier transform of a two-dimensional lattice of δ-functions. The top row shows the operations to create the direct lattice in (x, y) space. The bottom row shows the transforms of the functions and operations in the top row, leading to the reciprocal lattice which is the transform of the direct lattice.

In two dimensions, we first create a set of equally spaced points by multiplying a one-dimensional lattice in the x-direction by a single δ-function in the y-direction:

$$f_1(x,y) = \mathrm{comb}(x/a) \cdot \delta(y). \tag{4.89}$$

We now convolve this with a second similar function with axes x', y' and spacing a:

$$f_2(x',y') = \mathrm{comb}(x'/b) \cdot \delta(y'), \tag{4.90}$$

getting

$$f_{12} = f_1(x,y) \otimes f_2(x',y'), \tag{4.91}$$

That instructs us to put the array f_2 repeatedly with its origin at each of the δ-functions of f_1. The result is clearly a two-dimensional array of δ-functions with lattice spacings a and b. It has a repeat region, called the **unit cell**, which is a parallelogram with sides a and b and angle γ, which is the angle between the x and x' axes (Fig. 4.14(a)).

The Fourier transform F_1 of (4.89) is the convolution $\mathrm{comb}(k_x a/2\pi) \otimes 1(k_y)$, which is an infinite one-dimensional array of lines in the k_y-direction, spaced by $2\pi/a$ along the k_x-axis, which is parallel to x. Likewise, the transform F_2 of (4.90) is a similar array of lines spaced by $2\pi/b$ along the k'_x-axis, parallel to x'. Finally, we multiply these transforms to obtain the transform F_{12} of f_{12} (4.91). The product of two lines is zero, except at the point where they cross, so that F_{12} is a new two-dimensional array of δ-functions (Fig. 4.14(b)) called the **reciprocal lattice**. From the geometry, one sees that the new unit cell is a parallelogram similar to that of the original function, but rotated. It has

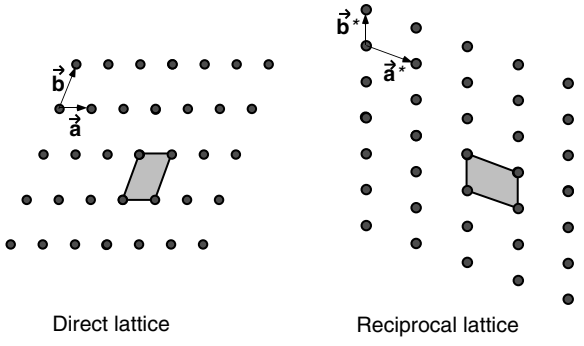

Figure 4.15
Relationship between the direct lattice and the reciprocal lattice vectors, defined respectively by (**a**, **b**) and (**a***, **b***). Note that $\mathbf{a}\cdot\mathbf{b}^* = 0$ and $\mathbf{b}\cdot\mathbf{a}^* = 0$. One unit cell of each lattice is shown shaded.

sides $a^* \equiv 2\pi/(a\sin\gamma)$ and $b^* \equiv 2\pi/(b\sin\gamma)$, which are normal to x' and x respectively (Fig. 4.15). Formally, we represent the direct unit cell by vectors **a** and **b**, and define the **reciprocal lattice vectors**

$$\mathbf{a}^* = 2\pi\frac{\hat{\mathbf{z}}\times\mathbf{b}}{|\mathbf{a}\times\mathbf{b}|}, \qquad \mathbf{b}^* = 2\pi\frac{\hat{\mathbf{z}}\times\mathbf{a}}{|\mathbf{a}\times\mathbf{b}|}, \tag{4.92}$$

$$\mathbf{b}\cdot\mathbf{a}^* = 0, \qquad \mathbf{a}\cdot\mathbf{b}^* = 0, \tag{4.93}$$

where $\hat{\mathbf{z}}$ is the normal to the plane. The denominator $|\mathbf{a}\times\mathbf{b}|$ has value equal to the area of the direct unit cell. In three dimensions, as shown in (4.112),

$$\mathbf{a}^* = 2\pi\frac{\mathbf{b}\times\mathbf{c}}{\mathbf{a}\times\mathbf{b}\cdot\mathbf{c}}, \tag{4.94}$$

etc., cyclically, where the triple product $\mathbf{a}\times\mathbf{b}\cdot\mathbf{c}$ is equal to the volume of the unit cell.

4.9 Correlation functions

A form of convolution function that is of great importance in statistics and has many applications in physics is the **correlation function**, which is formally defined as

$$h_C(x) = \int_{-\infty}^{\infty} f(x')\,g^*(x'-x)\,\mathrm{d}x'. \tag{4.95}$$

This is clearly the convolution of $f(x)$ with $g^*(-x)$. As its name implies, the function measures the degree of similarity between the functions f and g. Suppose the two tend to be similar in magnitude and phase, when referred to origins at 0 and x_0 respectively. Putting $x = x_0, f(x')$ and $g(x'-x_0)$ will then have about the same complex values and so $f(x')\,g^*(x'-x_0)$ will be positive and real. Thus the integral $h_C(x_0)$ will be large and positive. We shall use this function considerably in studying coherence in Chapter 11. Its Fourier transform is

$$H_C(k) = F(k)\,G^*(k). \tag{4.96}$$

4.9.1 Auto-correlation function and the Wiener–Khinchin theorem

A particular case of the correlation function is the **auto-correlation function**, h_{AC} which is defined by (4.95) with $f \equiv g$, i.e. by

$$h_{\mathrm{AC}}(x) = \int_{-\infty}^{\infty} f(x') f^*(x' - x)\, \mathrm{d}x', \tag{4.97}$$

i.e. $f(x) \otimes f^*(-x)$. Since the functions now have the same origin, the auto-correlation function clearly has a strong peak when $x = 0$. We get for the Fourier transform of h_{AC}:

$$H_{\mathrm{AC}}(k) = F(k)\, F^*(k) = |F(k)|^2. \tag{4.98}$$

In words, (4.98) states that the Fourier transform of the auto-correlation function is the square modulus of the transform of the function, also known as its **power spectrum**. From the Fourier inversion theorem, the statement is also true in reverse, up to a factor 2π. It is known as the **Wiener–Khinchin theorem**, and applies similarly in more than one dimension.

Useful information in the auto-correlation function is not limited to the peak at $x = 0$. For example, suppose that a function has a strong periodicity with wavenumber K_0 and period $\Lambda = 2\pi/K_0$. The functions $f(x')$ and $f^*(x' + n\Lambda)$ will then tend to be similar and so their product will be positive; thus periodic peaks in $h_{\mathrm{AC}}(x)$ will appear. The transform, the power spectrum H_{AC}, has a corresponding peak at $k = K_0$, and is thus useful for recognizing the existence of periodicities in the function $f(x)$.

In two and three dimensions, the correlation function finds many applications in pattern recognition, and the auto-correlation function has been widely used in the interpretation of X-ray diffraction patterns, where it is called the **Patterson function**. It is instructive to see how it is built up in a simple case in two dimensions (Fig. 4.16), where $f(x, y)$ consists of three equal real δ-functions. On each δ-point of $f(x', y')$ we put the origin of the function $f^*(-x, -y)$, which is just $f(x, y)$ rotated by 180°. We immediately see a strong point developing at the origin. This strong point at the origin is intrinsic to the auto-correlation of a real function. An experimental application of the spatial auto-correlation function will be discussed briefly in §12.7.

4.9.2 Energy conservation: Parseval's theorem

The process of Fourier transformation essentially takes a certain function $f(x)$ and represents it as the superposition of a set of waves. We shall see later, in Chapter 8, that Fraunhofer diffraction in optics is described by a Fourier

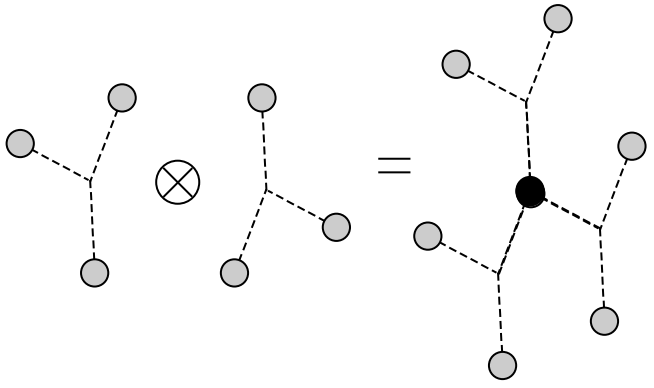

Figure 4.16

Auto-correlation of a two-dimensional function, consisting of three discs representing δ-functions (shown on left). The broken lines are inserted to guide the eye. It is convolved with itself, inverted through the origin, to give the auto-correlation. Notice that the strong spot at the origin is inherent.

transform, where $f(x)$ represents the amplitude distribution leaving the diffracting obstacle and $F(k)$ represents the amplitude distribution in the diffraction pattern. No light energy need be lost in this process, and it would therefore seem necessary that the total power leaving the object be equal to that arriving at the diffraction pattern. In mathematical terms, we expect that

$$\int_{-\infty}^{\infty} |f(x)|^2 \, \mathrm{d}x = C \int_{-\infty}^{\infty} |F(k)|^2 \, \mathrm{d}k. \tag{4.99}$$

The constant C was introduced because of the way in which the Fourier transform is defined; it has no physical significance. This is called **Parseval's theorem**. It can be deduced easily from our discussion of the auto-correlation function in §4.9.1. Applying the Fourier inversion theorem to (4.98), the inverse transform of $|F(k)|^2$ must be equal to $h_{\mathrm{AC}}(x)$. Writing this out explicitly, we get from (4.71)

$$\frac{1}{2\pi} \int_{-\infty}^{\infty} |F(k)|^2 \exp(\mathrm{i}kx) \, \mathrm{d}k = \int_{-\infty}^{\infty} f(x') f^*(x' - x) \, \mathrm{d}x'. \tag{4.100}$$

Now let $x = 0$ in this equation. This gives

$$\frac{1}{2\pi} \int_{-\infty}^{\infty} |F(k)|^2 \, \mathrm{d}k = \int_{-\infty}^{\infty} |f(x')|^2 \, \mathrm{d}x', \tag{4.101}$$

which is Parseval's theorem, and the factor $C = 1/2\pi$.

4.10 Advanced topic: Self-Fourier functions

If we consider the Fourier transform as an operator, which acts on a function to provide its transform, we can ask 'what are the eigenfunctions and eigenvalues of the operator?':

$$\mathcal{F}T[f(x)] = EF(x). \tag{4.102}$$

Although this might appear to be a purely mathematical question, we shall see in §14.6.1 that these eigenfunctions, or 'self-Fourier functions' have practical importance since they define the transverse modes of a laser with a confocal resonator. We already know of two functions that transform into themselves: the infinite array of δ-functions, (§4.4.2) for which the eigenvalue is $E = 2\pi/b$, and the Gaussian for which the eigenvalue is $E = \sqrt{2\pi\sigma^2}$. In fact there is an infinite number of self-Fourier functions, as can be seen from the following argument. To make it simple, we consider only real and symmetric functions, but a slightly more complicated formulation (Caola (1991)) covers all cases. Since $f(x)$ transforms to $F(k)$ and $F(k)$ transforms to $f(-x)$, clearly $f(x)+F(x)$ transforms to $F(k)+f(-k) = f(k)+F(k)$. However, amongst this multitude of possible functions there are some which are both wavenumber and space limited and have practical importance. These can be derived using the relationship between the transform of a function and those of its derivatives (Problem 4.1):

$$F^{(n)}(x) = \int \frac{\partial^n}{\partial x^n} f(x)\ \exp(-\mathrm{i}kx)\ \mathrm{d}x = (-\mathrm{i}k)^n F(k). \tag{4.103}$$

Now we can use the general idea above to generate the self-Fourier functions in the following way. Consider the differential equation

$$\left[\frac{\partial^n}{\partial x^n} + (-\mathrm{i}x)^n\right] f(x) = \alpha f(x). \tag{4.104}$$

Taking the Fourier transform of this equation, and using the Fourier inversion theorem, we get the identical equation in k-space:

$$\left[(-\mathrm{i}k)^n + \frac{\partial^n}{\partial k^n}\right] F(k) = \alpha F(k), \tag{4.105}$$

which must have identical solutions, up to a constant multiplier. We look in particular at the solutions for $n = 2$, which generates the laser modes:

$$\frac{\partial^2 f}{\partial x^2} - x^2 f = \alpha f, \tag{4.106}$$

which is the same equation as Schrödinger's equation for a simple-harmonic oscillator. The Hermite–Gauss functions are well known as its solutions. The first solution is the Gaussian, $f(x) = (\sqrt{2\pi}\sigma^2)^{-1} \exp(-x^2/2\sigma^2)$, which it is easy to verify by substitution and to show that $\alpha = 1$. This, we shall see later, is the amplitude cross-section of a single-mode laser. However, there are many higher-mode solutions of the equation. Thin vertical-cavity surface-emitting lasers (VCSEL) can oscillate in high-order modes which are solutions of the two-dimensional equation equivalent to (4.106):

$$\nabla^2 f - r^2 f = \alpha f, \tag{4.107}$$

some of the solutions of which are shown in Fig. 4.17, compared to observations.

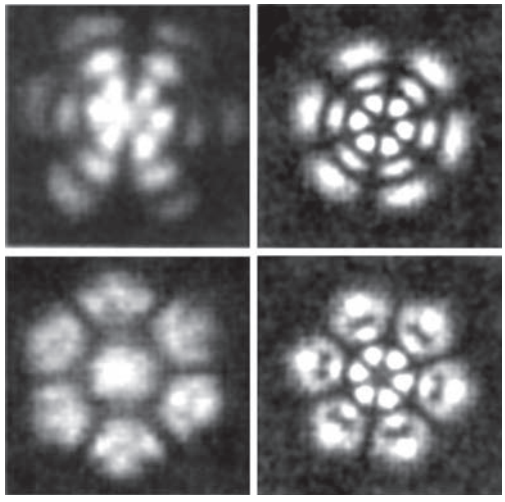

Figure 4.17

Self-Fourier functions in two dimensions, compared with observed transverse modes of VCSELs. (Calculations and experimental results courtesy of Yoav Yadin and Meir Orenstein)

Chapter summary

In this chapter we have outlined Fourier theory with emphasis on the physical, rather than mathematical, aspects. Fourier theory is widely used in optics because we are dealing with waves and oscillatory phenomena. We learnt:

- That the **Fourier series** was originally proposed as a way of analyzing periodic but non-sinusoidal wave-forms, and was later extended to non-periodic functions in the form of the **Fourier transform**;
- The important concept of spatial-frequency or reciprocal space, in which the Fourier transforms of spatial functions exist;
- The definition of the Fourier transform operation in one dimension for a general complex function, and discussed some examples which included a square pulse, a Gaussian function, a sine curve, Dirac's δ-function and a periodic array of δ-functions, and are summarized in Fig. 4.18;
- How to combine simple functions by using convolution and multiplication, which are related to one another by a Fourier transform;
- About **Fourier inversion**, which means that the Fourier transform of a Fourier transform recovers the original function, and will be seen later as the basis of optical imaging;
- About the basic structure of the **reciprocal lattice**, which is the Fourier transform of a periodic lattice in real space, and when extended to three dimensions becomes an important concept in crystallography;

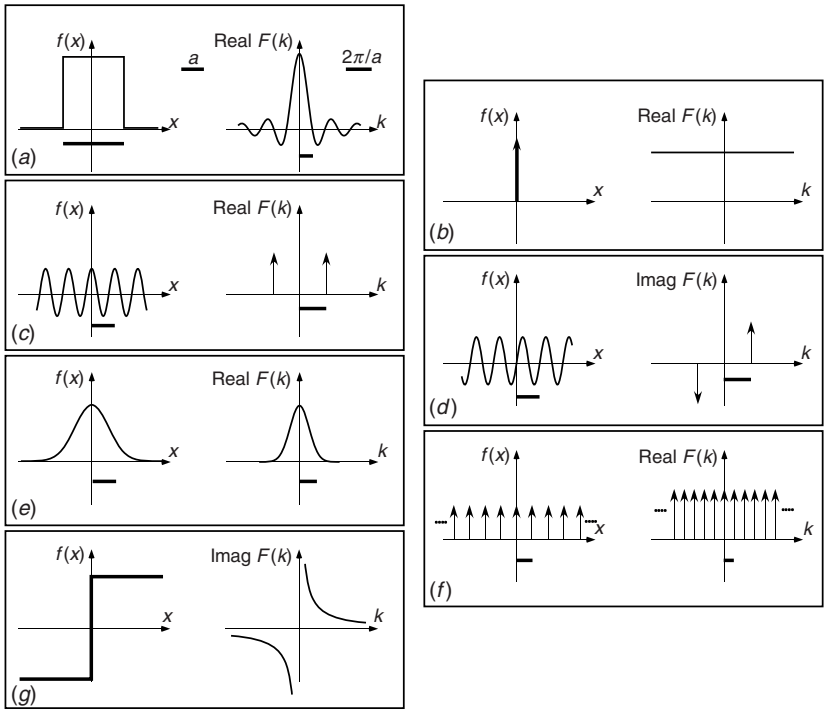

Figure 4.18 Fourier transforms of seven one-dimensional functions that are derived in the text, and will be widely used later in the book. Notice that $\sin(2\pi x/a)$ and the step function are antisymmetric functions, and have imaginary antisymmetric transforms. The scale bar in real space is a and in reciprocal space $2\pi/a$. The functions and transforms: (*a*) $\text{rect}(x/a) \Leftrightarrow a\,\text{sinc}(ka/2)$ (*b*) $\delta(x) \Leftrightarrow 1$
(*c*) $\cos(2\pi x/a) \Leftrightarrow \frac{1}{2}[\delta(k-a)+\delta(k+a)]$ (*d*) $\sin(2\pi x/a) \Leftrightarrow \frac{1}{2}\text{i}[\delta(k-a)-\delta(k+a)]$
(*e*) $\exp(-x^2/2\sigma^2) \Leftrightarrow \sigma\sqrt{2\pi}\exp(-k^2\sigma^2/2)$
(*f*) $\sum_{n=-\infty}^{\infty}\delta(x-na) \Leftrightarrow 2\pi/a\sum_{m=-\infty}^{\infty}(k-2\pi m/a)$ (*g*) $\text{sign}(x) \Leftrightarrow \text{i}/k$

- The Wiener–Khinchin theorem, which states that the transform of a correlation function is the power spectrum of the original function;
- Parseval's theorem, which relates the power spectrum and the intensity of the original function;
- A little about self-Fourier functions, which transform into themselves, and their applications.

Appendix: Formal derivation of the reciprocal lattice in three dimensions

The concept of the reciprocal lattice in three dimensions can be derived formally as follows. This is an alternative algebraic approach to the geometrical one used in §4.8.

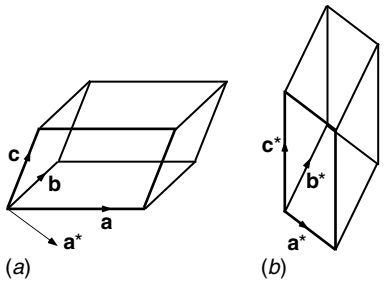

Figure 4.19
Relationship between the direct lattice and the reciprocal lattice vectors in three dimensions.

We define the positions of the δ-functions in an infinite periodic lattice in terms of three given **direct lattice vectors a**, **b** and **c** as

$$f(x,y,z) \equiv f(\mathbf{r}) = \sum_{\tilde{h},\tilde{k},\tilde{m}=-\infty}^{\infty} \delta(\mathbf{r} - \tilde{h}\mathbf{a} - \tilde{k}\mathbf{b} - \tilde{m}\mathbf{c}). \tag{4.108}$$

This puts a δ-function at every point of a periodic lattice whose unit cell is the parallelopiped whose sides are **a**, **b** and **c** (Fig. 4.19(a)).[5]

The Fourier transform of (4.108) is, writing **k** for the vector (k_x, k_y, k_z):

$$F(\mathbf{k}) = \sum_{\tilde{h},\tilde{k},\tilde{m}=-\infty}^{\infty} \exp[-\mathrm{i}\mathbf{k} \cdot (\tilde{h}\mathbf{a} + \tilde{k}\mathbf{b} + \tilde{m}\mathbf{c})]. \tag{4.109}$$

This expression can be simplified if we define three new vectors $\mathbf{a}^\star$ $\mathbf{b}^\star$ and $\mathbf{c}^\star$ such that

$$\mathbf{a} \cdot \mathbf{a}^\star = \mathbf{b} \cdot \mathbf{b}^\star = \mathbf{c} \cdot \mathbf{c}^\star = 2\pi \tag{4.110}$$

$$\mathbf{a}^\star \cdot \mathbf{b} = \mathbf{a}^\star \cdot \mathbf{c} = 0 \quad \text{and cyclically.} \tag{4.111}$$

In other words, $\mathbf{a}^\star$ is normal to **b** and **c** etc. These conditions are satisfied if

$$\mathbf{a}^\star = 2\pi \frac{\mathbf{b} \times \mathbf{c}}{\mathbf{a} \cdot \mathbf{b} \times \mathbf{c}} = 2\pi \frac{\mathbf{b} \times \mathbf{c}}{V}, \tag{4.112}$$

where V is the volume of the unit cell, and equivalently for $\mathbf{b}^\star$ and $\mathbf{c}^\star$.

The vectors $\mathbf{a}^\star$, $\mathbf{b}^\star$ and $\mathbf{c}^\star$ are not parallel, and so **k** can be expressed as a linear combination of them:

$$\mathbf{k} = \tilde{h}^\star\mathbf{a}^\star + \tilde{k}^\star\mathbf{b}^\star + \tilde{m}^\star\mathbf{c}^\star, \tag{4.113}$$

where $\tilde{h}^\star$, $\tilde{k}^\star$ and $\tilde{m}^\star$ are, for the present, any numbers. Then (4.109) becomes

$$\begin{aligned} F(\mathbf{k}) &= \sum_{\tilde{h},\tilde{k},\tilde{m}=-\infty}^{\infty} \exp[-\mathrm{i}(\tilde{h}\tilde{h}^\star\mathbf{a}^\star \cdot \mathbf{a} + \tilde{k}\tilde{k}^\star\mathbf{b}^\star \cdot \mathbf{b} + \tilde{m}\tilde{m}^\star\mathbf{c}^\star \cdot \mathbf{c})] \\ &= \sum \exp[-2\pi\mathrm{i}(\tilde{h}\tilde{h}^\star + \tilde{k}\tilde{k}^\star + \tilde{m}\tilde{m}^\star)]. \end{aligned} \tag{4.114}$$

[5] For a given lattice, there are many different ways of choosing **a**, **b** and **c**, but there are usually one or two that are obviously simplest.

This sum, for general $\tilde{h}^\star$, $\tilde{k}^\star$, $\tilde{m}^\star$, is usually zero, being an infinite sum of complex numbers that cancel since they are distributed uniformly around the unit circle. However, if $\tilde{h}^\star$, $\tilde{k}^\star$ and $\tilde{m}^\star$ are *integers*, every term is unity, and $F(\mathbf{k})$ is infinite. Thus $F(\mathbf{k})$ is a **three-dimensional array of δ-functions** on the lattice defined by the vectors $\mathbf{a}^\star$, $\mathbf{b}^\star$ and $\mathbf{c}^\star$. This array is called the **reciprocal lattice**. In two dimensions, this was illustrated in Fig. 4.15, and the equivalent three-dimensional structure is shown in Fig. 4.19(*b*).

Problems

4.1. Given that the transform of $f(x)$ is $F(k)$, find a general expression for the transform of $\int_0^x f(x')\,\mathrm{d}x'$.

4.2. The 'Hartley transform' of a real function $v(x)$ is defined as

$$H(k) = \int_{-\infty}^{\infty} v(x)[\cos kx + \sin kx]\,\mathrm{d}x. \tag{4.115}$$

Show that it is related to the Fourier transform by

$$H(k) = \mathrm{Re}[V(k)] - \mathrm{Im}[V(k)]. \tag{4.116}$$

Devise a method, using Fourier optics, to record the Hartley transform optically. Note that it contains all the information of the Fourier transform in a single real function, but only works for real functions. See Bracewell (1986) for a thorough discussion; an experimental method is given by Villasenor and Bracewell (1987).

4.3. Find the Fourier transform of a decaying series of δ-functions:

$$f(t) = \sum_{n=0}^{\infty} \delta(t - nt_0)\mathrm{e}^{-\alpha n}. \tag{4.117}$$

How can this result be used to understand the Fabry–Perot interferometer?

4.4. Derive the Fourier transform of a periodic triangular wave, defined in one period as $y = |x|$ $(-\pi < x \leq \pi)$. How can the result be related to the auto-correlation of a square pulse?

4.5. Use the result of the previous problem to simulate the results of the experiment on the guitar string described in Box 2.1.

4.6. The period of a square wave is b, the value being 1 for a period c within the cycle and 0 for $b - c$ (this is called 'duty cycle' $= c/b$). Use the convolution theorem to study how its Fourier transform changes as a function of c/b. What happens when $c/b \to 1$?

4.7. Show that the self-convolution of $\mathrm{sinc}(ax/2)$ is the same function multiplied by a constant.

4.8. Compare the functions $(f_1 \otimes f_2) \times f_3$ and $f_1 \otimes (f_2 \times f_3)$ and their transforms, when $f_1 = \sum_{n=-\infty}^{\infty} \delta(x - nb)$, $f_2 = \mathrm{rect}(x/b)$ and $f_3 = \exp(\mathrm{i}\alpha x)$.

4.9. The convolution has some odd properties. For example, a group of three δ-functions at intervals b can be represented as the product of the infinite periodic array $\sum \delta(x - nb)$ multiplied by $\mathrm{rect}(x/c)$ where c has any value between $2b + \epsilon$ and $4b - \epsilon$ (ϵ arbitrarily small). Show that the transform, which can be expressed as a convolution, is indeed independent of the argument of rect between these limits. (This problem is not easy!) The solution is discussed in detail by Collin (1991).

4.10. A periodic array of δ-functions has every fifth member missing. What is its Fourier transform?

4.11. The image of a thick black straight line at an angle to the x- and y-axes on a white background is digitized on a grid of $N \times N$ squares, so that a square is white or black depending on whether it is more or less than half covered by the line (Fig. 4.20). The digital Fourier transform of the line is then calculated. When N is small, the transform is predominantly along the k_x and k_y axes (transforms of elementary squares). As N increases, the transform approaches a limit that is predominantly along the axis at right-angles to the line. How does the transition take place?

4.12. A 'wavelet transform' is the Fourier transform of a function whose spectrum changes with time, and consists of a representation of the Fourier transform measured during an interval δt as a function of time (for examples see Combes *et al.* (1990)). It is often used in speech and music analysis. With the help of the convolution theorem, show that δt and the frequency resolution $\delta\omega$ of the wavelet transform are related by $\delta t \cdot \delta\omega \approx 2\pi$.

4.13. A long one-dimensional quasi-periodic array of δ-functions is created as follows. It has a basic period b, and within each cell there is a δ-function at either $x = 0$ or $x = h$ where $h < b/2$. The probability of each is 50%. Use the concept of the auto-correlation function to calculate the power spectrum of this array.

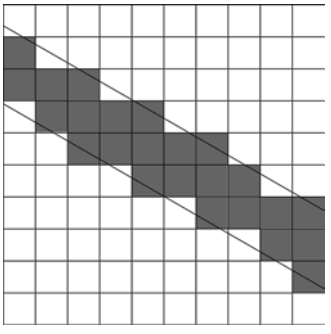

Figure 4.20
Digital representation of a diagonal line.

References

Bracewell, R. N. (1986), *The Hartley Transform*, Oxford: Oxford University Press.

Brigham, E. O. (1988), *The Fast Fourier Transform and its Applications*, Englewood Cliffs, NJ: Prentice-Hall International.

Caola, M. J. (1991), Self-Fourier functions, *J. Phys. A* **24**, 1143.

Collin, R. E. (1991), *Field Theory of Guided Waves*, 2nd edn., New York: IEEE.

Combes, J. M., Grossman, A. and Tchamitchian, Ph. (1990), *Time-frequency Methods and Phase Space*, Berlin: Springer.

Prestini, E. (2004), *The Evolution of Applied Harmonic Analysis: Models of the Real World*, Boston: Birkhäuser.

Villasenor, J. and Bracewell, R. N. (1987), Optical phase obtained by analogue Hartley transformation, *Nature* **330**, 735.

Walker, J. S. (1988), *Fourier Analysis*, New York: Oxford University Press.

5 Electromagnetic waves

This chapter will discuss the electromagnetic wave as a most important example of the general treatment of wave propagation presented in Chapter 2. We shall start at the point where the elementary features of classical electricity and magnetism have been summarized in the form of Maxwell's equations, and the reader's familiarity with the steps leading to this formulation will be assumed (see, for example, Grant and Phillips (1990), Jackson (1999), Franklin (2005)). It is well known that Maxwell's formulation included for the first time the displacement current $\partial \mathbf{D}/\partial t$, the time derivative of the fictitious displacement field $\mathbf{D} = \epsilon_0 \mathbf{E} + \mathbf{P}$, which is a combination of the applied electric field $\mathbf{E}$ and the electric polarization density $\mathbf{P}$. This field will turn out to be of prime importance when we come to extend the treatment in this chapter to wave propagation in anisotropic media in Chapter 6.

In this chapter we shall learn:

- about the properties of electromagnetic waves in isotropic linear media;
- about simple-harmonic waves with planar wavefronts;
- about radiation of electromagnetic waves;
- the way in which these waves behave when they meet the boundaries between media: the Fresnel coefficients for reflection and transmission;
- about optical tunnelling and frustrated total internal reflection;
- about electromagnetic waves in conducting media;
- some consequences of the time-reversal symmetry of Maxwell's equations;
- about electromagnetic momentum, radiation pressure and optical tweezers;
- about angular momentum of waves that have spiral wavefronts, instead of the usual plane wavefronts;
- what happens to waves in materials where both the electric and magnetic susceptibilities are negative, which has recently given rise to the new topic of left-handed, or negative refractive index materials.

Essentially the rest of the book consists of elaboration of these ideas, until the final chapter, which discusses the quantization of the electromagnetic field, an aspect that Maxwell could not have predicted in his lifetime and that is now one of the most vibrant areas of modern research.

5.1 Maxwell's equations and their development

Some of Maxwell's other major achievements were in colour vision, thermodynamics and statistical mechanics.

In his day, J. C. Maxwell did not have the modern concepts of vector differential operators (grad, div, curl) at his disposal. One of his major achievements was to summarize the classical properties of the electric fields **E** and **D**, the magnetic fields **H** and **B**, charge density ρ and current density **j**, in a set of 20 differential equations relating their various components! It was an almost incredible achievement that he could see that these equations led to wave propagation. Using vector operators, his results can today be summarized in *four* elegant and simple equations, and the derivation of the wave motion is much more transparent. The equations are as follows:

$$\text{Gauss's law in electrostatics becomes:} \quad \nabla \cdot \mathbf{D} = \rho, \tag{5.1}$$

$$\text{Gauss's law in magnetostatics becomes:} \quad \nabla \cdot \mathbf{B} = 0, \tag{5.2}$$

$$\text{Ampère's law becomes:} \quad \nabla \times \mathbf{H} = \frac{\partial \mathbf{D}}{\partial t} + \mathbf{j}, \tag{5.3}$$

$$\text{Faraday's law becomes:} \quad \nabla \times \mathbf{E} = -\frac{\partial \mathbf{B}}{\partial t}. \tag{5.4}$$

In vacuum, **D** and **E** are identical fields; the fact that in SI units, which will be used in this book, $\mathbf{D} = \epsilon_0 \mathbf{E}$, where ϵ_0 has a non-unit value, only reflects the fact that **D** and **E** are measured in different *units*. The same applies to the applied magnetic field **H** and the magnetic induction **B**, which is the measured field when magnetic polarization effects are taken into account. In a vacuum, $\mathbf{B} = \mu_0 \mathbf{H}$, where μ_0 reflects the difference in units. In a medium, **D** really does differ from **E**, and **B** from **H**. This is represented, in the case of a linear isotropic medium, by scalar dimensionless constants ϵ (dielectric constant), and μ (magnetic permeability):

$$\mathbf{D} = \epsilon \epsilon_0 \mathbf{E}, \tag{5.5}$$

$$\mathbf{B} = \mu \mu_0 \mathbf{H}. \tag{5.6}$$

The values of ϵ and μ are usually frequency dependent, as will be discussed in Chapter 10.

5.1.1 Electromagnetic waves in an isotropic linear non-conducting medium

The simplest case for which Maxwell's equations lead to a non-dispersive wave equation (2.6) is in a medium which is **isotropic, linear and non-conducting**, where charge density ρ and current density **j** are both zero. An **isotropic** medium is one in which all directions in space are equivalent, and there is no

Materials such as gases, monatomic liquids and glasses are examples of such media. Water and indium-tin-oxide are opaque conductors at low frequencies, but transparent and non-conducting at optical frequencies.

difference between right-handed and left-handed rotation. A **linear** medium is one in which the polarization produced by an applied electric or magnetic field is proportional to that field. Since interatomic electric fields are of the order of 10^{11} V m^{-1}, macroscopic laboratory electric fields (usually $< 10^8$ V m^{-1}) are small in comparison, and their effects are consequently linear. The oscillating fields produced by intense laser beams are often orders of magnitude larger and can cause **non-linear** response, which will be discussed briefly at the end of Chapter 13.

Then (5.1)–(5.4) become

$$\nabla \cdot \mathbf{D} = \epsilon\epsilon_0 \nabla \cdot \mathbf{E} = 0, \tag{5.7}$$

$$\nabla \cdot \mathbf{B} = \mu\mu_0 \nabla \cdot \mathbf{H} = 0, \tag{5.8}$$

$$\nabla \times \mathbf{H} = \frac{\partial \mathbf{D}}{\partial t} = \epsilon\epsilon_0 \frac{\partial \mathbf{E}}{\partial t}, \tag{5.9}$$

$$\nabla \times \mathbf{E} = -\frac{\partial \mathbf{B}}{\partial t} = -\mu\mu_0 \frac{\partial \mathbf{H}}{\partial t}. \tag{5.10}$$

Taking $(\nabla\times)$ of both sides of (5.10) and substituting (5.9) we have

$$\nabla \times (\nabla \times \mathbf{E}) = -\mu\mu_0 \frac{\partial}{\partial t}(\nabla \times \mathbf{H}) = -\mu\mu_0\epsilon\epsilon_0 \frac{\partial^2 \mathbf{E}}{\partial t^2}. \tag{5.11}$$

On expanding $\nabla \times (\nabla \times \mathbf{E}) = \nabla(\nabla \cdot \mathbf{E}) - \nabla^2\mathbf{E}$, (5.11) becomes

$$\nabla^2 \mathbf{E} = \epsilon\mu\,\epsilon_0\mu_0 \frac{\partial^2 \mathbf{E}}{\partial t^2}. \tag{5.12}$$

In Cartesians, $\nabla^2\mathbf{E}$ is the vector

$$\nabla \cdot (\nabla \mathbf{E}) \equiv (\nabla^2 E_x, \nabla^2 E_y, \nabla^2 E_z).$$

5.1.2 Wave velocity and refractive index

Following §2.2, we immediately see that the solution to (5.12) is a vector wave with velocity

$$v = (\epsilon\mu\,\epsilon_0\mu_0)^{-\frac{1}{2}}. \tag{5.13}$$

This value of c retains the metre and second as accurately as they have ever been defined, but makes c itself the fundamental constant – a decision made in 1986.

In free space, this velocity is $c = (\epsilon_0\mu_0)^{-\frac{1}{2}}$ which is an important fundamental constant, now defined as $2.997\,924\,58 \times 10^8$ m s^{-1} exactly. Following this definition, the SI defines μ_0 as $4\pi \times 10^{-7}$ H m^{-1} from which ϵ_0 can be calculated as $(\mu_0 c^2)^{-1} = 8.854 \times 10^{-12}$ F m^{-1}.

In accordance with the usual practice in optical work we shall assume in most of the book that the magnetic permeability μ of media is unity at the frequencies of light waves, unless otherwise stated. Recently the possibility of **negative refractive index** or **left-handed** materials has been raised, and a

requirement for these materials is that $\mu \neq 1$, but a discussion of these will be delayed till §5.10. Assuming then that $\mu = 1$, the ratio between the velocity of electromagnetic waves in a vacuum to that in an isotropic medium, which is the definition of **refractive index**, n, is then

$$n = c/v = \epsilon^{\frac{1}{2}}, \tag{5.14}$$

where again the value of ϵ at the right frequency must be used.

5.2 Plane wave solutions of the wave equation

The **plane wave** (cf. §2.5)

$$\mathbf{E} = \mathbf{E}_0 \exp[\mathrm{i}(\mathbf{k} \cdot \mathbf{r} - \omega t)] \tag{5.15}$$

is an important solution of (5.12) where $\omega/k = v$. For this wave-form, $\nabla \equiv -\mathrm{i}\mathbf{k}$ and $\partial/\partial t \equiv \mathrm{i}\omega$, and (§2.5.2) allows us to write (5.7)–(5.10) in the form

$$\mathbf{k} \cdot \mathbf{D} = \epsilon\epsilon_0 \mathbf{k} \cdot \mathbf{E} = 0, \tag{5.16}$$

$$\mathbf{k} \cdot \mathbf{B} = \mu_0 \mathbf{k} \cdot \mathbf{H} = 0, \tag{5.17}$$

$$\mathbf{k} \times \mathbf{H} = -\omega\mathbf{D} = -\omega\epsilon\epsilon_0 \mathbf{E}, \tag{5.18}$$

$$\mathbf{k} \times \mathbf{E} = \omega\mathbf{B} = \omega\mu_0 \mathbf{H}. \tag{5.19}$$

These equations immediately give us an insight into the disposition and size of the field vectors (Fig. 5.1): **D**, **H** and **k** form a right-handed mutually orthogonal set, as do **E**, **B** and **k**, and by virtue of the isotropy of the medium, also **E**, **H** and **k**. **Electromagnetic waves are therefore transverse**. Moreover, the magnitudes of **E** and **H** are related by

$$Z \equiv \frac{E}{H} = \frac{k}{\epsilon\epsilon_0\omega} = \sqrt{\frac{\mu_0}{\epsilon_0}}\,\frac{1}{\sqrt{\epsilon}}. \tag{5.20}$$

The impedance is the ratio of E to H; E has units of volts/metre (V m^{-1}) and H is measured in SI in amperes/metre (A m^{-1}), so that Z has dimensions volt/ampere = ohm.

The constant Z is called the **impedance** of the medium to electromagnetic waves. In free space $\epsilon = 1$ and $Z_0 = \sqrt{\mu_0/\epsilon_0} = c\mu_0 = 377$ ohms. Then, from (5.14),

$$Z = Z_0/n \tag{5.21}$$

relates the impedance of a medium to its refractive index.

The plane containing **D** and **k** is called the **plane of polarization**, which will be of paramount importance in Chapter 6.

The fact that equations (5.16)–(5.19) are completely real indicates that there are no phase differences between the oscillations of the electric and magnetic fields. **H** can thus be written

$$\mathbf{H} = \mathbf{H}_0 \exp[\mathrm{i}(\mathbf{k} \cdot \mathbf{r} - \omega t)], \tag{5.22}$$

where $\mathbf{H}_0$ is orthogonal to **k** and $\mathbf{E}_0$ and has magnitude E_0/Z.

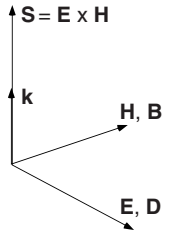

Figure 5.1

Disposition of vectors in an electromagnetic wave in an isotropic medium propagating along the direction of **k**.

5.2.1 Flow of energy in an electromagnetic wave

An important feature of electromagnetic waves is that they can transport energy. The vector describing the flow of energy is the **Poynting vector**, which can be shown in general to be

$$\mathbf{S} = \mathbf{E} \times \mathbf{H}. \tag{5.23}$$

It has dimensions of energy per unit time per unit area, and its absolute value is called the **intensity** of the wave. It is easy to see that this vector lies parallel to **k** in the isotropic medium. The time-averaged value of S, when **E** and **H** have the same phase, and are mutually orthogonal as in Fig. 5.1, is

$$\langle S \rangle = \langle E_0 \sin \omega t \, H_0 \sin \omega t \rangle = \frac{1}{2} E_0 H_0 = \frac{1}{2} E_0^2 / Z \tag{5.24}$$

(since the average value of $\sin^2 \omega t$ is $\frac{1}{2}$ over a time $\gg 1/\omega$).

If there is a phase difference between **E** and **H**, the mean value of the wave power $S = \langle EH \rangle$ depends on it. In particular, when the phase difference is 90°, as in an evanescent wave (§5.5.1), $S = 0$.

5.3 Radiation

Electromagnetic radiation is initiated by moving charges. Two types of source, a linearly accelerating charge distribution and an oscillating multipole, are of particular importance in optics and we shall discuss them briefly. A full treatment is given in the texts on electromagnetic theory.

5.3.1 Radiation by an accelerating charge

A charged particle moving at uniform velocity in a straight line is equivalent to an electric current, and produces a constant magnetic field. This does not radiate electromagnetic waves. However, if the particle accelerates, the magnetic field has a time derivative that results in an electric field too. Then, the cross product **S** of the electric and magnetic fields results in radiation of electromagnetic energy. For a particle of charge q moving with velocity $\mathbf{v}(t)$ and acceleration $\dot{\mathbf{v}}$, the radiative electric field at radius vector $\mathbf{r} \equiv \hat{\mathbf{n}} r$ is

$$\mathbf{E} = \frac{q}{4\pi\epsilon_0 r c^2} [\hat{\mathbf{n}} \times (\hat{\mathbf{n}} \times \dot{\mathbf{v}})], \tag{5.25}$$

$$\text{with magnitude} \quad |E| = \frac{q\dot{\mathbf{v}}}{4\pi\epsilon_0 c^2 r} \sin\theta, \tag{5.26}$$

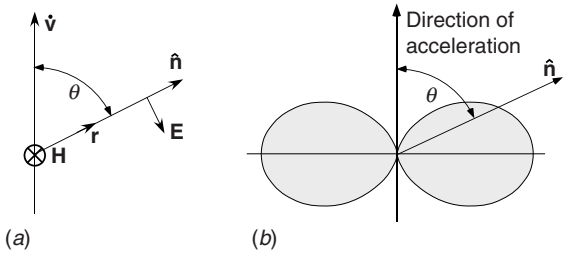

Figure 5.2

Radiation from an accelerating charge: (*a*) orientation of vectors, (*b*) section of the radiation polar diagram, which shows the intensity of radiation as a function of its direction. This has the form of a torus in three dimensions.

where θ is the angle between $\dot{\mathbf{v}}$ and $\hat{\mathbf{n}}$. The field lies in the plane containing these vectors, transverse to $\hat{\mathbf{n}}$, as shown in Fig. 5.2(*a*).

The magnetic field is given by $\mathbf{H} = Z_0^{-1}(\hat{\mathbf{n}} \times \mathbf{E})$ and is thus also transverse to $\hat{\mathbf{n}}$, but polarized normal to the $(\mathbf{v}, \hat{\mathbf{n}})$ plane. The fields are **retarded**, which means that $\mathbf{v}$ is evaluated a time r/c earlier than $\mathbf{E}$ and $\mathbf{H}$ are measured. Together, they result in energy being radiated predominantly in the plane normal to the direction of the acceleration. The Poynting vector is, from (5.26),

$$\mathbf{S} = \mathbf{E} \times \mathbf{H} = \frac{\hat{\mathbf{n}} q^2 \dot{\mathbf{v}}^2}{16\pi^2 \epsilon_0 c^3 r^2} \sin^2\theta, \tag{5.27}$$

which has maximum value in the direction normal to $\dot{\mathbf{v}}$. We can represent this by a **radiation polar diagram** in which the magnitude of $\mathbf{S}(\hat{\mathbf{n}})$ is represented as a polar graph with its centre at the radiating charge, Fig. 5.2(*b*). In the case of a charged particle traversing a circular orbit, as in a synchrotron, the radiation is then maximum in the plane tangential to the orbit and perpendicular to the instantaneous acceleration $\dot{\mathbf{v}}$. The total power radiated is then found by integrating (5.27) over the surface of a sphere of radius r:

$$P = \frac{q^2 \dot{\mathbf{v}}^2}{6\pi \epsilon_0 c^3}. \tag{5.28}$$

5.3.2 Radiation emitted by an oscillating dipole

At distances of the order of a or smaller we have near-field radiation, which is used for imaging in the near-field scanning optical microscope (§12.6.3).

The radiative system most frequently encountered in elementary optics is a periodically oscillating dipole. This arises, for example, in scattering theory (§13.2) when a wave is incident on a polarizable body – an atom, molecule or larger particle. The electric field of the wave polarizes the body and gives it a dipole moment which then oscillates at the wave frequency.

The radiated fields can be derived directly from §5.3.1. A point charge q has position $z(t) = a\cos\omega t$, representing a dipole with instantaneous moment $p = qz = qa\cos\omega t$. The acceleration is

$$\dot{\mathbf{v}} = -a\omega^2 \hat{\mathbf{z}} \cos\omega t. \tag{5.29}$$

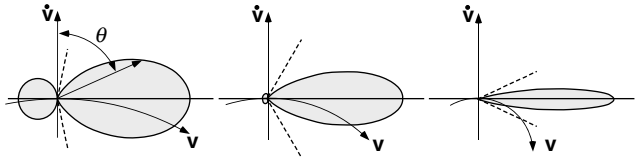

Figure 5.3
Synchrotron radiation. The diagram shows sections of the radiation polar diagrams in the plane of the orbit, for charged particle at $v/c = 0.2, 0.5$ and 0.9, transformed relativistically to the laboratory frame of reference. The broken lines show the axes along which the power becomes zero, which confine the radiated beam. The figures are scaled to the same maximum value; in fact, for a given value of $\dot{v}$, the maxima in the direction of $\mathbf{v}$ are in the ratio 2:8:1000 for the three examples.

Box 5.1 Synchrotron radiation

A **synchrotron** is a charged particle accelerator with the form of a ring in which electrons or other charged particles are accelerated during linear motion in an electric field, and uniform magnetic fields are used to constrain them to a periodic orbit of order 100 m radius. A detailed description of the physics is given by Wille (1991). A pulse of electrons initially accelerated to an energy of about 10 MeV is injected into the ring and travels around it many times, the accelerating field being synchronized (hence the name 'synchrotron') with each arrival of the pulse. X-radiation is then emitted by the electrons in the magnetic field regions, because of their centripetal acceleration. As the energy of the electrons increases, the magnetic fields have to be changed synchronously to keep the electrons in orbit. The energy loss by radiation increases fast, and equilibrium is reached at about 10 GeV. Several synchrotron radiation sources of this type operate around the world.

The calculation in §5.3.1 assumed that the charge motion is not relativistic, i.e. $v \ll c$. However, as $v \to c$ the radiative power increases enormously for two reasons: first, because of the dependence on $\dot{\mathbf{v}}^2$, and second because the radiation becomes more and more confined to a small angular range close to the direction of $\mathbf{v}$ when Fig. 5.2 is transformed to the laboratory frame of reference. The result of a relativistic calculation of the angular power distribution of the radiation is then shown in Fig. 5.3, where we emphasize the fact that the scale changes by a factor of 500 between (*a*) and (*c*).

The frequency spectrum of synchrotron radiation arises from Fourier analysis of what is essentially a short burst of radiation which is emitted every time an electron passes through the curved orbital region. In practice this contains considerable amounts of X-radiation concentrated into an intense almost-collimated beam of radiation. Important applications of synchrotron X-radiation which are discussed later in this book are X-ray diffraction by large molecules (§8.6), including phase retrieval methods for non-periodic structures (§8.8), and X-ray microscopy using Fresnel zone plates as imaging elements (§7.5).

Then, at distances large compared with a we have $\mathbf{E}$ and $\mathbf{H}$ transverse to $\hat{\mathbf{n}}$:

$$\mathbf{E} = \frac{-qa\omega^2}{4\pi\epsilon_0 c^2 r}[\hat{\mathbf{n}} \times (\hat{\mathbf{n}} \times \hat{\mathbf{z}})], \tag{5.30}$$

$$\mathbf{H} = Z_0^{-1}\hat{\mathbf{n}} \times \mathbf{E}. \tag{5.31}$$

The radiation polar diagram for the Poynting vector $\mathbf{S} = \mathbf{E} \times \mathbf{H}$ from such an oscillating dipole has the same $\sin^2\theta$ dependence as in (5.27), which was shown in Fig. 5.2(b). It is most important to appreciate that $\mathbf{S}$ has zero value along the axis $\hat{\mathbf{z}}$ of the dipole, emphasizing the fact that electromagnetic radiation is transversely polarized.

The total power radiated from the dipole is, like (5.28),

$$P = \frac{1}{6\pi\epsilon_0} \cdot \frac{p_0^2\omega^4}{c^3}\cos^2\omega t, \tag{5.32}$$

A heated body, such as a filament lamp, emits electromagnetic radiation because the electrons and atoms are in constant motion. They create random dipole moments, which radiate at a wide range of frequencies. This 'black-body radiation' is discussed in §14.1

where $p_0 = qa$ is the amplitude of the dipole moment oscillations. Since the average value of $\cos^2 x$ is $\frac{1}{2}$, the mean power radiated during a period $\gg \omega^{-1}$ is

$$\langle P \rangle = \frac{p_0^2\omega^4}{12\pi c^3\epsilon_0}. \tag{5.33}$$

A noticeable feature of this expression is the strong dependence on ω; the power radiated from a dipole oscillator is proportional to the *fourth power* of the frequency. One practical result of this dependence is the blue colour of the sky (§13.2.1); another one is a basic limitation to the transparency of glass and optical fibres (§10.2).

5.4 Reflection and refraction at an abrupt interface between two media

At a sharp boundary between two media, there are simple relationships that must be obeyed between the fields on the two sides. The components of the fields $\mathbf{E}$ and $\mathbf{H}$ parallel to the surface are equal on the two sides, whereas the normal components of $\mathbf{D}$ and $\mathbf{B}$ must likewise be continuous. Full proof of these conditions, which we shall use extensively in what follows, is given in the texts on electromagnetic theory. Application of the boundary conditions allows us to derive reflection and transmission coefficients for electromagnetic waves.

5.4.1 The Fresnel coefficients

Suppose that a plane electromagnetic wave with wave-vector $\mathbf{k}$ and electric field amplitude $\mathbf{E}_0$ is incident on a plane surface separating isotropic media with refractive indices n_1 and n_2. The angle of incidence between the incident

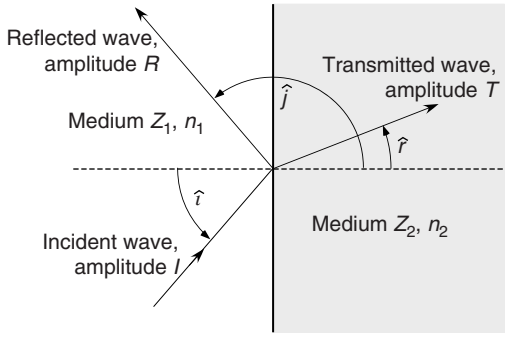

Figure 5.4
Incident, reflected and transmitted waves.

Other names which are commonly used for ∥ are p or TM (transverse magnetic), and for ⊥ are s (German: senkrechte) or TE (transverse electric).

wave-vector $\mathbf{k}$ and the normal to the surface $\hat{\mathbf{n}}$ is $\hat{\imath}$. Without loss of generality we can treat separately the two cases where the incident vector $\mathbf{E}$ lies in the plane defined by $\mathbf{k}$ and $\hat{\mathbf{n}}$, denoted by ∥, and that where $\mathbf{E}$ is normal to this plane, denoted by ⊥. Any other polarization, plane or otherwise (§6.2), can be considered as a linear superposition of these two cases.

Figure 5.4 shows the geometry of this situation. Notice that reflected and transmitted waves have been introduced. The plane containing the incident wave-vector $\mathbf{k}$, the reflected and transmitted wave-vector and the normal $\hat{\mathbf{n}}$ is the (x,z) plane, and the vector $\hat{\mathbf{n}}$ is along the z-direction. We denote the amplitudes (electric field magnitudes) of the incident, reflected and transmitted waves by I, R and T respectively. The magnitudes of the wave-vectors in the two media are k_1 and k_2 and clearly $k_1/n_1 = k_2/n_2 = k_0$ since both waves have the same frequency.

Consider first the ⊥ mode, so that the incident $\mathbf{E} = (0, I, 0)$. At $t = 0$,

$$\begin{aligned}
\text{incident wave:} \quad & E_y = E_{yI} = I\exp[-\mathrm{i}(k_1 z\cos\hat{\imath} + k_1 x\sin\hat{\imath})],\\
\text{reflected wave:} \quad & E_y = E_{yR} = R\exp[-\mathrm{i}(k_1 z\cos\hat{\jmath} + k_1 x\sin\hat{\jmath})],\\
\text{transmitted wave:} \quad & E_y = E_{yT} = T\exp[-\mathrm{i}(k_2 z\cos\hat{r} + k_2 x\sin\hat{r})].
\end{aligned} \tag{5.34}$$

Any changes of phase occurring on reflection and transmission will be indicated by negative or complex values of R and T. The magnetic fields are related by impedances $Z = E/H = Z_0/n$ and are perpendicular to $\mathbf{k}$ and $\mathbf{E}$. The fact that the reflected wave travels in the opposite z-direction to the others will be taken care of by the appropriate value of $\hat{\jmath}$ so that the Poynting vector, the energy flow, is in the correct direction. Given the direction of the field $\mathbf{E} = (0, E_y, 0)$, we find

$$\begin{aligned}
\text{incident wave:} \quad & H_z = E_{yI}Z_0^{-1}n_1\sin\hat{\imath},\\
& H_x = -E_{yI}Z_0^{-1}n_1\cos\hat{\imath};\\
\text{reflected wave:} \quad & H_z = E_{yR}Z_0^{-1}n_1\sin\hat{\jmath},\\
& H_x = -E_{yR}Z_0^{-1}n_1\cos\hat{\jmath};\\
\text{transmitted wave:} \quad & H_z = E_{yT}Z_0^{-1}n_2\sin\hat{r},\\
& H_x = -E_{yT}Z_0^{-1}n_2\cos\hat{r}.
\end{aligned} \tag{5.35}$$

The boundary conditions can then be applied. E_y is itself the parallel component, which is continuous, so from (5.34) at the point $x = 0$, $z = 0$ we have

$$I + R = T. \tag{5.36}$$

For $E_{yI} + E_{yR} = E_{yT}$ at any point in the plane $z = 0$, their oscillatory parts must be identical:

$$k_1 \sin\hat{\imath} = k_1 \sin\hat{\jmath} = k_2 \sin\hat{r}, \tag{5.37}$$

from which $\hat{\jmath} = \pi - \hat{\imath}$ and **Snell's law** follows:

$$\sin\hat{\imath} = \frac{k_2}{k_1}\sin\hat{r} = \frac{n_2}{n_1}\sin\hat{r} = n_r \sin\hat{r}, \tag{5.38}$$

where n_r is the relative refractive index between the two media. Continuity of the parallel component H_x at $(x, z) = (0, 0)$ gives

$$IZ_1^{-1}\cos\hat{\imath} + RZ_1^{-1}\cos\hat{\jmath} = TZ_2^{-1}\cos\hat{r}. \tag{5.39}$$

We define reflection and transmission coefficients $\mathcal{R} \equiv R/I$, $\mathcal{T} \equiv T/I$. Then, for this polarization (denoted by the subscript $\perp$) we have from (5.36), (5.37) and (5.21),

$$\mathcal{R}_\perp = \frac{n_1\cos\hat{\imath} - n_2\cos\hat{r}}{n_1\cos\hat{\imath} + n_2\cos\hat{r}} = \frac{\cos\hat{\imath} - n_r\cos\hat{r}}{\cos\hat{\imath} + n_r\cos\hat{r}}, \tag{5.40}$$

$$\mathcal{T}_\perp = \frac{2n_1\cos\hat{\imath}}{n_1\cos\hat{\imath} + n_2\cos\hat{r}} = \frac{2\cos\hat{\imath}}{\cos\hat{\imath} + n_r\cos\hat{r}}. \tag{5.41}$$

The coefficients for the $\parallel$ plane of polarization can be worked out similarly. When $\mathcal{R}$ and $\mathcal{T}$ refer to the component E_x, we find:

$$\mathcal{R}_\parallel = \frac{n_1\cos\hat{r} - n_2\cos\hat{\imath}}{n_1\cos\hat{r} + n_2\cos\hat{\imath}} = \frac{\cos\hat{r} - n_r\cos\hat{\imath}}{\cos\hat{r} + n_r\cos\hat{\imath}}, \tag{5.42}$$

$$\mathcal{T}_\parallel = \frac{2n_1\cos\hat{r}}{n_1\cos\hat{r} + n_2\cos\hat{\imath}} = \frac{2\cos\hat{r}}{\cos\hat{r} + n_r\cos\hat{\imath}}. \tag{5.43}$$

These functions are known as **Fresnel coefficients** and are shown in Fig. 5.5.

Fresnel's equations are valid also for imaginary or complex values of n or u, and examples will be discussed in §5.5.2 and §5.6 respectively.

The two cases are sometimes combined in the convenient forms

$$\mathcal{R} = \frac{u_1 - u_2}{u_2 + u_1}, \tag{5.44}$$

$$\mathcal{T} = \frac{2u_1}{u_2 + u_1}, \tag{5.45}$$

where

$$\text{for } \perp \quad u_1 \equiv n_1\cos\hat{\imath}, \quad u_2 \equiv n_2\cos\hat{r}, \tag{5.46}$$

$$\text{for } \parallel \quad u_1 \equiv n_1\sec\hat{\imath}, \quad u_2 \equiv n_2\sec\hat{r}. \tag{5.47}$$

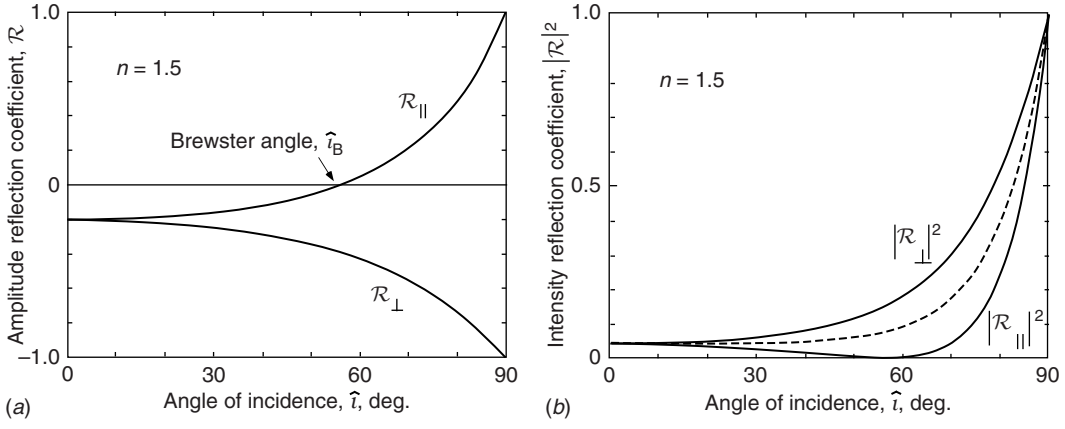

Figure 5.5

(*a*) Amplitude reflection coefficients $\mathcal{R}(\hat{\imath})$ at the surface of a medium of refractive index $n_r = 1.5$ for the ⊥ and ‖ polarizations. (*b*) Intensity reflection coefficients $|\mathcal{R}(\hat{\imath})|^2$. The broken line shows their average, which applies when the incident light is unpolarized.

This form is particularly useful in formulating the general theory of multilayer dielectric systems (§10.4), since both polarizations and all angles of incidence can be treated with the single pair of formulae.

At normal incidence, the reflection and transmission coefficients for the two polarizations are equal and are given by

$$\mathcal{R} = \frac{n_1 - n_2}{n_1 + n_2} = \frac{1 - n_r}{1 + n_r}, \tag{5.48}$$

$$\mathcal{T} = \frac{2n_1}{n_1 + n_2} = \frac{2}{1 + n_r}. \tag{5.49}$$

As an example, at an air–glass interface, where $n_r = 1.5$, the amplitude reflection coefficient $\mathcal{R}$ (5.48) is $-0.5/2.5 = -0.2$, and so the intensity reflection coefficient $\mathcal{R}^2 = 4\%$ (Fig. 5.5). This is a typical reflection coefficient for an uncoated glass surface.

5.4.2 Brewster angle

For the polarization plane parallel to the incidence plane, Fig. 5.5 indicates that the reflection coefficient is zero at a particular angle $\hat{\imath}_B$. For this condition we have

$$\begin{aligned} n_1 \cos\hat{r} - n_2 \cos\hat{\imath} &= 0, \\ \frac{\cos\hat{r}}{\cos\hat{\imath}} = \frac{n_2}{n_1} &= n_r = \frac{\sin\hat{\imath}}{\sin\hat{r}}. \end{aligned} \tag{5.50}$$

We leave it to the reader to confirm that this equation can be rewritten as

$$\tan\hat{\imath} = \cot\hat{r} = n_r. \tag{5.51}$$

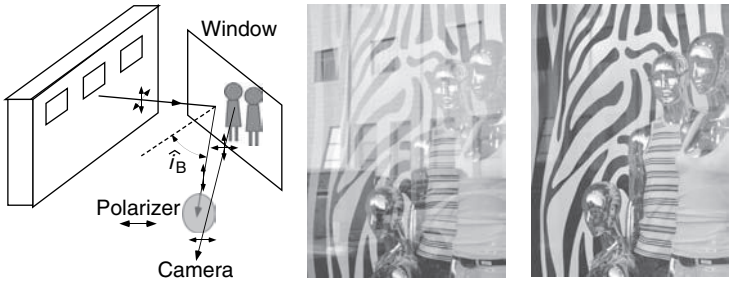

Figure 5.6
A shop window display is photographed at the Brewster angle with respect to the window pane. In unpolarized light, the view is dominated by the reflection of the street scene in the glass, but through a filter transmitting horizontally ‖-polarized light only, the reflection is eliminated and the display is clear.

The angle $\hat{\imath} = \hat{\imath}_B$ which is the solution of this equation is called the **Brewster angle**. At this angle of incidence, light of the parallel polarization is not reflected. A striking example of Brewster reflection is shown in Fig. 5.6.

5.5 Incidence in the denser medium

When $n_r < 1$, meaning that the incidence is in the denser medium, several interesting phenomena occur. First, we should point out that the fact that $\mathcal{T}$ can be greater than unity in (5.49), and (5.41) or (5.43) for certain angles, does not contradict the conservation of energy. We must calculate S in each case. For (5.49), putting $S = E^2 Z^{-1} = E^2 n Z_0^{-1}$ per unit area, the proportion of the energy transmitted is

$$\left(\frac{2n_1}{n_2+n_1}\right)^2 \frac{n_2}{n_1} = \frac{4n_1 n_2}{(n_1+n_2)^2} = \frac{4n_r}{(1+n_r)^2}, \tag{5.52}$$

which reaches a maximum value of 1 when $n_r = 1$. At non-normal incidence, the fact that the areas of transmitted and reflected beams are in the ratio $\cos\hat{\imath} : \cos\hat{r}$ must also be taken into account when calculating total energy flows.

5.5.1 Total internal reflection

In the usual situation, where $n_r < 1$, any angle of incidence results in a calculable angle of refraction $\hat{r}$. But if $n_r < 1$, there is no real solution for $\hat{r}$ if $\hat{\imath} < \sin^{-1} n_r \equiv \hat{\imath}_c$. This angle is called the **critical angle**, and above it both $|\mathcal{R}_\perp|$ and $|\mathcal{R}_\parallel|$ become unity. This phenomenon is called **total internal reflection**. How can the wave-field be described at angles $\hat{\imath} < \hat{\imath}_c$? We postulate for such angles a complex angle of refraction as a formal solution to Snell's law. It then turns out that the disturbance in the second medium is **evanescent**, as follows. For the equation

$$\sin\hat{r} = \frac{1}{n_r}\sin\hat{\imath} \equiv (1+\beta^2)^{\frac{1}{2}} > 1 \tag{5.53}$$

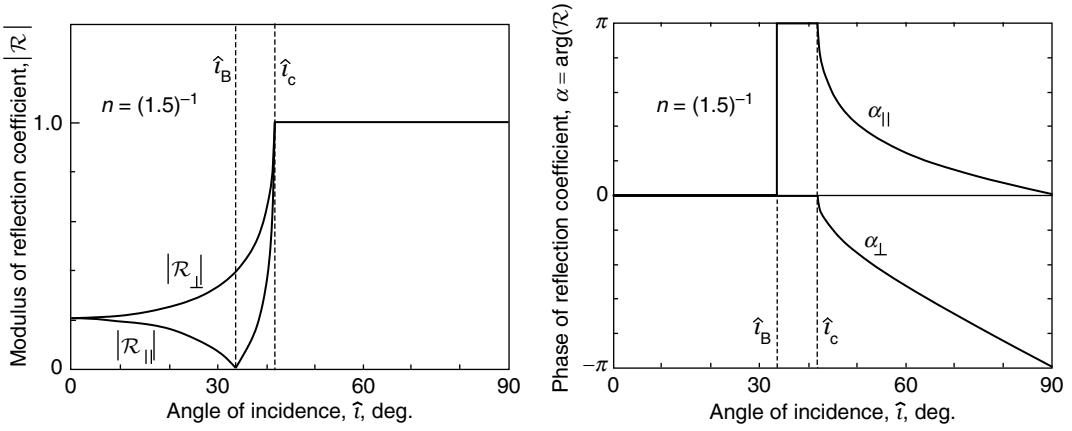

Figure 5.7

Modulus and phase of the reflection coefficient $\mathcal{R} = |R| \exp(i\alpha)$ at the surface when incidence is in the denser medium, $n_r = 1/1.5$. The Brewster angle is $\hat{i}_B$ and the critical angle $\hat{i}_c$.

we have

$$\cos\hat{r} = (1 - \sin^2\hat{r})^{\frac{1}{2}} = \pm i\beta \quad (\beta \text{ real and positive}). \tag{5.54}$$

Of the two signs for $\cos\hat{r}$, the upper and lower ones will be seen to apply to waves propagating along $+z$ and $-z$ respectively. Substituting in the equations for $\mathcal{R}$ and $\mathcal{T}$ (5.40)–(5.43) we obtain

$$\mathcal{R}_\perp = \frac{\cos\hat{i} \mp i n_r\beta}{\cos\hat{i} \pm i n_r\beta}, \tag{5.55}$$

$$\mathcal{T}_\perp = \frac{2\cos\hat{i}}{\cos\hat{i} \pm i n_r\beta}, \tag{5.56}$$

$$\mathcal{R}_\parallel = \frac{\pm i\beta - n_r\cos\hat{i}}{\pm i\beta + n_r\cos\hat{i}}, \tag{5.57}$$

$$\mathcal{T}_\parallel = \frac{\pm 2i\beta}{\pm i\beta + n_r\cos\hat{i}}. \tag{5.58}$$

As the reflection coefficients are both of the form

$$\mathcal{R} = \frac{p - iq}{p + iq} = \exp\left[-2i\tan^{-1}\left(\frac{p}{q}\right)\right] = \exp(-i\alpha), \tag{5.59}$$

it is clear that they represent complete reflection ($|\mathcal{R}| = 1$) but with a phase change α:

The reflection coefficient near $\hat{i}_c$ is a very steep function of $\hat{i}$, and this effect can be used to visualize surface defects on a transparent sample.

$$\alpha_\perp = \pm 2\tan^{-1}\frac{n_r\beta}{\cos\hat{i}}, \tag{5.60}$$

$$\alpha_\parallel = \mp 2\tan^{-1}\frac{n_r\cos\hat{i}}{\beta}. \tag{5.61}$$

Figure 5.7 shows the reflection coefficient for $n_r = 1.5^{-1}$ over the whole range of $\hat{i}$ from zero to $\pi/2$.

Neither of the transmission coefficients is zero, however, and so we must investigate the transmitted wave more closely. We shall write the space-dependent part of the transmitted wave in full:

$$E = E_0 \exp[-\mathrm{i}(kz\cos\hat{r} + kx\sin\hat{r})]$$
$$= E_0 \exp(\mp k\beta z)\exp[-\mathrm{i}kx(1+\beta^2)^{\frac{1}{2}}]. \qquad (5.62)$$

When the upper signs in (5.54)–(5.62) are chosen, the wave is evanescent and decays exponentially to zero as $z \to \infty$. The characteristic decay distance is $(k\beta)^{-1}$. As an example, a material with $n = 1.5$ has a critical angle of 41.8°. Then at an incident angle of 42.8°,

$$\beta = (2.25\sin^2 42.8° - 1)^{\frac{1}{2}} = 0.20$$

Evanescent penetration into the less dense medium at angles above the critical angle is used in surface plasmon resonance bio-sensors, for example, which respond only to surface physics and chemistry within the evanescent layer (§13.7)

and the decay distance is thus $\lambda/2\pi\beta \approx 0.8\lambda$.

The phenomena of total internal reflection and the consequent evanescent wave have several important uses. Various types of prism employing total internal reflection are used in optical instruments; a common application is found in the design of binocular field glasses. In optical waveguides and fibres (§10.1 and §10.2), repeated total internal reflection at the wall or an interface between media is used to transfer light energy along the length of the fibre, with negligible loss. In addition, the existence of the evanescent wave outside the fibre gives rise to one of the ways in which energy can be extracted without any mechanical disturbance.

5.5.2 Optical tunnelling, or frustrated total internal reflection

If light is totally reflected from a plane surface at an angle greater than the critical angle, but a second interface exists within the region of the evanescent wave, the reflection is no longer total, and we have the phenomenon of **optical tunnelling** or **frustrated total internal reflection** whereby a wave is partially transmitted through a region where it would be forbidden by geometrical optics. This is the electromagnetic equivalent to alpha-particle or electron tunnelling in quantum mechanics. A schematic experiment is shown in Fig. 5.10. This process has several applications, such as beamsplitters and optical waveguide couplers.

Calculation of the transmittance through the 'forbidden layer' is not difficult, once the effective refractive indices of the media are expressed in terms of u_1 and u_2 (5.44), (5.45), where clearly the value of u_2 in the air layer

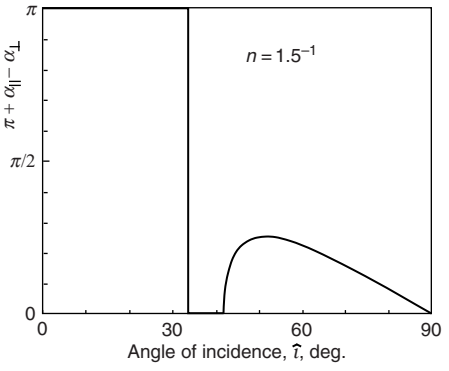

Figure 5.8

Phase difference $\pi + \alpha_\parallel - \alpha_\perp$ for $n_r = 1/1.5$ as a function of the angle of incidence. In the region of critical reflection, $\hat{\imath} > \hat{\imath}_c$, the maximum phase difference is about $\pi/4$ at $\hat{\imath} = 52°$.

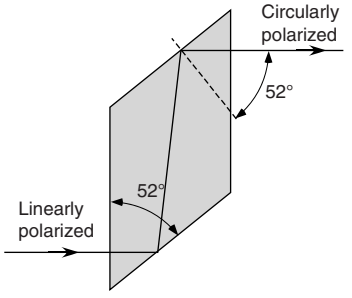

Figure 5.9

Fresnel rhomb.

Box 5.2 The Fresnel rhomb: an application of the phase change on total reflection

The phase changes (5.60) and (5.61) for the two polarizations for propagation in the z-direction have somewhat different dependence on the angle $\hat{\imath}$ in the region between $\hat{\imath}_c$ and $\pi/2$. Using the upper signs again in both equations, they can be seen to have the values 0 and π respectively at $\hat{\imath} = \hat{\imath}_c$ ($\beta = 0$), and π and 0 at $\hat{\imath} = \pi/2$. The difference $\alpha_\parallel - \alpha_\perp + \pi$ can be evaluated for any particular value of n_r, and is shown in Fig. 5.8 for $n_r = 1.5^{-1}$. When $\beta/\cos\hat{\imath} = 1$ the phase difference has its maximum value; for this case, it is $45° - \pi$ at $\hat{\imath} = 52°$.

Fresnel designed a circular polarizer that takes advantage of this property. Circularly polarized light, which will be discussed in §6.1.2, consists of the superposition of two waves with orthogonal polarization and a $\pm\pi/2$ phase difference between them. This phase difference might be introduced by total internal reflection, but from the figure you can see that for normal glass, a maximum difference only just larger than $\pi/4$ can be produced by a single reflection. Fresnel's rhomb (Fig. 5.9) uses two successive reflections at the required angle to introduce the required $\pi/2(-2\pi)$ shift in a single piece of glass called a **Fresnel rhomb**. An advantage of the rhomb over other methods of achieving circular or elliptic polarization is that it is almost independent of the wavelength and the angular range over which it works is quite large.

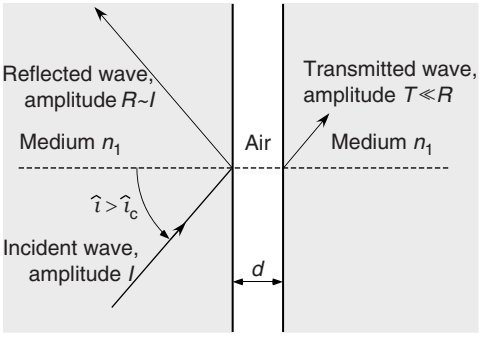

Figure 5.10
Tunnelling of a wave through the air gap between two media, spaced by $d \sim (k\beta)^{-1}$.

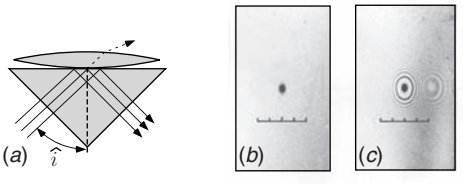

Figure 5.11
(*a*) Experiment to show optical tunnelling. (*b*) Observation with $\hat{\imath} > \hat{\imath}_c$. (*c*) Observation with $\hat{\imath} < \hat{\imath}_c$.

is imaginary. We can anticipate the technique to be developed in §10.4 for multilayer calculations and quote the result:

$$\mathcal{T} = \left[\cosh k\beta d + \tfrac{1}{2}\sinh k\beta d(n\cos\hat{\imath}/\beta - \beta/n\cos\hat{\imath})\right]^{-1}$$
$$\sim \mathrm{e}^{-k\beta d} \quad \text{at large } d. \tag{5.63}$$

It is easy to demonstrate the tunnelling by the experiment shown in Fig. 5.11(*a*). The second prism of Fig. 5.10 is replaced by a lens with a large (∼1 m) radius of curvature, which rests lightly on the horizontal hypotenuse of the prism, so that a variety of values of d are sampled simultaneously. Looking at the reflected light, a dark patch indicating frustrated reflection around the point of contact can be seen – Fig. 5.11(*b*). Altering the incidence in the prism to an angle below the critical angle returns u_2 to a real value and interference fringes (Newton's rings) replace the patch – Fig. 5.11(*c*). These can be used to calibrate the thickness profile of the forbidden layer and to confirm that significant tunnelling occurs up to thicknesses of about $\frac{3}{4}\lambda$.

5.5.3 Energy flow in the evanescent wave

The amplitude of the evanescent wave decays with increasing z, so clearly no energy can be transported in that direction, away from the interface. But on the other hand, the wave is there, and has an energy density, so we have to

show that energy transport within it is restricted to the directions parallel to the interface. For the $\perp$ wave in the second medium, substitution of (5.62) in (5.34) and (5.35) shows the fields to be

$$E_y = E_0 \exp(-k\beta z) \exp\left\{-\mathrm{i}\left[kx\left(1+\beta^2\right)^{\frac{1}{2}} - \omega t\right]\right\}, \tag{5.64}$$

$$\begin{aligned} H_z &= Z_0^{-1} \sin\hat{r}\, E_y = Z_0^{-1}(1+\beta^2)^{\frac{1}{2}} E_y \\ &= Z_0^{-1}(1+\beta^2)^{\frac{1}{2}} E_0 \exp\left\{-\mathrm{i}\left[kx\left(1+\beta^2\right)^{\frac{1}{2}} - \omega t\right]\right\}, \end{aligned} \tag{5.65}$$

$$\begin{aligned} H_x &= Z_0^{-1} \cos\hat{r}\, E_y = \mathrm{i} Z_0^{-1} \beta E_y \\ &= Z_0^{-1} E_0 \beta \exp\left\{-\mathrm{i}\left[kx\left(1+\beta^2\right)^{\frac{1}{2}} - \omega t + \pi/2\right]\right\}. \end{aligned} \tag{5.66}$$

So the Poynting vector has components

$$S_x = E_y H_z \sim E_y^2 (1+\beta)^{\frac{1}{2}}, \tag{5.67}$$

$$S_z = -E_y H_x \sim \mathrm{i}\beta E_y^2. \tag{5.68}$$

The imaginary value of S_z tells us that no energy is transported normal to the surface; it is clear from (5.64) and (5.66) **that E_y and H_x have a $\pi/2$ phase difference and so the average of their product is zero.** However, there is no phase difference between E_y and H_z and so $\langle S_x \rangle \neq 0$, and energy is transported in that direction.

5.6 Electromagnetic waves incident on a conductor

The media we have discussed so far have all been insulators, as a result of which we have been able to neglect the current term in the equation (5.3),

$$\nabla \times \mathbf{H} = \frac{\partial \mathbf{D}}{\partial t} + \mathbf{j}. \tag{5.69}$$

In order to understand what happens to an electromagnetic wave incident on a conductor we must bring this term into play, as the electric field $\mathbf{E}$ will induce a non-zero current density $\mathbf{j}$ if the conductivity σ is appreciable:

$$\mathbf{j} = \sigma \mathbf{E}. \tag{5.70}$$

We can substitute (5.70) into (5.69), at the same time replacing $\mathbf{D}$ by $\epsilon\epsilon_0\mathbf{E}$ to give

$$\nabla \times \mathbf{H} = \epsilon\epsilon_0 \frac{\partial \mathbf{E}}{\partial t} + \sigma \mathbf{E}. \tag{5.71}$$

Now, remembering that the wave is oscillatory with frequency ω, we replace the operator $\partial/\partial t$ by $-\mathrm{i}\omega$ and thus obtain the equation

$$\nabla \times \mathbf{H} = -\mathrm{i}\epsilon_0 E\omega \left(\epsilon - \frac{\sigma}{\mathrm{i}\omega\epsilon_0}\right). \tag{5.72}$$

The conductivity term can be absorbed into the dielectric constant by letting it be complex:

$$\tilde{\epsilon} = \epsilon + \frac{\sigma}{\mathrm{i}\omega\epsilon_0}. \tag{5.73}$$

This is an important result; propagation in a conductor can be treated formally as propagation in a medium with a complex dielectric constant. The reason is easy to see. In an insulator the dielectric field produces displacement current $\partial\mathbf{D}/\partial t$ in quadrature with it; in a conductor the real current density is in phase with $\mathbf{E}$, and thus the net effect is a total current at an intermediate phase angle, which is represented by a complex $\tilde{\epsilon}$.

As the mathematics is now similar to that in §5.1 for a real dielectric, we shall take the standard result, which defines a **complex refractive index** $\tilde{n} = c/v = \tilde{\epsilon}^{\frac{1}{2}}$, and substitute $\tilde{\epsilon}$ from equation (5.73) to give

$$\tilde{n} = \frac{c}{v} = \left(\epsilon + \frac{\mathrm{i}\sigma}{\epsilon_0\omega}\right)^{\frac{1}{2}}. \tag{5.74}$$

Let us assume ϵ to be of the order of unity. Then, substitution of values for σ and ω for metallic conductors shows the imaginary term to be completely dominant even at optical frequencies. We therefore write

$$\tilde{n} \approx (\mathrm{i}\sigma/\epsilon_0\omega)^{\frac{1}{2}} = (\sigma/2\epsilon_0\omega)^{\frac{1}{2}}(1 + \mathrm{i}). \tag{5.75}$$

The accepted nomenclatures for the complex refractive index are somewhat confusing: $\tilde{n} \equiv n + \mathrm{i}\tilde{k}$, or $\tilde{n} \equiv n(1 + \mathrm{i}\kappa)$. Here we use the former.

We can then write down the effect of applying a wave of frequency ω,

$$\mathbf{E} = \mathbf{E}_0 \exp[\mathrm{i}(kz - \omega t)] = \mathbf{E}_0 \exp[\mathrm{i}\omega(\tilde{n}z/c - t)], \tag{5.76}$$

normally to the surface $z = 0$ of a conductor; at depth z we have, from (5.75),

$$\mathbf{E}(z) = \mathbf{E}_0 \exp\left[-\left(\sigma\omega/2\epsilon_0 c^2\right)^{\frac{1}{2}} z\right] \exp\left\{\mathrm{i}\left[\left(\sigma\omega/2\epsilon_0 c^2\right)^{\frac{1}{2}} z - \omega t\right]\right\}. \tag{5.77}$$

This is an attenuated wave, with characteristic decay length l, called the **skin depth**, and wavelength λ_c inside the conductor given by

$$l = \lambda_c/2\pi = (2\epsilon_0 c^2/\sigma\omega)^{\frac{1}{2}}. \tag{5.78}$$

Thus, using $\tilde{n} \equiv n + \mathrm{i}\tilde{k}$, we have $n = \tilde{k} = \lambda/\lambda_c \gg 1$. The decay per wavelength $l/\lambda_c = 1/2\pi$ is independent of the frequency and implies that a wave travels less than a wavelength inside a conductor. However, when we come to substitute the value of the conductivity of metals into (5.78), we find that the value of l is very small compared with the free-space wavelength, indicating very large values of n and $\tilde{k}$. For example, at 1000 Hz the skin depth in copper is 2.1 mm and the wavelength in the metal 13 mm, compared with the free-space wavelength $\lambda = 3 \times 10^5$ m; at 10^8 Hz, the skin depth is 6 μm and the free-space wavelength 3 m.

If the conductivity were frequency independent, n would be very large even at optical frequencies, but this is not so; atomic and plasma resonances, which will be discussed in Chapter 13, change the picture completely. Typical values of $\tilde{n}$ for metals often used in optics at $\lambda = 600$ nm are: copper, $\tilde{n} = 0.2 + \mathrm{i}3.5$; silver, $\tilde{n} = 0.08 + \mathrm{i}4.2$; aluminium, $\tilde{n} = 1.02 + \mathrm{i}6.5$. The values of n are, surprisingly, less than or approximately 1.

5.6.1 Reflection by a metal surface

When using metal-coated mirrors at high angles of incidence, you should always remember that they can introduce phase changes, which may differ between the two principal polarizations.

Calculation of the reflection by a metal surface in principle requires substitution of the complex refractive index $\tilde{n}$ into Fresnel's equations (5.40) and (5.42). At long wavelengths, where $n = k \gg 1$, this gives us, for incidence at $\hat{\imath}$ in the $\parallel$ mode,

$$\mathcal{R}_\parallel = \frac{\cos\hat{r} - n(1-\mathrm{i})\cos\hat{\imath}}{\cos\hat{r} + n(1-\mathrm{i})\cos\hat{\imath}}. \tag{5.79}$$

Since $n \gg 1$ we can assume $\cos\hat{r} = 1$, whence

$$\mathcal{R}_\parallel = \frac{1 - n(1-\mathrm{i})\cos\hat{\imath}}{1 + n(1-\mathrm{i})\cos\hat{\imath}}. \tag{5.80}$$

For small angles of incidence $\hat{\imath}$, $\mathcal{R}_\parallel$ has the value $(1-n-\mathrm{i}n)/(1+n+\mathrm{i}n)$ which is close to -1, with a phase difference of about π between the reflected and incident waves. On approaching glancing incidence, the phase of the reflected wave changes continuously, reaching $\mathcal{R}_\parallel = +1$ at $\hat{\imath} = \pi/2$. The phase change occurs around what might be described as a 'quasi Brewster angle' at which the real and imaginary parts of $\mathcal{R}$ are comparable, i.e.

$$n\cos\hat{\imath} \approx 1; \tag{5.81}$$

here the value of $|\mathcal{R}|$ falls to a value less than unity.

However, at optical frequencies the values of n and $\tilde{k}$ are small. In particular, when $n < 1$ we might naively expect to see an anomaly for incidence at a critical angle $\hat{\imath}_c = \sin^{-1} n$ and total **external** reflection of light at greater angles. This is not so. In fact the subject of propagation of waves in an absorbing material with complex $\tilde{n}$ is complicated, in particular the interpretation of Snell's law

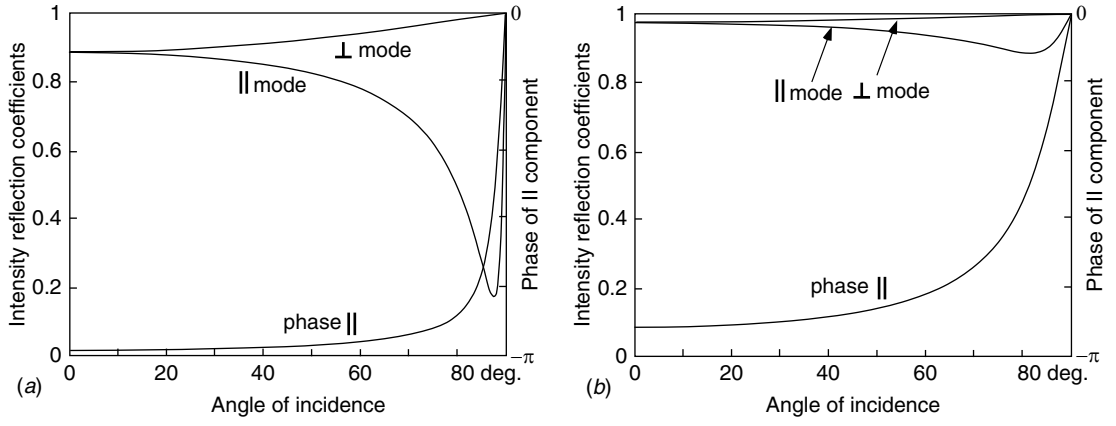

Figure 5.12

The reflectivity of metals, as a function of angle of incidence, showing $|\mathcal{R}_\parallel|^2$, $|\mathcal{R}_\perp|^2$ and the phase of the ‖ mode: (*a*) for a metal at very long wavelengths, with $n = k \gg 1$ and (*b*) for silver at $\lambda = 600$ nm, where $\tilde{n} = 0.08 + \mathrm{i}4.2$.

for a complex angle of refraction. It turns out that under these circumstances the **k**-vector is not normal to the wavefronts, because in an absorbing material at non-normal incidence energy can flow along the wavefront, and then it turns out that Snell's law does not apply to the **k**-vector as it does in transparent materials. Essentially, the reason is that when the light is strongly absorbed, the flow of energy **S** must be approximately normal to the interface, and this pulls **k** into a similar direction. The full mathematical development can be found in Sokolov (1960) and Born and Wolf (1999). As a result, the expected critical angle and total reflection are absent, and the reflectivities of metals, while often high, are less than unity. The phenomenon of the 'quasi Brewster angle' does seem to be a common feature. But it is interesting to note that when n is small it is the loss factor $\tilde{k}$ in the complex refractive index that is responsible for the high reflectivity; at normal incidence, for example,

$$|\mathcal{R}|^2 = \left|\frac{1 - n - \mathrm{i}\tilde{k}}{1 + n + \mathrm{i}\tilde{k}}\right|^2 = \frac{(1-n)^2 + \tilde{k}^2}{(1+n)^2 + \tilde{k}^2} \to 1 \tag{5.82}$$

when $\tilde{k} \gg n$. Figure 5.12 compares the long-wave theory (5.80) to a full calculation for silver at optical wavelength.

5.7 Reciprocity and time reversal: The Stokes relationships

The arguments in this section do not apply if the media have significant absorption, because (5.3) is not time reversible.

The reader may have noticed that the reflection coefficient (5.44) is negative when incidence is in the lower-index medium, and positive, with the same value, if the light ray is exactly reversed, so that it is incident in the denser medium. This reversal of the sign of the reflection coefficient when the light path is reversed is a feature of non-absorbing systems which arises in a very general manner. It is the result of the **time-reversal symmetry** of Maxwell's equations

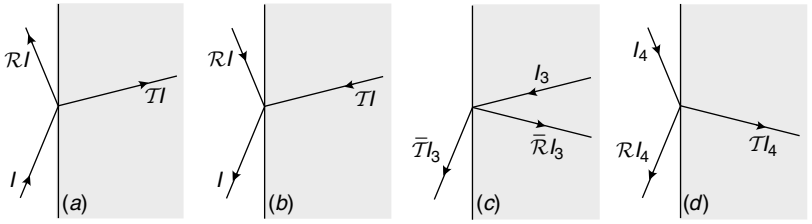

Figure 5.13

Reflection from opposite sides of an interface. (*a*) Usual situation, *I* incident from the left; (*b*) time-reversed situation; (*c*) I_3 incident from the right; (*d*) I_4 incident from the left.

in the absence of absorption mechanisms, which would be represented by a non-zero current density term **j** in (5.3).

If we change t in equations (5.9) and (5.10) to $-t$ we find no change in the resulting wave equation (5.12). So any set of related waves, such as the usual incident, reflected and transmitted trio, has an equally valid time-reversed set. But the effect of changing t to $-t$ in a wave is to reverse the direction of its propagation without affecting its amplitude, so that if we apply this procedure to the trio shown in Fig. 5.13(*a*), we get those in Fig. 5.13(*b*). The reflector is completely general here, except that it must be non-absorbing; it could be a single interface or any multilayer or other system satisfying this requirement. The incident, reflected and transmitted amplitudes I, R and T in both figures are related by coefficients $\mathcal{R} = R/I$ and $\mathcal{T} = T/I$. In Fig. 5.13(*b*) the amplitudes are unchanged, but it represents an unusual situation: there are *two* incident waves and *one* leaving the system. Obviously, some form of interference must be involved, but that is all within the framework of Maxwell's equations and the details don't matter to us. However, the situation in Fig. 5.13(*b*) can be represented by the superposition of two perfectly conventional trios, one incident from each side, which are shown in Fig. 5.13(*c*) and (*d*). The former has incidence from the reverse side, and reflection and transmission coefficients $\overline{\mathcal{R}}$ and $\overline{\mathcal{T}}$ respectively. In the figures, the amplitudes have been labelled accordingly. Equating amplitudes of Fig. 5.13(*b*) to the sum of the last two, gives us

$$I = \overline{\mathcal{T}}I_3 + \mathcal{R}I_4, \tag{5.83}$$

$$\mathcal{R}I = I_4, \tag{5.84}$$

$$0 = \overline{\mathcal{R}}I_3 + \mathcal{T}I_4, \tag{5.85}$$

$$\mathcal{T}I = I_3. \tag{5.86}$$

The result (5.87) is of key importance in many interferometers. For example, in the Fabry–Perot (§9.5.1) it explains the complementarity between the reflected and transmitted spectra.

These lead directly to the solutions

$$\overline{\mathcal{R}} = -\mathcal{R}, \tag{5.87}$$

$$1 = \mathcal{T}\overline{\mathcal{T}} + \mathcal{R}^2. \tag{5.88}$$

Equation (5.87) represents a general result, of which reflection at a dielectric surface is one example: **the reflection coefficients from opposite sides of a non-absorbing partial reflector are equal and opposite in sign**. Conservation of energy in the system is then expressed by (5.88).

The assumption that $\mathcal{R}$ and $\mathcal{T}$ are real quantities implies that neither reflection nor transmission of the wave introduces a phase change. But there are many cases, such as total internal reflection, §5.5.2, where this is not true. It is really quite easy to extend the argument to complex values of $\mathcal{R}$ and $\mathcal{T}$. The starting point is to realize that the time-reversed field corresponding to E is E^*. Although we shall not prove this in general (see Altman and Suchy (1991)), one can appreciate its significance in the case of total internal reflection, where the transmitted wave carries no energy and the reflection coefficient is $\mathcal{R} = \mathrm{e}^{\mathrm{i}\alpha}$. An incident wave I is reflected as $I\mathcal{R} = I\mathrm{e}^{\mathrm{i}\alpha}$. Now, in the time-reversed system, we begin with the field $(I\mathrm{e}^{\mathrm{i}\alpha})^*$, which is reflected with the same reflection coefficient into I^*. This demonstrates that using the complex conjugate wave in the time-reversed system is consistent in this example.

Now we replace I by I^* in Fig. 5.13(b) and then follow through the same calculation as in (5.83)–(5.86). This gives us the following two equations, which are valid for any partially reflecting non-absorbing system:

$$\mathcal{T}^*\overline{\mathcal{T}} + \mathcal{R}^*\mathcal{R} = 1, \tag{5.89}$$

$$\mathcal{T}^*\overline{\mathcal{R}} + \mathcal{R}^*\mathcal{T} = 0. \tag{5.90}$$

It is also possible to deduce phase relationships between the various reflection and transmission coefficients. For example, if we choose the arbitrary reference surface of reflection for a complex reflector such that $\mathcal{T}$ is real, (5.90) gives the **Stokes relations** in their complex form:

$$\overline{\mathcal{R}} = -\mathcal{R}^*, \tag{5.91}$$

$$1 = \overline{\mathcal{T}}\mathcal{T} + \mathcal{R}\mathcal{R}^*. \tag{5.92}$$

Without defining any particular reference surface, we can make a general statement about the phase *differences* δ between $\mathcal{T}$ and $\mathcal{R}$, and $\bar{\delta}$ between $\overline{\mathcal{T}}$ and $\overline{\mathcal{R}}$. By writing $\mathcal{T}$ and $\mathcal{R}$ in the form $A\exp(\mathrm{i}b)$ and substituting into (5.89) and (5.90), we find that $\delta + \bar{\delta} = \pi$ (Zeilinger (1981)). A symmetrical beamsplitter must then have $\delta = \bar{\delta} = \frac{1}{2}\pi$.

We conclude by reminding the reader that the above relationships are valid if the system is *non-absorbing*. Obviously, in an absorbing system no such generalization is possible; consider, for example, the properties of a metal foil painted green on one side!

5.8 Momentum of an electromagnetic wave: Radiation pressure

We saw in §5.2.1 that electromagnetic waves transport energy. They also transport momentum. The effect is very small, and needs delicate instrumentation

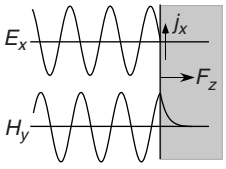

Figure 5.14

Wave-fields at the surface of an ideal conductor.

or intense light sources in order to observe it. Suppose that a plane wave with electric field amplitude E_{0x} is incident on a perfect conductor surface normal to z which therefore reflects it completely. This means that *twice* the momentum of the incident light is transferred to the conductor; the resulting force is called **radiation pressure**. Because the conductivity is infinite, the electric field at the surface has to be zero; in other words, the incident and reflected waves set up a standing wave which has a node of the electric field at the surface. As a result, the magnetic fields at the surface add, giving a total field there $H_y(z=0) = 2H_{0y}\cos\omega t$ (Fig. 5.14). Now this field at the surface decays very quickly within the skin depth of the conductor by inducing electric currents in the x-direction. The currents interact with the magnetic field H_y to produce a Lorentz force in the z-direction, which is the cause of the radiation pressure. Quantitatively, the current density is related to the magnetic field by Ampère's law (5.3) for the case where **E** and therefore **D** are zero:

$$j_x = \frac{\partial H_y}{\partial z} \tag{5.93}$$

and the Lorentz force $\mu_0 \mathbf{j} \times \mathbf{H}$ can be integrated throughout the reflector (much thicker than the skin depth) to give the total force

$$F_z = \mu_0 \int_{-\infty}^{0} j_x H_y \, \mathrm{d}z = \mu_0 \int_{-\infty}^{0} H_y \frac{\partial H_y}{\partial z} \, \mathrm{d}z = \frac{1}{2}\mu_0 H_y^2(z=0). \tag{5.94}$$

Now this force can be related to the Poynting vector of the incident wave, which is in this case

$$\mathbf{S} = \langle \mathbf{E} \times \mathbf{H} \rangle = E_{0x}H_{0y}\left\langle \cos^2\omega t \right\rangle = \frac{1}{2}E_{0x}H_{0y} = \frac{1}{2}Z_0 H_{0y}^2; \tag{5.95}$$

then, inserting the value of $H_y(z=0)$, the force is

$$F_z = 2\mu_0 H_{0y}^2 \left\langle \cos^2\omega t \right\rangle = \mu_0 H_{0y}^2 = 2S/c, \tag{5.96}$$

Figure 5.15

Optical tweezers: (*a*) A dielectric particle is attracted towards the maximum field intensity at the focus of a light beam by the gradient in electromagnetic energy density. (*b*) Geometric optics interpretation of the force: refraction creates transverse light momentum which is balanced by a force on the refracting particle.

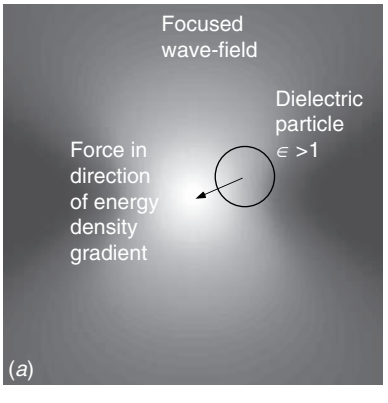

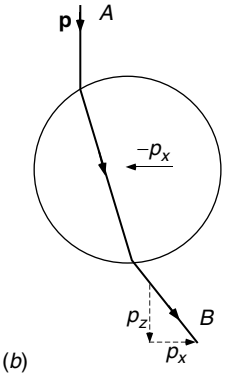

Box 5.3 Optical tweezers

Although radiation pressure is very small compared to everyday experience, it can be used to manipulate tiny particles and to measure forces applied to them by their surroundings. The systems used for this purpose are called **optical tweezers** (Ashkin (1970)). As we saw, light pressure is associated with the change in direction of a light wave (reflection in §5.8) and its magnitude is proportional to the energy density of the wave.

A small dielectric particle with $\epsilon > 1$ is placed in a region of non-uniform electric field. As a result, it becomes electrically polarized parallel to the field and then experiences a force towards the highest electric field in the same way as a piece of soft iron with $\mu > 1$ is attracted to a magnet, where the magnetic field is largest. Therefore, if light is brought to a focus, small dielectric particles are attracted to the focal point, where the electric field is largest. Conversely, a small bubble in a dielectric fluid is repelled from the focus. We can express this force quantitatively in terms of the potential energy $-\mathbf{p}\cdot\mathbf{E}$ of a dipole $\mathbf{p}$ in an electric field. If the dipole is induced by the field itself, the potential energy U and the force $-\nabla U$ on a particle of volume v are

$$U = -\frac{1}{2}v\epsilon_0(\epsilon - 1)E^2, \tag{5.97}$$

$$F = \frac{1}{2}v\epsilon_0(\epsilon - 1)\nabla(E^2). \tag{5.98}$$

The force pushes the particle towards the highest field. If we look at the distribution of light intensity $\frac{1}{2}c\epsilon_0E^2$ around the focus of a light beam (usually a laser, but the coherence is not essential) in Fig. 5.15(a) or Fig. 7.9, we see that the gradient of E^2 is always directed towards the focal point.

Another, 'semi-classical', way of looking at the trapping of a dielectric sphere by converging light uses ray optics combined with the momentum of electromagnetic waves. When a light ray such as A in Fig. 5.15(b) is refracted by the transparent particle, most of the light suffers a change in direction from A to B; a little is reflected at the surface, but this can be neglected. As a result of the change in direction, the wave acquires a transverse momentum, which must be balanced by an equal and opposite momentum of the particle, resulting in a force on it. Only when it is situated symmetrically about the point of maximum intensity do the forces on the two sides of the symmetry axis cancel to give stable equilibrium. This force can be used to manipulate particles and then make mechanical measurements on them.

using the value $Z_0 = c\mu_0$. The rate of momentum transport in the incident wave is half of this, and therefore has the value S/c. Once can then appreciate why the radiation pressure is so small, because c is so large: even a 1 W laser only produces a force of $1/c \approx 3 \times 10^{-9}$ newton when absorbed by an object!

5.9 Advanced topic: Angular momentum of a spiral wave

A spiral phase mask is used as a component in the super-resolution technique of STED (§12.6.4). The far-field diffraction pattern of a spiral wave always has a zero at its centre and this is the key to the resolution enhancement.

A wave with circular polarization carries angular momentum, a classical phenomenon (albeit rather difficult to prove directly from Maxwell's equations) that has a simple quantum equivalent: a photon has spin $\pm\hbar$, the sign depending on whether it has right- or left-handed circular polarization. A more recent discovery is a phenomenon akin to orbital angular momentum which is possessed by a wave with a spiral wavefront (Padgett and Allen (2000)). This wavefront is like a screw dislocation in a crystal, and has a singularity along its axis; we shall see that the photon equivalent has angular momentum $m\hbar$, where m can be any integer. Again, this is quite consistent with Maxwell's equations.

Suppose we create a monochromatic plane wave with transverse electric field in the (x, y) plane which we express in cylindrical polar coordinates:

$$E(\mathbf{r}, t) = E(r, \psi, z, t) = E_0(r) \exp[\mathrm{i}(\omega t - k_0 z - m\psi)]. \tag{5.99}$$

Clearly, at $r = 0$, all values of ψ refer to the same point in space, so that $E_0(0)$ has to be zero. **This wave has spiral wavefronts**. If we look at a given wavefront, ϕ =constant at given t, we have $k_0 z + m\psi$ = constant, meaning that as we go round a closed loop at given r, taking ψ from zero to 2π, z increases by $2\pi m/k_0 = m\lambda$. Since wavefronts are separated by λ, the wavefront looks like an m-start screw, left- or right-handed according to the sign of m (Fig. 5.16(c)). At radius r, the wavefront is therefore tilted locally with respect to the (x, y) plane by an angle θ whose tangent is the pitch $m\lambda$ divided by the perimeter of the loop $2\pi r$, $\tan\theta = m\lambda/2\pi r$. Now the momentum associated with the wave propagates normal to the wavefront, so it is clear that the result is angular momentum.

Quantitatively, consider an elementary area δA which transmits power $S(x, y)\delta A$. This is the axial component of power that is locally travelling in a spiral manner normal to the wavefront, at angle θ, and therefore the transverse component is $S\,\delta A \tan\theta$. This corresponds to transverse momentum rate $\delta p = S\,\delta A \tan\theta/c$ in the azimuthal direction. Substituting the value of $\tan\theta$, we have angular momentum rate

$$\delta L = r\,\delta p = \frac{rS\,\delta A}{c} \cdot \tan\theta = \frac{rS\,\delta A}{c} \cdot \frac{m\lambda}{2\pi r} = \frac{S\,\delta A\, m\lambda}{2\pi c}. \tag{5.100}$$

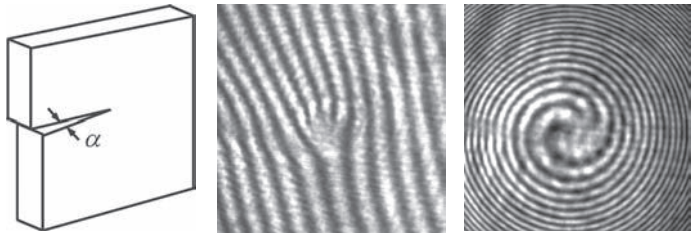

Figure 5.16
A spiral wave, created by separating the sides of a crack in a plastic sheet. (*a*) Construction of the phase plate; (*b*) an interference pattern between the spiral wave and a plane wave, showing a dislocation with $m = 3$; (*c*) interference pattern of the same spiral wave with a spherical wave. (Rotschild *et al.* (2004))

Thus the rate of angular momentum transfer by the complete beam, with power $P = \int S(x, y)\, \mathrm{d}A$ is $L = Pm\lambda/2\pi c = Pm/\omega$. Notice that this integral takes into account the facts that the beam is limited in extent and also has zero intensity along the singularity. It is important to see the quantum equivalent, where the beam is described by n photons per second, each with energy $\hbar\omega$. Substituting $P = n\hbar\omega$, we find $L = nm\hbar$, i.e. the **angular momentum per photon** is $m\hbar$.

There are several ways to construct a spiral wave, which include interference between laser modes (§14.6.1) and phase masks of various types. A particularly simple one uses the region around the termination of a crack in a plastic plate, where controlled separation between the two sides of the crack allows the value of m to be adjusted (Fig. 5.16). When a spiral wave is used to operate optical tweezers, the transfer of angular momentum to a trapped body results in its rotation, and the device is called an 'optical wrench'.

5.10 Advanced topic: Left-handed, or negative refractive index materials

Although they were first discussed by Veselago (1968) in a paper whose clarity makes it a delight to read, the properties of materials with negative refractive index were essentially ignored until brought to light by Pendry (2000). Since then, new materials with the required optical properties have been created, and most of the theoretical predictions for optics of such materials have been verified. In this section we shall outline the differences between the new and old physics, and give some examples of significant experimental results that have been obtained.

We start with the observation that (5.14) really ought to be written

$$n = c/v = \pm(\epsilon\mu)^{\frac{1}{2}}. \tag{5.101}$$

However, since the wave-vector $\mathbf{k} = n\mathbf{k}_0$ represents the direction in which the wave is propagating, we automatically assumed that n is positive. Now, to get the taste of the curious properties of the new materials, let us look at

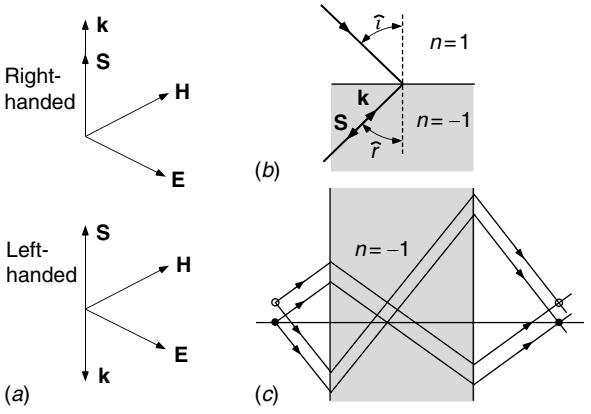

Figure 5.17
(*a*) Field and wave-vectors in a left-handed material, compared with a normal (right-handed) material. (*b*) Refraction of a ray at the interface between materials with $n = 1$ and $n = -1$. (*c*) Aberration-free imaging by a parallel-sided slab of material with $n = -1$ in air.

the situation that is obtained when both $\epsilon = -1$ and $\mu = -1$. We return to Maxwell's equations (5.9) and (5.10), which are now written

$$\nabla \times \mathbf{H} = \frac{\partial \mathbf{D}}{\partial t} = -\epsilon_0 \frac{\partial \mathbf{E}}{\partial t}, \tag{5.102}$$

$$\nabla \times \mathbf{E} = -\frac{\partial \mathbf{B}}{\partial t} = \mu_0 \frac{\partial \mathbf{H}}{\partial t}. \tag{5.103}$$

Substituting, as before, $\mathrm{i}\omega$ for $\partial/\partial t$ and $-\mathrm{i}\mathbf{k}$ for ∇, we have

$$\mathbf{k} \times \mathbf{H} = \epsilon_0 \omega \mathbf{E}, \tag{5.104}$$

$$\mathbf{k} \times \mathbf{E} = -\mu_0 \omega \mathbf{H}. \tag{5.105}$$

The Poynting vector, $\mathbf{S} = \mathbf{E} \times \mathbf{H}$ does not depend on ϵ and μ and is therefore unchanged. Now we redraw Fig. 5.1 as Fig. 5.17(*a*) and immediately see that **k** and **S** have *opposite* directions, i.e. the wave energy propagates counter to the wave-vector. Moreover, the triad [**E, H, k**] is left-handed, compared to normal materials in which it is right-handed; thus the name **left-handed materials**. The situation where **k** and **S** are not parallel will be discussed in greater detail in Chapter 6 as a common feature of anisotropic materials, but here we are discussing a basically isotropic material which exhibits the extreme case where the vectors are anti-parallel. Another way of describing this situation is to say that the wave and group velocities are in opposite direction. Since the former is $v = \omega/k$ and the latter $v_\mathrm{g} = \mathrm{d}\omega/\mathrm{d}k$, it becomes clear that the type of material involved is very dispersive (§2.4).

5.10.1 A lens with no spherical aberration: the superlens

Let us first consider the geometrical optics of a plane interface, normal to z, between vacuum with $n = 1$ and a left-handed material with $n = -1$. Most simply, we can just write Snell's law and deduce that $\sin \hat{r} = -\sin \hat{\imath}$; thus, with

no approximations, $\hat{r} = -\hat{\imath}$ or $\hat{r} = \pi + \hat{\imath}$. This is true, but bears a little analysis. The directions of the vectors **k** on the two sides of the interface in the (x, z) plane have components k_x in the plane and k_z normal to the interface, across which $\mathbf{E}_{xy}$ and $\mathbf{H}_{xy}$ are continuous. Now, following the spirit of §5.4.1, k_x must be identical on both sides. On the other hand, from Fig. 5.17(a), k_z is reversed. Thus the refraction angle of $\pi + \hat{\imath}$ is explained. Taking into account the fact that in the left-handed material **S** and **k** are anti-parallel, it follows that S is refracted at $-\hat{\imath}$.

We should remark that n might be complex (§5.6), but it is only its real part that determines the refractive behaviour.

Now consider refraction of light originating from a point source by a parallel-sided plate of material with $n = -1$. Since the light *rays* follow the routes determined by $\hat{r} = -\hat{\imath}$ it should be clear from Fig. 5.17(c) that the rays intersect exactly at the points shown, producing a 1:1 image in the rightmost plane. This is not a conventional image, whose magnification depends on the distances of object and image planes, but it must always have unit magnification, and since the relationship $\hat{r} = -\hat{\imath}$ contains no approximations, it has no classical aberrations (§3.7). In terms of imaging theory in physical optics, discussed in Chapter 12, it should at least be diffraction limited.

However, Pendry (2000) made a stronger claim than this. A point-like object of size a smaller than the wavelength λ radiates part of its energy into waves that have spatial frequencies up to $2\pi/a$, but as we have seen in §5.5.1 these waves propagate evanescently, and are therefore attenuated significantly in a distance of the order of a (§2.3.2). In normal imaging systems, these waves never contribute to the image, because at any reasonable distance their amplitudes are negligible; the fields with spatial frequency $2\pi/a$ decay as $\exp(-k_0\beta z)$, where $\beta = \sqrt{\lambda^2/n^2a^2 - 1} \approx \lambda/na$ (5.62). However, when n is negative, the waves *grow* exponentially at the same rate! In detail, one has to consider the exact boundary conditions for incidence of an evanescent wave at the boundary between media with $n = 1$ and $n = -1$ to show that the decaying wave converts into a growing wave. Now, when we look at the distances involved in Fig. 5.17(c), we see that in its passage from object to image, every ray traverses a path that is *exactly* half in the $n = 1$ medium and half in the $n = -1$ medium, so that the exponential decay of the evanescent wave in the former medium is exactly cancelled by the exponential growth in the latter. On this basis, image information on a scale smaller than the wavelength is also imaged by this type of lens, and for this reason it has been called a 'superlens'.

5.10.2 Achieving negative refractive index using meta-materials

In his paper, Veselago (1968) pointed out that an ionized gas plasma of the right density could provide values of $\epsilon < 0$, (§5.6) and by applying a magnetic field to the plasma, possibly μ could be made negative too. However, this

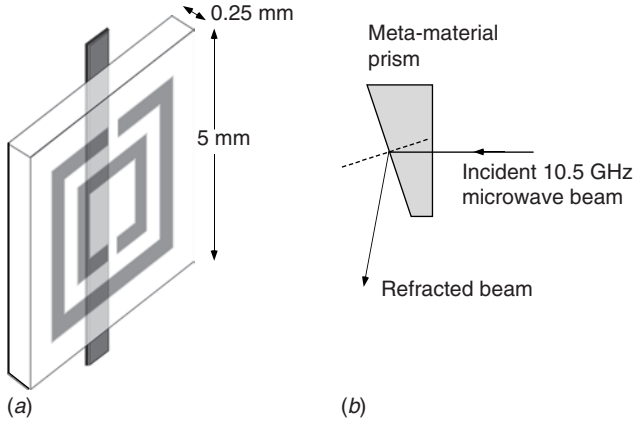

Figure 5.18 **A meta-material designed to have negative refractive index at 10.5 GHz. (*a*) One unit of the construction. Units were assembled on a square lattice with period 5 mm to provide the refracting medium. (*b*) Refraction experiment using a 18.4° prism cut from the meta-material, which refracted the microwaves by an angle of −61° ($n = -2.7$). (After Shelby *et al.* (2001))**

Meta-materials, with sub-wavelength structures, should be contrasted with *photonic crystals*, to be discussed in §10.5, where the array dimensions are comparable to the wavelength and the lattice structure is important.

was not followed up, and when work on the subject was revived after 2000, a different approach was taken. First, several metals have negative values of $\mathrm{Re}(\epsilon) = n^2 - \tilde{k}^2$ (§5.6), and silver is typically chosen because $\mathrm{Im}(\epsilon)$ is relatively small. The trouble is that there are no natural materials with negative μ. In order to obtain this, it is necessary to use resonant circuits, designed to be above resonance at the frequency of operation. The first materials of this sort were demonstrated by Smith *et al.* (2000) and Shelby *et al.* (2001), and worked at a frequency of 10.5 GHz ($\lambda = 3$ cm). A large number of small (mm-sized) double split ring resonators were etched in copper film and arranged on a lattice with period considerably shorter than the wavelength, so that they would behave as a continuum. Each ring is an inductor L, and the proximity of two rings created a capacitance C; the design was such that jointly the rings would have a resonance at a lower frequency $\sqrt{LC}$ than that of the wave, creating a phase difference of π between the applied and induced magnetic fields, and thus negative μ. The addition of parallel wires created an effective dielectric medium with a bulk plasma resonance (§13.3.4) frequency which could also be engineered to be below the wave frequency, creating the necessary negative ϵ. A prism constructed from this medium was shown experimentally to deviate a beam of microwaves by an angle corresponding to $n = -2.7$ (Fig. 5.18). The first evidence of sub-wavelength resolution by a superlens (§5.10.1) was also obtained by this system.

A composite material of this type, which behaves as a continuum despite its being constructed from a sub-wavelength array of small designed elements, is called a 'meta-material'. More recently, meta-materials have been constructed to provide negative refraction in the infra-red and optical regions; here, the

negative Re(ϵ) of silver or other metals can be employed (§5.6), together with nanometric-scale resonant structures to provide the negative μ.

Chapter summary

In this chapter we studied:

- Maxwell's equations and their solutions for harmonic waves;
- Plane waves and the relationship between their electric and magnetic fields;
- The Poynting vector, which describes energy flow in a wave;
- Radiation from accelerating charges, including synchrotron radiation;
- The derivation of Snell's law of refraction from boundary conditions at an interface;
- The Fresnel coefficients for reflection and refraction of plane waves at interfaces;
- Total internal reflection, optical tunnelling and evanescent waves;
- The optics of conducting media, which can be represented by a complex dielectric constant;
- Relationships between the reflection coefficients at opposite sides of a loss-less partial reflector;
- Momentum and angular momentum of electromagnetic waves;
- Optical tweezers, which use light pressure to manipulate tiny particles;
- Left-handed, or negative refractive index materials, and how they can be constructed from sub-wavelength-sized structures.

Problems

5.1. Two equal and opposite dipoles $\pm\mathbf{p}$ separated by vector $\mathbf{l}$ constitute a *quadrupole*. There are two generic types, with $\mathbf{l} \parallel \mathbf{p}$ and $\mathbf{l} \perp \mathbf{p}$. When $l \ll \lambda$, show that $\mathbf{E}_q(\mathbf{r})$, the field of an oscillating quadrupole, can be related to that of the dipole $\mathbf{E}_p$ by

$$\mathbf{E}_q = -\mathrm{i}k_0\mathbf{E}_p(\mathbf{l}\cdot\mathbf{r})/r, \tag{5.106}$$

and find the frequency dependence and radiation polar diagram for the power radiated by each of the generic types.

5.2. Estimate the pulse length and hence the peak frequency of synchrotron radiation from an electron travelling at velocity $v \approx c$ round a circle of

radius R. Use the facts that the electron only radiates within an angular range of $\psi = 2/\gamma$ (Fig. 5.3) around the line of sight, and it is travelling almost parallel to the line of sight at almost c.

5.3. Light tunnels between two prisms as in Fig. 5.10. What is the wave velocity in the tunnelling region? Now consider a Gaussian wave-group tunnelling through; can it propagate a signal faster than c? (For a discussion of this topic, see §13.5.)

5.4. Design a beamsplitter for wavelength 0.5 μm based on frustrated total internal reflection, based on two glass prisms with refractive index 1.5 separated by a layer of cement with refractive index 1.3.

5.5. Suppose that a reflector has a completely symmetrical construction (e.g. a quarter-wavelength-thick free-standing plate, which has non-zero reflection coefficient). What is the value of $\mathcal{R}$?

5.6. Show that at the Brewster angle the reflected and transmitted rays are orthogonal. When incidence is in the air, consider the reflected ray as originating in dipole radiation (Huygens-like) from surface dipoles on the interface, and show that the reflection coefficient for the $\parallel$ mode must indeed be zero at this angle. Can you extend this argument to Brewster-angle reflection when the incidence is *within* the medium, at an interface with air?

5.7. A pile of glass plates ($n = 1.5$) is used to polarize light by Brewster-angle reflection. If the incident light is incoherent and unpolarized, derive an expression for the degree of polarization (ratio of $\parallel$ to $\perp$) of the transmitted light as a function of the number of plates.

5.8. Magnesium fluoride (MgF_2) has refractive index 1.38. A $45°, 45°, 90°$ prism is constructed from this material and is used to turn a light beam by 90° by internal reflection at its hypotenuse. Relate the polarization vector after the reflection to that before, for both linearly and circularly polarized light (cf. §9.6).

5.9. A simple (free-electron) metal has conductivity σ. What thickness of it is necessary as a coating to make a beamsplitter that reflects and transmits equal intensities of a wave with frequency ω, and how much of the light is absorbed in the process? Ignore the substrate, to make things simpler.

5.10. An ellipsoidal dielectric particle is trapped by an optical tweezer. How will it align with respect to the optical axis?

5.11. A ball of plastic, $n = 1.5$ and 1 μm diameter is trapped in an optical tweezer employing a laser that has 10 mW focused into a 3 μm focal spot. Estimate how much force would be required to extract the ball from the trap.

5.12. Is a small, highly reflecting metal particle attracted or repelled by an optical tweezer?

5.13. A spiral wave with angular momentum given by $m = 1$ is reflected from a perfect mirror. Does the reflected wave have $m = +1$ or $m = -1$, and is angular momentum transferred to the mirror in the process?

5.14. Consider the design of an aplanatic lens (§3.8) using a material with refractive index -2.

References

Altman, C. and Suchy, K. (1991), *Reciprocity, Spatial Mapping and Time Reversal in Electromagnetics*, Dordrecht: Kluwer.

Ashkin, A. (1970), Acceleration and trapping of particles by radiation pressure, *Phys. Rev. Lett*. **24**, 156.

Born, M. and Wolf, E. (1999), *Principles of Optics*, Cambridge: Cambridge University Press.

Franklin, J. (2005), *Classical Electromagnetism*, San Francisco: Pearson/Addison-Wesley.

Grant, I. S. and Phillips, W. R. (1990), *Electromagnetism*, Chichester: Wiley.

Jackson, J. D. (1999), *Classical Electrodynamics*, New York: Wiley.

Padgett, M. and Allen, L. (2000), Light with a twist in its tail, *Contemp. Phys*. **41**, 275.

Pendry, J. B. (2000), Negative refraction makes a perfect lens, *Phys. Rev. Lett*. **85**, 3966.

Rotschild, C., Zommer, S., Moed, S., Hershcovitz, O. and Lipson, S. G. (2004), An adjustable spiral wave plate, *Appl. Opt*. **43**, 2397.

Shelby, R. A., Smith, D. R. and Schultz, S. (2001), Experimental verification of a negative index of refraction, *Science* **292**, 77.

Smith, D. R., Padilla, W. J., Vier, D. C., Nemat-Nasser, S. C. and Schultz, S. (2000), Composite medium with simultaneously negative permeability and permittivity, *Phys. Rev. Lett*. **84**, 4184.

Sokolov, A. V. (1960), *Optical Properties of Metals*, London: Blackie.

Veselago, V. G. (1968), The electrodynamics of substances with simultaneously negative values of ϵ and μ, *Sov. Phys. Uspekhi* **10**, 509.

Wille, K. (1991), Synchrotron radiation sources, *Rep. Prog. Phys*. **54**, 1005.

Zeilinger, A. (1981), General properties of lossless beamsplitters in interferometry, *Am. J. Phys*. **49**, 882.

6 Polarization and anisotropic media

As we saw in Chapter 5, electromagnetic waves in isotropic materials are transverse, their electric and magnetic field vectors **E** and **H** being normal to the direction of propagation **k**. The direction of **E** or rather, as we shall see later, the electric displacement field **D**, is called the **polarization** direction, and for any given direction of propagation there are two independent polarization vectors, which can be in any two mutually orthogonal directions normal to **k**. However, when the medium through which the wave travels is **anisotropic**, which means that its properties depend on orientation, the choice of the polarization vectors is not arbitrary, and the velocities of the two waves may be different. A material that supports two distinct propagation vectors is called **birefringent**.

In this chapter, we shall learn:

- about the various types of polarized plane waves that can propagate – linear, circular and elliptical – and how they are produced;
- how an anisotropic optical material can be described by a dielectric tensor $\boldsymbol{\epsilon}$, which relates the fields **D** and **E** within the material;
- a simple geometrical representation of wave propagation in an anisotropic material, the *n*-surface, which allows the wave propagation properties to be easily visualized;
- how Maxwell's equations are written in an anisotropic material, and how they lead to two particular orthogonally polarized plane-wave solutions;
- that the fields **D** and **B** of these plane waves remain transverse to **k** under all conditions, but **E** and **H**, no longer having to be parallel to **D** and **B**, are not *necessarily* transverse;
- that the Poynting vector **S** in an anisotropic material may not be parallel to the wave-vector **k**;
- about uniaxial and biaxial crystals, where the particular plane-wave solutions of Maxwell's equations are linearly polarized;
- about optically active materials with helical structures where these solutions are circularly polarized;
- about materials where anisotropy can be induced by external electric, magnetic or stress fields;
- a little about meta-materials with sub-wavelength structures, which have interesting 'designer-controlled' properties.

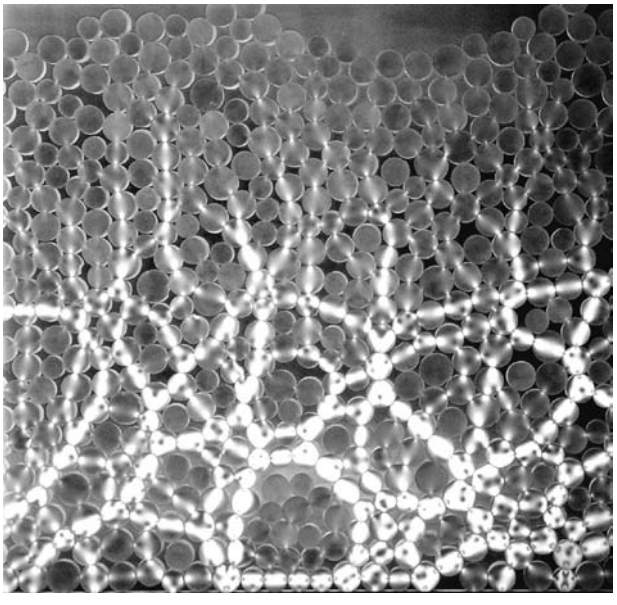

Figure 6.1 **An assembly of plastic discs with varying diameters are sandwiched between two vertical glass plates, but can move freely in the vertical plane under their own weight. The assembly is visualized between crossed polarizers. The transmitted light picture uses the photo-elastic properties (§6.9.2) of the plastic to visualize 'force chains' between the discs, showing that their weight is supported by chains of touching particles. This experiment models the structure and mechanics of sand-piles. (Experiment by Sarel Matza and Yuval Regev)**

Polarization of light has numerous applications, ranging from microscopy to studies of the magnetic fields in far-away galaxies. Many of them can easily be seen if we look at the world around us through a polarizing film, which selectively passes light with a particular direction of the vector **E**. For example, light from the blue sky is partially polarized, and when it is reflected from a car windscreen, the photo-elastic effect visualizes the strain pattern in the glass. Figure 6.1 shows a dramatic application of this effect in a study of the mechanics of granular materials.

6.1 Polarized light in isotropic media

Before we enter the complications of anisotropic media, we shall study two important plane-wave solutions of Maxwell's equations in an **isotropic medium**, and see how they are produced. These are waves that have well-defined **polarization**.

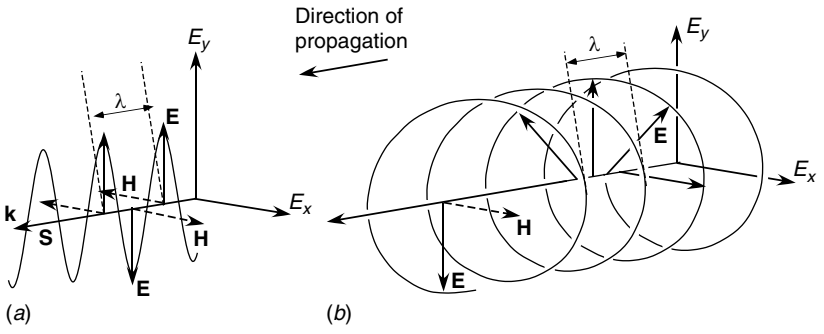

Figure 6.2
Electric field vector at time $t = 0$ for (*a*) linearly polarized and (*b*) circularly polarized waves.

6.1.1 Linearly polarized light

A homogeneous polarized light wave can be described either as a superposition of two linearly polarized waves with orthogonal polarizations, or as a superposition of two circularly polarized waves with opposite senses. Such descriptions do not apply to inhomogeneous waves, such as a spiral wave (§5.9).

The simplest basic periodic solution to Maxwell's equations is a plane wave in which **E**, **H** and **k** form a triad of mutually perpendicular vectors. This is called a **linearly polarized** (or **plane-polarized**) wave: $\mathbf{E} = E_y$, $\mathbf{H} = -H_x$ and $\mathbf{k} = k_z$ in Fig. 6.2(*a*). The vectors **E** and **k** define a plane called the **plane of polarization**. We have

$$\mathbf{E} = \mathbf{E}_0 \exp[\mathrm{i}(\mathbf{k} \cdot \mathbf{r} - \omega t)], \tag{6.1}$$

$$\mathbf{H} = \mathbf{H}_0 \exp[\mathrm{i}(\mathbf{k} \cdot \mathbf{r} - \omega t)]. \tag{6.2}$$

The energy flow or Poynting vector $\mathbf{S} = \mathbf{E} \times \mathbf{H}$ is parallel to **k**. For a given direction of **k** any pair of orthogonal polarizations can be chosen to represent independent ways of fulfilling these requirements.

6.1.2 Circularly polarized light

In a medium that responds linearly to electric and magnetic fields (i.e. we assume B is proportional to H, and D to E), any linear superposition of the above two linearly polarized waves is also a solution of Maxwell's equations. A particularly important case is that in which the two waves are superposed with a phase difference of $\pi/2$ (either positive or negative) between them. If we take the example where **k** is in the z-direction, and the two linearly polarized waves have equal amplitudes

$$\mathbf{E}_{01} = E_0\hat{\mathbf{x}}, \quad \mathbf{E}_{02} = E_0\hat{\mathbf{y}}, \tag{6.3}$$

in which $\hat{\mathbf{x}}$ and $\hat{\mathbf{y}}$ are unit vectors along the x- and y-axes, we have the superposition with $\pi/2$ phase difference

$$\mathbf{E} = E_0\hat{\mathbf{x}} \exp[\mathrm{i}(kz - \omega t)] + E_0\hat{\mathbf{y}} \exp[\mathrm{i}(kz - \omega t + \pi/2)]. \tag{6.4}$$

Remembering that the real electric field is the real part of this complex vector, we have

$$\mathbf{E}^{\mathrm{R}} = E_0\hat{\mathbf{x}}\cos(kz - \omega t) + E_0\hat{\mathbf{y}}\sin(kz - \omega t). \tag{6.5}$$

At given z, this represents a vector of length E_0 which rotates around the z-axis at angular velocity ω. The sense of rotation is clockwise as viewed by an observer; this is called **right-handed circularly polarized light**.

Alternatively, if we were to freeze the wave at time $t = 0$, the vector $\mathbf{E}^{\mathrm{R}}$ has the form

$$\mathbf{E}^{\mathrm{R}} = E_0(\hat{\mathbf{x}}\cos kz + \hat{\mathbf{y}}\sin k\hat{z}). \tag{6.6}$$

This vector, when drawn out as a function of z, traces out a right-handed screw (Fig. 6.2(b)). The magnetic field traces a similar screw, describing $\mathbf{H} \perp \mathbf{E}$.

If the phase difference between the two linearly polarized components is $-\pi/2$, a second independent polarization, in which the sense of rotation of $\mathbf{E}$ is anti-clockwise, is created. This is called **left-handed circularly polarized light.** At given t, the vector traces out a left-handed screw.

6.1.3 Elliptically polarized light

The superposition described in §6.1.2 need not involve two linearly polarized waves of equal amplitude. If the two waves have amplitudes E_{0x} and E_{0y}, then it is easy to see that the vector in Fig. 6.2 traces out a screw of elliptical cross-section. Similarly, at constant z, the vector $\mathbf{E}^{\mathrm{R}}$ traces out an ellipse. This type of light is called **elliptically polarized light** and also has left- and right-handed senses.

6.1.4 Fundamental significance of polarized types

Linearly polarized light is not a pure photon state, but is a superposition of photons with positive and negative spin.

When we introduce quantum optics in Chapter 14, we shall see that the quantum statistics of the electromagnetic field are equivalent to those of an ensemble of identical particles with Bose statistics. These are called **photons**. In order to have such statistics, they must have integral spin. Moreover, we shall see that in order to conserve angular momentum when light interacts with atoms, this must be ± 1 units of $\hbar$. It therefore emerges that the closest equivalent to a single photon is a wave with circular polarization, right-handed for spin $= +1$ and left-handed for spin $= -1$ (Problem 6.17). Linearly polarized light should then be rightly considered as the superposition of two circularly polarized waves with opposite handedness; the direction of polarization achieved then depends on the phase difference between the two circularly polarized waves.

6.1.5 Partially polarized and unpolarized light

Light generated by a discharge or filament lamp is generally not polarized. What this really means is that such light can be described as a superposition of many linearly polarized waves, each having its own random plane of polarization and individual phase. Moreover, because the light is not strictly monochromatic, the phase relation between the waves changes with time. Such a chaotic collection of waves has no discernable polarization properties and is called **unpolarized**. Sometimes, such light has a statistical preference for a particular plane of polarization because of some anisotropy in the medium and is **partially polarized**. An example is light from blue sky, where scattering provides the anisotropy (§13.2.2).

It is sometimes necessary to describe the degree of polarization of a light wave. There are several ways of doing this, which are described in detail in specialized texts (e.g. Azzam and Bashara (1989)). Basically, incoherent partially polarized light (the most general practical case) can be described by an unpolarized intensity plus a polarized intensity, the latter of which has an axis, degree of elliptical polarization and sense of rotation. It is possible to express these properties in terms of four parameters, which form a four-element vector called the **Stokes vector**. A polarizing element or mirror, which changes the polarization state of a wave, can then be described by a 4×4 matrix called a **Müller matrix**, which multiplies the Stokes vector of the incident wave to give that of the outgoing one. If the light is coherent, fewer parameters are needed to describe it, since an unpolarized coherent component does not exist. We shall not use these descriptions in the rest of this book, and therefore will not discuss them further.

6.1.6 Orthogonal polarization states

Two modes of polarization are called **orthogonal** if their electric field vectors are orthogonal in the conventional manner:

$$\mathbf{E}_1 \cdot \mathbf{E}_2^* = 0. \tag{6.7}$$

The electric field vector intended here is the complex amplitude[1] which multiplies $\exp[\mathrm{i}(\mathbf{k} \cdot \mathbf{r} - \omega t)]$. For example, for linearly polarized waves, these amplitudes are two real vectors which are orthogonal in the usual geometric sense; $\mathbf{E}_1$ normal to $\mathbf{E}_2$ implies that

[1] **E** as observed is a real electric field. The complex **E** used in the mathematics here is a complex function whose real part is the observed field. The relationship between the two, the Hilbert transform, was discussed in §4.5.1.

$$E_{1x}E_{2x} + E_{1y}E_{2y} = 0. \tag{6.8}$$

Two circularly polarized waves with opposite senses are likewise orthogonal. From (6.4) we have

$$\mathbf{E}_1 = E_0(\hat{\mathbf{x}} + \mathrm{i}\hat{\mathbf{y}}), \quad \mathbf{E}_2 = E_0(\hat{\mathbf{x}} - \mathrm{i}\hat{\mathbf{y}})$$
$$\mathbf{E}_1 \cdot \mathbf{E}_2^* = E_0^2(\hat{\mathbf{x}} \cdot \hat{\mathbf{x}} + \mathrm{i}^2\hat{\mathbf{y}} \cdot \hat{\mathbf{y}}) = 0. \tag{6.9}$$

Any elliptically polarized mode has an orthogonal companion; the two can be shown to have the same ellipticity but with major and minor axes interchanged and opposite senses.

6.2 Production of polarized light

There is no way of creating a beam of polarized light from a beam of unpolarized light without either wasting part of its energy or changing its geometrical properties.

Any dependence of the propagation properties of light on its polarization can be used, in principle, to produce polarized light. Two well-known phenomena having this property are reflection at the surface of a dielectric (§5.4) and scattering by small particles (§13.2.2). Other methods, which will be discussed in more detail later, involve crystal propagation (§6.8.3) and selective absorption (dichroism, §6.2.2).

The action of 'polarizing light' essentially means taking unpolarized light and extracting from it a beam of polarized (linear, circular or elliptical) light. The rest of the light, which is sometimes just as well polarized in an orthogonal orientation, is wasted, or may be used for some other purpose. There is no way of reorganizing the light so as to get a single beam of polarized light from an unpolarized source without making the beam either broader or more divergent. Such a process, were it possible, could be used to defy the second law of thermodynamics! (Problem 6.10).

6.2.1 Polarization by reflection

One of the easiest ways to polarize light is to reflect it from a plane dielectric surface between two media at the Brewster angle (§5.4.2):

$$\hat{\imath}_\mathrm{B} = \tan^{-1} n_r, \tag{6.10}$$

where n_r is the ratio between their refractive indices. At this angle, the reflection coefficient for the $\parallel$ component is zero; thus the reflected light is completely polarized in the $\perp$ direction (Fig. 6.3). However, even for this component the reflection coefficient is small (typically 5–6%) so that this method of polarization is quite inefficient. The polarization is also complete only for a specified angle of incidence. By stacking several plates in series, each one of which reflects some of the $\perp$ component, the transmitted $\parallel$ component can be polarized

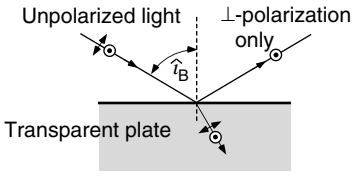

Figure 6.3
Polarization by reflection at the Brewster angle. The reflected light is ∥-polarized, since the reflection coefficient $\mathcal{R}_\perp = 0$.

reasonably well, with less angular sensitivity (Problem 5.7). Polarization by Brewster-angle reflection has one important practical property; it is automatically calibrated in the sense that the geometry alone defines exactly the plane of polarization. It is also extremely sensitive to surface quality and structure, a property that is exploited in the technique of **ellipsometry** for investigating interfaces (Azzam and Bashara (1989), Tompkins (2006)).

Crystal polarizers use total internal reflection to separate polarized components from unpolarized light, and must be used if the highest quality of polarization is required. We shall discuss these in more detail in §6.8.3.

6.2.2 Polarization by absorption

Several materials, both natural and synthetic, absorb different polarizations by different amounts. This behaviour is called **dichroism**. It is widely used to polarize light linearly, and may also be used to polarize it circularly.

A well-known mechanism that polarizes light linearly by this effect is a parallel grid of conducting wires separated by less than one wavelength. This system transmits most of the light when its electric polarization vector is normal to the wires. No diffraction orders are created (§8.5.3) if the separation is less than λ. But if the electric field vector is parallel to the wires, currents are induced in them and the wave energy is absorbed. So an incident unpolarized beam emerges polarized fairly well normal to the wires.[2] Polarizers of this sort are constructed by microfabrication or ion-implantation of gold or silver strips on a transparent dielectric substrate. The most common polarizing material, 'Polaroid', also uses this mechanism (see Box 6.1).

6.2.3 Extinction ratio

A measure of the effectiveness of a polarizer is gained by passing unpolarized light through two identical devices in series. If the two transmit along parallel axes, a single component is transmitted by both, and the output intensity is I_1. If the two polarizers are now 'crossed', so that the transmitting axes are perpendicular, ideally no light would be transmitted, but in practice a small intensity I_2 passes. Careful orientation of the polarizers minimizes this value.

[2] This is popular and easy to demonstrate using centimetre microwaves.

Box 6.1 Dichroic polarizers: Polaroid film

Polaroid film,[3] developed by Edwin Land in 1932, works like the array of thin conducting wires, which are in this case produced chemically. It is manufactured in two different ways. The original method consisted of putting many microscopic needle-shaped crystals of iodoquinine sulphate (herapathite) into a transparent nitrocellulose film, which was then stretched to align the crystals. In 1938 Land improved the process and the Polaroid film we now use consists of a stretched film of polyvinyl alcohol dyed with iodine. The oriented conducting polymeric chains behave similarly to the wire grid. This material is cheap to produce and can be made in thin sheets of almost unlimited size.

The ratio I_1/I_2 is called the **extinction ratio**. In good crystal polarizers this may be as high as 10^7, and a similar value can be obtained for clean reflectors exactly at the Brewster angle. Polaroid typically gives a value of 10^3.

6.3 Wave propagation in anisotropic media: A generalized approach

In the next two sections we shall discuss the way in which the electromagnetic wave propagation theory in Chapter 5 must be extended to take into account the anisotropic (orientation dependent) properties of the material. This will be done at a purely phenomenological level; no account will be given of the atomic or molecular origin of the anisotropy, which is a subject well outside the scope of this book.

6.3.1 Huygens' construction

We shall first discuss the general relationship between propagation of waves and rays and anisotropic properties. This was first done in about 1650 by Huygens, who considered 'wavelets' originating from points on a given wavefront AB of *limited extent*, as in Fig. 6.4 (see also Fig. 2.6(*b*)). If the velocity is a function of the direction of propagation, the wavelets are not spherical; we shall see that they are in fact ellipsoidal. The new wavefront A_1B_1 is then the common tangent to the wavelets, as shown. But the *position* of the wavefront A_1B_1 moves sideways, showing that the light ray which it represents is at an angle to the wave-vector. This is a common feature of crystal propagation: **the Poynting**

[3] The widely used polarizing film commonly called 'Polaroid' should not be confused with instant Polaroid photographic film, which has now been made obsolete by the digital camera.

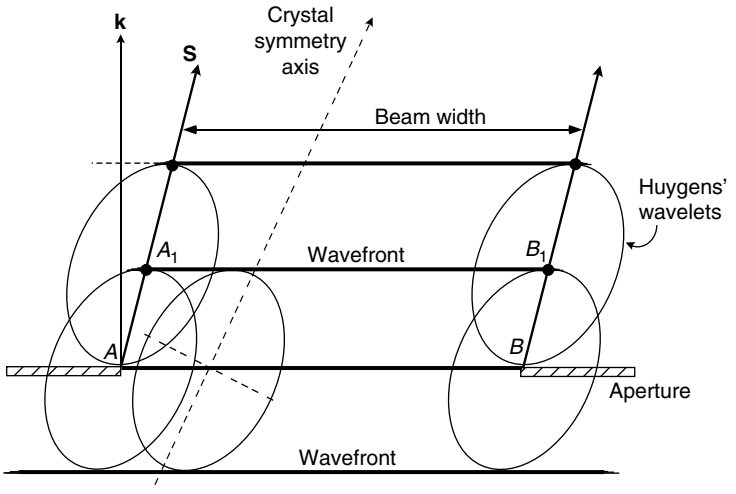

Figure 6.4

Huygens' principle applied to propagation of a limited beam in an anisotropic medium. The black spots emphasize the points where the wavefront is tangent to the wavelets; these points are not necessarily on the symmetry axes of the ellipsoid.

vector S, represented by the direction AA_1 of the light ray, is not in general parallel to k.

The *n*-surface in optics is analogous to the Fermi surface of a metal in solid-state physics. The same idea can be applied to any type of wave propagation.

6.3.2 The refractive-index surface, or *n*-surface

The exact relationship between the velocity anisotropy and **S** can easily be visualized by a geometrical method. To establish the method we need a small amount of formal mathematics. For monochromatic light at frequency ω_0 the refractive index, since it is a function of the direction of propagation, can be written as a vector:

$$\mathbf{n} = \frac{c\mathbf{k}}{\omega_0}, \tag{6.11}$$

where **k** has the value of the wave-vector measured in the medium for propagation in that direction, and the vector **n** has the same direction.

Now the phase velocity is $v = \omega/k$. The group velocity $\mathbf{v}_\mathrm{g}$, which is the velocity of propagation of *energy* and therefore corresponds in direction to **S**, has components, by extension of §2.4,

$$v_{\mathrm{g}x} = \frac{\partial\omega}{\partial k_x}, \quad v_{\mathrm{g}y} = \frac{\partial\omega}{\partial k_y}, \quad v_{\mathrm{g}z} = \frac{\partial\omega}{\partial k_z}. \tag{6.12}$$

This is written in vector terminology:

$$\mathbf{v}_\mathrm{g} = \nabla_k\,\omega \equiv \left(\frac{\partial\omega}{\partial k_x}, \frac{\partial\omega}{\partial k_y}, \frac{\partial\omega}{\partial k_z}\right) \tag{6.13}$$

$$= \frac{c}{\omega_0}\left(\frac{\partial\omega}{\partial n_x}, \frac{\partial\omega}{\partial n_y}, \frac{\partial\omega}{\partial n_z}\right) = \frac{c}{\omega_0}\nabla_n\,\omega. \tag{6.14}$$

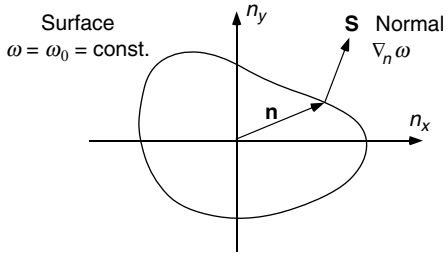

Figure 6.5
Construction of the *n*-surface, which is a polar plot of the value of *n* as a function of the direction of propagation $\hat{\mathbf{k}}$. The Poynting vector **S** has direction normal to the surface; **n** is defined as parallel to the propagation vector **k**.

We shall now represent the propagation properties in the medium by the vector **n**. At a particular value $\omega = \omega_0$ this has a given value for each direction of propagation and therefore can be represented by a closed surface.[4] The radius vector, from the origin to the surface, in each direction is equal to the value of n for propagation in that direction. We shall call this the **refractive-index surface**, or ***n*-surface**. In other texts, for example Born and Wolf (1999), it is called the **inverse surface of wave-normals**. Since (6.14) is analogous to the well-known electrostatic relationship $\mathbf{E} = -\nabla V$, which shows that lines of electric field E are normal to the equipotential surfaces V= constant, it follows similarly that the vector $\mathbf{v}_g$ (6.14) is normal to the surface of constant ω, i.e. **normal to the *n*-surface**. The velocity v_g can be identified with the Poynting vector **S** (§5.2.1) since both represent the transfer of energy.

In general, once we have found the n-surface for a given material at frequency ω_0, we can investigate wave propagation in that material geometrically. For a given wave-vector **k** (Fig. 6.5), we find the appropriate value of n as the radius of the n-surface in direction **k**, and the direction of **S** as the normal to the n-surface at that point. Clearly, in an isotropic material the n-surface is a sphere, and $\mathbf{S} \parallel \mathbf{k}$.

6.4 Electromagnetic waves in an anisotropic medium

We shall now solve Maxwell's equations when the dielectric properties of the medium are anisotropic. As in most of Chapter 5, we assume no magnetic polarization (i.e. $\mu = 1$) since this is usually the case in transparent media at optical frequencies. For harmonic plane waves of the form

$$E = E_0 \exp[\mathrm{i}(\mathbf{k} \cdot \mathbf{r} - \omega t)] \tag{6.15}$$

[4] If there is no propagation possible in a certain direction, the surface does not exist in that orientation, and is therefore not closed. This happens if, for example, the propagation is evanescent in that direction. See §6.10, for example.

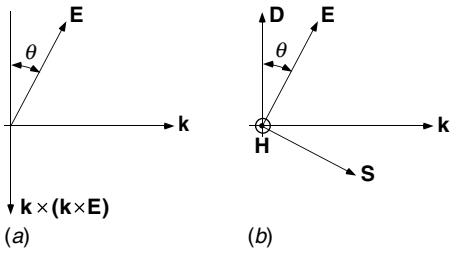

Figure 6.6
(*a*) The vectors **k**, **E** and **k** × (**k** × **E**); (*b*) vectors **D**, **E**, **S**, **k** and **H** for a wave.

we once again use the operator substitutions (§2.2) as we did in §5.1:

$$\frac{\partial}{\partial t} = -\mathrm{i}\omega, \quad \nabla = \mathrm{i}\mathbf{k}. \tag{6.16}$$

Maxwell's equations in an uncharged insulator then emerge as:

$$\nabla \cdot \mathbf{B} = 0 \Rightarrow \mathrm{i}\mathbf{k} \cdot \mathbf{B} = 0, \tag{6.17}$$

$$\nabla \cdot \mathbf{D} = 0 \Rightarrow \mathrm{i}\mathbf{k} \cdot \mathbf{D} = 0, \tag{6.18}$$

$$\nabla \times \mathbf{H} = \frac{\partial \mathbf{D}}{\partial t} \Rightarrow \mathrm{i}\mathbf{k} \times \mathbf{H} = -\mathrm{i}\omega\mathbf{D}, \tag{6.19}$$

$$\nabla \times \mathbf{E} = -\frac{\partial \mathbf{B}}{\partial t} \Rightarrow \mathrm{i}\mathbf{k} \times \mathbf{E} = \mathrm{i}\omega\mathbf{B}. \tag{6.20}$$

These equations should be compared with (5.16)–(5.19). Notice that **D** and **B** are transverse (normal to **k**). Substituting $\mu_0\mathbf{H}$ for **B** (non-magnetic material), we take (**k**×) equation (6.20) and get

$$\mathbf{k} \times (\mathbf{k} \times \mathbf{E}) = \mu_0\omega\mathbf{k} \times \mathbf{H} = -\mu_0\omega^2\mathbf{D}. \tag{6.21}$$

This equation relates the vectors **k**, **E** and **D**. In the isotropic case, $\mathbf{D} = \epsilon_0\epsilon\mathbf{E}$, giving $\mathbf{k} \times (\mathbf{k} \times \mathbf{E}) = -k^2\mathbf{E} = -\mu_0\omega^2\epsilon_0\epsilon\mathbf{E}$, which can easily be seen to revert to (5.13).

In anisotropic media the electric field is not necessarily transverse to **k**, but the displacement field **D** is always transverse.

First we look at the disposition of the vectors in (6.21). The vector $\mathbf{k} \times (\mathbf{k} \times \mathbf{E})$ lies in the plane of **k** and **E**, normal to **k**. For the equation to have a solution at all, **D must therefore lie in the plane of k and E**. We also know from (6.18) that **D** is normal to **k**, as illustrated in Fig. 6.6. This condition defines what we shall call a **characteristic wave**, which is a propagation mode for the material. For such a wave, there is an angle θ between **E** and **D** and

$$|\mathbf{k} \times (\mathbf{k} \times \mathbf{E})| = k^2 E \cos\theta = \mu_0\omega^2 D. \tag{6.22}$$

The wave velocity is thus given by

$$v^2 = \frac{\omega^2}{k^2} = \frac{E\cos\theta}{\mu_0 D}. \tag{6.23}$$

Finally, from (6.17)–(6.19), the magnetic fields **B** and **H** are normal to **k** and to **D**, so that a full picture of the disposition of the vectors **D**, **E**, **k**, **H** and the Poynting vector $\mathbf{S} = \mathbf{E} \times \mathbf{H}$ can be drawn, Fig. 6.6(*b*).

The problem we have to solve for a particular medium is, having chosen the direction of the wave-vector **k**, to identify the characteristic waves, which means finding those directions of **D** that result in coplanar **D**, **E** and **k**. Then the wave velocity and refractive index $n = c/v$ can be found from (6.23). There will be in general two distinct solutions for each direction of **k** (under some circumstances they may be degenerate). The polarizations of the two characteristic waves will be found to be orthogonal (§6.1.6). Thus when we construct the *n*-surface (§6.3.2) we shall find it to be doubly valued (i.e. two values of *n* in each direction), which leads to many interesting and important properties. For this reason, anisotropic optical crystals are called **birefringent**.

6.5 Crystal optics

In this section we shall first describe how the dielectric properties of an anisotropic material are described by a tensor (or matrix), which can be represented geometrically by means of an ellipsoid. We then go on to use the geometry of the ellipsoid to find the characteristic waves for the material and their velocities. These define the shape of the *n*-surface, from which all the optical properties can then be deduced.

6.5.1 The dielectric tensor

Three principal dielectric constants are needed to describe the relationship between **D** and **E**; in the most general case they are all different.

Crystals are anisotropic because of their microscopic structure. Here we shall only consider the anisotropy as a continuum phenomena, because interatomic distances are orders of magnitude smaller than the light wavelength. In an anisotropic linear dielectric medium, the vectors **D** and **E** are proportional in magnitude, but not necessarily parallel, so that we write a tensor relationship

$$\mathbf{D} = \epsilon_0 \boldsymbol{\epsilon} \mathbf{E}. \tag{6.24}$$

In (6.24) the dielectric tensor, $\boldsymbol{\epsilon}$, represents the matrix

$$\boldsymbol{\epsilon} = \begin{pmatrix} \epsilon_{11} & \epsilon_{12} & \epsilon_{13} \\ \epsilon_{21} & \epsilon_{22} & \epsilon_{23} \\ \epsilon_{31} & \epsilon_{32} & \epsilon_{33} \end{pmatrix}. \tag{6.25}$$

Its meaning is straightforward. If an electric field $\mathbf{E} = (E_1, E_2, E_3)$ is applied, the resulting displacement field **D** has components (D_1, D_2, D_3) where

$$D_i = \epsilon_0 [\epsilon_{i1} E_1 + \epsilon_{i2} E_2 + \epsilon_{i3} E_3]. \tag{6.26}$$

The theory of linear algebra shows that there always exist three **principal axes** ($i = 1, 2, 3$) for which $\mathbf{D}_i$ and $\mathbf{E}_i$ are parallel. We then have three **principal dielectric constants** ϵ_i defined by

$$\frac{D_{1i}}{E_{1i}} = \frac{D_{2i}}{E_{2i}} = \frac{D_{3i}}{E_{3i}} = \epsilon_0 \epsilon_i. \tag{6.27}$$

The three principal axes are mutually orthogonal and, for a non-absorbing crystal, the ϵ_i's are real. By using these three axes as x, y and z, the tensor (6.25) can be written in a simpler diagonal form, which we shall use as far as possible:

$$\boldsymbol{\epsilon} = \begin{pmatrix} \epsilon_1 & 0 & 0 \\ 0 & \epsilon_2 & 0 \\ 0 & 0 & \epsilon_3 \end{pmatrix}. \tag{6.28}$$

In a non-absorbing medium, ϵ_1, ϵ_2 and ϵ_3 are real; this can be shown to be equivalent to $\epsilon_{ji} = \epsilon_{ij}^*$ in (6.25), and is the definition of a Hermitian tensor. The process of rotating the tensor so that (x, y, z) become principal axes is called **diagonalizing the tensor** and the technique for doing it is discussed in every book on linear algebra. The most general crystal, called a **biaxial crystal** for reasons which will be apparent later, has three distinct values for $\epsilon_1, \epsilon_2, \epsilon_3$; in crystals with higher symmetry, **uniaxial crystals**, two of the values are equal (say, $\epsilon_1 = \epsilon_2$). If all three are equal, the material is isotropic.

6.5.2 The index ellipsoid, or optical indicatrix

To carry out our plan of presenting crystal optics geometrically we need to represent the tensor as an ellipsoid. In general, the ellipsoid with semi-axes a, b, c is the surface

$$\frac{x^2}{a^2} + \frac{y^2}{b^2} + \frac{z^2}{c^2} = 1. \tag{6.29}$$

In formal terms this can be written

$$(x, y, z) \begin{pmatrix} a^{-2} & 0 & 0 \\ 0 & b^{-2} & 0 \\ 0 & 0 & c^{-2} \end{pmatrix} \begin{pmatrix} x \\ y \\ z \end{pmatrix} = 1, \tag{6.30}$$

$$\text{or, in shorthand} \quad \mathbf{r} \cdot \mathsf{M} \cdot \mathbf{r} = 1. \tag{6.31}$$

The inverse to (6.24) is

$$\mathbf{E} = \epsilon_0^{-1} \boldsymbol{\epsilon}^{-1} \cdot \mathbf{D}, \tag{6.32}$$

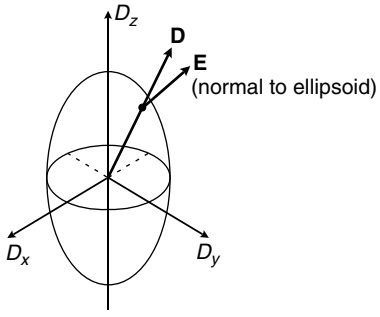

Figure 6.7
The optical indicatrix and the relationship between **D** and **E**. **E** is normal to the surface of the indicatrix.

where, for the diagonal form (6.28),

$$\boldsymbol{\epsilon}^{-1} \equiv \begin{pmatrix} \epsilon_1^{-1} & 0 & 0 \\ 0 & \epsilon_2^{-1} & 0 \\ 0 & 0 & \epsilon_3^{-1} \end{pmatrix}. \tag{6.33}$$

We can now study the geometrical meaning of the formal equation $\epsilon_0 \mathbf{D} \cdot \mathbf{E} = 1$ which becomes, using (6.32),

$$\mathbf{D} \cdot \boldsymbol{\epsilon}^{-1} \cdot \mathbf{D} = 1. \tag{6.34}$$

This is represented by the ellipsoid (6.30) if (x,y,z) replaces $\mathbf{D}$, $\epsilon_1 = a^2$, $\epsilon_2 = b^2$ and $\epsilon_3 = c^2$, i.e.

$$\frac{D_x^2}{\epsilon_1} + \frac{D_y^2}{\epsilon_2} + \frac{D_z^2}{\epsilon_3} = 1. \tag{6.35}$$

Thus the ellipsoid, Fig. 6.7, has semi-axes $\epsilon_1^{\frac{1}{2}}$, $\epsilon_2^{\frac{1}{2}}$, $\epsilon_3^{\frac{1}{2}}$ which we shall see to be three principal values of the refractive index n (remember that in an isotropic medium $n = \epsilon^{\frac{1}{2}}$: §5.1.2). To understand the meaning of the ellipsoid, we imagine **D** varying in direction, its length being calculated at each point so that $\mathbf{D} \cdot \mathbf{E} = 1$ (in units of energy density). The tip of the vector **D** then traces out the ellipsoid. The vector **E** can be shown to have the direction of the normal to the ellipsoid at the tip of **D** (Fig. 6.7).[5]

The polarization vector of a propagating wave determines its velocity.

[5] Proof: the tangent plane to the ellipsoid (6.29) at (x_1,y_1,z_1) is

$$\frac{xx_1}{a^2} + \frac{yy_1}{b^2} + \frac{zz_1}{c^2} = 1. \tag{6.36}$$

A vector normal to this plane is $(x_1/a^2, y_1/b^2, z_1/c^2)$. Replacing (x_1,y_1,z_1) by **D** and a^2 by ϵ_1, etc., shows this normal to be in the direction of **E**.

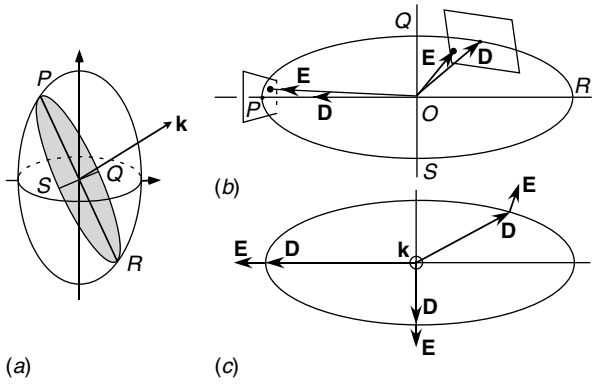

Figure 6.8
(*a*) The elliptical section of the indicatrix *PQRS* which is normal to **k**. (*b*) The tangent planes are indicated at two points on *PQRS* to show that on the axes (at *P*, for example) **D**, **E** and **k** are coplanar, but not at other points. (*c*) Projection of **E** on the plane of the ellipse emphasizes the fact that only at the extrema are **D, E** and **k** coplanar.

The refractive index n for the wave with polarization vector **D** then follows simply:

$$n^2 = \frac{c^2}{v^2} = \frac{c^2\mu_0 D}{E\cos\theta} = \frac{\epsilon_0 c^2 \mu_0 D^2}{\epsilon_0 ED\cos\theta} = D^2 \tag{6.37}$$

since $\epsilon_0 ED\cos\theta = \epsilon_0 \mathbf{E}\cdot\mathbf{D} = 1$ at all points on the ellipsoid and $\epsilon_0\mu_0 c^2 = 1$. Thus $n = |D|$. In other words, **the radius vector of the ellipsoid in each direction equals the refractive index of the medium for a wave with polarization vector D in that direction**. This ellipsoid is called the **index ellipsoid** or **optical indicatrix**. Notice, by the way, that the values have come out correctly in a principal direction, x for example; the ellipsoid has semi-axis $\epsilon_1^{\frac{1}{2}}$, which is just the refractive index for a wave polarized in that direction. It is most important to realize that it is the **polarization direction, not the propagation direction, which determines the velocity of the wave**. Waves propagating in different directions, but with the same polarization vector, travel at the same velocity.

6.5.3 Characteristic waves

We now have to determine the polarizations and velocities of the characteristic waves for a given propagation direction **k**. We saw, in §6.4, that the requirement for characteristic waves is that **D**, **E** and **k** have to be coplanar. We now have the means to find them. We proceed as follows, given the propagation vector **k**:

1. We find all possible polarizations **D**. These lie in a plane normal to **k** since **D** is always transverse (6.18).
2. We construct **E** for each **D** using the indicatrix. Recall that **E** is normal to the surface of the indicatrix at the tip of **D** (§6.5.2).
3. We look for coplanar **D**, **E** and **k**.

Figure 6.8 illustrates these stages. In stage 1, we construct a plane normal to **k** through the origin. It intersects the indicatrix in an ellipse. In stage 2, we

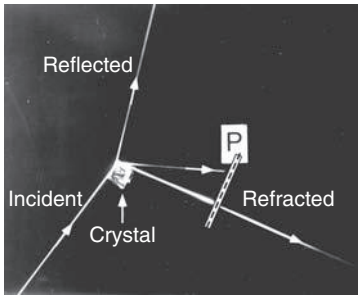

Figure 6.9

Photograph of refraction of an unpolarized laser beam by a crystal of sodium nitrate ($NaNO_3$), whose natural growth facets form a prism. A reflected beam and two refracted beams are visible, showing the existence of two refractive indices. At *P* the refracted beams meet a polarizer, which transmits only one beam.

construct **E** normal to the indicatrix at each point on the intersection ellipse. By symmetry, stage 3 selects the points which are on the major and minor axes of the intersection ellipse as those for which **E** lies in the (**k, D**) plane. Thus there are always **two characteristic waves** for propagation with a particular **k**, and *OP* and *OQ* in the figure represent their polarization vectors, which must be orthogonal. Their refractive indices are given by the lengths of *OP* and *OQ*. The existence of two waves with different refractive indices and polarizations is shown by the photograph in Fig. 6.9.

6.5.4 The *n*-surface for a crystal

The *n*-surface is constructed from two sheets, representing two orthogonal polarization states.

We can get a good idea of the shape of the *n*-surface in three dimensions by working out its sections in the (x, y), (y, z) and (z, x) planes. Without loss of generality, assume the indicatrix to have minor, intermediate and major axes of lengths n_1, n_2 and n_3 along the x, y and z-axes respectively.

Start with **k** along x and consider what happens as it rotates in the (x, y) plane, as in Fig. 6.10. When **k** is along the x-axis, the ellipse *PQRS* of Fig. 6.8 has its major and minor axes $OZ = n_3$ and $OY = n_2$. When **k** rotates around z, OZ is always the major axis, but the minor axis changes gradually from OY to $OX = n_1$, which value it reaches when **k** is along y. Plotting the two values of n on a polar plot as a function of the direction of k gives us the section of the n-surface in the (x, y) plane. Figure 6.11(a) shows the result. There is a circle, radius n_3, corresponding to polarization in the z-direction and an ellipse (n_2, n_1)[6] corresponding to polarizations orthogonal to z and **k**.

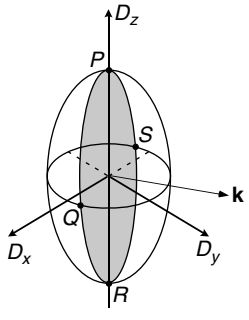

Figure 6.10

Section of the indicatrix when k lies in the (*x*, *y*) plane.

In the same way we construct the sections in the (y, z) plane (Fig. 6.11(b)) and (z, x) plane (Fig. 6.12). The latter figure shows the circle of radius n_2 to intersect the ellipse (n_3, n_1) at four points A. These correspond to two circular sections of the indicatrix (Fig. 6.13), and the directions **k** corresponding to the OA's are called **optic axes**. For propagation in these directions, the two characteristic waves are degenerate (and so in fact any two orthogonal polarizations could be chosen for characteristic waves). Since there are two such orientations OA, the general crystal ($n_3 \neq n_2 \neq n_1$) is called **biaxial**. It is quite easy to see that

[6] Meaning the ellipse with major axis n_2 and minor axis n_1.

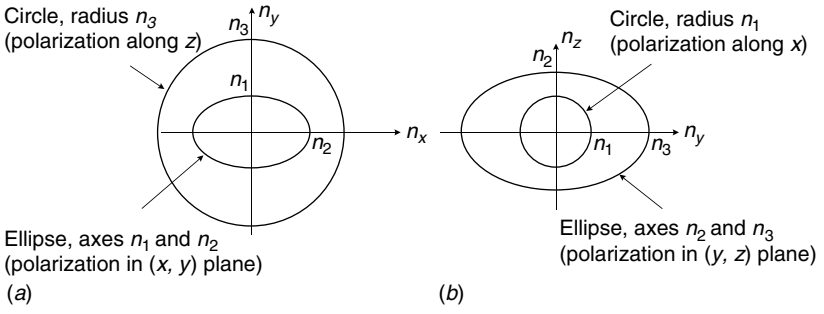

Figure 6.11

Sections of the *n*-surface (*a*) in the (*x*, *y*) plane and (*b*) in the (*y*, *z*) plane.

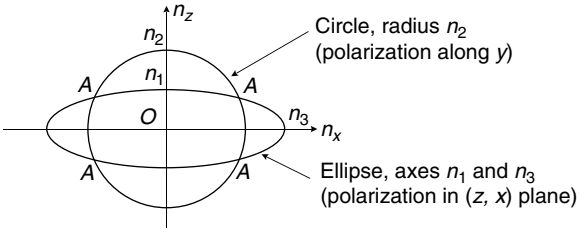

Figure 6.12

Section of the *n*-surface in the (*z*, *x*) plane. The two directions *OA* are the optic axes.

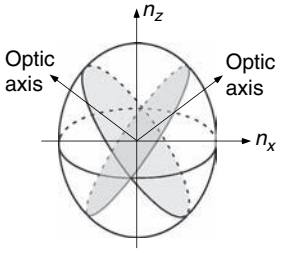

Figure 6.13

Two circular sections of the indicatrix.

there are no other circular sections of the general ellipsoid, so there are no other optic axes.

Construction of the complete *n*-surface can now be done, qualitatively, by interpolation, and this will serve us sufficiently for understanding the physics of crystal optics. One octant of the surface is shown in Fig. 6.14. The surface clearly has two branches, which we shall call 'outer' and 'inner'. They touch along the optic axis, which is the only direction for which the refractive indices of the two characteristic waves are equal. The other octants are constructed by reflection.

6.5.5 Ordinary and extraordinary rays

Once we have constructed the *n*-surface, it is in principle a simple matter to deduce the polarizations and Poynting vectors **S** of the two characteristic waves in any given direction (Fig. 6.15). We associate with each direction of **k** and characteristic polarization a **ray** that travels in the direction of **S**. The ray is what is actually seen when a wave travels through a crystal (Fig. 6.16), and the existence of two rays for any given **k** direction gives rise to the well-known phenomenon of the double image (see Fig. 1.3). Two types of ray can be defined:

– an **ordinary ray,** for which **S** and **k** are parallel;
– an **extraordinary ray,** for which **S** and **k** are not parallel.

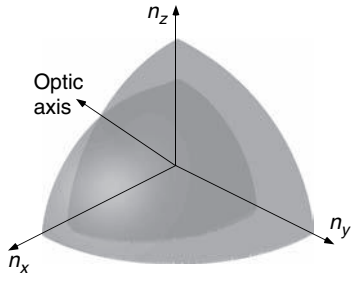

Figure 6.14

One octant of the *n*-surface for a biaxial crystal, showing the inner and outer branches.

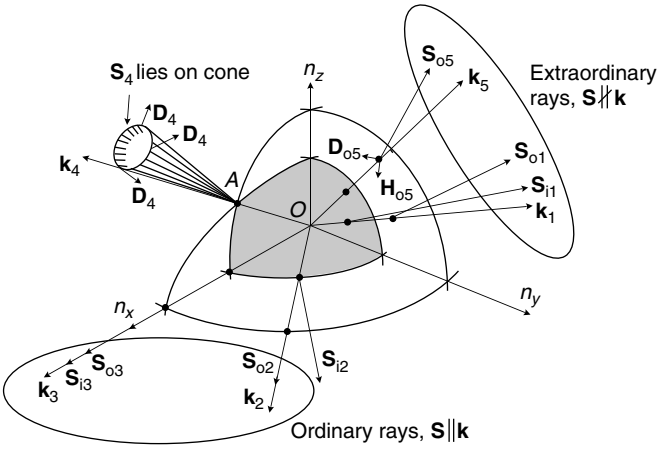

Figure 6.15

The *n*-surface for a biaxial crystal. Suffix 'i' refers to the inner branch, which is shaded, and 'o' to the outer branch. $\mathbf{k}_1$ represents the most general direction for which there are two extraordinary rays. $\mathbf{k}_2$ lies in a symmetry plane, and there is one ordinary and one extraordinary ray. $\mathbf{k}_3$ lies along a symmetry axis, and there are two ordinary rays. $\mathbf{k}_4$ is along the optic axis *OA* and **S** is located on a cone, in a direction depending on the polarization vector **D**. $\mathbf{k}_5$ is used to show how the vector **H** is constructed normal to **k** and **S**, and **D**, normal to **k** and **H**.

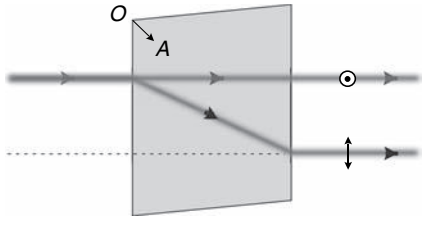

Figure 6.16

An unpolarized light ray splits into two as it traverses a crystal plate; this is the origin of the term **birefringent**. The angles between extraordinary rays and the interface clearly do not satisfy Snell's law. The optic axis is in direction *OA*.

Since Snell's law applies to the directions of **k**, it applies to **S** as well only for ordinary waves. In general we find one general and two special cases, which are illustrated by Fig. 6.16:

1. In an arbitrary direction $\mathbf{k}_1$ both surfaces give rise to extraordinary rays. Once **S** and **k** are known, the magnetic field vector **H** is determined by being their common normal, and the polarization vector **D** by being the common normal to **k** and **H**.
2. If $\mathbf{k}_2$ lies in a symmetry plane (x, y), (y, z) or (z, x) there is one ordinary and one extraordinary ray.
3. If $\mathbf{k}_3$ lies along one of the axes x, y or z, both rays are ordinary, despite their having different values of n.

6.5.6 Conical propagation

A peculiar form of propagation occurs when **k** is along the optic axis ($\mathbf{k}_4$ in Fig. 6.15). Because of the degeneracy of n, **any polarization can be chosen** (§6.5.4), **but each one gives rise to a different S**. The various **S**'s possible lie on a cone, one edge of which is along the optic axis. If we have a plate of a biaxial crystal, and an unpolarized light beam is incident on it so that it is refracted into the optic axis, the light spreads out into a conical surface inside the crystal, and exits the plate as a ring. This phenomenon is called **external conical refraction.** Conical refraction also occurs in **photonic crystals**, which are discussed in §10.5.

6.6 Uniaxial crystals

Many crystals have a dielectric tensor that has only two distinct principal values. Then (6.28) becomes

$$\boldsymbol{\epsilon} = \begin{pmatrix} \epsilon_1 & 0 & 0 \\ 0 & \epsilon_1 & 0 \\ 0 & 0 & \epsilon_3 \end{pmatrix}. \tag{6.38}$$

It follows that the indicatrix is a spheroid (ellipsoid of revolution) with one semi-axis of length n_3 and circular section of radius n_1. Visualizing the n-surface via its sections gives once again a two-branched surface. One branch is a sphere of radius n_1; the other is a spheroid with semi-axis n_1 and section of radius n_3. It is immediately apparent that the two branches touch along the n_z-axis, which is the only optic axis (Fig. 6.17(a)). Hence the name for such crystals, **uniaxial crystals.** It is usual to refer to n_1 as the **ordinary** index (n_o) and n_3 as the **extraordinary** index (n_e); if $n_\mathrm{e} > n_\mathrm{o}$, the crystal is said to be **positive uniaxial**, and if $n_\mathrm{e} < n_\mathrm{o}$, **negative uniaxial**. Table 6.1 gives several examples.

Table 6.1. Refractive indices of some common biaxial and uniaxial crystals at $\lambda = 589$ nm

Crystal	Principal refractive indices			
	n_1	(n_o)	n_2	n_3 (n_e)
Mica [typically $(KF)_2(Al_2O_3)_3(SiO_2)_6(H_2O)$]	1.582		1.587	1.552
Lithium borate [LiB_3O_5]	1.578		1.601	1.621
Lithium niobate [$LiNbO_3$]	2.30			2.21
Calcite, or Iceland spar [$CaCO_3$]	1.66			1.49
Potassium di-hydrogen phosphate, KDP [KH_2PO_4]	1.51			1.47
Crystalline quartz [SiO_2]	1.54			1.55
Sapphire [Al_2O_3]	1.768			1.760
Sodium nitrate [$NaNO_3$]	1.59			1.34
Calomel [Hg_2Cl_2]	1.97			2.66
Ice [H_2O]	1.309			1.311

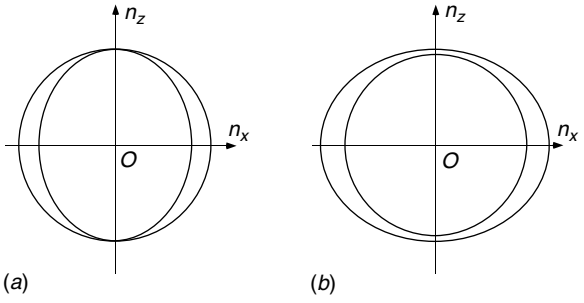

Figure 6.17
Axial sections of the *n*-surface of uniaxial crystals: (*a*) such as calcite, (*b*) such as quartz, which is also optically active.

6.6.1 Propagation in a uniaxial crystal

It follows from the form of the *n*-surface, as the reader will easily verify, that:

1. For a general **k** there is one ordinary and one extraordinary ray;
2. For **k** along the optic axis, there are two degenerate ordinary rays;
3. For **k** normal to the optic axis, two ordinary rays propagate with indices n_o and n_e. The former is polarized along the optic axis (z) and the latter in the orthogonal direction in the (x, y) plane.
4. Conical propagation does not occur.

6.6.2 Optical activity

When a linearly polarized wave enters a quartz crystal along its optic axis, it is found that the plane of polarization rotates at about 22° per mm of propagation.

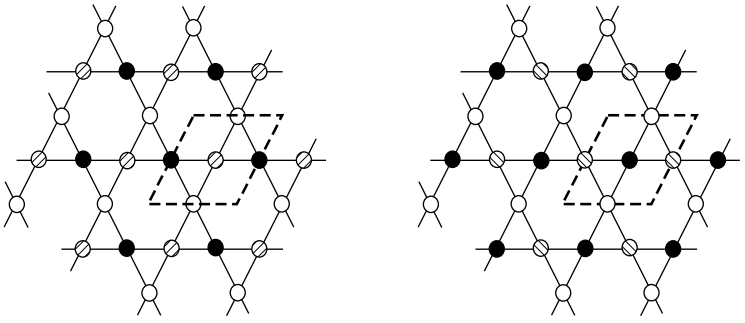

Figure 6.18

Positions of silicon atoms in right- and left-handed quartz, projected on a plane normal to the optic axis. The broken line outlines the unit cell, within which there are atoms at levels of 0, $\frac{1}{3}$ and $\frac{2}{3}$ of the cell height, indicated by open, shaded and filled circles respectively. These form helices of opposite sense in the two diagrams.

Optical activity, in which the plane of polarization rotates with propagation, is the only birefringent property that can be associated with an isotropic medium, such as a liquid.

Quartz is a uniaxial crystal, so this is not consistent with the behaviour that we have described so far. The continuous rotation of the plane of polarization is known as **optical activity** and can occur in any material, crystalline or non-crystalline, having a helical structure – such as quartz which occurs naturally in both right- and left-handed versions (Fig. 6.18). Sugar solutions are the most well-known examples of non-crystalline optically active media; dextrose rotates the polarization in a right-handed sense, whereas laevulose is the opposite.

Phenomenologically the dielectric properties of an optically active uniaxial crystal can be described by a Hermitian dielectric tensor with imaginary off-diagonal components.[7] We write

$$\boldsymbol{\epsilon} = \begin{pmatrix} \epsilon_1 & \mathrm{i}a & 0 \\ -\mathrm{i}a & \epsilon_1 & 0 \\ 0 & 0 & \epsilon_3 \end{pmatrix}. \tag{6.39}$$

This tensor satisfies $\epsilon_{ij} = \epsilon_{ji}^*$, i.e. is Hermitian, and can be diagonalized to give principal values $\epsilon_1 + a, \epsilon_1 - a$ and ϵ_3. The principal polarizations are, respectively, $\mathbf{D}_1 = (1, \mathrm{i}, 0), \mathbf{D}_2 = (1, -\mathrm{i}, 0), \mathbf{D}_3 = (0, 0, 1)$. The first two represent circularly polarized waves propagating along the z-axis, since they show $\pi/2$ phase differences between the oscillations of their x and y components.

When a wave propagates parallel to z in such a medium we can now see why its plane of polarization rotates. A linearly polarized wave can be constructed from the superposition of two circularly polarized waves of opposite senses:

$$\mathbf{D}_\mathrm{r} = D_0(1, \mathrm{i}, 0) \exp[\mathrm{i}(n_\mathrm{r} k_0 z - \omega t)], \tag{6.40}$$

$$\mathbf{D}_\mathrm{l} = D_0(1, -\mathrm{i}, 0) \exp[\mathrm{i}(n_\mathrm{l} k_0 z - \omega t)], \tag{6.41}$$

[7] We shall derive such a tensor for a magneto-optical medium in §13.3.5.

in which the refractive indices n_r and n_l are, respectively, $(\epsilon_1 \pm a)^{\frac{1}{2}}$. Their mean is $\bar{n}$ and difference δn. Combined:

$$\mathbf{D} = \mathbf{D}_r + \mathbf{D}_l = 2D_0 \left(\hat{\mathbf{x}} \cos \frac{1}{2}\delta n\, k_0 z + \hat{\mathbf{y}} \sin \frac{1}{2}\delta n\, k_0 z \right) \exp[\mathrm{i}(\bar{n} k_0 z - \omega t)]. \tag{6.42}$$

The angle of the plane of polarization, $\tan^{-1}(D_x/D_y) = \frac{1}{2}\delta n\, k_0 z$, increases continuously with z. The rate of 22° per mm gives, for green light, $\delta n \approx 7 \times 10^{-5}$. Because this value is so small, quartz behaves as a normal uniaxial crystal for propagation in all directions except very close to the optic axis. Its n-surface is shown schematically in Fig. 6.17(*b*).

Corn syrup is a popular and inexpensive material that shows strong optical activity.

An isotropic optically active material, such as sugar solution, can be described by an n-surface consisting of two concentric spheres, with radii n_r and n_l.

6.7 Interference figures: Picturing the anisotropic properties of a crystal

A useful and beautiful way of characterizing the anisotropic properties of crystals is to observe the interference pattern between the two characteristic waves, presented as a function of the angle of incidence of the light. These patterns, called **interference figures** or **conoscopic figures**, have symmetry related to that of the n-surface, and provide quantitative information about the differences between n_x, n_y and n_z. In white light, the figures are beautifully coloured. To see the interference figure, place a parallel-sided crystal plate between crossed polarizers. If the crystal is large enough, simply look through this sandwich at a distant extended source, so that each point in the image corresponds to parallel light that has crossed the crystal at a different angle. If the sample is small, the same effect can be obtained in a microscope by using the condenser to focus a distant source to a point in the crystal, and then observing the far-field image in the back focal plane of the microscope objective. The two methods are shown in Fig. 6.19. Sometimes a quarter-wave plate is added before the condenser lens.

The basic principle underlying interference figures is that the optical path lengths of the two characteristic waves differ within the crystal plate, and therefore if both are excited together, and both have field components parallel to the analyzer, they will interfere to give an interference pattern. Since the path differences are a function of the direction of propagation, but not of the position in the crystal, a clear interference pattern will be seen in the far field (§9.3.3). The exact details of the patterns are quite complicated, mainly because the two waves in the crystal are refracted to different angles and therefore do not travel

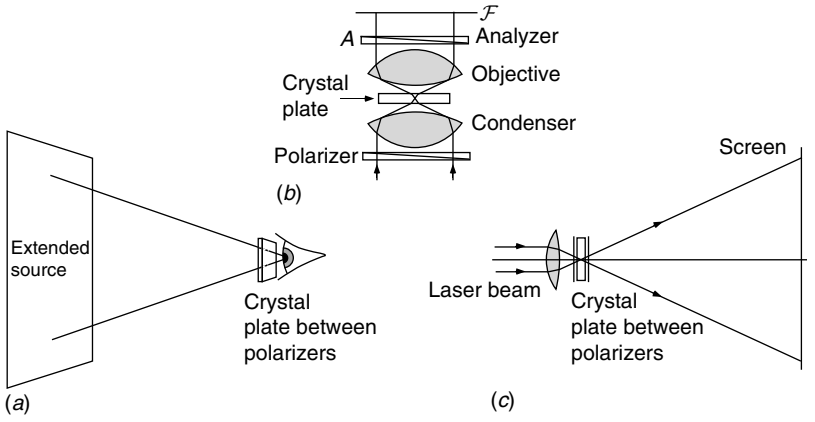

Figure 6.19

Three methods of observing interference figures in crystals. (*a*) A distant extended source is observed through a parallel-sided crystal slab placed between crossed polarizers, so that each point on the source provides illumination in a different direction. (*b*) In a microscope the condenser is used to focus linearly polarized light to a point in the crystal, and the transmitted light is observed through a crossed analyzer in the back focal plane of the objective. (*c*) A laser beam is focused into the crystal sandwiched between polarizers and its projection observed on a screen.

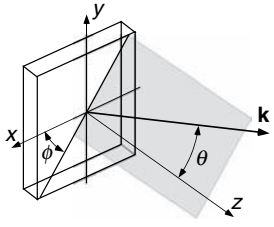

Figure 6.20

Coordinates for describing conoscopic figures.

An interference figure arises because the optical path difference between the characteristic waves is a function of the angle of incidence.

parallel to one another, but a good qualitative understanding can be obtained if this fact is ignored. A full analysis can be found in Born and Wolf (1999) and a practical description in the website of Derochette (2008).

We shall consider the case of a crystal plate with thickness h placed between crossed polarizer and analyzer (Fig. 6.20). In this case, an isotropic material would give a completely black field. The waves travel within the crystal in a direction defined by the polar angle θ, measured with respect to the normal to the crystal plate, and the azimuthal angle ϕ. The ϕ axis is defined such that the polarizer and analyzer transmit waves with electric field along $\phi = 0$ and $\phi = \pi/2$ respectively. Now, as we mentioned before, here we assume that the two characteristic waves travel at the *same* angle θ within the crystal (this corresponds to a different angle θ_{ext} outside the crystal because of Snell's law, but this does not affect the qualitative observations). The two characteristic waves travelling in direction (θ, ϕ) have refractive indices $n_1(\theta, \phi)$ and $n_2(\theta, \phi)$, and polarization vectors at azimuthal angles $\psi(\theta, \phi)$ and $\pi/2 + \psi(\theta, \phi)$. Their optical paths within the crystal are therefore $hn_1 \cos\theta$ and $hn_2 \cos\theta$ and their amplitudes within the crystal are proportional to $\cos\psi$ and $\sin\psi$ respectively. When they interfere at the crossed analyzer, their amplitudes are multiplied respectively by $\sin\psi$ and $-\cos\psi$, giving interference fringes with intensity profile

$$I(\theta, \phi) = I_0 \cos^2\psi \, \sin^2\psi \, \sin^2[(n_1 - n_2)hk_0 \cos\theta]. \tag{6.43}$$

Since we are looking in the far field, the observation shows this light intensity as a function of θ_{ext}.

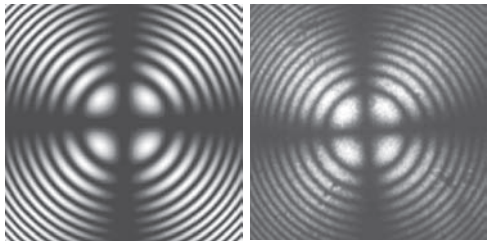

Figure 6.21
Interference figure of a uniaxial crystal: (*a*) theoretical result (6.44); (*b*) observed figure in a crystal of lithium niobate ($LiNbO_3$) at $\lambda = 632$ nm.

6.7.1 Interference figures in uniaxial crystals

In a uniaxial crystal (§6.6) the n-surface has a spherical branch with radius n_o and a spheroidal branch with polar radius n_o and equatorial radius n_e, so that $n_1 = n_o$ and $n_2 = n_o + (n_e - n_o)\sin^2\theta$, when $\theta = 0$ is the optic axis. The polarization vectors of the characteristic waves are respectively tangential and radial. It follows simply that for a crystal plate with faces normal to the optic axis, the interference figure is given by

$$I(\theta, \phi) = I_0 \cos^2\phi \, \sin^2\phi \, \cos^2[hk_0(n_e - n_o)\sin^2\theta \cos\theta]. \qquad (6.44)$$

This picture is shown in Fig. 6.21, and can be seen to have circular fringes of gradually increasing density, crossed by dark radial fringes at $\phi = 0$ and $\pi/2$. Putting (6.44) equal to zero, the azimuthal fringe zeros are at angles $hk_0(n_e - n_o)\sin^2\theta\cos\theta = m\pi$ or for small θ, $\theta^2 \approx m\lambda/2h(n_e - n_o)$. This implies quadratically spaced fringes – essentially Newton's rings between the spherical and spheroidal branches of the n-surface. When the optic axis lies in the plane of the plate, a different interference figure is observed. This can be understood by the same method, and is left as an exercise for the reader (Problem 6.11).

6.7.2 Interference figure of a biaxial crystal

When the crystal plate is biaxial, we shall not try to describe the situation analytically since we never gave an analytical form for the n-surface for a biaxial crystal in §6.5.4. A complete analysis has been given by Berry *et al.* (1999). However, the general principles should be clear. We assume that the plate is normal to one of the symmetry axes of the indicatrix, Fig. 6.22(*a*), so that the optic axes are in two centro-symmetrically disposed directions $\pm(\theta_a, \phi_a)$. Around these directions, we saw that $n_1 - n_2$ goes *linearly* through zero because the inner and outer surfaces of the n-surface are conical with apices touching at the optic axes. We therefore expect a black spot (because there is no path difference) along each optic axis, with *equally spaced*, approximately circular

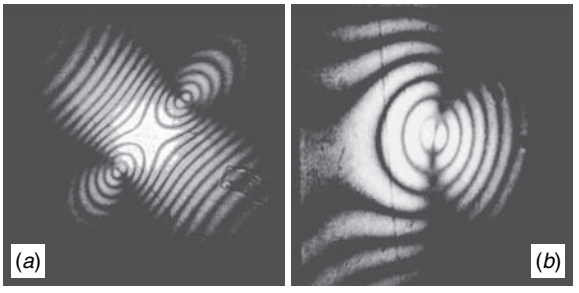

Figure 6.22

Interference figure of a biaxial crystal obtained using a piece of an overhead projector slide sandwiched between crossed polariods. This was done using the method of Fig. 6.19(*c*), since the angle between the *z*-axis and the optic axes is 39°: (*a*) with the *z*-axis at centre of the field of view; (*b*) with the optic axis at the centre.

fringes around it, representing the conical shapes of the touching branches (Fig. 6.22(*b*)). Now if we choose **k** in a starting direction slightly displaced from an optic axis, and from there go in a complete circle of 2π around the axis while observing the angle ψ of the polarization vector of the characteristic waves, we see from Fig. 6.15 ($\mathbf{k}_4$) that ψ changes by only π. Thus in the biaxial case there is only one dark diametric fringe crossing each of the points $\pm(\theta_a, \phi_a)$, not two as in the uniaxial case. In fact the uniaxial case corresponds to a merger of the two optic axes, with the diametric fringes mutually orthogonal.

Next we can look at the centre point $\theta = 0$ on the interference figure. Here the phase difference is $hk_0(n_i - n_j)$, where n_i and n_j are two of the principal refractive indices. This phase difference can be determined absolutely by counting fringes out to one of the optic axes, where it has become zero.

A simple demonstration of the interference figure can easily be made using an extruded plastic film, such as overhead projector film, as a biaxial crystal. The film is sandwiched between crossed polaroid filters and has been called a 'black light sandwich'. The film acts as a biaxial crystal because of the photo-elastic effect (§6.9.2); the thickness dimension has been compressed, one direction has been stretched, and the third one remains unstressed. Since this device can be produced in large sheets, there is no need to observe it under a microscope, and the configuration of Fig. 6.19(*a*) can conveniently be used, but it is difficult to see both optic axes simultaneously because of the large angle between them (Fig. 6.22).

6.8 Applications of propagation in anisotropic media

To follow the propagation of a wave of given **k** and polarization state in an anisotropic medium we first have to express its **D** vector as a superposition of those of the two characteristic waves for the same **k**. We then follow each one according to its refractive index, and recombine the two at a later stage. If there is an interface to another medium, it is necessary to ensure continuity of

the fields, which involves applying Snell's law separately to each characteristic wave (§6.8.2).

6.8.1 Quarter- and half-wave plates

Polarizers used on cameras often have a quarter-wave plate attached to them. Why?

A linearly polarized plane wave is incident normally (z-direction) on a parallel-sided crystal slab of thickness l, such that its plane of polarization bisects those of the two characteristic waves propagating in the same direction; their **D** vectors will define the x- and y-axes. The two characteristic waves have refractive indices n_1 and n_2, whose mean is $\bar{n}$ and difference δn. We have

$$\mathbf{D} = D_0\hat{\mathbf{x}}\exp[\mathrm{i}(n_1k_0z - \omega t)] + D_0\hat{\mathbf{y}}\exp[\mathrm{i}(n_2k_0z - \omega t)], \tag{6.45}$$

which, at $z = 0$, combine to give the incident wave $\mathbf{D} = D_0(1, 1, 0)\exp(-\mathrm{i}\omega t)$. At non-zero z, (6.45) can be written

$$\mathbf{D} = D_0\left[\hat{\mathbf{x}}\exp\left(-\frac{1}{2}\mathrm{i}\delta n\,k_0z\right) + \hat{\mathbf{y}}\exp\left(\frac{1}{2}\mathrm{i}\delta n\,k_0z\right)\right]\exp[\mathrm{i}(\bar{n}k_0z - \omega t)]. \tag{6.46}$$

Some particular cases are of great importance.

1. When $\frac{1}{2}\delta n\,k_0z = \pi/4$ the phase difference between the $\hat{\mathbf{x}}$ and $\hat{\mathbf{y}}$ components has the value $\pi/2$. The incident linearly polarized wave has become circularly polarized. A plate with this thickness, $l = \pi/(2k_0\delta n) = \lambda/(4\delta n)$, is called a **quarter-wave plate**. If the plane of polarization of the incident wave is in the second bisector of $\hat{\mathbf{x}}$ and $\hat{\mathbf{y}}$ the opposite sense of rotation is obtained, and if it does not exactly bisect $\hat{\mathbf{x}}$ and $\hat{\mathbf{y}}$, the outgoing wave is elliptically polarized. In the reverse situation, a quarter-wave plate converts circularly polarized light into linearly polarized. According to the values given in §6.5.5, a quarter-wave plate for $\lambda = 590$ nm made from mica has thickness about 0.025 mm.

2. A plate of the same material with twice the above thickness can easily be seen to reflect the plane of polarization in the (x, z) and (y, z) planes, and therefore also reverses the sense of rotation of an incident circularly or elliptically polarized wave. It is called a **half-wave** plate.

6.8.2 The Pöverlein construction

The n-surface construction lends itself easily to the graphical solution of refraction problems at interfaces between crystals. We should remember that Snell's law, arising as it does from the continuity of E and H at the interface, is *always* true for the **k** vector directions. Now suppose that we consider the refraction of light from, say, a homogeneous material of index n_1 into the crystal. Figure 6.23 shows the section of the n-surface in the plane of incidence, which

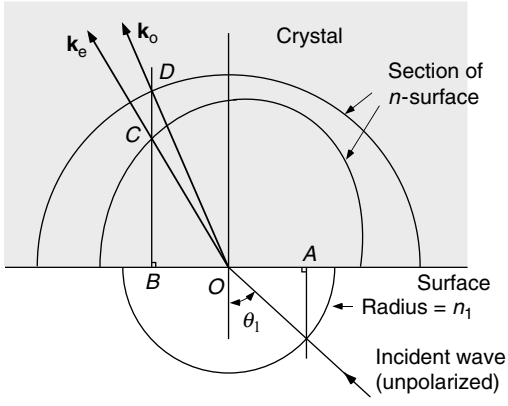

Figure 6.23

Illustrating the Pöverlein construction. *OB* is the projection of both $\mathbf{k}_o$ and $\mathbf{k}_e$ on the interface, and is equal to the projection *OA* of the incident $\mathbf{k}$ vector.

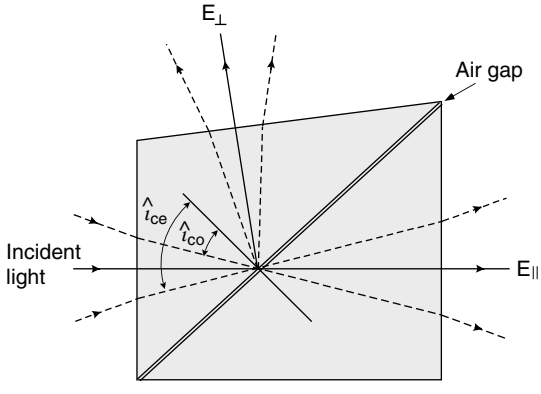

Figure 6.24

Glan air polarizing prism. The chief ray is indicated by a full line, and is normal to the entrance and exit surfaces. The broken lines represent the limits of the angular field for which the polarization is complete. If the air gap is filled with a low-index cement, a more stable structure is obtained, but the angular field is reduced.

contains the $\mathbf{k}$ vectors of the incident and refracted rays as well as the normal to the surface. The construction described by the figure equates the projections $k \sin\theta = k_0 n(\theta) \sin\theta$ (OA for the incident wave and OB for the two refracted waves) on the interface. It is known as **Pöverlein's construction** and can also be used for refraction at an interface between different birefringent materials.

6.8.3 Crystal polarizers

Crystal polarizers separate the two orthogonal polarizations by using the fact that the critical angle is a function of the refractive index and therefore depends on the polarization state. A typical example is the Glan prism which is generally constructed from calcite. The construction is illustrated by Fig. 6.24, the optic axes of both halves of the device being normal to the plane of the diagram. Clearly, when the angle of incidence at the air layer is between the critical angles

$\sin^{-1} n_o$ and $\sin^{-1} n_e$, only the extraordinary polarization is transmitted. The reflected wave is mainly ordinary polarization, but contains some extraordinary. The crystal is cut so that this interface lies half-way between the two critical angles when light is incident normally on the input surface.

If the two halves are cemented with a glue having refractive index n_B between n_o and n_e, variants on this idea – the **Glan–Thompson** and **Nicol prisms** – are obtained. In this case there is a critical angle only for the ordinary wave. The Nicol prism is constructed around natural cleavage angles of the calcite.

6.9 Induced anisotropic behaviour

External fields of many types can create anisotropy in an otherwise isotropic material. Both linear and non-linear effects arise.

The discussion so far has assumed that the anisotropy of a crystal is the result of its structure. There are, however, many instances in which the properties of an isotropic material (such as a liquid, polymer or a cubic crystal) become anisotropic because of some external field; in addition, the optical properties of many anisotropic materials can be changed by applied fields. We shall describe below a few examples of such behaviour, but the description should not be considered in any way as exhaustive. Some other aspects of induced dielectric effects will be discussed in Chapter 13. A much more detailed description will be found in the book by Yariv (1989).

6.9.1 The electro-optic effect

Application of an external electric field can cause induced anisotropy. Two types of effect are common. First, many isotropic materials such as glass, and liquids such as nitrobenzene, become uniaxial with their optic axis along the direction of the electric field. Since there is no way that an isotropic material could be sensitive to the sign of the field, the effect has to be proportional to the square (or a polynomial including only even powers) of the applied field E_0:

$$n_e - n_o \propto E_0^2. \tag{6.47}$$

This is called the **Kerr effect**.

On the other hand, crystals without a centre of symmetry in the atomic arrangement of their unit cell are able to distinguish between positive and negative fields and so the electro-optic effect can depend on any power of the field; in particular, a linear effect is possible. Its magnitude can also be a function of the orientation of the field and so a complete description of the effect, even at a phenomenological level, becomes quite involved. It is usual

to describe the electro-optic effect in terms of parameters that relate directly to the distortion of the indicatrix, (6.32), which is written explicitly:

$$\frac{D_x^2}{n_1^2} + \frac{D_y^2}{n_1^2} + \frac{D_z^2}{n_3^2} = 1. \tag{6.48}$$

We shall consider here only one example, the **Pockels effect** in a uniaxial crystal. In this effect the application of the field E_0 parallel to the optic axis makes equal and opposite linear changes in n_1, the refractive indices for the two polarizations perpendicular to the applied field. It is usual to write the distorted indicatrix in the form

$$D_x^2\left(\frac{1}{n_1^2} + rE_0\right) + D_y^2\left(\frac{1}{n_1^2} - rE_0\right) + \frac{D_z^2}{n_3^2} = 1, \tag{6.49}$$

in which we have assumed that the changes in n are very small. Then the actual changes in the x- and y-axes of the ellipsoid are $\pm\delta n_1 \approx \mp rE_0 n_1^3/2$. Clearly, the crystal is now biaxial. It follows that a wave propagating along z, for example, can become elliptically polarized in the same way as we discussed in §6.8.1 and a slab crystal of thickness l in the z-direction will act as a quarter-wave plate when

$$lE_0 = \lambda/4rn_1^3. \tag{6.50}$$

The product lE_0 is a voltage that is independent of the thickness of the slab and is called the **quarter-wave voltage**, typically 500 V. Both the Kerr effect and the linear electro-optic effects such as the Pockels effect can be used to make an electrically operated optical shutter by placing the sample or crystal between crossed polarizers.

6.9.2 The photo-elastic effect

This effect was first investigated by Maxwell, who used gelatin, and was the subject of his third paper, published when he was 19 years old in 1850.

A strain field can affect the indicatrix of an isotropic medium such as glass, Perspex (lucite or polymethyl-methacrylate) or various epoxy resins. One can imagine the indicatrix being distorted when the medium stretches and this is, qualitatively, the basis of the effect. The material becomes uniaxial with its axis along that of the strain; the birefringence $n_o - n_e$ is then proportional to the difference between the strain components along the axis and normal to it. To observe the effect, it is then necessary to place the sample between crossed polarizer and analyzer, with their axes at 45° to the strain axis. The effect is of considerable importance as a method of visualizing strain fields in complicated two-dimensional bodies, models of which can be constructed from the above materials (Figs. 6.1 and 6.25).

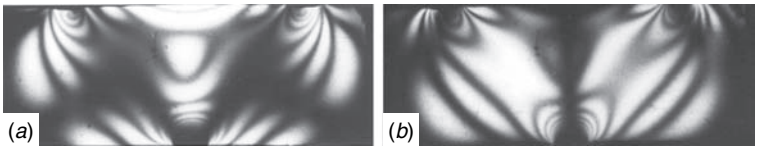

Figure 6.25
An example of the photo-elastic effect. A piece of strained Perspex is observed in monochromatic light between crossed polarizers, oriented (*a*) at ±45° and (*b*) 0° and 90° to the edges of the strip.

6.9.3 The magneto-optic effect

Many isotropic diamagnetic materials, including glass and water, become optically active when a magnetic field is applied to them, the induced optic axis being parallel to the applied field $\mathbf{B}_0$. Then, if a wave propagates with $\mathbf{k} \parallel \mathbf{B}_0$, its plane of polarization rotates, in one sense if $\mathbf{k}$ is in the same direction as $\mathbf{B}_0$, and in the other sense if they are opposite. The effect can be used to measure magnetic fields and visualize field patterns (see Box 6.2).

We describe this in a manner identical to (6.39), in which the parameter a is proportional to B_0, $a = r_\mathrm{B} B_0$. A microscopic model that illustrates this effect for an electron plasma will be described in §13.3.5. It then follows from (6.41) that the two refractive indices, for left- and right-handed polarizations, satisfy $\delta n = n_\mathrm{l} - n_\mathrm{r} = n^3 r_\mathrm{B} B_0$ when $r_\mathrm{B} B_0 \ll n^{-2}$. The angle of rotation of the plane of polarization per unit propagation distance is then $\frac{1}{2} k_0\, \delta n = \frac{1}{2} k_0 n^3 r_\mathrm{B} B_0$. The constant $V = \frac{1}{2} k_0 n^3 r_\mathrm{B}$ is called **Verdet's constant**, and is approximately proportional to λ^{-2}. At $\lambda = 546$ nm, for water, $V = 20\,\mathrm{deg\,T^{-1}\,m^{-1}}$ and for the commonly used magneto-optic indicator europium selenide (EuSe) below the temperature 7 K, $V = 10^8\,\mathrm{deg\,T^{-1}m^{-1}}$.

There is an important difference between optical activity in a crystal and the magneto-optic effect which emphasizes the properties of the magnetic field as a pseudo-vector.[8] If a wave propagates through an *optically active* crystal, is reflected normally by a mirror and then returns through the crystal, the net rotation of the plane of polarization is zero, because the mirror interchanges left- and right-handed circularly polarized components, and so the rotation resulting from the first passage is cancelled in the second. However, if the same experiment is carried out with a *magneto-optic* material, the propagation being parallel to $\mathbf{B}_0$, not only is the handedness of the wave reversed on reflection, but also the sign of the magneto-optic effect, because after the reflection the direction of $\mathbf{k}$ is reversed with respect to $\mathbf{B}_0$. So the net result of the two passages is twice the effect of the single one. A similar analysis of the electro-optic effect vis-á-vis birefringence (which will be left as an exercise to the reader), shows no such distinction. This property of the magneto-optic effect allows us to

[8] A screw remains left- or right-handed from whichever end you look at it. But the helix traced out by an electron in a magnetic field as it comes towards you reverses its helicity if you reverse the field direction.

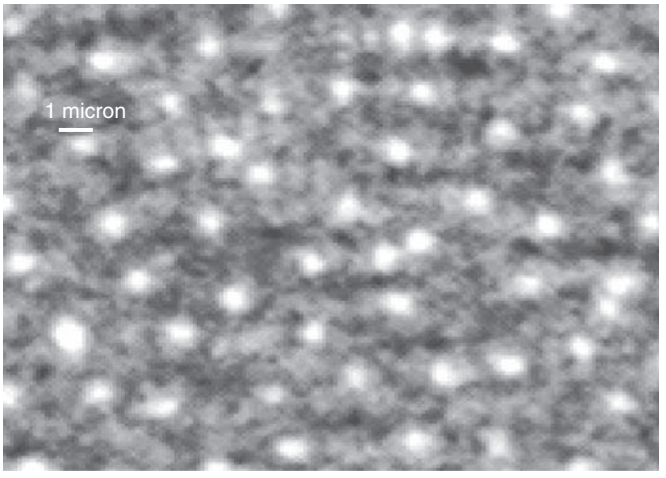

Figure 6.26
Quantized flux vortices in niobium visualized using the magneto-optic effect in europium selenide at 4 K. The average magnetic field applied is only 4×10^{-4} T. (Photograph courtesy of Daniel Golubchik; Golubchik *et al.* (2009))

construct a one-way light valve, or **isolator**. If we have a magneto-optic plate in a field such that the rotation obtained is $\pi/4$, and it is sandwiched between polarizer and analyzer with their axes separated by this angle, a wave in one direction will be transmitted by both polarizers. A wave in the other direction, however, will find itself with polarization exactly orthogonal to the polarizer when it leaves the device, and so is absorbed. This type of device is widely used in microwave equipment.

Box 6.2 An application of the magneto-optic effect: visualizing flux vortices in superconductors

When a magnetic field is applied to a type-II superconductor, it does not penetrate it uniformly, but the field is concentrated into quantized flux vortices, each one having a magnetic flux of $\pm\hbar/2e$, where $\hbar$ is Planck's constant and e is the electron charge. The size of the penetration region, which is a normal conductor, is the superconducting coherence length. It is quite a challenge to visualize these flux vortices, since the value of the magnetic field is only about 10^{-4} tesla. The magneto-optic effect can be used to do this (Fig. 6.26). A film of europium selenide (EuSe) and a reflecting layer of aluminium are deposited on a superconductor, which is then cooled to liquid helium temperature. The reflected light is observed between crossed polarizers in a microscope, and when a small magnetic field is applied, the flux vortices become visible. The field has to be small enough that the distance between them is greater than a few micrometres, otherwise the microscope cannot resolve individual vortices.

6.10 Advanced topic: Hyperbolic propagation in meta-materials

We assumed throughout this chapter that the eigenvalues of the dielectric tensor are positive, and that the axes of the optical indicatrix, which are the square roots of the eigenvalues, are therefore real. Does this have to be so? Do there exist materials whose eigenvalues are negative or complex, which could lead to different types of propagation? The answer is certainly yes. During the years up to about 1960, much work was carried out on propagation of radio waves in a plasma of electrons and ions in a magnetic field, out of which arose the geometrical formalism developed in this chapter. Such waves have been extensively studied in the Earth's ionosphere (Budden (1966)). In Chapter 13, there is a short discussion of the dielectric tensor of such a medium, from which it can easily be seen that in certain frequency regions (determined by the bulk plasma and cyclotron frequencies) the eigenvalues of $\boldsymbol{\epsilon}$ are indeed negative. What this means in terms of propagation is that the refractive index is imaginary for waves with certain propagation directions and polarizations, resulting in evanescent propagation of these waves (§2.3.2).

In recent years, the optics of composite materials has received considerable attention. Such materials are built out of several components with different optical properties. We have already discussed one example of such a 'meta-material' in §5.10.2, where sub-wavelength structures having resonant properties were used to create materials with negative values of both ϵ and μ, leading to real negative refractive index. Another example, which will be discussed in §10.5, is the 'photonic crystal', where the structure of a composite optical material is designed to be periodic, with lattice spacing commensurate with the wavelength. Then, interference between waves internally reflected within the material influences its optical properties strongly. In this section we shall derive some of the properties of a simpler composite system having anisotropic properties, which can lead to negative ϵ for some polarizations.

In §5.6 we discussed the optical properties of metals, and pointed out that several of the noble metals have complex dielectric constants with negative real parts. Silver is a good example because the imaginary part of ϵ is relatively small. It is possible to construct an anisotropic composite material from alternating thin layers of such a metal and a transparent dielectric. Of course, the material is only transparent for short distances because of $\mathrm{Im}(\epsilon)$, but we shall ignore this fact in the following discussion. Using elementary electrostatics we can calculate the effective dielectric constant of such a structure made from two dielectrics with thicknesses $d_{1,2}$ and $\epsilon_{1,2}$. When an electric field is applied parallel to the layers, $E_\parallel$ is conserved at the interfaces and the mean field $\bar{D}$ is the weighted mean of the fields $D = \epsilon E$ in the two types of layer, giving:

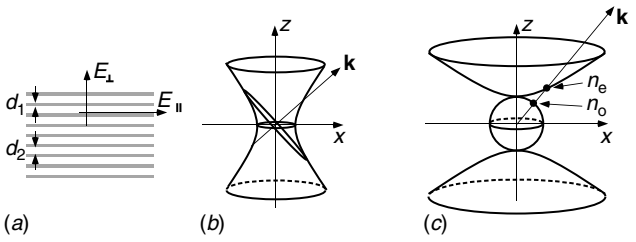

Figure 6.27 An anisotropic material is constructed from alternating layers of silver ($\epsilon < 0$) and aluminium oxide ($\epsilon > 0$). (*a*) Layer structure, where $d \ll \lambda$; (*b*) the indicatrix is a hyperboloid of one sheet, which replaces the index ellipsoid of §6.5.2; (*c*) the refractive-index surface consists of a sphere of radius n_o touching a hyperboloid of two sheets. Along the asymptotic cone, the extraordinary refractive index n_e diverges to ∞.

$$\epsilon_\parallel = \frac{\bar{D}}{\bar{E}} = \frac{d_1\epsilon_1 + d_2\epsilon_2}{d_1 + d_2}. \tag{6.51}$$

On the other hand, when **E** is perpendicular to the layers, $D_\perp$ is conserved at the interface, and the mean field $\bar{E}$ is the weighted mean of the fields $E = D/\epsilon$. Thus

$$\epsilon_\perp = \frac{\bar{D}}{\bar{E}} = \frac{d_1 + d_2}{d_1/\epsilon_1 + d_2/\epsilon_2}. \tag{6.52}$$

Now suppose that the two values of ϵ have opposite signs. Then $\epsilon_1 + \epsilon_2$ will have opposite sign to $\epsilon_1^{-1} + \epsilon_2^{-1}$. In the range of d_1/d_2 between $|\epsilon_1/\epsilon_2|$ and $|\epsilon_2/\epsilon_1|$, we find that $\epsilon_\parallel$ and $\epsilon_\perp$ also have opposite signs.

A material with the above properties, illustrated in Fig. 6.27(*a*), behaves as a uniaxial material because there are two parallel orientations (x and y) and one perpendicular one (z). But now, because of the opposite signs of the principal values of ϵ, the indicatrix becomes a hyperboloid of one sheet instead of the spheroid of §6.6:

$$\frac{D_x^2}{\epsilon_\parallel} + \frac{D_y^2}{\epsilon_\parallel} + \frac{D_z^2}{\epsilon_\perp} = 1. \tag{6.53}$$

This represents a hyperboloid of one sheet if $\epsilon_\parallel > 0$ and $\epsilon_\perp < 0$, and a hyperboloid of two sheets if the signs are reversed.

A practical example uses layers with equal thicknesses of silver ($\epsilon = -2.4 + \mathrm{i}0.25$) and aluminium oxide ($Al_2O_3$) ($\epsilon = +3.2$). Then the real parts of $\epsilon_\parallel = +0.4$ and $\epsilon_\perp = -9.6$, leading to an axially symmetric hyperboloidal indicatrix of one sheet with axes $n_1 = n_2 = 0.63$ and $n_3 = \mathrm{i}3.1$ (Fig. 6.27(*b*)). Following through the procedure to construct the refractive-index surface we find a sphere for the ordinary waves and a hyperboloid of two sheets for the extraordinary waves; the two surfaces touch along the optic axis, which is the z-axis (Fig. 6.27(*c*); compare to Fig. 6.17(*a*)). What is interesting to note is that the extraordinary refractive index diverges along the asymptotic cone of

the hyperboloids, a fact that has been used to achieve extremely high spatial resolution, essentially by using such a material as an immersion lens (§3.8). Such a lens has been called a 'hyperlens' (Jacob *et al.* (2006), Lee *et al.* (2007)).

Chapter summary

In this chapter we studied polarized light, and how its passage through crystals is related to their anisotropic properties. We saw that:

- In an **isotropic** medium, a plane wave can be described as a superposition of two orthogonally polarized characteristic waves, which are degenerate.
- In an **anisotropic** medium, the characteristic waves may not be degenerate and their polarizations and propagation velocities are determined by the parameters of the medium. The characteristic waves may be linearly or circularly polarized.
- The dielectric properties of a crystal can be represented by a dielectric tensor, which is described geometrically by an index ellipsoid (optical indicatrix).
- We can represent the refractive and polarization properties of a medium by a refractive-index surface (n-surface) which is a polar plot of the refractive index n as a function of the wave-vector direction $\hat{\mathbf{k}}$. The surface is double-valued in an anisotropic medium; the polarizations and Poynting vectors of the characteristic waves are then related geometrically to its form.
- Interference figures are an attractive method of visualizing the anisotropic properties of a material.
- Unpolarized light can be polarized by a variety of effects, ranging from Brewster angle reflection to the use of devices constructed from crystals.
- Anisotropic properties can be induced in isotropic materials by means of external fields, the important ones being electric, magnetic and stress fields.
- Artificial anisotropic materials can be constructed using sub-wavelength structures built up from materials with different isotropic dielectric properties, and these can have designed properties that are not found in normal materials.

Problems

6.1. A beam of light is known to be partly unpolarized and partly circularly polarized. How would you find the proportions of each?

6.2. Devise a method to find *absolutely* the sense of rotation of an elliptically polarized wave (i.e. not by comparison with a known material).

6.3. A quartz plate has thickness d and its optic axis makes an angle 45° to its faces. A ray of unpolarized light enters normal to the plate and leaves as two separate polarized rays. Given that $n_o = 1.544$ and $n_e = 1.533$, find the separation between the two exiting rays.

6.4. Mica (biaxial) has refractive indices 1.587 and 1.582 for propagation normal to the cleavage plane, and the third value is 1.552. A sheet of cleaved mica, observed between crossed polarizers, is seen to have a purple colour, i.e. it transmits red and blue light, but not green. Estimate the thickness of the sheet. How does the colour change (*a*) as the mica is turned in its own plane, (*b*) as one of the polarizers is turned in its own plane? What is the angle between the normal to the sheet and the optic axis?

6.5. A parallel beam of sodium light (spectral doublet with $\lambda = 589.3$ nm and 589.6 nm passes through a pair of parallel polarizers separated by a calcite plate whose optic axis lies in the plane of its faces, at 45° to the axes of the polarizers. One line of the doublet is transmitted and one is absorbed. Calculate the thickness of the plate, given that in the above spectral region:
$n_e = 1.486$ and $\mathrm{d}n_e/\mathrm{d}\lambda = -3.53 \times 10^{-5}\mathrm{nm}^{-1}$,
$n_o = 1.658$ and $\mathrm{d}n_o/\mathrm{d}\lambda = -5.88 \times 10^{-5}\mathrm{nm}^{-1}$.

6.6. Design a Glan polarizer, made from two calcite prisms separated by an air gap. Calculate the optimum angles of the two prisms, their crystal orientations with respect to the optic axis, and the angular range over which the transmitted polarization is pure, and the extinction ratio for the reflected wave at the centre of the range. Repeat the design for a cemented prism, using an optical cement with refractive index equal to the smaller of n_e and n_o.

6.7. How is Pöverlein's construction used to describe *reflection* at the plane surface of a crystal? An unpolarized ray enters obliquely into a

parallel-sided crystal plate, whose optic axis is at an arbitrary angle. The ray is reflected to and fro between the surfaces many times. Into how many distinct rays does it separate after N reflections?

6.8. Corn syrup is an excellent example of an isotropic optically active medium. Linearly polarized white light is incident on a sample of length 10 cm, and as the analyzer is rotated a complete spectrum of colours can be observed. Estimate the difference in refractive index $n_l - n_r$, given that the mean value is 1.50.

6.9. A linearly polarized light beam is incident normally on a parallel-sided transparent plate. After transmission, it is reflected back to its starting point by a plane metal-coated mirror. Compare the final state of polarization to the initial state for the following types of plate:
(a) a birefringent plate with its optic axes in arbitrary directions;
(b) a plate showing the Pockels effect, with the applied electric field parallel to the light beam;
(c) an optically active plate, with optic axis parallel to the light beam;
(d) a magneto-optic plate with applied magnetic field parallel to the light beam.

6.10. Consider possible practical ways of creating a completely polarized light beam from an unpolarized source. For example, a polarizing prism is used to create two orthogonally polarized beams, one of which is then rotated in polarization before the two are recombined. Show that the brightness of the output beam can never exceed that of the input (brightness is defined as power per unit area, per unit wavelength interval, per unit solid angle for a given polarization) and therefore the second law of thermodynamics is obeyed.

6.11. What does the interference figure look like for a uniaxial crystal with the optic axis in the plane of the slab?

6.12. A stack of glass plates ($n = 1.5$) is used to polarize incoherent light incident at the Brewster angle. What fraction of the transmitted light is polarized after transmission through a stack of N plates?

6.13. From Fig. 6.22 estimate the three refractive indices of the polymer sheet, given that its thickness is 0.10 mm and mean refractive index 1.49.

6.14. What would the interference figure of a parallel-sided sample of an isotropic optically active material (such as sugar solution) look like?

6.15. In photo-elastic experiments, a quarter-wave plate is often added between the polarizer and the sample. What is its effect on the observations?

6.16. In the photo-elastic effect in an isotropic material the degree of birefringence, $n_o - n_e$, is proportional to the difference between the principal stresses, $p_x - p_y$. Describe the pattern of fringes that is observed in a plastic model of a cantilever beam of uniform cross-section, rigidly supported horizontally at one end, and with a weight at the other. What orientation of polarizers is necessary to make the effect clearest?

6.17. A right-handed circularly polarized wave with wavelength λ is incident in the z-direction on a half-wave plate made from a crystal with principal refractive indices (for x- and y-polarizations) n_1 and n_2.
   (a) What is the thickness of the plate?
   (b) Show that the wave exits the plate with left-handed circular polarization.
   (c) Use the fact that the torque exerted by an electric field **E** on a dipole **p** is $\mathbf{p} \times \mathbf{E}$ to find the torque exerted on the plate as it reverses the circular polarization.
   (d) Show that your result agrees with the quantum interpretation that right- and left-handedly polarized photons have angular momenta of $\pm\hbar$ respectively.

References

Azzam, R. M. A. and Bashara, N. M. (1989), *Ellipsometry and Polarized Light*, 2nd edn., North Holland: Amsterdam.

Berry, M. V., Bhandari, R. and Klein, S. (1999), Black plastic sandwiches demonstrating biaxial optical anisotropy, *Eur. J. Phys*. **20**, 1.

Born, M. and Wolf, E. (1999), *Principles of Optics*, 7th edn., Cambridge: Cambridge University Press.

Budden, K. G. (1966), *Radio Waves in the Ionosphere*, Cambridge: Cambridge University Press.

Derochette, J. M. (2008), http://jm-derochette.be/conoscopy.htm.

Golubchik, D., Polturak, E., Koren, G. and Lipson, S. G. (2009), A high resolution magneto-optical system for imaging of individual magnetic flux quanta, *Optics Express* **17**, 16160.

Jacob, Z., Alexseyev, L. V. and Narimanov, E. (2006), Optical hyperlens: far-field imaging beyond the diffraction limit, *Optics Express* **14**, 8247.

Lee, H., Liu, Z., Xiong, Y., Sun, C. and Zhang, X. (2007), Development of optical hyperlens for imaging below the diffraction limit, *Optics Express* **15**, 15886.

Tompkins, H. A. (2006), *A User's Guide to Ellipsometry*, New York: Dover.

Yariv, A. (1989), *Quantum Electronics*, New York: Wiley.

7 The scalar theory of diffraction

Why did it take so long for the wave theory of light to be accepted, from its instigation by Huygens in about 1660 to the conclusive demonstrations by Young and Fresnel in 1803–12? In retrospect, it may be that Huygens did not take into account the wavelength; as a result the phenomenon of interference, particularly destructive interference, was missing. Only when Huygens' construction was analyzed in quantitative detail by Young and Fresnel did interference fringes and other wavelength-dependent features appear, and when these were confirmed experimentally the wave theory became generally accepted. It was because the wavelength, as measured by Young, was so much smaller than the size of everyday objects that special experiments had to be devised in order to see the effects of the waves; these are called 'diffraction' or 'interference' experiments and will be the subject of this chapter. Even so, some everyday objects, such as the drops of water that condense on a car window or the weave of an umbrella, do have dimensions commensurate with the wavelength of light, and the way they diffract light from a distant street light is clearly visible to the unaided eye (Fig. 7.1).

The distinction between the terms diffraction and interference is somewhat fuzzy. We try to use the term **diffraction** as a general term for all interactions between a wave and an obstacle, with **interference** as the case where several separable waves are superimposed. However, it is not always possible to maintain this distinction; the name 'diffraction grating', for example, is too well entrenched to be changed. But with this terminology, interference becomes a special case of diffraction, in an analogous way to the Fourier series being a special case of the Fourier transform. For this reason we are going to study diffraction first, as the more general situation.

In this chapter we shall learn:

- how we can describe most diffraction problems in terms of a scalar wave theory, and what are the limitations to this theory;
- how we express Huygens' principle for scalar waves;
- about the difference between Fresnel (near-field) and Fraunhofer (far-field) diffraction;
- the experimental conditions needed for Fresnel diffraction;
- about Fresnel diffraction experiments with circular obstacles;

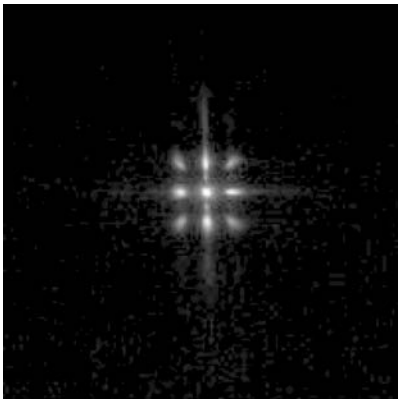

Figure 7.1
Diffraction pattern observed when looking through a silk scarf at a distant street light. The original picture showed the spectrum of the lamp, but this cannot be seen in monochrome rendering. The scarf was draped over the camera lens.

- how a zone plate focuses light;
- about the propagation of Gaussian beams, which will be applied later to laser beams;
- about the Gouy phase shift when a wave goes through a focus;
- how we calculate Fresnel diffraction patterns of slits and edges;
- how zone plates are applied to X-ray microscopy using synchrotron radiation.

7.1 The scalar-wave theory of diffraction

The formulation of a diffraction problem essentially considers an incident free-space wave whose propagation is interrupted by an obstacle or mask which changes the amplitude and/or phase of the wave locally by a well-determined factor. The observer at a given point, or set of points on a screen (the eye's retina, for example), measures a wave-field corresponding to the superposition of the part of the incident field that was not affected by the obstacle and other fields that were generated in order to satisfy Maxwell's equations at points on the obstacle, according to appropriate boundary conditions. An example of a problem that has been solved this way is the diffraction of a plane wave by a perfectly conducting sphere; this is called **Mie scattering** and a detailed account of it is given by Born and Wolf (1999), Bohren (1983) and van de Hulst (1984).

Unfortunately the class of analytically soluble problems of this type is too small for general use and a considerably simpler approach has been developed, based on Huygens' principle (§2.6.1). This approach describes most diffraction phenomena in a satisfactory, if not completely quantitative manner. It makes the basic approximation that **the amplitude and phase of the**

electromagnetic wave can be adequately described by a scalar variable, and that effects arising from the polarization of waves can be neglected. It is called the **scalar-wave approximation**. Below, we shall develop this approach intuitively, giving its mathematical justification in an appendix to this chapter.

7.1.1 Limitations to the scalar-wave approximation

Despite the limitations, scalar-wave diffraction theory is surprisingly accurate even under conditions where you might expect it not to be!

In principle, a scalar-wave calculation should be carried out for each component of the vector wave, but in practice this is rarely necessary. On the other hand, a simple example will illustrate the type of conditions under which the direction of polarization might be important. We consider how we would begin the problem of diffraction by a slit in a perfectly conducting sheet of metal. Considering each point on the plane of the sheet as a potential radiator, we see that:

1. points on the metal sheet will not radiate at all, because the field **E** must be zero in a perfect conductor;
2. points in the slit well away from its edges can radiate equally well in all polarizations;
3. points close to the edge of the slit will radiate better when **E** is perpendicular to the edge of the slit than when **E** is parallel. This occurs because $\mathbf{E}_{\parallel}$ changes smoothly from zero in the metal to a non-zero value in the slit, whereas $\mathbf{E}_{\perp}$ is not continuous and can therefore change abruptly at the edge (§5.4).

The slit thus produces a diffraction pattern appropriate to a rather smaller width when the illumination is polarized parallel to its length. Because such differences are limited to a region within only about one wavelength of the edge of the obstacle, they become most noticeable for objects with much fine detail on the scale of less than a few wavelengths. For example, the efficiency of metal-coated diffraction gratings (§9.2.5) is almost always polarization dependent, and closely spaced wire grids with spacings of the order of 2 μm are efficient polarizers at infra-red wavelengths. The most common polarizers (Polaroid, §6.2.2) use this effect.

Having voiced these reservations, we now invite the reader, for the time being, to forget that light consists of two oscillating vector fields, and imagine the vibration to be that of a single complex scalar variable ψ with angular frequency ω and wave-vector $\mathbf{k}_0$ having magnitude ω/c in its direction of propagation. Because ψ represents a complex scalar field it has both amplitude and phase. The time-dependent wave-factor $\exp(-\mathrm{i}\omega t)$ is of no importance in this chapter, since it is carried through all the calculations unchanged. It will therefore be omitted.

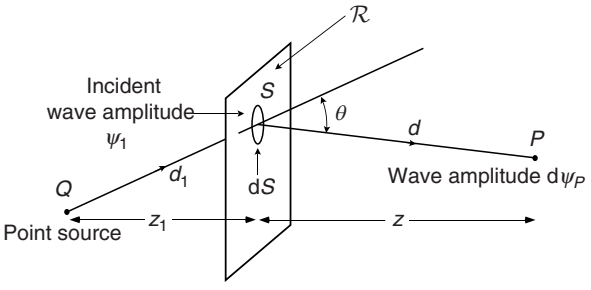

Figure 7.2

Definition of quantities for the diffraction integral. The wave at *P* originates from *Q* and is diffracted by screen $\mathcal{R}$.

7.1.2 Reformulating Huygens' construction

A reminder: Huygens considered each point on a wavefront as a virtual source for a new spherical wave, called a 'wavelet', and the envelope of the wavelets after a given time defined a new wavefront.

Let us try intuitively to build a theory of diffraction based on Huygens' principle of the re-emission of scalar waves by points on a surface spanning the aperture. A more rigorous, but still scalar-wave, derivation of the same theory was derived by Kirchhoff and is given as an appendix to this chapter. But most of the parts of the formulation can be written down intuitively, and we shall first derive it in such a manner.

We shall consider the amplitude observed at a point P arising from light emitted from a point source Q and scattered by a plane mask $\mathcal{R}$ (Fig. 7.2). We shall suppose that if an element of area $\mathrm{d}S$ at S on $\mathcal{R}$ is disturbed by a wave ψ_1 this same point acts as a coherent secondary emitter of strength $bf_S\psi_1\mathrm{d}S$, where f_S is called the **transmission function** of $\mathcal{R}$ at point S. The factor b is the strength with which the reradiation occurs, for unit disturbance, and its value will be derived subsequently. In the simplest examples f_S is zero where the mask is opaque and unity where it is transparent, but it is easy to imagine intermediate cases, including complex values of f_S which change the phase of the incident light by a given amount. The coherence of the re-emission is important; the phase of the emitted wave must be exactly related to that of the initiating disturbance ψ_1, otherwise the diffraction effects will change with time.

From its dimensions, b is an 'inverse scattering length'.

The scalar wave emitted from a point source Q of strength a_Q can be written as a spherical wave of wavenumber $k_0 = 2\pi/\lambda$ (§2.5.3),

$$\psi_1 = \frac{a_Q}{d_1}\exp(\mathrm{i}k_0 d_1), \tag{7.1}$$

and consequently $\mathrm{d}S$ acts as a secondary emitter of strength $ba_S = bf_S\psi_1\,\mathrm{d}S$, so that the contribution to ψ received at P is

$$\begin{aligned}\mathrm{d}\psi_P &= bf_S\psi_1 d^{-1}\exp(\mathrm{i}k_0 d)\,\mathrm{d}S \\ &= bf_S a_Q(dd_1)^{-1}\exp[\mathrm{i}k_0(d+d_1)]\,\mathrm{d}S.\end{aligned} \tag{7.2}$$

By including waves that also go in the reverse direction, Huygens reached an absurd situation where there was no unique solution to a propagation problem. He solved this by assuming the inclination factor in the reverse direction to be zero.

The total amplitude received at P is therefore the integral of this expression over the plane $\mathcal{R}$:

$$\psi_P = ba_Q \int\int_{\mathcal{R}} \frac{f_S}{dd_1} \exp[\mathrm{i}k_0(d + d_1)] \, \mathrm{d}S. \tag{7.3}$$

The quantities f_S, d and d_1 are all functions of the position S. It will be shown in the appendix that the factor b should really contain an inclination factor $g(\theta)$ too; i.e. the strength of a secondary emitter depends on the angle between the directions of the incident and scattered radiation, θ in Fig. 7.2. Huygens intuitively considered this factor to be unity in the forward direction and zero in the reverse, as shown in §2.6.1 and Fig. 7.20, and he was not far wrong! However, we shall ignore this inclination factor for the time being, because we shall be using a paraxial approximation where the angles of scattering are small.

7.1.3 Paraxial approximation for scalar diffraction

Diffraction calculations involve integrating the expression (7.3) (or its more rigorous counterpart (7.73)), under various conditions representing real experiments. We shall consider a classification which will help to make the principles clearer. First let us restrict our attention mainly to a system illuminated by a plane wave. We do this by taking the source Q to a very distant point and making it very bright; we therefore make d_1 and a_Q very large while maintaining their ratio constant:

$$a_Q/d_1 = A. \tag{7.4}$$

Now we shall consider the situation where we let $\mathcal{R}$ coincide with a plane wavefront of the incident wave. The axis of the system is defined as the normal to $\mathcal{R}$ through its origin O. If we denote the position of S by vector $\mathbf{r}$ in the plane of $\mathcal{R}$, f_S is replaced by $f(\mathbf{r})$ and (7.3) becomes

$$\psi = Ab \exp(\mathrm{i}k_0 z_1) \int\int_{\mathcal{R}} \frac{f(\mathbf{r})}{d} \exp(\mathrm{i}k_0 d) \, \mathrm{d}^2\mathbf{r}, \tag{7.5}$$

where z_1 is the normal distance from Q to $\mathcal{R}$. The factor $\exp(\mathrm{i}k_0 z_1)$, being constant over the plane $\mathcal{R}$, will henceforth be absorbed into A. The intensity observed at P is

$$I = |\psi|^2 \equiv \psi\psi^*. \tag{7.6}$$

Diffraction effects can conveniently be classified into **Fresnel**, or **near-field** and **Fraunhofer** or **far-field** types depending on the way in which the phase $k_0 d$ changes as we cross the mask $\mathcal{R}$. This depends on the relative values of the distance d between the point S and the point of observation, the extent of $\mathcal{R}$ for which $f(\mathbf{r})$ is not zero (i.e. the size of the mask's transmitting region) and the

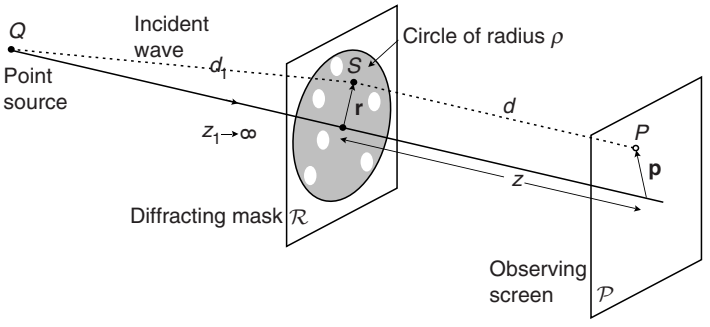

Figure 7.3
Elements of a diffraction calculation in the Fresnel approximation.

wavelength $\lambda = 2\pi/k_0$. If $k_0 d$ is found to vary linearly with $\mathbf{r}$, the diffraction is called **Fraunhofer diffraction**; if the variation has non-linear terms of size greater than about $\pi/2$, the diffraction is called **Fresnel diffraction**. We can translate this statement into quantitative terms if we define a circle of radius ρ which just includes all the transmitting regions of $\mathcal{R}$ (Fig. 7.3). We now observe the diffraction in the plane $\mathcal{P}$ normal to the axis at distance z from the mask. Then at a point P in this plane, at vector distance $\mathbf{p}$ from the axis, the phase $k_0 d$ of the wave from $\mathbf{r}$ is

$$k_0 d = k_0 (z^2 + |\mathbf{r} - \mathbf{p}|^2)^{1/2} \simeq k_0 z + \frac{1}{2} k_0 z^{-1} (r^2 - 2\mathbf{r} \cdot \mathbf{p} + p^2) + \cdots, \qquad (7.7)$$

where we have assumed that r and p are small compared with z. This expression contains:

- the constant term $k_0 \left(z + \frac{1}{2} p^2 / z \right)$,
- the term $k_0 \mathbf{r} \cdot \mathbf{p}/z$ which is linear in r, and
- the quadratic term $\frac{1}{2} k_0 r^2 / z$.

Now since the largest value of r that contributes to the problem is ρ, the maximum size of the quadratic phase term is $\frac{1}{2} k_0 \rho^2 / z$. This means that Fresnel or Fraunhofer conditions are obtained depending on whether $\frac{1}{2} k_0 \rho^2 / z$ is considerably greater or less than about $\pi/2$. In terms of wavelength λ this gives us:

$$\text{Fresnel, or near-field diffraction: } \rho^2 \geq \lambda z; \qquad (7.8)$$

$$\text{Fraunhofer, or far-field diffraction: } \rho^2 \ll \lambda z. \qquad (7.9)$$

This example illustrates where the terms 'near-field' and 'far-field' have their origin.

For example, if a hole of diameter 2 mm is illuminated by light of wavelength 5×10^{-4} mm, Fresnel diffraction patterns will be observed at distances z less than 2 m, and Fraunhofer diffraction at much greater distances. Calculation of the patterns will show that the transition from one type to the other is gradual.

We can remark at this stage that when the mask is illuminated by a point source at a finite distance z_1, as in Fig. 7.3, (7.7) can easily be modified.[1] The phase of the wave at P is then

$$k_0(d_1+d) = k_0\left[\left(z_1^2+r^2\right)^{1/2} + (z^2+|\mathbf{r}-\mathbf{p}|^2)^{1/2}\right]$$
$$\simeq k_0(z+z_1) + \frac{k_0 r^2}{2}\left(z^{-1}+z_1^{-1}\right) + \frac{k_0 p^2}{2z} - \frac{k_0}{z}\mathbf{r}\cdot\mathbf{p} + \cdots. \tag{7.10}$$

An equivalent differentiation between Fresnel and Fraunhofer diffraction classes then arises with z replaced by $1/\left(z^{-1}+z_1^{-1}\right)$ in (7.8) and (7.9):

$$\text{Fresnel diffraction: } \rho^2 \geq \lambda/\left(z^{-1}+z_1^{-1}\right); \tag{7.11}$$

$$\text{Fraunhofer diffraction: } \rho^2 \ll \lambda/\left(z^{-1}+z_1^{-1}\right). \tag{7.12}$$

Replacement of z^{-1} by $z^{-1}+z_1^{-1}$ can be applied to all the results in §7.2.

7.1.4 Experimental observation of diffraction patterns

In Chapter 11, we shall see that astronomers essentially use the quality of diffraction patterns to measure the size of stellar sources.

Using a point source of monochromatic light or a coherent wavefront from a laser, it is easy to observe diffraction patterns of both types. When using a conventional source, such as a discharge or other lamp, it is important to make sure that it is really small enough for the radiated wave to be a true spherical wave. In other words, the spherical waves emitted by various points in the source, assuming it to have finite extent D, must coincide to an accuracy of better than $\frac{1}{4}\lambda$ over the transmitting part of $\mathcal{R}$, which is the circle of radius ρ. The requirement for this is easily seen to be

$$D\rho/z_1 < \frac{1}{4}\lambda. \tag{7.13}$$

As we shall see in Chapter 11, this amounts to saying that the radiated wave is **coherent** across the transmitting part of the mask. For our 2 mm circular hole, at a distance $z_1 = 1$ m the source must have dimensions $D < 0.1$ mm; at a distance of 1 km a 10 cm diameter street lamp will suffice.

To observe Fresnel patterns, it is only necessary to put a screen at the required distance z. Figure 7.4 shows the 'shadow' of a paperclip illuminated by a point source, which is a typical Fresnel diffraction pattern.

[1] When the object is one-dimensional, for example a slit or series of slits, it is possible to replace the point source Q by a line or slit source. Each point of the line source produces a diffraction pattern from the obstacle, and provided these are identical and not displaced laterally they will lie on top of one another and produce an intensified version of the pattern from a point source. This requires the line source and slit obstacle to be accurately parallel, but no new physical ideas are involved.

Figure 7.4

Fresnel diffraction fringes around the shadow of a paperclip.

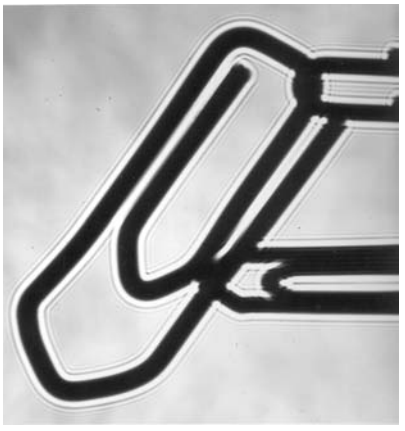

To observe Fraunhofer patterns, we must make the quadratic term in r small enough to satisfy either condition (7.9) or (7.12). One way of doing this is to make both z and z_1 very large; more conveniently we can make $z = -z_1$ by using a lens to put the observing screen in a plane conjugate to the source. For example, we can look directly at the source, so that the retina of the eye is conjugate to the plane of the source, and by inserting the obstacle anywhere along the line of sight (close to the pupil is best) the Fraunhofer pattern can be observed. Defocusing the eye converts the pattern into a Fresnel pattern. For quantitative work one uses a point source with a lens giving a parallel beam, or else an expanded collimated laser beam, either of which is equivalent to infinite z_1. The Fraunhofer pattern is then observed on a screen at a large enough z, or else in the focal plane of a converging lens, which is conjugate to the infinite z. Many of the photographs in this book were taken with an optical diffractometer, Fig. 8.2(b), which is constructed on the above principle.

7.2 Fresnel diffraction

Diffractive optics is a growing field where optical elements are designed using diffraction principles, allowing more flexibility in design than glass optics. However, the wavelength dependence is a problem.

The following sections will be devoted to examples of Fresnel diffraction in a few simple systems. Fraunhofer diffraction and its applications will be discussed separately in Chapters 8 and 9 since they are far more important as analytical tools. But the more general case of Fresnel diffraction has applications in holography (§12.5), in the design of diffractive optics and in imaging at wavelengths where refractive optics is not feasible (§7.5), and historically was of crucial importance in clinching the validity of the wave theory of light (§7.2.4 and §1.1.3).

The basic integral to be evaluated is equation (7.5):

$$\psi = Ab \int\int_{\mathcal{R}} \frac{f(\mathbf{r})}{d} \exp(\mathrm{i}k_0 d)\, \mathrm{d}^2 r. \tag{7.14}$$

For any given situation this integral can obviously be evaluated numerically, but we gain little physical intuition from numerical solutions, so we shall leave them as a last resort, or when accurate values are required. The first class of problems we shall deal with have axial symmetry, and the integral can be performed analytically in several cases. Then we shall discuss the use of amplitude–phase diagrams, which illustrate some of the principles of diffraction rather well in a geometrical manner.

7.2.1 The Fresnel approximation, and evaluation of the Huygens scattering strength

Fresnel, in about 1810, realized that for apertures small compared to the distance z to the screen (radius $\rho \ll z$), d in the exponent of (7.14) can be expanded by the binomial theorem, and terms beyond the quadratic one neglected, as in §7.1.3. The integral can then be written[2]

$$\psi = Ab \iint_{\mathcal{R}} \frac{f(\mathbf{r})}{\sqrt{z^2 + r^2}} \exp\left[\mathrm{i}k_0 \left(z + \frac{r^2}{2z} \right) \right] \mathrm{d}^2 r$$

$$= Ab \exp(\mathrm{i}k_0 z) \iint_{\mathcal{R}} \frac{f(\mathbf{r})}{\sqrt{z^2 + r^2}} \exp\left(\mathrm{i}k_0 \frac{r^2}{2z} \right) \mathrm{d}^2 r. \tag{7.15}$$

This can now be integrated by parts, provided that the aperture $\mathcal{R}$ has axial symmetry, extending out to radius R. Using the variable $s \equiv r^2$, from which $\mathrm{d}^2 r = 2\pi r \, \mathrm{d}r = \pi \, \mathrm{d}s$, we write the factor $h(s) \equiv f(r)/\sqrt{z^2 + r^2}$. Then the integral becomes

$$\psi = Ab \exp(\mathrm{i}k_0 z) \int_{\mathcal{R}} h(s) \exp\left(\mathrm{i}k_0 \frac{s}{2z} \right) \pi \, \mathrm{d}s \tag{7.16}$$

$$= \pi Ab \exp(\mathrm{i}k_0 z) \frac{2z}{\mathrm{i}k_0} \left\{ \left[h(R^2) \exp\left(\mathrm{i}k_0 \frac{R^2}{2z} \right) - h(0) \right] \right.$$

$$\left. - \int_0^{R^2} \frac{\mathrm{d}h}{\mathrm{d}s} \exp\left(\mathrm{i}k_0 \frac{s}{2z} \right) \mathrm{d}s \right\}. \tag{7.17}$$

In order to evaluate b, we consider the case of a very large aperture where $f(r) = 1$, which negligibly affects the propagation of the incident plane wave.

[2] The inclination factor $g(\theta)$ could be included here, since θ can be expressed in terms of $\mathbf{r}$ and z, but since it has a value of 1, according to Huygens, or between 1 and $\frac{1}{2}$ according to Kirchhoff (Appendix), we do not include it here, as it makes no important difference to the results.

We determine the inverse scattering length b by observing that a very large aperture negligibly affects near-field wave propagation on its axis.

We can then make two reasonable assumptions: first that R is large enough for $h(R^2)$ to be neglected with respect to $h(0)$, and then that the integral on the second line of (7.17) is negligible, because the integrand is a small function $\mathrm{d}h/\mathrm{d}s \sim z^{-3}$ multiplied by a rapidly oscillating one. The integral (7.17) then simplifies to

$$\begin{aligned}\psi &= -\exp(\mathrm{i}k_0 z)\frac{2\pi A b z}{\mathrm{i}k_0}h(0)\\ &= -Ab\exp(\mathrm{i}k_0 z)\frac{2\pi}{\mathrm{i}k_0},\end{aligned} \tag{7.18}$$

Since $h(0) = f(0)/z = 1/z$. But on making the aperture large enough for its effects to be negligible, the result must be identical to that which we would have obtained without an aperture at all, namely $A\exp(\mathrm{i}k_0 z)$, from which it follows that

$$b = \frac{-\mathrm{i}k_0}{2\pi} = \frac{-\mathrm{i}}{\lambda}. \tag{7.19}$$

This result is also derived rigorously in the appendix.

7.2.2 Fresnel diffraction by apertures with axial symmetry

In systems with axial symmetry, the value of ψ on the axis $p = 0$ can be evaluated by direct integration of (7.15), giving

A concept called 'Fresnel zones' allowed off-axis diffraction patterns to be qualitatively appreciated, but is hardly necessary today because the integrals can be calculated numerically.

$$\psi = \frac{\mathrm{i}k_0 A}{2z}\int_0^\infty f(s)\exp\left(\frac{\mathrm{i}k_0 s}{2z}\right)\mathrm{d}s. \tag{7.20}$$

The integral is clearly of Fourier transform type, although the limits of integration are from zero (not $-\infty$) to ∞, which can be shown to make negligible difference in many physical situations. For off-axis points, $p \neq 0$, the integrals usually have to be calculated numerically, but one important exception is discussed in §7.3.

We shall consider four important examples:

1. a circular hole of radius $R \ll 2z/k_0$, for which $f(s) = 1$ when $s < R^2$, otherwise 0;
2. a circular disc of radius R, for which $f(s) = 1$ when $s > R^2$, otherwise 0;
3. a zone plate, for which $f(s)$ is periodic, and which acts like a lens;
4. a beam with Gaussian amplitude profile, $f(s) \sim \exp(-\alpha s)$, where α can be either real or complex. In the latter case, the imaginary part of α indicates that the wavefront not only has a Gaussian profile, but is also converging or diverging, depending on its sign.

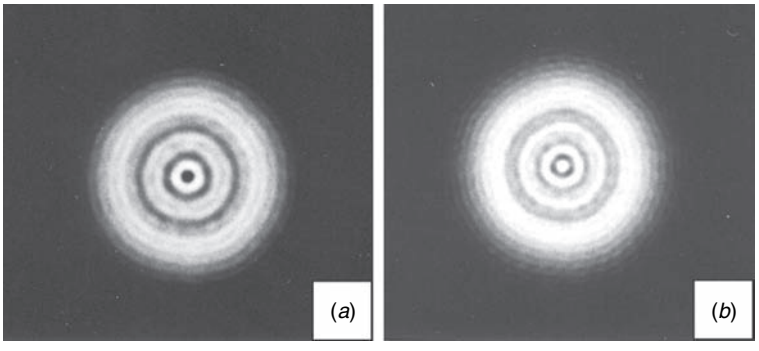

Figure 7.5
Fresnel diffraction patterns of a circular hole: (*a*) when $kR^2/2z = 2n\pi$ and (*b*) when $kR^2/2z = (2n+1)\pi$.

7.2.3 The circular hole

The integral becomes, under the conditions (1) above,

$$\psi = \frac{\mathrm{i}k_0 A}{2z}\int_0^{R^2} \exp\left(\frac{\mathrm{i}k_0 s}{2z}\right) \mathrm{d}s \tag{7.21}$$

$$= A\left[\exp(\mathrm{i}k_0 R^2/2z) - 1\right]. \tag{7.22}$$

The observed intensity is

$$|\psi|^2 = 2A^2\left[1 - \cos(k_0 R^2/2z)\right]. \tag{7.23}$$

As the point of observation moves along the axis, the intensity at the centre of the pattern alternates periodically with z^{-1} between zero and four times the incident intensity A^2 (Fig. 7.5).

7.2.4 The circular disc

For case (2) we have to evaluate the integral (7.17) from a lower limit $s = R^2$ out to a large value. Following through the integration by parts, we obtain

$$\psi = Az\exp(\mathrm{i}k_0 z)h(R)$$

$$= A\exp(\mathrm{i}k_0 z)\frac{z}{\sqrt{z^2+R^2}}. \tag{7.24}$$

Thus the intensity on the axis, when $R \ll z$, is

$$|\psi|^2 \approx A^2 \tag{7.25}$$

for all values of z. This surprising result, that there is *always* a bright spot at the centre of the diffraction pattern of a disc (Fig. 1.3), finally converted the opponents to the wave theory of light when it was experimentally verified by Fresnel and Arago (§1.1.3). Fresnel diffraction has thus been of vital importance to the development of optics.

Repeating the Fresnel–Arago experiment today using a laser source is very easy (Appendix B), but of course lasers were not available in 1818!

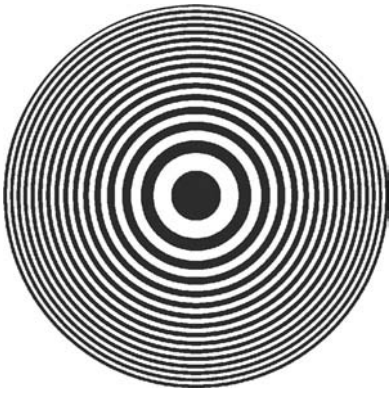

Figure 7.6
Zone plate with square-wave profile $\frac{1}{2}[1 - \cos(\pi r^2/R_0^2)]$ rounded to 0 or 1, as shown in Fig. 7.7.

7.2.5 The zone plate

A zone plate is a series of transparent and opaque rings (Fig. 7.6) whose radii are calculated so that on the axis, at a certain distance, the transmitted waves all have the same phase. For a long time, the zone plate was little more than an amusing physical toy to illustrate Fresnel diffraction. In recent years, its significance has been enhanced as providing a simple model for understanding holograms (§12.5) and it has found applications in X-ray microscopy (§7.5) and in the emerging technology of **diffractive optics**. A zone plate can be made by photo-lithography of an absorbing film by photo-reducing a drawing like that shown in Fig. 7.6, which is calculated so as to make $g(s)$ a periodic function of s with period $2R_0^2$ (Fig. 7.7). The simplest form would have an all-positive sinusoidal profile

$$g(s) = \frac{1}{2}\left[1 + \cos\left(\frac{\pi s}{R_0^2}\right)\right], \tag{7.26}$$

but this is not usually very practical because photo-lithography of absorbing films is not a linear process and only values of $g(s) = 0$ or 1 can be produced accurately. We therefore consider the square-wave profile

$$\begin{aligned} g(s) &= 1 \quad \text{for} \quad 2nR_0^2 < s < (2n+1)R_0^2, \\ g(s) &= 0 \quad \text{for} \quad (2n+1)R_0^2 < s < (2n+2)R_0^2. \end{aligned} \tag{7.27}$$

The Fourier series for this function (§4.2.1) has δ-function-like orders with amplitudes $G_m = (-1)^{(m-1)/2}2/m\pi$ at $m = 0$ and odd values of m. Therefore, from (7.20), the zone plate concentrates an incident plane wave to a series of foci at axial positions given by $k_0/2z = m\pi/R_0^2$ for these values of m, i.e. at

$$z_m = k_0 R_0^2/2m\pi = R_0^2/m\lambda. \tag{7.28}$$

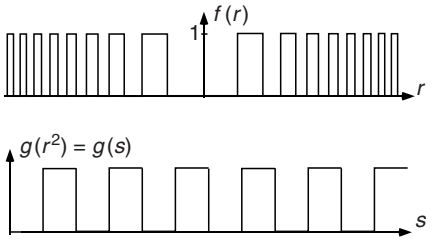

Figure 7.7
Functions $f(r)$ and $g(s)$ (where $s = r^2$) for a zone plate.

The order m has amplitude $ik_0 G_m/2z_m$. Since both z_m and G_m are proportional to $1/m$, all the foci with odd m have equal amplitudes. This is a mathematical quirk that is true for the symmetrical square wave only, but means that in general the higher order foci cannot be neglected (see §7.5). The wave corresponding to $m = 0$ focuses at infinite z, and is a continuation of the incident plane wave. The other foci are at both positive and negative distances, corresponding to both converging and diverging lenses, and in practical applications the unwanted orders have to be blocked. As will be seen in §9.2.4, the first-order focus cannot contain more than 10% of the incident power; this is called the **diffraction efficiency**.

The field of diffractive optics is based on the fact that a zone plate behaves as a lens, but it is easy to introduce corrections for aberrations. Their chromatic aberration has the opposite sign to that of glass lenses. Several camera lens companies now manufacture lenses combining both diffractive and refractive elements.

The zone plate behaves in a similar way to a lens. If we concentrate on one particular focus, $m = +1$ say, we can see from §7.1.3 that if illumination is provided by a point source at distance z_1 (Fig. 7.2) the position of the image moves out to satisfy

$$\frac{1}{z_1} + \frac{1}{z} = \frac{\lambda}{R_0^2}, \tag{7.29}$$

which makes the zone plate equivalent to a lens with focal length R_0^2/λ. It clearly suffers from serious chromatic aberration (see Problem 7.4). Such 'lenses' are now used for X-ray microscopy (§7.5) and as the basis of diffractive optical systems.

In diffractive optical systems, zone-plate lenses are used to replace refractive lenses. It is then important to improve the efficiency by creating only a single focus. This requires a phase mask, of the form $g(s) = \exp\left(i\pi s/R_0^2\right)$, whose Fourier transform is a single δ-function, and must be manufactured by photolithography in a transparent material (Problem 7.6). This is the equivalent of a blazed grating, to be discussed in §9.2.5.

7.3 Propagation of a Gaussian light beam

One of the few Fresnel diffraction problems that can be solved analytically at all points (x, y, z), not just on the axis, starts with a wavefront that has an axially symmetric Gaussian profile (see also Problem 7.13). The reason that

Propagation of Gaussian beams is very important in laser physics. It is usually treated by solution of the Helmholtz equation (7.60).

this is analytically soluble is that the Fresnel propagator $\exp[ik_0(\mathbf{r}-\mathbf{p})^2/2z]$ is also Gaussian, albeit with an imaginary variance iz/k_0. This problem is very important because it demonstrates clearly how a light beam propagates; it is particularly relevant to laser beams, which do in fact usually have a Gaussian profile (§9.5.4). We shall use it here to model such a beam as it propagates through a focal point. The topic of Gaussian beam propagation is dealt with thoroughly in detail in texts on laser physics and photonics, such as Siegman (1986) and Saleh and Teich (1991).

First, consider the way in which a light wave having a converging spherical wavefront with radius of curvature R focuses to a point at $z = R$. Within the Fresnel (paraxial) approximation, we write the wave amplitude in the plane $z = 0$ as

$$\psi(x, y, 0) = \exp(-ik_0 r^2/2R). \tag{7.30}$$

Now, from (7.5), we express the amplitude at the point (x_0, y_0, z) as

$$\psi(x_0, y_0, z) = \exp(ik_0 z)\frac{ik_0}{2\pi z}\int\int_0^\infty \exp(-ik_0 r^2/2R)\exp\left(\frac{ik_0(\mathbf{r}-\mathbf{r_0})^2}{2z}\right)\mathrm{d}^2 r. \tag{7.31}$$

This integral can be evaluated easily once one realizes that it is a convolution between two Gaussian functions with complex arguments. Actually they are imaginary arguments here, but shortly we shall require them to be complex. Thus we write (7.31) as

$$\begin{aligned}\psi(x_0, y_0, z) &= \exp(ik_0 z)\frac{ik_0}{2\pi z}\left\{\exp(-ik_0 r^2/2R) \otimes \exp(ik_0 r^2/2z)\right\} \\ &\equiv \exp(ik_0 z)\frac{ik_0}{2\pi z} q(r).\end{aligned} \tag{7.32}$$

The convolution $q(r)$ can easily be evaluated by taking the Fourier transform $Q(k)$ of $q(r)$, which is the product of two Gaussians, equal to a single Gaussian, and transforming $Q(k)$ back into r space. It is necessary to keep track of the prefactors in the transformations, including a factor $4\pi^2$ which enters from the two-dimensional Fourier inversion theorem (the square of the 2π prefactor in (4.70)), after which we find

$$\psi(x_0, y_0, z) = \exp(ik_0 z)\frac{R}{z-R}\exp\left[\frac{ik_0\left(x_0^2+y_0^2\right)}{2(z-R)}\right]. \tag{7.33}$$

As you might expect, its value diverges to infinity at the focal point $z = R$, where the phase is indeterminate. The intensity falls as $(z-R)^{-2}$: the inverse square law. Notice also that the sign of ψ changes as we go through the focus, indicating a phase jump of π, known as the **Gouy phase shift**. We shall study this phase shift in more detail later. The wavefront structure is illustrated in Fig. 7.8.

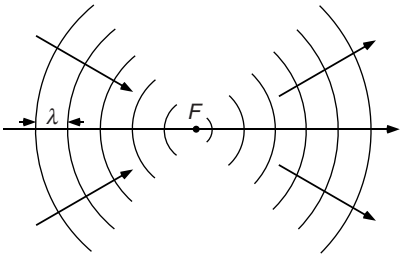

Figure 7.8
Wavefronts of a spherical wave converging to a focus and then diverging from it. Notice the phase shift of π as the wave goes through the focus.

The calculation above is unphysical, since we assumed that the input wave amplitude is constant out to infinity, while still using the paraxial approximation. Now we shall put this right by replacing the incident wave curvature $1/R$ by a complex value which will ensure that the wave energy is limited to a small region near the axis. Specifically, we write

$$\frac{1}{R} = \frac{1}{R_0} + \frac{1}{\mathrm{i}k_0\sigma^2}, \tag{7.34}$$

which means that the wavefront has radius of curvature R_0 and has a Gaussian parameter σ (as in §4.4.3). Then, in the plane $z = 0$ we have

$$\psi(x, y, 0) = \exp(-r^2/2\sigma^2)\exp(-\mathrm{i}k_0 r^2/2R_0), \tag{7.35}$$

$$|\psi| = \exp(-r^2/2\sigma^2). \tag{7.36}$$

The paraxial conditions will be fulfilled if $\lambda \ll \sigma \ll R_0$. Now, for the complex curvature R from (7.34), we substitute in (7.33),

$$\frac{1}{z - R} = \frac{R_0^2 + k_0^2\sigma^4}{z\left(R_0^2 + k_0^2\sigma^4\right) - R_0 k_0^2\sigma^4 - \mathrm{i}R_0^2 k_0\sigma^2}. \tag{7.37}$$

This rather formidable-looking expression has the structure $A/[B(z) + \mathrm{i}C]$ which has maximum value when $B(z) = 0$, i.e. at the position $z = z_\mathrm{w}$ where

$$z_\mathrm{w} = \frac{R_0 k_0^2\sigma^4}{R_0^2 + k_0^2\sigma^4}. \tag{7.38}$$

At this position, the wave amplitude is

$$\psi(x_0, y_0, z_\mathrm{w}) = \exp(\mathrm{i}k_0 z_\mathrm{w})\frac{R}{z - R}\exp\left[\frac{-\left(x_0^2 + y_0^2\right)}{2w^2}\right], \tag{7.39}$$

where the **waist radius** w is defined by

$$w^2 = \frac{R_0^2\sigma^2}{R_0^2 + k_0^2\sigma^4}. \tag{7.40}$$

When $z = z_\mathrm{w}$ the light beam is narrowest (hence the term 'waist') and most intense. It is closer than the focal point $z = R_0$ although it does approach the focus as σ increases. On the other hand, as $\sigma \to 0$, the waist approaches the

The 'intensity transport equation' relates the rate of change of intensity along the axis to the curvature of the wavefront (Problem 2.8). Then, if the intensity has a maximum, the wavefronts must have zero curvature, i.e. be planar.

input plane $z = 0$. Another important observation is that in the plane of the waist the wavefront is planar. This is clear because in the exponent in (7.39) the multiplier of $x_0^2 + y_0^2$ is real. Evaluating (7.33) at all points shows that the wavefronts, while initially concentric around the focal point, become flatter as the wave approaches the waist. This means that the wavefronts cannot be separated by equal distances λ (only concentric spheres or coaxial cylinders could satisfy this requirement), and therefore there has to be a more extended phase anomaly of the Gouy type in that region. Figure 7.9(a) shows the way in which the Gaussian beam becomes confined as it goes through the waist, and the corresponding form of the wavefronts.

Now let us look at the prefactor to the exponent in (7.33) with the complex curvature:

$$\frac{R}{z-R} = \left[\frac{z}{R} - 1\right]^{-1} = \left[\frac{z}{R_0} - 1 + \frac{\mathrm{i}k_0 z}{\sigma^2}\right]^{-1}, \tag{7.41}$$

$$= -1 + \frac{\mathrm{i}k_0\sigma^2}{R_0} \tag{7.42}$$

on inserting the value for z_w from (7.38). On integrating (7.39) the total intensity of the beam is then found to be $2\pi\sigma^2$, confirming that energy is indeed conserved.

We can compare w with the radius of the spot in the focal plane $z = R_0$ by direct substitution in (7.39). Then

$$\psi(x_0, y_0, R_0) = \exp(\mathrm{i}k_0 R_0)\frac{\mathrm{i}k_0\sigma^2}{R_0}\exp\left[\frac{-k_0^2\left(x_0^2+y_0^2\right)\sigma^2}{2R_0^2} + \frac{\mathrm{i}k_0^2\left(x_0^2+y_0^2\right)}{2R_0}\right]. \tag{7.43}$$

The amplitude in this plane has the Gaussian form $\exp\left(-r_0^2/2s^2\right)$, where $s = R_0/k_0\sigma$; anticipating Chapter 8, this is the Fraunhofer diffraction pattern of a Gaussian mask. The position of the waist can be found by a simple geometrical construction using the Gaussian parameters σ and s, as shown in Fig. 7.9(c). The size of the waist can be written simply in terms of σ and s from (7.40):

$$w^{-2} = \sigma^{-2} + s^{-2}, \tag{7.44}$$

which shows again that w is smaller than both σ and s, and that a broader beam, with larger σ, creates a more tightly focused waist (§4.4.3).

The Gouy phase shift has been employed in optical interferometers to obtain an achromatic phase shift, independent of the wavelength.

Now we shall look in more detail at the way in which the intensity and phase of the Gaussian beam change as we go through the waist. Once again substituting (7.34) into (7.33), this time at axial points $(0, 0, z)$ we have

$$\psi(0, 0, z) = \frac{1}{(z/R_0 - 1) - \mathrm{i}z/k_0\sigma^2}\exp(\mathrm{i}k_0 z). \tag{7.45}$$

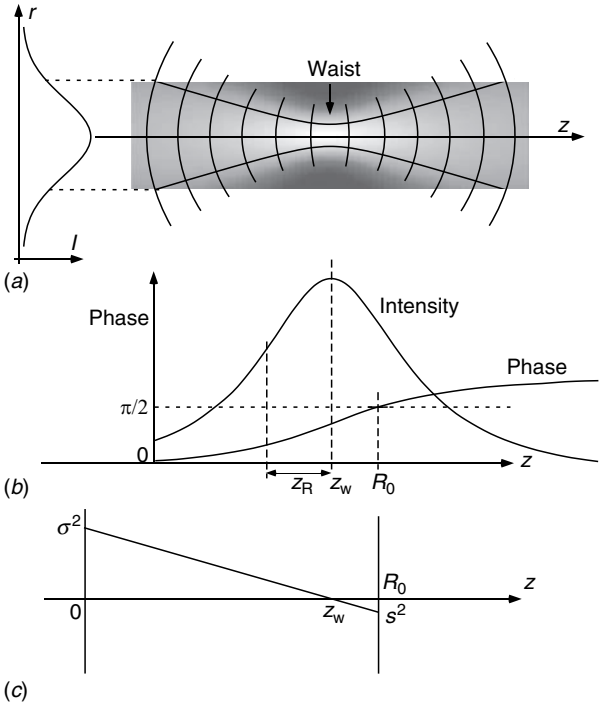

Figure 7.9

(*a*) Wavefronts of a Gaussian wave converging to a focus and then diverging from it. The shape of the 'waist' structure is shown by drawing the locus of the 1/e points of the Gaussian in each plane. (*b*) Intensity of the wave along the axis, showing the peak at the waist, and its phase relative to a propagating plane wave of the same frequency. The phase graph shows the Gouy phase shift in the waist region, where its gradient is maximum. (*c*) A simple construction to find the position of the waist, as a function of the Gaussian parameters σ in the incident plane $z = 0$ and s in the focal plane $z = R_0$.

This has intensity profile along the axis

$$I(z) = \left[\left(\frac{z}{R_0} - 1\right)^2 + \frac{z^2}{k_0^2\sigma^4}\right]^{-1}. \tag{7.46}$$

This is a bell-shaped curve whose maximum is at $z = z_w$ and whose height falls to half of the peak at $z_w \pm z_R$ where $z_R \approx z_w^2/k_0\sigma^2 = k_0 w^2$. This distance is called the **Rayleigh length**. The **depth of focus**, which is the distance between the two axial positions at which the focal spot has blurred to twice the area it had at the waist, equals $2z_R$.

The phase of the wave now changes through the waist in a continuous manner. Relative to the continuous plane wave $\exp(ik_0 z)$, the phase of (7.45) is

$$\phi(z) = \arctan\left[\frac{zR_0}{k_0\sigma^2(z - R_0)}\right]. \tag{7.47}$$

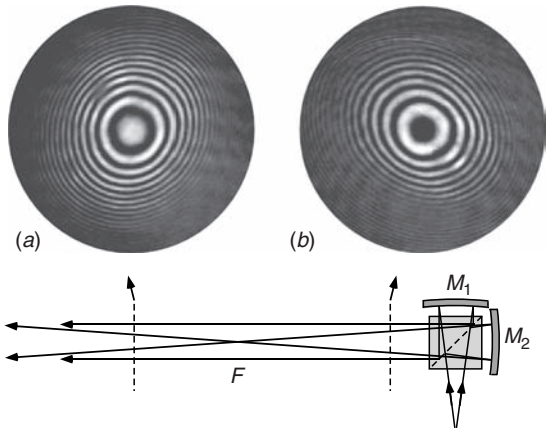

Figure 7.10
The Gouy effect. The photographs show interference patterns between a plane wave and a focused spherical wave with Gaussian profile (*a*) after the focus, *F*, and (*b*) before it. The experimental set-up is sketched below; the mirrors M_1 and M_2 have different focal lengths. The phase change of π in the relative phase is clear, since the central fringe is bright in (*a*) and dark in (*b*).

This goes from zero to π in a continuous manner, having maximum gradient at the waist and value $\pi/2$ at the focus. It is called the **Gouy phase**. The intensity and phase changes along the axis are shown in Fig. 7.9(*b*), and the Gouy phase change is illustrated by an interference experiment in Fig. 7.10.

7.4 Fresnel diffraction by linear systems

There is no simple analytical method to evaluate the Fresnel integral (7.15) for systems without circular symmetry, and either numerical or graphical methods must be used. The latter give us some physical insight into the rather beautiful forms of Fresnel diffraction patterns. In Cartesian coordinates, (7.15) becomes

$$\psi = \frac{\mathrm{i}k_0 A}{2\pi z}\int\!\!\int_{\mathcal{R}} f(x,y)\exp\left[\frac{\mathrm{i}k_0}{2z}(x^2+y^2)\right]\mathrm{d}x\,\mathrm{d}y. \tag{7.48}$$

As an example of the use of graphical methods, we shall briefly consider systems in which $f(x,y)$ can be expressed as the product of two functions, $f(x,y) = g(x)h(y)$, so that (7.48) becomes

$$\psi = \frac{\mathrm{i}k_0 A}{2\pi z}\int_{-\infty}^{\infty} g(x)\exp\left(\frac{\mathrm{i}k_0}{2z}x^2\right)\mathrm{d}x\int_{-\infty}^{\infty} h(y)\exp\left(\frac{\mathrm{i}k_0}{2z}y^2\right)\mathrm{d}y. \tag{7.49}$$

Amplitude–phase diagrams have also been widely used for solving diffraction problems that do have analytical solutions, because they give a lot of qualitative insight into the origins of features of a diffraction pattern.

The two integrals can then be evaluated independently.

7.4.1 Graphical integration by amplitude–phase diagrams

Integrals of the type

$$\psi = \int_{x_1}^{x_2} f(x)\exp[\mathrm{i}\phi(x)]\,\mathrm{d}x \tag{7.50}$$

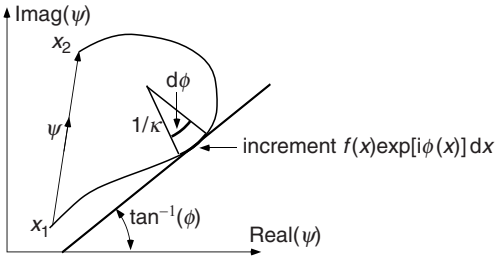

Figure 7.11
Complex plane diagram of the integral $\psi = \int_{x_1}^{x_2} f(x)\exp[\mathrm{i}\phi(x)]\,\mathrm{d}x$.

can be evaluated by representing the real and imaginary parts of ψ as coordinates in the complex plane. We represent each infinitesimal increment of ψ

$$\mathrm{d}\psi = f(x)\exp[\mathrm{i}\phi(x)]\,\mathrm{d}x \tag{7.51}$$

by a vector of length $f(x)\,\mathrm{d}x$ at angle $\phi(x)$ to the real axis. The value of ψ is then the vector sum of the increments, which is the vector joining the x_1 and x_2 ends of the curve formed by all the increments head-to-tail. This is called an **amplitude–phase diagram**, and the physics emerges from the geometry of the resulting curve which is drawn schematically in Fig. 7.11. The geometrical properties of the generated curve can best be appreciated by expressing its curvature κ as a function of position σ measured along the curve. Then, from Fig. 7.11, $\kappa = \mathrm{d}\phi/\mathrm{d}\sigma$ and $\mathrm{d}\sigma = f(x)\mathrm{d}x$, so that

$$\kappa = \frac{1}{f(x)}\frac{\mathrm{d}\phi}{\mathrm{d}x}. \tag{7.52}$$

Classically, amplitude–phase diagrams have been extensively used to evaluate complex integrals of the Fresnel type, but of course today they have largely been displaced by numerical methods. However, construction of an amplitude–phase diagram for an integral often provides an intuitive feeling for the result and this can shorten the way to physical meaning. For example, as $f(x) \to 0$ or $\mathrm{d}\phi/\mathrm{d}x$ is large, the curvature becomes very large and the curve winds itself into a limiting dot and does not contribute to the integral. As a result, the most important parts in defining the value of a complex integral are those where $f(x)$ is large and the phase ϕ has a turning point, $\mathrm{d}\phi/\mathrm{d}x = 0$. Evaluating the integral by considering these points alone is called the **method of stationary phase**. Below, we shall briefly describe the method as applied to Fresnel diffraction by linear systems.

7.4.2 Diffraction by a slit

Let us consider the problem of diffraction by a single long slit defined in the plane $\mathcal{R}$ from x_1 to x_2, so that $g(x) = 1$ between these limits and is zero

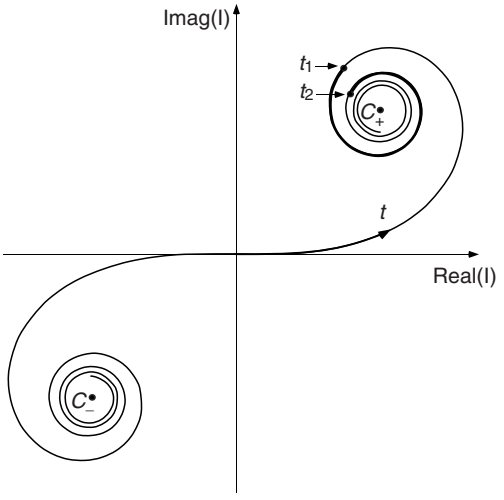

Figure 7.12
The Cornu spiral. The section from $t = t_1$ to t_2 is shown emphasized, and the complex amplitude observed is given by the vector between these two points. The intensity is the square of this vector.

elsewhere; $h(y) = 1$ everywhere. The integral (7.49) for ψ then gives the amplitude and phase of the disturbance at P, the axial point $(0, 0, z)$:

$$\psi = \frac{\mathrm{i}k_0 A}{2\pi z} \int_{x_1}^{x_2} \exp\left(\frac{\mathrm{i}k_0}{2z}x^2\right) \mathrm{d}x \int_{-\infty}^{\infty} \exp\left(\frac{\mathrm{i}k_0}{2z}y^2\right) \mathrm{d}y. \tag{7.53}$$

The second integral in (7.53) can be evaluated analytically (see §7.3) as $\sqrt{2\pi z/k_0}\mathrm{i}$. The first integral can be written in terms of the dimensionless variable $t = x\sqrt{k_0/z} \equiv \beta x$:

$$\mathcal{I} = \frac{1}{\beta} \int_{\beta x_1}^{\beta x_2} \exp\left(\frac{\mathrm{i}t^2}{2}\right) \mathrm{d}t. \tag{7.54}$$

From (7.52), the amplitude–phase diagram for this integral has the property that its curvature equals the distance from the origin, as measured along the curve. It is called the **Cornu spiral** and is illustrated in Fig. 7.12. In fact, the x- and y-axes are, respectively, the **Fresnel integrals** $\int_0^t \cos(t'^2/2)\,\mathrm{d}t'$ and $\int_0^t \sin(t'^2/2)\,\mathrm{d}t'$. To calculate the diffraction pattern from the slit we take a series of values of t_1 and t_2 such that $(t_1 - t_2)/\beta$ is the width of the slit, and measure the vector length between the points on the spiral at t_1 and t_2. This gives the amplitude and phase of ψ at P, which is opposite $x = 0$. Repeating the calculation as a function of the starting value t_1, which relates the point of observation P on the axis to the lateral position of the slit, gives the complete pattern. It will be seen, then, that diffraction patterns become quite intricate when both t_1 and t_2 are in the 'curls' of the spiral – i.e. when $(t_1 - t_2)$ is typically of the order of, or greater than, 10. Figure 7.13 shows the calculated intensity

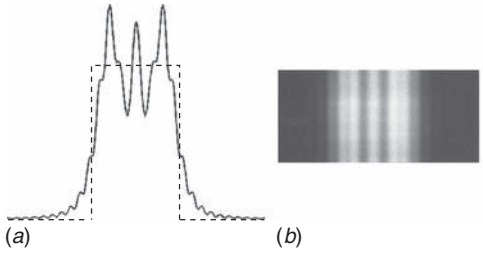

Figure 7.13

(*a*) Amplitude of the Fresnel diffraction pattern calculated for a slit of width 0.9 mm observed with $z = 20$ cm, $z_1 = 28$ cm and $\lambda = 0.6$ μm. The geometrical shadow is indicated by the broken lines. (*b*) Photograph of the diffraction pattern observed under these conditions.

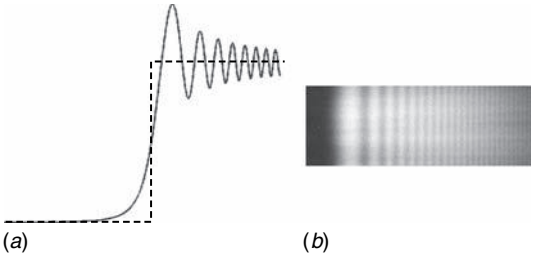

Figure 7.14

The Fresnel diffraction pattern of a single straight edge: (*a*) calculated from (7.54), where the geometrical shadow is shown as a broken line; (*b*) photographed. The edges of the shadow of the paperclip in Fig. 7.4 also show this phenomenon.

and the diffraction pattern observed for a value of $(t_1 - t_2) = 8.5$. Using light of wavelength 0.6 μm in (7.54) this corresponds to $(x_1 - x_2)^2/z \simeq 7$ μm – for example, a slit 2.7 mm wide at $z = 1$ m.

7.5 Advanced topic: X-ray microscopy

We shall see in §13.3.3 that the refractive index of materials for X-rays is very slightly less than unity ($n - 1 \sim -10^{-6}$) so that useful lenses cannot be constructed for use at such wavelengths. Another possibility for X-ray imaging is to use glancing-angle mirrors employing total *external* reflection, but because of the difficulties involved in accurate figuring of the ellipsoidal surfaces of such mirrors they have not so far been able to achieve high enough resolution for microscopy, although they are employed in X-ray astronomy. However, in Fresnel's zone plate we have an alternative focusing element consisting of a series of rings that are alternately transparent and opaque to X-rays. As a result of advances in microfabrication (Unger *et al.* (1987)), such zone plates can now be constructed from gold on a transparent substrate at a scale which makes them suitable for X-ray microscopy. A typical layout for an

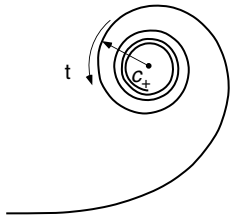

Figure 7.15

Cornu-spiral construction for the edge wave observed in the shadow region. As t advances, the vector rotates just like the wave from a line source; hence the term 'edge wave'.

Box 7.1 Diffraction by a single edge: the edge wave

A commonly observed diffraction pattern that can be easily recognized as resulting from the geometrical properties of the Cornu spiral is the pattern from a straight edge. Here, this is defined as an aperture extending from a finite value of t to infinity and its diffraction pattern is shown in Fig. 7.14. Fringes of this type are commonly seen around the shadow of any sharply defined object, and in a microscope might be used to judge the degree of defocus of such an object. The vector representing $\psi(t)$ joins the point t to C_+. When t is positive, so that $t = 0$ is in the geometrical shadow, the vector simply rotates about C_+, becoming monotonically shorter with continuously increasing and slowly accelerating phase as $t \to \infty$ (Fig. 7.15). This is almost identical with the phase variation of a wave coming from a line source. As a result, the edge appears to be a bright line; this is known as an **edge wave**, and explains why a sharp edge appears to be highlighted when observed from the shadow region. In the illuminated part, the fringes result from interference between the edge wave and the transmitted wave.

X-ray microscope based on a synchrotron radiation source (§5.3.1) is shown in Fig. 7.16.

Supposing that we use a wavelength of 5 nm, and require a focal length of 1 mm. The scale of the rings is then given by (7.29):

$$R_0 = \sqrt{f\lambda} = 2.7\,\mu\text{m}. \tag{7.55}$$

The nth ring has a radius $R_0\sqrt{n}$, and its thickness is approximately $R_0/\sqrt{n}$, so that if there are to be several hundred rings we require fabrication with a lateral scale resolution of 50 nm. Such structures have been made by electron-beam writing on a photo-resist film which, following several etching and electroplating stages, results in a zone plate of gold rings 150 nm thick which is sufficient to absorb X-rays of this wavelength. The zone plate is supported on a 120 nm thick X-ray-transparent silicon nitride substrate.

The transverse resolution limit of a zone plate is given by the width of its finest (outermost) ring.

We can calculate the resolution limit of such a 'lens' using the methods that will be developed in §12.2. First of all, the transverse resolution limit is equivalent to that of a lens with outer diameter D equal to that of the zone plate. We shall assume it to have N rings so that, from (7.27), $s_{\max} = D^2/4 = 2NR_0^2$. Then the resolution limit $\delta x_{\min}$, using (7.29) for the focal length f is

$$\delta x_{\min} = f\theta_{\min} = \frac{1.22f\lambda}{D} = \frac{1.22f\lambda}{2\sqrt{2N}R_0} = \frac{1.22R_0}{2\sqrt{2N}}. \tag{7.56}$$

This is can usefully be compared with the thickness of the outermost ring, which is $\sqrt{2N}R_0 - \sqrt{2N-1}R_0 \simeq R_0/\sqrt{2N}$ for large N. In other words, the transverse resolution limit is approximately equal to the scale of the finest ring, which is determined by the fabrication technique (about 50 nm). The longitudinal

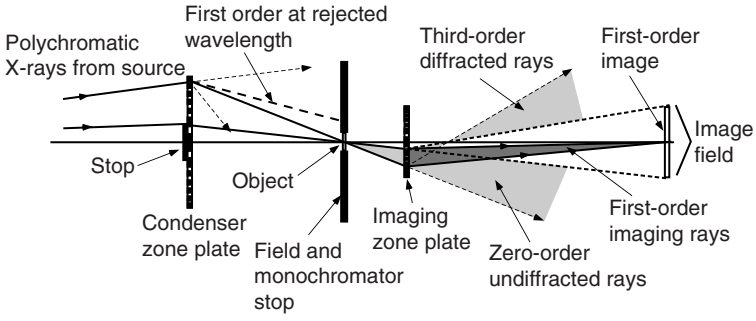

Figure 7.16

Schematic layout of the X-ray microscope at BESSY based on a synchrotron source. For clarity, rays are shown on one side of the axis only. It uses two Fresnel zone plates, the first as a condenser and the second for imaging. (After Niemann *et al.* (1986))

resolution is wavelength dependent. The images, at positions given by (7.28) where the primary image $n = 1$ is the only one of interest (the others are blocked by appropriately placed baffles), are ideally sharp only when $N \to \infty$. Otherwise, from the Fourier theory for a finite number N of oscillations (§8.5.3), we have the relative width of the image:

$$\frac{\delta L}{L} = \frac{1}{N}, \tag{7.57}$$

$$\delta L = \frac{R_0^2 k_0}{2N\pi} = \frac{1}{N}\left(\frac{R_0^2}{\lambda}\right) = \frac{D^2}{8N^2\lambda}. \tag{7.58}$$

As is usual in imaging systems, the longitudinal and transverse resolutions are related by

$$\frac{\delta L}{\lambda} \simeq \left(\frac{\delta x_{\min}}{\lambda}\right)^2, \tag{7.59}$$

i.e. the longitudinal resolution limit approximately equals the square of the transverse resolution limit, when both are measured in units of the wavelength. The transverse resolution limit is about 4λ, and so the longitudinal limit is about 16λ. The poor depth discrimination indicated by the last figure, which might be seen as a disadvantage, has been put to good use in forming tomographic images, where a number of views from different directions are synthesized mathematically into a three-dimensional picture of the object.

An example of an image is shown in Fig. 7.17. An alternative technique, inverting the X-ray diffraction pattern with the aid of phase retrieval, will be discussed in §8.8. The main problem that needs solution is the poor efficiency of the zone plate (<10%) which means that high X-ray dosages are necessary for imaging and therefore the technique is only available at synchrotron or other high intensity sources; the high intensity is also not healthy for biological samples. A phase-modulated zone plate, particularly if it can be blazed (§9.2.5), is clearly one answer here.

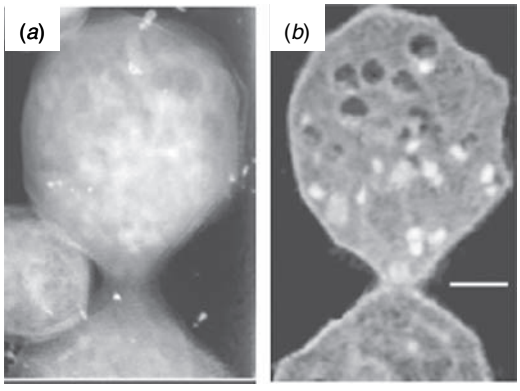

Figure 7.17
Images of budding yeast made using X-rays with $\lambda = 2.4$ nm: (*a*) projection image and (*b*) a section obtained by tomographic reconstruction from a series of projections in different directions. The scale bar on (*b*) is 0.5 μm. (Courtesy of C. Larabell; Larabell and Le Gros (2004))

Chapter summary

This chapter was devoted to the diffraction of optical waves and the subject of near-field, or Fresnel, diffraction in particular. We saw:

- That a full solution of wave propagation using Maxwell's equations is too difficult under most circumstances, and can be replaced by a scalar-wave diffraction theory, which is much easier to visualize and calculate;
- Some limitations of the scalar-wave theory and when it *cannot* be used;
- How to formulate scalar-wave diffraction by an obstacle by using Huygens' wavelets;
- That diffraction problems can be conveniently classed as **near-field** (Fresnel) and **far-field** (Fraunhofer) diffraction; the latter class has such far-reaching consequences that the next chapter will be devoted to it specifically;
- Some solutions for near-field, or Fresnel, diffraction by axially symmetric objects, where the necessary integrals can be performed analytically;
- How a Fresnel zone plate can be constructed to behave like a diffractive lens, and that this is the source of a new industry of 'diffractive optics';
- That Gaussian light beam propagation can be treated as a Fresnel diffraction problem;
- That there is a **Gouy phase shift** of π when a wave goes through a focus;
- How to use an **amplitude–phase diagram** for solving diffraction problems graphically or numerically;
- That Fresnel zone plates are being used today for imaging with soft X-rays, for which no lenses are available.

Appendix: The Huygens–Kirchhoff diffraction integral

Kirchhoff reformulated the diffraction problem for a scalar wave, which we derived intuitively in §7.1.2, in a more rigorous manner as a boundary-value problem. In the next two sections, (7.3) will be rederived, with an explicit form for the inclination factor $g(\theta)$.

An electromagnetic field within a bounded region of space can be uniquely determined by the boundary conditions around this region. Kirchhoff showed that this approach is consistent with the idea of reradiation by points on a wavefront through the aperture. Since we are dealing with harmonic fields having time dependence $\exp(-\mathrm{i}\omega t)$, the wave equation (2.49) becomes

$$\nabla^2\psi = -\frac{\omega^2}{c^2}\psi = -k_0^2\psi, \tag{7.60}$$

which refers to any component of the electric or magnetic wave-field. This is called the **Helmholtz equation**. We shall see that the field $\psi(0)$ at a point inside the bounded region can be written in terms of ψ and its derivatives on the boundary of the region. In simple cases where these are determined by external waves originating from a point source the result is very similar to the one which we have already found intuitively.

The exact mathematics for the diffraction integral

In problems involving boundaries it is often convenient to study the properties of the differences between two solutions of an equation rather than of one solution alone, since the boundary conditions become simpler to handle. The diffraction integral provides one such example, and we shall compare the required solution $\psi(\mathbf{r})$ of (7.60) with a trial solution

$$\psi_\mathrm{t} = \frac{a_\mathrm{t}}{r}\exp(\mathrm{i}k_0 r), \tag{7.61}$$

which is a spherical wave (2.48) radiating from the origin. This wave satisfies (7.60) except at $\mathbf{r} = 0$. This origin we shall define as the point of observation P, at which ψ has the value $\psi(0)$. The two wave-fields ψ (to be calculated) and ψ_t (the convergent reference wave) satisfy the equation

$$\psi\nabla^2\psi_\mathrm{t} - \psi_\mathrm{t}\nabla^2\psi = -\psi k_0^2\psi_\mathrm{t} + \psi_\mathrm{t}k_0^2\psi = 0 \tag{7.62}$$

at all points except $\mathbf{r} = 0$, because both ψ and ψ_t are solutions of (7.60). We shall now integrate expression (7.62) throughout a volume $\mathcal{V}$ bounded by a

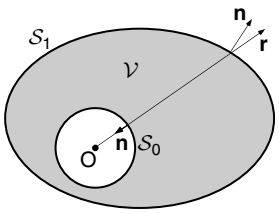

Figure 7.18

The surface for integration, shown as a two-dimensional section. $\mathcal{V}$ lies between $\mathcal{S}_0$ and $\mathcal{S}_1$. Since $\mathcal{S}_0$ is a sphere surrounding a hole in $\mathcal{V}$, its outward normal vector n is anti-parallel to r.

surface $\mathcal{S}$. The volume integral can be changed by Green's theorem to a surface integral:

$$\iiint_{\mathcal{V}} (\psi \nabla^2 \psi_t - \psi_t \nabla^2 \psi)\, \mathrm{d}V = \iint_{\mathcal{S}} (\psi \nabla \psi_t - \psi_t \nabla \psi) \cdot \mathbf{n}\, \mathrm{d}S, \qquad (7.63)$$

$\mathbf{n}$ being the outward normal to the surface $\mathcal{S}$ at each point. Because the integrand (7.62) is zero, the integrals (7.63) are also zero, provided that the region $\mathcal{V}$ does not include the origin $\mathbf{r} = 0$. The surface $\mathcal{S}$ is therefore chosen to have two parts, as illustrated in Fig. 7.18: an arbitrary outer surface $\mathcal{S}_1$ and a small spherical surface $\mathcal{S}_0$ of radius δr (much less than one wavelength) surrounding the origin. Volume $\mathcal{V}$ lies between the two surfaces, and $\mathbf{n}$, being the outward normal from $\mathcal{V}$, is therefore inward on $\mathcal{S}_0$ and outward on $\mathcal{S}_1$.

Over this two-sheet surface we thus have, for (7.63)

$$\left[\iint_{\mathcal{S}_0} + \iint_{\mathcal{S}_1}\right] (\psi \nabla \psi_t - \psi_t \nabla \psi) \cdot \mathbf{n}\, \mathrm{d}S = 0. \qquad (7.64)$$

We can evaluate the gradient of ψ_t from (7.61):

$$\nabla \psi_t = \frac{a_t \mathbf{r}}{r^2} \mathrm{i}k_0 \exp(\mathrm{i}k_0 r) - \frac{a_t \mathbf{r}}{r^3} \exp(\mathrm{i}k_0 r) = \frac{a_t \mathbf{r}}{r^3} (\mathrm{i}k_0 r - 1) \exp(\mathrm{i}k_0 r) \qquad (7.65)$$

and substitute in (7.64) to obtain

$$\iint_{\mathcal{S}_0 + \mathcal{S}_1} \frac{a_t}{r^3} \exp(\mathrm{i}k_0 r)[\psi (\mathrm{i}k_0 r - 1)\mathbf{r} + r^2 \nabla \psi] \cdot \mathbf{n}\, \mathrm{d}S = 0. \qquad (7.66)$$

The $\mathcal{S}_0$ contribution can be evaluated directly, since over the small sphere of radius δr we can consider ψ to be constant, equal to $\psi(0)$. Also, since $\mathbf{n}$ is then the unit vector parallel to $-\mathbf{r}$, we have $\mathbf{r} \cdot \mathbf{n} = -r$ and can substitute $r^2\, \mathrm{d}\Omega$ for $\mathrm{d}S$. Thus

$$\begin{aligned} &\iint_{\mathcal{S}_0} \frac{a_t}{r^3} \exp(\mathrm{i}k_0 r)[\psi(0)(\mathrm{i}k_0 r - 1)\mathbf{r} + r^2 \nabla \psi(0)] \cdot \mathbf{n} r^2\, \mathrm{d}\Omega \\ &\quad = -\iint_{\mathcal{S}_0} a_t \exp(\mathrm{i}k_0 r)[\psi(0)(\mathrm{i}k_0 r - 1) - r \nabla \psi(0) \cdot \mathbf{n}]\, \mathrm{d}\Omega, \end{aligned} \qquad (7.67)$$

evaluated at $r = \delta r$, $\mathrm{d}\Omega$ being the element of solid angle. In the limit as $\delta r \to 0$ there is only one term which does not approach zero and that is

$$-\iint_{\mathcal{S}_0} a_t \exp(\mathrm{i}k_0 \delta r)\psi(0)\mathrm{d}\Omega \to -4a_t \pi \psi(0), \qquad (7.68)$$

since $k_0\, \delta r \ll 1$. Equation (7.66) therefore gives, cancelling a_t,

$$\iint_{\mathcal{S}_1} \frac{1}{r^3} \exp(\mathrm{i}k_0 r)[\psi (\mathrm{i}k_0 r - 1)\mathbf{r} + r^2 \nabla \psi] \cdot \mathbf{n}\, \mathrm{d}S = 4\pi \psi(0). \qquad (7.69)$$

This expression is the analytical result of the wave equation (7.60). To summarize, it relates the value of the scalar wave ψ at the origin to its values and gradients on an arbitrary surface $\mathcal{S}_1$ surrounding the origin at a non-negligible distance from it.

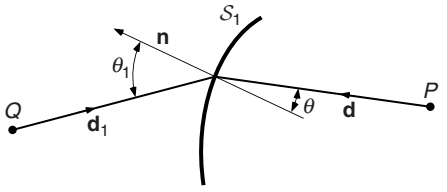

Figure 7.19
Part of the surface $\mathcal{S}_1$ showing normal, vectors and angles.

Illumination by a point source

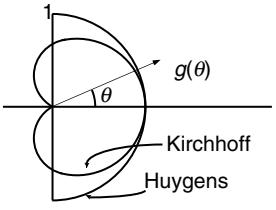

Figure 7.20
The inclination factor $g(\theta)$ for $\theta_1 = 0$ displayed in polar coordinates. The Kirchhoff result can be compared to Huygens' guess.

Suppose now that the disturbance on $\mathcal{S}_1$ originates from a point source Q. We consider a point S on $\mathcal{S}_1$ at $\mathbf{r} = \mathbf{d}$ which also lies a distance $\mathbf{d}_1$ from Q (Fig. 7.19). The incident wave at S has amplitude $(a_Q/d_1)\exp(\mathrm{i}k_0 d_1)$ and if the transmission function at this point is f_S, the reradiated values of $\psi(\mathbf{d})$ and its gradient are then

$$\psi(\mathbf{d}) = \frac{f_S a_Q}{d_1}\exp(\mathrm{i}k_0 d_1), \tag{7.70}$$

$$\nabla\psi = \frac{f_S a_Q \mathbf{d}_1}{d_1^3}(\mathrm{i}k_0 d_1 - 1)\exp(\mathrm{i}k_0 d_1), \tag{7.71}$$

as in (7.65). Substituting these values into (7.69) gives

$$a_Q \iint_{\mathcal{S}_1} f_S \exp[\mathrm{i}k_0(d + d_1)]\left[\frac{\mathbf{d}\cdot\mathbf{n}}{d_1 d^3}(\mathrm{i}k_0 d - 1) - \frac{\mathbf{d}_1\cdot\mathbf{n}}{d d_1^3}(\mathrm{i}k_0 d_1 - 1)\right]\mathrm{d}S$$
$$= -4\pi\psi(0). \tag{7.72}$$

The scalar products can be seen from the diagram to be $\mathbf{d}\cdot\mathbf{n} = d\cos\theta$ and $\mathbf{d}_1\cdot\mathbf{n} = -d_1\cos\theta_1$. When d and d_1 are both very much greater than the wavelength, we can neglect 1 with respect to $k_0 d$ and then, with the angles θ and θ_1 defined as in Fig. 7.19,

$$\psi(0) = -\frac{\mathrm{i}k_0 a_Q}{2\pi}\iint_{\mathcal{S}_1}\frac{f_S}{d d_1}\exp[\mathrm{i}k_0(d + d_1)]\left(\frac{\cos\theta + \cos\theta_1}{2}\right)\mathrm{d}S. \tag{7.73}$$

This is the theoretical basis for the expression (7.3) which we have already used in our diffraction calculations. It contains two extra pieces of information. The first is a definite form $\frac{1}{2}(\cos\theta + \cos\theta_1)$ for the inclination factor $g(\theta)$, which is shown in Fig. 7.20 where it is compared with the Huygens guess (§2.6.1). For paraxial conditions, $g(\theta) = \cos\theta = \cos\theta_1 \simeq 1$ as assumed in (7.3). In the backward direction $\cos\theta = -1$ and $g(\theta) = 0$. The second point of interest is that the scattering strength $b = -\mathrm{i}k_0/2\pi = -\mathrm{i}/\lambda$ has been derived directly (7.19).

Problems

7.1. A plane wave is incident normally on a mask containing a 1 mm hole. What is the furthest distance from the mask at which one can observe a diffraction pattern with zero intensity at its centre?

7.2. A 5 mm diameter disc is used to demonstrate the classic experiment showing the bright spot at the centre of its Fresnel diffraction pattern. The screen is at 1 m distance. What irregularity in the edges of the disc can be tolerated? Estimate the diameter of the bright spot on the screen.

7.3. Calculate the distances of the bright and dark fringes from the edge of the geometrical shadow in the diffraction pattern of a straight edge, observed in parallel light on a screen at 1 m distance from the edge.

7.4. What is the dispersive power (§3.7.3) of a Fresnel zone plate, considered as a lens? Design an achromatic doublet using a zone plate and a glass lens.

7.5. Find the variation of intensity along the axis of an annular aperture with inner and outer radii R_1 and R_2 illuminated by parallel light.

7.6. What efficiency would you expect to obtain from a zone plate with all rings transparent, but with phases (*a*) alternately 0 and π, (*b*) cyclically $0, \pi/2, \pi, 3\pi/2$? How is the latter related to a blazed grating (§9.2.5)?

7.7. A pinhole camera forms an image of a distant object on a screen at distance d from the pinhole. What diameter of pinhole gives the sharpest image? (Take into account both diffraction and convolution of the image with the aperture of the pinhole.)

7.8. Use the Cornu spiral to calculate the Fresnel diffraction pattern of a slit of width 1 mm on a screen at 1 m distance, when illuminated by parallel light. Compare this with the Fraunhofer pattern, obtained by inserting a lens of focal length 1 m immediately after the slit.

7.9. Devise a method of using amplitude–phase diagrams for Fraunhofer diffraction patterns, and apply it to finding the pattern of a periodic array of six thin slits.

7.10. Use the Cornu spiral to design a linear zone plate, by choosing slits with positions and widths such that all their contributions to ψ have the same sign.

7.11. Study the design of the X-ray microscope in Fig. 7.16 and see what are the trade-offs between the field of view and efficiency of imaging, which arise because of the need to block the centre of the zone plate.

7.12. Show that computations of Fresnel diffraction patterns can conveniently be carried out by calculating the two-dimensional Fourier transform of the object function, multiplied by a quadratic phase function $\exp(-i\alpha r^2)$, and show how to relate α to the experimental conditions. Illustrate your answer with some examples.

7.13. The transmission function of an annular mask is given by $f(r,\theta) = \delta(r - R_0)g(\theta)$, i.e. the mask is only transparent around the ring of radius R_0, but has arbitrary complex transmission function $g(\theta)$ around it. Using the Fresnel approximation, show that the diffraction pattern $I(\mathbf{p})$ is independent of z except for its scale, which depends linearly on z. For the case $g(\theta) = 1$, show that the diffraction pattern is given by a Bessel function (Appendix A). For this reason, beams which are limited by an annular aperture are called **Bessel beams** or **non-diffracting beams**.

References

Bohren, C. F. (1983), *Absorption and Scattering of Light by Small Particles*, New York: Wiley.

Born, M. and Wolf, E. (1999), *Principles of Optics*, 7th edn., Cambridge: Cambridge University Press.

Larabell, C. A. and Le Gros, M. A. (2004), X-ray tomography generates 3-D reconstructions of the yeast, *Saccharomyces cerevisiae*, at 60 nm resolution, *Mol. Biol. Cell* **15**, 957.

Niemann, B., Sarafis, V., Rudolph, D., Schmal, G., Meyer-Ilse, W. and Gutmann, P. (1986), X-ray microscopy with synchrotron radiation at the electron storage ring BESSY in Berlin, *Nucl. Instrum. Methods Phys. Res.* **A246**, 675.

Saleh, B. E. A. and Teich, M. C. (1991), *Fundamentals of Photonics*, New York: Wiley.

Siegman, A. E. (1986), *Lasers*, Sausalito, CA: University Science Books.

Unger, P., Bögli, V., Beneking, H., Niemann, B. and Guttmann, P. (1987), X-ray microscope images with Fresnel zone plates fabricated by electron beam nanolithography, *Microelectron. Eng.* **6**, 565.

van de Hulst, H. C. (1984), *Scattering of Light by Small Particles*, New York: Dover.

8 Fraunhofer diffraction and interference

The difference between Fresnel and Fraunhofer diffraction has been discussed in Chapter 7, where we showed that Fraunhofer diffraction is characterized by a **linear** change of phase over the diffracting obstacle, contrasting the quadratic phase change responsible for Fresnel diffraction. Basically, **Fraunhofer diffraction is the limit of Fresnel diffraction when the source and the observer are infinitely distant from the obstacle**. When the wavelength is very short and the obstacles are very small, such conditions can be achieved in the laboratory; for this reason Fraunhofer diffraction is naturally observed with X-rays, electrons, neutrons, etc., which generally have wavelengths less than 1 Å. The study of Fraunhofer diffraction has been fuelled by its importance in understanding the diffraction of these waves, particularly by crystals. This has led to our present-day knowledge of the crystalline structures of materials and also of many molecular structures. Figure 8.1 shows a famous X-ray diffraction pattern of a crystal of haemoglobin, from about 1958, whose interpretation was a milestone in visualizing and understanding biological macromolecules. The techniques used in interpreting such pictures will be discussed in the later parts of the chapter.

In optics, using macroscopic objects in a finite laboratory, the linear phase change can be achieved by illuminating the object with a beam of parallel light. It is therefore necessary to use lenses, both for the production of the parallel beam and for the observation of the resultant diffraction pattern.

In this chapter we shall learn:

- how to observe Fraunhofer diffraction patterns;
- about the relationship between Fraunhofer diffraction and the Fourier transform;
- why phase information in the patterns is lost in the recording process;
- some examples of diffraction patterns;
- general principles of Fraunhofer diffraction;
- about interference between several identical apertures;
- about three-dimensional Fraunhofer diffraction, and its importance in crystallography;
- how, in practice, it is often possible to retrieve the lost phases;
- how this has improved both modern crystallography and the Hubble Space Telescope.

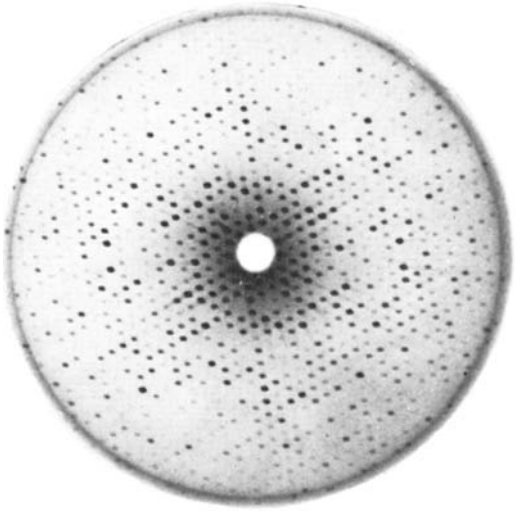

Figure 8.1
Precession photograph of haemoglobin. X-ray diffraction by crystals is an important application of Fraunhofer diffraction. (By courtesy of M. F. Perutz)

8.1 Fraunhofer diffraction in optics

8.1.1 Experimental observation of Fraunhofer patterns

How to observe Fraunhofer diffraction patterns in the laboratory and in the street.

In (7.10) we showed the optical path from an axial point source Q at distance z_1 to the general point P in the observation plane at z, via a point S in the mask plane $\mathcal{R}$ (as in Fig. 7.3), to be

$$\overline{QSP} \simeq z + z_1 + \frac{1}{2}\left(z^{-1} + z_1^{-1}\right) r^2 + \frac{1}{2} z^{-1}(p^2 - 2\mathbf{r}\cdot\mathbf{p}) + \cdots, \qquad (8.1)$$

where S is at $\mathbf{r} \equiv (x, y)$ and P at $\mathbf{p} \equiv (p_x, p_y)$ in their respective planes, with origins on the axis of illumination. Let P now be defined by the direction cosines $(\tilde{l}, \tilde{m}, \tilde{n})$ of the line OP joining the origin of the mask to P. Then, when $p \ll z$ we can write $\mathbf{p} = (z\tilde{l}, z\tilde{m})$, and

$$\begin{aligned} \overline{QSP} &\simeq z + z_1 + \frac{1}{2}\left(z^{-1} + z_1^{-1}\right) r^2 + \frac{1}{2} z\left(\tilde{l}^2 + \tilde{m}^2\right) - x\tilde{l} - y\tilde{m} \\ &\simeq z + z_1 - x\tilde{l} - y\tilde{m} + \cdots. \end{aligned} \qquad (8.2)$$

In the last line above, all second- and higher-order terms have been neglected. It is this linear dependence on x and y that is the origin of the great importance of Fraunhofer diffraction. As was pointed out in §7.1.4, experimental conditions can easily be devised so that the second-order terms are zero, even for quite

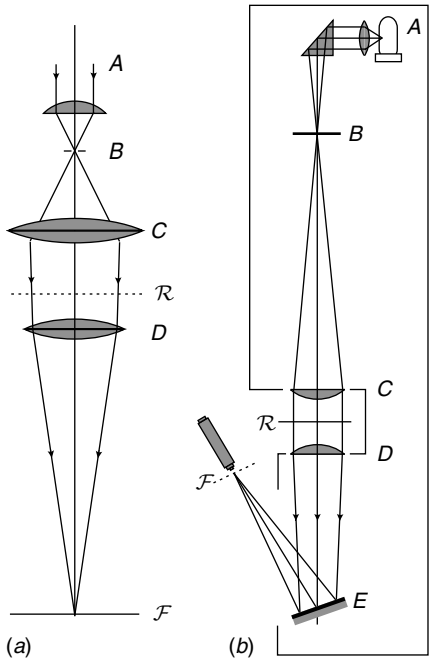

Figure 8.2

Set-ups for laboratory experiments on Fraunhofer diffraction: (*a*) using a laser source (*A*); (*b*) optical diffractometer, where the source *A* is a mercury discharge lamp. In the diagrams *B* is a pinhole to ensure spatial coherence over the mask; *C* and *D* are high quality lenses, *E* is an optically flat mirror. The diffraction pattern of a mask at $\mathcal{R}$ is seen in the plane $\mathcal{F}$.

large **r**. An everyday situation is when $z_1 = -z$ (observing screen conjugate to the point source Q); this arises when you look at a distant point source such as a monochromatic (sodium) street lamp, with the diffracting mask right in front of your eye.

Quantitative laboratory experiments are carried out with the aid of lenses or lens combinations, as in Fig. 8.2(*a*). The point source, a laser beam focused on a pinhole, is situated at the focal point B of the first lens C, so that a plane wave is incident on the mask $\mathcal{R}$, and thus $z_1 \to \infty$. The light leaving the mask passes through a second lens D, and the observation plane is the focal plane $\mathcal{F}$ of that lens, so that $z \to \infty$. Each point in this plane corresponds to a vector $(z\tilde{l}, z\tilde{m})$. Clearly the observation plane is conjugate to the point source, irrespective of the distance between the two lenses.

Many of the older photographs in this book were taken with an **optical diffractometer**, shown in Fig. 8.2(*b*), which was designed for accurate experiments of this sort. It was developed in the 1950s as an 'analogue computer' (Taylor and Lipson (1964)) for solving X-ray crystal diffraction problems, which will be discussed in §8.6. Although this instrument today seems old-fashioned, the use of a conventional discharge lamp source instead of a laser does avoid the appearance of laser speckle and spurious interference fringes in the diffraction patterns, which you might notice in some of the newer figures, although we took pains to avoid them!

Figure 8.3

(*a*) Illustrating the geometry of Fraunhofer diffraction by a two-dimensional object; (*b*) detail of the region *OZX*.

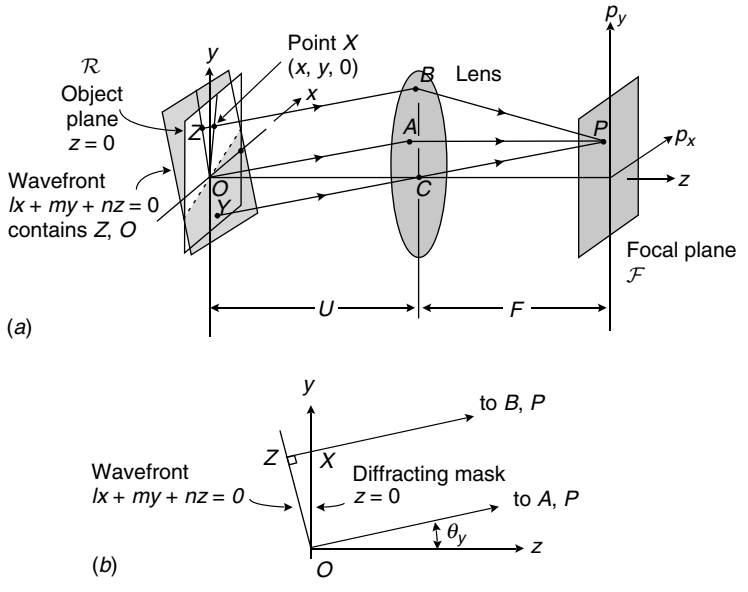

8.2 Fraunhofer diffraction and Fourier transforms

Fraunhofer diffraction experiments are an excellent way of learning about Fourier transforms.

We shall now examine the argument in §8.1.1 in more detail, for the case illustrated by Fig. 8.3 in which the incident light is a plane wave parallel to the optical axis and observation is in the focal plane of the second lens.

Consider a plane wave travelling along the z-axis (Fig. 8.3) and incident at $z = 0$ on a mask with amplitude transmission function $f(x,y)$. The diffracted light is collected by a lens of focal length F situated in the plane $z = U$.

All light waves leaving the screen in a particular direction are focused by the lens to a point in the focal plane. In the figure XB, OA, YC are all parallel and are focused at P. The amplitude of the light at P is therefore the sum of the amplitudes at X, O, Y, etc., each with the appropriate phase factor $\exp(\mathrm{i}k_0\overline{XBP})$, etc., where $\overline{XBP}$ indicates the optical path from X to P via B, including the path through the lens.

Now the amplitude at X, the general point (x,y) in the plane $z = 0$, is simply the amplitude of the incident wave, assumed unity, multiplied by the transmission function $f(x,y)$. To calculate the optical path $\overline{XBP}$ we remember that according to Fermat's principle (§2.6.4) the optical paths from the various points *on a wavefront* to its focus are all equal. The direction of XB, OA, ... is represented by direction cosines $(\tilde{l}, \tilde{m}, \tilde{n})$. Then the wavefront normal to them, through O, which focuses at P is the plane

$$\tilde{l}x + \tilde{m}y + \tilde{n}z = 0 \tag{8.3}$$

and the optical paths from the wavefront to P, i.e. $\overline{OAP}$ and $\overline{ZBP}$ are equal. Now ZX is just the projection of OX onto the ray XB, and this can be expressed as the component of the vector $(x, y, 0)$ in the direction $(\tilde{l}, \tilde{m}, \tilde{n})$, namely,

$$ZX = \tilde{l}x + \tilde{m}y. \tag{8.4}$$

Thus,

$$\overline{XBP} = \overline{OAP} - \tilde{l}x - \tilde{m}y. \tag{8.5}$$

The amplitude at P is obtained by integrating $f(x, y) \exp(\mathrm{i}k_0\overline{XBP})$ over the screen, ignoring the prefactor $\mathrm{i}k_0/2\pi z$ from (7.20):

$$\psi_P = \exp(\mathrm{i}k_0\overline{OAP}) \iint f(x, y) \exp[-\mathrm{i}k_0(\tilde{l}x + \tilde{m}y)]\, \mathrm{d}x\, \mathrm{d}y. \tag{8.6}$$

We define

$$u \equiv \tilde{l}k_0, \qquad v \equiv \tilde{m}k_0 \tag{8.7}$$

to represent the position of P, and write

$$\psi(u, v) = \exp(\mathrm{i}k_0\overline{OAP}) \iint f(x, y) \exp[-\mathrm{i}(ux + vy)]\, \mathrm{d}x\, \mathrm{d}y. \tag{8.8}$$

The Fraunhofer diffraction pattern amplitude is therefore given by the two-dimensional Fourier transform of the mask transmission function $f(x, y)$.

The Fraunhofer pattern is an expression of the wave transmitted by the mask as a superposition of plane waves, each travelling in a different direction. This is the Fourier transform.

The coordinates (u, v) can also be related to the angles of diffraction θ_x and θ_y between the vector $(\tilde{l}, \tilde{m}, \tilde{n})$ and the vertical and horizontal planes, respectively, containing the axis. Then $\tilde{l} = \sin\theta_x$, $\tilde{m} = \sin\theta_y$, and

$$u = k_0 \sin\theta_x, \qquad v = k_0 \sin\theta_y. \tag{8.9}$$

The coordinates (p_x, p_y) of P can be related exactly to u and v only if the details of the lens are known. For paraxial optics, the direction cosine $\tilde{n} \approx 1$ and

$$p_x = F\tilde{l}/\tilde{n} \approx uF/k_0, \qquad p_y = F\tilde{m}/\tilde{n} \approx vF/k_0, \tag{8.10}$$

where F is the effective focal length of the lens. It would be useful if the linear approximation could be preserved out to larger angles, and lenses with this property have been designed. In general, however, one has to work at small angles for the $(p_x, p_y) : (u, v)$ relationship to be linear.

When we observe a diffraction pattern, or photograph it, we measure the intensity $|\psi(u, v)|^2$, and the exact value of $\overline{OAP}$ is irrelevant. We then have from (8.8)

$$|\psi(u, v)|^2 = \left| \iint f(x, y) \exp[-\mathrm{i}(ux + vy)]\, \mathrm{d}x\, \mathrm{d}y \right|^2. \tag{8.11}$$

8.2.1 The phase of the Fraunhofer diffraction pattern

Although the phase of the diffraction pattern is lost when we photograph it, there are ways of retrieving or recording it. See §8.8 and §12.5 where these are described.

The intensity of the diffraction pattern is independent of the exact distance OC between the mask and the lens, in that this distance only affects the phase factor $\exp(\mathrm{i}k_0\overline{OAP})$. For some purposes, it is necessary to know the phase of the diffraction pattern also, for example if the diffracted wave is to be allowed to interfere with another coherent light wave as in some forms of pattern recognition or holography (§12.5).

Now the factor $\exp(\mathrm{i}k_0\overline{OAP})$ is quite independent of $f(x,y)$, since it is determined by the geometry of the optical system. It is very easy to calculate it for the particular case where $f(x,y)$ is $\delta(x)\,\delta(y)$. This represents a pinhole in the mask at O. Then the diffraction pattern is, from (8.8),

$$\begin{aligned}\psi(u,v) &= \exp(\mathrm{i}k_0\overline{OAP})\int \delta(x)\exp(-\mathrm{i}ux)\,\mathrm{d}x\int \delta(y)\exp(-\mathrm{i}vy)]\,\mathrm{d}y\\ &= \exp(\mathrm{i}k_0\overline{OAP}).\end{aligned} \tag{8.12}$$

However, we know that the action of the lens in general is to focus the light from the pinhole. Of particular interest is the case where the mask is in the front focal plane ($OC = F$). Then the wave leaving the lens is a plane wave with wavefronts normal to the z-axis:

$$\psi(u,v) = \exp(\mathrm{i}k_0\overline{OAP}) = \text{constant}. \tag{8.13}$$

Therefore, **when the object is situated in the front focal plane of the lens, the Fraunhofer diffraction pattern represents the true complex Fourier transform** of $f(x,y)$. For all other object positions the intensity of the diffraction pattern is that of the Fourier transform, but the phase is not.

8.2.2 Fraunhofer diffraction in obliquely incident light

Diffraction gratings are usually illuminated at an angle in order to increase their resolving power (§9.2.2)

If the plane wave illuminating the mask in Fig. 8.3 does not travel along the z-axis, the foregoing treatment can be adjusted in a rather simple manner. Specifically, when the incident wave-vector has direction cosines $(\tilde{l}_0, \tilde{m}_0, \tilde{n}_0)$ the phase of the wave reaching the point (x,y) on the mask is advanced by $k_0(\tilde{l}_0 x + \tilde{m}_0 y)$ with respect to that at the origin. Thus the retardation of the component from (x,y) with respect to that from $(0,0)$ is $k_0[(\tilde{l}-\tilde{l}_0)x+(\tilde{m}-\tilde{m}_0)y]$. The integral (8.6) is now

$$\begin{aligned}\psi_P = \exp(\mathrm{i}k_0\overline{OAP})\iint f(x,y)\\ \times\ \exp\{-\mathrm{i}k_0[(\tilde{l}-\tilde{l}_0)x+(\tilde{m}-\tilde{m}_0)y]\}\,\mathrm{d}x\,\mathrm{d}y.\end{aligned} \tag{8.14}$$

This can still be written in the form (8.8)

$$\psi(u,v) = \exp(\mathrm{i}k_0\overline{OAP}) \iint f(x,y)\exp[-\mathrm{i}(ux+vy)]\,\mathrm{d}x\,\mathrm{d}y, \tag{8.15}$$

provided that u and v are redefined:

$$u = k_0(\tilde{l}-\tilde{l}_0), \qquad v = k_0(\tilde{m}-\tilde{m}_0). \tag{8.16}$$

Now, remembering that $(\tilde{l},\tilde{m})$ are defined as sines of the angles (θ_x,θ_y), we see that u and v can be written

$$u = k_0(\sin\theta_x - \sin\theta_{x0}), \qquad v = k_0(\sin\theta_y - \sin\theta_{y0}). \tag{8.17}$$

This formulation will be important when we study the resolution limits of diffraction gratings (§9.2.2) and incoherent imaging (§12.2.5).

8.3 Examples of Fraunhofer diffraction by one- and two-dimensional apertures

In this section we shall apply the theory developed above to some specific examples. The results will be illustrated by experimental photographs, which demonstrate that the theory really works well in practice.

8.3.1 Fraunhofer diffraction by a slit

We represent a slit of width a by the function

$$f(x,y) = \mathrm{rect}(x/a) = \begin{cases} 1 & |x| \le a/2, \\ 0 & |x| > a/2. \end{cases} \tag{8.18}$$

Notice that the slit is considered to be infinitely long in the y-direction. The function $f(x,y)$ separates trivially into a product of functions of x and y only (the latter being the constant 1) and so, from §4.3.2,

$$\begin{aligned}\psi(u,v) &= \int_{-a/2}^{a/2} \exp(-\mathrm{i}ux)\,\mathrm{d}x \int_{-\infty}^{\infty} \exp(-\mathrm{i}vy)\,\mathrm{d}y \\ &= \frac{2\sin(au/2)}{u}\,\delta(v) = a\,\mathrm{sinc}(au/2)\,\delta(v).\end{aligned} \tag{8.19}$$

The intensity of the Fraunhofer diffraction pattern along the axis $v = 0$ is

$$|\psi(u,0)|^2 = a^2\,\mathrm{sinc}^2(au/2). \tag{8.20}$$

The function introduced here, $\mathrm{sinc}(x) \equiv \sin(x)/x$, shown in Fig. 8.4($a$), was discussed in §4.3.2, but is so important that we repeat its properties here. It has

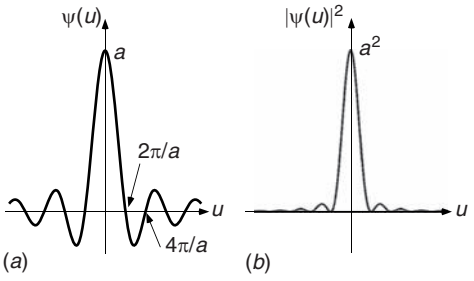

Figure 8.4
(*a*) Form of the function sinc(*x*). (*b*) The intensity of diffraction by a slit of width *a*, $a^2\,\mathrm{sinc}^2(\frac{1}{2}au)$.

The function sinc(*x*), (Fig. 8.4(*a*)), the diffraction pattern of a slit, occurs frequently in diffraction theory.

a maximum of 1 at $x = 0$, since $\sin(x) \approx x$ for small values of x, and is zero at regular intervals where $x = m\pi$, m being a non-zero integer. The values of the interleaving maxima are approximately proportional to $\left(m + \frac{1}{2}\right)^{-1}$; this result arises if we assume that these maxima lie half-way between the zeros, which is not quite true. Figure 8.4(*b*) shows the observed intensity, $|\psi(u,0)|^2$. The zeros in this function occur at angles given by

$$k_0 a \sin\theta = 2m\pi, \quad a\sin\theta = m\lambda. \tag{8.21}$$

The sharp edges of an aperture give rise to oscillatory side-bands; smoothing the edges reduces the prominence of these oscillations.

8.3.2 Diffraction by a blurred slit, represented by a triangular function

We now assume that the transmission function at the edges of the slit varies continuously and linearly with x so as to define a slit of the same width a as before, but with blurred edges. This will demonstrate that the effect of blurring the sharp edges is to reduce the prominence of the side-bands in the diffraction pattern. Consider

$$f(x,y) = \begin{cases} 1 - |x|/a & |x| \le a, \\ 0 & |x| > a. \end{cases}$$

This slit has **effective width** (defined as $\int f(x)\,\mathrm{d}x\,/f_{\max}$; see §8.3.5) equal to a, the same as that of the previous slit (§8.3.1). Then, integrating by parts, one finds

$$\psi(u,v) = \left[\frac{1}{a}\int_0^a (a-x)\exp(-\mathrm{i}ux)\,\mathrm{d}x + \frac{1}{a}\int_{-a}^0 (a+x)\exp(-\mathrm{i}ux)\,\mathrm{d}x\right] \times \int_{-\infty}^{\infty} \exp(-\mathrm{i}vy)\,\mathrm{d}y = a\,\mathrm{sinc}^2(au/2)\,\delta(v). \tag{8.22}$$

The form of $\psi(u,0)$ is the same as shown in Fig. 8.4(*b*). It is everywhere positive, reaching zero at values of u given by

$$au/2 = m\pi; \quad a\sin\theta = m\lambda. \tag{8.23}$$

The positions of these zeros are thus exactly the same as for the uniform slit; since their effective widths are the same this result is not surprising. But the maxima of the side-bands produced are much less; their intensities are proportional to $(2m+1)^{-4}$. Further smoothing of the function $f(x,y)$ at the edges of the slit results in even weaker side-bands. A very smooth function is the Gaussian discussed in §4.4.3 and §8.3.6 whose transform has no side-bands at all. Notice that the diffraction pattern intensities in both this case and that of the sharp-edged slit (§8.3.1) are functions centro-symmetrical about $(u,v)=(0,0)$, since $f(x,y)$ is real.

8.3.3 Diffraction pattern of a rectangular hole

The diffraction pattern of a rectangular aperture is a two-dimensional 'sinc' function with dimensions inversely proportional to those of the aperture itself.

Now we consider a rectangular hole of sides a and b, parallel to the x- and y-axes respectively,

$$f(x,y) = \mathrm{rect}(x/a)\,\mathrm{rect}(y/b). \tag{8.24}$$

Since this function is the product of independent functions of x and y, (8.8) can be written as a product:

$$\psi(u,v) = \int_{-a/2}^{a/2} \exp(-\mathrm{i}ux)\,\mathrm{d}x \int_{-b/2}^{b/2} \exp(-\mathrm{i}vy)\,\mathrm{d}y. \tag{8.25}$$

Since the origin is at the centre of the aperture the function is even and therefore has a real transform. Thus

$$\psi(u,v) = ab\,\mathrm{sinc}\left(\tfrac{1}{2}ua\right)\,\mathrm{sinc}\left(\tfrac{1}{2}vb\right), \tag{8.26}$$

each factor being similar to that derived for a uniform slit (8.19). The diffraction pattern has zeros at values of ua and vb equal to non-zero multiples of 2π. Thus the zeros lie on lines parallel to the edges of the slit, given by the equations

$$u = m_1\frac{2\pi}{a} \quad \text{and} \quad v = m_2\frac{2\pi}{b}. \tag{8.27}$$

The centre peak, for example, is bounded by lines given by $m_1 = \pm 1$ and $m_2 = \pm 1$, which form a rectangle whose dimensions are inversely proportional to those of the diffracting aperture (Fig. 8.5). The peaks off the u- and v-axes are very weak, and are difficult to bring out in a photograph.

8.3.4 Diffraction pattern of apertures with axial symmetry

Axially symmetric apertures have diffraction patterns described by Bessel functions (Appendix A).

The diffraction pattern of a circular aperture is most important, since almost all optical systems have axial symmetry, and their elements are bounded by circular apertures. But now the integral (8.11) is more difficult to evaluate

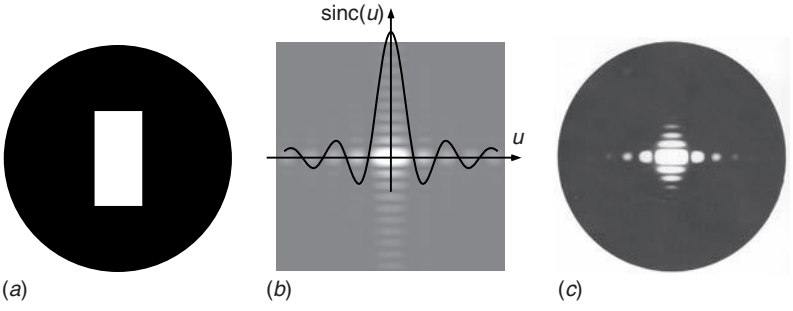

Figure 8.5 **(*a*) A rectangular aperture, with vertical-to-horizontal aspect ratio $b/a \approx 2$. (*b*) The calculated diffraction pattern amplitude along the x-axis, of form $\mathrm{sinc}(ua/2)$ superimposed on the calculated amplitude of the diffraction pattern $|\mathrm{sinc}(au/2)\mathrm{sinc}(vb/2)|$. (*c*) The observed diffraction pattern. Notice that the vertical-to-horizontal aspect ratio is now $b/a \approx \frac{1}{2}$.**

since the limits are not independent. It is necessary to use polar coordinates both for points in the aperture and in the diffraction pattern. If (r, θ) are the polar coordinates in the aperture

$$x = r\cos\theta \quad \text{and} \quad y = r\sin\theta, \tag{8.28}$$

and if (ζ, ϕ) are the polar coordinates in the diffraction pattern,

$$u \equiv \zeta\cos\phi \quad \text{and} \quad v \equiv \zeta\sin\phi. \tag{8.29}$$

Thus equation (8.8) becomes

$$\psi(\zeta,\phi) = \int_0^{2\pi}\int_0^{\infty} \exp[-\mathrm{i}(r\zeta\cos\phi\cos\theta + r\zeta\sin\phi\sin\theta)]\, r\,\mathrm{d}r\,\mathrm{d}\theta$$

$$= \int_0^{2\pi}\int_0^{\infty} \exp[-\mathrm{i}r\zeta\cos(\theta-\phi)] r\,\mathrm{d}r\,\mathrm{d}\theta. \tag{8.30}$$

The diffraction patterns shown in this chapter were mainly photographed using the diffractometer shown in Fig. 8.2(*b*).

This integral must be performed in terms of Bessel functions (Appendix A). First, we calculate the outer (θ) integral, which is the diffraction pattern of a thin annular aperture. Let it have radius r and thin width $\delta r \ll r$. The symmetry dictates that the result will be independent of ϕ, so we can put $\phi = 0$ and then the formulation (A.1) gives us

$$\psi(\zeta,\phi)_{\mathrm{a}} = \psi(\zeta,0)_{\mathrm{a}} = \int_0^{2\pi} \exp[-\mathrm{i}r\zeta\cos(\theta)] r\,\delta r\,\mathrm{d}\theta \tag{8.31}$$

$$= 2\pi r\delta r J_0(r\zeta). \tag{8.32}$$

In Fig. 8.6, (8.32) is compared with an experimental observation. The zero-order Bessel function has a sharp central peak (actually the narrowest that can be obtained from any real and positive aperture within the bounds of r) and quite a strong ring structure, which is clearly evident in the photograph.

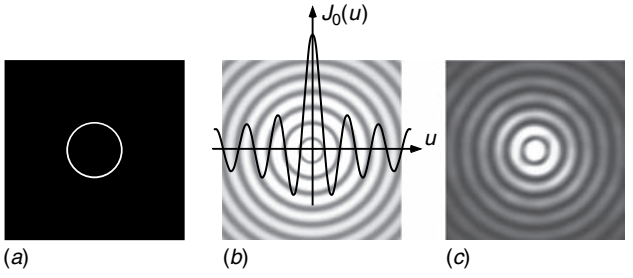

Figure 8.6
(*a*) Annular aperture. (*b*) Form of the function $J_0(u)$, the radial amplitude distribution in the diffraction pattern of an annular aperture, superimposed on the two-dimensional form of the amplitude $|J_0(\zeta)|$. (*c*) Observed Fraunhofer diffraction pattern of an annular aperture.

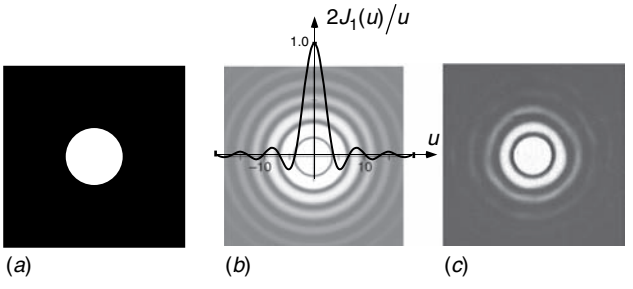

Figure 8.7
(*a*) Circular aperture. (*b*) Form of function $2J_1(u)/u$, the radial amplitude distribution in the diffraction pattern of a circular aperture, superimposed on the two-dimensional form of the amplitude $|J_1(\zeta)/\zeta|$. (*c*) Observed Fraunhofer diffraction pattern of a circular hole.

The diffraction pattern of a circular hole is obtained by integrating (8.32) from 0 to R. The integral can be performed using power series (A.2) and shown to be the **Airy function**:

$$\psi(\zeta,\phi) = \frac{2\pi R J_1(\zeta R)}{\zeta} = \pi R^2 \left[\frac{2J_1(\zeta R)}{\zeta R}\right]. \tag{8.33}$$

The form of (8.33) is interesting and very important. $J_1(x)$ is equal to $x/2$ at small values of x and therefore, like $\mathrm{sinc}(x)$, the function $2J_1(x)/x$ has a finite value of unity at $x = 0$. It then decreases to zero, becomes negative and continues to oscillate with a gradually decreasing period that tends to a constant as in Fig. 8.7(*b*).

The diffraction pattern is shown in Fig. 8.7(*c*). The central peak is known as the **Airy disc**, and it extends to the first zero, which occurs at $x = 3.83$, or at angle $\zeta/k_0 = 0.61\lambda/R$. As one would expect from the properties of Fourier transforms, the radius of the Airy disc is inversely proportional to the radius of the hole.

It should also be noted from equations (8.26) and (8.33) that the amplitude at the centre of the diffraction pattern is proportional to the area of the hole, and therefore the intensity at that point is proportional to the square of the area. This result makes sense when we realize that the linear dimensions of the diffraction pattern are inversely proportional to those of the hole. Thus the total energy

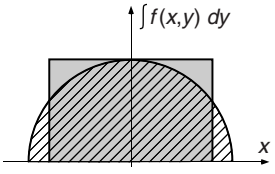

Figure 8.8

The 'effective width' of a circular aperture. The shaded rectangle and the hatched circle have equal areas.

flow in the diffraction pattern, which is proportional to the area of the hole, is mainly concentrated in a region that is inversely proportional to that area.

8.3.5 Section of a diffraction pattern through the origin: effective width

The effective width is a useful tool for estimating the scale of a diffraction pattern.

The derivation of the form of the diffraction pattern in terms of a Bessel function does not really throw any light upon the physics of the problem. If it had not been that Bessel functions appear in other physical problems, their properties would not have been studied and we should be no nearer an acceptable solution when the equation (8.33) had been derived. It is, however, possible to see a rough solution in terms of the concepts discussed in §8.3.1 and §8.3.2.

Suppose we have a function $f(x,y)$ whose diffraction pattern is $\psi(u,v)$. Along the axis $v=0$, we have in general

$$\psi(u,0) = \iint f(x,y)\exp(-\mathrm{i}ux)\,\mathrm{d}x\,\mathrm{d}y$$
$$= \int_{-\infty}^{\infty}\left[\int_{-\infty}^{\infty} f(x,y)\,\mathrm{d}y\right]\exp(-\mathrm{i}ux)\,\mathrm{d}x. \qquad (8.34)$$

This means that the axial value $\psi(u,0)$ is the Fourier transform of the integral $f_0(x) = \int f(x,y)\,\mathrm{d}y$. This has converted the two-dimensional Fourier transform into a one-dimensional one whose properties might be easier to appreciate intuitively. For many functions, we can define an 'effective width' $w_{\mathrm{eff}} = \int f_0(x)\,\mathrm{d}x/\max(f_0)$, and the diffraction pattern along the axis then has a characteristic dimension $2\pi/w_{\mathrm{eff}}$.

As an example, we can apply this to the circular aperture. The integral is a semicircular function and its effective width is $\pi R/2$ (Fig. 8.8). A slit with width w_{eff} has diffraction pattern along the u-axis

$$\psi(u,0) = w_{\mathrm{eff}}\,\mathrm{sinc}(\pi uR/4), \qquad (8.35)$$

which has its first zero when $uR = 4$. This agrees quite well with the exact value, $uR = 3.83$, from the Bessel function.

8.3.6 Diffraction pattern of a Gaussian mask

The diffraction patterns of the apertures studied so far show noticeable outer rings or side-bands, which arise as the result of the sharp cut-off at the edge of the aperture. We saw an example in §8.3.2 of how these can be reduced by blurring the edges. You can see this qualitatively because blurring corresponds to convolution with a 'smearing function' whose transform multiplies the diffraction pattern and reduces the intensity of the outer parts where the

rings are. A sufficiently smooth function has no side-bands at all. We can illustrate this by using the Gaussian function, and we consider a circular aperture whose transmission function is

$$f(x,y) = \exp[-(x^2+y^2)/2\sigma^2]. \tag{8.36}$$

This also represents a Gaussian light beam incident on the plane $\mathcal{R}$ in a diffractometer, and the same problem was discussed in §7.3. Since this function, despite its axial symmetry, can be written as the product of independent Gaussian functions of x and y, we have the Fourier transform from (4.48):

$$\begin{aligned}\psi(u,v) &= 2\pi\sigma^2 \exp(-u^2\sigma^2/2 - v^2\sigma^2/2)\\ &= 2\pi\sigma^2 \exp(\zeta^2\sigma^2/2).\end{aligned} \tag{8.37}$$

The result is also a Gaussian spot, and is the most well-known example of a 'self-Fourier function' (§4.10). In the diffraction plane at distance $F = R_0$, using the paraxial form $\zeta = k_0 r/F$ we have the Gaussian $\psi(r) = 2\pi\sigma^2 \exp\left(-k_0^2 r^2\sigma^2/2R_0^2\right)$ which is the same result as we obtained by Fresnel diffraction (7.43).

8.4 Some general diffraction principles

If a mask only absorbs light, its diffraction pattern is centro-symmetrical. If it changes the phase too, the diffraction pattern may not be centro-symmetrical

Having worked through a number of specific examples, we shall now discuss some general principles that apply to Fraunhofer diffraction, and are of great importance in gaining an intuitive understanding of these patterns.

8.4.1 Diffraction by an object with phase variation only

There are many objects, including many natural ones, that do not absorb light appreciably but change its phase on transmission. Any ordinary piece of window glass will do this; it is transparent, but its thickness is not uniform and light passing through different parts of it suffers a varying amount of phase retardation. If the refractive index of the glass is n, the optical difference between two paths including different thicknesses t_1 and t_2 is

$$(n-1)(t_1 - t_2) \tag{8.38}$$

and consequently an incident plane wave emerges from the glass sheet with wavefronts that may no longer be planar (Fig. 8.9). Since waves of different phases but the same amplitudes are represented by complex amplitudes with the same modulus, this situation can be represented by a complex transmission function $f(x,y)$ with constant modulus and is called a **phase object**. When calculating the Fraunhofer diffraction pattern of a phase object it is important to realize that, because the transmission function $f(x,y)$ is a complex function, **the diffraction pattern may not be centro-symmetric** (§4.2.1).

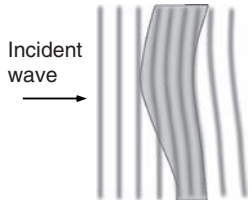

Figure 8.9

Distortion of a plane wavefront by a non-uniform glass plate.

We shall take as an example a thin prism of angle $\alpha \ll 1$ and refractive index n. The thickness t of the prism at position x is αx (Fig. 8.10) and its transmission function is thus

$$\begin{aligned} f(x,y) &= \exp[\mathrm{i}k_0(n-1)t] \\ &= \exp[\mathrm{i}k_0(n-1)\alpha x]. \end{aligned} \tag{8.39}$$

The prism is assumed to be infinite in extent along both x- and y-directions. The diffraction pattern corresponding to $f(x,y)$ is then

$$\begin{aligned} \psi(u,v) &= \int_{-\infty}^{\infty} \exp[\mathrm{i}k_0(n-1)\alpha x] \exp(-\mathrm{i}ux)\,\mathrm{d}x \int_{-\infty}^{\infty} \exp(-\mathrm{i}vy)\,\mathrm{d}y \\ &= \delta[u-(n-1)k_0\alpha]\,\delta(y). \end{aligned} \tag{8.40}$$

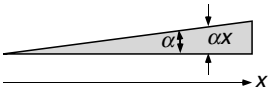

Figure 8.10

A thin prism of angle α.

The diffracted wave thus travels in the direction represented by

$$u = k_0(n-1)\alpha, \quad v = 0. \tag{8.41}$$

Substituting for u this gives $\theta \approx (n-1)\alpha$ for small θ. The light thus remains concentrated in a single direction, but is deviated from the incident by the same angle as deduced from geometrical optics. Notice that (8.40) is *not centro-symmetric*, since it consists of a single δ-function which is not at the origin.

8.4.2 Addition of diffraction patterns

Since diffraction is a linear process, diffraction pattern *amplitudes* can be combined algebraically. This often allows the diffraction patterns of relatively complicated objects to be derived if their transmission functions can be expressed as an algebraic sum of simpler ones. The separate components of the object must of course be expressed with respect to the same origin, and the complete transform is then obtained by summing the complex amplitudes of the component transforms. For example, it is possible to derive the diffraction pattern of three slits by adding the transform of the two outer ones to that of the inner one, or the diffraction pattern of a rectangular frame by subtracting the transform of the inner rectangle from that of the outer one. In every case one must be careful about the prefactors of the Fourier transforms. Some examples of this sort are included as problems.

Diffraction pattern amplitudes can be combined algebraically.

8.4.3 Complementary screens: Babinet's theorem

Babinet's theorem relates the Fraunhofer diffraction patterns of two complementary screens. Two screens are said to be **complementary** if they each

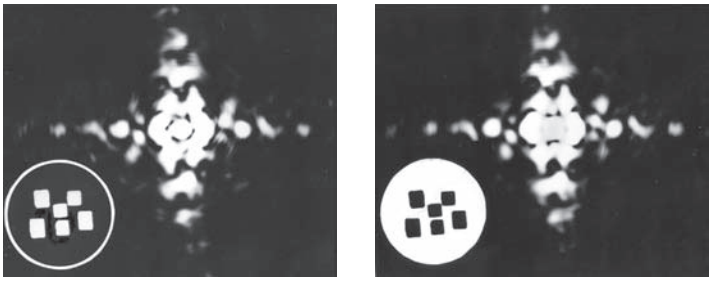

(*a*) (*b*)

Figure 8.11
Babinet's theorem. Diffraction patterns of two complementary masks (shown as insets) when illuminated by a Gaussian beam. The positive mask (*a*) was cut from metal foil and the negative (*b*) produced by evaporating metal through it onto a flat glass plate.

Box 8.1 Demonstration of Babinet's theorem

Experimental confirmation of Babinet's theorem is an interesting exercise, mainly because of the strength of the central peak. If the unobstructed beam is very large, and one of the masks is mainly transparent, the peak is extremely strong for that mask and usually dominates its diffraction pattern, whereas it is negligible for the other mask. To get a convincing experimental confirmation of the theorem, the following rules should therefore be followed.

1. The edges of the unobstructed beam should be blurred. This suppresses the outer parts of its transform. In fact, using a Gaussian beam gives the most concentrated central peak with the weakest wings.
2. The positive and negative masks should each be about 50% transmitting, to give the strongest diffraction patterns in both cases.
3. The masks should contain fine detail so as to give rise to a strong diffraction pattern well outside the central peak.

consist of openings in opaque material, the openings in one corresponding exactly to the opaque parts of the other. Then the diffraction patterns of two such screens are exactly the same except for a small region near the origin. For example, the pattern of a set of opaque discs should be the same as that of a set of equally sized holes similarly arranged, except around the origin. The theorem is illustrated by the masks and diffraction patterns shown in Fig. 8.11.

The theorem can be proved on general grounds using the scalar theory of diffraction. Suppose that the amplitudes of the diffraction patterns of two complementary screens when illuminated by a certain beam are ψ_1 and ψ_2. Now, the diffraction function for a combination of apertures can be obtained by adding the separate (complex) functions. If we add ψ_1 and ψ_2 we should obtain the diffraction function for the unobstructed beam. If this beam is large in extent, the sum of ψ_1 and ψ_2 is then confined to a small region round the centre; the rest is blank. Therefore the sum of ψ_1 and ψ_2 must be zero

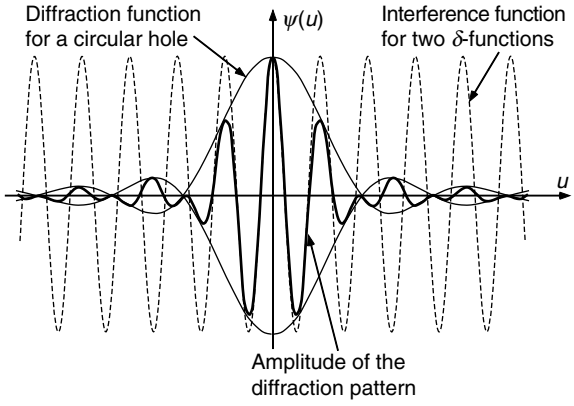

Figure 8.12
The diffraction pattern of two circular holes is the product of the diffraction function and the interference function. The former is the Airy disc pattern (§8.3.4) and the latter is a cosine function.

everywhere except for this small central region. The moduli of ψ_1 and ψ_2 outside this region must therefore be equal, their phases differing by π. The intensity functions are the same.

8.5 Interference

The relationship between interference and diffraction is like that between the Fourier series and transform.

We have so far considered only the effect of modifying a single wavefront; we shall now consider the effects occurring when two or more wavefronts interact. These effects are called **interference**. In this section, we shall concern ourselves mainly with wavefronts from identical masks.

For identical apertures we can make use of the principle of convolution (§4.7). For example, two similar parallel apertures can be considered as the **convolution** of one aperture with a pair of δ-functions, one at the origin of each. The interference pattern is therefore the product of the diffraction pattern of one aperture and that of the pair of δ-functions (§4.4.1). We can therefore divide such an interference problem into two parts – the derivation of the Fourier transform of the single aperture and that of the set of δ-functions. The transform of the single aperture is called the **diffraction function** and that of the set of δ-functions is called the **interference function**; the complete diffraction pattern is the product of the two. This is shown for two circular holes in Fig. 8.12.

8.5.1 Interference pattern of two circular holes

We can regard a pair of circular holes, with separation a, as the result of convolving a single hole with a pair of δ-functions. Now from §4.4.1 the

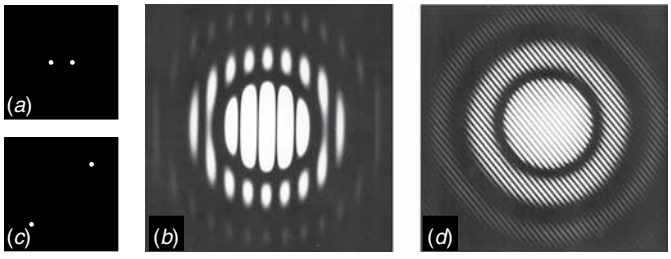

Figure 8.13
Experimental diffraction patterns of pairs of circular holes: (*a*, *b*) separated by about five times their diameter; (*c*, *d*) separated by about 18 times their diameter. Note that the fringes are normal to the line joining the holes.

transform of the two δ-functions is given by

$$\psi(u, v) = 2\cos(ua/2). \tag{8.42}$$

Thus the diffraction pattern of the two holes is the diffraction pattern of one of them multiplied by a cosine function, varying in a direction parallel to the separation a, Fig. 8.13.

The zeros of the function (8.42) occur at values of θ given by

$$ua/2 = \left(m + \frac{1}{2}\right)\pi, \tag{8.43}$$

where m is an integer. Since $u = k\sin\theta = 2\pi\sin\theta/\lambda$, this simplifies to

$$a\sin\theta = \left(m + \frac{1}{2}\right)\lambda. \tag{8.44}$$

It will be realized that what we have achieved is a rather roundabout method of deriving an expression for Young's fringes. There are, however, several reasons for using this approach: first, we have derived the full expression for the profile of the fringes, not just the spacing; second, we have demonstrated use of the convolution method in a simple example; and, third, we have prepared the ground for more complicated systems, such as those that follow.

8.5.2 Interference pattern of two parallel apertures of arbitrary shape

Convolution is a powerful tool that can often be used to break down a complicated structure into simpler ones.

We can regard a pair of similar parallel apertures (Fig. 8.14) as the convolution of a single aperture with two δ-functions. The diffraction pattern is therefore the product of the diffraction pattern of a single aperture and the interference function, which is a set of sinusoidal fringes. This is illustrated in Fig. 8.15. The argument is obviously applicable to a pair of apertures of any shape.

Figure 8.14
Pair of parallel apertures with quite a complicated structure.

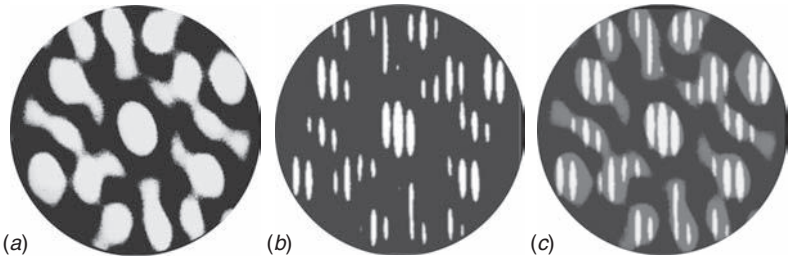

Figure 8.15
(*a*) Diffraction pattern of one of the apertures in Fig. 8.14. (*b*) Complete diffraction pattern of the mask in Fig. 8.14. (*c*) Superposition of (*a*) and (*b*) showing that (*b*) is (*a*) multiplied by a cosine function.

8.5.3 Interference pattern of a regular array of identical apertures

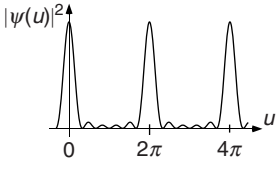

Figure 8.16
Diffraction by six parallel slits. Form of the function $\sin^2(uNd/2)/\sin^2(ud/2)$ for $N = 6$.

An array of apertures can be regarded as the convolution of a set of δ-functions with one aperture. From §4.4.2 we find that, if the δ-functions form a regular one-dimensional lattice with spacing d, the transform is

$$\psi(u,v) = \sum_{n=0}^{N-1} \exp(-\mathrm{i}und), \tag{8.45}$$

where N is the number of apertures. When $N \to \infty$, the sum is (§4.4.2)

$$\psi(u,v) = \sum_{m=-\infty}^{\infty} \delta(u - 2\pi m/d). \tag{8.46}$$

The index m is called the **order of diffraction**. When N is finite, the sum of the geometrical series (8.45) is

$$\psi(u,v) = \frac{1 - \exp(-\mathrm{i}uNd)}{1 - \exp(-\mathrm{i}ud)}. \tag{8.47}$$

The intensity is given by

$$I(u,v) = |\psi(u,v)|^2 = \frac{\sin^2(uNd/2)}{\sin^2(ud/2)}. \tag{8.48}$$

This expression, which is plotted in Fig. 8.16 for $N = 6$, has some interesting properties. It is zero whenever the numerator is zero except when the denominator is also zero; then it is N^2. As the number of apertures increases, the number of zeros increases and the pattern becomes more detailed. Two examples are shown in Fig. 8.17. The peaks of intensity N^2 – called the **principal maxima** – become outstanding compared to the smaller subsidiary maxima, of

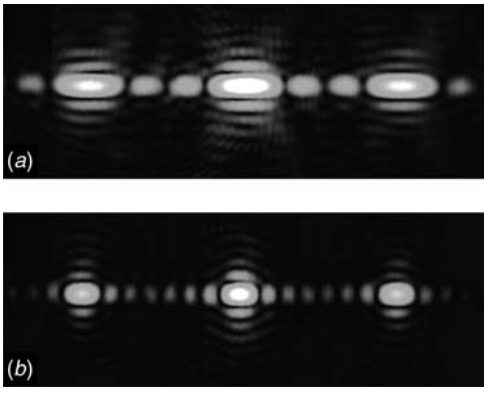

Figure 8.17
Region of u between about $\pm 2\pi/d$ of the diffraction patterns of N parallel slits: (a) $N = 4$; (b) $N = 8$. In this experiment, the slit arrays were masked by a circular aperture, whose transform is convolved with (8.48).

which there are $N - 2$ between the principal maxima. In fact, these principal maxima approximate to the δ-functions of (8.46), namely $\delta(u - 2m\pi/d)$.

The conditions for the production of principal maxima are that $ud/2 = m\pi$. Since for normal incidence $u = 2\pi \sin\theta/\lambda$, we have

$$d \sin\theta = m\lambda, \tag{8.49}$$

the well-known equation for the diffraction grating.

8.5.4 Diffraction gratings

The diffraction grating is a one-dimensional periodic array of similar apertures. If the grating is used in transmission, the apertures are narrow slits; if in reflection they are narrow mirrors. Because they are important interferometric instruments, gratings will be discussed in depth in §9.2; here we shall only briefly outline the Fraunhofer diffraction theory of the basic grating, because it provides a useful basis for understanding other systems, such as the hologram and image formation. If each slit has transmission function $b(x)$, and the line spacing is d, the complete transmission function is

$$f(x) = b(x) \otimes \sum_{n=-N/2}^{N/2} \delta(x - nd), \tag{8.50}$$

where a total number N slits has been assumed. When $N \to \infty$, the transform of the $\sum$ is given by (8.46) and

$$\psi(u) = B(u) \sum_{m=-\infty}^{\infty} \delta(u - 2\pi m/d). \tag{8.51}$$

Now we should recall the general definition of u (8.16); for light incident at angle θ_0 to the axis, and diffracted to angle θ, we have

$$u = \frac{2\pi}{\lambda}(\sin\theta - \sin\theta_0). \tag{8.52}$$

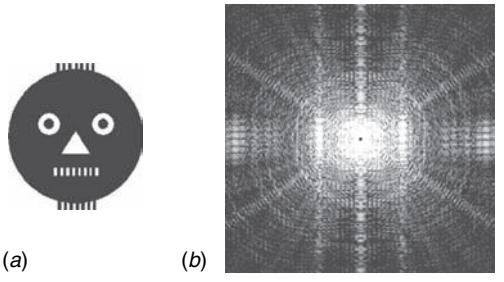

Figure 8.18
(*a*) Face of a gentleman. (*b*) His diffraction pattern. Contrast has been enhanced, and the δ-function at the origin has been masked, in order to bring out the various details discussed in the text.

Box 8.2 An example including many of the principles of two-dimensional diffraction patterns

In this example, we shall try to construct the diffraction pattern of the gentleman illustrated in Fig. 8.18(*a*). The mask is considered as a two-dimensional amplitude object, with zero phase at all points, and transmission function either 0 or 1.

First, we use Babinet's theorem which relates the function to a complementary mask in which the face is white on a black background, and all information lies within a bounded region. The radius of this bounded region r determine the smallest detail in the pattern, $u_0 \equiv 2\pi/r$. The result is a δ-function at the origin. Next, we consider the two eyes. They are annuli of diameter about $r/4$ and so they contribute a J_0 function centred on the origin, with rings having radii approximately multiples of $4u_0$. Because there are two eyes, these rings are crossed by vertical fringes spaced by $2u_0$. The nose is a triangle. Its transform has three-fold symmetry, but because it is a real function, the diffraction pattern also has a centre of symmetry; therefore the pattern has six-fold symmetry. The major features of the triangle are its edges. These create streaks in the directions normal to the edges, and these streaks dominate the pattern, forming a six-pointed star. The teeth, beard and hair are periodic functions limited by a rectangular border, longer in the horizontal direction. The transforms of these functions are each a periodic set of δ-functions, separated by about $24u_0$, each convolved with a sinc$\times$sinc function (the transform of a rectangular aperture) stretched in the vertical direction. Since there are three such arrays, one with phase π different from the other two, this pattern is crossed by some rather complicated horizontal interference fringes with spacing about u_0. Having descibed these details, we can now compare them with the calculated diffraction pattern of the gentleman's portrait in Fig. 8.18(*b*).

Since $\sin\theta$ and $\sin\theta_0$ lie between -1 and 1, the maximum *observable* value of u is $4\pi/\lambda$. So that, although (8.51) is defined for all m, the diffraction condition is in general

$$m\lambda = d(\sin\theta - \sin\theta_0). \tag{8.53}$$

The amplitudes of the various orders of diffraction are given by the transform of the individual aperture, $B(u)$. A common example is a square-wave grating (Ronchi ruling) where $b(x) = \mathrm{rect}(2x/d)$. Without repeating the details, one immediately sees from Fig. 4.3 that the even orders of diffraction are missing and the odd orders have steadily decreasing intensity. Although Fig. 4.3 does not show the zero order, it must be added here because $b(x)$ is positive definite and $\psi(0)$ is its integral (see §8.3.5), which is non-zero. The existence of a strong zero order for a positive-definite function has important consequences, which will be discussed in §9.2.4 and §12.5.

A finite grating (all *real* gratings are, of course, finite) is given by summing (8.50) to finite N. This is conveniently expressed by multiplying the infinite sum by a 'window function' of length Nd which 'transmits' only N δ-functions. Then the grating is represented by

$$f(x) = b(x) \otimes \left[\sum_{n=-\infty}^{\infty} \delta(x - nd) \cdot \mathrm{rect}(x/Nd) \right]. \tag{8.54}$$

Notice the order of the operations (i.e. the positions of the large brackets); it is important to carry out the product first, and the convolution afterwards, in order to represent a finite number of complete slits. The reverse order might give incomplete slits at the end. The difference here is minor, but it is not difficult to construct examples for which the order of convolution and product is very important. Convolution and multiplication are *not* associative.

The diffraction pattern of (8.54)

$$\psi(u) = B(u) \cdot \left[\sum \delta\left(u - \frac{2\pi m}{d}\right) \otimes \mathrm{sinc}\left(\frac{uNd}{2}\right) \right] \tag{8.55}$$

has the following characteristics. There are well-defined orders of diffraction (for large N) as defined in (8.53) but each one has a $\mathrm{sinc}(uNd/2)$ profile. This has width (from the peak to the first zero) $\Delta u = 2\pi/Nd$, which is $(1/N)$ of the distance between the orders.

8.5.5 Interference pattern of a lattice of pinholes

The diffraction pattern of a two-dimensional array retains the angles of the original object.

We can now extend our results to an array of pinholes, periodic in x and y, which we may call a two-dimensional lattice. We can approach this through a set of four pinholes, at positions $\pm(x_1, y_1), \pm(x_2, y_2)$, see Fig. 8.19(*a*). We have to evaluate the expression

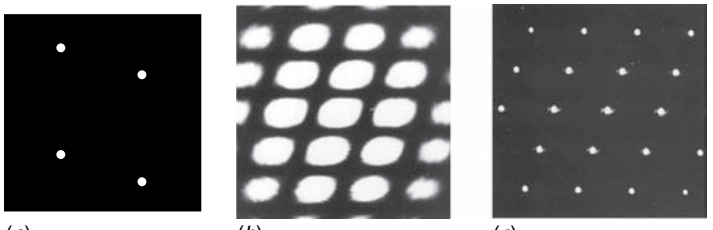

Figure 8.19
(*a*) Two pairs of pinholes; (*b*) diffraction pattern of (*a*), showing crossed fringes; (*c*) reciprocal lattice – the diffraction pattern of an extended lattice of pinholes based on (*a*) as unit cell.

$$\begin{aligned}\psi(u,v) &= \sum \exp[-\mathrm{i}(ux+vy)] \\ &= 2[\cos(ux_1+vy_1)+\cos(ux_2+vy_2)] \\ &= 4\cos\left(u\frac{x_1+x_2}{2}+v\frac{y_1+y_2}{2}\right)\cos\left(u\frac{x_1-x_2}{2}+v\frac{y_1-y_2}{2}\right).\end{aligned} \tag{8.56}$$

As in §8.5.1, we see that this function has maxima at values of u and v given by the equations

$$\begin{aligned}u(x_1+x_2)+v(y_1+y_2) &= 2m_1\pi, \\ u(x_1-x_2)+v(y_1-y_2) &= 2m_2\pi,\end{aligned} \tag{8.57}$$

where m_1 and m_2 are integers. The interference pattern is therefore the product of two sets of linear fringes, each set being perpendicular to the separation of the pairs of holes (Fig. 8.13). Such **crossed fringes** are shown in Fig. 8.19(*b*).

Box 8.3 The symmetry of diffraction patterns

The Fourier transform of a two-dimensional function has the same axial symmetry as the original function, since rotating the object by a certain angle rotates the transform by the same angle. In addition, if the function is real, the transform intensity must be centro-symmetrical. Now, if the function has an even-fold axial symmetry, the centro-symmetry occurs naturally, but if it has odd-fold symmetry, the centro-symmetry has to be added. This results in a striking difference between the patterns of odd- and even-fold masks, which is illustrated by Fig. 8.20, where the diffraction pattern of a regular hexagon of holes is compared with that of a regular pentagon. These patterns have six- and *ten*-fold symmetry respectively. There are also important qualitative differences between the patterns. The former (6) is the square of a continuous real function, which has either positive or negative values, and therefore its square has clear and continuous zero lines. However, the latter (5) is the square modulus of a complex function, which can go from positive to negative without passing through zero. The zero regions therefore do not need to be continuous. This difference can be seen in the figure.

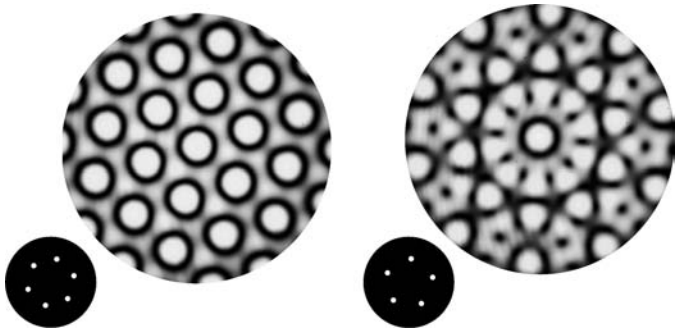

Figure 8.20

Diffraction patterns of a regular hexagon of holes and a regular pentagon of holes. The pentagon must be produced very accurately for the diffraction pattern to have 10-fold symmetry, since any slight error produces a pattern that has clear two-fold symmetry! (Experiment by Igor Yulevich)

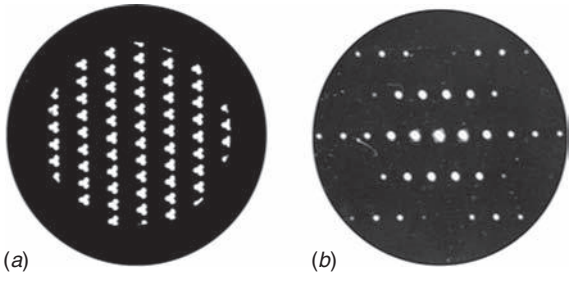

Figure 8.21

(*a*) A lattice of parallel apertures. (*b*) Diffraction pattern of (*a*).

By reasoning analogous to that of §8.5.3, we can see that as the lattice of pinholes, with these four points providing the unit cell, increases in extent, the conditions for constructive interference become more precisely defined. In the limit, the interference pattern then becomes a collection of points, also arranged on a lattice (Fig. 8.19(*c*)). This is called the **reciprocal lattice** of the original (**direct**) lattice, because u and v are reciprocally related to the separations of the pairs of holes in Fig. 8.19(*a*). The concept was discussed mathematically in Chapter 4 as the Fourier transform of a periodic array of δ-functions, and is the basis of crystal diffraction (§8.6.3).

8.5.6 Interference pattern of a lattice of parallel apertures

If we have an extended lattice of similar apertures such as Fig. 8.21(*a*), we may consider it as the convolution of a single aperture with the lattice having translations **a** and **b**. Then the diffraction pattern (Fig. 8.21(*b*)) is the product of the interference function due to the lattice and the diffraction pattern of the single aperture. In other words, the reciprocal lattice pattern is multiplied by the diffraction pattern of the unit. When the unit is simple, then the influence of the diffraction function is clear; if the pattern is more complicated, as in Fig. 8.22(*a*), the result is still true, but the diffraction function is more difficult to recognize. Note that there may be several choices for **a** and **b**, but the final

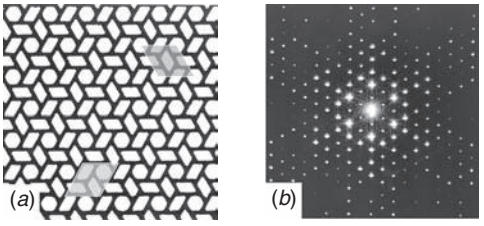

Figure 8.22
(*a*) Provided that the object repeats exactly, one can always define a unit cell, which may not be unique; two possibilities are shown shaded. (*b*) Diffraction pattern of (*a*).

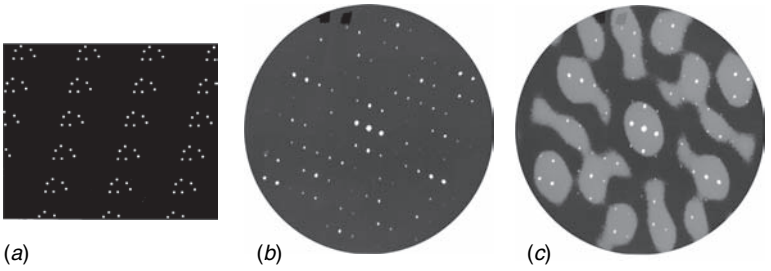

Figure 8.23
(*a*) Set of holes representing a lattice of chemical molecules. (*b*) Diffraction pattern of (*a*). (*c*) Diffraction pattern of a unit of (*a*), with (*b*) superimposed.

result is always the same! Figure 8.23 shows a set of holes representing a lattice of molecules (*a*) and its diffraction pattern (*b*). The relationship to the diffraction function is shown in (*c*).

We may look upon the diffraction pattern of a repeated unit in another way. A single unit of Fig. 8.23(*a*) gives a particular diffraction function; the effect of putting the units on a lattice is, apart from making the pattern stronger, to make the diffraction pattern observable only at the reciprocal lattice points. This process is called **sampling**; it is important in dealing with diffraction by crystals, and has many applications in image processing and communication theory.

If we regard the set of apertures as a two-dimensional diffraction grating, the reciprocal lattice represents its set of orders. Each reciprocal lattice point is an order of diffraction (§8.5.3), specified now by *two* integers, $\tilde{h}^\star$ and $\tilde{k}^\star$, instead of one. In three dimensions (§8.6) we shall see that three integers are needed.

The Earth's atmosphere behaves rather like a random mask in front of a telescope. In §12.7, you can see how Fraunhofer diffraction is used to overcome this problem.

8.5.7 Diffraction by a random array of parallel apertures

Suppose that the diffracting object consists of a collection of parallel apertures arranged randomly. We can regard the collection as the convolution of the single aperture with a set of δ-functions representing the aperture positions.

We therefore need to determine the diffraction pattern of a set of N randomly arranged δ-functions. This problem is expressed mathematically as

$$\psi(u,v) = \int\int \sum_{n=1}^{N} \delta(x-x_n)\,\delta(y-y_n)\exp[-\mathrm{i}(ux+vy)]\,\mathrm{d}x\,\mathrm{d}y$$
$$= \sum \exp[-\mathrm{i}(ux_n+vy_n)], \qquad (8.58)$$

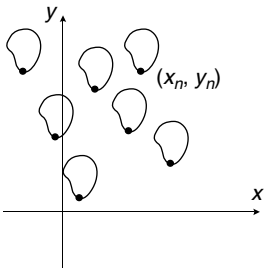

Figure 8.24

A random set of similar apertures, showing the origin (x_n, y_n) of an individual one.

where the nth aperture has random origin at (x_n, y_n) (Fig. 8.24). This sum cannot be evaluated in general. But the intensity of the transform

$$I(u,v) = |\psi(u,v)|^2 \tag{8.59}$$

can be evaluated by writing the square of the sum (8.58) as a double sum:

$$|\psi(u,v)|^2 = \left|\sum_{n=1}^{N} \exp[-\mathrm{i}(ux_n + vy_n)]\right|^2$$
$$= \sum_{n=1}^{N}\sum_{m=1}^{N} \exp\{-\mathrm{i}[u(x_n - x_m) + v(y_n - y_m)]\}. \tag{8.60}$$

Now since x_n and x_m are random variables, $(x_n - x_m)$ is also random and so the various terms usually make randomly positive or negative contributions to the sum. There are two exceptions to this statement. First, the terms with $n = m$ in the double sum all contribute a value $\mathrm{e}^{\mathrm{i}0} = 1$, and there are N of them, so that the expected value of the double sum (8.60) is N. Second, when $u = v = 0$, *all* the terms in the sum contribute 1, and the value of (8.60) is N^2, so that we can write the statistical expectation:

$$I(u,v) = N + N^2\overline{\delta}(u,v), \tag{8.61}$$

where $\overline{\delta}(u,v)$ has the value of unity at $(u,v) = (0,0)$ and is zero elsewhere (Kronecker delta). The function (8.61) represents a bright spot of intensity N^2 at the origin and a uniform background of intensity N.

Of course a truly random distribution does not exist in practice and the above description must really be modified. First, if the N points all lie within a finite region (say a square of side D) the terms in the double sum (8.60) will all have positive values even if u and v deviate from zero by as much as $\pi/2D$. So the spot at the origin has a finite size, of this order of magnitude. Second, the randomness of the distribution might be restricted to avoid the overlapping of neighbouring apertures. This can be shown to result in a weak structure appearing in the background term. Third, because N is finite, the oscillatory terms in (8.60) do not cancel exactly and there are fluctuations in the uniform background which are called 'speckle'.

Speckle patterns are the interference patterns of a finite number of randomly phased waves.

We now recall that the object was expressed as the convolution of a single aperture with the random array of δ-functions. Its diffraction pattern is then the product of the diffraction pattern of a single object and the function (8.61). At all points except the origin and its immediate vicinity the result is an intensity just N times the intensity of the single aperture's diffraction pattern. Only at the origin itself there appears a bright spot, with intensity N^2 times that of the zero order of the single aperture diffraction pattern. The result is illustrated by Fig. 8.25. If the number of apertures becomes *very* large, the bright spot is the only observable feature. However, if the *phases* of the apertures are

Figure 8.25
(*a*) Mask of random parallel apertures; (*b*) diffraction pattern of one unit of (*a*); (*c*) complete diffraction pattern of (*a*); the centre inset is an under-exposed part of the diffraction pattern showing the strong spot at the centre, at the end of the arrow. Notice also that the region around the central spot is dark, indicating some correlations between the positions of the apertures, since they cannot overlap.

random, as well as their positions, the central peak may be completely absent. A practical application of this analysis to astronomical imaging, called **speckle interferometry**, will be discussed in §12.7.

8.6 Three-dimensional interference

Fraunhofer diffraction by three-dimensional obstacles has been of major importance in the development of modern science, because it has allowed us to visualize the structures of materials down to the atomic scale. The most important application is diffraction by a crystal. It is not just a straightforward extension from one and two dimensions to three. The theory developed so far has essentially described the diffraction pattern as the solution of a boundary-value problem, in which the incident wave on the surface (mask) was allowed to develop according to Huygens' principle, as expressed mathematically by the Kirchhoff–Huygens theory. If the scattering object is three-dimensional, the boundary conditions are over-defined, and a diffraction pattern consistent with all of them may not exist. In fact we shall see that the Fourier transform alone does not describe the diffraction pattern, but another condition, described by the construction of the Ewald sphere has also to be satisfied, and tells us *which parts* of the transform contribute to the pattern.

8.6.1 Crystals and convolutions

Crystallography has been a major motivation for studying Fraunhofer diffraction. Many crystal structures were elucidated intuitively using the principles in this chapter.

Crystals are three-dimensional gratings and diffract waves of compatible wavelengths: neutrons, electrons, atoms and X-rays. The general principles of diffraction by any of these waves are the same; just the relevant parameters must be used. The discussion here will centre around X-rays. The theory was originally developed by M. von Laue for the **weak scattering** case, which means that the probability of a wave being scattered *twice* within the crystal is negligible.

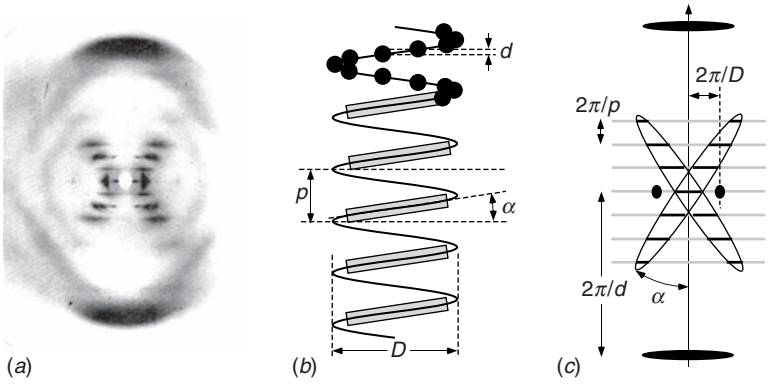

Figure 8.26

Interpretation of the X-ray diffraction by Na-DNA strands. (*a*) The diffraction pattern. (*b*) The basic features of the helix used in the interpretation. Only one set of tilted apertures is shown and the black dots represent P atoms. (*c*) Diffraction patterns of these features. (Bragg (1975))

Box 8.4 Example: X-ray diffraction by DNA strands

Probably the most famous X-ray diffraction pattern of a non-crystalline material ever taken is that of Na-DNA strands photographed by Rosalind Franklin in 1952. J. D. Watson wrote in *The Double Helix*: 'The instant I saw the picture my mouth fell open and my pulse began to race. The pattern was unbelievably simpler than those obtained previously ('A' form). Moreover, the black cross of reflections which dominated the picture could arise only from a helical structure.'

You can understand this from what we have learnt so far. First, the sample was a random collection of strands with the same orientation, so the diffraction pattern is the same as that of a single strand, except for the zero order, which was masked out. Then, as Bragg (1975) points out, the diffraction pattern shown in Fig. 8.26(*a*) is dominated by scattering from the heavy P atoms arranged regularly along a helix, at equal intervals d along the z-axis. The helix itself, seen from the side, appears *roughly* as two periodic arrays of slits inclined at the pitch angle $\pm\alpha$ (Fig. 8.26(*b*)), and separated by the pitch length p. This gives a periodic set of lines with spacing $2\pi/p$ normal to k_z multiplied by a 'sinc' stretched out along lines at $\pm\alpha$ to k_z. Furthermore, the regular spacing of P atoms in the base-pairs along the z-direction gives strong reflections at $k_z = \pm 2\pi/d$. These features are shown in Fig. 8.26(*c*). You can deduce from the picture that p/d is about 10, which means that there are 10 P atoms in each turn of the spiral – correct. The strong spots along the k_x-axis result from the predominance of P atoms along the edges of the strand in the side projection, lines of atoms at $x = \pm D/2$.

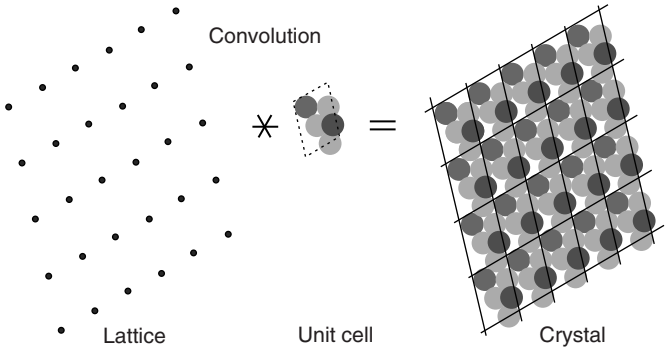

Figure 8.27
Two-dimensional representation of a crystal structure as the convolution between the lattice and a unit cell.

A crystal is a collection of atoms. From the point of view of X-ray diffraction, since X-rays are scattered only by electrons,[1] a crystal can be considered as a periodic set of positions represented by δ-functions, convolved with the electron density function of the group of atoms being repeated, which may be one or more molecular units. The periodic set of δ-functions is called the **crystal lattice** and the repeated spatial volume associated with each δ-function is called the **unit cell**. The group of atoms resides in the same position and orientation in every unit cell. Therefore we can regard the crystal as composed of the unit cell contents convolved with the lattice positions. These ideas are illustrated in two dimensions in Fig. 8.27. This would lead to an infinite crystal. We therefore limit its extent by multiplying the lattice by a shape function, the external boundary.

From the convolution theorem, therefore, we see that **the transform of the electron density of the crystal is the transform of the lattice, convolved with that of the shape function, and multiplied by the transform of the contents of the unit cell**. This is a *complete* outline of the theory of X-ray diffraction. All that remains is to fill in the details! In the following section we shall discuss diffraction by the crystal lattice, and in §8.8.2 we shall touch on the problems involved in determining the atomic positions within the unit cell.

8.6.2 Diffraction by a three-dimensional lattice

We are concerned with the diffraction pattern produced by a three-dimensional lattice of δ-functions. Suppose we have an incident wave with wave-vector $\mathbf{k}_0$, and that it is diffracted to a direction with vector $\mathbf{k}$. In order to conserve energy, the incident and diffracted waves must have the same frequency,

$$\omega_0 = ck, \tag{8.62}$$

and therefore the moduli of $\mathbf{k}$ and $\mathbf{k}_0$ must be equal,

$$|\mathbf{k}| = |\mathbf{k}_0|. \tag{8.63}$$

[1] Neutrons are scattered by the nuclei of the atoms, and so neutron diffraction investigates the density of nuclear matter.

Elastic scattering: no energy is lost by the scattered wave. Inelastic scattering: energy is lost to, or gained from excitations (e.g. phonons) in the scattering object.

Alternatively, we can say that the waves must have the same time variation, $\exp(-\mathrm{i}\omega_0 t)$, since this must pass unchanged through the calculation of diffraction by a *stationary* lattice. This is called **elastic scattering**. The condition (8.63) can be represented geometrically by saying that $\mathbf{k}_0$ and $\mathbf{k}$ must be radius vectors of the same sphere, which is called the **Ewald sphere, reflecting sphere** or **sphere of observation** (Fig. 8.28). An order of diffraction satisfying this condition is called a Bragg reflection, after W. L. Bragg who, in 1912, introduced the idea of reflection of X-rays by lattice planes.

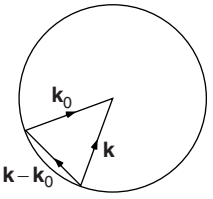

Figure 8.28

Ewald sphere, or sphere of observation.

We can now calculate the total wave scattered by a lattice of δ-function point scatterers. The point $\delta(\mathbf{r}-\mathbf{r}')$ scatters a wave of complex amplitude proportional to the incident wave at that point, i.e. $b_\mathrm{s}\exp[\mathrm{i}\mathbf{k}_0\cdot\mathbf{r}']$, where b_s is the scattering strength.[2] In the direction $\mathbf{k}$ this wave will have amplitude

$$\begin{aligned}\psi &= b_\mathrm{s}\exp[\mathrm{i}\mathbf{k}_0\cdot\mathbf{r}']\,\exp[\mathrm{i}\mathbf{k}\cdot(\mathbf{r}-\mathbf{r}')]\\ &= b_\mathrm{s}\exp[\mathrm{i}\mathbf{k}\cdot\mathbf{r}]\exp[\mathrm{i}(\mathbf{k}_0-\mathbf{k})\cdot\mathbf{r}'].\end{aligned}\tag{8.64}$$

The total diffracted beam with wave-vector $\mathbf{k}$ is therefore given by summing (8.64) over all positions $\mathbf{r}'$ of the lattice of δ-functions with unit-cell vectors $\mathbf{a}$, $\mathbf{b}$, $\mathbf{c}$. Following §4.8,

$$f(\mathbf{r}') = b_\mathrm{s}\sum_{\tilde{h},\tilde{k},\tilde{l}=-\infty}^{\infty}\delta(\mathbf{r}-\tilde{h}\mathbf{a}-\tilde{k}\mathbf{b}-\tilde{l}\mathbf{c})\quad(\tilde{h},\tilde{k},\tilde{l}\text{ integers}),\tag{8.65}$$

which reduces to the summation

$$\Psi(\mathbf{k}) = b_\mathrm{s}\exp(\mathrm{i}\mathbf{k}\cdot\mathbf{r})\sum_{\tilde{h},\tilde{k},\tilde{l}=-\infty}^{\infty}\exp\{\mathrm{i}[(\mathbf{k}-\mathbf{k}_0)\cdot(\tilde{h}\mathbf{a}+\tilde{k}\mathbf{b}+\tilde{l}\mathbf{c})]\}.\tag{8.66}$$

In the same way as we saw in §4.12, the summation is clearly zero unless the phases of all the terms are multiples of 2π:

$$(\mathbf{k}-\mathbf{k}_0)\cdot(\tilde{h}\mathbf{a}+\tilde{k}\mathbf{b}+\tilde{l}\mathbf{c}) = 2\pi s\quad(s\text{ is an integer}).\tag{8.67}$$

One trivial solution to this equation which also satisfies (8.63) is

$$\mathbf{k}-\mathbf{k}_0 = 0\quad(s=0).\tag{8.68}$$

But there is also a host of other solutions.

Each reciprocal lattice vector represents a vector distance between atomic planes in the crystal.

8.6.3 Reciprocal lattice in three dimensions

These other solutions to (8.67) can be derived by means of a reciprocal lattice (§8.5.5). The vectors $\mathbf{k}-\mathbf{k}_0$ between points in the reciprocal lattice are also

[2] When the value of b_s is very small, multiple scattering of the waves, which would be proportional to b_s^2, can be neglected. This is true for X-rays and neutrons, but not for electrons. See Cowley (1995).

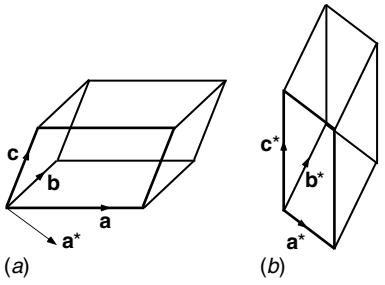

Figure 8.29
(*a*) Direct lattice unit cell. (*b*) Reciprocal lattice unit cell. In (*a*) the vector **a*** is shown to be normal to **b** and **c**.

solutions of (8.67). In three dimensions, the reciprocal lattice vectors $\mathbf{a}^\star$, $\mathbf{b}^\star$ and $\mathbf{c}^\star$ are defined in terms of the real lattice vectors, which were shown in the appendix to Chapter 4 to be

$$\begin{aligned} \mathbf{a}^\star &= 2\pi V^{-1}\, \mathbf{b} \times \mathbf{c}, \\ \mathbf{b}^\star &= 2\pi V^{-1}\, \mathbf{c} \times \mathbf{a}, \\ \mathbf{c}^\star &= 2\pi V^{-1}\, \mathbf{a} \times \mathbf{b}, \end{aligned} \tag{8.69}$$

where $V = \mathbf{a} \cdot \mathbf{b} \times \mathbf{c}$ is the volume of the unit cell in real space.

It now follows that if $(\mathbf{k} - \mathbf{k}_0)$ can be written as the sum of integral multiples of $\mathbf{a}^\star$, $\mathbf{b}^\star$ and $\mathbf{c}^\star$,

$$(\mathbf{k} - \mathbf{k}_0) = \tilde{h}^\star \mathbf{a}^\star + \tilde{k}^\star \mathbf{b}^\star + \tilde{l}^\star \mathbf{c}^\star \quad (\tilde{h}^\star, \tilde{k}^\star, \tilde{l}^\star \text{ are integers}), \tag{8.70}$$

the summation (8.66) diverges; otherwise it is zero. This defines the three-dimensional reciprocal lattice of δ-functions at the points (8.71) (Fig. 8.29).

When X-rays are reflected by angle 2θ from a single set of lattice planes spaced by a, (8.63) gives $(k - k_0) = (4\pi/\lambda)\sin\theta$ and (8.70) simplifies to the well-known **Bragg law of diffraction**,

$$n\lambda = 2a \sin\theta, \tag{8.71}$$

where we replaced $\tilde{h}^\star$ by the conventional n.

The observed diffraction pattern consists of those beams that satisfy both (8.63) and (8.71). The two conditions are represented geometrically by the Ewald sphere and the reciprocal lattice respectively. One therefore draws the Ewald sphere and the reciprocal lattice superimposed and looks for intersections (Fig. 8.30). The sphere passes through the origin of reciprocal space (because $\mathbf{k} - \mathbf{k}_0 = 0$ is a point on it) and its centre is defined by the direction of the vector $\mathbf{k}_0$. Mathematically, the exact intersection of a sphere and a set of discrete points is negligibly probable; but because neither an exactly parallel beam nor a purely monochromatic source of X-rays exists, the sphere has a non-zero thickness and diffraction by a crystal does in fact occur. (One important point is the trivial solution (8.68) which ensures that at least one 'diffracted' beam – the unscattered one – exists to carry away the incident energy.) When 'white' X-rays are used, containing a broad band of wavelengths, many diffracted

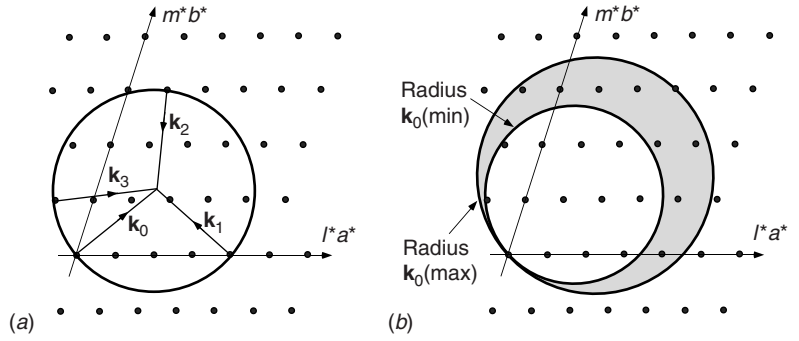

Figure 8.30

(*a*) Two-dimensional representation of the intersection between the Ewald sphere of observation and the reciprocal lattice, showing directions of the incident beam $\mathbf{k}_0$ and of three possible diffracted beams $\mathbf{k}_1$, $\mathbf{k}_2$ and $\mathbf{k}_3$. (*b*) With broad-band radiation, $\mathbf{k}_0$ is not well defined, and all reciprocal lattice points in the shaded region between the two spheres representing the maximum and minimum values of $\mathbf{k}_0$ will reflect; the resulting diffraction pattern is called a 'Laue photograph' and can be used to determine the lattice structure and orientation of a crystal (Fig. 8.31).

Figure 8.31

Laue photograph of beryl. It shows crystal diffraction using 'white' X-rays having a large range of wavelengths. (From Lipson (1970))

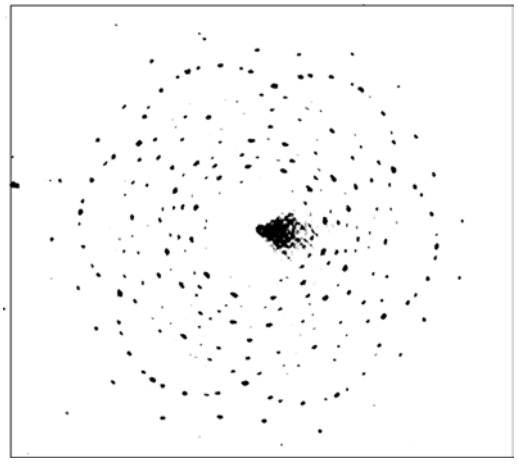

In Fig. 8.21 we saw an example of the diffraction pattern of a crystal with a complicated unit cell.

beams can occur, and we have a 'Laue photograph', but quantitative interpretation of such pictures is difficult and they are mainly used for qualitative purposes (Fig. 8.31). By controlling the direction of the incident beam $\mathbf{k}_0$ and moving the crystal and recording screen in appropriate ways, it is possible to produce a section of the reciprocal lattice with, say, one of the indices $\tilde{h}^\star$, $\tilde{k}^\star$, $\tilde{l}^\star$ constant. Such a photograph is shown in Fig. 8.1.

8.6.4 Diffraction by a complete crystal

We can see from Figs. 8.1 and 8.22 that the intensities of the orders of diffraction vary in an irregular way; some are strong and some weak. This variation

arises as it did in Fig. 8.21 as a result of multiplying the reciprocal lattice (the interference function) by the transform of the atomic positions within the unit cell, the diffraction function. A major part of crystallography consists of interpreting these variations (§8.8.2). In the case of X-ray and neutron diffraction it is usually correct to assume that the scattering is weak, so that only single scattering events need to be taken into account. Electron diffraction is different, and corrections must be applied for multiply scattered waves. The results are too complicated to discuss here (see Cowley (1995)) but also contribute to the differences between the intensities of the various orders. One can also see that the spots in Fig. 8.1 have finite size. This is caused by the geometry of the apparatus – finite size of X-ray focus, angular divergence of beam and so on. Even if these factors could be allowed for, however, the spots would still have a non-zero size because of the shape function of the crystal (§8.6.1). This effect can only be observed if the sample is very small in at least one dimension (e.g. a nano-crystal or a surface).

8.7 Inelastic scattering: The acousto-optic effect

Acousto-optic devices are also used for laser scanning and modulation.

Another three-dimensional diffraction effect that can conveniently be treated in the weak scattering limit by the concepts of the reciprocal lattice and observation sphere is the **acousto-optic effect**, which is basically a situation in which a sinusoidal refractive index modulation is impressed on an initially uniform material by a longitudinal sound or ultrasonic wave. Acousto-optic cells are widely used as fast optical switches or shutters, because they allow an incident optical wave to be diffracted selectively into a chosen direction by application of an acoustic signal. Moreover, since the frequency of the diffracted wave is shifted by an amount equal to the acoustic wave frequency, acousto-optic devices can also be used for changing a laser frequency in a controlled manner. If the acoustic wave is not sinusoidal, the acousto-optic cell can be used as a spectrum analyzer.

A particularly simple case is that of an ultrasonic plane wave propagating in a homogeneous compressible material such as water.[3] Because of the finite compressibility of water, the local density and hence refractive index responds to the oscillating pressure of the ultrasonic wave, creating a propagating sinusoidal modulation of amplitude A to the refractive index:

$$n(\mathbf{r}) = n_{\mathrm{W}} + A\cos(\mathbf{q}\cdot\mathbf{r} - \Omega t), \tag{8.72}$$

where n_{W} is the refractive index of water at atmospheric pressure and the ultrasonic wave has frequency Ω and wave-vector $\mathbf{q}$. The velocity of sound in water

[3] Water is a good medium for demonstrating the effect. Crystals such as $PbGeO_4$ have been developed to use it for solid-state applications.

is $v_s \approx 1200\,\mathrm{m\,s^{-1}}$, and so for a frequency $\Omega = 2\pi \times 10$ MHz, the wavelength $2\pi/q$ of the ultrasonic wave is about 0.1 mm, $\gg \lambda_{\mathrm{light}}$. The water behaves as a three-dimensional phase grating with this period, and because $v_s \ll c$ we first assume that an incident light wave sees it as a stationary modulation.

This is a well-defined problem, but one whose exact solution is elusive because the incident wave is refracted as well as diffracted by the medium. We only discuss here a very approximate approach that illustrates the physics of the problem; further details can be found in the books by Born and Wolf (1999), Korpel (1997) and Yariv (1991).

Diffraction of light by a weak three-dimensional sinusoidal grating can be treated by the same techniques that we used for crystal diffraction.[4] The grating is represented by a three-dimensional scattering function $f(\mathbf{r})$. In §13.3.1 we shall see formally that $n - 1$ for a material is proportional to its density, and since the scattering strength is also proportional to the density we can write $f(\mathbf{r}) = \eta[n(\mathbf{r}) - 1]$ to represent this, where η is a constant depending on the material.

Now the modulation in (8.72) $A \ll 1$ (typically $< 10^{-6}$), so that

$$\begin{aligned} f(\mathbf{r}) &= \eta[n_{\mathrm{W}} - 1 + A\cos(\mathbf{q}\cdot\mathbf{r} - \Omega t)] \\ &= \eta[n_{\mathrm{W}} - 1] + \frac{1}{2}\eta A \exp[\mathrm{i}(\mathbf{q}\cdot\mathbf{r} - \Omega t)] + \frac{1}{2}\eta A \exp[-\mathrm{i}(\mathbf{q}\cdot\mathbf{r} - \Omega t)]. \end{aligned} \tag{8.73}$$

The Fourier transform of this function in reciprocal space $\mathbf{u}$ is

$$F(\mathbf{u}) = (n_{\mathrm{W}} - 1)\delta(\mathbf{u}) + \frac{1}{2}\mathrm{i}A\,\mathrm{e}^{-\mathrm{i}\Omega t}\delta(\mathbf{u} - \mathbf{q}) + \frac{1}{2}\mathrm{i}A\,\mathrm{e}^{\mathrm{i}\Omega t}\delta(\mathbf{u} + \mathbf{q}), \tag{8.74}$$

which represents three δ-functions, a strong one at the origin and two weak ones at $\pm\mathbf{q}$, oscillating at $\pm\Omega$ respectively. When we recall the time-variation $\exp(\mathrm{i}\omega t)$ of the incident light, this means that the diffracted waves have frequencies ω and $\omega \pm \Omega$ respectively.

The diffraction problem is then represented by the superposition of the sphere of observation on this Fourier transform (Fig. 8.32). It is shown first for incidence normal to $\mathbf{q}$ in Fig. 8.32(*a*); it is clear that there is no diffracted beam in this case. There are only two angles of incidence at which diffraction occurs, $\pm\alpha$, shown for $+\alpha$ in Fig. 8.32(*b*). The angles α are clearly given by

$$q = \pm 2k_0 \sin\alpha. \tag{8.75}$$

Putting $q = 2\pi/\Lambda$ and $k_0 = 2\pi/\lambda$, this translates to

$$\lambda = 2\Lambda \sin\alpha, \tag{8.76}$$

[4] We should remark that the wavelength of light is so large compared to the interatomic spacing that any crystalline reciprocal lattice points are completely off scale (by about five orders of magnitude) compared to the region of reciprocal space discussed here.

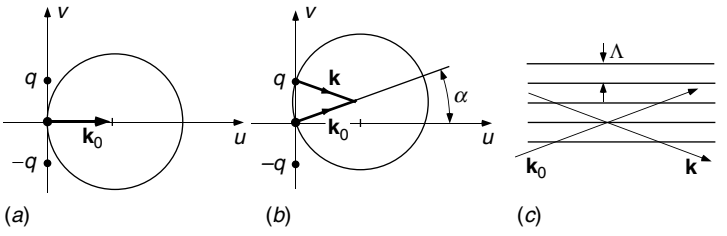

Figure 8.32

Reciprocal space construction for diffraction of an incident wave-vector $\mathbf{k}_0$ by an ultrasonic wave of wave-vector $\mathbf{q}$: (*a*) normal incidence; (*b*) at the angle α for Bragg diffraction; (*c*) interpretation in terms of Bragg's law.

which is the familiar form of the Bragg diffraction formula (8.71) for lattice planes with spacing Λ (see Fig. 8.32(*c*)).

Generally, the size of a sample or crystal used for acousto-optic experiments may not be large compared with the acoustic wavelength. In such a case, the transmission function is multiplied by a shape function (§8.6) with value 1 within the sample, 0 outside. In its transform, each of the three δ-functions is therefore convolved with the transform of the shape function, giving it a finite size. This means that the Bragg condition (8.76) need not be fulfilled exactly.

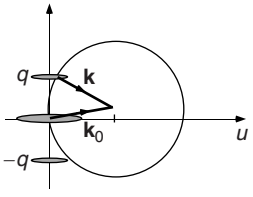

Figure 8.33

Reciprocal space construction for diffraction by an ultrasonic wave in a thin sample.

An extreme case occurs when the sample is thin in the direction normal to $\mathbf{q}$, so that the transform points are greatly elongated in this direction (Fig. 8.33). Diffraction can then be observed for incidence in any direction. It is easy to show that these angles satisfy the two-dimensional diffraction grating equation for oblique incidence (8.53). This is called the **Raman–Nath** scattering limit. In this limit, the diffraction pattern can be calculated by representing the sample as a thin phase grating. If the thickness of the sample is d, and we assume $\mathbf{q}$ to be parallel to the x-direction, we have optical thickness $d[n_\mathrm{W} + A\cos(qx - \Omega t)]$ and therefore the sample behaves as a grating with

$$f(x) = \exp[\mathrm{i}k_0 d(n_\mathrm{W} + A\cos(qx - \Omega t))]. \tag{8.77}$$

If the amplitude of the phase variation $k_0 dA \ll 1$ its Taylor expansion and Fourier transform are

$$f(x) = \exp(\mathrm{i}k_0 d n_\mathrm{W})[1 + k_0 dA\cos(qx - \Omega t)], \tag{8.78}$$

$$F(u) = \exp(\mathrm{i}k_0 d n_\mathrm{W})\left[\delta(u) + \frac{1}{2}\mathrm{i}Ak_0 d\,\mathrm{e}^{-\mathrm{i}\Omega t}\delta(u-q) + \frac{1}{2}\mathrm{i}Ak_0 d\,\mathrm{e}^{\mathrm{i}\Omega t}\delta(u+q)\right], \tag{8.79}$$

indicating the formation of weak first orders surrounding a strong undiffracted zero order. If $Ak_0 d$ is larger, the Fourier transform can be performed by the use of Bessel functions (Appendix A) and shows that the diffracted orders m have amplitudes proportional to $J_m(Ak_0 d)$. Experimentally, it is not difficult to reach the conditions where higher orders have appreciable intensities.

Because the velocity of light is much greater than that of sound, the light essentially sees the grating as stationary. However, the time-dependent amplitudes of the δ-functions $Ak_0 d\,\exp(\pm\mathrm{i}\Omega t)$ do have practical effects. Since the

two diffracted waves are shifted in frequency by $\pm\Omega$ they can, for example, interfere to give a moving fringe pattern. The frequency shift can be simply interpreted as a Doppler effect when the wave is reflected by a moving grating (Problem 8.13), or as the condition for conservation of energy when a phonon is either absorbed or emitted by a photon.

8.8 Advanced topic: Phase retrieval in crystallography

Phase retrieval is an important solution to the phase problem (§8.2.1).

When a diffraction pattern is recorded by photography or any other energy detector, the phase of the wave is lost. Diffraction is such a powerful method of investigating the structure of matter that it is imperative to find a way of applying an inverse Fourier transform to a diffraction pattern in order to reveal directly the structure of the diffracting object. However, the reverse transform has to be applied to the *complex amplitude* pattern, and if the phases are lost, this is not known completely. This is called the **phase problem**, and finding a solution to it, called **phase retrieval**, is extremely important in crystallography and other imaging problems.

Although in principle the phase problem can have no general solution (there is an infinite number of mathematical functions that give the same diffraction pattern intensities), in practice the addition of some reasonable constraints usually leads to a unique solution, and techniques have been developed by which this solution can be found. For their pioneering work in phase retrieval in crystallography, Hauptman and Karle were awarded the Nobel prize for chemistry in 1985. As a result, the interpretation of most crystalline X-ray diffraction patterns has today become a fairly straightforward technical matter, although supplementary techniques are still needed for the most complicated crystals (§12.1.5). The most difficult part is often the preparation of the crystal itself! In this section we discuss the ideas behind the solutions in crystallography, where the diffraction pattern of the crystal is sampled at the reciprocal lattice points (§8.5.6) only. In §8.9 we shall use similar methods for the determination of phase errors in optical systems from image data (notably the Hubble Space Telescope).

8.8.1 A-priori information and constraints

As we pointed out above, some constraints are required to make the solution unique. In crystallography, the object function is the electron density of a crystal which is *real* and *positive*. In an optical system, the object to be determined might be the phase in the aperture stop, where the amplitude is assumed to

be uniform. The second piece of *a-priori* information is an estimate of the dimensional extent of the object, which in crystallography is given by the dimensions of the unit cell of a crystal (known from the reciprocal lattice) and the number of atoms in it; in the optical case this would be the size and shape of the aperture stop.

8.8.2 Direct methods in crystallography

The determination of the crystal structure from the intensities of its X-ray diffraction spots alone is called a **direct method**, and should be contrasted with other techniques which require the addition of further information, such as the heavy-atom method outlined in §12.1.5. Although such methods were first proposed around 1950, their need for quite considerable computations delayed their development till the 1970s, when powerful electronic computers became generally available. In this section we shall outline the ideas behind the direct method, with a simple example. Two useful reviews of the field have been given by Woolfson (1971) and Hauptman (1991).

We saw in §8.6 that a crystal can be described by the convolution between the molecular electron density (or that of a group of molecules with some well-defined geometrical relationship) and the crystal lattice. The diffraction pattern of the former is then sampled at the reciprocal lattice points. The distances and angles between the diffraction spots allow the reciprocal lattice, and hence the real lattice, to be determined easily.

The amplitude of the diffraction pattern at reciprocal lattice point $\mathbf{h}$, defined by (8.71)

$$\mathbf{h} = \tilde{h}^\star \mathbf{a}^\star + \tilde{k}^\star \mathbf{b}^\star + \tilde{l}^\star \mathbf{c}^\star \tag{8.80}$$

is related to the electron density $\rho(\mathbf{r})$ within the unit cell by

$$F(\mathbf{h}) = V^{-1} \iiint_{\text{cell}} \rho(\mathbf{r}) \exp(-\mathrm{i}\mathbf{h} \cdot \mathbf{r}) \, \mathrm{d}^3\mathbf{r}, \tag{8.81}$$

which is the three-dimensional Fourier transform of $\rho(\mathbf{r})$.

Suppose the cell contains N atoms, and for simplicity let each one have electron density $Zs(\mathbf{r})$ with respect to its own origin, where $s(\mathbf{r})$ represents the shape of a 'typical' atom.[5] The difference between one atom and another is here contained in the value of Z, the atomic number. The electron density ρ can then be expressed by the convolution between $s(\mathbf{r})$ and a set of N δ-functions at the

[5] The 'shape of a "typical" atom' is assumed here for pedagogical purposes, and is not a requirement of the method.

atomic positions $\mathbf{r}_j$, where the jth δ-function has strength Z_j. Equation (8.81) can then be written as a sum:

$$F(\mathbf{h}) = S(\mathbf{h}) \sum_{j=1}^{N} Z_j \exp(-\mathrm{i}\mathbf{h} \cdot \mathbf{r}_j), \tag{8.82}$$

where $S(\mathbf{h})$ is the transform of $s(\mathbf{r})$ and is a smooth and reasonably well-known function. Finally, the intensity measured at reciprocal lattice point $\mathbf{h}$ is $|F(\mathbf{h})|^2$:

$$\begin{aligned} |F(\mathbf{h})|^2 &= |S(\mathbf{h})|^2 \left| \sum_{j=1}^{N} Z_j \exp(-\mathrm{i}\mathbf{h} \cdot \mathbf{r}_j) \right|^2, \\ &= |S(\mathbf{h})|^2 \sum_{j=1}^{N} \sum_{k=1}^{N} Z_j Z_k \exp[-\mathrm{i}\mathbf{h} \cdot (\mathbf{r}_j - \mathbf{r}_k)]. \end{aligned} \tag{8.83}$$

In (8.83) there are four unknowns for each position j – these are Z_j and the three components of $\mathbf{r}_j$ – and there are N values of j; in all, $4N$ unknowns. Therefore, if $|F(\mathbf{h})|^2$ is measured at more than $4N$ different values of $\mathbf{h}$, *in principle* there is enough information for all the variables to be determined. Since the measurement of this number of reflections, or even many more, is usually possible, the problem should not only be soluble but even over-determined! The question is, how can the solution be found?

The discussion here will centre around a few key points with the intention of making the ideas clear without mathematical complexity. In this vein, consider a crystal of molecular units each having N *identical* point atoms. Thus all the Z_js are equal, and since the atoms are considered as δ-functions we put $S(\mathbf{h}) = 1$. Now consider the two functions $\rho(\mathbf{r})$ and $\rho^2(\mathbf{r})$. They are

$$\rho(\mathbf{r}) = \sum_{j=1}^{N} \delta(\mathbf{r} - \mathbf{r}_j), \tag{8.84}$$

$$\rho^2(\mathbf{r}) = \beta \sum_{j=1}^{N} \delta(\mathbf{r} - \mathbf{r}_j). \tag{8.85}$$

The former is *required* to be positive (§8.8.1) and the second is obviously so.[6] The Fourier transform of (8.84) is $F(\mathbf{h})$ and that of (8.85) is its auto-correlation

$$F(\mathbf{h}) \otimes F^*(-\mathbf{h}) = \sum_{\mathbf{k}} F(\mathbf{k}) F^*(\mathbf{k} - \mathbf{h}). \tag{8.86}$$

But also, from (8.84) and (8.85), $\rho^2(\mathbf{r}) = \beta\rho(\mathbf{r})$ and so (8.86) becomes

$$\beta F(\mathbf{h}) = \sum_{\mathbf{k}} F(\mathbf{k}) F^*(\mathbf{k} - \mathbf{h}). \tag{8.87}$$

[6] The factor β represents the ratio between $\delta(x)$ and its square – unknown, but definitely positive. Its value is irrelevant here. Remember that the δ-function is a mathematical abstraction representing a real atom.

This is known as **Sayre's equation** for point atoms. Let us now separate the amplitude and phase of each $F(\mathbf{h})$ by writing $F(\mathbf{h}) = E(\mathbf{h}) \exp[i\phi(\mathbf{h})]$. It then follows on multiplying (8.87) by $F^*(\mathbf{h})$ that

$$\beta E^2(\mathbf{h}) = \sum_{\mathbf{k}} E(\mathbf{h})E(\mathbf{k})E(\mathbf{k}-\mathbf{h}) \exp\{i[-\phi(\mathbf{h}) + \phi(\mathbf{k}) - \phi(\mathbf{k}-\mathbf{h})]\}. \tag{8.88}$$

A practical method of getting a good first approximation to the solution is based on this equation, observing that $\beta E^2(\mathbf{h})$ is positive.

Measurement of the diffraction pattern gives us values for $E(\mathbf{h})$ for many values of $\mathbf{h}$. We should recall (§4.2.1) that for real ρ, $F(\mathbf{h}) = F^*(-\mathbf{h})$, so that $E(\mathbf{h}) = E(-\mathbf{h})$ and $\phi(\mathbf{h}) = -\phi(-\mathbf{h})$. The method for determining the phases goes as follows, and can be followed using the example in Fig. 8.34. First, note that the actual values of the phases ϕ are determined by the origin of the unit cell, which is in principle arbitrary, although the symmetry of the molecule will often dictate some preferred choice. In a three-dimensional case, the phases of any three of the diffraction spots $\mathbf{h}_1, \mathbf{h}_2$ and $\mathbf{h}_3$ (usually the strongest three) can therefore be assigned arbitrary values of zero provided that the vectors are not linearly related. Moreover, if the molecule is centro-symmetric, choosing the origin at the centre of symmetry makes all the phases zero or π. Now prepare a table of $E(\mathbf{h})E(\mathbf{k})E(\mathbf{h} \pm \mathbf{k})$, for all measured values of $\mathbf{h}$ and $\mathbf{k}$, as in Fig. 8.34(*b*). Then choose the largest entry. For the value of (8.88) to be positive it is *most likely* that this term will make a positive contribution to the sum, since it is its largest term. If so, the sum of the phases will be zero:

$$\phi(\mathbf{h}) \pm \phi(\mathbf{k}) \doteq \phi(\mathbf{h} \pm \mathbf{k}), \tag{8.89}$$

in which the sign $\doteq$ is to be read as 'expected to be equal to'. It is very likely that one or more of the three vectors involved in this equation has been assigned phase 0. By repeating the process for the various entries in the table in descending order, a series of relationships between the phases is obtained, with reliability depending on the value of the triple product $E(\mathbf{h})E(\mathbf{k})E(\mathbf{h} \pm \mathbf{k})$. This allows us to express all the phases in terms of the three chosen to be zero and the phases of a small number of additional prominent spots, whose phases are represented by symbols $a, b, c \ldots$

The next stage in the determination involves reconstructing the object from the known amplitudes and the estimated phases. Since some of them have been given arbitrary symbols, it is necessary to perform a series of reconstructions, with various values assigned to the symbols. The set of phases that reconstructs an object with the least negative parts and having the closest similarity to a-priori expectations of the structure (number of atoms, bond lengths etc.) is assumed to be roughly correct. An improvement to the phases is found by retransforming this approximate structure with all the negative electron densities set to zero. The phases calculated this way are then used, together

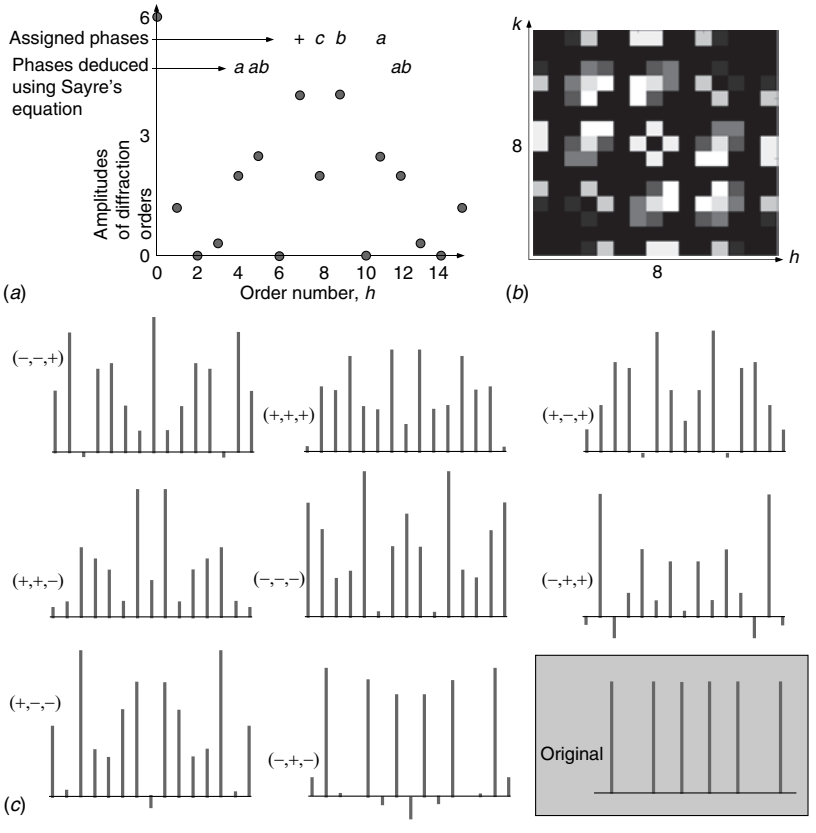

Figure 8.34 Illustrating the direct method in crystallography, for a linear centro-symmetric array of six atoms. (*a*) The diffraction amplitudes $E(h)$ observed at sixteen reciprocal lattice points. (*b*) The table of triple products $E(h)\,E(k)\,E(h-k)$ in pictorial form, where white is largest. Three spots are assigned arbitrary phases *a*, *b* and *c*, and phases of the others are determined by applying (8.89). (*c*) The original object, and its reconstruction using the diffraction spots whose phases have been related to *a*, *b* and *c*, for the eight possibilities where they each have values ±1. Clearly (−, +, −) best satisfies the a-priori conditions: that there are six identical atoms, and the the function is positive definite.

with the measured amplitudes, to return a better structure, and this process is iterated several times until the required degree of accuracy is obtained. The process works better in two and three dimensions than in one because increasing the dimensionality increases the number of possible relations.

8.8.3 A centro-symmetrical example of the direct method

The method described above is so important in modern crystallography that we shall illustrate it with a simple one-dimensional example, as shown in Fig. 8.34.

We use a centro-symmetrical example, consisting of six equal point 'atoms' known to be at integer points x in the region $(1, 16)$, and arranged symmetrically about $x = 8$. This is the a-priori information, in addition to the measured diffraction amplitudes, square roots of the intensities, shown in Fig. 8.34(a). The symmetry means that the phases are either zero or π (i.e. signs '+' or '−'). In one dimension we can arbitrarily assign '+' to the one strongest diffraction spot (excluding that at the origin), at $h = 7$; three more strong spots are assigned phases a at $h = 11$, b at $h = 9$ and c at $h = 8$. Figure 8.34(b) shows the table of triple products $E(h)E(k)E(h-k)$ in pictorial form, where the brightest pixels correspond to the largest values. The phases of as many as possible of the spots ($h = 4, 5, 7, 8, 9, 11$ and 12) are determined in terms of a, b and c by using (8.89). Assigning $+$ and $-$ to each of a, b and c in turn gives eight different reconstruction estimates for the original function when (a) is retransformed using the known values of $E(h)$ with the appropriate phases. These are shown in (c) together with the original function. Without knowing the original function, it is clear that choosing phases $a = -, b = +, c = -$ reconstructs a function that has the clearest six points on a dark background. This provides a good starting point for the iterative stage of the retrieval, which determines the phases of the remaining spots.

8.9 Advanced topic: Phase retrieval in an optical system – the Hubble Space Telescope and COSTAR

When the Hubble Space Telescope was launched in 1990, it was soon discovered that the images were blurred due to unexpectedly large aberrations of the 2.4 m primary mirror. The question immediately arose as to whether the exact form of the aberrations could be deduced from analysis of the blurred images of point stars (Fig. 8.35), which would enable the design and installation of a correction system. The aberrated images are essentially diffraction patterns of the aperture stop considered as a phase mask, whose value represents the aberration. In this section we shall show how this was done analytically by phase retrieval.

Phase retrieval was one of the methods used to design correction optics for the Hubble Space Telescope in 1990.

After the first pictures were received, data on the aberrated images of point stars photographed at known wavelengths in several planes near the paraxial focus were made available to a number of research groups who each used a different analytical technique to determine the aberration. One of the groups used a phase retrieval method (Fienup *et al.* (1993)). The substantial agreement between the results of the various groups encouraged the design of a correction system, COSTAR,[7] which was successfully installed

[7] Corrective Optics Space Telescope Axial Replacement.

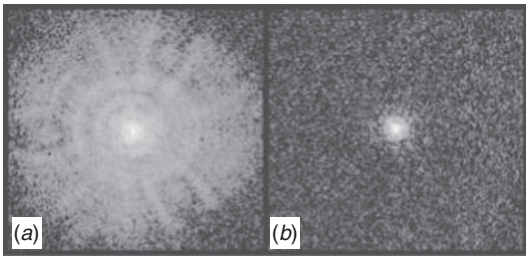

Figure 8.35
An example of the monochromatic image of a point star as observed by the Hubble Space Telescope (*a*) before correction by COSTAR, and (*b*) after correction. (Courtesy of NASA)

during a Space Shuttle mission in 1994, and which restored to the telescope its intended diffraction-limited performance. Certainly, this must have been the most expensive eyeglasses ever made! The various methods of analysis used for determining the aberration function are described in a series of papers in a special feature issue of the journal *Applied Optics* (Vol. 32, no. 10, 1993).

The basic algorithm for finding the phases is due to Gershberg and Saxton (1972) and was written to derive a mask transmission function, given its outer bound and the measured intensity of its diffraction pattern. It was initially developed, with Fresnel rather than Fourier transforms, for achieving phase-contrast from defocused electron microscope images (Misell (1973)) and further developments are discussed by Fienup (1982).

For a problem of the Hubble telescope type, where there is an unknown phase aberration in the aperture, we consider Fraunhofer diffraction at wavelength λ by a complex mask which is described by the function

$$f(x,y) = a_0(x,y)\exp[\mathrm{i}\phi(x,y)]. \tag{8.90}$$

Here $a_0(x,y) = 1$ in the transparent regions of the aperture stop and zero otherwise, and $\exp[\mathrm{i}\phi(x,y)]$ describes the aberration.[8] The point spread function (§12.2.1) is described by the intensity of the Fourier transform of the mask function, $|F_0(u,v)|^2$, and is photographed as the image of a distant isolated star. When the telescope is defocused, the image plane is moved an axial distance Δ from the focal plane $z = L$ and an additional quadratic phase is introduced (in the paraxial limit): $\exp\left\{\frac{1}{2}\mathrm{i}k_0(x^2+y^2)[1/(L+\Delta) - 1/L]\right\}$. An example of an aberrated image is shown in Fig. 8.35(*a*). The problem here is to deduce $\phi(x,y)$ from $|F_0(u,v)|^2$ and $a_0(x,y)$ knowing only the intensity $|F|^2$ as a function of Δ.

The method uses an iterative algorithm in which the mutual transform relation between mask and image is repeatedly applied, the known values of a_0 and $|F_0|$ being used as constraints at each stage. It works as follows. We begin by assigning a trial phase function ϕ_1, which must have no symmetry (otherwise that symmetry may permeate the solution):

$$f_1(x,y) = a_0(x,y)\exp[\mathrm{i}\phi_1(x,y)]. \tag{8.91}$$

[8] The aperture stop of the Hubble telescope has an off-axis central obscuration.

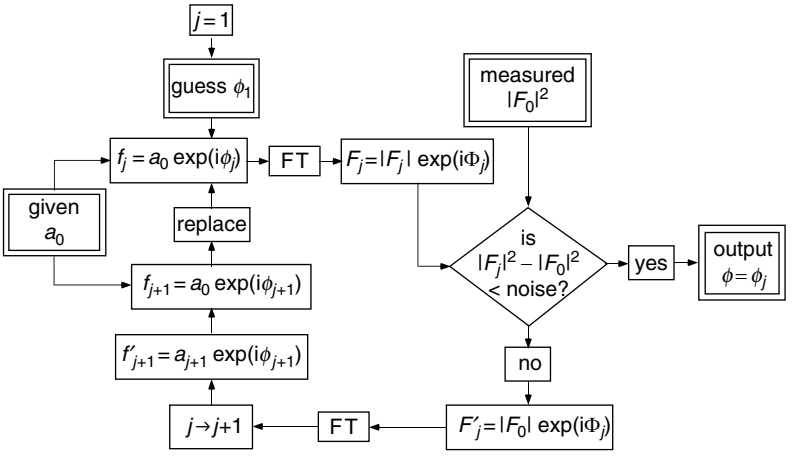

Figure 8.36
Phase-retrieval algorithm.

The Fourier transform $F_1(u,v) = |F_1(u,v)| \exp i\Phi_1(u,v)$ is calculated. In the next stage, the value of the modulus $|F_1(u,v)|$ is replaced by the known value, $|F_0(u,v)|$ (the square root of the intensity of the image). The new function $F'_1(u,v) = |F_0(u,v)| \exp i\Phi_1(u,v)$ is then inversely transformed to get a new estimate of the aperture function: $f'_2(x,y) = a_2(x,y) \exp[i\phi_2(x,y)]$. The modulus a_2 is next replaced by the known value a_0 and the new function $f_2(x,y) = a_0(x,y) \exp[i\phi_2(x,y)]$ replaces f_1 in (8.91). This process is iterated as many times as necessary to achieve a stable solution (Fig. 8.36). It will be clear if this solution is correct, when it reproduces the known image to within its noise limits; however, the program might possibly stagnate to a value that is clearly incorrect but does not improve with further iteration. This problem can be overcome by using out-of-focus images ($\Delta \neq 0$), where the image data $F(u,v)$ are spread over a larger region of the (u,v) plane, and the results are found to be more reliable;[9] the quadratic phase resulting from the known defocus can afterwards be removed analytically. The most reliable results in fact come from using several values of Δ within one algorithm which shifts periodically from one to another during the iterations. Once the value of ϕ_n has stabilized to the value which reproduces $|F_0(u,v)|^2$ within its noise level, the form of the aberration has been determined, and can be compared to that obtained by other methods (e.g. Barrett and Sandler (1993)). To demonstrate the performance of the algorithm, we show in Fig. 8.37 a simulated example in which the point spread function for coma aberration was initially calculated, and this was used as input to the algorithm described above in order to retrieve the phase error in the aperture stop. We shall not go into the details of the optics used to correct the aberration in COSTAR, but the excellent astronomical images (Fig. 8.38) obtained after the correction are witness to the power of this technique.

[9] Astronomers often use out-of-focus images of point stars for critical alignment of telescope optics, for the same reason.

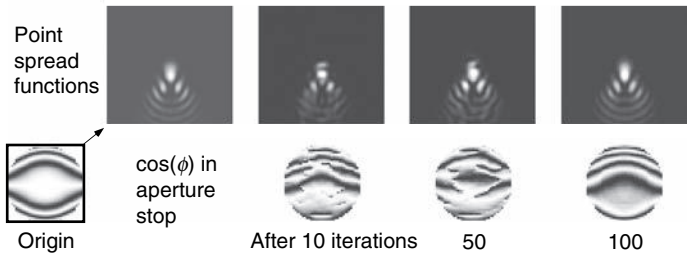

Figure 8.37 A simulated example to illustrate phase retrieval for a circular aperture. The source aperture has third-order coma and the measured point spread function is shown. The algorithm started with a random phase guess and finds the phase function by iteration. The difference between the retrieved functions and the source, shown on the right, is a constant phase which does not affect the point spread function.

Chapter summary

In this chapter we discussed the principles of Fraunhofer diffraction by two- and three-dimensional objects.

- We saw that a Fraunhofer diffraction pattern can be described mathematically by a Fourier transform.
- We saw that when we can observe only the intensity (square modulus) of the transform, we lose all information on the phase; this led to a major problem in interpreting patterns: the 'phase problem'.
- We calculated several examples of diffraction by amplitude masks, and saw that they are all centro-symmetric because the object function is real.
- We saw some examples of diffraction by phase masks, where the patterns are not centro-symmetric.
- We learnt how to describe interference patterns, which are diffraction patterns of repeated basic apertures, by the convolution operation.
- In three-dimensional diffraction, we saw that the three-dimensional Fourier transform is sampled by the Ewald or observation sphere, which represents all possible diffraction conditions that conserve photon energy.
- We learnt that three-dimensional Fourier transforms are the basis of X-ray and neutron crystallography.
- We saw how to represent the acousto-optic effect as a three-dimensional diffraction example, where photon energy is not conserved because energy can be exchanged with acoustic waves.

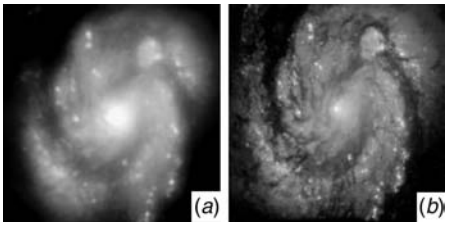

Figure 8.38

Comparison between images of the core of the galaxy M100 (*a*) before and (*b*) after mounting COSTAR on the Hubble Space Telescope. (Courtesy of NASA)

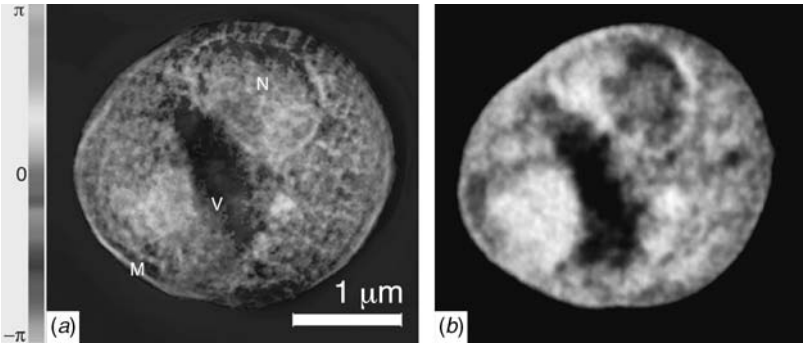

Figure 8.39

(*a*) Phase image with 30 nm resolution of a yeast cell made with 750 eV X-rays using phase retrieval, compared with (*b*) a scanning X-ray image showing absorption data (at 540 nm). The original published colour image (*a*) shows both absorption and phase data, but the grey-scale reproduction here shows mainly the phase contribution. (Courtesy of C. Jacobsen; Shapiro *et al.* (2005))

Box 8.5 Phase retrieval used in X-ray microscopy

Another field in which phase retrieval has recently been successful is in creating images of small non-periodic biological entities such as cells directly from their soft X-ray scattering patterns. Here there is no crystal, so the method of §8.9 has to be used (Shapiro *et al.* (2005)). It is interesting to note that the object in this case has both absorption and phase structures; its diffraction pattern is not centro-symmetrical. Both can be determined by phase retrieval when the boundary of the object is constrained sufficiently well (adaptively, during the procedure) and the pattern is sampled at very closely separated spatial frequencies. This requires the incident X-ray beam to be considerably larger than the sample diameter, so that its diffractive spreading is smaller than the required spatial frequency resolution. The method needs scattering data with exceptionally high signal-to-noise ratio and dynamic range, and this is obtained by averaging many samples made with different exposures. An example of the image of a yeast cell made by this method is shown in Fig. 8.39, where the result is compared with an absorption image of the same cell produced by scanning with an X-ray beam focused by means of a zone plate (§7.2.5). The two techniques of X-ray scanning and phase retrieval have also been employed together, by analyzing a series of small area diffraction patterns in order to improve resolution further (Thibault *et al.* (2008)).

- **We studied examples of phase retrieval, where the diffraction pattern intensity and a-priori information about the object are used to solve the phase problem algorithmically. We saw examples of how these methods have been applied to two different types of problem: interpretation of X-ray diffraction patterns, and correction of the optics of the Hubble Space Telescope.**

Problems

All diffraction patterns in these problems are of Fraunhofer type. In numerical problems, assume that $\lambda = 0.5\ \mu\text{m}$.

8.1. Deduce the diffraction pattern of a set of four equally spaced slits by considering them as
(a) a pair of pairs of slits,
(b) a double slit in the centre, flanked by a second double slit with three times the spacing. Show that both methods give the same answer.

8.2. Deduce the diffraction pattern of a square frame by subtracting the pattern of a square from that of a slightly larger one.

8.3. Find the diffraction pattern of a group of four pinholes at the points $(x,y) = (a,0)$, $(-a,0)$, (b,a) and $(-b,-a)$ by using the concept of the reciprocal lattice.

8.4. A mask consists of an array of 5×3 small circular holes. Find its diffraction pattern. Alternate holes in both directions are now covered with plates that change the phase of their transmission functions by π. What is the diffraction pattern now?

8.5. An elliptical aperture has semi-axes a and b. Calculate its diffraction pattern.

8.6. In the apparatus of Fig. 8.2 to observe Fraunhofer diffraction patterns, a slit aperture of width 1 mm in the mask plane $\mathcal{R}$ gives rise to a diffraction pattern in the plane $\mathcal{F}$ with effective width 1 mm. What is the effective focal length of the lens D? Suggest two lenses from which a telephoto lens of this focal length could be constructed.

8.7. Figure 8.40 shows 20 apertures and Fig. 8.41 shows 20 diffraction patterns. All the patterns were photographed to the same scale, but may have had different exposures. Match each pattern to its aperture and find its correct orientation.

Figure 8.40

Masks for Problem 8.7.

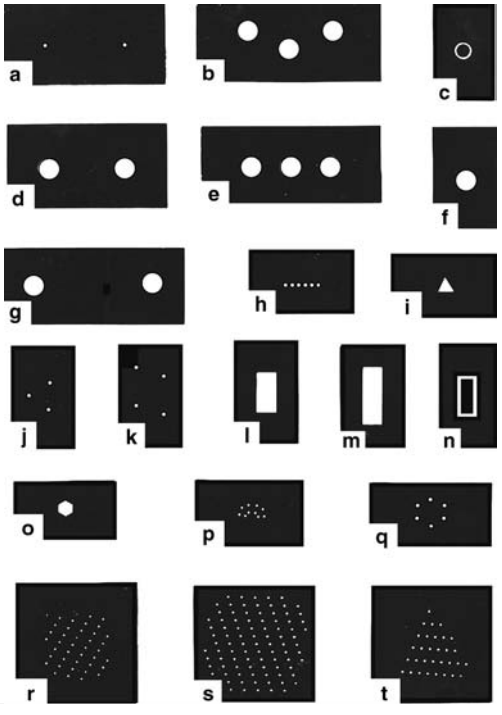

Figure 8.41

Diffraction patterns for Problem 8.7.

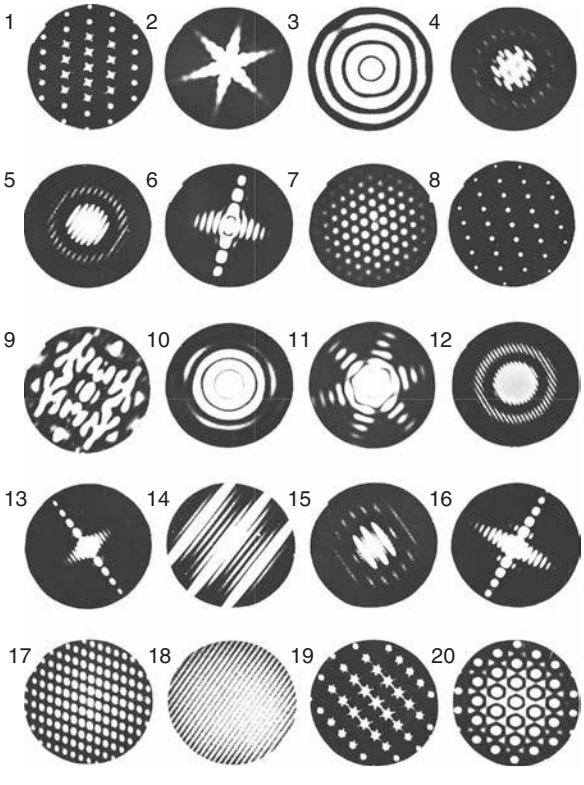

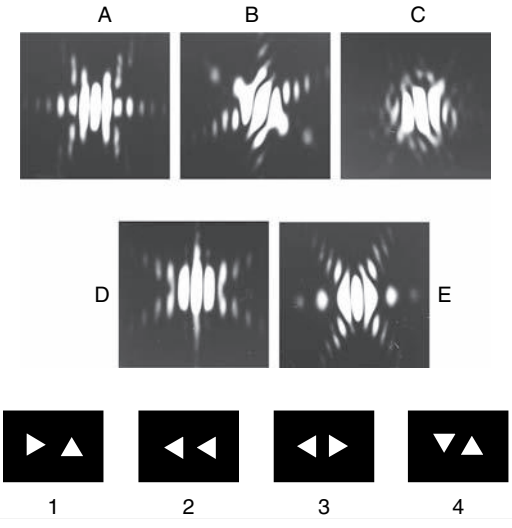

Figure 8.42
Four masks and five diffraction patterns.

8.8. A diffraction pattern intensity is observed to be centro-symmetric. Can you deduce from this that the mask transmission function is real?

8.9. Figure 8.42 shows five diffraction patterns and four masks each consisting of a pair of triangular holes. Which pattern corresponds to each mask? The fifth pair of holes corresponds to a pair of holes not shown; what is it? There are two symmetry-related solutions.

8.10. What is the Fraunhofer diffraction pattern of a mask in the form of a chessboard with opaque and transparent squares?

8.11. A square aperture is half-covered by a sheet of transparent film which introduces a phase lag of $\pi/2$. What is its diffraction pattern?

8.12. Calculate the diffraction pattern intensity of a mask consisting of six holes at the corners of a regular hexagon. Now repeat the calculation with one extra hole in the centre. Show how comparison of the two diffraction patterns allows the phase to be determined at each point. Use this calculation to explain the heavy-atom method in crystallography.

8.13. A plane wave of wavelength λ_0 is normally incident on a diffraction grating moving transversely at velocity $v \ll c$ in a direction normal to its slits. Find the wavelengths of the various diffraction orders.

8.14. A mask has many horizontal rows of holes. The rows are equally spaced in the vertical direction, and within each row the holes are equally spaced. However, the holes in a given row are randomly situated with

Figure 8.43

Mask for Problem 8.14.

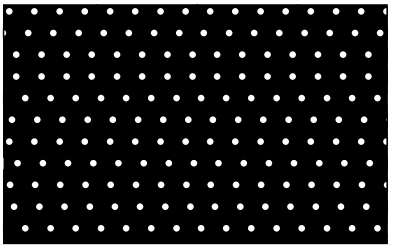

Figure 8.44

Diffraction pattern for Problem 8.17.

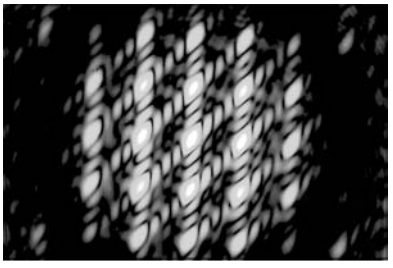

respect to those in the rows above or below it (see Fig. 8.43). What is its diffraction pattern? Hint: use the auto-correlation function.

8.15. The atoms in a crystal are regularly spaced on a lattice of spacing a, but vibrate randomly about their equilibrium positions because of thermal effects. The r.m.s. vibration amplitude is $b \ll a$. Show that the diffraction spots remain sharp but become weaker at large distances from the origin of the reciprocal lattice, and that there is a continuous background which increases with that distance. This is called the **Debye–Waller effect.**

8.16. Find the diffraction pattern of a triangular hole in an opaque screen. Hint: it is easier to calculate the diffraction pattern of the differential of this mask.

8.17. Figure 8.44 shows the diffraction pattern of a certain mask, consisting of holes in an opaque screen. Describe the mask as fully as you can.

8.18. An antenna array used in radio astronomy consists of a set of antennae equally spaced along a north–south line. By reciprocity, the detection pattern of the antenna array is just the same as the radiation pattern if the antennae were radiating at the same wavelength. The spacing between the antennae is smaller than the wavelength. Show that the array only receives radiation from a specific direction in the N–S plane, and that the direction can be chosen by introducing equal phase delays between adjacent antennae. This is called a **phased array**.

Figure 8.45
Diffraction pattern of a piece of woven gauze.

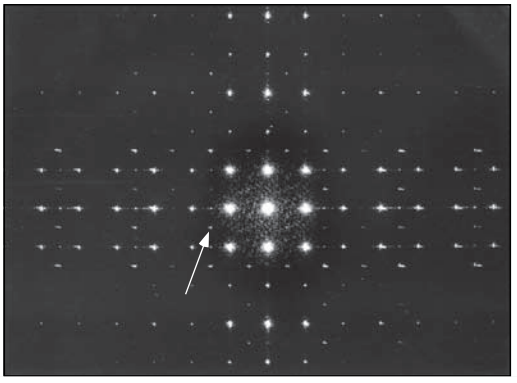

8.19. The **Mills cross** antenna used in radio astronomy consists of two orthogonal linear phased arrays (see previous problem) of N equally spaced antennae. The two arrays have one common antenna, at the point where they cross. Two signals are recorded; one is the sum of the responses of the two arrays and the other is the difference between their responses. Show that subtracting the intensity of one signal from that of the other gives an output that is the equivalent of an $N \times N$ matrix of antennae.

8.20. Figure 8.45 shows the diffraction pattern of a piece of woven gauze. Explain as many features of the diffraction pattern as you can, including in particular the weak spots at the midpoints (one is shown by the arrow).

8.21. A perfect crystal is disturbed by a single phonon with wavelength equal to a few times the interatomic spacing. Draw the reciprocal lattice for this crystal. Deduce the diffraction pattern for waves with wavelength about one-tenth of the lattice spacing, using the Ewald sphere construction. This is the basis of phonon spectroscopy of crystals using slow neutrons (Squires (1996)).

References

Barrett, T. K. and Sandler, D. G. (1993), Artificial neural network for determination of Hubble Space Telescope aberration from stellar images, *Appl. Opt*. **32**, 1720.

Born, M. and Wolf, E. (1999), *Principles of Optics*, Cambridge: Cambridge University Press.

Bragg, W. L. (1975), *The Development of X-ray Analysis*, eds. D. C. Phillips and H. Lipson, London: Bell.

Cowley, J. M. (1995), *Diffraction Physics*, Amsterdam: North Holland.

Fienup, J. R. (1982), Phase retrieval algorithms: a comparison, *Appl. Opt*. **21**, 2758.

Fienup, J. R., Marron, C. J., Schultz, T. J. and Selden, J. H. (1993), Hubble Space Telescope characterization by using phase retrieval algorithms, *Appl. Opt*. **32**, 1747.

Gershberg, R. W. and Saxton, W. O. (1972), A practical algorithm for the determination of phase from image and diffraction plane pictures, *Optik*, **35**, 237.

Hauptman, H. A. (1991), The phase problem of X-ray crystallography, *Rep. Prog. Phys*. **54**, 1427.

Korpel, A. (1997), *Acousto-Optics*, New York: Marcel Dekker.

Lipson, H. S. (1970), *Crystals and X-rays*, London: Wykeham Publications.

Misell, D. L. (1973), An examination of an iterative method for the solution of the phase problem in optics and electron optics: I, II, *J. Phys. D: Appl. Phys*. **6**, 2200 and 2217.

Shapiro, D. *et al*. (2005), Biological imaging by soft x-ray diffraction microscopy, *PNAS* **102**, 15343.

Squires, G. L. (1996), *Introduction to the Theory of Thermal Neutron Scattering*, New York: Dover.

Taylor, C. A. and Lipson, H. (1964), *Optical Transforms*, London: Bell.

Thibault, P., Dierolf, M., Menzel, A. *et al*. (2008), High-resolution scanning X-ray diffraction microscopy, *Science* **321**, 379.

Watson, J. D. (1968), *The Double Helix*, Harmondsworth: Penguin.

Woolfson, M. M. (1971), Direct methods in crystallography, *Rep. Prog. Phys*. **34**, 369.

Yariv, A. (1991), *Optical Electronics*, Philadelphia: Holt, Reinhart and Winston.

9 Interferometry

In Chapter 8 we discussed the theory of Fraunhofer diffraction and interference, emphasizing in particular the relevance of Fourier transforms. In this chapter we shall describe the applications of interference to measurement; this is called **interferometry**. Some of the most accurate dimensional measurements are made by interferometric means using waves of different types, electromagnetic, matter, neutron, acoustic etc. One current highlight of optical interferometry is the development of detectors that can measure dimensional changes as small as 10^{-19} m, which should be induced by gravitational waves emitted by cataclysmic events in the distant Universe. A picture of one such interferometer, which has two orthogonal arms each 4 km in length, is shown in Fig. 9.1 and the design of this instrument will be discussed in more detail in §9.7.

An enormous variety of interferometric techniques has been developed during the years, and we shall limit ourselves in this chapter to a discussion of examples representing distinctly different principles. There are several monographs on interferometry that discuss practical aspects in greater detail, for example Tolansky (1973), Steel (1983), Hariharan (2003) and Hariharan (2007).

In this chapter we shall learn about:

- Young's basic two-slit interferometer and its capabilities;
- interference in a reflecting thin film;
- diffraction gratings: how they work and how they are made, their resolving power and their efficiency;
- two-beam interferometers of several types;
- Michelson's interferometer and its most important applications;
- the Sagnac effect and optical gyroscopes;
- multiple-beam interferometry;
- the Fabry–Perot étalon: its structure and resolving power;
- laser resonators and the modes they support;
- Berry's geometrical phase in interferometry;
- gravitational wave detectors.

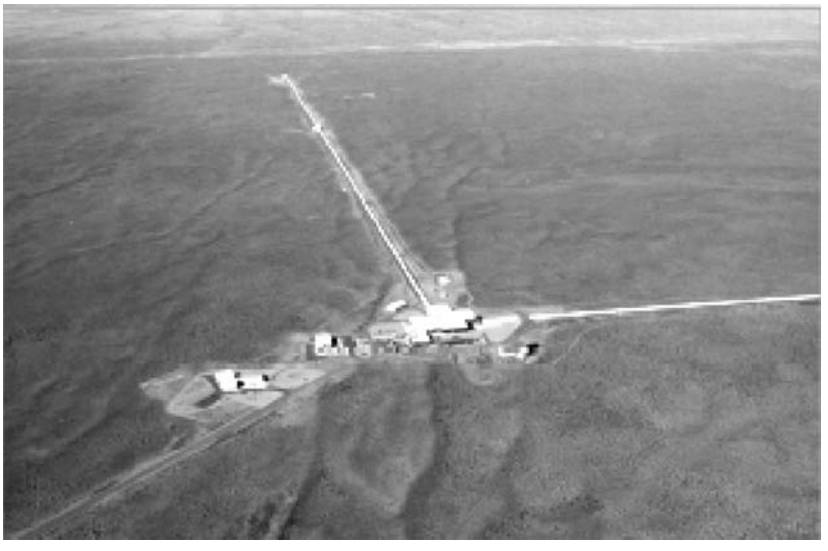

Figure 9.1
Aerial photograph of the gravitational wave detector LIGO at Hanford, WA, USA. The two arms are 4 km in length and are oriented NW and SW. The optical layout of this interferometer is shown in Fig. 9.35. (Photograph courtesy of the LIGO Laboratory)

9.1 Interference between coherent waves

Interference can only occur between waves that have a constant phase difference between them, called 'coherent waves'.

The discovery of interference effects by Young (§1.1.3) enabled him to make the first interferometric measurement, a determination of the wavelength of light. Even this primitive system, a pair of slits illuminated by a common point source, can be surprisingly accurate, as we shall see in §9.1.1.

The use of a common source was necessary to ensure that the interfering waves were coherent. In general, interference is possible between waves of any non-zero degree of mutual coherence (see §11.3), but for the purposes of this chapter we shall simply assume that waves are either completely **coherent** (in which case they can interfere) or **incoherent** (in which case no interference effects occur between them). The concept of complete coherence between two waves implies that there is a fixed phase relationship between them, and the interference effects observed are therefore stationary in time; they can therefore be observed with slowly responding instruments such as the eye or photography. We combine coherent waves by adding their complex amplitudes, and then calculate the intensity by taking the square modulus of the sum; we combine incoherent waves by calculating their individual intensities first, and then adding, and there are no interference effects. The need for coherence between the interfering waves generally dictates at optical frequencies that they must all originate from the same source; the various ways of dividing an incident wave into separate parts and interfering them, after they have been influenced by the system to be measured, constitute the different interferometers.

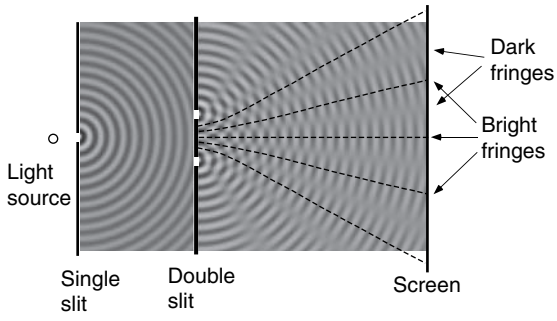

Figure 9.2

Set-up for Young's fringes. A source illuminates a single slit which then provides coherent illumination at two slits in an opaque screen. Young's original set-up was different, and is shown in Fig. 1.2.

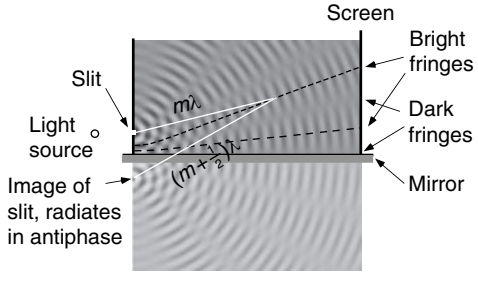

Figure 9.3

Set-up for Lloyd's mirror fringes. Notice the phase change on reflection, which results in the zero-order fringe being dark. The lower half of the picture shows the fringe pattern as seen through the mirror.

9.1.1 Young's fringes

Young's fringe experiment, which he carried out in 1801, constitutes the basic interferometer, and it is worth dwelling briefly on some of its basic aspects. According to Huygens' principle, each slit behaves as a source of coherent waves, and the wavefronts are circular in the two-dimensional projection shown in Fig. 9.2. The maxima and minima of the interference pattern arise at points where the waves interfere **constructively** (amplitudes add) or **destructively** (amplitudes subtract). In the simplest case, where the two slits emit with the same phase, constructive interference occurs when the path difference is an integer number of wavelengths and destructive interference when the number is integer-plus-half. The loci of such points lie on a family of hyperbolae whose foci are at the two slits. In three dimensions we replace the slits by pinholes and the loci of the fringes are a family of hyperboloids having their foci on the pinholes. Their intersection with a plane screen at a large distance gives approximately straight fringes.

At large distances, Young's fringes lie on planes intersecting in the centre-line midway between the two slits.

One simple way of producing two coherent sources is to use a single point source and its image in a plane mirror; this is called the **Lloyd's mirror** experiment and is shown in Fig. 9.3. If the source is nearly in the plane of the mirror, the separation of the source and its image is quite small, and well-separated interference fringes can be produced. Obviously, however, the zero-order fringe – that which is equidistant from the two sources – lies on the

mirror itself; but if one extrapolates back to the position where it should be, one finds that there is a minimum of intensity there, not a maximum. There is therefore some asymmetry between the source and its image; this can be traced to the change of phase that occurs when light is reflected from a medium of higher refractive index (§5.4) or from a conductor (§5.6.1).

Although one would not usually employ Young's fringes for high-resolution measurements of wavelength, it is of interest to see what could be achieved. The slits are represented by a transmission function consisting of two δ-functions separated by distance a (§8.5.1) and we showed that the amplitude of the diffraction pattern observed on a distant screen (Fraunhofer conditions) is then

$$\psi(u) = 2\cos(ua/2). \tag{9.1}$$

Writing this in terms of the angular variable $\sin\theta$, where $u = k_0 \sin\theta$,

$$\psi(\sin\theta) = 2\cos\left(\frac{1}{2}k_0 a \sin\theta\right); \tag{9.2}$$

$$I = |\psi(\sin\theta)|^2 = 4\cos^2\left(\frac{1}{2}k_0 a \sin\theta\right). \tag{9.3}$$

If two separate wavenumbers k_1 and k_2 contribute to the source, the intensities add incoherently and so, assuming equally bright sources,

$$I = 4\left[\cos^2\left(\frac{k_1 a}{2}\sin\theta\right) + \cos^2\left(\frac{k_2 a}{2}\sin\theta\right)\right]. \tag{9.4}$$

The two sets of $\cos^2$ fringes will be out of phase and therefore cancel one another to give a uniform intensity when, for integer m,

$$\frac{k_1 a}{2}\sin\theta - \frac{k_2 a}{2}\sin\theta = (2m+1)\frac{\pi}{2}. \tag{9.5}$$

A primitive condition for wavelength resolution is, intuitively, that at least one such cancellation will occur at an observable angle $\theta < 90°$; this occurs if $\delta k \equiv k_1 - k_2 > \pi/a$ or, for $|k_1 - k_2| \ll \bar{k} \equiv (k_1 + k_2)/2$, in terms of wavelength $\lambda = 2\pi/k$,

$$\frac{\delta k}{\bar{k}} = (-)\frac{\delta\lambda}{\bar{\lambda}} > \frac{\bar{\lambda}}{2a}. \tag{9.6}$$

Even a simple pair of slits separated by 1 mm can be used as a spectrometer with an accuracy of 1/40%, but it is not a convenient or efficient means of doing spectroscopy.

This is called the **limit of resolution**; its inverse, $\bar{\lambda}/\delta\lambda$ is called the **resolving power**. For example, if $a \sim 1$ mm and $\lambda \sim 0.5$ nm, a resolving power of order 4000 has been achieved, which is quite good for such a primitive experiment. In fact, if the sources are bright, one could map the fringe profile accurately, and fit it to (9.4) thereby improving the accuracy greatly. If the source contains more than two wavelengths, as shown in Fig. 9.4, more sophisticated techniques are

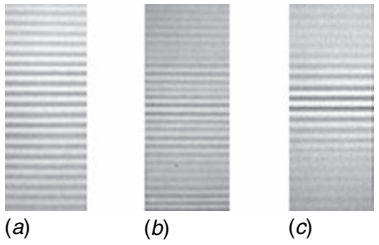

Figure 9.4
Interference fringes from (*a*) a monochromatic source, (*b*) a polychromatic line source (mercury lamp), (*c*) a broad-band source.

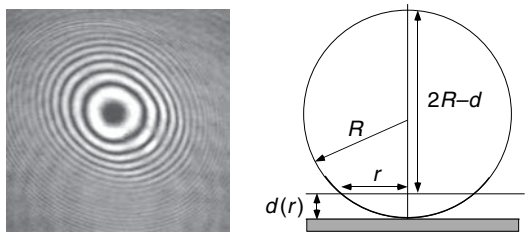

Figure 9.5
(*a*) Newton's rings in light reflected from a glass plate and a lens in contact with it. (*b*) Construction to find $d(r)$.

required, such as Fourier transform spectroscopy (§11.5), but this discussion contains all the physics of all two-beam interferometry!

9.1.2 Newton's rings

We saw in the first chapter that Newton observed ring-like interference fringes between light reflected from a plane surface and a curved surface in contact with it (Fig. 9.5(*a*)). However, he failed to appreciate the significance, and missed discovering light waves! It is easy to see (now) the origin of the effect. The curved surface is usually obtained using a long focal-length lens, and we denote by R the radius of curvature of the lens surface which contacts the plane surface at $r = 0$. Then the separation $d(r)$ between the plane and the curve is given by Euclid: $r^2 = d(2R - d) \approx 2Rd$ (Fig. 9.5(*b*)). In monochromatic light, the reflected waves at radius r then have a phase difference $\delta\phi(r) = 2dk_0(r) + \pi$, the π arising from the reflection coefficients at the two surfaces, which are equal but have opposite signs (§5.7). As a result, dark interference fringes are seen whenever the waves are in antiphase, i.e. $\delta\phi =$ odd π. This defines a set of dark circles with $2k_0 d(r) = 2m\pi$ where m is an integer:

$$2k_0 r^2/2R = 2m\pi, \qquad r = \sqrt{R\lambda\, m}. \tag{9.7}$$

We then see a set of circular fringes with radii proportional to the square roots of the natural numbers, on a scale proportional to $\sqrt{R\lambda}$, a picture that appears commonly in interference between a spherical wave and a plane wave, or two spherical waves (see, for example, Fig. 9.15(*b*)). When the light is not monochromatic, each wavelength gives its own set of fringes scaled by $\sqrt{\lambda}$ and

Box 9.1 Interference in films of oil and soap bubbles

An everyday situation that gives rise to interference fringes is a thin film, either in the form of a soap bubble or a film of oil on a wet road. Here, the interference occurs between pairs of sources that are images of the same point on an extended source, often the sky, in the two surfaces of the film. This way, coherence between the two interfering waves is achieved despite the fact that the source is obviously incoherent. We would not use this situation for measuring the wavelength, because the separation of the two surfaces is usually too small, but it can often be used to determine the thickness of the film. The brilliant colours observed when the source is white are often a great help in distinguishing between the various orders of interference. Notice that when the film of a soap bubble becomes very thin, no light is reflected; the film is black. This occurs because the reflection coefficients from the two sides have opposite signs (§5.7), and so when the path difference between the two reflected waves is much smaller than the wavelength, *destructive* interference occurs. The opposite is true of a film of oil on water, when the refractive index of the oil is less than that of water. In that case the two reflection coefficients have the same sign, and the interference between waves reflected from a very thin film is *constructive*.

the composite pattern becomes blurred after a few fringes. Young actually used Newton's rings, and not the two-slit experiment, to deduce the wavelength of light of various colours.

9.2 Diffraction gratings

A great practical improvement over the two-slit system is the **diffraction grating**, which is a one-dimensional periodic array of similar apertures, usually narrow slits or mirrors, which makes the fringes (9.1) much sharper than a sinusoidal function. We have seen in §8.5.3 that the diffraction pattern of such an array is a periodic series of δ-functions $\sum F_m \delta(u - u_m)$, called **orders of diffraction**, whose strengths F_m are determined by the exact shape and dimensions of the apertures. The positions of the δ-functions u_m are determined only by the period of the array; from (8.52),

$$u = k_0(\sin\theta - \sin\theta_0) = u_m = 2\pi m/d, \tag{9.8}$$

where m is the **order of diffraction**. Because k_0 enters the definition of u, the angle of diffraction θ depends on the wavelength $\lambda = 2\pi/k_0$; this dependence makes diffraction gratings important tools for spectroscopy. We shall discuss

them in the framework of the scalar approximation, despite the real need for a vector formulation, as pointed out in §7.1 (Hutley (1982)).

9.2.1 Production of diffraction gratings

To appreciate some aspects of the succeeding theory, we need a little acquaintance with methods of production of diffraction gratings. The first serious gratings were made by scribing a series of lines on glass or metal with a fine diamond. Rowland used an accurate screw to translate the diamond laterally through a small distance between each pair of lines. Obviously much is implied in this sentence: the diamond and the flat upon which the grating is to be ruled must be carefully chosen; the screw and flat must be accurately adjusted relative to each other; the diamond point must not change during the ruling operation; and the temperature of the whole apparatus must be kept constant so that no irregular expansions occur. Thus, machines for making gratings, called **ruling engines**, are extremely complicated and costly.

Diffraction grating production has developed from individual gratings inscribed on an optically flat plate, to mass production of replicas made from a master grating, and to gratings produced by holography and photo-lithography.

Most high-quality gratings today are **holographic diffraction gratings**. As will be pointed out in §12.5, holograms are essentially *complicated* diffraction gratings. They can also be designed to be *simple* diffraction gratings. The development of high-resolution photo-resists for the microelectronic industry has made it possible to photograph a very fine interference pattern between plane waves. This produces, in a single exposure, a grating with many thousands of lines. For example, if two coherent plane waves from a laser with wavelength of say 0.5 μm interfere at an angle of $2\alpha = 60°$, the interference pattern has Young's fringes with a spacing $\lambda/2 \sin\alpha = 0.5$ μm. Because the laser lines are very sharp the number of fringes is enormous, and a grating many centimetres long can be produced in a single exposure. This technique completely avoids the problem of errors in line position, which is very troublesome in ruled gratings.

Another advantage of the holographic grating is that the line spacing can be arranged to be non-uniform in a planned way so as to correct for known aberrations in the associated optics or to reduce the number of accessory optical elements required. For example, a self-focusing grating can be produced by using as the source of the grating the interference pattern between two spherical waves.

The main use of diffraction gratings is for spectroscopy. The quality of a diffraction grating is judged by the apparent spectral width of a monochromatic line, and the absence of ghosts (§9.2.3).

Most serious diffraction gratings are reflection gratings, being either ruled on an optically flat reflecting surface, or being produced holographically on such a surface by etching through the developed photo-resist. This preference arises because reflection gratings are generally **phase gratings**, whose efficiency, both in theory and in practice, can be considerably larger than that of transmission gratings (§9.2.4). Gratings can also be produced on cylindrical and spherical surfaces in order to add a further dimension to the possible correction of aberrations.

9.2.2 Resolving power

One of the most important functions of a diffraction grating is the measurement of the wavelengths of spectral lines; because we know the spacing of the grating we can use equation (9.8) to measure wavelengths absolutely. The first question we must ask about a grating is 'What is the smallest separation between two wavelengths that will result in two separate peaks in the spectrum?' This defines the **limit of resolution**. We shall see that the limit results from the finite length of a grating.

The problem can be considered in terms of §8.5.3, where we saw that the diffraction pattern of a finite number of equally spaced apertures has both principal and secondary maxima. In the case of N slits there are $N-1$ zero values of the intensity between the principal maxima. If two different wavelengths are present in the light falling on a grating, the intensity functions will add together; we need to find the conditions under which the principal maxima can clearly be discerned as double. We therefore have to consider in more detail the exact shape of the interference function.

From (8.48), the intensity function (normalized to unity at $u = 0$) is

$$I(u) = \frac{\sin^2(uNd/2)}{N^2 \sin^2(ud/2)}. \tag{9.9}$$

This has principal orders with $I(u) = 1$ at $u = 2m\pi/d$ and zeros at

$$u = 2(m + p/N)\pi/d, \tag{9.10}$$

where p is an integer $1 \leq p \leq N - 1$. Between the zeros are subsidiary orders. Now if the intensities of the two incident wavelengths are equal, their combined intensity is the sum of two functions like (9.9), when expressed in terms of the angle θ. A reasonable criterion for resolution was suggested by Rayleigh, who considered that the two wavelengths would just be resolved if the principal maximum of one intensity function coincided in angle with the first zero ($p = 1$) of the other (Fig. 9.6(a)). This is a useful criterion, if a little pessimistic, and will be discussed further in §9.5.2 and in §12.2.1 where it is used in an imaging context. Using the Rayleigh criterion, we find from (9.10) that the first zero is separated from the main order by $\delta u = 2\pi/Nd$. Now from the definition of u as in (9.8), we can write, for a given angle θ,

$$\frac{\delta u}{u} = \frac{\delta k}{k} = -\frac{\delta\lambda}{\lambda}. \tag{9.11}$$

The **resolving power** is defined as $\lambda/\delta\lambda_{\min}$, which for order m, at $u = 2\pi m/d$, is

$$\frac{\lambda}{\delta\lambda_{\min}} = \frac{uNd}{2\pi} = mN. \tag{9.12}$$

This result shows that the resolving power obtainable does not depend solely upon the line spacing; if a coarse grating is made, a higher order can be used

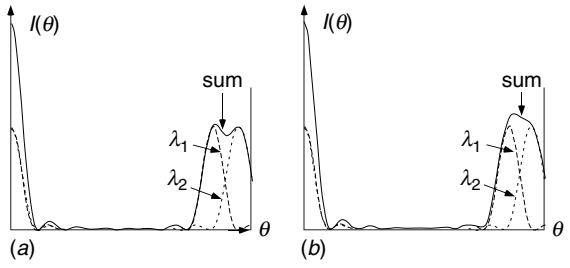

Figure 9.6
The addition of two diffraction-grating functions for two just-resolved wavelengths λ_1 and λ_2, showing resolution of the two wavelengths according to (*a*) the Rayleigh criterion, and (*b*) the Sparrow criterion (§9.5.2).

and the resolving power may be as good as that of a finer grating. If L is the total length of the grating, $d = L/N$ and the resolving power is equal to

$$\frac{\lambda}{\delta\lambda_{\min}} = mN = \frac{Nd}{\lambda}(\sin\theta - \sin\theta_0) = \frac{L}{\lambda}(\sin\theta - \sin\theta_0). \tag{9.13}$$

Thus, **for given angles of diffraction θ and incidence θ_0, the resolving power depends only on the total length of the grating**. The highest resolving power is obtained when $\theta_0 \to -\pi/2$ and $\theta \to \pi/2$, whence

$$\frac{\lambda}{\delta\lambda_{\min}} \to \frac{2L}{\lambda}. \tag{9.14}$$

Gratings should therefore be made as long as possible. In fact, we might as well just make a pair of slits at distance L apart, although they would use the light very inefficiently. This situation, Young's slits, has already been discussed in §9.1.1. For example, from (9.14) with $\lambda = 0.5\,\mu$m, a grating 5 cm long should give a resolving power approaching 2×10^5 although it is difficult to use θ and θ_0 around 90°. Another important resolution criterion, due to Sparrow, is discussed in §9.5.2.

9.2.3 Effects of periodic errors: ghosts and side-bands

Ghosts are satellite orders of diffraction surrounding a principal order, and may be mistaken by a spectroscopist for fine structure in a spectral line.

There is one type of error that often arises in ruled gratings and does not affect the resolving power but is nevertheless undesirable for other reasons; this is a periodic error in line position. It can arise from a poor screw or by a badly designed coupling between the screw and the table carrying the grating (§9.2.1), and has the effect of enhancing some of the secondary maxima.

As an example we shall analyze the situation where errors in line position are repeated every qth line; the true spacing is qd, and therefore q times as many orders will be produced. Most of them will be very weak, but some may be strong enough to be appreciable compared with the main orders. To make the problem soluble analytically we assume the line positions x_p to contain a small error which is sinusoidal in position, having maximum size $\epsilon \ll d$,

$$x_p = pd + \epsilon \sin 2\pi p/q. \tag{9.15}$$

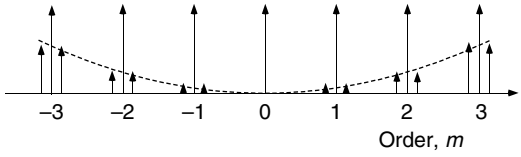

Figure 9.7

Representation of the principal orders of diffraction and ghost orders from a grating with periodic errors in line position. The broken line shows the dependence of the ghost intensities on m^2.

The grating is then represented by the set of δ-functions

$$f(x) = \sum_p \delta(x - pd - \epsilon \sin 2\pi p/q), \tag{9.16}$$

whose Fourier transform is

$$\begin{aligned} F(u) &= \sum_p \exp[-iu(pd + \epsilon \sin 2\pi p/q)] \\ &\approx \sum_p [\exp(-iupd)\,(1 - iu\epsilon \sin 2\pi p/q)] \end{aligned} \tag{9.17}$$

since $\epsilon \ll d$. On writing $\sin 2\pi p/q$ as $\frac{1}{2}i[\exp(-2i\pi p/q) - \exp(2i\pi p/q)]$, this is easily shown to be

$$\begin{aligned} F(u) = &\sum_m \delta\left(u - \frac{2\pi m}{d}\right) - \frac{u\epsilon}{2} \sum_m \delta\left[u - \frac{2\pi}{d}\left(m + \frac{1}{q}\right)\right] \\ &+ \frac{u\epsilon}{2} \sum_m \delta\left[u - \frac{2\pi}{d}\left(m - \frac{1}{q}\right)\right], \end{aligned} \tag{9.18}$$

where m is the order of diffraction. The summations show that, in addition to the principal maxima, there are also maxima at angles given by the two 'orders' $m + 1/q$ and $m - 1/q$. That is, each order m is flanked by two weak satellite lines, with intensities proportional to $u^2\epsilon^2$ (i.e. $\epsilon^2 \sin^2\theta$), at a separation of $1/q$ of the principal orders (Fig. 9.7). These lines are called **ghosts**. Such errors in line position do not result in ghosts around the zero order.

The idea that periodic displacements in position from the points of a regular lattice leads to ghost orders of diffraction has applications in many areas of physics, of which we shall mention three:

1. Thermal motion of the atoms of a crystal can be analyzed as a superposition of sinusoidal displacements to their periodic lattice positions, called **phonons**, each of which results in ghost orders. These, together, give a diffuse background and apparent broadening to the otherwise sharp X-ray diffraction spots from the crystal; this is called the **Debye–Waller effect**.
2. In the study of alloys, **superlattices** arise when there is spatial ordering of each component within the basic lattice, sometimes in quite a complicated manner (e.g. Cu–Zn). Superlattices can also be created artificially in semiconductors by deposition of atoms in a calculated sequence. The existence of a superlattice is indicated by the appearance of ghost orders of diffraction

between the main X-ray diffraction spots. A particularly important example occurs in antiferromagnetic materials (e.g. MnF_2) where the atomic spins are ordered on a lattice that is different from the crystal lattice, and ghost orders are then evident in the diffraction pattern of slow neutrons, whose spin causes them to interact with the atomic spins. The ghosts are absent in an X-ray diffraction pattern of the same crystal because X-rays are not spin-sensitive.

3. The one-dimensional analysis carried out in this section is equivalent to the spectral analysis of a **frequency modulated** (FM) radio wave. The ghost orders of diffraction, which contain the information on the frequency and amplitude of the modulation, are called **side-bands** in telecommunications (see §10.2.4).

9.2.4 Diffraction efficiency: influence of the slit profile

The discussion of gratings has so far concentrated on the **interference function**, the Fourier transform of the set of δ-functions representing the positions of the individual apertures. This transform has now to be multiplied by the **diffraction function**, which is the transform of one aperture.

Let us first consider a simple amplitude transmission grating for which the apertures are slits, each with width b (which obviously must be less than their separation d). The diffraction function is then the transform of such a slit (§8.3.1),

$$\psi(u) = b\,\mathrm{sinc}(bu/2). \tag{9.19}$$

At the order m, $u_m = 2\pi m/d$. For the first order, as b is varied, the maximum value of $\psi(u_1)$ is easily shown to occur when $b = d/2$; thus the optimum slit width is half the spacing. But even with this value the efficiency of the grating is dismally small. The light power P_m reaching the various orders is proportional to the values of $|\psi(u_m)|^2$ namely,

$$P_0 \propto d^2/4, \quad P_{\pm1} \propto d^2/\pi^2, \quad P_{\pm2} = 0, \quad P_{\pm3} \propto d^2/9\pi^2, \text{ etc.} \tag{9.20}$$

Since $b = d/2$, this grating transmits exactly one half of the incident light, and therefore the fraction of the light intensity diffracted into the first order is

$$\eta = \frac{1}{2}\frac{P_1}{\sum_{m=m(\min)}^{m(\max)} P_m} \approx 10\%. \tag{9.21}$$

This factor η is called the **diffraction efficiency** and is defined in general as the fraction of the incident light diffracted into the strongest non-zero order. The figure of 10% can hardly be improved upon, within the limitations of real, positive transmission functions; the way to higher efficiencies is through the use of **phase gratings**.

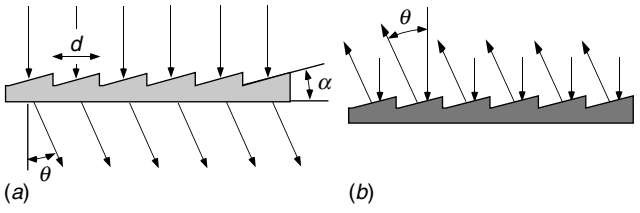

Figure 9.8

(*a*) Blazed transmission grating. The value of θ must satisfy the two equations $n\lambda = d\sin\theta$ and $\theta \approx (n-1)\alpha$. (*b*) Blazed reflection grating. The value of θ must satisfy the two equations $n\lambda = d\sin\theta$ and $\theta = 2\alpha$.

9.2.5 Blazed gratings

A blazed grating concentrates the diffracted energy into a particular order. It can be very efficient, but only in a given wavelength region.

The discussion in the previous section shows us how inefficient an amplitude transmission grating must necessarily be. Rayleigh originated the idea of combining the effects of refraction or reflection with interference to make a phase grating that could concentrate most of the intensity in one particular order. The principle is illustrated by Fig. 9.8. Each element in the transmission grating shown in Fig. 9.8(*a*) is made in the form of a prism, of which the angle is such that the deviation produced is equal to the angle of one of the orders of diffraction; correspondingly, in Fig. 9.8(*b*) a reflection grating is shown in which each element is a small mirror.

Such gratings are widely used. Instead of using any available sharp diamond edge for ruling a grating, a special edge is selected that can make optically flat cuts at any desired angle. Gratings so made are called **blazed gratings**. It will be noted that a diffraction grating can be blazed only for one particular order and wavelength, and the high efficiency applies only to a restricted wavelength region.

The scalar-wave theory of the blazed grating is an elegant illustration of the use of the convolution theorem. Suppose that a plane wavefront incident normally on the grating is deviated by angle β on being reflected or transmitted by an individual facet. For a reflection grating, $\beta = 2\alpha$ is determined by the geometry only; for a transmission grating it may be wavelength dependent too, but we shall restrict our interest to the former. Following the analysis in §8.4.1, the individual facet is represented by a phase ramp of form $\exp(\mathrm{i}k_0 x\sin\beta)$. We now describe the individual facet, of width b, by the complex transmission function $g(x) = \mathrm{rect}(x/b)\,\exp(\mathrm{i}k_0 x\sin\beta)$. The complete grating is therefore represented by

$$f(x) = g(x) \otimes \sum \delta(x - nd) \tag{9.22}$$

$$= [\mathrm{rect}(x/b)\,\exp(\mathrm{i}k_0 x\sin\beta)] \otimes \sum \delta(x - nd). \tag{9.23}$$

The Fourier transform of (9.23) is

$$F(u) = [\delta(u - k_0\sin\beta) \otimes \mathrm{sinc}(ub/2)] \cdot \sum \delta(u - 2\pi m/d)$$

$$= \mathrm{sinc}[b(u - k_0\sin\beta)/2] \cdot \sum \delta(u - 2\pi m/d). \tag{9.24}$$

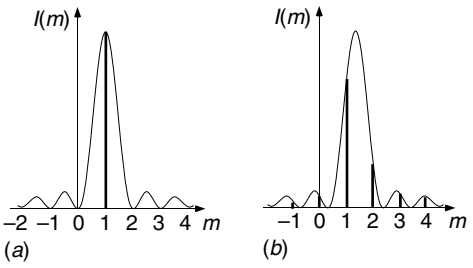

Figure 9.9

Diffracted intensity in the orders of a blazed grating; (*a*) at the wavelength for which the blazing was designed (all energy goes, theoretically, into the +1 order); (*b*) at a slightly different wavelength (the +1 order predominates, but other orders appear weakly).

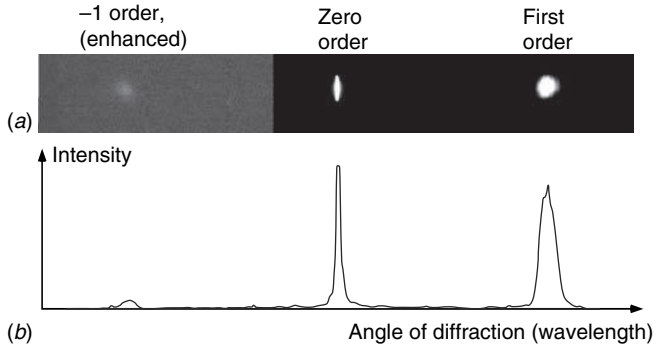

Figure 9.10

Zero order and first orders of diffraction from a narrow band source, measured using a reflection grating blazed for the first order. (*a*) Photograph of the spectrum (−1 order has been enhanced); (*b*) measured profile of (*a*).

One sees in Fig. 9.9(*a*) that the maximum of the envelope function (sinc), which indicates the value of u giving the highest intensity, has moved from the origin to $k_0 \sin\beta$. If $k_0 \sin\beta = 2\pi m_0/d$, this coincides with order m_0 (usually, but not necessarily, the first order). This way, β can be chosen to maximize the intensity in a specified order, for a given wavenumber k_0. The corresponding wavelength is called the **blazing wavelength**.

We can now calculate the diffraction efficiency. At the blazing wavelength the intensity I_m of the order m is given by $|F(2\pi m/d)|^2$:

$$I_m = \mathrm{sinc}^2\left[\frac{b\pi}{d}(m - m_0)\right]; \tag{9.25}$$

in the ideal case (complete transmission or reflection) where $b = d$, $I_m = 0$ for all orders except $m = m_0$. The diffraction efficiency in the m_0th order is therefore 100%! In practice, a grating with $b = d$ is difficult to construct; there are usually some obstructed regions at the edges of the facets. Then we have $b < d$ and the orders $m \neq m_0$ have small but non-zero intensities, with a consequent reduction in the efficiency (see Fig. 9.10).

At a wavenumber $k_1 \neq k_0$ the phase ramp is $\exp(ik_1 x \sin\beta)$ and

$$F(u) = \text{sinc}[b(u - k_1 \sin\beta)/2] \cdot \sum \delta(u - 2\pi m/d) \tag{9.26}$$

$$I_m = \text{sinc}^2 \left[\frac{b\pi}{d} \left(m - m_0 \frac{k_1}{k_0} \right) \right], \tag{9.27}$$

in which we used the blazing condition to write $\sin\beta$ in terms of k_0. This is illustrated by Fig. 9.9(*b*); the diffraction efficiency is no longer 100%, but can still be quite high if $k_1 \approx k_0$. The modification for non-zero angle of incidence is simple, and will be left as a problem to the reader (Problem 9.5). It should be remarked that the blazing wavelength can be altered somewhat by changing the angle of incidence.

In detail, the structure of a diffraction grating is comparable in scale with the wavelength, and so the scalar theory of diffraction is not really adequate. In particular, polarization-dependent effects are very much in evidence. A fuller discussion is given by Hutley (1982).

9.3 Two-beam interferometry

With a strain sensitivity $\delta l/l$ of 10^{-22} achieved by LIGO, interferometry is now the most sensitive measurement method in physics.

As well as answering basic questions about the nature of light, the phenomenon of interference also opened up vast possibilities of accurate measurement. As we have seen, even Young's fringes can give quite an accurate measure of the wavelength of light, and with more carefully designed equipment optical interferometry has become the most accurate measurement technique in physics. In this section we shall describe several interferometers based on the interference of two separate waves, with examples of their applications. For measurement purposes it is usual today to employ laser light sources, as indicated schematically in the figures; only when imaging is required as part of the interferometer (such as in interference microscopy, §12.4.5) are quasi-monochromatic sources preferred to avoid laser speckle.

9.3.1 Jamin and Mach–Zehnder interferometers

These interferometers use partial reflection at a beamsplitter to create two separate coherent light waves, and recombine them at a second beamsplitter. Note that in both cases there are two output beams. The optical path lengths can be compared, and small differences detected. The Jamin form is very stable to mechanical disturbances, but is less flexible in that the beams are relatively close to one another (Fig. 9.11). In the Mach–Zehnder interferometer a greater separation is possible (Fig. 9.12). Both interferometers can be adjusted, using

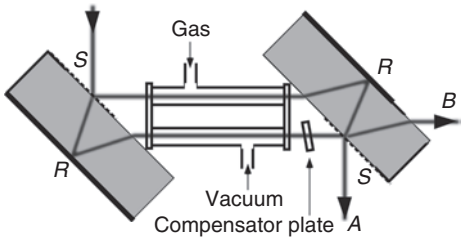

Figure 9.11

Jamin interferometer used for the measurement of refractive index of a gas. At *R* the glass plates are fully reflecting, and at *S* they are about 50% reflecting. The interference is visible at outputs *A* and *B*.

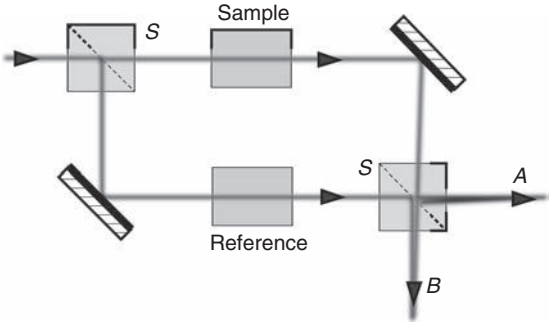

Figure 9.12

Mach–Zehnder interferometer. In this illustration we use cube beamsplitters *S* with reflectivity about 50%. The output can be observed at *A* or *B*.

a white light source, to have zero path difference under specified conditions. A typical application of either is to the measurement of refractive index of gases. In Fig. 9.11, one sees that the two beams go through closed glass tubes of length L, one of which is evacuated and the other contains gas at a known pressure. The difference in optical path $\overline{\delta l}$ then allows the refractive index of the gas to be measured:

$$\overline{\delta l} = (n-1)L. \tag{9.28}$$

In a measurement of this type one does not actually measure a fringe shift, but uses a compensator (usually a parallel glass plate of known thickness and refractive index inserted at a variable angle to one of the beams) to bring the fringes back to the initial (null) position. Then, for example, electronic detection might allow the null position to be sensed to about 10^{-3} fringes. From (9.28), for $L = 20\,\text{cm}$ and $\lambda = 0.5\,\mu\text{m}$, an accuracy of measurement $\delta n = \pm 10^{-3}\lambda/L = \pm 2.5 \times 10^{-9}$ would be achievable.

9.3.2 Michelson interferometer

The Michelson interferometer uses a single beamsplitter to produce two beams that are not only widely separated but also propagate in directions at right angles. These two features make it a very versatile instrument and it is the best

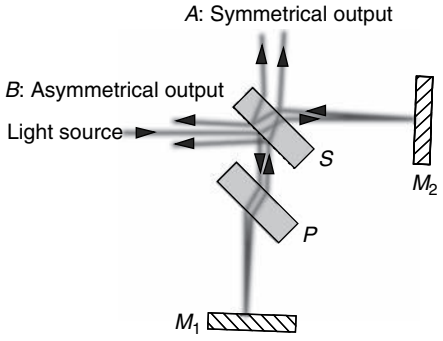

Figure 9.13

Michelson interferometer. The beamsplitter *S* is coated on the upper surface to reflect and transmit about 50% of the light, and *P* is the compensating plate. The output can be observed at *A* or *B*.

The Michelson interferometer, which compares waves travelling in different directions, has many modifications such as the Fourier transform spectrometer (§11.5) and the Twyman–Green interferometer (Box 9.2); it can be applied to many different types of measurement.

known of all the interferometers. It should not be confused with the Michelson stellar interferometer, which will be described in §11.8.1.

The principle is illustrated in essence in Fig. 9.13. Light enters from the left and is partly reflected and partly transmitted by the beamsplitter S, which has amplitude reflection and transmission coefficients $\mathcal{R}$ and $\mathcal{T}$ respectively. The two beams are reflected from the mirrors M_1 and M_2, and return to the beamsplitter. After a second reflection or transmission of each beam, the resultant interference fringes are observed at A or B. Notice that the amplitudes of the two waves interfering at A are $\mathcal{R}\overline{\mathcal{T}}$ and $\overline{\mathcal{R}}\mathcal{T}$. Following the argument in §5.7, these are equal in magnitude and have opposite signs for an ideal loss-less beamsplitter, and so when the path lengths via M_1 and M_2 are equal, complete *destructive* interference is observed; the zero-order fringe is black![1] The exit at A, where complete destructive interference can be expected, at least in theory, is often called the **symmetric** exit. On the other hand, at B the amplitudes are $\mathcal{R}^2$ and $\mathcal{T}\overline{\mathcal{T}}$, which both have the same sign but may not be equal, so that the zero fringe is bright, but complete destructive interference is unlikely. This may be called the **asymmetric** exit. Because the rays reflected from M_2 have to pass through three thicknesses of the beamsplitter S, whereas those reflected from M_1 have to pass through only one, Michelson inserted a compensating plate at P to give equality between the two paths. This plate is needed because glass is dispersive and so only by having the same amount of the same glass in both beams can the optical paths be made equal at *all* wavelengths. This plate must therefore be of the same thickness as S and placed at the same angle. Today, a cube beamsplitter is often used in place of Michelson's partially silvered plate beamsplitter, and the compensator is unnecessary.

Different geometries of fringes can be created in the Michelson interferometer by changing the angles and positions of the mirrors.

With the Michelson interferometer many different sorts of fringes can be obtained – straight, curved, or completely circular, in monochromatic or white light. These can all be understood in terms of a single theory if we regard the problem as a three-dimensional one, the different sorts of fringes resulting from looking at the same three-dimensional pattern from different directions.

[1] With real-life beamsplitters, this may not be so.

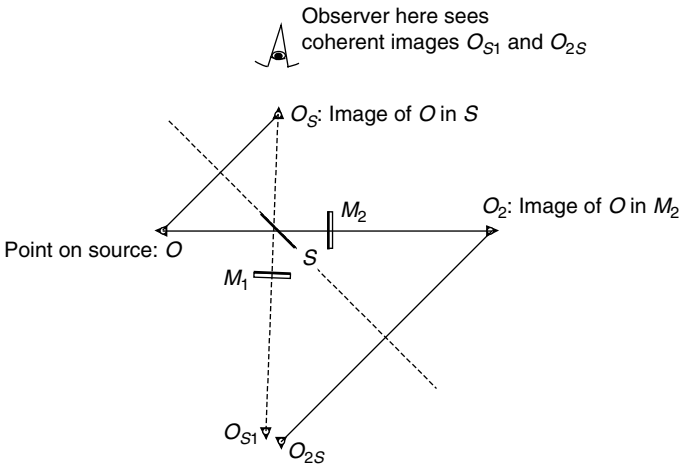

Figure 9.14

Principle of the Michelson interferometer observing an extended incoherent source. The observer sees, by reflection in the beamsplitter and the two mirrors, two virtual images of the source point O, at O_{S1} and O_{2S}. These images are coherent, and therefore interfere. For simplicity, the beamsplitter is assumed to have no thickness and the compensation plate has therefore been omitted. Note that M_1 is slightly tilted from the horizontal.

The source can be a broad one, but we can simplify the understanding of the interferometer by considering one 'ray' at a time, coming from one point on the source. Then two virtual images of this point, produced via the two routes to A or to B, interfere to give the observed pattern. If we ignore the finite thickness of the components, which does not affect the argument, we see from Fig. 9.14 that O has images at O_S and O_2 in S in M_2 respectively; O_S has an image O_{S1} in M_1, and O_2 has an image O_{2S} in S. The images O_{S1} and O_{2S} are the two virtual coherent sources that give rise to interference.

It can easily be seen that O_{S1} and O_{2S} can be brought as closely together as we require. Small adjustments in the position and angles of M_1 and M_2 can change their relative positions. The different sorts of fringes arise from various relative positions of O_{S1} and O_{2S}, and the scales of the fringes depend upon their separation.

Consider an observer at A, from where the two virtual sources are seen to radiate in antiphase. The same argument would follow at B, but there the two virtual sources are seen in phase. If O_{S1} and O_{2S} are side-by-side, the situation is just like Young's experiment, and we get a set of straight fringes, normal to the vector $O_{S1}O_{2S}$. The fringes are actually hyperbolic, as in Fig. 9.17(b), but are indistinguishable from straight fringes in most practical situations (§9.1.1). The closer the points, the wider the fringe separation. Another situation is for O_{2S} to be behind or in front of O_{S1}. The directions of constructive and destructive interference then lie on cones around the line $O_{S1}O_{2S}$. From Fig. 9.15(a) we see that, on a screen at distance $L \gg O_{2S}O_{S1} \equiv s$ the wave amplitude at P, the point corresponding to an angle of observation θ, is

$$\psi_P = \mathcal{R}T\left[\exp(\mathrm{i}k_0\overline{O_{2S}P}) - \exp(\mathrm{i}k_0\overline{O_{S1}P})\right] \tag{9.29}$$

$$= 2\mathcal{R}T\exp\left[\frac{1}{2}\mathrm{i}k_0(\overline{O_{2S}P} + \overline{O_{S1}P})\right]\sin\left[\frac{1}{2}k_0(\overline{O_{2S}P} - \overline{O_{S1}P})\right]. \tag{9.30}$$

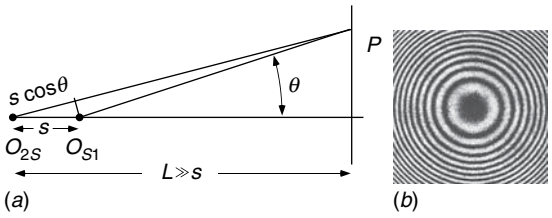

Figure 9.15

(*a*) Path difference at *P* between waves at angle θ to the axis, when O_{2S} lies behind O_{S1}. (*b*) Circular fringes seen in a Michelson interferometer.

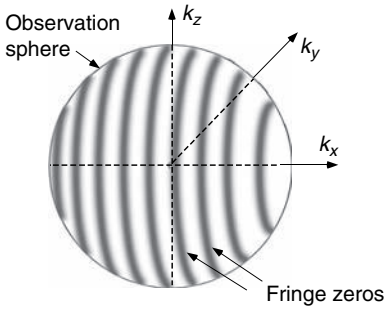

Figure 9.16

Schematic representation of the Fourier transform of two points – plane sinusoidal fringes – cutting the sphere of observation.

For this large L, $\frac{1}{2}(\overline{O_{2S}P} - \overline{O_{S1}P}) \simeq \frac{1}{2}s\cos\theta$, so the observed intensity can be written

$$|\psi_P|^2 = 4(\mathcal{R}T)^2 \sin^2\left[\frac{1}{2}k_0 s\cos\theta\right] = 2(\mathcal{R}T)^2[1-\cos(k_0 s\cos\theta)]. \quad (9.31)$$

Notice that $(\mathcal{R}T)^2$ always has value less than $\frac{1}{4}$ since $\mathcal{R}^2+\mathcal{T}^2 \le 1$, so $|\psi_P|^2$ is never negative. This defines a set of circular fringes (of constant θ) in the plane containing P. The exact value of s determines whether the centre ($\theta = 0$) will be bright or dark, and the scale of the fringe pattern is determined by s. Suppose that s is such that the centremost dark ring has order m_0, i.e. $k_0 s = (m_0+\delta)2\pi$, where $0 \le \delta < 1$. The succeeding dark rings have lower orders $m = m_0 - 1$, $m_0 - 2$, etc. For small angles θ, dark ring m appears at θ_m where

$$\begin{aligned}\cos(k_0 s\cos\theta) &\approx \cos\left[k_0 s\left(1-\frac{1}{2}\theta^2\right)\right] \\ &= \cos\left[(m_0+\delta)2\pi - \frac{1}{2}k_0 s\theta^2\right] = \cos 2m\pi = 1, \quad (9.32)\end{aligned}$$

whence $\frac{1}{2}k_0 s\theta^2 = (m_0+\delta-m)2\pi$. Notice the square-root dependence of the angular radius on the order, just like the zone plate (§7.2.5), in Fig. 9.15(*b*).

Following the discussion of crystallography in §8.6.4, it is instructive to consider this problem, and other interferometers, in terms of their Fourier transforms. The three-dimensional Fourier transform of the two points is a set of planar sinusoidal fringes, represented in Fig. 9.16. The different fringes observed are different aspects of this Fourier transform.

To understand this statement we make use once again of the concept of the sphere of observation (§8.6.4). Now, however, we are dealing with coherent

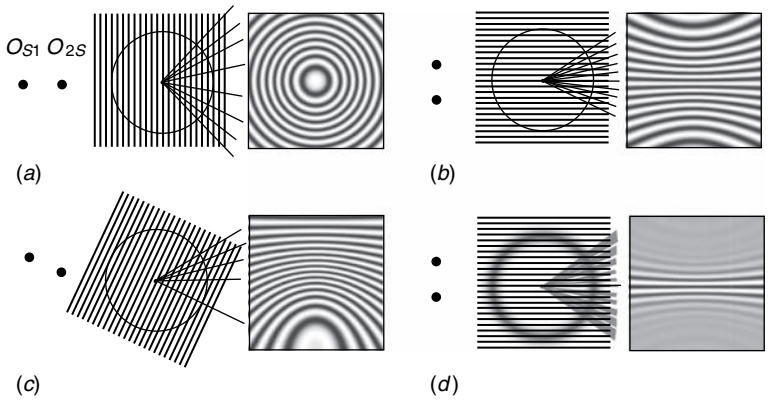

Figure 9.17

Different types of fringes from Michelson interferometer: (*a*) and (*b*) show how circular and 'straight' fringes are produced as the result of different dispositions of O_{S1} and O_{2S} and (*c*) shows an intermediate type of fringe pattern; (*d*) shows how broadened fringes are produced if a range of wavelengths, such as white light, is used.

sources and not scatterers so that their phase difference is always zero and does not depend upon an incident beam $\mathbf{k}_0$. Thus the factor $\exp(\mathrm{i}\mathbf{k}_0 \cdot \mathbf{r}')$ in (8.64) must be replaced by unity; this can be done by putting $\mathbf{k}_0 = 0$, which results in the observation sphere having radius $2\pi/\lambda$ and being *centred on the origin* of reciprocal space. The sphere of observation therefore penetrates the Fourier transform, and has its centre on a maximum (Fig. 9.16).

As the points O_{S1} and O_{2S} become closer, the fringe separation $2\pi/O_{S1}O_{2S}$ becomes larger, and as the disposition of the points changes the transform rotates into different orientations. Figure 9.17 shows how different types of fringes arise, when the intersection is projected onto the observation screen. If white light is used, the sphere must be considered to have finite thickness and only the zero-order fringe is sharp and the others are coloured and soon merge together. Such coloured fringes are the best way of identifying the zero-order interference.

The coloured fringes in a Michelson interferometer have another important application. By studying their profile in detail, we can measure the spectrum of the source. This method is called **Fourier spectroscopy** and will be discussed in detail in §11.5.

9.3.3 Localization of fringes

Fringes are localized in space when the light source is spatially incoherent. The concept is particularly important in interference microscopy because incoherent illumination gives superior images.

So far we have considered the interference fringes orginating from a single point source O. If the source is coherent, the beamsplitter divides the incident light into two waves that are mutually coherent at all points in space, and the fringes can be observed anywhere where they overlap after they exit the interferometer. The fringes are then said to be **delocalized**. This is the case when a laser is used as the source. On the other hand, if the source is extended and incoherent, such as the sky, each point on it creates its own fringe pattern in a different place; the various fringe patterns superimpose and generally cancel

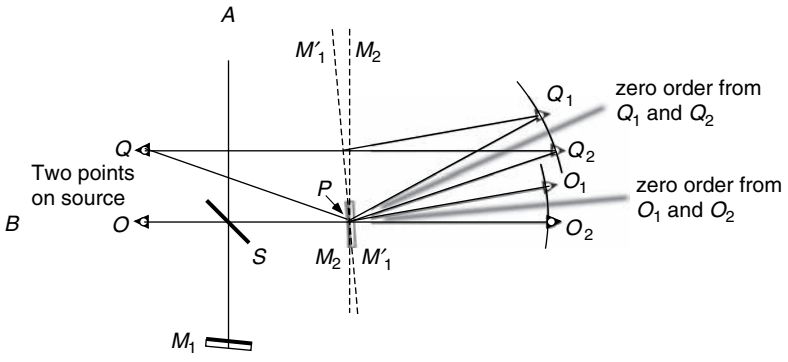

Figure 9.18 Construction based on Fig. 9.14 to show localization of fringes from an extended incoherent source in the Michelson interferometer, when the path difference is zero. An observer at *A* or *B* sees the two mirrors superimposed, intersecting at *P*, and the two virtual images O_1 and O_2 of the source point *O*. These images are equidistant from *P* and therefore the zero-order fringe, which bisects O_1O_2, must go through *P*. Likewise for a second source point *Q*. The zero-order fringe is therefore localized at *P*, which is on the mirrors.

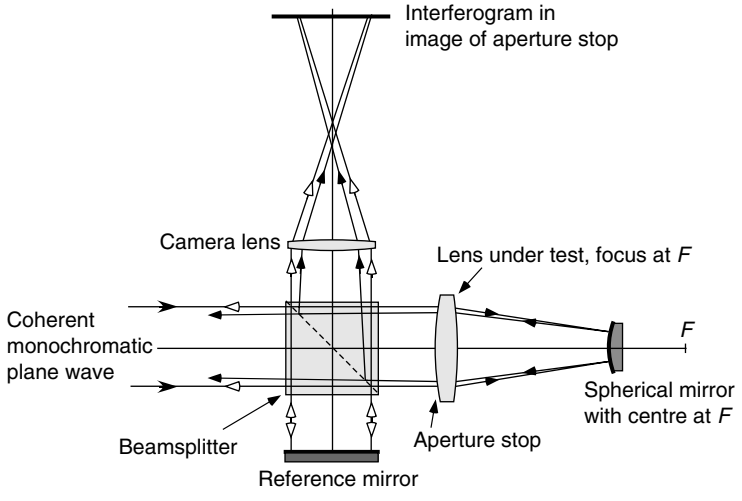

Figure 9.19 Configuration of a Twyman–Green interferometer for testing the quality of a lens. The reference mirror position can be moved in a controlled manner vertically, to get a series of interferograms from which the phase error can be deduced.

one another. However, there may be a region where all the fringe patterns coincide and, even with a broad incoherent source, a fringe pattern can be seen **localized** in this region. In the Michelson interferometer, for example, we shall see that the fringes are localized in the region of the mirrors M_1 and M_2, which the observer sees as coincident.

Returning to the construction in Fig. 9.14, we can see that we get the same result if we replace M_1 by its image M_1' in *S* and locate the images of *O* in M_1' and M_2 (Fig. 9.18). The observer sees these two images either directly (from *B*) or through the beamsplitter (from *A*). When the distances of M_1 and M_2 from the beamsplitter are equal, but they have slightly different tilt angles, M_2

Box 9.2 Optical testing: the Twyman–Green interferometer

One of the practical uses of the Michelson interferometer is to test an optical component. We saw that the simplest fringe pattern that can be obtained is a set of straight-line fringes, called an **interferogram**, obtained when a monochromatic plane wave is incident. By careful adjustment of the mirror angles, the output light field at A or B can even be made to be uniformly illuminated; however, this is difficult to do because the instrument is *very* sensitive to optical (phase) defects in any of the components; just the same, we shall assume that this is indeed possible. The **Twyman–Green** is a Michelson interferometer which uses this sensitivity to test optical components. The idea is shown in Fig. 9.19 for testing a lens. The lens is mounted in a configuration where, if it is ideal, it will convert an incident plane wave into an exiting plane wave, but any defects will affect the planarity of the exiting wave. The same principle can easily be used to test other optical components. In the configuration shown, this requires an extra component – a high-quality spherical mirror with radius less than the focal length of the lens; an optical workshop needs to have components of this sort available.

At the exit from the interferometer we place a camera focused on the aperture stop of the lens, so that deviations from the straight-line fringe pattern at a particular point on the interferogram can be associated directly with the corresponding point on the lens, so that if corrections are to be made by polishing, we know exactly where to make them.

Other interferometers could also be used in a similar manner, but the Michelson is very convenient because the two interfering paths are well separated. Another advantage is that it is easy to measure the phase errors quantitatively by modulating the position of the reference mirror in several steps. The fringes then move transversely, and by comparing the interferograms obtained at each step, the phase error can easily be deduced. This method is called **phase-stepping interferometry** and we leave it as a problem (9.9) to write a formula that gives the phase (relative to a fixed reference) from the interferograms at four mirror position separated by $\lambda/8$.

and M_1' intersect at P. Then O_1 and O_2 lie on an arc with centre at P, and therefore by simple geometry the zero-order fringe, which is equidistant from both O_1 and O_2, must pass through the intersection. This is true for any other source point such as Q. As a result, the zero-order fringe is localized along the intersection line. The argument can easily be extended to show that the higher-order fringes are also localized in the plane of the mirrors to a good degree of approximation. The same argument applies to fringes in a thin film, where the fringes are localized in the plane going through the geometrical intersection between the two surfaces, which is approximately that of the film

itself. Localization of fringes in incoherent light can be investigated in other interferometer types by representing them as a pair of mirrors in the same way.

Michelson and Morley set out to measure the velocity of the Earth relative to the supposed 'aether', but had no success. The answer was, of course, special relativity.

9.3.4 The Michelson–Morley experiment

One of the most important experiments leading to the modern era of physics was carried out by Michelson and Morley around 1887, employing the superb accuracy that Michelson's genius enabled him to extract from his interferometer. He was concerned by the fact that in order to explain the aberration of light – the apparent change of the direction of light from a star that occurs because the Earth is in motion around the Sun – Fresnel had had to assume that the 'aether' (the assumed medium in which electromagnetic waves propagate) must be at rest as an opaque body moves through it. He therefore set himself the task of measuring the velocity of the Earth with respect to the aether.

Starting with the assumption that the Earth's velocity relative to the aether was of the same order of magnitude as its orbital velocity, Michelson showed that his interferometer could make the measurement with reasonable certainty. The difficulty was that the effect to be measured is a second-order one. The velocity of light could be found only by measuring the time taken for a light signal to return to its starting point, and the difference between the time for a journey *up and down* the path of the Earth and that *across* the path, to take the two extremes, is a second-order quantity derived as follows.

According to classical physics, the time t_1 for the up-and-down journey of a path L is

$$t_1 = \frac{L}{c+v} + \frac{L}{c-v}, \tag{9.33}$$

where v is the velocity of the Earth. For the transverse passage the light would effectively have to travel a longer path $L' = 2L[1 + (v^2/c^2)]^{\frac{1}{2}}$, the time taken being $t_2 = L'/c$. Expanded to second order in v/c we have

$$t_1 \approx \frac{2L}{c}\left(1 + \frac{v^2}{c^2}\right); \qquad t_2 \approx \frac{2L}{c}\left(1 + \frac{1}{2}\frac{v^2}{c^2}\right). \tag{9.34}$$

The time difference $t_1 - t_2 = (L/c)(v^2/c^2)$, which corresponds to a path difference of Lv^2/c^2. If v is small compared with c, it would appear that the measurement of this quantity would not be possible.

But *was* it too small? The orbital velocity of the Earth is about 10^{-4} of the velocity of light. If L is 1 m the path difference is about 10^{-8} m, or about $\lambda/50$; this was too small for measurement using visual techniques, but large enough to suggest that with some modification a measurable effect might be expected.

The chief factor in producing a measurable path difference was an increase in the path L; the interferometer was mounted on a stone slab of diagonal

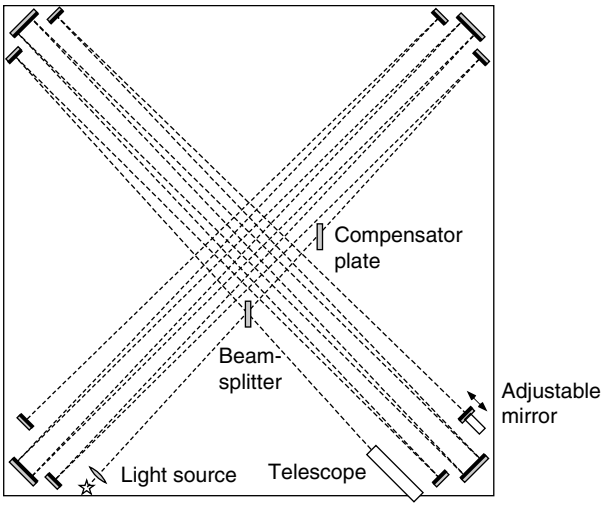

Figure 9.20

Interferometer used in the Michelson–Morley experiment. The output was observed visually through the telescope. (After Michelson (1927))

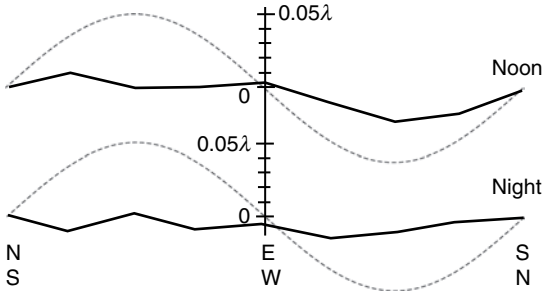

Figure 9.21

Typical diurnal variation of the fringe shift. The broken line shows $\frac{1}{8}$ of the displacement expected from the orbital velocity of the Earth. (After Michelson (1927))

about 2 m floating in a bath of mercury (Fig. 9.20) and the light was reflected so that it traversed this diagonal several times, giving a total distance L of 11 m. Since there was no a-priori knowledge of what might be the direction of the path of the Earth, the whole apparatus could be rotated and the maximum difference in path should be 22 times that previously calculated – just under half a fringe. Michelson and Morley were confident that they could measure this to an accuracy of about 5%.

This experiment is described in some detail because it is one of the most important experiments in optics. It illustrates the importance of developing techniques to measure very small quantities, for which Michelson was awarded the Nobel prize in 1907; the complete account of the care taken in avoiding spurious effects is well worth reading in the original (Michelson (1927)). The result was most surprising and disappointing; no certain shift greater than 0.01λ was found (Fig. 9.21). The broken line in Fig. 9.21 shows $\frac{1}{8}$ of the displacement expected from the orbital velocity of the Earth. It appeared the velocity of the Earth was zero!

There was just the possibility that the orbital velocity of the Earth at the time of the experiment happened to cancel out the drift velocity of the Solar System. This could not happen at all seasons of the year and therefore more measurements were made at intervals of several months. The result was always zero. This result was one of the mysteries of nineteenth-century physics. It was perplexing and disappointing to Michelson and Morley, whose skill and patience seemed to have been completely wasted. But in 1905 Einstein came forward with a new physical principle, relativity, the main assumption of which is that the velocity of light is invariant whatever the velocity of the observer, which was completely in accordance with the experiments. Thus, out of an apparently abortive experiment, a new physical principle received its confirmation and a new branch of physics had its beginning.

Although Michelson and Morley's results predated the theory of relativity, Einstein apparently did not know about them.

9.4 Common-path interferometers

Because the two counter-propagating beams travel equal paths, a common-path interferometer can be used with broad-band light.

In a common-path interferometer, which was first used in 1851 by Fizeau, the two interfering beams traverse identical, or almost identical paths, but propagate in opposite directions. As a result, with almost no trouble it can be set up to give white-light fringes, since the two path lengths are automatically equal. Small differences can be introduced by making offsets from the ideal counter-propagating condition. Figure 9.22 shows the two simplest forms, but other variants using more mirrors are possible. There are as usual two output waves; one at A, which is easily accessible, and one at B, which returns in the direction of the source. There is no need for the compensating plate of the Michelson interferometer because both beams pass through the beamsplitter plate an equal number of times. If the amplitude reflection coefficient of the splitter is $\mathcal{R}$ and its transmission coefficient $\mathcal{T}$, clearly one of the waves at A has amplitude $\mathcal{T}^2$ and the other $\mathcal{R}\overline{\mathcal{R}}$. The waves therefore interfere destructively when there is zero path distance at this exit (see §5.7), but cancel exactly only if $\mathcal{T}^2 = \mathcal{R}^2$; this requires a carefully chosen beamsplitter. On the other hand, at B, we have two waves with amplitudes $\mathcal{T}\overline{\mathcal{R}}$, which therefore interfere *constructively* at zero path difference, with unit contrast for any values of $\mathcal{T}$ and $\mathcal{R}$.

If light passes through the interferometer at an angle as shown in Fig. 9.22(*a*), a path difference is introduced because the two counter-propagating beams do not coincide exactly. But the two emerging rays are always parallel, so if an extended incoherent source is used it follows from §9.3.3 that the fringe pattern is **localized at infinity**. In versions of the interferometer that have a beamsplitter and an *odd* number of mirrors, e.g. Fig. 9.22(*b*), the two beams can be separated by a controlled amount, while remaining equal in length, and the B exit is more accessible.

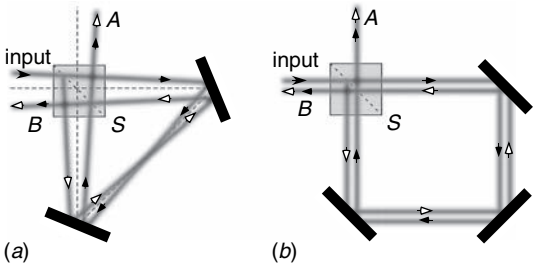

Figure 9.22

Two common-path interferometers: (*a*) constructed with a beamsplitter and two mirrors (triangular interferometer) and (*b*) with a beamsplitter and three mirrors. *S* is the beamsplitter plate. The first type can be used as a shearing interferometer (Fig. 11.15) in which the two beams are offset by a thick plate, which can be rotated about a vertical axis. The second type is more versatile, particularly for investigations involving the Sagnac effect.

Figure 9.23

Conceptual diagram of Fizeau's experiment to determine the velocity of light in moving water. The water tubes must be several metres long in order to get a measurable effect.

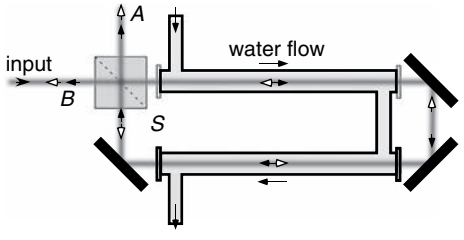

9.4.1 Velocity of light in a moving medium

Fizeau's measurements of the velocity of light in moving water differed from the expected result by about 55%, an error that could not be explained classically.

The common-path interferometer is important for two reasons. The first is historical; it provided the first way of measuring relativistic effects in light propagation. In 1851, Fizeau constructed an interferometer of this type to measure the velocity of light in moving water (Fig. 9.23). The water flows as shown in the figure, and so one of the light beams propagates parallel to the flow velocity, and the second one anti-parallel to it. The difference in velocity between the two waves could thus be measured. Of course, the classical theory of motion in a moving frame of reference that gave light velocities $c_+ = c/n+v$ and $c_- = c/n-v$ for the two cases, did not explain the results, and Fizeau found it necessary to employ an 'aether drag' coefficient $(1 - n^{-2})$ to explain them (this term had previously been introduced by Fresnel to explain anomalous results of stellar aberration due to the motion of the Earth, §9.3.4). Einstein's theory of relativity explains the results correctly by showing c_+ and c_- to be

$$c_\pm = \frac{c/n \pm v}{1 \pm v/nc}. \tag{9.35}$$

It is interesting that, unlike the Michelson–Morley experiment, the relativistic correction to be measured is first order in v, and can therefore be observed fairly easily even at low velocity.

9.4.2 The Sagnac effect and optical gyroscopes

Measuring the small phase shift introduced in a common-path interferometer in a rotating frame of reference allows its rate of rotation to be deduced.

An important modern application of the common-path interferometer pioneered by Sagnac in 1913 is to make an **optical gyroscope**. Suppose that the whole interferometer rotates in its plane at an angular velocity Ω. A phase difference is produced between the two counter-propagating beams; this is called the **Sagnac effect**. Because it involves light propagating in a non-inertial (rotating) system it should properly be treated by general relativity (Chow *et al.* (1985)); however, since no gravitational field is involved, special and general relativity give the same result, as follows.[2]

Since the interferometer used to investigate the Sagnac effect is usually built with the light travelling in a coiled optical fibre, we can consider for simplicity a circular interferometer of radius R, with path length L between the first and second passage of light through the beamsplitter. For a single turn, $L = 2\pi R$, but several turns may be involved. The velocity is $v = R\Omega$ and the light travels in a medium of refractive index n. Using the velocity-addition formula for an inertial frame, in one sense (clockwise, the same as Ω) the velocity of light is c_+ and in the other sense (counter-clockwise) it is c_- (9.35). These velocities represent the two speeds of light as measured in the laboratory frame. During the time t_+ that the clockwise light takes to traverse the length L of the interferometer, the beamsplitter moves a distance $R\Omega t_+$, so that $c_+ t_+ = L + R\Omega t_+$. Likewise, for the counter-clockwise sense, $c_- t_- = L - R\Omega t_-$. Combining these two, we find

$$\Delta t = t_+ - t_- = L\left[\frac{1}{c_+ - R\Omega} - \frac{1}{c_- + R\Omega}\right]. \tag{9.36}$$

Substituting for c_+ and c_-, (9.35), we find

$$\Delta t = \frac{2LR\Omega}{c^2 - R^2\Omega^2} \simeq \frac{2LR\Omega}{c^2}. \tag{9.37}$$

Note that n does not appear in this equation. Since the length of one turn is $2\pi R$, the result can also be written as $4NA\Omega/c^2$, where A is the area of one turn and N is the number of turns. It appears that this dependence on the area of

[2] A classical approach says that in vacuum the light takes time $\Delta t = L/c$ to traverse the loop, during which the beamsplitter moves a distance $\Delta t R\Omega = LR\Omega/c$, which shortens one path and lengthens the other. The phase difference introduced is therefore $\Delta\phi_0 = 2k_0 LR\Omega/c$. This result is correct for vacuum, but suggests that in a medium k_0 should be replaced by nk_0 and Δt by $n\Delta t$, resulting in $n^2\Delta\phi_0$, which is incorrect. Thus, confirmation that the Sagnac effect is independent of n provides a confirmation of special relativity.

the circuit is quite general when the Sagnac effect is calculated for polygonal interferometers such as those shown in Fig. 9.22. The proof of this is left as a problem for the reader (9.11).

This time difference can be translated to a phase difference or a frequency difference, depending on the method of sensing it. In an interferometric optical gyroscope, a light wave of frequency ω enters the interferometer, and the phase difference $\omega\Delta t$ is measured. The effect is very small, and it is usual to increase it by making L very long by using a coil of optical fibre; the fact that the fibre is made of glass does not affect the result because (9.37) does not involve n. R is simply made as large as practically convenient (it determines the size of the instrument). For example, if $L = 100\,\text{m}$, $R = 0.1\,\text{m}$, $\Omega = 1\,\text{rad}\,\text{s}^{-1}$ and $\lambda = 0.5\,\mu\text{m}$, the phase shift is

$$\Delta\phi = \omega\Delta t = \frac{2\pi c}{\lambda} \cdot \frac{2LR\Omega}{c^2} \simeq 0.8\,\text{rad}. \tag{9.38}$$

If the refractive index of the fibre depends on the light intensity, and the light is not equally divided between the two circulating beams, a phase difference is introduced which has to be distinguished from the Sagnac effect.

It is quite practical to measure such a phase shift, but a useful gyroscope must be accurate to about 10^{-3} times the rate of rotation of the Earth, $15^\circ\,\text{hr}^{-1}$, so that phase shifts of order 10^{-7}rad would have to be measured. Because of attenuation, the longest practical value for L is a few kilometres.

We shall not go into the various sensitive detection techniques that have been developed nor into the problems that have had to be solved in order to develop this effect into a successful technology. Many of the problems centre around non-reciprocal or non-linear processes in the fibre materials (§13.6.2), which affect the propagation of the clockwise and counter-clockwise wave differently and thus mimic the Sagnac effect.

9.5 Interference by multiple reflections

By using N multiple reflections, we essentially increase the maximum phase difference between the beams by $N - 1$ and therefore improve the resolving power of an interferometer.

Two-beam interference provided both an initial verification of the wave theory of light and a method of measuring the wavelength a monochromatic wave. Because, as we showed in §9.1.1, the intensity distribution in two-beam interference is sinusoidal, the maxima and minima are quite broad. In multiple-beam interference we essentially maximize (9.12) by using both large *m and N*. The conditions for reinforcement of N beams are then $N/2$ times more precise than those for the reinforcement of two, and very sharp maxima can be obtained.

We have already discussed one way of using multiple-beam interferometry, the diffraction grating, in which a set of accurately constructed periodic apertures gave us a set of interfering waves with regularly incremented phases. Another way of producing such a set of waves uses multiple reflections from a plane-parallel transparent plate, or between parallel mirrors. As the wave is reflected backwards and forwards, a constant addition to its phase is made in each cycle, and if a little of the wave is extracted at each reflection, the result is

Figure 9.24
Ring laser gyroscope.

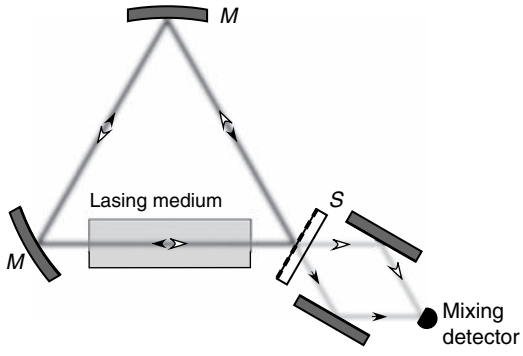

Box 9.3 The ring laser gyroscope

The ring laser gyroscope (Fig. 9.24) represents another way of using the Sagnac effect. A closed loop resonator is constructed with (at least) three mirrors defining a cycle of length L assumed, for simplicity, to be filled with a lasing material of refractive index n. The laser operates (see §14.6.1) at a resonance frequency for which the cycle length is a whole number m of wavelengths λ/n. When the resonator rotates, the light travelling clockwise satisfies

$$L + tR\Omega = L\left(1 + \frac{n}{c}R\Omega\right) = m\lambda_+/n, \tag{9.39}$$

whereas the anti-clockwise wave satisfies

$$L - tR\Omega = L\left(1 - \frac{n}{c}R\Omega\right) = m\lambda_-/n. \tag{9.40}$$

The very small wavelength difference is

$$\Delta\lambda = \lambda_+ - \lambda_- = \frac{2LRn^2\Omega}{cm}, \tag{9.41}$$

assuming that the same mode number m is optimum in both senses. Then, translating this small $\Delta\lambda$ into a frequency difference between the exiting waves we have, using $\lambda = nL/m$ from (9.39) and (9.40),

$$\Delta f = \frac{\Delta\lambda\, c}{n\lambda^2} = \frac{2LRn\Omega}{m\lambda^2} = \frac{2R\Omega}{\lambda}. \tag{9.42}$$

Measuring Δf allows Ω to be determined. This approach has, of course, assumed a 'circular triangle', but gives the result approximately. An estimate of its value, for $R = 0.1\,\text{m}$, $\Omega = 1\,\text{rad}\,\text{s}^{-1}$ and $\lambda = 0.5\,\mu\text{m}$ is 0.4 MHz. In principle, measurement of such a frequency (or less when Ω is much smaller) should not be difficult, but early efforts to implement laser ring gyroscopes were bedevilled by frequency locking; as $\Delta f \to 0$, scattering in the optics caused the two counter-propagating modes to become mixed, therefore stimulating emission at the same frequency. Further details are given by Lefèvre (1993).

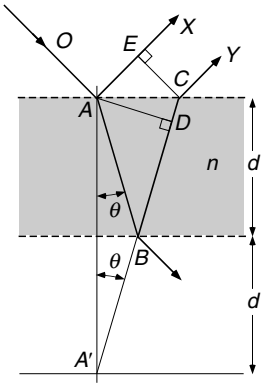

Figure 9.25

Path differences for rays reflected from top and bottom of plane film.

a set of waves with progressively increasing phase. We shall therefore consider the problem of multiple reflections between two parallel surfaces each having amplitude reflection coefficient $\mathcal{R}$ and transmission coefficient $\mathcal{T}$; if we assume that no energy is lost, then by (5.91)

$$\mathcal{R}^2 + \mathcal{T}\overline{\mathcal{T}} = 1. \tag{9.43}$$

Let us first calculate the phase difference introduced in one cycle. Consider the wave transmitted by a plate of thickness d and refractive index n, when the wave travels at angle θ to the normal *within the medium* (Fig. 9.25). The optical path lengths $\overline{AE}$ and $\overline{DC}$ are equal. Therefore the optical path difference between the rays going to X and to Y is $\overline{ABD} = n(AB + BD)$. By constructing A', which is the reflection of A in the lower surface, it is clear that

$$AB + BD = A'D = 2d\cos\theta \tag{9.44}$$

so that the phase difference between the interfering wavefronts AD is

$$2\pi\overline{ABD}/\lambda = k_0\overline{ABD} = 2k_0 nd\cos\theta \equiv g. \tag{9.45}$$

It is important to emphasize that the path difference is *not* twice AB, the projected thickness of the plate. Moreover, g *decreases* (like $\cos\theta$) as the angle of incidence *increases*. Both these points are somewhat counter-intuitive.

Now let us look at the amplitudes of the multiply reflected waves (Fig. 9.26). We should remember (§5.7) that $\mathcal{R}$ is defined for reflection from one side of each reflector – let's say the inside. So reflection from the outside will have coefficient $\overline{\mathcal{R}} = -\mathcal{R}$. The amplitudes of the waves are as shown in the figure. An exiting wave, either in reflection or transmission, will combine the waves having these amplitudes with phase increments g at each stage. The situation is very similar to the diffraction grating except that the waves have steadily decreasing amplitudes.

Let us consider the transmitted light. The series is

$$\psi(g) = \mathcal{T}\overline{\mathcal{T}}\sum_{p=0}^{\infty}\mathcal{R}^{2p}\exp(\mathrm{i}pg). \tag{9.46}$$

This function can be evaluated by two methods:

- as a geometric series with factor $\mathcal{R}^2\exp(\mathrm{i}g)$ relating successive terms,
- as a Fourier series with coefficients $a_p = \mathcal{R}^{2p}$.

First, we can evaluate (9.46) as a geometric series. This is the conventional method of attacking the problem. We write

$$\psi(g) = \mathcal{T}\overline{\mathcal{T}}\sum_{p=0}^{\infty}[\mathcal{R}^2\exp(\mathrm{i}g)]^p, \tag{9.47}$$

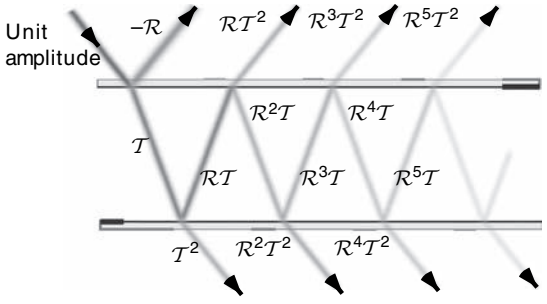

Figure 9.26
Multiple internal reflections in a transparent plate. $\mathcal{R}$, $\mathcal{T}$ and $\overline{\mathcal{T}}$ refer to amplitudes.

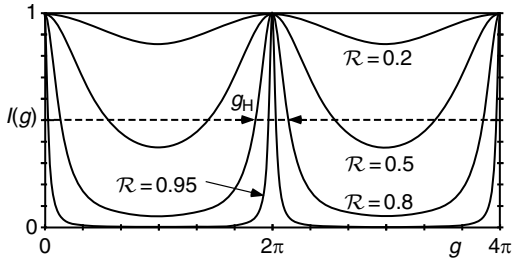

Figure 9.27
Form of $I(g)$ from (9.49) for different values of $\mathcal{R}$. Increasing the reflectivity decreases the line-width.

which is a geometrical series having sum

$$\psi(g) = \mathcal{T}\overline{\mathcal{T}}/[1 - \mathcal{R}^2 \exp(ig)]. \tag{9.48}$$

The intensity

$$\begin{aligned} I(g) = |\psi(g)|^2 &= \mathcal{T}^2\overline{\mathcal{T}}^2/(1 + \mathcal{R}^4 - 2\mathcal{R}^2\cos g) \\ &= \frac{\mathcal{T}^2\overline{\mathcal{T}}^2}{(1-\mathcal{R}^2)^2 + 4\mathcal{R}^2\sin^2(g/2)} \\ &= \left(\frac{\mathcal{T}\overline{\mathcal{T}}}{1-\mathcal{R}^2}\right)^2 \cdot \frac{1}{1 + F\sin^2(g/2)}, \end{aligned} \tag{9.49}$$

where $F \equiv 4\mathcal{R}^2/(1-\mathcal{R}^2)^2$ and $\mathcal{F} = (\pi/2)F^{1/2}$ is called the **finesse**.

Expression (9.49) has some interesting features. We notice that the function has periodic maxima of value $[\mathcal{T}\overline{\mathcal{T}}/(1-\mathcal{R}^2)]^2$ at $g = 2m\pi$. If there is no absorption, $[\mathcal{T}\overline{\mathcal{T}}/(1-\mathcal{R}^2)]^2 = 1$, and so we reach the apparently paradoxical conclusion that, **even if the transmission coefficient $\mathcal{T}$ is almost zero**, at $g = 2m\pi$ all the light is transmitted! Of course it is not really a paradox; the strong transmitted wave results from constructive interference between many multiply reflected weak waves. When F is large ($\mathcal{R} \simeq 1$) these maxima are very narrow; between them the function has value of order $1/F \ll 1$ (Fig. 9.27). The contrast, or visibility, of the fringes, which we shall define formally in §11.3.2, is then $F/(2+F)$, approaching unity when F is large.

Table 9.1. Values of half-peak width and finesse for different values of $\mathcal{R}$.

$\mathcal{R}$	0.5	0.6	0.7	0.8	0.9	0.95	0.98
$2g_H/2\pi$	0.54	0.36	0.24	0.15	0.07	0.03	0.01
Finesse $\mathcal{F}$	1.9	2.8	4.2	6.7	14	33	100

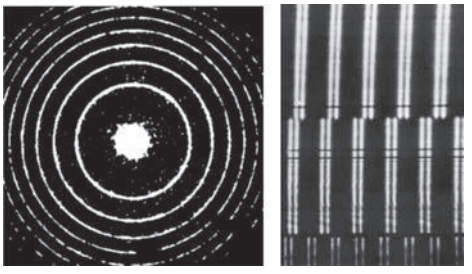

(*a*) (*b*)

Figure 9.28

(*a*) Fringes obtained with a He-Ne laser using a 3 mm thick parallel-sided glass plate coated with aluminium, giving $\mathcal{R}^2 \approx 80\%$ on both sides. (Prepared by Sarit Feldman and Shahar Hirshfeld) (*b*) Multiple-reflection fringes in birefringent mica. Cleaved mica has atomically flat surfaces. (From Tolansky (1973))

We can calculate the half-width of the peaks from (9.49). The intensity has fallen to half its peak value when $F\sin^2(g/2) = 1$. Thus

$$g_H = 2\sin^{-1}\left(F^{-\frac{1}{2}}\right) \approx 2F^{-\frac{1}{2}}. \tag{9.50}$$

If $\mathcal{R} \to 1$, the width $w = 2g_H \simeq 4(1-\mathcal{R})$. Table 9.1 shows the values of $2g_H/2\pi$, the width of the peaks relative to their spacing, as a function of of $\mathcal{R}$. For comparison it should be noted that the corresponding value for Young's fringes is 0.50, so that unless $\mathcal{R} > 0.6$ no improvement in sharpness is obtained by multiple reflections.

Evaluating (9.46) as a Fourier series gives a result that can be expressed as a convolution.

A second way of treating the summation (9.46) is to consider it as a Fourier series with coefficients $\mathcal{R}^{2p}$. The result is a periodic function with period $\Delta g = 2\pi$ and the wave-form is the Fourier transform of the coefficients $\mathcal{R}^{2p}$, where p is considered as a continuous variable. This function is an exponential and its Fourier transform is easily calculated; it is called a **Lorentzian** function. We leave this approach as a problem for the reader (Problem 9.12).

The reflected wave behaves in a complementary manner. Then there is almost complete reflection for all values of g, except for narrow dark lines at $g = 2m\pi$. The inversion occurs because the first reflection is from outside the cavity and has amplitude $-\mathcal{R}$, which is in antiphase to all the other reflections.

Multiple-reflection interference effects can be seen when any of the parameters in (9.45), $g = 2k_0 nd\cos\theta$, changes, namely k_0 (or λ), n, d or θ. Fig. 9.28(*a*) shows the ring pattern of sharp fringes that occur in convergent light through a plane-parallel glass plate coated to make $\mathcal{R} \to 1$, wherever $g = 2n\pi$. The

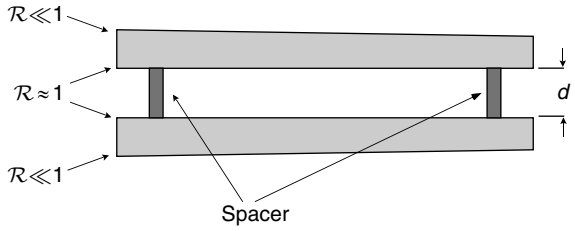

Figure 9.29
Schematic construction of a Fabry–Perot étalon. The outer surfaces are not quite parallel to the inner ones.

pattern is observed as a function of θ for constant n, d and k_0 in the far field (camera focused on infinity). Figure 9.28(b) shows a detail of the pattern observed in a mica sheet where d occasionally changes at molecular steps on the surface. Moreover, because mica is birefringent, there are two values of n and the fringes appear double.

9.5.1 The Fabry–Perot interferometer or étalon

An important practical application of interference by multiple reflections is the Fabry–Perot interferometer. Its basic construction is simplicity itself: it consists of two flat glass plates, arranged in a mechanical support with spacers between them so that they are parallel to one another. The two inner surfaces are coated so as to have a high reflection coefficient, but to transmit a small amount of light (Fig. 9.29). This simple description glosses over several important qualifications that can make the Fabry–Perot an expensive instrument. First, the plates must be flat to a very high degree of accuracy (better than $\lambda/50$). Second, the inner surfaces (reflective) must be very accurately parallel to one another. Third, the distance d, which can be very large (centimetres in laboratory instruments, to kilometres in LIGO – §9.7) must not change with time, due to temperature or other fluctuations. On the other hand, the outer surfaces of the plates are largely irrelevant. They must be optically flat, but play no part in the analysis. It is convenient if they are not quite parallel to the inner surfaces, or are anti-reflection coated, so as not to give rise to reflections which could confuse the interference pattern.

A good adjustable Fabry–Perot étalon is a masterpiece of opto-mechanical engineering, demanding glass surfaces with very high quality polishing, because of the repeated reflections.

9.5.2 Resolving power of the Fabry–Perot étalon

If an extended monochromatic source of light is observed through the interferometer, sharp bright rings are seen at angles θ given by $2k_0 nd\cos\theta = 2m\pi$, or $nd\cos\theta = m\lambda/2$. In this case, n is the refractive index of the air (or other medium) between the plates. Just like the Michelson interferometer fringes, these rings have radii basically depending on the square roots of the natural numbers (see equation (9.32)).

The finesse $\mathcal{F}$ of a Fabry–Perot tells you how much better is its resolving power than that of a two-beam interferometer.

But the rings are now very sharp and so a high resolving power is obtained. The form of $I(g)$ (9.49) does not allow us to use the Rayleigh criterion to determine this, because the function has no zeros, so we will use a different estimate, the **Sparrow criterion**, which actually corresponds better to visual or photographic acuity than does Rayleigh. This criterion expresses the resolution limit in terms of the joint intensity curve when observing two closely separated wavelengths of equal intensity. They are considered resolved when the intensity at the midpoint between the peaks shows a minimum (Fig. 9.6(*b*)). Mathematically, the closest separation at which this occurs is expressed by requiring that in (9.49), $\mathrm{d}^2I/\mathrm{d}g^2 = 0$ at the midpoint. The differentiation easily shows that this occurs at $g = 2m\pi \pm 2g_\mathrm{H} = 2m\pi \pm 2/\sqrt{F}$. Thus the separation between the two wavelength peaks has to be greater than $2g_\mathrm{H}$ for them to be resolved. As a result, the resolving power is

$$g/2g_\mathrm{H} = 2\pi m\sqrt{F}/4 = m\left(\pi\sqrt{F}/2\right) = m\mathcal{F}. \tag{9.51}$$

Comparing this with the result for a diffraction grating $g/\delta g = mN$ (9.12), we see that the finesse $\mathcal{F}$ can be interpreted as the number of slits N in an ideal diffraction grating which would have the same resolving power in the same order as the Fabry–Perot. The great advantage of the Fabry–Perot arises from large values of *both* $\mathcal{F}$ and the order m.

The resolving power (9.51) is equal to $\lambda/\delta\lambda$, $d/\delta d$ or $n/\delta n$, depending on what is being measured. For example, in a laboratory Fabry–Perot we might have an intensity reflection coefficient $\mathcal{R}^2 = 0.95$ and plate separation $d = 2.5\,\mathrm{cm}$; then for $\lambda = 0.5\,\mu\mathrm{m}$, $m = 2d/\lambda = 10^5$ at the centre of the ring pattern and $F = 1500$, $\mathcal{F} = 61$. Then $g/\delta g = 1.2 \times 10^7$, which is considerably better than the other interferometers considered so far. However, in order to get such resolution, the phase after more than $2\mathcal{F}$ reflections must be accurate to better than $\lambda/4$, so the plates must be flat and *parallel* over the area used to $\lambda/8\mathcal{F}$, in this example to $\lambda/500$, which is about 10 Å! A much more extreme situation where $d = 4\,\mathrm{km}$ is considered in §9.7.

The Fabry–Perot interferometer is widely used for studying the fine structure of spectral lines. If a source emits several lines, the overlapping ring patterns may be confusing, and it is usual to separate out the line of interest by also passing the light through a 'lesser' spectrometer, such as a prism or diffraction grating (Fig. 9.30). The limited spectral region separated out by this spectrometer must be such that all the rings observed as one group (satellite of the same spectral line for example) do indeed have the same order m. This means that the region must be smaller than $\delta\lambda = \lambda/2m$, which is called the **free spectral range** of the interferometer.

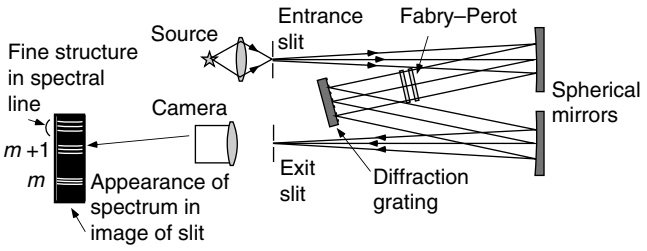

Figure 9.30
Use of Fabry–Perot étalon for high-resolution spectroscopy. The étalon is adjusted so that the rings cross the slit image as shown on the left, and each order m exhibits the fine structure around that wavelength.

9.5.3 Multiple reflections in an amplifying medium

A subject that has become of great importance with the advent of the laser is the effect of an amplifying medium on the behaviour of a multiple reflection interferometer, since this is the basis of laser resonators (§3.9 and §14.6.1). Suppose that the laser medium amplifies the wave-field by factor G during a single round trip. Then (9.46) becomes

$$\psi(g) = \mathcal{T}\overline{\mathcal{T}} \sum_{p=0}^{\infty} (\mathcal{R}^2 G)^p \exp(\mathrm{i}pg). \tag{9.52}$$

The result obtained would be similar to (9.49) if $\mathcal{R}^2 G$ were less than unity. For large enough G, the value becomes unity and the sum is

$$\psi(g) = \mathcal{T}\overline{\mathcal{T}} \sum_{p=0}^{\infty} \exp(\mathrm{i}pg) \tag{9.53}$$

$$= \mathcal{T}\overline{\mathcal{T}} \sum_{q=0}^{\infty} \delta(g - 2\pi q). \tag{9.54}$$

The spectrum is a series of ideally sharp lines; for this function $g_{\mathrm{H}} = 0$. This is the basic reason that laser lines are so sharp. Now if one asks what happens if $\mathcal{R}^2 G$ becomes greater than unity, one is asking a question that is unphysical because the series diverges. In practice, in a continuous-wave laser the amplification factor G eventually settles down, at high enough intensity, to a value equal to $\mathcal{R}^{-2}$, so that stability is achieved at that intensity. In a pulsed laser the amplification is large as the pulse starts, and gradually gets smaller as the population inversion is wiped out. The number of terms in the series for which $\mathcal{R}^2 G$ is greater than unity remains finite; towards the end of the pulse G falls below unity and the series terminates. This indicates that (9.53) should be summed to a finite value of p, and a small but non-zero linewidth $\delta g \sim 1/p_{\max}$ results.

One would expect from the above arguments that a continuous-wave laser would emit a number of perfectly sharp lines (longitudinal modes) separated by $\delta k = \pi/nd$ (from (9.54)) indicating a wavelength separation $\delta\lambda = \lambda^2/2nd$. As will be discussed in §14.7, the lines are not ideally sharp because of noise

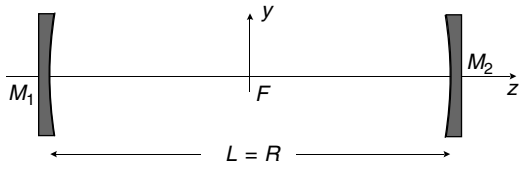

Figure 9.31
Confocal resonator.

(spontaneous emission) and thermal fluctuations; in addition, the number of frequencies emitted is rather small (sometimes only one) centred around the wavelength for which the gain G is maximum.

The modes of a confocal resonator are a set of bounded self-Fourier functions, of which the Gaussian is the best known.

9.5.4 The confocal resonator: transverse modes

One widely used example of a periodic system of the type discussed in §3.9 is the confocal resonator, for which $L = R_1 = R_2$ (Fig. 9.31). This is marginally stable in the geometrical sense, and the foci of the two mirrors coincide (hence the name). If such a resonator contains an amplifying (lasing) medium, we have a system that closely approximates that discussed in the previous section, in that geometrical optics does not predict any light leakage, even for mirrors of finite size. We shall not discuss the properties of this resonator in detail, but use it to illustrate the idea of **transverse mode patterns**.

Consider the amplitude $a(x, y)$ of light travelling to the right in the common focal plane (Fig. 9.31). Since this is the light amplitude in the focal plane, the amplitude at the other focal plane of the mirror M_2 (which is coincident with it) must be its Fourier transform $A(u, v)$ (§8.2), but the light is travelling to the left. However, this system is symmetrical about the focal plane and so the direction of travel of the waves is unimportant, and a stable mode of operation is seen when the Fraunhofer diffraction pattern is identical to the original function $a(x, y)$ in amplitude and phase at each point.

In §4.10 we discussed 'self-Fourier functions', which have the property that the function and its Fourier transform are identical in form. The relevant functions in the present context, limited to a small paraxial region, are the Gaussian function in particular, and in addition the set of Gauss–Hermite polynomials that should be familiar to any student of quantum mechanics as the wave-functions of a harmonic oscillator.[3] They are expressed as

$$a_n(x) = H_n(x/\sigma)\exp(-x^2/2\sigma^2), \tag{9.55}$$

where the functions $H_n(x)$ obey the recurrence relation:

$$2xH_n = H_{n+1} + 2nH_{n-1}, \quad H_0 = 1, \tag{9.56}$$

[3] The wave-function in p-space is the Fourier transform of that in q-space, and the Hamiltonian of the harmonic oscillator, which can be written $\mathcal{H} = \frac{1}{2}(p^2 + q^2)$, is invariant on interchanging p and q.

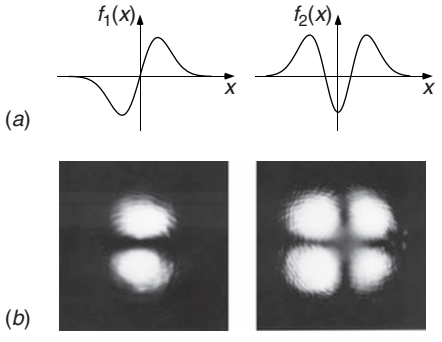

Figure 9.32
(*a*) Examples of Gauss–Hermite functions; (*b*) photographs of (01) and (11) transverse laser modes.

which gives $H_1 = 2x$, $H_2 = 4x^2 - 2$, etc. In Fig. 9.32(*a*) we show two examples of these functions.

In two dimensions any product of the form

$$a_{lm}(x,y) = H_l(x/\sigma)H_m(y/\sigma)\exp[-(x^2+y^2)/2\sigma^2] \tag{9.57}$$

satisfies our requirements. They can be seen as the intensity distribution across the output beam of a slightly misaligned continuous-wave laser; two examples are shown in Fig. 9.32(*b*). The various functions are known as **transverse modes** and are referred to by the number pair (l, m). They should be compared with the similar modes in optical fibres (§10.2), although their origin there is rather different.

For the basic Gaussian mode, we recognize the beam within the resonator as a Gaussian beam (§7.3) with a waist at the centre point. Thus, for the symmetrical arrangement where $R_1 = R_2 \equiv R_0$ in the terms of §3.9,

$$\begin{aligned} \sigma^2 &= s^2 = k_0 R_0/\sigma^2, \\ \sigma &= \sqrt{R_0/k_0} = \sqrt{R_0\lambda/2\pi}. \end{aligned} \tag{9.58}$$

The waist has Gaussian parameter w, where from (7.40)

$$w^2 = \frac{R_0^2\sigma^2}{R_0^2 + k_0^2\sigma^4} = \frac{\sigma^2}{2}. \tag{9.59}$$

This is the basis of a single-mode laser, which creates an output beam with a Gaussian profile.

9.6 Advanced topic: Berry's geometrical phase in interferometry

Two waves with orthogonal polarizations cannot interfere directly. It is therefore important to ensure that the initial polarization of a wave entering an interferometer is preserved or restored before the interference pattern is

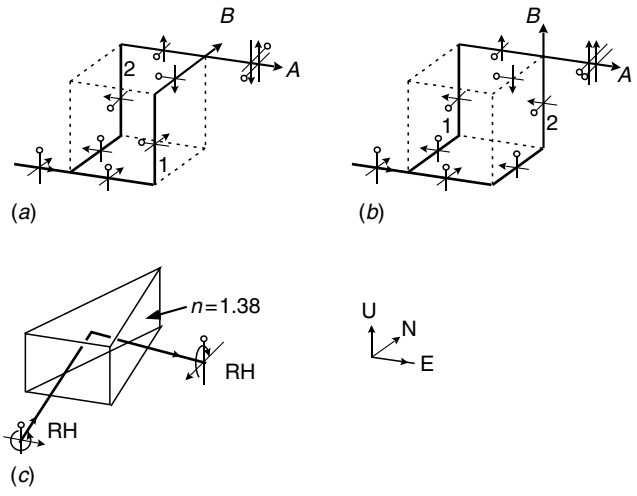

Figure 9.33

'Cubical Mach–Zehnder' interferometers, each with zero path difference and two routes between the beamsplitters. In (*a*) the routes labelled 1 and 2 have LH and RH helicities respectively, whereas in (*b*) they both have RH helicity; (*c*) shows the relationship between the field vectors on reflection at the special mirrors in this example.

observed. From a practical point of view, polarization changes within an interferometer often occur when light is reflected at oblique incidence from a mirror or beamsplitter, and also when the light path does not lie in a single plane. Even if interference occurs, the phase may be different from a naive expectation, because of phase changes on reflection.

If the light path is not planar, further phase changes can arise for topological reasons, depending on whether the light path describes a right-handed or left-handed helical route; such phases are called **geometrical** or **Berry phases** (Berry (1984, 1987)). We shall illustrate this phenomenon with a simple example.

The discussion is considerably simplified if we build our interferometer with polarization-preserving mirrors and beamsplitters. These are not conventional laboratory components; in general, reflection at a mirror reverses the sense of a circularly polarized wave, but this can be avoided if internal reflection occurs at a dielectric–air interface so that the angle of incidence is between the Brewster angle and the critical angle. In such a case the phase changes introduced preserve the sense of circular polarization. Since the angle of incidence should be 45° we can use a prism of, say, magnesium fluoride, ($n < \sqrt{2}$) as shown in Fig. 9.33(*c*). We emphasize that the above mirrors have been introduced in order to simplify the following discussion; they have no effect on the value of the Berry phase.

With such polarization-preserving reflectors we can construct a three-dimensional Mach–Zehnder interferometer in which the light beams traverse the edges of a cube. The edges of the cube are exactly equal, so we expect, a priori, that there will be constructive interference at exit A and destructive interference at B. Two possible constructions for the interferometer using different cube edges, each having path difference zero, are shown in Fig. 9.33. In each of the interferometers, we follow through the orientation of the **E**

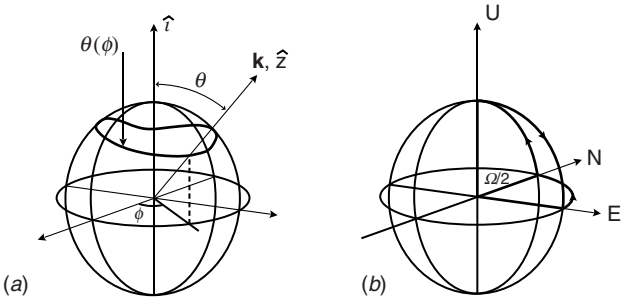

Figure 9.34

(*a*) Construction of a general k-route on the surface of a sphere; (*b*) construction of locus ENUE appropriate to the cube interferometer in Fig. 9.33(*a*). $\Omega/2$ is the spherical angle enclosed by the three axes.

vector of the incident wave after successive reflections; this is done for initially $\parallel$ ($\uparrow$) and $\perp$ ($\circlearrowleft$) fields. What appears in Fig. 9.33 is that in version (*a*) there is *destructive* interference at A (the exiting fields have opposite orientations) while in (*b*) there is *constructive* interference.

The difference can be traced to the sense of rotation of the light beams. Designating the three directions by North, East and Up as shown, in (*a*) beam 1 goes EUNE while beam 2 goes ENUE; the first is a rudimentary left-handed helix, while the second is right-handed. In (*b*), both beams are ENUE, which is right-handed. It is the different sequences of the finite rotations which introduce the π phase difference between the two cases. This phase change is topological in origin, and depends only on the geometry of the system; it is an example of a wide range of such phase changes, in classical and quantum physics, which were initially derived on general grounds by Berry (1984). They are identically zero in two-dimensional arrangements.

Berry's phase provides a method of creating arbitrary and controllable *achromatic* phase differences between two waves; compare this to the Gouy effect (§7.3) which can create an achromatic π phase shift only.

For any chosen three-dimensional interferometer the geometrical phase can be deduced by plotting the propagation vectors **k** of the waves as they traverse the two arms of the interferometer as two loci on the surface of a sphere, as in Fig. 9.34(*a*). Before the initial beamsplitter the **k**-vectors of the two waves coincide, and likewise after the second one. Thus the two loci have common end-points. If we define Ω as the solid angle subtended at the centre of the sphere by the segment of the sphere enclosed between the two loci, we shall show that the topological phase difference between the two is $\pi - \Omega/2$. This construction makes it easy to calculate the geometrical phase for any interferometer (Problem 9.16). Clearly, if the interferometer lies in a plane, $\Omega = 0$.

This construction can be derived in the case of electromagnetic waves as follows (Lipson (1990)). We shall assume that the changes in **k** are continuous (so that the loci on the sphere are uniquely defined, although in the example we quoted there are actually discontinuous changes in **k** at the mirrors!). We postulate an observer of the electromagnetic wave who travels slowly along each of the routes, measuring the vector field in his own frame of reference, which changes continuously so that the local z-axis always coincides with **k**. In order to maintain this situation, the observer has to rotate his frame, and we define $\boldsymbol{\alpha}(t)$ as his angular velocity with respect to the laboratory frame.

In the frame rotating at $\boldsymbol{\alpha}$, we relate the time derivative of a general vector $\mathbf{V}$ to that in the inertial frame by

$$\left(\frac{\partial \mathbf{V}}{\partial t}\right)_{\text{rotating frame}} = \left(\frac{\partial \mathbf{V}}{\partial t}\right)_{\text{inertial frame}} - \boldsymbol{\alpha} \times \mathbf{V}. \tag{9.60}$$

We can apply this to Maxwell's equations (5.9) and (5.10) which yield, in the observer's space,

$$\nabla \times \mathbf{H} = \epsilon_0 \left(\frac{\partial \mathbf{E}}{\partial t} - \boldsymbol{\alpha} \times \mathbf{E}\right); \tag{9.61}$$

$$\nabla \times \mathbf{E} = -n_0 \left(\frac{\partial \mathbf{H}}{\partial t} - \boldsymbol{\alpha} \times \mathbf{H}\right). \tag{9.62}$$

The other two Maxwell equations ((5.7) and (5.8)) are unchanged. The wave equation which replaces (5.12) then follows as

$$\frac{\partial^2 \mathbf{E}}{\partial t^2} + \boldsymbol{\alpha} \times \frac{\partial \mathbf{E}}{\partial t} = c^2 \nabla^2 \mathbf{E}. \tag{9.63}$$

This equation is analogous to that obtained in classical mechanics for Foucault's pendulum swinging on a rotating Earth, in which the second term arises from the Coriolis force.

In contrast to the usual wave equation (5.12), a linearly polarized plane wave is not a solution of (9.63); however, left- and right-handed circularly polarized waves are solutions. Substituting waves

$$\mathbf{E}_{\pm} = E_0(1, \pm \mathrm{i}, 0) \exp[\mathrm{i}(\omega t - kz)], \tag{9.64}$$

we immediately find the dispersion relation

$$c^2 k^2 = \omega^2 \pm \alpha_z \omega \;\Rightarrow\; \omega_{\pm} \approx ck \pm \alpha_z/2 \tag{9.65}$$

when $\alpha \ll \omega$. The phase difference between the waves along the two routes now results from the slight difference between the velocities that arises if α_z is positive for one and negative for the other, as a result of their opposite helicities.

The phase difference between beginning and end of a route is

$$\int_0^{z,t} (k\,\mathrm{d}z - \omega\,\mathrm{d}t) \pm \frac{1}{2}\int_0^t \alpha_z\,\mathrm{d}t = \Delta\Phi_0 \pm \frac{1}{2}\int_0^t \alpha_z\,\mathrm{d}t \equiv \Delta\Phi_0 + \gamma, \tag{9.66}$$

$\Delta\Phi_0$ indicating the usual (kinetic) phase difference expected from the optical path length of the route. The extra term γ can be easily interpreted by the construction on the sphere. The direction of $\mathbf{k}$ has angular position (θ, ϕ), Fig. 9.34(a). Then the locus is the curve $\theta(\phi)$ and $\boldsymbol{\alpha}$ is the sum of the two orthogonal components:

$$\boldsymbol{\alpha}(t) = \frac{\mathrm{d}\phi}{\mathrm{d}t}\hat{\imath} + \frac{\mathrm{d}\theta}{\mathrm{d}t}\hat{\jmath}, \tag{9.67}$$

where $\hat{\imath}$ is the unit vector to the pole and $\hat{\jmath}$ is the common normal to $\hat{\imath}$ and $\mathbf{k}$. Thus the projection of $\boldsymbol{\alpha}$ on the z-axis in the rotating coordinates, defined as being parallel to $\mathbf{k}$, is

$$\alpha_z = \frac{\mathrm{d}\phi}{\mathrm{d}t}(\hat{\imath}\cdot\hat{z}) = \frac{\mathrm{d}\phi}{\mathrm{d}t}\cos\theta. \tag{9.68}$$

Integrating this along the route gives

$$\gamma = \frac{1}{2}\int_0^t \alpha_z\,\mathrm{d}t = \frac{1}{2}\int_0^t \frac{\mathrm{d}\phi}{\mathrm{d}t}\cos\theta\,\mathrm{d}t = \frac{1}{2}\int \cos\theta(\phi)\mathrm{d}\phi. \tag{9.69}$$

For a closed loop, the solid angle subtended at the centre of the sphere is $\Omega = \oint[1-\cos\theta(\phi)]\,\mathrm{d}\phi = 2(\pi-\gamma)$. Thus, when we have drawn on the sphere the $\mathbf{k}$-routes corresponding to the two arms of the interferometer, $\gamma = \pi - \Omega/2$, where Ω is the solid angle subtended by the enclosed segment. We recall that this γ corresponds to one of the circularly polarized waves. The wave with opposite sense gives $-\gamma$, and the *difference* between the two, namely 2γ, is directly measurable since $\Delta\Phi_0$ in (9.66) cancels out. Experiments on variations of the cube interferometer carried out by Chaio *et al.* (1988) and on propagation in helically coiled fibres by Tomita and Chaio (1986) confirm this result. In the cube interferometer we described in Fig. 9.33, $\gamma = \pi/2$, and it is the phase difference $2\gamma = \pi$ which results in the destructive interference (Fig. 9.33(*b*)).

9.7 Advanced topic: The gravitational-wave detector LIGO

The Laser Interferometer Gravitational-wave Observatory (LIGO) is based on three interferometers with the highest resolution ever built (Smith (2009); Abbott *et al.* (2009)). Here, we shall describe the optics of these interferometers briefly because they incorporate many of the ideas discussed in this and other chapters. They are designed as instruments for detecting the gravitational waves emitted by dramatic astrophysical events such as coalescing black holes or neutron stars and supernova explosions. Such a wave, as it passes the Earth, should result in minute relative movements of massive bodies separated by a vector distance normal to the wave propagation direction.

In order to detect such relative movement, and to estimate the direction of the source, the idea is to compare the change in separation between two pairs of suspended masses, one pair being oriented along the x-direction, and the other along y. The sign of the change, i.e. elongation or shortening of the vector, depends on the polarization of the gravitational wave; this is a quadrupole field and not a dipole field as in an electromagnetic wave, and if the polarization is in the most favourable orientation parallel to one of the interferometer axes

it causes equal and opposite effects in the two orthogonal directions. On the other hand, an unfavourable polarization at 45° to the axes would cause no effect. The expected peak frequency of gravitational waves from such sources is between 40 and 2000 Hz, so that in order to obtain sufficient sensitivity the size of the separation between the masses must be several kilometres; even this is many orders of magnitude less than the wavelength, since the waves propagate at the velocity of light. As a result, the expected signal amplitude is only about 10^{-9} nm. In order to eliminate noise arising from man-made sources and seismic events, three interferometers have been built, in Washington and Louisiana states in the USA, separated by more than 3000 km, and a third in northern Italy. Only events that are recorded simultaneously at these observatories will be considered as true signals.

The structure of each LIGO interferometer is a Michelson interferometer augmented by a 4 km spherical Fabry–Perot resonator in each arm. The Michelson interferometer gives an output that measures the difference between the path lengths in the two arms. The resonator mirrors are designed to be in the middle of the stable region (§3.9), where the stability number $(1 - L/R_1)(1 - L/R_2) = 0.33$ or 0.67. The light source is a highly stabilized single-mode 10 W Nd-YAG laser, and interference is detected in the A (symmetric) exit, light at the B exit being returned to the system by a 'recycling mirror'. From §9.5.2 the high resolving power achieved is $2m\mathcal{F} = 4L\mathcal{F}/\lambda$, since it behaves as a Michelson interferometer in which the path length in each of the two arms is multiplied by the effective number of reflections, the finesse $\mathcal{F}$. Thus, for the experimental parameters $L = 4$ km, $\mathcal{F} = 20$, $\lambda = 1.0$ μm, we expect a resolving power of about 3×10^{11}. However, this formula is based on the Sparrow criterion, and advanced techniques of fringe detection allow much better detection than this by accurate curve fitting to a known line-shape. Without entering into technical details, when a photon flux of p photons per second is used, and results are integrated for T seconds, the resolving power can be increased by a factor of order $\sqrt{pT}$, which has a value of about 10^{11} for a 10 W laser and $T = 1$ s. Thus the expected resolving power is about 10^{22}. Currently, a frequency-dependent resolving power peaking at 10^{21} has been measured for wave frequencies between about 100 Hz and 3 kHz. For the 4 km separation between two test masses, this corresponds to a positional sensitivity of about 4×10^{-9} nm and is considered sufficient to detect astrophysical events as far away as 10^7 parsecs.

One should notice that since the dynamic range of the photon detectors is finite, and one wishes to detect with photon-limited sensitivity, it is essential to work under conditions of *almost* destructive interference at the A exit of the interferometer where a sufficiently small signal can be expected. Most of the light therefore leaves through the B exit, where the recycling mirror, essentially creating a new resonator in phase with both of the Fabry–Perots, allows the reflected energy to be reused. Figure 9.35 shows the optical layout of a LIGO schematically and Fig. 9.1 showed an aerial photograph of the LIGO

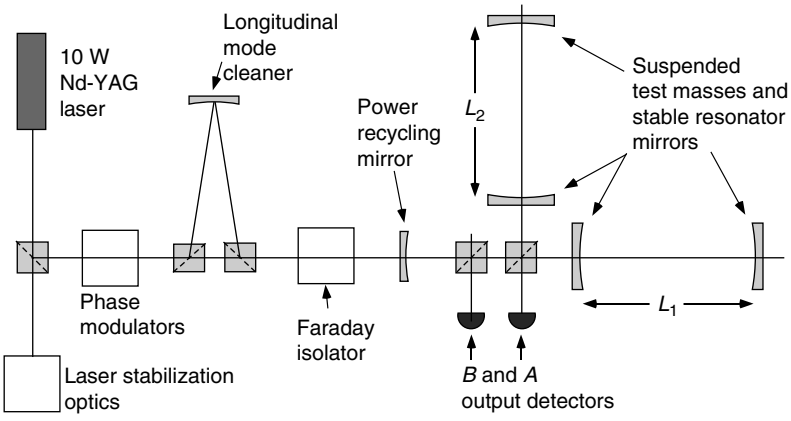

Figure 9.35 The optical layout of the Michelson–Fabry–Perot interferometer of a Laser Interferometry Gravitational-wave Observatory. It is powered by a 10 W near infra-red frequency laser and has two 4 km long Fabry–Perot étalons in the arms of a Michelson interferometer. Interference is observed at A and the light reflected to B is mainly returned by a recycling mirror. The longitudinal mode cleaner selects a single longitudinal mode of the laser output.

at Hanford, WA. From the optical point of view, the system works optimally, but many improvements, including an increase of the input energy, are planned for the near future.

Chapter summary

In this chapter we showed how optical interference can be used as an accurate measurement tool.

- We saw that even a simple set-up like Young's slits or a thin film of material can make surprisingly accurate wavelength measurements.
- We studied diffraction gratings, as an extension of the idea of Young's slits, and saw how to optimize their resolving power and efficiency, particularly by using blazed reflection gratings.
- We learnt how several types of two-beam interferometer work, including the famous Michelson interferometer, and studied their applications.
- We derived the Sagnac effect in a rotating frame of reference and saw how it is used to construct an optical gyroscope.
- We saw how the use of multiple reflections in the Fabry–Perot interferometer results in very high resolution, which makes it a useful tool for atomic spectroscopy.

- We studied the physical optics of laser resonators.
- We learnt about Berry's geometrical phase in optical systems with helical properties.
- We saw the principles of a LIGO interferometer, used by astronomers to look for far-away cosmic catastrophes by detecting gravitational waves.

Problems

9.1. An amplitude diffraction grating has amplitude transmission function of the form $f(x) = \frac{1}{2}(1 + \cos Kx)$. What is its diffraction efficiency $\eta(m)$ in the various orders m?

9.2. An amplitude diffraction grating (i.e. one that does not affect the phase) has a transmission function $f(x)$ $(\in 0 < x < d)$ which is real and positive. What function maximizes the diffraction efficiency in the first order?

9.3. An echelon grating has construction like a staircase, with highly reflecting treads of width b and height h. It has N steps (Fig. 9.36). Deduce its Fraunhofer diffraction pattern, and the resolving power attainable for high-resolution spectroscopy.

9.4. Find the resolving power of a diffraction grating according to the Sparrow criterion, when the intensities of the two wavelengths to be resolved are equal.

9.5. A reflection grating is blazed for $\lambda = 700$ nm in the first order at normal incidence. The zero order is found to have intensity 0.09 compared to the first order at that wavelength. Assuming the grating to be constructed of flat mirrors, find the relative intensities of the other orders. Find also the relative intensities at $\lambda = 500$ nm.

9.6. A grating constructed of flat mirrors is blazed for a certain wavelength λ_0 in the first order, when light is normally incident. Find how the blazing wavelength depends on the angle of incidence.

9.7. Why does a soap film appear black in reflected light as its thickness approaches zero? Light reflected from a certain film has a spectrum that peaks at 666 nm, 545 nm and 462 nm. What is its thickness? Take the refractive index as 1.4 and assume normal incidence.

Figure 9.36
Echelon grating.

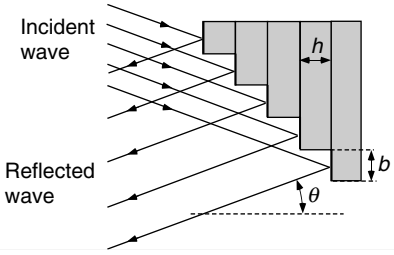

9.8. A Michelson interferometer is used in exactly parallel monochromatic light, and is adjusted so that the two optical paths SM_1 and SM_2 differ by exactly $\lambda/2$. The output intensity is therefore zero. Where has the energy gone?

9.9. The phase-step method, which is used in many commercial interferometers, works as follows. A Twyman–Green interferometer produces a certain interferogram whose intensity is given by $I_0(x,y)$ on the camera sensor. The reference mirror is moved by a distance $\lambda/8$ thereby changing the phase difference between the interfering waves by $\pi/2$. The new interferogram is $I_1(x,y)$. Two further steps of the same size give interferograms $I_2(x,y)$ and $I_3(x,y)$. Derive a formula for determining the phase difference between any two points on the interferogram. For example, if in I_0 a certain point has locally minimum intensity and at another point the intensity is locally maximum, the phase difference (modulo π) is presumably $\pi/2$, but this is a simple case, and in any event your formula should not be limited to giving the phase only to modulo π.

9.10. Where are fringes from a broad source localized in (*a*) interference from a thin film, (*b*) a Mach–Zehnder interferometer? Can multiple-reflection fringes be localized, and if so, under what conditions?

9.11. A Sagnac interferometer has polygonal form, not the circle assumed in the approximation in §9.4.2. Show that the result $\Delta t = 4NA\Omega/c^2$ is true for this case.

9.12. In a Fabry–Perot interferometer with spacing d, the amplitude of each reflected wave is attenuated by the factor $\mathcal{R}^2$ compared to the previous one. Consider the images of a source point (δ-function) multiply reflected in the two parallel reflectors. Show that the diffraction pattern of the array so produced is that of a diffraction grating with spacing $2d$ and an exponentially decaying envelope. Thus find the profile of each order and the resolving power of the interferometer. Relate your answer to (9.50).

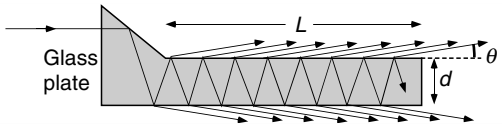

Figure 9.37
Lummer–Gherke plate.

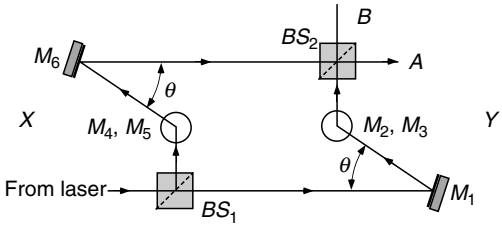

Figure 9.38
Berry-phase interferometer. The lower figures show views of the interferometer from *X* and *Y* in order to make the three-dimensional structure clear.

9.13. A Fabry–Perot interferometer is constructed with plates that are not quite parallel. Assuming the reflection coefficient of each plate to be close to unity and the mean separation to be d, work out approximately how the resolving power is affected by the small angle θ between the plates. You may find it convenient to use the method described in the previous problem.

9.14. A Lummer–Gherke plate is constructed as in Fig. 9.37. It uses multiple reflection at internal angles just less than critical in a parallel-sided plate of thickness d, length L and refractive index n to create a large number of parallel output beams. Find the phase difference between them, as a function of the output angle θ. What is the resolving power?

9.15. A Gaussian beam resonates in a stable resonator for which $R_1 \neq R_2$. Find the sizes of the waist and the beams at the two mirrors.

9.16. The interferometer constructed by Chaio *et al.* (1988) to investigate the Berry phase is shown in Fig. 9.38. Draw the routes followed by the two waves on the **k**-sphere and find the phase difference between the interference patterns observed for right- and left-handed circularly polarized light traversing the interferometer, as a function of θ. (Answer in their paper.)

9.17. Perform ray traces for the rays in the LIGO resonators, given their stability numbers.

References

Abbott, B. *et al.* (2009), The Laser Interferometer Gravitational Wave Observatory, *Rep. Prog. Phys*. **72**, 076901.

Berry, M. V. (1984), Quantal phase factors accompanying adiabatic changes, *Proc. R. Soc. London* **A 392**, 45.

Berry, M. V. (1987), Interpreting the anholonomy of light, *Nature* **326**, 277.

Chaio, R. Y., Antaramian, A., Ganga, K. M., Jaio, H. and Wilkinson, S. R. (1988), Observation of a topological phase by means of a non-planar Mach–Zehnder interferometer, *Phys. Rev. Lett*. **60**, 1214.

Chow, W. W., Gea-Banacloche, J., Pedrotti, L. M. *et al*. (1985), The ring laser gyro, *Rev. Mod. Phys*. **57**, 61.

Hariharan, P. (2003), *Optical Interferometry*, San Diego: Academic Press.

Hariharan, P. (2007), *Basics of Interferometry*, Amsterdam: Elsevier.

Hutley, M. C. (1982), *Diffraction Gratings*, London: Academic Press.

Lefèvre, H. (1993), *The Fiber-Optic Gyroscope*, Boston: Artech House.

Lipson, S. G. (1990), Berry's phase in optical interferometry: a simple interpretation, *Opt. Lett*. **15**, 154.

Michelson, A. A. (1927, 1995), *Studies in Optics*, University of Chicago Press, reprinted by Dover Publications, New York.

Smith, J. R. (2009), The path to enhanced and advanced LIGO gravitational-wave detectors, *Class. Quant. Gravity* **26**, 114013.

Steel, W. H. (1983), *Interferometry*, Cambridge: Cambridge University Press.

Tolansky, S. (1973), *An Introduction to Interferometry*, New York: Wiley.

Tomita, A. and Chaio, R. Y. (1986), Observation of Berry's topological phase using a coiled optical fiber, *Phys. Rev. Lett*. **57**, 937.

10 Optical waveguides and modulated media

In this chapter we shall meet examples of electromagnetic wave propagation in systems containing fine dielectric structure on a scale of the order of the wavelength, where the scalar-wave approximation is inadequate. Clearly, in these cases we have to solve Maxwell's equations directly. On writing the equations, we shall discover that they bear a close similarity to those of quantum mechanics, where the dielectric constant in Maxwell's equations is analogous to the potential in Schrödinger's equation. This opens up a vast arsenal of methods, both analytical and numerical, which have been developed for their solution.

We first discuss the **optical waveguide**, already familiar in everyday life as the optical fibre, which has caused a revolution in the communications industry (Agrawal (2002)). The second topic is the **dielectric multilayer system** which, in its simplest form (the quarter-wave anti-reflection coating) has been with us for more than a century, but can today be used to make optical filters of any degree of complexity (MacLeod (2001)).

Following these examples, we shall briefly discuss their application to **photonic crystals**, structures with periodic refractive index leading to optical band gaps, whose behaviour can immediately be understood in terms of the quantum analogy (Joannopoulos *et al.* (2008)). Photonic crystals have always existed. First, many of the bright colours of insects, butterflies and bird feathers are the result of diffraction by microscopic periodic structures (Fig. 10.1), and these can usually be recognized by the tendency of the colours to change with direction of observation (as opposed to flowers, which have colours of chemical origin) (Zi *et al.* (2003); Biró *et al.* (2007)). Second, opals are periodically ordered collections of microscopic silica spheres, and their colours result from their periodicity. In recent years, artificial photonic crystals have been widely researched and they are used in commercial products such as photonic crystal fibres.

In this chapter we shall study:

- light propagation in a planar optical waveguide consisting of a layer of higher n sandwiched between layers of lower n;
- solutions of Maxwell's equations for this system, which are analogous to bound states of a potential well in Schrödinger's equation;
- propagation in optical waveguides and fibres;

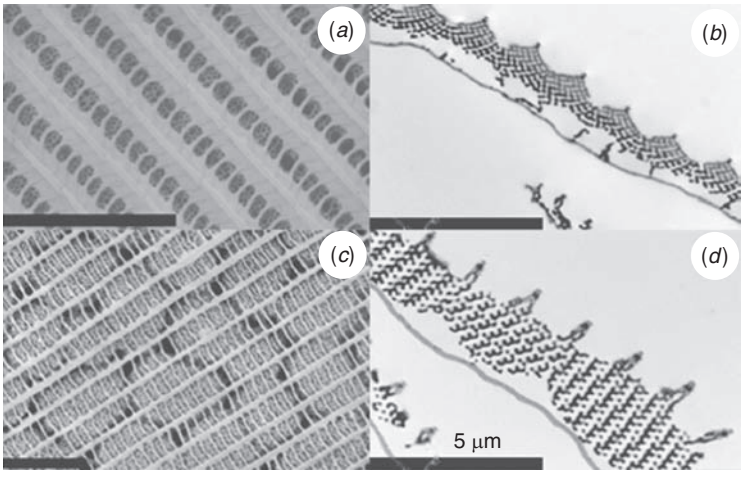

Figure 10.1
Scanning and transmission electron micrographs of the scales on the wings of the butterfly *C. remus*: (*a*) and (*c*) SEM pictures of dorsal and ventral scales, respectively; (*b*) and (*d*) TEM micrograph of the same. All scale bars correspond to 5 μm. (Biró *et al.* (2007))

- solutions of Maxwell's equations in a medium consisting of many layers with different values of n;
- multilayer mirrors made from periodic layer structures;
- filters resulting from defects in periodic structures;
- wave propagation in three-dimensional periodic structures, called photonic crystals, where Maxwell's equations become analogous to Schrödinger's equation for an electron in a periodic lattice;
- photonic crystal fibres.

10.1 Optical waveguides

Transmission of light along a rod of transparent material by means of repeated total internal reflection at its walls must have been observed countless times before it was put to practical use. In this section we shall describe the geometrical and physical optical approaches to this phenomenon, and derive some of the basic results for planar and cylindrical guides, the latter of which is a model for the optical fibre. Optical fibres have many uses, two of which will be described briefly at the end of the section; the first is for transmitting images, either faithfully or in coded form, without the use of lenses; the second is for optical communication. A further application in which the properties of periodic multilayers are also involved will be discussed in §10.4.

10.1.1 Geometrical theory of wave guiding

The principle of the optical fibre can be illustrated by a two-dimensional model (corresponding really to a very wide strip rather than a fibre) shown in Fig. 10.2.

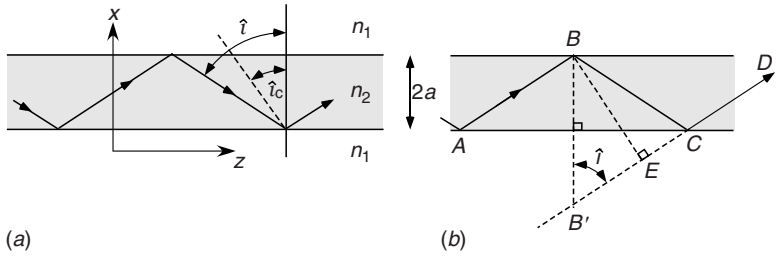

Figure 10.2

Geometrical optics of light propagation along a fibre in one dimension. In (*b*), *BE* is the wavefront common to rays *AB* and *CD*.

The geometrical model is simple, but, since it does not take into account phase differences on reflection, gives inaccurate answers.

The strip has thickness $2a$ and refractive index n_2, and is immersed in a medium of lower refractive index n_1. A plane wave incident inside the strip at angle $\hat{\imath}$ to the x-axis is reflected completely at the wall (§5.5.1) if $\hat{\imath}$ is greater than the critical angle $\hat{\imath}_c = \sin^{-1}(n_1/n_2)$. Since the two sides of the strip are parallel, the wave is then reflected to and fro at the same angle repeatedly, ideally with no losses (Fig. 10.2(*a*)). According to geometrical optics, any ray with $\hat{\imath} < \hat{\imath}_c$ can propagate in this way. However, physical optics requires us to look at the sum of all the waves travelling in the same direction, and to ensure that they interfere constructively. If we do this we naively calculate the phase difference between adjacent waves travelling parallel to one another to be (Fig. 10.2(*b*))

$$\Delta\phi = k_0(\overline{BC} - \overline{EC}) = n_2 k_0 \, B'E = 4n_2 k_0 a \cos\hat{\imath}, \tag{10.1}$$

where k_0 is 2π divided by the wavelength in free space. The requirement for constructive interference is then (as in §9.5)

$$\Delta\phi = 4n_2 k_0 a \cos\hat{\imath} = 2m\pi. \tag{10.2}$$

Each integer value of m defines an allowed mode of propagation. There will always be at least one solution to (10.2) given by $m = 0$, $\hat{\imath} = \pi/2$. As can be seen from Fig. 10.3(*a*) the number of additional solutions having $\hat{\imath} > \hat{\imath}_c$ is the integer part of

$$\frac{2n_2 k_0 a}{\pi} \cos\hat{\imath}_c = \frac{2n_2 k_0 a}{\pi} \left(1 - n_1^2/n_2^2\right)^{\frac{1}{2}}. \tag{10.3}$$

Now unfortunately the calculation is not quite as simple as this, because we have neglected to take into account the phase change $\alpha(\hat{\imath})$ which occurs on reflection at angles exceeding the critical (§5.5.2). We should then write instead of (10.2)

$$\Delta\phi = 4n_2 k_0 a \cos\hat{\imath} + 2\alpha(\hat{\imath}) = 2m\pi. \tag{10.4}$$

The solution $m = 1$, $\hat{\imath} = \pi/2$ is now the first solution because $\alpha(\pi/2) = \pi$. However, since $\alpha(\hat{\imath}_c) = 0$, there will usually be one mode less than suggested by (10.3), as shown in Fig. 10.3(*b*). The modes for the two principal polarizations will not be identical because of the difference between $\alpha_\parallel$ and $\alpha_\perp$.

The modes described above, with $\hat{\imath} > \hat{\imath}_c$, are theoretically loss-less modes, and can propagate along an ideal fibre as far as the absorption coefficient of the medium will permit. In addition there are lossy modes with $\hat{\imath} < \hat{\imath}_c$, which

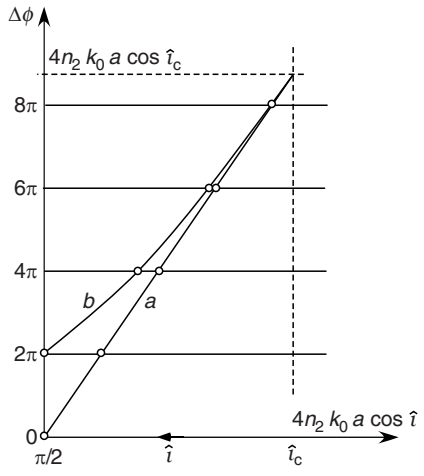

Figure 10.3

Graphical determination of the number of modes propagating in a slab; equation (10.2) is represented by *a*, equation (10.4) by *b*.

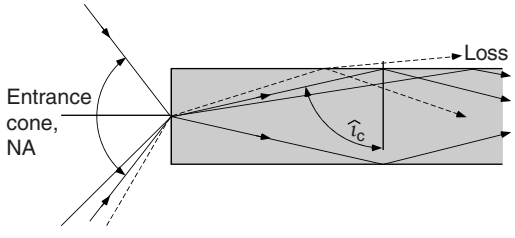

Figure 10.4

Cone of angles allowing light to enter propagating modes.

die away after a certain number of reflections, and are important only for very short fibres.

The above geometrical approach does in fact give a fairly complete picture of propagation in the slab, including in particular the features of propagation modes and differences between the $\perp$ and $\parallel$ polarizations. In addition, it is easy to see that the wave entering the slab (and fibres in general) must do so at an angle sufficiently close to the axis that critical reflection occurs. This means a restriction on possible angles of incidence in the exterior medium at the end of the slab. From Fig. 10.4, it is easy to show that the angle of the entrance cone corresponding to the critical angle for reflection at the interface is given by $\sin^{-1}\left(\sqrt{n_2^2 - n_1^2}\right)$, which seriously influences the efficiency with which incoherent light can be fed into it, particularly when $n_2 - n_1 \ll n_1$. The sine of this angle, i.e. $\sqrt{n_2^2 - n_1^2}$, is then called the 'numerical aperture' (NA) of the slab, in line with the use of the term in microscopy (§12.2.5). However, the geometrical approach becomes clumsy to use quantitatively in any extension of this simple model. Two cases are of great importance. First, there is the optical fibre, which has a cylindrical cross-section, and supports some modes in which the light rays spiral around the axis and are not confined to a single plane (**skew rays**). Second, both slab waveguides and optical fibres can have continuously varying refractive index, in which case there is no well-defined plane at which

Light collection systems require large NA for efficiency, whereas communication systems require small NA to prevent dispersion.

critical reflection occurs, but the angle $\hat{\imath}$ changes gradually along z, as in the situation of a mirage, §2.6. These are called **graded index** systems and are very important practically.

These problems are better treated by a more general approach in which Maxwell's equations are solved from scratch in the required environment. The method is much more fruitful, and has the enormous advantage of highlighting the similarity of the electromagnetic wave equation to Schrödinger's equation for matter waves (§2.2.1). Solutions to this latter equation, with which the reader may well be familiar from studies of quantum mechanics (see, e.g., Cohen-Tannoudji *et al.* (1977)) help us both to solve particular problems easily and to develop a taste for possible useful configurations. In fact, many quantum-mechanical concepts such as tunnelling and the band theory of solids have found direct application to optical waveguides in analogous situations.

10.1.2 Maxwell's wave equation for a planar waveguide

Maxwell's equations for the slab provide a much richer set of solutions than the geometrical approach.

Continuing our two-dimensional planar model for a waveguide we shall now construct and solve the wave equation for the same system as was shown in Fig. 10.2. Specifically, we have propagation in the z-direction, while the refractive index $n(x)$ varies in the x-direction. There is no functional dependence on y in this model, but we have $\perp$ polarization ($E = E_y$ only, also called s or TE polarization) or $\parallel$ polarization (E in (x, z) plane, also called p or TM polarization) as two independent possibilities (cf. §5.4).

The wave equation begins with (5.11):

$$-\frac{\epsilon}{c^2}\frac{\partial^2 \mathbf{E}}{\partial t^2} = \nabla \times (\nabla \times \mathbf{E}) = \nabla(\nabla \cdot \mathbf{E}) - \nabla^2 \mathbf{E}. \tag{10.5}$$

As we saw in Chapter 6, Gauss's law, $\nabla \cdot \mathbf{D} = 0$, does not imply $\nabla \cdot \mathbf{E} = 0$ unless ϵ is a homogeneous (i.e. spatially uniform) scalar number. In the present situation this is not so. Recalling that $\epsilon(x) = n^2(x)$,

$$\begin{aligned} 0 = \nabla \cdot \mathbf{D} = \epsilon_0 \nabla \cdot (\epsilon \mathbf{E}) &= \epsilon_0(\epsilon \nabla \cdot \mathbf{E} + \nabla\epsilon \cdot \mathbf{E}) \\ &= \epsilon_0 \epsilon \nabla \cdot \mathbf{E} + \epsilon_0 E_x \frac{\partial \epsilon}{\partial x}. \end{aligned} \tag{10.6}$$

Now the wave equation (10.5) becomes:

$$\frac{\epsilon}{c^2}\frac{\partial^2 \mathbf{E}}{\partial t^2} = \nabla^2 \mathbf{E} - \nabla(\nabla \cdot \mathbf{E}) = \nabla^2 \mathbf{E} + \nabla\left(E_x \frac{1}{\epsilon}\frac{\partial \epsilon}{\partial x}\right), \tag{10.7}$$

which reduces to the usual Maxwell wave equation (5.12) if the term

$$\nabla\left(E_x \frac{1}{\epsilon}\frac{\partial \epsilon}{\partial x}\right) \tag{10.8}$$

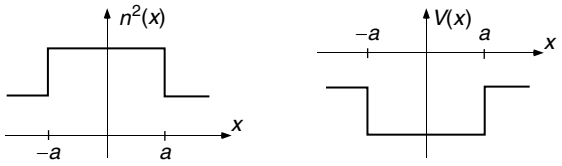

Figure 10.5
Refractive index profile $n(x)$ for the slab, and the equivalent Schrödinger potential.

is small enough with respect to $\nabla^2\mathbf{E}$ to be neglected. For the $\perp$ mode, $E_x = 0$ and so (10.8) is identically zero. But for the $\parallel$ mode $E_x \neq 0$, although in many examples $\partial\epsilon/\partial x = 0$ except for a limited number of discontinuities. In what follows, we shall assume that the term (10.8) is negligible, in which case there is no difference between the equations for $\perp$ and $\parallel$ (although the *boundary conditions* they satisfy are not identical); this is called the **weak guiding approximation**.

An optical fibre is the 3D equivalent of a square potential well in quantum mechanics.

For the wave $E = E(x)\exp[\mathrm{i}(k_z z - \omega t)]$ propagating in the z-direction, we can substitute into (10.7) $\partial/\partial z = \mathrm{i}k_z$, $\partial/\partial t = -\mathrm{i}\omega$ and $\partial/\partial y \equiv 0$ and get

$$\frac{\partial^2 E}{\partial x^2} - k_z^2 E = \frac{-1}{c^2}\epsilon\omega^2 E = \frac{-n^2(x)}{c^2}\omega^2 E, \tag{10.9}$$

$$\frac{\partial^2 E}{\partial x^2} = \left[k_z^2 - n^2(x)k_0^2\right]E. \tag{10.10}$$

For analogy's sake we write Schrödinger's time-independent wave equation in the same way so that the similarity can be seen:

$$\frac{\partial^2 \psi}{\partial x^2} = \frac{2m}{\hbar^2}[-\mathcal{E} + \mathcal{V}(x)]\psi. \tag{10.11}$$

One sees immediately that there will be corresponding solutions for refractive index profile $-n^2(x)$ and potential well $\mathcal{V}(x)$. Then $-k_z^2$ corresponds to the energy eigenvalue $\mathcal{E}$. It is also clear that a propagating mode, for which k_z is real, corresponds to a bound state in quantum mechanics, for which $\mathcal{E} < \mathcal{V}(\infty)$.

The specific form of $n(x)$ that represents the optical slab waveguide shown in Fig. 10.5 is

$$n(x) = n_2 \quad (|x| < a, \text{ called the } \mathbf{core}), \tag{10.12}$$

$$n(x) = n_1 < n_2 \quad (|x| \geq a, \text{ called the } \mathbf{cladding}) \tag{10.13}$$

and is equivalent to a square-well potential. The guided wave solutions of this problem therefore (using the quantum-mechanics analogy of a particle in a potential well to guide us directly to the solution) lie in the region $n_1^2 k_0^2 < k_z^2 < n_2^2 k_0^2$. If we therefore define

$$n_2^2 k_0^2 - k_z^2 \equiv \alpha^2, \qquad k_z^2 - n_1^2 k_0^2 \equiv \beta^2,$$

$$\alpha^2 + \beta^2 = \left(n_2^2 - n_1^2\right)k_0^2 \equiv V^2, \tag{10.14}$$

we have, in the core region $|x| < a$,

$$\frac{\partial^2 E}{\partial x^2} = -\alpha^2 E$$
$$\Rightarrow\ E = E_{2\mathrm{s}} \cos \alpha x + E_{2\mathrm{a}} \sin \alpha x, \tag{10.15}$$

where the suffices 's' and 'a' refer to 'symmetrical' and 'antisymmetrical' modes. In the cladding region, $|x| > a$, we have likewise:

$$\frac{\partial^2 E}{\partial x^2} = \beta^2 E$$
$$\Rightarrow\ E = E_{1l} \mathrm{e}^{\beta x} + E_{1r} \mathrm{e}^{-\beta x} \quad (\beta \geq 0), \tag{10.16}$$

where suffices l and r indicate 'left' and 'right'. Within the core of the slab, the function is wave-like (oscillatory); in the cladding it is evanescent, and for E to remain finite it must decay as $\exp(-\beta|x|)$ at large $|x|$. The core and cladding solutions join together in a continuous fashion, which will shortly be detailed. The complete function is therefore 'trapped' or 'localized' in a region centred on the core. This is the essence of the guided wave.[1] The inherent symmetry of the system about the plane $x = 0$ has suggested using symmetrical and antisymmetrical solutions in (10.15). Considering just the region $x > 0$ ($x < 0$ follows by symmetry or antisymmetry), clearly only the solutions (10.16) with $E_{1l} = 0$ are acceptable. At $x = a$ the field components E_y, E_z, H_y and H_z parallel to the interface (see §5.4.1) must be continuous. For the $\perp$ mode, $E_z = 0$ and continuity of E_y then requires, for the cosine solution to (10.15),

$$E_{2\mathrm{s}} \cos \alpha a = E_{1r} \mathrm{e}^{-\beta a}. \tag{10.17}$$

The field H_z can be calculated from Maxwell's equation (5.4) for the $\perp$ case $\mathbf{E} = (0, E_y, 0)$:

$$-\frac{\partial \mathbf{B}}{\partial t} = \frac{\mathrm{i}\,\omega}{c^2 \epsilon_0} \mathbf{H}$$
$$= \nabla \times \mathbf{E} = \left(\frac{\partial E_y}{\partial z}, 0, -\frac{\partial E_y}{\partial x} \right), \tag{10.18}$$

whence continuity of H_z implies continuity of $\partial E_y / \partial x$. Thus the analogy with Schrödinger's equation is complete. For the cosine solution to (10.15) this gives

$$\alpha E_{2\mathrm{s}} \sin \alpha a = \beta E_{1r} \mathrm{e}^{-\beta a}. \tag{10.19}$$

Dividing (10.19) by (10.17):

$$\alpha a \tan \alpha a = \beta a. \tag{10.20}$$

[1] We could extend the analogy by allowing β to be imaginary, and k_z complex. Then we should arrive at the lossy modes. This is left as an exercise to the reader.

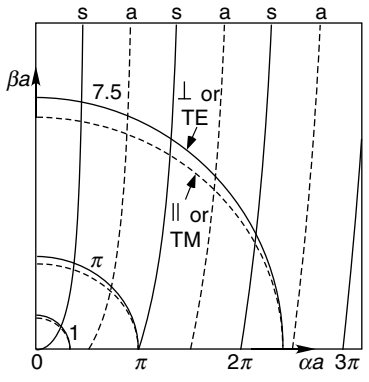

Figure 10.6 Graphical construction to find the ⊥ polarized modes in a waveguide slab according to (10.20) and (10.21). The curves labelled 's' and 'a' represent $\beta a(\alpha a)$ for the symmetric and antisymmetric modes respectively. A circle (full line), radius aV, represents (10.14), and is shown for several values of a. Intersection between a circle and one of the curves represents a mode. Intersections with the ellipses (broken lines) represent schematically the solutions for the ∥ modes, although in practice the difference between the circles and corresponding ellipses would be very small. The cut-off of each mode, being defined by $\beta = 0$ is the same for both ⊥ and ∥ polarizations.

Similarly, choosing the sine solution to (10.15) gives

$$-\alpha a \cot \alpha a = \beta a. \tag{10.21}$$

We can repeat the calculation for the ∥ polarization for which $\mathbf{H} = (0, H_y, 0)$. The arguments analogous to (10.17)–(10.19) then lead to the equations, equivalent to (10.20) and (10.21),

$$\frac{\alpha a}{n_1^2} \tan \alpha a = \frac{\beta a}{n_2^2}, \tag{10.22}$$

$$-\frac{\alpha a}{n_1^2} \cot \alpha a = \frac{\beta a}{n_2^2}. \tag{10.23}$$

In practice the difference between n_1 and n_2 is often extremely small, in which case there is negligible difference between the two types of solution.

We shall limit our attention to the ⊥ mode, for which (10.20) and (10.21) are eigenvalue equations whose solutions define particular values of α and β. These must satisfy $\alpha^2 + \beta^2 = V^2$, a constant, from (10.14). Only certain values of k_z result, and these correspond to **propagation modes** of the slab. The equations cannot be solved analytically, but the solutions can be found graphically by plotting βa as a function of αa according to (10.20) and (10.21) and finding their intersections with the circle representing (10.14), Fig. 10.6.

No matter how small the thickness of a symmetrical slab, there is always one propagation mode.

The circle has radius Va, and as a increases, one finds more and more intersections with the curves. Only the quadrant $\alpha, \beta > 0$ is relevant since β was defined as positive, and the figure is symmetrical about the β-axis. The

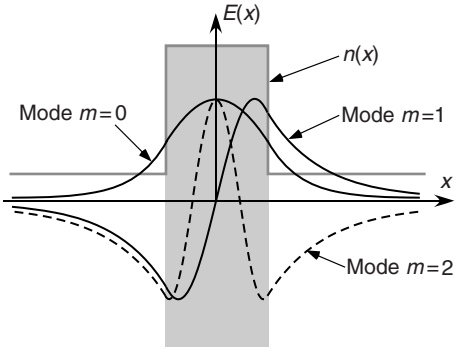

Figure 10.7

$E(x)$ for the modes $m = 0$, 1 and 2 in a slab, normalized to the same maximum value. Note that, as m increases, the size and extent of the field outside the slab also increases.

‖ mode solution is obtained by replacing β by β', where $\beta' = \beta n_1^2/n_2^2$. The circle $\alpha^2 + \beta^2 = V^2$ then becomes the ellipse $\alpha^2 + \beta'^2 \left(n_2^2/n_1^2\right) = V^2$, as shown schematically by dashed curves in Fig. 10.6. An important feature that appears from Fig. 10.6 is that the number of propagating modes is finite. There is always at least one mode (even as $V \to 0$); in general, the number of modes is $1 + p$, where p is the integer part of $2aV/\pi$ (see §10.1.1).

Typical forms of $E(x)$ are shown in Fig. 10.7. Alternate solutions are symmetric (cosine-like, with $E_{2a} = 0$ in (10.15)) and antisymmetric (sine-like, with $E_{2s} = 0$). The lowest mode ($m = 0$) has a single peak in the centre of the slab; higher modes have more and more peaks.

10.1.3 Dispersion

The velocity of a mode is determined mainly by the refractive index of the medium in which most of the energy is concentrated.

Another important feature of the propagation is the **intra-mode dispersion relation**, which describes the way in which the phase velocity of propagation depends on the frequency for a given mode. In general, the relationship will differ from mode to mode, and is often described in terms of an **effective refractive index**, defined as $n_{\text{eff}} = k_z(\omega)/k_0$. The significance of dispersion with regard to the transmission of information was discussed in §2.4 and §2.7. We have considered the frequency $\omega = k_0 c$ as a constant in the analysis so far. In order to create a dispersion curve, we now have to look at the dependence of k_0 on k_z (the propagation wave-vector along the slab). It is easiest to do this by reading off from the intersections in Fig. 10.6 the values of α and β as a function of V, which is proportional to k_0. Then we calculate from (10.14)

$$k_z = \left(\beta^2 + n_1^2 k_0^2\right)^{\frac{1}{2}}. \tag{10.24}$$

The result is shown schematically in Fig. 10.8. It will be seen by following a given mode m:

1. Propagation starts when $\beta = 0$, i.e. at $k_0 = m\pi/2a\left(n_2^2 - n_1^2\right)^{\frac{1}{2}}$.
2. When β is small, $k_z \approx n_1 k_0$; the wave propagates as if in the cladding medium, i.e. $n_{\text{eff}} = n_1$.

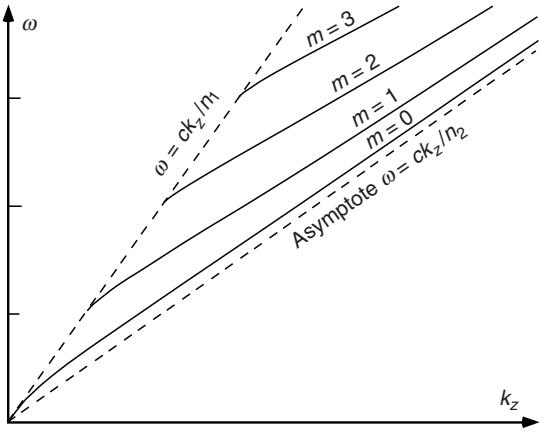

Figure 10.8
Dispersion curves for different modes m for a slab waveguide, calculated for $n_2 = 2$ and $n_1 = 1$. The graphs show the relationship between frequency ω and propagation wavenumber k_z for the first few modes. The effective refractive index is $n_{\text{eff}} = k_z/k_0 = ck_z/\omega$ and the group velocity for pulse propagation is $\mathrm{d}\omega/\mathrm{d}k_z$.

3. As k_0 increases, $\beta \to V$, and so $k_z \to \left(V^2 + n_1^2 k_0^2\right)^{\frac{1}{2}} = n_2 k_0$; propagation is then dominated by the core, i.e. $n_{\text{eff}} \to n_2$.
4. The mode group velocity is less than the asymptotic value c/n_2 throughout most of the curve.

From the physical point of view, when one looks at the distribution of energy (E^2 from Fig. 10.7), it is clear that the propagation velocity is dominated by the medium in which most of the energy is located.

10.1.4 Single-mode waveguide

The slab with only a single propagating mode ($n = 0$) is particularly important for communication purposes, and is called a **single-mode waveguide**. The reason for its importance is that in a multi-mode guide the wave and group velocities, ck_0/k_z and $c\mathrm{d}k_0/\mathrm{d}k_z$, which can be found from Fig. 10.8, differ from mode to mode and as a result information sent along a fibre in wave-group form will be distorted when several modes propagate simultaneously. Use of a single-mode waveguide avoids this cause of distortion, although pulse spreading due to the non-linear form of $k_z(k_0)$ within the single mode still occurs.

In order to make a single-mode guide, we require $Va < \pi/2$. This implies

$$a < 0.25\lambda / \left(n_2^2 - n_1^2\right)^{\frac{1}{2}}, \tag{10.25}$$

where λ is the free-space wavelength. Although a symmetrical waveguide always has at least one mode, an asymmetrical one may have no modes at all if its width is very small (Problem 10.4).

10.2 Optical fibres

The discussion has so far centred around the one-dimensional waveguide. Although this configuration has many applications, by far the most common

For the idea of using optical fibres for long-distance communication, C. K. Kao received the Nobel prize in 2009.

wave-guiding system is an optical fibre. The basic geometry is a cylindrical core of glass with refractive index n_2 embedded in a cladding medium of index n_1. Ideally the cladding is infinite in extent, but in practice it is cylindrical, coaxial with the core, and has a large enough diameter to contain the evanescent waves (10.16) out to many times their decay distance β^{-1}.

We shall not repeat the slab calculation for the cylindrical case except to the extent that new features emerge. The equation that is to be solved is (10.7) with $\epsilon \equiv n^2(r)$, in the weak-guiding approximation. Since the boundary between the two media has axial symmetry, it is convenient to rewrite the equation for scalar E in cylindrical polar coordinates (r, θ, z):

$$\frac{\partial^2 E}{\partial x^2} + \frac{\partial^2 E}{\partial y^2} - \left[k_z^2 - n^2(x,y)k_0^2\right] E = 0 \tag{10.26}$$

becomes

$$\frac{\partial^2 E}{\partial r^2} + \frac{1}{r}\frac{\partial E}{\partial r} + \frac{1}{r^2}\frac{\partial^2 E}{\partial \theta^2} - \left[k_z^2 - n^2(r)k_0^2\right] E = 0. \tag{10.27}$$

Because of the axial symmetry, it is possible to write $E(r,\theta)$ as the product of two functions, $R(r)\Theta(\theta)$; (10.27) is then

$$\frac{\Theta\,\mathrm{d}^2R}{\mathrm{d}r^2} + \frac{\Theta}{r}\frac{\mathrm{d}R}{\mathrm{d}r} + \frac{R}{r^2}\frac{\mathrm{d}^2\Theta}{\mathrm{d}\theta^2} - \left[k_z^2 - n^2(r)k_0^2\right] R\Theta = 0. \tag{10.28}$$

Dividing by $R\Theta$, and multiplying by r^2,

$$\frac{r^2}{R}\frac{\mathrm{d}^2R}{\mathrm{d}r^2} + \frac{r}{R}\frac{\mathrm{d}R}{\mathrm{d}r} + \frac{1}{\Theta}\frac{\mathrm{d}^2\Theta}{\mathrm{d}\theta^2} - r^2\left[k_z^2 - n^2(r)k_0^2\right] = 0, \tag{10.29}$$

which contains terms which are either functions of r or of θ, but not both. Thus the equation breaks up into two, one in r, the other in θ, each of which must be independent and equal to a constant, which we denote by l^2. They are

$$\frac{1}{\Theta}\frac{\mathrm{d}^2\Theta}{\mathrm{d}\theta^2} = \text{constant} \equiv -l^2 \tag{10.30}$$

$$\text{and} \quad \frac{r^2}{R}\frac{\mathrm{d}^2R}{\mathrm{d}r^2} + \frac{r}{R}\frac{\mathrm{d}R}{\mathrm{d}r} - r^2\left[k_z^2 - n^2(r)k_0^2\right] = l^2. \tag{10.31}$$

The sum of these two equations is (10.29). Equation (10.30) introduces a new feature that did not appear in the planar waveguide and is related to the skew rays of §10.1.1. Any solution of it must satisfy $\Theta(2\pi) = \Theta(0)$, i.e.

$$\Theta(\theta) = A\cos l\theta + B\sin l\theta, \tag{10.32}$$

The azimuthal modes are a feature of fibres that did not appear in the slab waveguide, but they have few uses.

where l is a non-negative integer and A and B are arbitrary constants. Looking at this part of the solution alone, we see that the light intensity E^2 is modulated angularly with an even number of peaks in the full circle. These are called **azimuthal modes** (Fig. 10.9). We have already met such modes in the confocal resonator in §9.5.4.

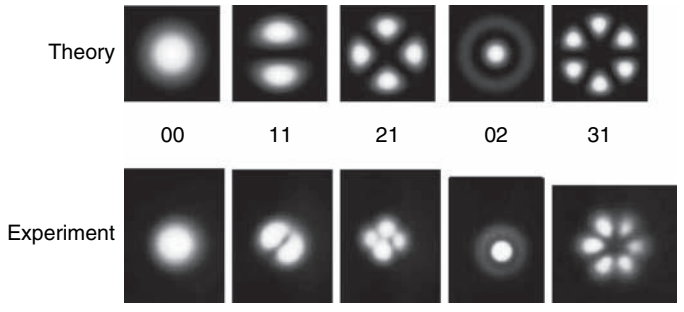

Figure 10.9
Intensity distribution photographed for several modes in a circular fibre, compared to the theory. The experiment was carried out at 633 nm on a fibre that has only a single mode at 1550 nm. The first mode number is azimuthal; the second, radial. (Courtesy of Nikolai Berkovitch and Evgeny Orski)

10.2.1 Step-index fibres

The radial equation (10.31) is no easier to solve than was (10.10) and gives radial modes that are oscillatory in the core and evanescent in the cladding. Note that the l^2 term can be included as if it were an additional dielectric constant $-l^2/k_0^2r^2$; because r^{-2} diverges at $r = 0$ the field of modes with $l \neq 0$ must vanish there. In the simplest case, a step-index fibre, $n(r) = n_2$ $(r < a)$ and $n(r) = n_1$ $(r > a)$. The analysis is similar to that for the slab, with the cosine and sine functions replaced by Bessel functions J_0 and J_1 (see Appendix A). Some typical mode structures are shown in Fig. 10.9. Only one mode can propagate if $a < 0.383\lambda/\left(n_2^2 - n_1^2\right)^{\frac{1}{2}}$, see (10.25), and **single-mode fibres** with this property are very important for communication purposes because of their relatively small dispersion. If n_2 and n_1 are very close, the maximum core diameter $2a$ of a single-mode fibre can be considerably larger than λ. For example, using $n_2 = 1.535$ and $n_1 = 1.530$, a fibre with $2a < 6.2\lambda$ will support only a single mode.

10.2.2 Graded-index fibres

A different method of combating dispersion is to use alternating sections of fibre with positive and negative dispersion.

At this point we recall from §2.7 that one of the results of non-linear dispersion on the propagation of a wave-packet is to cause a progressive increase in its width. This eventually poses a limit to the repetition rate at which packets can be propagated without their merging. It turns out that the step-index fibre, even in the single-mode variety, has sufficient dispersion within a single mode to stimulate a search for fibres with lower dispersion for long-distance communication purposes. This has led to the development of **graded-index fibres**, in which the refractive index $n(r)$ is a continuous function of the radius. A commonly found profile for $n^2(r)$ is parabolic. This has smaller dispersion than the step-index fibre, although there is no proof that this profile has minimum dispersion; indeed a slightly lower power than parabolic produces some

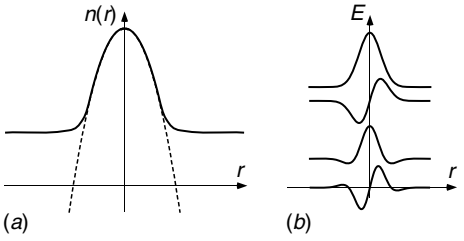

Figure 10.10
(*a*) Refractive index profile of a parabolic graded-index fibre (full line), and the mathematical model (broken line). (*b*) Radial dependence of the wave-field in the first four modes (separated vertically for clarity).

improvement. However, the parabolic profile $n^2(r) = A - br^2$ reminds us of the harmonic oscillator potential in quantum mechanics and since Schrödinger's equation has a simple solution for this model we shall pursue it briefly. In practice, the parabolic profile is limited to the central region only and is merged into a uniform cladding, as shown in Fig. 10.10(*a*), which represents a cladded parabolic-index fibre, whose parameters can be adjusted so that it has a single mode only, still preserving minimal dispersion. A full discussion is given by Ghatak and Thyagarajan (1980).

The equation (10.29) can be taken as the starting point by substituting $n^2(r) = n_2^2 - b^2r^2$. Clearly, all that has been said already about azimuthal modes applies in this case too, since the form of $n^2(r)$ was not involved in (10.30). The radial equation (10.31) can be written

$$\frac{\mathrm{d}^2R}{\mathrm{d}r^2} + \frac{1}{r}\frac{\mathrm{d}R}{\mathrm{d}r} + R\left(U - \alpha^2r^2 - \frac{l^2}{r^2}\right) = 0, \tag{10.33}$$

where $U = n_2^2k_0^2 - k_z^2$ and $\alpha = k_0b$. This makes it analogous to the two-dimensional harmonic oscillator equation in quantum mechanics, where the total energy is U and the potential energy is α^2r^2. It suggests to us a solution of the form

$$R = \mathrm{e}^{-\alpha r^2/2}f(r), \tag{10.34}$$

where $f(r) = \sum_{j=p_0}^{p} a_jr^j$ is a finite polynomial series; this is the classical Sommerfeld solution of the quantum mechanical harmonic oscillator equation.

Substitution of (10.34) into (10.33) and comparison of coefficients of r^p, together with the requirement for p to be a finite integer (i.e. $a_k = 0$ for all $k > p$) leads us directly to the following conclusions:

1. There are independent symmetric and antisymmetric solutions for even and odd l respectively. For $l \neq 0$, $R(0)$ must be zero.
2. The value of $p_0 = l$. This means that the radial function can have at most $p - l + 1$ peaks, since it is a polynomial with this number of terms multiplied by the Gaussian. Typical mode patterns look like Fig. 10.10(*b*).
3. The allowed values $U = n_2^2k_0^2 - k_z^2 = 2\alpha(p+1)$. The value 2α is analogous to $h\nu$ in the quantum harmonic oscillator; the 'ground-state energy' ($p = 0$) is $h\nu$, and not $\frac{1}{2}h\nu$, because it is a two-dimensional system.

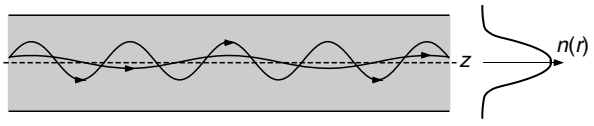

Figure 10.11
Ray equivalents of two modes in a parabolic graded-index fibre.

So the dispersion equation for the lowest mode (using $k_0 = \omega/c$ and $\alpha = k_0 b$) is

$$n_2^2 k_0^2 - 2bk_0 = k_z^2. \tag{10.35}$$

This lowest mode has $l = p = 0$, so that the electric field has amplitude

$$E(r) = R(r) = \mathrm{e}^{-k_0 b r^2/2}; \tag{10.36}$$

it is a simple Gaussian profile. The radius $r = (k_0 b)^{-\frac{1}{2}}$ is just the inflexion point on this profile, so that $(k_0 b)^{-\frac{1}{2}}$ is essentially the radius of the equivalent core (compare Fig. 10.10(*b*) with Fig. 10.7). But do not take this result too seriously; it only applies to an infinite parabolic profile, and is altered significantly by the presence of a cladding medium, which must necessarily exist since n can never fall below about 1.5.

Propagation of Gaussian beams in free space is discussed in §7.3.

One can see qualitatively the origin of the lesser dispersion in a graded-index fibre from Fig. 10.11. In the figure, the mode with the shorter path length is confined to the region where $n(x)$ is largest, while the mode with the longer path length enters regions of smaller refractive index. The two parameters – refractive index and path length – partially compensate, and give a dispersion that is less than in a step-index fibre. The dispersion of the glass itself must also be taken into account; in the normal dispersion region (§13.3.2), $\partial^2\omega/\partial k^2$ for glass conveniently has the opposite sign to that for the fibre dispersion, and further compensation is possible.

10.2.3 Production of fibres

A few words about how fibres are produced will take the above discussion out of the realm of pure theory. Fibres are made commercially in many-kilometre lengths from specially prepared low absorption glasses. First, a short cylindrical glass rod (preform), several centimetres in diameter, is prepared with a central core of higher refractive index than the outer region. This is heated and drawn through a small orifice with diameter equal to the outer diameter required of the fibre (see Fig. 10.22). The inner structure all scales down in proportion. A typical absorption spectrum for a fibre glass is shown in Fig. 10.12. Notice that the units on the abscissa are dB/km, where one dB is a loss of intensity of transmitted light by $10^{0.1}$ (B is the 'Bel' which corresponds to one decade loss; $3\,\mathrm{dB} = 10^{0.3} \approx 0.5$).

The problem of a slab waveguide bent to a radius can be solved analytically, and is found to be analogous to a quantum-mechanical system – the tunnel diode!

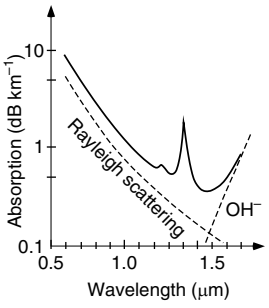

Figure 10.12

Typical absorption coefficient for a fibre glass, as a function of wavelength. The limits for Rayleigh scattering and far-infra-red OH^- band absorption are shown as broken lines. (After Gloge (1979))

A similar method of production is used for graded-index fibres. In this case, the original glass preform is constructed from axial layers of glass of differing refractive indices, often deposited chemically by vapour deposition from sources of gradually varying composition.

Light losses from fibres come from several sources. Absorption in the glass, as mentioned above, is one; tremendous development activity has resulted in this factor becoming negligible at some wavelengths, even for hundreds of kilometres. Rayleigh scattering (§13.2) is important at short wavelengths and arises because glass is not a crystalline material and therefore has unavoidable statistical density fluctuations. Losses because of incomplete total internal reflection in a step-index fibre are effectively avoided by the interface between n_2 and n_1 being buried well inside the cladding, so that it cannot be damaged or dirtied; *a fortiore* in the graded-index system where the interface is undefined. With practical dimensions, loss via the evanescent wave in the cladding can also be made negligible, although when the fibre is bent losses from this source can become noticeable.

10.2.4 Communication through optical fibres

A single-mode waveguide for optical communication typically has a core diameter 8 μm.

Optical fibres have now become the standard transmission medium for telephones and data, known as telecom and datacom. A typical system starts with a light-emitting diode or semiconductor laser, emitting at the wavelength where the fibre absorption and dispersion are least (1.3–1.5 μm; see Fig. 10.12), whose output intensity or phase is modulated according to the signals to be transmitted. The light is focused into a fibre. At the far end, the light is reconverted to an electronic signal by a photo-detector. The maximum distance for transmission is limited by losses in the fibre, which we discussed above. It may therefore be necessary to amplify the signal at intervals on very long routes. This can be done by terminating the fibre as with a photo-detector, amplifying the signal electronically, removing noise that does not correspond to the transmission code and then retransmitting. In the late 1980s, the invention of an erbium-doped fibre amplifier (EDFA) (§14.5.3) revolutionized the field, as it became no longer necessary to leave the optical domain in order to amplify the signal, this being done internally within the fibre and with great uniformity. Moreover, the ability to modulate light at tremendous rates, superseding 100 Gbit/s (10^{11} s^{-1}), explains the ongoing drive towards an 'all optical' system; electronic circuits cannot work efficiently, if at all, at these rates. The invention of the EDFA was the main reason for the communications industry to shift to 1.5 μm dispersion-free fibres, as no equivalent could be efficiently produced for other wavelength regions.

The great attraction of optical fibres for data transmission lies in the potential amount of data that can be transmitted simultaneously on a single fibre, compared with about 24 'telephone conversations' on conventional copper cable. If we suppose that the light transmitted has frequency f, and that a single conversation covers a band of frequencies of width f_1 then, by mixing various conversations each with a different intermediate frequency, in principle f/f_1 conversations can all be used to modulate the light wave simultaneously. For optical communication, $f \approx 10^{15}\,\mathrm{s}^{-1}$. In practice systems are limited to $f_1 > 10$ Gbit/s ($10^{10}\,\mathrm{s}^{-1}$) as a result of fibre non-linearity, dispersion (§2.7 and §10.1.3) and the speed of the electronics. While dispersion effects are commonly resolved by having alternating fibre segments of positive and negative dispersion, non-linear effects are harder to overcome and are still a bottleneck to higher modulations (Agrawal (2007)). It follows that $f/f_1 \approx 10^5$. Technology is nowhere near capable of using this enormous potential; but the attraction remains. This ability to interleave data channels in the wavelength domain is known as wavelength-division multiplexing (WDM), the first products of which became commercially available in 1996. Channel multiplexing can be done in the time domain as well, leading to optical time-division multiplexing (OTDM). In 2001, a record-breaking WDM system transmitted 273 channels, each having $f_1 = 40$ Gbit/s, for 117 km.

10.2.5 Imaging applications

For image transmission, the mode structure of light transmission in a fibre is unimportant; we are only concerned that the light be transmitted from one end to the other. A bundle of fibres is arranged in an organized array and the end is cut across cleanly. At the other end the fibres are arranged in the same way. What happens in-between is unimportant. An image projected on one end is then seen at the other end. This type of device is invaluable as a method of transmitting images from inaccessible regions; one important medical application is the 'endoscope' used for the internal examination of patients. The resolution of the image is just determined by the diameter of each fibre, which is typically 20–50 μm. By changing the ordering of the fibres at the far end, an image can be coded, for example changed from a circular field of view to a slit-like field. Or the reordering may be simply a rotation; inverting an image by means of a fibre bundle is cheaper, is less bulky and introduces less aberration than would a lens system although its resolution is limited (Fig. 10.13).

Another approach to the transmission of images through optical fibres uses a phase-conjugate mirror, which is described in §13.6.3.

The subject of fibre optics is comprehensively covered by review articles and books at all levels, for example Gloge (1979), Saleh and Teich (1991) and Agrawal (2002). The book by Al-Azzawi (2007) describes many practical details and experiments.

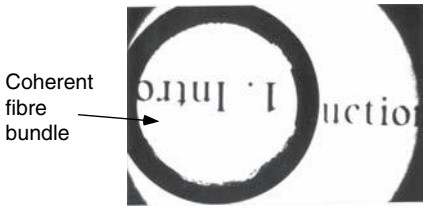

Figure 10.13
Inversion of an image using a coherent fibre bundle. This device is part of a night-vision image intensifier.

10.3 Propagation of waves in a modulated medium

Another practically important electromagnetic wave propagation problem arises when the refractive index of the medium is modulated periodically (MacLeod (2001)). Continuing the vein of our analogy to solved quantum-mechanical problems, we immediately seek guidance from the behaviour of an electron in a periodic crystal potential. The solutions that emerge indeed have many similarities to the well-known Bloch waves, and show band gaps that are entirely analogous to those found in the electronic structure of crystals (see, for example, Kittel (2005)). The treatment here is mainly limited to one dimension, but can also be extended to three-dimensional periodic media (Yablonovitch (1993)). In §10.5 the results derived here will be extended a little into such systems. The analogy to quantum mechanics remains as the basic theme.

10.3.1 General method for multilayers

The multilayer formulation here describes each layer by a matrix, and uses linear algebra to get the general results. It is very convenient for numerical computations.

The refractive system that interests us, called a **dielectric multilayer system**, consists of a series of layers of transparent media having various refractive indices, deposited on top of each other on a substrate. A light wave is incident from free space in a direction at angle $\hat{\imath}$ to the normal, and we calculate the way in which it is reflected and transmitted. In this section, we shall set up the general framework for solving such problems and then consider a particular case, that of the periodic stack. The narrow-band interference filter will be shown as an example of its application.

Let us first consider the case of normal incidence. Waves entering the layered system along the x-axis (Fig. 10.14) are partially reflected at the various interfaces. In any layer m there are in general two waves, one travelling in each of the $+x$ and $-x$ directions. We shall assume E to be polarized in the y-direction. We label their complex amplitudes E_m^+ and E_m^- at the right-hand side (interface with layer $m+1$). The phase difference for either of them is

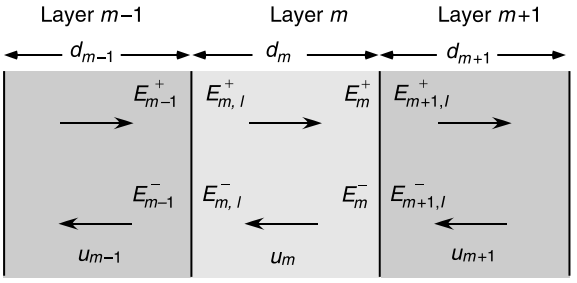

Figure 10.14
Parameters for the multilayer calculation.

$g_m = k_m d$, where k_m is the wavenumber in the medium, i.e. $k_m = k_0 n_m$. Thus the wave amplitudes at the left-hand side of the layer are

$$E^+_{ml} = E^+_m \mathrm{e}^{+\mathrm{i}g_m}, \tag{10.37}$$

$$E^-_{ml} = E^-_m \mathrm{e}^{-\mathrm{i}g_m}. \tag{10.38}$$

Now the total electric field must be continuous at the interface, so that

$$E^+_{ml} + E^-_{ml} = E^+_{m-1} + E^-_{m-1}. \tag{10.39}$$

Substituting:

$$E^+_m \mathrm{e}^{+\mathrm{i}g_m} + E^-_m \mathrm{e}^{-\mathrm{i}g_m} = E^+_{m-1} + E^-_{m-1}. \tag{10.40}$$

Likewise, we deal with the magnetic fields, which are in the z-direction. The amplitude of the wave propagating in the $+x$-direction is $H^+ = nZ_0^{-1}E^+$, and that in the $-x$-direction is $H^- = -nZ_0^{-1}E^-$. Thus, like (10.40),

$$H^+_m \mathrm{e}^{+\mathrm{i}g_m} + H^-_m \mathrm{e}^{-\mathrm{i}g_m} = H^+_{m-1} + H^-_{m-1}. \tag{10.41}$$

Rewrite (10.40) and (10.41) in terms of the total fields

$$E_m = E^+_m + E^-_m \tag{10.42}$$

$$\text{and} \quad Z_0 H_m = u_m \left(E^+_m - E^-_m\right) \equiv n_m \left(E^+_m - E^-_m\right). \tag{10.43}$$

Here, n_m has been replaced by u_m; the change in notation corresponds to that in §5.4.1, and is discussed further in §10.3.2.[2] We have two new equations:

$$E_{m-1} = E_m \cos g_m + \frac{\mathrm{i}Z_0 H_m}{u_m} \sin g_m, \tag{10.44}$$

$$Z_0 H_{m-1} = \mathrm{i}u_m E_m \sin g_m + Z_0 H_m \cos g_m, \tag{10.45}$$

which can be written in matrix form:

$$\begin{pmatrix} E_{m-1} \\ Z_0 H_{m-1} \end{pmatrix} = \begin{pmatrix} \cos g_m & \mathrm{i}u_m^{-1} \sin g_m \\ \mathrm{i}u_m \sin g_m & \cos g_m \end{pmatrix} \begin{pmatrix} E_m \\ Z_0 H_m \end{pmatrix} \equiv \mathsf{M}_m \begin{pmatrix} E_m \\ Z_0 H_m \end{pmatrix}. \tag{10.46}$$

[2] It is common in many books to put $Z_0 = 1$ at this stage because its value always cancels out.

The behaviour of the complete system, defined by the set of parameters (g_m, u_m) for each layer, can now be found by matrix multiplication. As a result, we have the relationship between (E_0, Z_0H_0), which contains both the incident wave and the reflected wave, and (E_N, Z_0H_N) representing the transmitted wave:

$$(E_0, Z_0H_0) = \prod_{m=1}^{N} \mathsf{M}_m \cdot (E_N, Z_0H_N). \tag{10.47}$$

Now the reflection and transmission coefficients $\mathcal{R}$ and $\mathcal{T}$ follow. Since $E_0^- = \mathcal{R}E_0^+$, $Z_0H_0^+ = u_0E_0^+$ and $Z_0H_0^- = -u_0E_0^-$,

$$(E_0, Z_0H_0) = [(1+\mathcal{R}), u_0(1-\mathcal{R})], \tag{10.48}$$

where the incident field is assumed to have unit value. Obviously $E_N^- = 0$, since there is no reflected wave in the $-x$-direction in the last layer, so that

$$(E_N, Z_0H_N) = (\mathcal{T}, u_N\mathcal{T}). \tag{10.49}$$

The approach used here works also with complex refractive indices (§13.3); see surface plasmon resonance (§13.7) as an example. If n is complex, $\det\{\mathsf{M}\} \neq 1$.

The resulting matrix equation

$$(1+\mathcal{R}, u_0(1-\mathcal{R})) = \prod_{m} \mathsf{M}_m \cdot (\mathcal{T}, u_N\mathcal{T}) \tag{10.50}$$

is easily solved by equating coefficients as will be seen in the example which follows. Notice, for future use, that the determinant $\det\{\mathsf{M}\} = 1$. This implies conservation of energy; as a result, $\det\{\prod_m \mathsf{M}_m\} = 1$.

10.3.2 Oblique incidence

The case of oblique incidence is easily dealt with, and will remind the reader why u was introduced. Suppose that the incident wave in free space is at an angle $\hat{\imath}$ to the x-axis. Then its angle $\hat{r}_m$ in the mth layer is given by Snell's law

$$\sin\hat{\imath} = n_m \sin\hat{r}_m. \tag{10.51}$$

The phase difference g_m now contains the x-component of $\mathbf{k}$ in the medium, i.e. $k_0 n_m \cos\hat{r}_m$:[3]

$$g_m = k_0 n_m d_m \cos\hat{r}_m. \tag{10.52}$$

As we saw in §5.4.1 it is now possible to express the boundary conditions for $\parallel$ and $\perp$ fields by introducing effective indices of refraction,

$$u_m = n_m \sec\hat{r}_m \quad (\parallel \text{ polarization}), \tag{10.53}$$

$$u_m = n_m \cos\hat{r}_m \quad (\perp \text{ polarization}), \tag{10.54}$$

[3] It is a common error to assume, by erroneous intuition, that oblique incidence makes the layers 'seem thicker', and to write $g = k_0 nd/\cos\hat{r}$. A physical explanation, which underlies what appears here, is given in §9.5.1 for the Fabry–Perot interferometer.

into the Fresnel coefficients for normal incidence, giving (5.43) and (5.44). The same argument applies here, where $\hat{r}_m$ is the angle of refraction within each medium.

10.3.3 Single-layer anti-reflection coating: lens blooming

Although the reflection coefficient at a single interface between air and a transparent medium, of the order of 4% as calculated in §5.4.1, might seem small, it represents a serious loss of light in optical systems such as compound lenses and instruments which contain many surfaces. The reflection coefficient can be greatly reduced by coating the surfaces with one or more thin layers of materials with different refractive indices. Such **anti-reflection coatings** are the most widespread use of dielectric multilayers. We shall illustrate the basic idea with the simplest case, a single-layer coating, which by suitable design can reduce the reflection coefficient to zero at a specific wavelength, and is quite effective at neighbouring ones.

For one layer with parameters (g, u) between air (u_0) and a substrate with index u_s, we have (10.46) and (10.50),

$$\begin{pmatrix} 1+\mathcal{R} \\ u_0(1-\mathcal{R}) \end{pmatrix} = \begin{pmatrix} c & \mathrm{i}u^{-1}s \\ \mathrm{i}us & c \end{pmatrix} \begin{pmatrix} \mathcal{T} \\ u_s\mathcal{T} \end{pmatrix}, \tag{10.55}$$

where $c \equiv \cos g$ and $s \equiv \sin g$. We shall use u instead of the refractive index n, so that the results will be generally applicable to any angle of incidence and polarization. We now require $\mathcal{R} = 0$, for which (10.55) gives the pair of equations

$$1 = (c + \mathrm{i}su_s/u)\mathcal{T}, \tag{10.56}$$

$$u_0 = (\mathrm{i}us + cu_s)\mathcal{T}. \tag{10.57}$$

Eliminating $\mathcal{T}$ by dividing (10.57) by (10.56) leads to the complex equation

$$u_0 = \left[u_s + \mathrm{i}cs\left(u - u_s^2/u\right)\right] \Big/ \left(c^2 + s^2u_s^2/u^2\right). \tag{10.58}$$

Clearly, the imaginary part must be zero. Since $u \neq u_s$ (otherwise the deposited layer would simply be part of the substrate) c or s must be zero. If $s = 0$, it follows that $c = \pm 1$, but the equation cannot be satisfied because $u_0 \neq u_s$. Therefore $c = 0$, $s = \pm 1$ and

$$u_0 u_s = u^2. \tag{10.59}$$

The value $s = \pm 1$ implies $g = (\text{odd})\,\pi/2$; the optical thickness of the layer is an odd number of quarter-wavelengths. Usually, a single quarter-wave is chosen. As an example, at normal incidence the refractive index needed to provide an anti-reflection coating at an interface with air ($u_0 = 1$) is the square root of that of the substrate. On glass with $u_s = n_s \simeq 1.6$, the most common

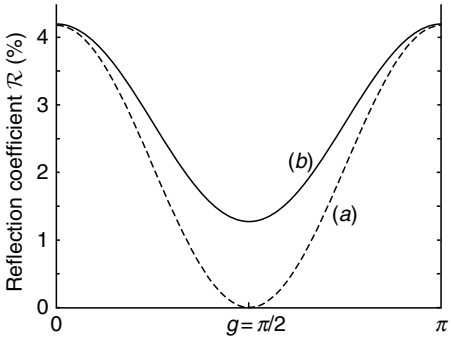

Figure 10.15
Reflection coefficient for a quarter-wave anti-reflection coating on glass with $n = 1.52$, calculated for minimum reflectance at normal incidence: (*a*) ideal, $u = \sqrt{1.52}$; (*b*) magnesium fluoride, $u = 1.38$.

Glass coated with a single $\lambda/4$ layer for green light shows a slight purplish reflection, because the layer reflects rather more in the blue and red.

coating material is magnesium fluoride, which can easily be deposited by evaporation and has a refractive index of 1.38, which is approximately correct. The reflection coefficient as a function of wavelength for this case is shown in Fig. 10.15. It is always smaller than that of uncoated glass.

The use of more than one layer allows broader-band anti-reflection coatings to be designed, with better overall quality, but we shall not discuss them here (see MacLeod (2001)).

It is easy to see the physical basis of the single-layer anti-reflection coating. By choosing a layer with u equal to the geometric mean of the air and the medium u_s, we have created two interfaces with equal reflection coefficients (5.34). Separating them by an optical distance of $\lambda/4$ ensures that the waves reflected from the two will be in antiphase and therefore interfere destructively.

10.3.4 Periodic multilayers: selective mirrors

An important and much more challenging problem is the inverse: given the spectral properties of a stack, to calculate the values of (g_m, u_m) needed.

We shall only solve one multilayer problem in any detail, although the reader will realize that (10.47) and a small computer in fact allow calculation of the properties of *any* combination of layers that are non-absorbing, if the various (g_m, u_m) are given.

In order to create a highly reflective multilayer, we want to do the opposite to what we did with the anti-reflecting layer. So we need *constructive* interference between the partially reflected waves. This can be achieved by making interfaces that have alternately positive and negative reflection coefficients of equal value, and separating them by half-wavelength path differences (i.e. quarter-wavelength thick layers again) as in Fig. 10.16. Let us try this idea out.

We construct a periodic system from two types of layer, which we call H for 'high' refractive index and L for 'low'. Their effective refractive indices are u_H and u_L respectively, and we shall let their optical thicknesses be equal, $g_H = g_L = g$. The system contains q pairs of these layers on a substrate with refractive index u_s. Equation (10.47) then becomes (with $c \equiv \cos g$ and $s \equiv \sin g$)

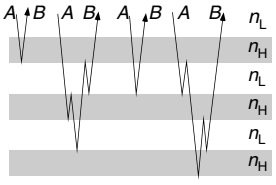

Figure 10.16

Arbitrary multiply reflected waves in a multilayer. Notice that any wave from *A* has the same phase at *B* (modulo 2π) if every layer has optical thickness $\lambda/4$, when phase changes on reflection have been taken into account.

$$\begin{pmatrix} E_0 \\ Z_0 H_0 \end{pmatrix} = \left[\begin{pmatrix} c & \mathrm{i}u_\mathrm{L}^{-1} s \\ \mathrm{i}u_\mathrm{L} s & c \end{pmatrix} \begin{pmatrix} c & \mathrm{i}u_\mathrm{H}^{-1} s \\ \mathrm{i}u_\mathrm{H} s & c \end{pmatrix} \right]^q \begin{pmatrix} E_N \\ Z_0 H_N \end{pmatrix}$$
$$= \begin{pmatrix} c^2 - u_\mathrm{H} u_\mathrm{L}^{-1} s^2 & \mathrm{i}cs\left(u_\mathrm{H}^{-1} + u_\mathrm{L}^{-1}\right) \\ \mathrm{i}cs(u_\mathrm{H} + u_\mathrm{L}) & c^2 - u_\mathrm{L} u_\mathrm{H}^{-1} s^2 \end{pmatrix}^q \begin{pmatrix} E_N \\ Z_0 H_N \end{pmatrix} \tag{10.60}$$

$$\equiv (\mathsf{M}_p)^q \begin{pmatrix} E_N \\ Z_0 H_N \end{pmatrix}. \tag{10.61}$$

It is easiest to evaluate $(\mathsf{M}_p)^q$ algebraically when it is first diagonalized by rotating the vectors $(E, Z_0 H)$, because if

$$\mathsf{M} = \begin{pmatrix} \lambda_1 & 0 \\ 0 & \lambda_2 \end{pmatrix},$$
$$\text{then} \quad \mathsf{M}^q = \begin{pmatrix} \lambda_1^q & 0 \\ 0 & \lambda_2^q \end{pmatrix}. \tag{10.62}$$

The values of λ are given by

$$\det\{\mathsf{M}_p - \lambda \mathsf{I}\} = 0$$
$$= \det\{\mathsf{M}_p\} - \lambda \mathrm{trace}\{\mathsf{M}_p\} + \lambda^2$$
$$= 1 - \lambda \mathrm{trace}\{\mathsf{M}_p\} + \lambda^2. \tag{10.63}$$

Writing 2ξ for the trace (sum of diagonal components) (10.63) gives:

$$\lambda = \xi \pm \sqrt{\xi^2 - 1}. \tag{10.64}$$

Now ξ has the value

$$\xi = c^2 - \frac{1}{2}\left(\frac{u_\mathrm{H}}{u_\mathrm{L}} + \frac{u_\mathrm{L}}{u_\mathrm{H}}\right) s^2. \tag{10.65}$$

Note that $(u_\mathrm{H}/u_\mathrm{L} + u_\mathrm{L}/u_\mathrm{H}) \geq 2$ for any $u_\mathrm{H}, u_\mathrm{L}$. Then ξ can easily be seen to have the following characteristics (remember that $c^2 + s^2 = 1$):

- its maximum value, obtained when $c = \pm 1,\ s = 0$, is 1.
- its minimum value, when $c = 0,\ s = \pm 1$ is $-\frac{1}{2}(u_\mathrm{H}/u_\mathrm{L} + u_\mathrm{L}/u_\mathrm{H})$ which is always less than -1.

Therefore there exist regions of c and s for which λ is real (around $g = 0, \pi \ldots$) and complex (around $g = \pi/2, 3\pi/2 \ldots$), as shown in Fig. 10.17. In general we have

$$\lambda_1 \lambda_2 = 1. \tag{10.66}$$

The particular case where $g = (\mathrm{odd})\,\pi/2$ is particulary easy to treat, since the matrix M_p is already diagonal in its unrotated form; i.e. $(E_m, Z_0 H_m)$ is an

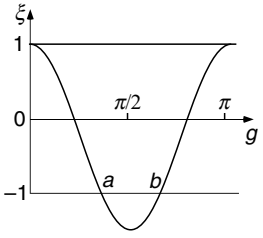

Figure 10.17
Eigenvalues of the matrix for a periodic multilayer.

eigenvector. Here $\lambda_1 = u_H/u_L$, $\lambda_2 = u_L/u_H$ and the optical thickness of each layer is

$$ud = g/k_0 = (\text{odd})\frac{\pi}{2} \times \frac{\lambda}{2\pi} = (\text{odd})\frac{\lambda}{4}. \tag{10.67}$$

We have for (10.50)

$$\begin{pmatrix} 1+\mathcal{R} \\ u_0(1-\mathcal{R}) \end{pmatrix} = \begin{pmatrix} \lambda_1^q & 0 \\ 0 & \lambda_2^q \end{pmatrix} \begin{pmatrix} \mathcal{T} \\ u_s\mathcal{T} \end{pmatrix}, \tag{10.68}$$

which can be solved for $\mathcal{R}$:

$$\mathcal{R} = \frac{u_0\lambda_1^q - u_s\lambda_2^q}{u_0\lambda_1^q + u_s\lambda_2^q}. \tag{10.69}$$

Now from (10.66), one of $|\lambda_1|, |\lambda_2|$ must be > 1, so that $|\mathcal{R}| \to 1$ as $q \to \infty$. In other words, in the region of real λ, around $g = (\text{odd})\,\pi/2$, the system behaves as a mirror. In fact, it is quite easy to get a very good mirror. Suppose that $u_H/u_L = 2$ (approximately the ratio for the commonly used pair zinc sulphide–magnesium fluoride) at normal incidence; then for $g = \pi/2$, (10.67) gives $\xi = -\frac{5}{4}$ and $\lambda_1 = -\frac{1}{2}$, $\lambda_2 = -2$. Thus, for five periods, say, and $u_s/u_0 = 1.5$,

$$\mathcal{R} = \frac{\left(-\frac{1}{2}\right)^5 - 1.5(-2)^5}{\left(-\frac{1}{2}\right)^5 + 1.5(-2)^5} = -0.9987. \tag{10.70}$$

The intensity reflection coefficient is then $\mathcal{R}^2 = 0.9974$. This method allows us to make highly reflecting mirrors for selected wavelengths, for which each layer has optical thickness of an odd number (usually one) of quarter-wavelengths. It is used routinely for making laser resonator mirrors since the losses achieved (even under real conditions) are much less than in metal mirrors. The region where λ_1 and λ_2 are real extends for a region around $g = (\text{odd})\,\pi/2$. Its boundaries are given by putting $\lambda_1 = \lambda_2 = 1$, whence $\xi = 1$ and (10.67) leads to

$$-1 = c^2 - \frac{1}{2}\left(\frac{u_H}{u_L} + \frac{u_L}{u_H}\right)s^2, \tag{10.71}$$

which simplifies to

$$\cos g = \pm\left(\frac{u_H - u_L}{u_H + u_L}\right). \tag{10.72}$$

These two solutions define the points a and b in Fig. 10.18; the region of high reflectivity around $(\text{odd})\pi/2$ has width

$$\Delta g = 2\sin^{-1}\left(\frac{u_H - u_L}{u_H + u_L}\right) = 2\sin^{-1}\mathcal{R}_{HL}, \tag{10.73}$$

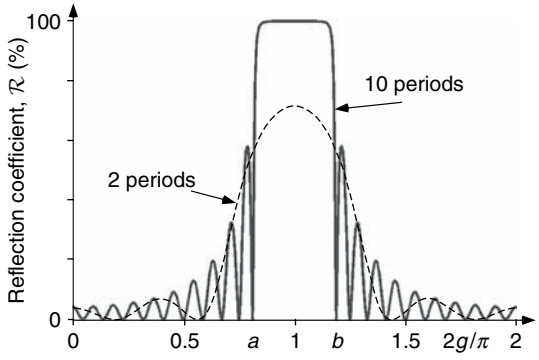

Figure 10.18
Reflectivity of periodic multilayers with 2 and 10 periods.

The effect on the shape of the reflectance curve is similar to that of adding terms to a Fourier series (Fig. 4.1).

where $\mathcal{R}_{HL}$ is the Fresnel reflectivity of the interface from §5.4.1. Notice that the width of the reflecting region does not depend on the number of periods, q. However, q does affect the flatness of $\mathcal{R}$ within the band.

In the region where λ_1 and λ_2 are complex, they take the form $\lambda = \exp(\pm i\phi)$ where $\xi = \cos\phi$. As an example, consider $g = (\text{even})\pi/2$, where M_p is already diagonal. Then $\phi = 0$ and we find $\mathcal{R} = (u_0 - u_s)/(u_0 + u_s)$. This is the reflectivity of the substrate as if the multilayer were not there; the multilayer has no effect when the layer optical thicknesses are multiples of half a wavelength.

Calculation of $\mathcal{R}$ for values of g other than integer multiples of $\pi/2$ is tiresome algebraically, and is best done numerically, directly from (10.60). The example mentioned above, $u_H/u_L = 2$, $q = 10$ and $u_s/u_0 = 1.5$ gives the result shown in Fig. 10.18. The general features are high reflectivity around $g = (\text{odd})\,\pi/2$ and low reflectivity around $(\text{even})\pi/2$, with the transition where $\cos g = \pm\mathcal{R}_{HL}$.

Finally, we once again stress the analogy with the band theory of electrons in crystals. When the period of the crystal is half the wavelength of the electrons, we are exactly in the middle of the band gap. The band gap is then seen as equivalent to the region of high reflectivity (zero transmission) of the multilayer.

10.3.5 Interference filters

Interference filters are essential in high-power applications, for example Raman studies, because the unwanted energy is reflected rather than absorbed, which would damage the filter.

An important application of dielectric multilayers is to the design of interference filters. In the preceding section we showed that highly reflective and non-absorbing wavelength-selective mirrors can be made by using quarter-wave-thick layers of different dielectric media. This idea can be extended to the design of filters with transmission characteristics satisfying almost any specification. We shall use symbols H, L to represent quarter-wave layers of indices n_H, n_L respectively.

The most common filter is a narrow-band interference filter based on the properties of the Fabry–Perot étalon (§9.5.1). Suppose that we make a pair of reflecting surfaces by using quarter-wave assemblies (HLHL. . .) and separate them by a spacer corresponding to the first (or higher, m) order of the

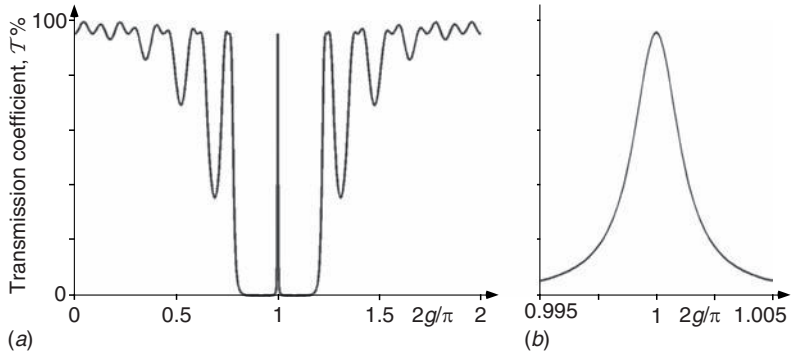

Figure 10.19

(*a*) Transmittance of the interference filter $(HL)^5H^2(LH)^5$ on a glass substrate, as a function of $2g/\pi$; (*b*) shows the region $0.995 < 2g/\pi < 1.005$ expanded.

Fabry–Perot. Ignoring the substrate for simplicity, the amplitude reflection coefficient at normal incidence for a set of q pairs HL is, from (10.69),

$$\mathcal{R} \simeq \frac{n_{\mathrm{H}}^{2q} - n_{\mathrm{L}}^{2q}}{n_{\mathrm{H}}^{2q} + n_{\mathrm{L}}^{2q}}. \tag{10.74}$$

The thickness of the spacer, for order $m = 1$, is given by $t = \lambda/2n$, implying a single half-wave layer. We then have a layer system that can be described symbolically as $(HL)^qH^2(LH)^q$ in which the two consecutive H layers make the half-wave layer. This has a pass band given by (9.56)

$$\frac{\delta\lambda}{\lambda} = \frac{\delta g}{g} = \frac{F^{-\frac{1}{2}}}{2\pi m} = \frac{1-\mathcal{R}^2}{4\pi\mathcal{R}} = \frac{n_{\mathrm{H}}^{2q} n_{\mathrm{L}}^{2q}}{\pi\left(n_{\mathrm{H}}^{4q} - n_{\mathrm{L}}^{4q}\right)}. \tag{10.75}$$

The Fabry–Perot type of filter has a transmission band with a Lorentzian bell-shaped profile, which is not ideal. A rectangular shape would be preferable; see Problem 10.8.

Very accurate coating techniques have been developed to produce such filters (and many others of more intricate design) with many tens of layers. For example, using zinc sulphide ($n_{\mathrm{H}} = 2.32$) and magnesium fluoride ($n_{\mathrm{L}} = 1.38$), with $q = 5$ (21 layer filter)

$$\frac{\delta\lambda}{\lambda} = 1.7 \times 10^{-3}.$$

For $\lambda = 500\,\mathrm{nm}$, $\delta\lambda = 0.9\,\mathrm{nm}$. The filter is non-transmitting in the region of complete reflection of the quarter-wave periodic assembly, about 100 nm on each side of the pass band. This is typical of what can be achieved with multilayer filters (Fig. 10.19).

Since this book is intended to explain physical principles without going into technical details, we will not continue with a discussion of more advanced filter designs. Clearly, more than two different materials can be used, and layer thicknesses do not need to be limited to integer multiples of $\lambda/4n$. Some ideas that can be explored by the reader, with the aid of a simple computer program written to evaluate $\mathcal{R}(g)$ and $\mathcal{T}(g)$, are included as problems at the end of the chapter.

Box 10.1 Thin-film solar cells

The first solar cell was created by Charles Fritts in the late nineteenth century using selenium as the photosensitive material. Following this, after the discovery of semiconductors, considerable work was done on solar cells using p-n junctions in the 1950s. The intrinsic region, 'i' of a p-i-n junction, absorbs photons and creates electron-hole pairs, which are separated by the internal field; this uses the reverse of the mechanism described in §14.5.5, where light-emitting and laser diodes are discussed. However, the importance of sunlight as a renewable energy source has highlighted this work and led to important new developments. Amongst the many methods of producing these junctions, the thin-film solar cell is a technique that exploits the optical properties of multilayer stacks in conjunction with the semiconductor properties of the materials themselves both to capture the light and to create electricity. The main benefits of the thin-film technique lie in its low cost of production, the possibility of making devices with large areas and the modestly high conversion efficiency. An efficiency of over 20% can be achieved for copper indium gallium selenide cells, although at the time of writing these are not in widespread use.

Figure 10.20 shows schematically the cross-section of a tandem silicon thin-film solar cell. A multilayer anti-reflection coating is first deposited on one side of a glass substrate to maximize the transmitted light at all wavelengths that can be absorbed. A transparent conductive (doped zinc oxide or indium tin oxide) layer is next deposited on the other side of the glass as the first solar cell layer, followed by an α-Si p-i-n layered solar cell junction. The oxide layer is one electrical contact and must be transparent, highly conductive and, more recently, structured in order to scatter the shorter wavelengths transversely into the α-Si layer while letting the longer wavelengths continue straight on. An intermediate multilayer reflector then reflects back the shorter wavelength light into the junction layer again, while transmitting the wavelengths too long to be absorbed. This has been found to increase the efficiency dramatically, since wavelengths too long to be absorbed by the first p-i-n junction pass through the reflector and can then be absorbed by a second micro-crystalline silicon p-i-n junction layer, which has a narrower band gap. Finally, a metallic layer serves as a back contact and also reflects the longer wavelength light back into the second absorbing layer. The two junction layers are in series and therefore their currents have to be matched, which is not a trivial problem! At present, much work is under way to create diffractive structures on the transparent conducting layer that influence not only the optics but also the way the micro-crystalline silicon layer grows.

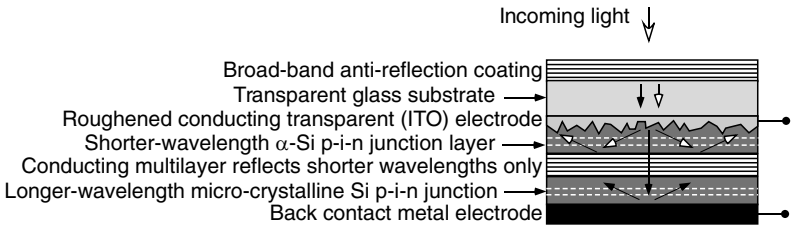

Figure 10.20

Design details of a two-stage tandem solar cell, using p-i-n junctions in two types of silicon having different band gaps. The longer-wavelength light is signified by arrows with black heads, and the shorter-wavelength by white-headed arrows.

10.4 Advanced topic: An omnidirectional reflector

Most of the discussion of propagation in one-dimensional periodic media above has concentrated on the dependence of the propagation on wavelength. An interesting question was asked by Fink *et al.* (1998) concerning the dependence on angle: could a multilayer stack be designed that reflected efficiently at all angles of incidence in both polarizations? The motive behind this question was the possibility of constructing an efficient hollow (air-cored) circular waveguide for transmitting light power, for use in laser surgery. This would require extremely good reflection at all relevant angles to prevent damaging the waveguide. Now of course, if the question refers to *all* angles of incidence, the answer must be 'no', since at the Brewster angle the reflection coefficient of the p-polarization is zero. However, if the incident light enters from air, only angles in the media less than the critical angle are relevant, and under these conditions, the answer is 'yes' when the right materials are chosen. If the multilayer stack is constructed from two materials with refractive indices n_{L} and n_{H}, when the light enters from air into the former, the condition for not exceeding the Brewster angle at the interface between the two is $\sin^{-1}(1/n_{\mathrm{L}}) < \tan^{-1}(n_{\mathrm{H}}/n_{\mathrm{L}})$, which is always obeyed if $n_{\mathrm{L}} > \sqrt{2}$, a condition easy to fulfil. However, more manipulation of the refractive indices is necessary to ensure that at all angles of incidence from 0 to the critical, complete reflection is obtained at the same wavelength. The calculation depends mainly on the refractive indices chosen, following which the thicknesses of the layers can be tuned to achieve the highest reflection at the wavelength of interest. It is useful to represent the band edges, at which $\mathcal{R} = 1$ (10.72), as a function of angle on a diagram where 'positive' angles represent $\parallel$ or p-polarization, and 'negative' angles $\perp$ or s-polarization. This is done in Fig. 10.21, which shows two examples, one with $n_{\mathrm{L}} < \sqrt{2}$ illustrating the zero band gap at the Brewster angle, and one with sufficiently high indices for a band gap common to all angles of incidence and both polarizations to be formed. In the figure, the ordinate nd/λ represents the wavelength, where the product nd is assumed equal for both layers; then, clearly, the centre of the band gap at normal incidence is at 0.25, the quarter-wave condition.

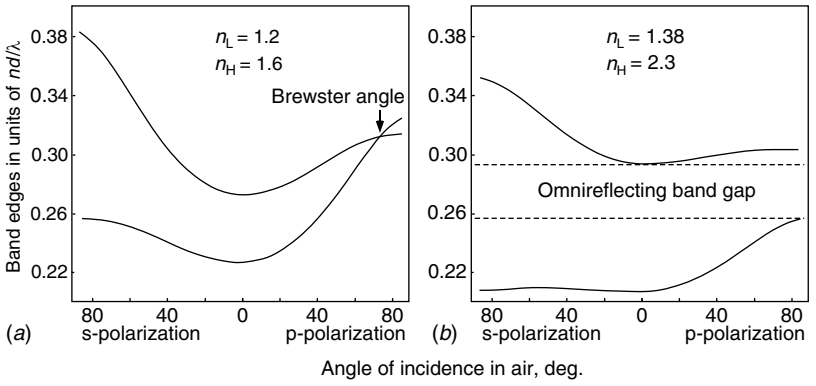

Figure 10.21

Reflecting band gaps for multilayer stacks as a function of incidence angle in air for s- and p-polarizations: (*a*) for the case $n_L < \sqrt{2}$ where the gap for the p-polarization closes at the Brewster angle; (*b*) for higher refractive indices, where there is a region of frequencies for which complete reflection occurs at all angles of incidence. The two curves in each figure show the values of $g/2\pi$ at the edges of the reflection band, as a function of angle of incidence from air.

Figure 10.22

Preform made from a rolled polystyrene–As_2Se_3 sheet and the extruded fibre. On the right, SEM images of the cross-section showing multilayers surrounding the hollow core. (Courtesy of Yoel Fink; Abouraddy *et al.* (2007))

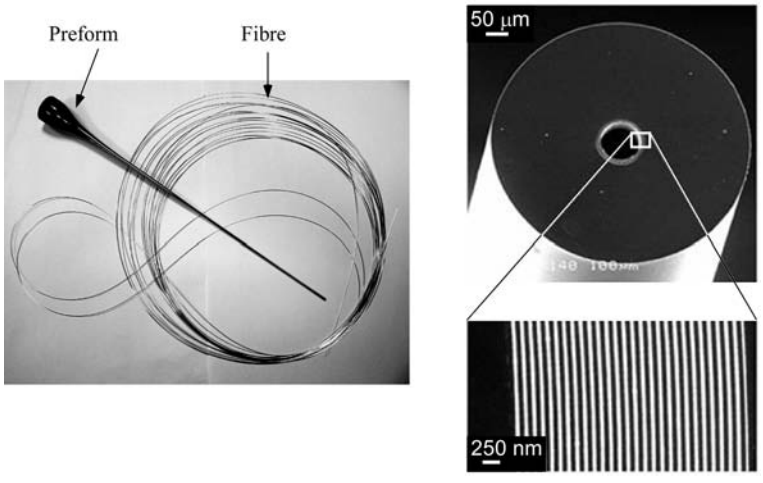

This technique has been successfully applied to producing hollow optical fibres for transmitting high-power carbon-dioxide laser light at 10 μm wavelength. The multilayer system is made by coating a polystyrene sheet ($n_L = 1.6$) with an arsenic selenide (As_2Se_3) ($n_H = 2.7$) layer, the two having the optimum thickness ratio. The sheet is then rolled into a multi-walled cylinder as a preform and is then drawn down into a fibre with a size reduction calculated so that the layers have the right thicknesses for the omnidirectional band gap to contain the wavelength 10 μm. An example of the rolled preform and extruded fibre is shown in Fig. 10.22.

10.5 Advanced topic: Photonic crystals

This chapter has emphasized the strong analogy between the properties of light waves as described by Maxwell's equations and those of matter waves described by Schrödinger's equation. In particular, the analogy between the optical properties of periodic multilayers and the electronic structure of metal and semiconductor crystals, where frequency bands appear in which propagation is forbidden, suggests that two- and three-dimensional optical crystals might be designed to have specifically interesting and useful properties. These are called 'photonic crystals'. Indeed, such structures, with optical properties changing periodically on the scale of a fraction of an optical wavelength, exist in nature. Michelson (*Studies in Optics*, Chapter 15) pointed out that the colours of opals and peacock feathers, for example, might be explicable on the basis of a microscopic periodicity in their structure, and more recently this has been studied quantitatively (Zi *et al*. (2003)).

The original motivation for studying photonic crystals was to produce lasers with essentially zero threshold for lasing, the threshold being the level at which stimulated emission starts to dominate spontaneous emission (Chapter 14). Spontaneous emission, as we shall see in §14.4.2, is initiated by zero-point fluctuations in modes of the electromagnetic field in the laser cavity. By creating a cavity in surroundings in which waves cannot propagate at the lasing frequency, the threshold could be reduced to zero. By analogy with an insulator, such as diamond, which is a periodic crystal with an omnidirectional band gap at a particular electron energy (the Fermi energy), the idea was to create a photonic crystal with similar properties, within which a laser cavity could be carved, essentially creating a defect in the crystal. The laser light in the defect cavity would then be coupled to the outside world by tunnelling through a finite barrier to a waveguide created by another defect in the crystal, designed so as to form a low-loss waveguide. Only recently have there been some developments in this direction, using two-dimensional photonic crystals.

The basic idea, and how it was developed first using microwaves in structures that could be drilled and cast on the laboratory bench, is described dramatically by Yablonovitch (1993). It quickly became clear that the face-centred-cubic or diamond lattices held the most promise for photonic crystals with completely overlapping band gaps in all directions, or 'optical insulators'. The calculations involved in developing this idea in more than one dimension are quite complicated, as are those for electronic band structures, and generally need sophisticated computer programs for their implementation. It appears that obtaining complete overlap of forbidden propagation bands for all polarizations requires a refractive index ratio of at least 2 between the maximum and minimum values in the diamond lattice and its derivatives, while in the simple cubic lattice, for example, complete overlap cannot be achieved without a ratio greater than about 3.

To illustrate the basic ideas, we can look at a simple approximate model analogous to the 'nearly-free electron model' used in solid-state physics to derive band structures (Kittel (2005)). The solid-state model allows analytical calculation of the electronic properties of a material with a weak sinusoidal potential $V(\mathbf{r}) = V_0 + 2V_1 \cos(\mathbf{g} \cdot \mathbf{r})$, where $V_1 \ll V_0$. Being based on Schrödinger's scalar-wave equation for electrons, it clearly ignores the polarization properties of electromagnetic waves. Here, we shall solve the equivalent optical problem where $\epsilon(x) = \epsilon_b + 2\epsilon_1 \cos(\mathbf{g} \cdot \mathbf{r})$ and $\epsilon_1 \ll 1$. In fact, although many photonic crystals that have been produced do not satisfy the condition that $\epsilon_1 \ll 1$, some interesting experiments have been carried out with photonic crystals that have been 'written' into a medium using non-linear optics (§13.6.2), in which case $\epsilon_1 \approx 10^{-3}$ for which this model is entirely appropriate, and will be described briefly in Box 10.2.

From (10.5)

$$-\frac{\epsilon}{c^2}\frac{\partial^2 \mathbf{E}}{\partial t^2} = \nabla \times (\nabla \times \mathbf{E}) = \nabla(\nabla \cdot \mathbf{E}) - \nabla^2 \mathbf{E} = -\nabla^2 \mathbf{E}. \quad (10.76)$$

Since the variations in ϵ are assumed to be very small, we can put $\nabla \cdot \mathbf{E} = 0$.[4] Now for a sinusoidal wave of frequency ω, (10.76) can then be written:

$$\nabla^2 \mathbf{E} + \frac{\epsilon \omega^2}{c^2}\mathbf{E} = \nabla^2 \mathbf{E} + k_0^2[\epsilon_b + \epsilon_1 \exp(\mathrm{i}\mathbf{g} \cdot \mathbf{r}) + \epsilon_1 \exp(-\mathrm{i}\mathbf{g} \cdot \mathbf{r})]\mathbf{E} = 0. \quad (10.77)$$

Bloch's theorem in solid-state physics showed that the general solution of Schrodinger's equation in a periodic potential is a modulated plane wave having the general form $u_g(\mathbf{r}) \exp(\mathrm{i}\mathbf{k} \cdot \mathbf{r})$, where $u_g(\mathbf{r})$ is a function with the same wave-vector $\mathbf{g}$ as the potential. Inspired by this, we consider as a trial solution the simplest periodically modulated function, which is the superposition of two plane waves with wave-vectors $\mathbf{k}$ and $\mathbf{k} - \mathbf{q}$:

$$E = a \exp[\mathrm{i}\mathbf{k} \cdot \mathbf{r}] + b \exp[\mathrm{i}(\mathbf{k} - \mathbf{q}) \cdot \mathbf{r}]. \quad (10.78)$$

Substituting E into (10.76), we find

$$\begin{aligned} &a[-k^2 + \epsilon_b k_0^2] \exp(\mathrm{i}\mathbf{k} \cdot \mathbf{r}) + b[-|\mathbf{k} - \mathbf{q}|^2 + \epsilon_b k_0^2] \exp(\mathrm{i}(\mathbf{k} - \mathbf{q}) \cdot \mathbf{r}) \\ &\quad + k_0^2 \epsilon_1 \{a \exp(\mathrm{i}(\mathbf{k} + \mathbf{g}) \cdot \mathbf{r}\} + a\{\exp(\mathrm{i}(\mathbf{k} - \mathbf{g}) \cdot \mathbf{r}\} \\ &\quad + k_0^2 \epsilon_1 \{b \exp(\mathrm{i}(\mathbf{k} + \mathbf{g} - \mathbf{q}) \cdot \mathbf{r}\} + b\{\exp(\mathrm{i}(\mathbf{k} - \mathbf{g} - \mathbf{q}) \cdot \mathbf{r}\} = 0. \quad (10.79) \end{aligned}$$

[4] $\nabla \cdot \mathbf{D} = \nabla \cdot (\epsilon \mathbf{E}) = \epsilon \nabla \cdot \mathbf{E} + \nabla \epsilon \cdot \mathbf{E}$, where the last term is negligible if the variations in ϵ are small.

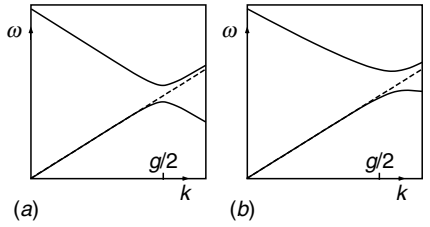

Figure 10.23
$\omega(k) = ck_0$ for a weak photonic crystal with lattice vector $\mathbf{g}$ as a function of k calculated from (10.86) (*a*) along the axis $\mathbf{k} \parallel \mathbf{g}$, (*b*) along an axis at 30° to $\mathbf{g}$. The broken line shows the relationship for the unmodulated medium, $\omega = kc/\sqrt{\epsilon_b}$.

In the same way as we derived Fourier coefficients in Chapter 4, we separate this equation into parts by multiplying first by $e^{-i\mathbf{k}\cdot\mathbf{r}}$ and integrating from $-\infty$ to $+\infty$, and then likewise by $e^{-i(\mathbf{k}-\mathbf{q})\cdot\mathbf{r}}$. We then get two equations:

$$\left(k_0^2\epsilon_b - k^2\right) a - \epsilon_1 k_0^2 b[\delta((\mathbf{g}-\mathbf{q})\cdot\mathbf{r}) + \delta((\mathbf{g}+\mathbf{q})\cdot\mathbf{r})] = 0, \quad (10.80)$$

$$\left(k_0^2\epsilon_b - |\mathbf{k}-\mathbf{q}|^2\right) b - \epsilon_1 k_0^2 a[\delta((\mathbf{g}-\mathbf{q})\cdot\mathbf{r}) + \delta((\mathbf{g}+\mathbf{q})\cdot\mathbf{r})] = 0, \quad (10.81)$$

in which the δ is unity when its argument is zero, otherwise zero. These δ-functions are zero, unless $(\mathbf{g}-\mathbf{q})\cdot\mathbf{r} = 0$ or $(\mathbf{g}+\mathbf{q})\cdot\mathbf{r} = 0$, i.e. $\mathbf{g} = \pm\mathbf{q}$. This is Bloch's theorem. The case $\mathbf{g} = +\mathbf{q}$ will be sufficient to illustrate the physics; we then have

$$a\left(k_0^2\epsilon_b - k^2\right) + bk_0^2\epsilon_1 = 0, \quad (10.82)$$

$$ak_0^2\epsilon_1 + b\left(k_0^2\epsilon_b - |\mathbf{k}-\mathbf{g}|^2\right) = 0. \quad (10.83)$$

The solution to these equations is given by the 'secular determinant'

$$\begin{vmatrix} k_0^2\epsilon_b - k^2 & k_0^2\epsilon_1 \\ k_0^2\epsilon_1 & k_0^2\epsilon_b - |\mathbf{k}-\mathbf{g}|^2 \end{vmatrix} = 0, \quad (10.84)$$

which represents a quadratic equation with two solutions for k_0^2 at each value of k. We solve it for k_0^2 because $ck_0 = \omega$, so that we can directly obtain the dispersion relation $\omega(k)$:

$$\left(k_0^2\epsilon_b - k^2\right)\left(k_0^2\epsilon_b - |\mathbf{k}-\mathbf{g}|^2\right) - k_0^4\epsilon_1^2 = 0, \quad (10.85)$$

$$k_0^2 = \frac{\epsilon_b\left(k^2 + |\mathbf{k}-\mathbf{g}|^2\right) \pm \sqrt{\epsilon_b^2\left(k^2 - |\mathbf{k}-\mathbf{g}|^2\right)^2 + \epsilon_1^2 k^2 |\mathbf{k}-\mathbf{g}|^2}}{2\left(\epsilon_b^2 - \epsilon_1^2\right)}. \quad (10.86)$$

In particular, when $|\mathbf{k}-\mathbf{g}|^2 = k^2$, i.e. the projection of $\mathbf{k}$ on $\mathbf{g}$ is $g/2$, the two values are $\omega^2 = c^2k^2\epsilon_b^{-1}(1 \pm \epsilon_1/\epsilon_b)$. The form of the two solutions for $\omega(k)$ along the axis $\mathbf{k} \parallel \mathbf{g}$ is shown in Fig. 10.23. What is important is to see that there is a band gap, of width proportional to ϵ_1, within which region no travelling wave can propagate inside the medium. As we saw in §10.3.4, the propagation in the gap is evanescent (§5.5.2). In fact, the complete solution for all $\mathbf{k}$ can be represented within the region $|\mathbf{k}\cdot\mathbf{g}| < g^2/2$, which is called the

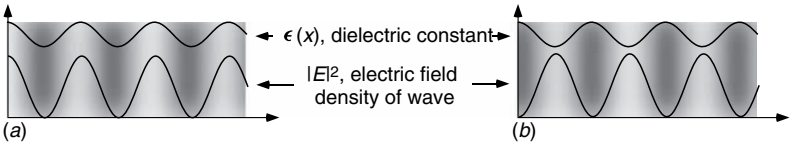

Figure 10.24 **The wave energy density $|E|^2$ related to the dielectric constant variations for the two standing waves with k at the zone edge. The wave on the left has its maximum field in the regions of highest ϵ and thus has lower frequency than the wave on the right, where the maximum field samples regions of lowest ϵ.**

'Brillouin zone', and lies between two planes normal to the vectors $\mathbf{k} = \pm\mathbf{g}/2$. It corresponds to the unit cell of the reciprocal lattice (§4.8) of the periodic structure. The upper branch has generally b large and a small, and the lower branch the opposite. But on the zone boundaries, where $\mathbf{k} \cdot \hat{\mathbf{g}} = \pm g/2$, the two solutions correspond to $a = \pm b$. Then the physical explanation for the splitting is clear: the two solutions are standing waves, and one solution has its maximum fields in the higher ϵ region, with consequently lower frequency, and the other has its maximum fields in the lower ϵ region, and higher frequency (Fig. 10.24).

So far, we have learnt nothing new, but have an analytical approach to the multilayer problem. Admittedly, the solution is only approximate; the assumed solution (10.78) is not exact, but is a good approximation provided that $\epsilon_1 \ll \epsilon_b$.[5]

The reason for doing the calculation this way is that it shows how the solution can be visualized if we know the free-space wave-vector $\mathbf{k}$ and the lattice vector $\mathbf{g}$. We can now see how a more complex material behaves. Supposing the dielectric constant has a two- or three-dimensional periodic structure which can be represented by superposition of several periodic functions with wave-vectors $\mathbf{g}_m$ and amplitude ϵ_m. Then the basic solution to the problem will be a superposition of waves with vectors $\mathbf{k} \pm \mathbf{g}_m$, and band gaps at the appropriate boundaries of the Brillouin zones normal to $\pm\mathbf{g}_m/2$. In two dimensions, for example, we can derive the dispersion relation $\omega(\mathbf{k})$ for a dielectric constant periodic in both x and y on a square lattice: $\epsilon(x, y) = \epsilon_b + 2\epsilon_1[\cos(gx) + \cos(gy)]$. The problem then reduces to a 3×3 secular determinant (10.84) and a surface representing $\omega(k)$ would then look like the illustration in Fig. 10.25. It is interesting to notice that there is no band gap at the corner of the Brillouin zone; a band gap there would indicate an additional periodic potential of the form $\cos[g(x + y)]$.

Another way of representing the result is to draw the surface representing the value of k as a function of its direction for a constant wave frequency $\omega = ck_0$, i.e. the refractive-index surface (Chapter 6), since $k = n\omega/c$.[6] In

[5] The exact solution is the series $\sum a_m \exp(\mathrm{i}k_1 + mg)$. See, for example, Kittel (2005).
[6] This is analogous to the Fermi surface in a metal.

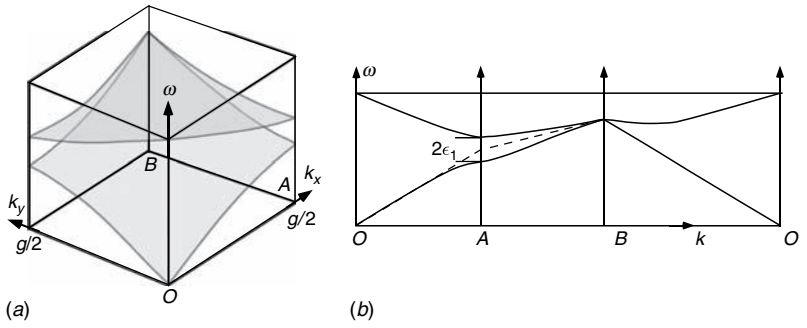

Figure 10.25 (*a*) A sketch of $\omega(\mathbf{k})$ for a two-dimensional periodic dielectric constant $\epsilon(x, y) = \epsilon_b + 2\epsilon_1[\cos(gx) + \cos(gy)]$. The shaded curves show contours of constant ω on the lower branch. (*b*) The values of $\omega(\mathbf{k})$ along three sections of (*a*). The broken lines in (*b*) show the result for a homogeneous medium, where $\omega = c|k|/\sqrt{\epsilon_b}$. Notice that the band gap is zero at the diagonal corner *B*.

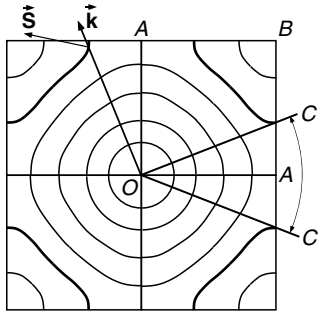

Figure 10.26 Contours of constant ω corresponding to the lower band in Fig. 10.25. These contours are, in a three-dimensional photonic crystal, the index surfaces of Chapter 6. At the frequency of the contour emphasized, at the point shown near the zone edge, the wave-vector **k** and Poynting vector **S** are not in the same direction; also, at that frequency, waves with directions in the sector *CC*, for example, do not propagate in this band.

the two-dimensional crystal the surface becomes a curve which is one of the contours indicated in Fig. 10.25(*a*) and shown in Fig. 10.26. This representation teaches us how waves propagate in a photonic crystal. In a photonic crystal the symmetry of the index surface follows that of the reciprocal lattice, rather than that of the dielectric tensor (Problem 10.9). Clearly, following the methods described in §6.3.2, we find that there are directions near the zone boundaries, i.e. when the wavelength of the light in the crystal is near to half the lattice spacing, the ray-vector **S** can have a different direction from the wave-vector **k**, and in certain directions no wave can propagate. In addition, one should note that when this idea is applied to the upper band in Fig. 10.25, the direction of **S** is opposite to that of **k**; this means that the crystal behaves as a left-handed or negative refractive index material (§5.10).

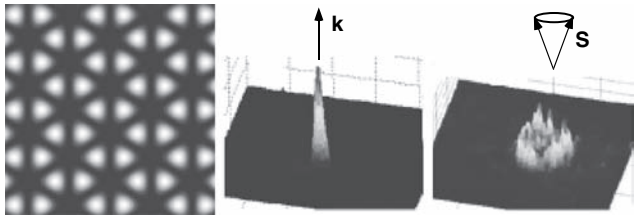

Figure 10.27 **Conical refraction by a honeycomb-lattice photonic crystal induced in a photo-refractive crystal. (*a*) The illumination pattern, formed by interference of three waves at 120°; (*b*) the input beam (crystal switched off); (*c*) the conical diffraction ring exiting the honeycomb lattice.**

Box 10.2 Photonic crystals written into a non-linear medium

A beautiful and fundamental investigation which brings together topics from several chapters of this book uses a technique in which photonic crystals are created in a photo-refractive crystal (§13.6.2) by illuminating it with a light intensity pattern with the required periodicity. In such crystals, the non-linear properties result in a refractive index variation controlled by the illumination pattern. A weak probe beam with a wavelength longer than that of the control illumination can then be used to investigate the optical properties of the photonic crystal without destroying or modifying it. The crystal that has been used (Peleg *et al.* (2007)) is SBN ($Sr_{0.75}Ba_{0.25}Nb_2O_6$), with $\epsilon_b = 5.5$, and changes $\epsilon_1/\epsilon_b \approx 10^{-3}$.

In one of these experiments a photonic crystal with a two-dimensional honeycomb-like lattice was written into the substrate material by using the interference pattern between three waves at angles of 120°, creating a photonic crystal with six-fold symmetry (Fig. 10.27(*a*)). The forbidden band for this structure (the 'graphene' structure) behaves in the same way as the model photonic crystal described in §10.5 except that the structure is hexagonal and there are six points at which the band gap is zero. The optical behaviour of the crystal around these orientations is analogous to that around the optic axis of a biaxial crystal (§6.5) where the inner and outer branches of the refractive-index surface touch at a singular point. Now we saw in §6.5.6 that one of the results of the point-like singularity is the phenomenon of **conical refraction**. In these experiments, it was indeed observed that when the photonic crystal was 'switched on', a conical distribution of output energy was observed when light was incident along the optic axis (Fig. 10.27(*b*) and (*c*)).

Chapter summary

This chapter discussed the propagation of optical waves in materials whose dielectric constant or refractive index is real but varies with position. Such problems, when formulated in terms of Maxwell's equations, were shown to be analogous to problems in quantum mechanics, where the negative of the refractive index plays the part of the potential in Schrödinger's equation. The wave propagation was then found to be defined by specific modes, which are the analogies of quantum stationary states.

- In an optical waveguide the wave propagates in the z-direction, guided by a local maximum in the refractive index. An example that has found widespread applications is the optical fibre. Various propagation modes were found, depending on the exact form of the index maximum; an important case was 'single-mode' propagation, which has many applications in optical communication.
- We developed the general theory of propagation in dielectric multilayers, using Maxwell's equations, which can be applied to a wide variety of problems, several of which were discussed in detail. In addition to solutions analogous to those of quantum mechanics, a new feature appears that is not present in Schrödinger's equation, the dependence on polarization; this allows polarization-sensitive structures to be devised.
- When the refractive index variation has periodic structure, solutions analogous to electron waves in crystals appear, indicating band-gap structure. In a one-dimensional periodic structure of dielectric multilayers, certain wavelengths cannot propagate, providing an almost perfect mirror. Defects in such periodic structures, such as a single additional layer that breaks the symmetry, allow filters with designated properties to be invented.
- Following the above discussion, we extended the treatment to two- and three-dimensionally periodic structures. The concept of a universally reflecting multilayer, similar in concept to an insulator in band-structure theory, was developed, and allowed efficient optical fibres to be designed.
- We developed an approximate method, based on the 'nearly-free electron' model in the band theory of metals, to understand some of the basic properties of multi-dimensional photonic crystals.

Problems

10.1. Incoherent light is to be focused onto the plane end of a multi-mode fibre, with core refractive index n_2 and cladding n_1. What is the largest useful numerical aperture (NA) of the focusing optics? Can this be increased by making the end of the fibre non-planar?

10.2. Show that the brightness (Problem 6.10) of light entering an optical fibre cannot be increased by tapering the input end, so as to collect light over a larger area and concentrate it (optical funnel).

10.3. Show that the numbers of $\perp$ and $\parallel$ modes in a slab waveguide are equal. If the cladding has higher losses than the core, which type of mode travels further?

10.4. An asymmetrical slab waveguide of thickness a and refractive index n_2 is made on a substrate of index n_0 and is covered with cladding of index n_1. What is the smallest value of a/λ for which a single mode propagates, assuming that $n_2 - n_1 \ll n_2 - n_0$?

10.5. An interference filter has transmission wavelength λ and bandwidth $\delta\lambda$ when light is incident normally on it. How do λ and $\delta\lambda$ change as the filter is tilted with respect to the incident light? Take into account the effect of polarization.

10.6. Design a multilayer cube beamsplitter operating at oblique incidence, which transmits one polarization completely and reflects 99% of the other.

10.7. Using physical ideas only, explain why the multilayer mirror system 'glass $(\mathrm{HL})^{q+1}$ air' has a lower reflection coefficient than 'glass $(\mathrm{HL})^{q}\mathrm{H}$ air', despite the latter having one layer less. The symmetrical arrangement $(\mathrm{HL})^{q}\mathrm{H}$ is called a **quarter-wave stack** and is widely used in filter design.

10.8. Write a computer program to study multilayer systems built from two materials H and L on a substrate. Use it to calculate $\mathcal{R}(g)$ and $\mathcal{T}(g)$, $\in$ $0 < g < 2\pi$. Investigate the following ideas with it:
(a) broad-band, sharp-edged filters using the idea of coupled potential wells – 'glass $(\mathrm{HL})^{q}\mathrm{H}(\mathrm{HL})^{p}\mathrm{H}(\mathrm{HL})^{q}$ air', where p is small;
(b) high- and low-pass filters based on a multilayer mirror in which the layer thickness changes monotonically through the stack.

10.9. The refractive index surface of a regular crystal (Fig. 6.14) has to be orthorhombic, which is the symmetry of the dielectric tensor, independent of the crystal symmetry. Why can that of a photonic crystal be different?

References

Abouraddy, A. F., Bayinder, M., Benoit, G. *et al*. (2007), Towards multimaterial multifunctional fibres that see, hear, sense and communicate, *Nature Materials* **6**, 336.

Agrawal, G. P. (2002), *Fiber-optic Communication Systems*, 3rd edn., New York: Wiley-Interscience.

Agrawal, G. P. (2007), *Non-linear Fiber Optics*, 2nd edn., Amsterdam: Elsevier.

Al-Azzawi, A. (2007), *Fibre-optics: Principles and Practices*, Boca Raton, FL: CRC/Taylor and Francis.

Biró, L. P., Kertész, K., Vértesy, Z. *et al.* (2007), Living photonic crystals: butterfly scales, nanostructure and optical properties, *Mater. Sci. Eng. C* **27**, 941.

Cohen-Tannoudji, C., Diu, B. and Laloe, F. (1977), *Quantum Mechanics*, New York: Wiley-Interscience.

Fink, Y., Winn, J. N., Fan, S. *et al*. (1998), A dielectric omnidirectional reflector, *Science* **282**, 1679.

Ghatak, A. and Thyagarajan, K. (1980), Graded index optical waveguides, in *Progress in Optics*, XVIII, 1, Amsterdam: North-Holland.

Gloge, D. (1979), The optical fibre as a transmission medium, *Rep. Prog. Phys*., **42**, 1777.

Joannopoulos, J. D., Meade, R. D. and Winn, J. N. (2008), *Photonic Crystals: Molding the Flow of Light*, 2nd edn., Princeton: Princeton University Press.

Kittel, C. (2005), *Introduction to Solid State Physics*, 8th edn., Hoboken, NJ: Wiley.

Macleod, H. A. (2001), *Thin Film Optical Filters*, 3rd edn., Bristol: Institute of Physics Publishing.

Peleg, O., Bartal, G., Freedman, B. *et al*. (2007), Conical diffraction and gap solitons in honeycomb photonic lattices, *Phys. Rev. Lett*. **98**, 103901.

Saleh, B. E. A. and Teich, M. C. (1991). *Fundamentals of Photonics*, New York: Wiley-Interscience.

Yablonovitch, E. (1993), Photonic band-gap structures, *J. Opt. Soc. Am*. **B10**, 283.

Zi, J., Yu, X., Li, Y. *et al*. (2003), Coloration strategies in peacock feathers, *PNAS* **100**, 12576.

11 Coherence

The coherence of a wave describes the accuracy with which it can be represented by a pure sine wave. So far we have discussed optical effects in terms of **coherent** waves whose wave-vector **k** and frequency ω are known exactly; in this chapter we intend to investigate the way in which uncertainties and small fluctuations in **k** and ω can affect the observations in optical experiments. Waves that appear to be pure sine waves only if they are observed in a limited space or for a limited period of time are called **partially coherent** waves, and we shall see in this chapter how we can measure deviations of such waves from their pure counterparts, and what these measurements tell us about the source of the waves.

The classical measure of coherence was formulated by Zernike in 1938 but had its roots in much earlier work by Fizeau and Michelson in the late nineteenth century. Both of these scientists realized that the contrast of interference fringes between waves travelling by two different paths from a source to an observer would be affected by the size, shape and spectrum of the source. Fizeau suggested, and Michelson carried out,[1] experiments which showed that the angular diameter of a star could indeed be measured by observing the degradation of the contrast of interference fringes seen when using the star as a source of light (§11.8.1). Michelson also used interference to measure the spectral quality of a light source (§11.5), and both of these accomplishments are described in his book *Studies in Optics* (Michelson (1927)). But this work was done without a formal theoretical basis, which was later provided for classical light sources by Zernike in 1938 and extended to quantized systems by Glauber in 1963. Once the formal basis of coherence theory was understood and tested, it was possible to use it to make detailed measurements of optical sources. This was first done in radio astronomy by Ryle, who in 1958 developed 'aperture synthesis' (§11.8) as a method of mapping radio stars, and in recent years the same methods have been realized in optical astronomy, so that it is now possible not only to measure angular diameters but also to image actual features on stellar surfaces. An aerial photograph of a modern optical aperture synthesis array observatory is shown in Fig. 11.1. This observatory can produce stellar images with resolution equivalent to that of a

[1] Michelson makes no reference to Fizeau's work, and probably developed the idea independently.

Figure 11.1
Aerial photograph of the Navy Prototype Optical Interferometer (NPOI), at the Lowell Observatory, Flagstaff, AZ. (Courtesy of M. Collier)

telescope having an aperture diameter equal to that of the maximum extent of the array, which is about 450 m.

In this chapter we shall learn:

- about amplitude and phase fluctuations in real light waves;
- the concept of coherence, and how it is expressed quantitatively as a complex coherence function;
- how the coherence function can be measured;
- about temporal coherence, and how it is related to the spectral linewidth of the source by the Wiener–Khinchin theorem;
- about Fourier transform spectroscopy, which is a practical application of temporal coherence measurements;
- about spatial coherence, and how it is related to the source geometry by the van Cittert–Zernike theorem;
- how spatial coherence measurements made with large telescope arrays are being used to make detailed images of distant stellar objects.

11.1 Coherence of waves in space and time

The coherence properties of the waves are in general functions of both time and space. However, in order to make the concepts clear we shall consider them as functions of time and spatial dimensions independently. In a very schematic manner, Fig. 11.2 compares a completely coherent wave with one that is partially coherent in time (it appears to be a perfect sine wave only when

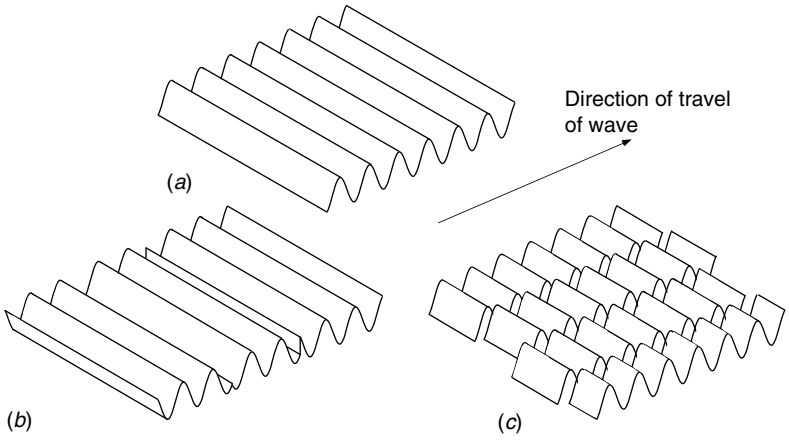

Figure 11.2
Schematic partially coherent waves: (*a*) perfectly coherent wave; (*b*) wave with spatial coherence only; (*c*) wave with temporal coherence only.

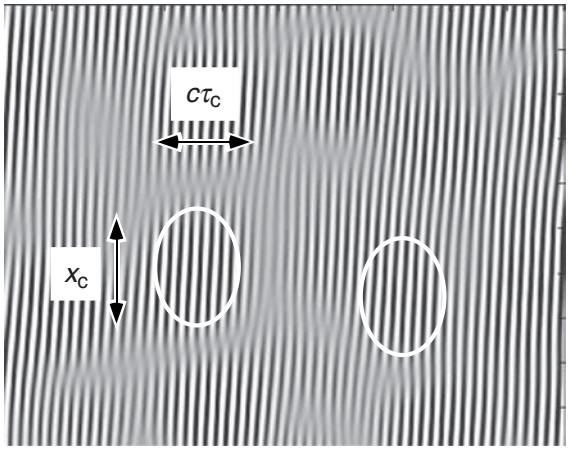

Figure 11.3
Simulation of a plane wave that is partially coherent in both position and time, showing the coherence distance x_c and the coherence time τ_c. Coherence regions, within which on average the wave looks like a plane wave, are indicated by ellipses.

observed for a limited time – called the **coherence time** τ_c) and another that is partially coherent in space (it appears to be a sinusoidal plane wave only if observed over a limited region of its wavefront – the **coherence distance**, x_c). Figure 11.3 shows a simulation of a wave with partial coherence in both temporal and spatial domains, and how this leads to a **coherence region** or volume in three dimensions, within which the wave cannot be distinguished from a simple plane wave. The simulation was carried out by the method described in §11.1.1.

In this chapter we shall study fluctuations in phase and intensity of real light waves only at a classical level. However, some of the most exciting areas of modern optics have grown out of the application of coherence theory to quantum systems and lasers, and in Chapter 14 we shall see how this leads to new results, some of which are inconsistent with the classical description.

11.1.1 Properties of real light waves

Let us try to describe clearly what we know about a real light wave, emitted by a classical monochromatic light source. We know that the light we see at any moment comes from a large number of atoms, each making a transition between the same pair of energy levels, but that the emission from any one atom is no way related to that from any other atom. In fact, a careful spectroscopic analysis shows us that the light is not really monochromatic in the strict sense of the word; it contains components of various wavelengths within a certain range, called the **linewidth**. Typically, the ratio of linewidth to wavelength might be 10^{-6}, and when the linewidth is much less than the average wavelength one uses the term **quasi-monochromatic** for such radiation. The physical reasons for a non-zero linewidth will be discussed in more detail in §11.2, but just as an example we remark that at a finite temperature all the atoms in the emitting material (a gas, for example) are moving randomly in various directions, and so the emission from each atom is Doppler shifted by a different amount.

In a laser, which is a non-classical source, emission from the various atoms is strongly related, and the discussion in this section is not accurate.

We now ask exactly what such a light wave looks like. We can answer the question by performing a Fourier synthesis based on the remarks in the previous paragraph. We take a number of sine waves, having frequencies randomly chosen within a specified range representing the linewidth of the radiation, and add them together. We have done this in Fig. 11.4, where three examples of continuous waves have each been generated from about 20 sine waves with frequencies randomly chosen within a specified interval. What we see is a complicated beat phenomenon; the amplitude of the wave is not a constant, but fluctuates in a rather haphazard fashion. The average length of a beat is related to the range of frequencies involved. If there is no rational relationship between the frequencies themselves, the waveform never repeats itself and is an example of **chaotic light**, §14.2.3. In the figure, we have also indicated the phase of the wave relative to a coherent wave at the mid-frequency. One observes that the phase is more-or-less constant within each group, but jumps – often sharply – in the regions between wave-groups, particularly where the amplitude is small.

Real light waves have intrinsic intensity and phase fluctuations, usually on a time-scale of nanoseconds to picoseconds.

The wave-trains in Fig. 11.4 can also be looked at in a different way. We can consider each beat as an independent wave-group; the complete wave-train is then a series of such wave-groups emitted at random intervals. This description turns out to be convenient for some purposes. However, we must emphasize that the individual wave-groups must *not* be interpreted as photons, quantum units of light energy. Apart from the fact that the model has been created by completely classical thinking, and therefore cannot produce a quantized particle, the rate of repetition of the wave-group is determined entirely by the spread of frequencies. If the wave-groups were photons, their average rate of occurrence would depend on the *intensity* of the wave, and not the linewidth.

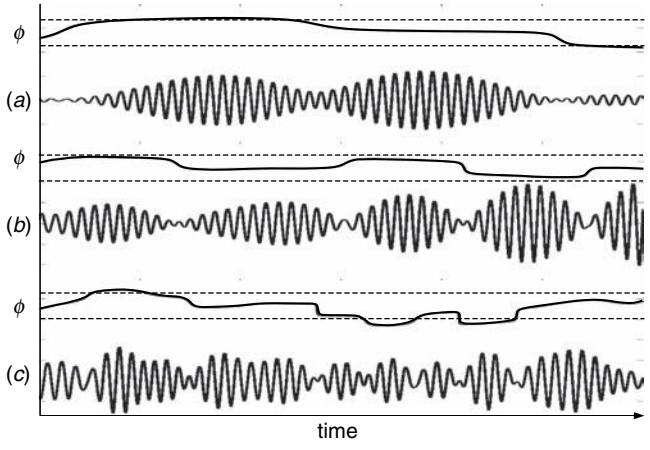

Figure 11.4 Three impure sine waves, showing the amplitude and phase fluctuations resulting from a spread in component frequencies. Each wave is generated from 20 components with frequencies randomly distributed in the range $\pm\frac{1}{2}\epsilon$ about ω_0. The phase fluctuations are shown relative to a perfect wave at ω_0, and 2π phase jumps have been eliminated ('unwrapped'). The horizontal broken lines are separated by 2π. Notice that within each wave-group the phase is fairly constant, but changes randomly from group to group; the phase changes occur where the wave amplitude is small. The values of ω_0/ϵ are as follows: (*a*) 24, (*b*) 12, (*c*) 6.

11.1.2 The amplitude and phase of quasi-monochromatic light

Let us try to develop the ideas of the previous section a little further with the help of a simple model. It is important at this stage to recall the definition of an average or mean value of a function $g(t)$ during an interval of duration T lasting from $-T/2$ to $T/2$:

$$\langle g\rangle_T = \frac{1}{T}\int_{-T/2}^{T/2} g(t)\,\mathrm{d}t. \tag{11.1}$$

For mathematical convenience we shall work with the complex wave-field $f = f^{\mathrm{R}} + \mathrm{i}f^{\mathrm{I}}$; one should remember, however, that observable physical fields are real and are given by f^{R}. However, in optics we can only measure the intensity $I(t) \equiv |f(t)|^2$; for a pure sine wave, which is described by the complex function $f(t) = a\exp(\mathrm{i}\,\omega t)$, the intensity is constant.

We assume all the component waves to have the same amplitude; this makes the mathematics easier, without affecting the physics.

Now picture a quasi-monochromatic light beam that is represented at a given point in space by the superposition of a large number N of waves with equal amplitude a. Each one has a random phase ϕ_n and a frequency ω_n randomly chosen within the range $\omega_0 \pm \epsilon/2$ where $\epsilon \ll \omega_0$ (Fig. 11.4). The amplitude and intensity of the combined wave are

$$f(t) = a\sum_{n=1}^{N} \exp[\mathrm{i}(\omega_n t + \phi_n)], \tag{11.2}$$

$$I(t) = |f(t)|^2 = a^2 \left|\sum_{n=1}^{N} \exp[\mathrm{i}(\omega_n t + \phi_n)]\right|^2, \tag{11.3}$$

which can be written as a double sum

$$I(t) = a^2 \sum_n \sum_m \exp\{\mathrm{i}[(\omega_n - \omega_m)t + \phi_n - \phi_m]\}. \tag{11.4}$$

The most noticeable features of the waves of Fig. 11.4, which are simulations of (11.2) are the fluctuations in intensity (11.4) on a time-scale of $2\pi/\epsilon$. However, since the simulations were performed with a finite number N of waves, we have to be sure that the fluctuations are not smoothed out by making N very large. We can do this by calculating the **variance** in the intensity. If you sample a variable x statistically, the variance describes how far away from its mean a particular sample is likely to be. This is quantified by the mean square deviation $\Delta x^2 \equiv \langle (x - \langle x\rangle)^2\rangle$, which is easily shown[2] to be equal to $\langle x^2\rangle - \langle x\rangle^2$. The square root of the variance shows the range within which x varies about its mean value. We can apply this to the intensity as described by (11.4).

First, the long-term average of (11.4) is the mean intensity $\langle I\rangle$. This is given by

$$\langle I(t)\rangle_T = \frac{a^2}{T}\int_{-T/2}^{T/2} \sum_n \sum_m \exp\{\mathrm{i}[(\omega_n - \omega_m)t + \phi_n - \phi_m]\}\,\mathrm{d}t. \tag{11.5}$$

When T is very large, the terms $\exp[\mathrm{i}(\omega_n - \omega_m)t]$ perform many oscillations within the integral and average to zero. But if $n = m$, this exponent is $\mathrm{e}^{\mathrm{i}0} = 1$ and the integral is equal to T. Thus, only the N terms for which $n = m$ contribute to the mean intensity, giving

$$\langle I\rangle_T = \frac{a^2}{T}\int_{-T/2}^{T/2} \sum_{n=1}^{N} 1\,\mathrm{d}t = a^2 N. \tag{11.6}$$

This confirms intuitive expectations that **for an incoherent wave, the total intensity is the sum of the intensities of the individual components**. The term $\langle I^2\rangle$ can be calculated similarly. Now there is a quadruple summation, but we deal with it similarly:

$$\langle I^2\rangle = \frac{a^4}{T}\int_{-T/2}^{T/2} \sum_n \sum_m \sum_p \sum_q \exp\{\mathrm{i}[(\omega_n - \omega_m + \omega_p - \omega_q)t + \phi_n - \phi_m + \phi_p - \phi_q]\}\,\mathrm{d}t. \tag{11.7}$$

[2] See any elementary book on statistics.

This time, the terms that do not average to zero are the N^2 terms for which $n = m$ and $p = q$, but *also* another N^2 for which $n = q$ and $m = p$. Thus

$$\langle I^2 \rangle_T = 2a^4 N^2, \tag{11.8}$$

from which the variance is

$$\Delta I^2 \equiv \langle I^2 \rangle_T - \langle I \rangle_T^2 = a^4 N^2. \tag{11.9}$$

This important result says that **the magnitude of the fluctuations in intensity ΔI of a quasi-monochromatic wave is equal to its mean intensity**. The fluctuations are *macroscopic* and result in an intensity that, when looked at on a short enough time-scale of order $1/\epsilon$, fluctuates essentially between 0 and twice the mean intensity, as we saw in the simulations.

Calculation of many other statistical properties of quasi-monochromatic waves can be based on this model. It particular, it can be used to show, as illustrated by the simulation, that there is no correlation between the phases measured at times separated by much more than $2\pi/\epsilon$. This will be seen to be the **coherence time** of the wave.

11.1.3 The spectrum of a random series of wave-groups

We remarked that the beat patterns in Fig. 11.4 can also be described visually as a random succession of wave-groups of duration $2\pi/\epsilon$. Such a series does indeed have similar spectral characteristics. Consider for example a wave-group defined by the Gaussian of §4.4.3:

$$f(t) = A \exp(-\mathrm{i}\omega_0 t) \exp(-t^2/2\sigma^2), \tag{11.10}$$

whose Fourier transform is

$$F(\omega) = 2\pi A (2\pi\sigma^2)^{\frac{1}{2}} \exp[-(\omega - \omega_0)^2 \sigma^2/2]. \tag{11.11}$$

A random series of such groups is

$$f_{\mathrm{r}}(t) = \sum_{n=1}^{N} f(t - t_n), \tag{11.12}$$

where t_n is the random centre point of the nth wave-group. Now the transform of (11.12) is

$$F_{\mathrm{r}}(\omega) = F(\omega) \sum_n \exp(-\mathrm{i}\omega t_n), \tag{11.13}$$

$$|F_{\mathrm{r}}(\omega)|^2 = |F(\omega)|^2 \sum_{n,m=1}^{N} \exp[-\mathrm{i}\omega(t_m - t_n)] = N|F(\omega)|^2 \tag{11.14}$$

by the same reasoning as (11.6). $|F_r(\omega)|^2 \equiv J(\omega)$ is called the **spectral intensity** or **power spectrum**. The phase of $F_r(\omega)$ is indeterminate, so we can conclude that the spectral intensity is like that of the single wave-group (11.10), but has random phase. The series of wave-groups reproduces exactly the spectrum of Fig. 11.4 and is therefore a good physical representation of the wave. One should compare this result to that obtained in §8.5.7 for the Fraunhofer diffraction pattern of a random array of identical apertures.

11.2 Physical origin of linewidths

So far we have introduced the width of a spectral line, or the finiteness of a wave-train, simply as a parameter to be reckoned with; now we shall enquire briefly into the physical causes of line broadening in gases, where the emitting atoms or molecules are almost independent. In this discussion, the word 'molecule' can be exchanged for 'atom' in all cases.

White light is a limiting case. When the bandwidth becomes very large, the wave-groups become δ-functions, and white light can be considered as a series of such δ-functions occurring at random intervals.

11.2.1 Natural linewidth

A spectral line has its origin in a quantum transition in which a molecule changes its state from level A to level B, with energies E_A and E_B respectively; a wave of frequency $\omega_0 = (E_A - E_B)/\hbar$ is emitted at the same time (§14.4.2). However, no energy level except the ground state is an exact stationary state because of fluctuations of the environmental electromagnetic field (§14.2.3), and therefore has a finite lifetime. As a result a molecule in level A will decay to a lower level after an average time T_A. According to the uncertainty principle, the value of E_A is therefore uncertain to the extent $\delta E \approx h/T_A$, where h is Planck's constant. The corresponding frequency width of the emitted wave is $\delta\omega = 2\pi\left(T_A^{-1} + T_B^{-1}\right)$. This is called the **natural linewidth**; it is generally smaller than the Doppler and collision linewidths discussed in the following sections, but can be achieved experimentally under conditions where the environmental effects are neutralized (Haroche and Kleppner (1989); Foot (1991)).

11.2.2 Doppler broadening

Let us consider radiation from an isolated molecule in a gas at temperature T. If the molecule, mass m, has velocity v_x along the line of sight while the transition is taking place, the spectral line will appear shifted by the Doppler effect. The Maxwell distribution of velocities along a particular axis (x) in a

perfect gas is Gaussian:

$$f(v_x)\mathrm{d}v_x = C\exp\left(\frac{-mv_x^2}{2k_\mathrm{B}T}\right)\mathrm{d}v_x, \tag{11.15}$$

and the Doppler shift in the observed frequency is

$$\omega - \omega_0 = \omega_0 v_x/c, \tag{11.16}$$

so that

$$F(\omega) = C\exp\left[\frac{-m(\omega-\omega_0)^2c^2}{2\omega_0^2 k_\mathrm{B}T}\right]. \tag{11.17}$$

This effect has broadened an ideally sharp spectral line into a line with a Gaussian profile (see §4.4.3), where

$$\sigma = \omega_0(k_\mathrm{B}T/mc^2)^{\frac{1}{2}}. \tag{11.18}$$

It is common to express spectral linewidths in terms of the **half-width** (§4.4.3) which is 2.36σ for a Gaussian. In terms of wavelength, rather than frequency, we find the half-width to be $2.36\lambda_0(k_\mathrm{B}T/mc^2)^{\frac{1}{2}}$.

As an example, we can take the Kr^{84} line for which $\lambda_0 = 5600$ Å, $m = 1.4\times 10^{-22}$ g. At $T = 80$ K, (11.18) gives a half-width of 1.6×10^{-11} m ≈ 0.002 Å, which agrees reasonably with the observed value of 0.003 Å.

11.2.3 Pressure or collision broadening

Considering an isolated molecule does not give us the whole story. There will always be collisions between the various molecules in a real gas. According to the kinetic theory of gases (see, for example, Jeans (1982)), a particular molecule will expect to be free for an average time

$$\tau_1 \propto T^{\frac{1}{2}}P^{-1} \tag{11.19}$$

between collisions, where T is the absolute temperature and P is the gas pressure.

Now consider what happens if an emitting molecule suffers a collision. We may suppose that the shock of the collision will at the very least destroy phase correlation between the emitted waves before and after the collision. The emission from all the molecules in the gas will therefore appear like a series of uncorrelated bursts of radiation each of average duration τ_1. From the model of §11.1.3, this suggests that τ_1 plays the role of the coherence time. The actual durations can be assumed to have a Poisson distribution of mean value τ_1, from which it can easily be shown that the spectral intensity $J(\omega)$ has a Lorentzian form with shape

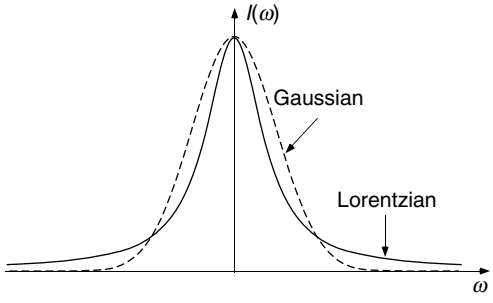

Figure 11.5
Comparison between Lorentzian and Gaussian functions. The Lorentzian has much longer 'tails' than the Gaussian.

$$J(\omega) = \frac{1}{1 + (\omega - \omega_0)^2 \tau_1^2}. \tag{11.20}$$

We have already met this function in our discussion of multiple-reflection fringes (§9.5). From Fig. 11.5 we see that it is superficially similar to the Gaussian but has a much slower decay in its wings.

In practice, temperature and pressure in a gas cause both Doppler and collision broadening in various degrees, and observed spectral lines are rarely exactly Gaussian or exactly Lorentzian. Moreover, many spectral lines are multiplets with complicated fine structure, but from the point of view of optical coherence theory they can often just be considered as having a single empirical width, just like the **effective width** of a function defined in §8.3.5. In condensed matter, linewidths are further complicated by interactions between neighbouring molecules.

11.3 Quantification of the concept of coherence

The coherence function describes the correlation between a wave-field at two different points in space or time.

In the previous sections we have described some of the characteristics of real light waves. In order to understand how they affect optical experiments, it is necessary to develop a quantitative framework to describe their properties statistically. The coherence function γ which will be defined in this section is a measure of coherence between two values of a wave-field, $f(\mathbf{r}_1, t_1)$ and $f(\mathbf{r}_2, t_2)$. **Coherence means that, given $f(\mathbf{r}_1, t_1)$, a recipe exists to estimate the amplitude and phase of $f(\mathbf{r}_2, t_2)$.** The better this recipe works on the average the better the coherence, and the closer the function γ is to unity. An example of a recipe applying to a plane wave would be: 'propagate the wave by multiplying its complex amplitude by $\exp[\mathrm{i}(\omega(t_2 - t_1) - \mathbf{k} \cdot (\mathbf{r_2} - \mathbf{r_1}))]$'. We shall find it simplest to talk about the two limiting cases mentioned in the introduction.

- **Temporal coherence**, which measures the coherence between $f(\mathbf{r}, t_1)$ and $f(\mathbf{r}, t_2)$, i.e. between two values of the wave-field at the same point $\mathbf{r}$ but different times. Temporal coherence allows us to define a **coherence time** τ_c, the

maximum $t_2 - t_1$ for which the recipe works well. As we have seen in §11.1.2, τ_c is intimately connected with the bandwidth of a quasi-monochromatic wave, and we shall show that the degree of temporal coherence is related quantitatively to the spectrum of the wave-field.

- **Spatial coherence**, which is a measure of the coherence between $f(\mathbf{r}_1, t)$ and $f(\mathbf{r}_2, t)$, i.e. between two values of the wave-field at different points measured at the same time t. In analogy to τ_c one can define a **coherence region** around $\mathbf{r}_1$ for which the recipe is valid. This region need not be circular.

11.3.1 The mutual coherence function

We shall now make these concepts more quantitative by defining a mutual coherence function based on the idea of correlation which was introduced in §4.9. We shall write $t_1 = t$ and $t_2 = t + \tau$ and assume that the coherence properties do not change with time and therefore depend only on the difference $\tau = t_2 - t_1$ (this is called the 'assumption of stationarity'). The **complex degree of mutual coherence**, or briefly **coherence function**, is a normalized correlation function defined as

$$\gamma(\mathbf{r}_1, \mathbf{r}_2, \tau) = \frac{\langle f(\mathbf{r}_1, t) f^*(\mathbf{r}_2, t+\tau)\rangle}{(I_1 I_2)^{\frac{1}{2}}}, \tag{11.21}$$

where the I_j's are the mean intensities at $\mathbf{r}_1$ and $\mathbf{r}_2$:

$$I_j \equiv \langle f(\mathbf{r}_j, t) f^*(\mathbf{r}_j, t)\rangle_t. \tag{11.22}$$

In view of the assumption of stationarity, γ does not depend on t; in the same spirit, we shall assume stationarity in position as well as time, and assume that γ only depends on the vector separation $\mathbf{r} = \mathbf{r_2} - \mathbf{r_1}$. Substituting $\mathbf{r} = 0$ and $\tau = 0$ gives $\gamma(0, 0) = 1$, showing that γ is indeed normalized. To make the physics clear, we shall only study the limiting cases of temporal and spatial coherence defined above.

11.3.2 The visibility of interference fringes and interferometric methods of measuring the coherence function

Figure 11.6 shows a thought-experiment that helps us to clarify the concept of coherence and shows how the coherence function can be measured. It is constructed from two loss-less single-mode optical fibres[3] (§10.2) A_1B_1 and A_2B_2

[3] The need for loss-less propagation is not necessary, but both fibres should attenuate by the same amount. This is certainly the case in stellar interferometers, which are one of the embodiments of the optical stethoscope.

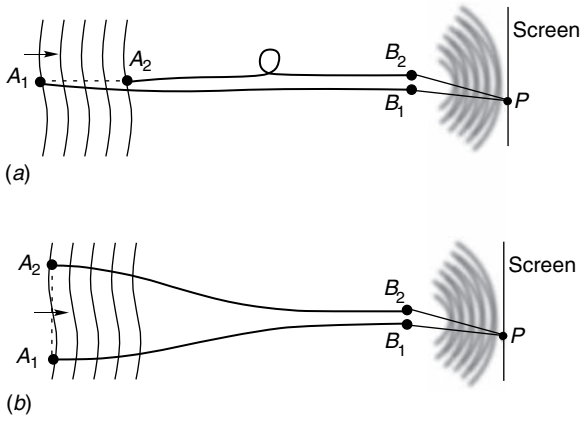

Figure 11.6
The idea of the 'optical stethoscope'. The instrument would measure in (*a*) the temporal coherence and in (*b*) the spatial coherence.

of exactly equal length, whose ends B_1 and B_2 are supported close together, a few wavelengths apart. We might call it an 'optical stethoscope', and it can actually be constructed, although not perhaps in the flexible form envisaged here. In later sections, we shall discuss in detail two implementations: the **Fourier transform spectrometer** (§11.5), which measures the temporal coherence using a Michelson interferometer (§9.3.2), and the **Michelson stellar interferometer**, and its modern derivatives (§11.8.1), which measures the spatial coherence of light waves of cosmic origin.

The fibre ends A_1 and A_2 are placed in the quasi-monochromatic wave field, whose coherence properties we want to analyze, and which originates in a distant source of small angular size. A_1 and A_2 can sample this field at any two points we choose, and because the fibres are loss-less we assume that the light amplitudes emitted at B_1 and B_2 are the same as those sampled at A_1 and A_2, with equal time delays resulting from their equal lengths. B_1 and B_2 radiate as point sources and we observe the interference fringes on a screen a few centimetres away. If B_1 and B_2 radiate coherently, the interference fringes are clear; if B_1 and B_2 are incoherent, there will be no interference fringes. There can also be an intermediate situation, in which poorly visible fringes can be seen; this occurs when B_1 and B_2 are **partially coherent**. Figure 11.6 shows two basic configurations, which will be discussed in detail later. If the two points A_1 and A_2 are situated one behind the other, as in (*a*), in the direction of propagation of the light, they essentially sample the wave at the same place, but at different times separated by $\tau = A_1A_2/c$, and the contrast of the fringes measures the temporal coherence. If the points are side-by-side, in the same wavefront but separated by **r**, as in (*b*), the contrast measures the spatial coherence.

The contrast of interference fringes formed by quasi-monochromatic light can be quantified by defining the **visibility** V:

$$V \equiv \frac{I_{\max} - I_{\min}}{I_{\max} + I_{\min}}, \tag{11.23}$$

where I is the local intensity of the fringe pattern. If the fringes are well-developed, the minima have almost zero intensity compared to the maxima, and so $V \approx 1$. On the other hand, if the fringes are weak, and there is little difference between the minimum and maximum values of intensity, $V \sim 0$. At a general point P on the screen the field is defined as g and the local intensity is $\langle |g^2| \rangle$. Now the field g measured at P is the sum of the fields g_1 radiated by B_1 and g_2 radiated by B_2 at time t. We denote B_1P by x_1 and B_2P by x_2, and their mean by x, whence:

$$g_1(P,t) = \frac{1}{x} f\Big(B_1, t - \frac{x_1}{c}\Big), \tag{11.24}$$

$$g_2(P,t) = \frac{1}{x} f\Big(B_2, t - \frac{x_2}{c}\Big), \tag{11.25}$$

in which the $1/x$ term arises because B_1 and B_2 are point-source-like radiators. It is essentially a constant and will eventually cancel out in this argument. The intensity at P is

$$I(P) = \big\langle (g_1 + g_2)\left(g_1^* + g_2^*\right)\big\rangle = \big\langle g_1 g_1^*\big\rangle + \big\langle g_2 g_2^*\big\rangle + \big\langle g_1 g_2^*\big\rangle + \big\langle g_1^* g_2\big\rangle . \tag{11.26}$$

We shall now show that **if the intensities $\langle |f(B_1)|^2 \rangle$ and $\langle |f(B_2)|^2 \rangle$ are equal, the visibility is a direct measure of the degree of mutual coherence** between A_1 and A_2, i.e. $V = |\gamma_{A_1A_2}(0)|$.[4] We have

$$\begin{aligned} g_1 g_2^* &= \frac{1}{x^2} f\Big(B_1, t - \frac{x_1}{c}\Big) f^*\Big(B_2, t - \frac{x_2}{c}\Big) \\ &= \frac{1}{x^2} f\Big(B_1, t - \frac{x_1}{c}\Big) f^*\Big(B_2, t - \frac{x_1}{c} - \tau_p\Big), \end{aligned} \tag{11.27}$$

where we have defined $\tau_p = (x_2 - x_1)/c$. Since B_1 and B_2 are only a few wavelengths apart, this τ_p is at most a few periods long and therefore much shorter than the coherence time τ_c. We can now use the assumption of stationarity and the fact that during $\tau_p f \sim \mathrm{e}^{\mathrm{i}\omega_0 t}$ to write

$$\big\langle g_1 g_2^*\big\rangle = \frac{1}{x^2} \langle f(B_1, t) f^*(B_2, t)\rangle \exp(-\mathrm{i}\,\omega_0 \tau_p). \tag{11.28}$$

Assume for simplicity that the optical stethoscope is constructed so that the intensities incident on and exiting the two fibres are equal to I. We then have from (11.26)

$$\begin{aligned} I(P) = \frac{1}{x^2} [2I &+ \langle f(A_1) f^*(A_2)\rangle \exp(-\mathrm{i}\,\omega_0 \tau_p) \\ &+ \langle f^*(A_1) f(A_2)\rangle \exp(\mathrm{i}\,\omega_0 \tau_p)]. \end{aligned} \tag{11.29}$$

[4] The notation $\gamma_{A_1A_2}(0)$ is short for $\gamma[\mathbf{r}(A_1), \mathbf{r}(A_2), 0]$. In principle, an optical stethoscope could be made for measuring $\gamma_{A_1A_2}(\tau)$ by using fibres differing in length by $c\tau$.

Since from (11.21) $\langle f(A_1)f^*(A_2)\rangle = I\gamma_{A_1A_2}(0)$, which can be written in the form $I|\gamma_{A_1A_2}(0)|e^{i\Delta}$, we can put (11.29) in the form

$$\begin{aligned} x^2 I(P) &= 2I + 2I|\gamma_{A_1A_2}(0)|\cos(\omega_0\tau_p + \Delta) \\ &= 2I[1 + |\gamma_{A_1A_2}(0)|\cos(\omega_0\tau_p + \Delta)]. \end{aligned} \tag{11.30}$$

From the definition (11.23) it now follows that the visibility of the fringes is

$$V = |\gamma_{A_1A_2}(0)|, \tag{11.31}$$

when the intensities $I_1 = I_2$. The value of Δ in (11.31) can be read from the shift of the fringe pattern from the symmetrical position ($\tau_p = 0$) on the screen. It is a measure of the actual mean phase difference between the wave-fields at A_1 and A_2. The optical stethoscope thus provides us with direct means of measuring the degree of coherence of a wave-field between any two points A_1 and A_2. We now show how it can be used specifically to measure temporal and spatial coherence.

11.4 Temporal coherence

11.4.1 The temporal coherence function

We now return to the situation described in Fig. 11.6(*a*). Since the source is distant, the wavefront changes insignificantly between A_1 and A_2, but the latter sees the wave as it was at A_1 a time τ earlier. It follows that the optical stethoscope measures $\gamma(\tau)$ where $\tau = A_1A_2/c$; in this section we can drop the position variable $\mathbf{r}$ in $\gamma(\mathbf{r}, \tau)$. The visibility of the fringes in the stethoscope is then $V = |\gamma(\tau)|$ where

$$\gamma(\tau) = \frac{\langle f(t)f^*(t+\tau)\rangle}{I} = \frac{\langle f(t)f^*(t+\tau)\rangle}{\langle f(t)f^*(t)\rangle}. \tag{11.32}$$

Now for a pure sine wave we have $f(t) = a\exp(i\,\omega_0 t)$, whence

$$\gamma(\tau) = \exp(-i\,\omega_0\tau). \tag{11.33}$$

It is therefore common to refer to $\gamma(\tau)\exp(+i\,\omega_0\tau)$, whose departure from unity represents the departure of the wave-form from the pure sinusoid, as the **temporal coherence function**. For a quasi-monochromatic source $|\gamma(\tau)|$ has a typical form illustrated in Fig. 11.7. By definition $\gamma(0) = 1$, and as τ increases $|\gamma(\tau)|$ falls monotonically to zero. For any wave with such a $|\gamma(\tau)|$ we can define the coherence time τ_c as the value at which $|\gamma(\tau_c)| = 1/e$; for instance the random collection of Gaussian wave-groups mentioned in §11.1.3 has $\tau_c = \sqrt{2}\sigma$. For quasi-monochromatic light, τ_c is of order of magnitude 10^{-9} s. The form shown in Fig. 11.7 is not typical of laser light (§14.7.1).

A multi-mode laser emits frequencies ω_n that are equally spaced within the linewidth ϵ. As a result, the coherence function has a periodic structure, and is not monotonically decreasing.

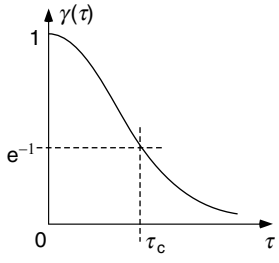

Figure 11.7

Coherence function for a typical quasi-monochromatic source.

11.4.2 Temporal coherence and auto-correlation

The form of $\gamma(\tau)$ in (11.32) is the same as the auto-correlation function discussed in §4.9.1, when we use (11.1) to express the average values by integrals. Since $f(t)$ is real and the average is taken over a long time T, the **Wiener–Khinchin theorem** relates the power spectrum of $f(t)$ to the Fourier transform of $\gamma(\tau)$:

$$|F(\omega)|^2 = I\int_{-\infty}^{\infty}\gamma(\tau)\mathrm{e}^{-\mathrm{i}\omega\tau}\mathrm{d}\tau; \tag{11.34}$$

and

$$|F(-\omega)|^2 = |F(\omega)|^2 \equiv J(\omega). \tag{11.35}$$

Equation (11.34) shows that if $\gamma(\tau)$ can be measured, the **spectral intensity** $J(\omega)$ can be deduced by a Fourier transform; this leads to an important form of spectroscopy, called **Fourier transform spectroscopy**, or **Fourier transform infra-red spectroscopy** (FTIR) because it is mainly used in the infra-red part of the spectrum.

11.5 Fourier transform spectroscopy

In 1898 Michelson showed that a two-beam interferometer could be used for spectral analysis by recording fringes as the path difference is increased, which essentially measures $\gamma(\tau)$. (Remember that the coherence theory being discussed here dates from the 1930s.) In Michelson's time the idea was difficult to implement because of the necessity for a Fourier transform in order to convert the observations into a conventional spectrum, although Michelson made some headway by intuitive methods and even constructed an analogue computer for the purpose of reconstructing spectra. The advent of electronic computers has of course changed the situation. Because of the basic simplicity of construction of a Michelson interferometer and its efficiency in terms of signal-to-noise ratio (§11.5.2) Fourier transform spectroscopy is widely employed in modern physics and chemistry (see, e.g., Bell (1972)). It is mainly used in the infra-red, both because good enough mechanical stability is difficult to achieve for work in the visible, and also because it can make better use of background-limited detectors typical of the IR region. Thus, the abbreviation FTIR (Fourier Transform Infra-Red spectroscopy) is often used for this technique.

As shown in Fig. 11.8, the incident wave $f(t)$ is split into two approximately equal parts, which travel along different paths before recombining with equal amplitudes at the detector. If the two paths have lengths differing by d it is clear that the waves arriving at a given instant at D originated at the source at times separated by $\tau = d/c$. This is essentially the situation described by

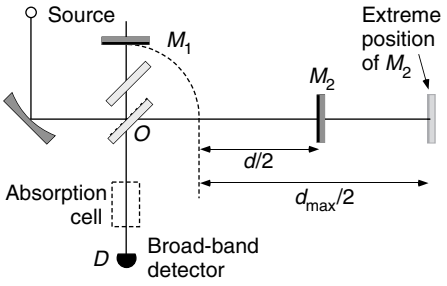

Figure 11.8

A Michelson interferometer (Fig. 9.13) as used for Fourier transform spectroscopy. The path difference is $d = 2(OM_2 - OM_1)$. For studying the absorption spectrum of a sample, it is placed in the position indicated, while the source has a broad emission spectrum; then the result is compared to the spectrum obtained without the absorption cell.

Fig. 11.6(*a*). The instrument is adjusted so that the interference fringes form a circular pattern (like Fig. 9.15(*b*)), at whose centre D the detector is positioned. Ideally, the detector can be as large as the central fringe when d has its maximum value, $d_{\max}$. It measures the intensity of the recombined wave in the A output (§9.3.2):

$$I_{\mathrm{M}}(\tau) = \mathcal{R}T\langle|f(t) - f(t+\tau)|^2\rangle \tag{11.36}$$

$$= \mathcal{R}T\langle I(t)\rangle[2 - \gamma(\tau) - \gamma^*(\tau)]. \tag{11.37}$$

By taking the Fourier transform of this equation, the symmetrized power spectrum $J(\omega) + J(-\omega)$ can be calculated. Clearly, the signal I_{M} is real and symmetrical and so is $J(\omega)$ (11.35); however, the part of the spectrum for $\omega < 0$ has no practical physical significance. Writing the transform out explicitly and replacing τ by d/c we have

$$J(\omega) = \frac{1}{2c}\int_{-d_{\max}}^{d_{\max}} [I - I_{\mathrm{M}}(d/c)/2\mathcal{R}T]\exp[-\mathrm{i}\omega d/c]\,\mathrm{d}d. \tag{11.38}$$

Relying on the symmetry of I_{M}, the interferogram only needs to be measured for one sign of d (with a short excursion into the other to allow the zero of d to be identified exactly). As a result the integral above can be written in terms of wavenumber $k = \omega/c$:

$$J(ck) = \frac{1}{c}\int_{0}^{d_{\max}} [I - I_{\mathrm{M}}(d/c)/2\mathcal{R}T]\cos(kd)\,\mathrm{d}d. \tag{11.39}$$

This equation is the basic algorithm for Fourier transform spectroscopy; the measured data are $I_{\mathrm{M}}(d/c)$ and the derived spectrum is $J(\omega)$.

In (11.38) we have introduced finite limits to the Fourier integral because there are no data for $d > d_{\max}$ and so the best estimate for this region would be $I_{\mathrm{M}} = 2I\mathcal{R}T$. This sharp cut-off to the integral results in a spectrum with limited resolution (§11.5.2). Furthermore, it introduces 'false detail' into the spectrum, in the same way as will be discussed in §12.2.5, and the technique of apodization (Problem 11.6) is often used mathematically to improve the line-shape obtained.

The above treatment can be extended to the case where a material with unknown index of refraction $n(\omega)$ is inserted in one arm of the interferometer.

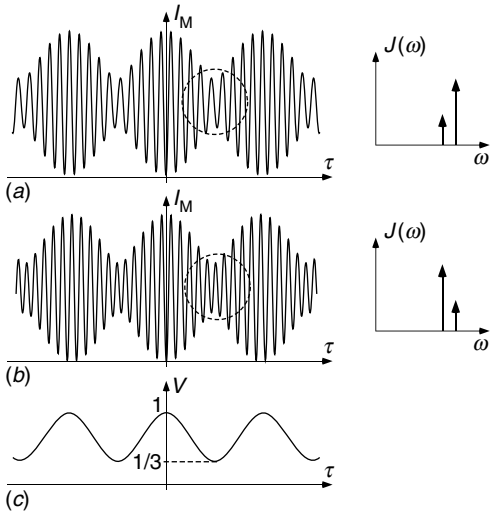

Figure 11.9

The Fourier interferogram $I_M(\tau)$ when the source spectrum is an asymmetrical doublet, to show how the asymmetry is encoded in the fringes. Between (*a*) and (*b*) the relative intensities of the two components have been interchanged. The main differences between the two fringe patterns are in the circled regions. The visibility, which is the same in both cases, is shown in (*c*).

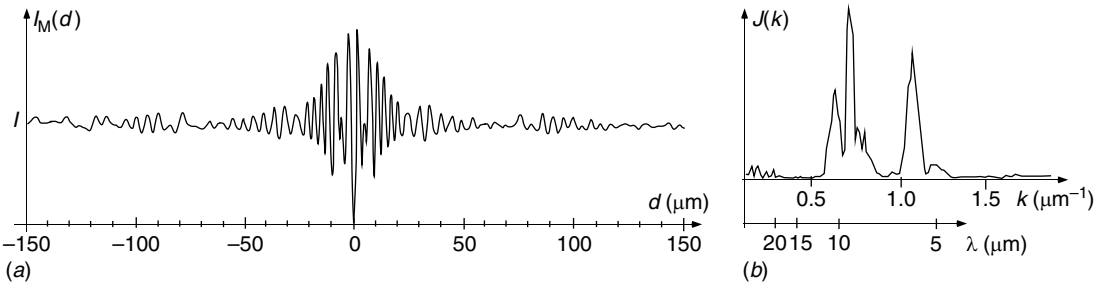

Figure 11.10

(*a*) Interferogram from a broad-band infra-red source, and (*b*) the calculated spectrum.

One then gets non-symmetrical functions $I_M(\tau)$ and $\gamma(\tau)$, and consequently the Fourier transform will have an imaginary part. The value of $n(\omega)$ can then be calculated from the ratio between the imaginary and the real parts of the transform. This is called **asymmetric Fourier transform spectroscopy** (Parker (1990); Problem 11.5).

11.5.1 Two examples of Fourier spectroscopy

In Figs. 11.9 and 11.10 we show two examples of Fourier spectroscopy. The first illustrates Michelson's original approach, via the visibility function, and shows why measuring $V(\tau)$ alone is insufficient to determine the spectrum uniquely. The second example is typical of a modern commercial Fourier spectrometer.

(*a*) Let us consider how to investigate a spectral line with fine structure around frequency ω_0. Its spectral intensity can be represented by a δ-function $\delta(\omega - \omega_0)$ convolved with a 'fine-structure function' $s(\omega)$ which, as its name

suggests, is limited to a region of frequency $\epsilon \ll \omega_0$. The function $J(\omega)$, which is the spectrum repeated symmetrically about the origin, is

$$J(\omega) = s(\omega) \otimes \delta(\omega - \omega_0) + s(-\omega) \otimes \delta(\omega + \omega_0). \tag{11.40}$$

The interferogram is its Fourier transform:

$$\begin{aligned} I - I_{\mathrm{M}}(\tau) &= \frac{1}{2}[S(\tau)\ \exp(-\mathrm{i}\omega_0\tau) + S^*(\tau)\ \exp(\mathrm{i}\omega_0\tau)] \\ &= \frac{1}{2}|S(\tau)|\{\exp[\mathrm{i}\phi_S(\tau)]\exp(-\mathrm{i}\omega_0\tau) + \exp[-\mathrm{i}\phi_S(\tau)]\exp(\mathrm{i}\omega_0\tau)\} \\ &= |S(\tau)|\cos[\omega_0\tau - \phi_S(\tau)], \end{aligned} \tag{11.41}$$

where we expressed $S(\tau)$ in terms of its magnitude and phase as $|S(\tau)|\exp[\mathrm{i}\phi_S(\tau)]$.

Now since the fine structure is restricted to a small frequency region ϵ, the transform of S varies on a time-scale ϵ^{-1}, so that it is appropriate to describe (11.41) as an oscillatory function (fringes) with a slowly varying envelope, which gives the visibility as $V = |S(\tau)|$. In order to obtain $s(\omega)$ uniquely, we also need to measure the phase $\phi_S(\tau)$ which is recorded in the phase of the fringes in (11.41). There is often no way of overcoming this problem by phase retrieval (§8.8 and §8.9) because there are clearly at least two candidate functions $s(\omega)$ and $s(-\omega)$ that have the same $|S(\tau)|$, and in spectroscopy the difference between them may be important; however, prior knowledge may enable them to be distinguished. We learn from this that in order to get reliable spectra, we have to record all the fringes in detail and perform a full numerical Fourier transform, which was impossible in Michelson's day without computers.

An example that illustrates this is shown in Fig. 11.9. A source emits a narrow asymmetrical doublet consisting of two waves with intensities a^2 at frequency $(\omega_0 - \epsilon/2)$ and b^2 at $(\omega_0 + \epsilon/2)$. You can see from the figure that the fringes are different (again, as in §11.1.1, particularly in the regions where the amplitude is small) but the visibility of the fringes is the same for both. We shall leave to the reader the details of the calculation, which are easy enough to carry out either analytically or by computation.

(*b*) The second example (Fig. 11.10) is from an automated Fourier transform spectrometer. Today, commercial Fourier transform spectrometers do not give access to the interferogram itself, but compute the spectrum directly; the spectrum shown in this figure was obtained on an old machine that had some manual features! It measures $\gamma^{\mathrm{R}}(\tau)$ by recording $I_{\mathrm{M}}(d)$ as d scans the region from $-d_1$ to $d_{\max}$. If the instrument is adjusted perfectly, $I_{\mathrm{M}}(d) = I_{\mathrm{M}}(-d)$, and it is only necessary to include a small negative region to allow the zero of d to be determined accurately. The example shows a central part of an interferogram and the spectrum deduced from it, using (11.39).

11.5.2 Resolution and sensitivity

The resolution limit of a Fourier spectrometer can be estimated in the following manner. Suppose that a monochromatic wave of wavelength λ is measured, and as the path difference d changes from 0 to $d_{\max}$ we record m fringes, the mth fringe having minimum intensity like the zero order. Now change λ to $\lambda_1 = \lambda + \delta\lambda$. For a certain value of $\delta\lambda$, $m - \frac{1}{2}$ fringes will be recorded between 0 and $d_{\max}$, so that the fringe intensity at $d_{\max}$ is now a maximum, and not a minimum. Clearly these can be resolved; if both wavelengths were incident simultaneously, and had equal intensities, the fringes would be in antiphase and cancel one another out at $d_{\max}$, a clearly observable situation. Thus, $\delta\lambda$ can be resolved if

$$d_{\max} = m\lambda = \left(m - \frac{1}{2}\right)(\lambda + \delta\lambda)$$
$$= m\lambda + m\delta\lambda - \frac{1}{2}\lambda - \frac{1}{2}\delta\lambda. \tag{11.42}$$

Neglecting the last term because $\delta\lambda \ll \lambda$, we have $\frac{1}{2}\lambda = m\delta\lambda$ or resolving power:

$$\frac{\lambda}{\delta\lambda} = 2m. \tag{11.43}$$

Compare this with the resolving power of a diffraction grating (9.12), $\lambda/\delta\lambda = mN$, where N is the number of slits, i.e. the number of interfering waves. In the Michelson case, $N = 2$. In the case of the diffraction grating, we showed that this is also equal to $2L/\lambda$, where L is the length of the grating. In the present case it is the same, where L is the length of travel of the mirror, i.e. $d_{\max}/2$. The difference is that with a diffraction grating this is a theoretical limit, requiring perfect ruling, whereas in the Fourier spectrometer it can actually be realized.

When background radiation at the detector cannot be neglected, the Fourier spectrometer has an advantage over conventional spectrometers that use diffraction gratings or prisms. If the output of a spectrometer is measured with a single detector, the spectrum must be scanned in some way, and so for part of the time (between spectral lines) very little light reaches the detector from the source, although background radiation is always received. On the other hand, with the Fourier spectrometer an average of half the input light reaches the detector at the A exit at any instant. The other half leaves through the B exit where, in principle, a second detector can be placed. The Fourier spectrometer then has a distinct advantage (called the **Fellgett advantage**) in the signal-to-noise attainable. This is the reason for the success of this type of spectrometer in the infra-red region, where background radiation – thermal emission from the instrument itself – is inevitable.

A Fourier spectrometer for astronomy, where every photon is immensely valuable, indeed uses two detectors at *A* and *B*. The interferometric signal is then the difference between the two detector outputs. (Connes and Connes (1966))

A further advantage, the **Jacquinot advantage**, over grating or prism instruments arises in the throughput of radiation, which in a conventional

spectrometer is limited by the input slit width. In the Fourier spectrometer, the detector (which is the exit pupil) can be as large as the central interference ring at $d_{\max}$, and the resulting throughput may be an order of magnitude higher. This applies to all spectral regions, including the visible.

11.6 Spatial coherence

We recall that the concept of temporal coherence was introduced as an attempt to give a quantitative answer to the following question. At a certain instant of time we measure the phase of a propagating light wave at a given point. If the wave were a perfect sinusoidal plane wave, $A\exp(-\mathrm{i}\,\omega_0 t)$, we should then know the phase at any time in the future. But in a real situation, for how long after that instant will an estimate made in the above way be reliable? The gradual disappearance of our knowledge of the phase was seen to result from uncertainty of the exact value of ω_0, and could be related quantitatively to the finite width of the spectral line representing the wave.

The second coherence concept, that of **spatial coherence**, is concerned with the phase relationship at a given instant between waves at various points in a plane normal to the direction of propagation. If the wave were a perfect plane wave, whose propagation direction is known exactly, this plane would be a wavefront, and definition of the phase at one point P in it provides the recipe to determine the phase at every other point.[5] This can be done for each component wavelength if the wave is not monochromatic, so that a wave does not have to be monochromatic in order to be spatially coherent. In practice, we can ask the question: if we know the value of the phase at P, how far away from P can we go and still make a correct estimate of the phase to within, say, $\pi/2$?

A spatially coherent wave need not have temporal coherence. But a wave with temporal coherence must arise from one or more phase-related sources, and therefore must be spatially coherent.

In a similar way that we found **temporal** incoherence to be related to uncertainty in the **frequency** ω_0 of the wave (and hence in the magnitude of the wave-vector, $|k|$), we shall see that **spatial incoherence is related to uncertainty in the direction of the wave-vector, $\hat{\mathbf{k}}$**. And uncertainty in the direction of **k** arises when the source of the light is not a point source, but is extended. Therefore the size of the source is important.

11.6.1 A qualitative investigation of spatial coherence

We saw in §11.3.2 that if we sample the wave-train with our optical stethoscope at two points A_1 and A_2 situated one behind the other we see interference fringes only if the distance A_1A_2 is less than $c\tau_c$. Spatial coherence can be approached

[5] This argument could be rephrased for a spherical wavefront emanating from a source at a finite distance.

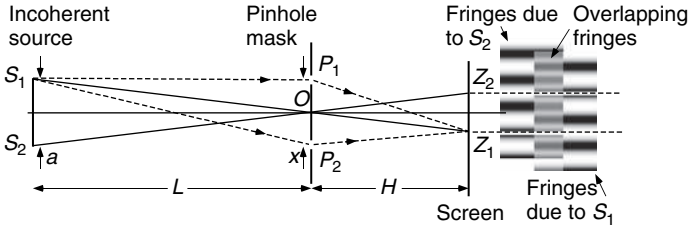

Figure 11.11

Spatial coherence. The figure shows on the right the interference fringes created by points S_1 and S_2 on an extended incoherent source; when these fringes are in antiphase, the coherence is zero.

in the same way, and can be illustrated by the following simple one-dimensional experiment.

Suppose that an incoherent, quasi-monochromatic source, of linear dimensions a, is used to illuminate a mask $\mathcal{P}$ containing a pair of pinholes P_1 and P_2 separated by x (Fig. 11.11). The appearance of a fringe pattern on a screen indicates coherence between the wave amplitudes at the two pinholes. The source is at distance L and the screen at distance H from the pinholes; for simplicity we assume $L, H \gg a, x$, and all angles to be small.

Consider the point S_1 at one end of the source. This point on its own illuminates the pinholes coherently and therefore produces a fringe pattern on the screen. The zero order of the fringe pattern appears at Z_1, corresponding to zero difference between the optical paths $\overline{S_1P_1Z_1}$ and $\overline{S_1P_2Z_1}$. Z_1 lies on the line S_1O joining S_1 to the point O half-way between the two pinholes. The period of the interference fringes is given by $H\lambda/x$. Now consider S_2 at the other end of the source, distant a from S_1. This gives a fringe pattern with the same period, with its zero order at the point Z_2, on the line S_2O. The two sets of fringes overlap, and since S_1 and S_2 are mutually incoherent, their intensities must be added. When Z_1Z_2 is equal to half the fringe spacing, the fringe patterns from S_1 and S_2 will be spatially in antiphase, and so no fringes will be visible on the screen. We can say that the spatial coherence between the two pinholes has disappeared when

$$\frac{1}{2}H\lambda/x = Z_1Z_2 = aH/L; \tag{11.44}$$

$$x = L\lambda/2a. \tag{11.45}$$

The result can be stated as follows. Because of the size of the source a, or more usefully its **angular** size $\alpha = a/L$, the fields at neighbouring points on the mask are only coherent if the distance between the points is less than

$$x_c = \lambda/2\alpha. \tag{11.46}$$

The coherence distance x_c is the largest distance between the two pinholes for which fringes are visible.

This maximum distance x_c is called the **coherence distance** in the plane of the pinholes. Notice in particular the reciprocal relationship between x_c and α.

We have neglected, in this discussion, the effect of all points such as S_3 in-between S_1 and S_2, and thereby introduced an error of about 2. This will be corrected in §11.6.3 by a more complete analysis.

When the argument is extended to two dimensions, a source of limited angular dimensions defines a two-dimensional region within which both pinholes must be situated in order to be coherently illuminated. This region is called the **coherence area** or **coherence region**.

The relationship between the coherence area, or strictly the coherence function, and the source dimensions will be shown in §11.6.3 to be that between Fourier transforms, at least when the source has a small angular diameter α. This relationship can be very useful in practice, and is the basis of the technique of aperture synthesis which will be discussed in §11.8.

11.6.2 The spatial coherence function

We return now to the idea of the optical stethoscope probing a quasi-monochromatic wave-field and assume that A_1 and A_2 are approximately on the same wavefront.[6] To be specific we assume that τ_c is much longer than τ, which is the difference between the times of arrival of the wavefronts at A_1 and A_2. Equation (11.31) is again valid, but now $|\gamma_{A_1A_2}(\tau = 0)|$ depends only on the lateral distance between A_1 and A_2 since the only effect of a change in their longitudinal distance will be to multiply $\gamma_{A_1A_2}(0)$ by $e^{i\omega_0\tau}$. We then call $\gamma_{A_1A_2}(0)$ the **complex spatial coherence function**. Usually, stationarity applies and γ depends only on the vector $\mathbf{r}$ connecting A_1 and A_2; it can then be written $\gamma(\mathbf{r})$.

An instrument that implements the above scheme almost exactly is the Michelson stellar interferometer (§11.8.1) where $A_{1,2}$ are the entrance mirrors and $B_{1,2}$ the second pair of mirrors.

11.6.3 The van Cittert–Zernike theorem

Observe that the units in the Fourier transform relating f and F are a transform pair: the argument of the exponent in the Fourier transform is the product $ik_0(x\theta_x + y\theta_y)$.

This theorem is the spatial equivalent of the Wiener–Khinchin theorem (§4.9.1) and was proved independently by van Cittert and by Zernike. It relates $\gamma(\mathbf{r})$ by a Fourier transform to the intensity distribution $I(\theta_x, \theta_y)$ in the source. We consider a distant quasi-monochromatic incoherent source of angular extent α (outside which its intensity is zero – Fig. 11.12) illuminating the observation plane. All angles in the figure will be assumed to be small. The amplitude at point S on the source is described in terms of the wavenumber k_0 and the angular coordinates (θ_x, θ_y) as $f(\theta_x, \theta_y)$, where $|f|^2 = I(\theta_x, \theta_y)$ is its intensity, and the amplitude received at $P(x = 0)$ is then its far-field diffraction pattern

[6] The importance of A_1 and A_2 being within a coherence length of the same wavefront will be emphasized in the discussion of aperture synthesis in §11.8.

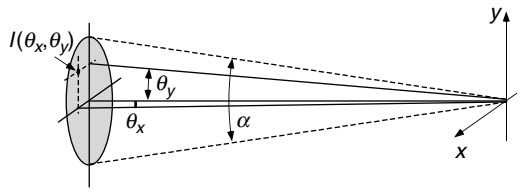

Figure 11.12
Illustrating the van Cittert–Zernike theorem. $I(\theta_x, \theta_y)$ represents the angular intensity profile of the source (usually a star) and $\gamma(k_0x, k_0y)$ is measured in the observation plane.

$F(k_0x, k_0y)$. Now the spatial coherence function of this field F can be formulated as a convolution:

$$\gamma(\mathbf{r}) = \frac{F(k_0x', k_0y')F(k_0x' - k_0x, k_0y' - k_0y)}{|F|^2} = \frac{F(k_0\mathbf{r}) \otimes F^*(k_0 - \mathbf{r})}{|F|^2}. \tag{11.47}$$

The Fourier transform of the convolution is the product of $f(\theta_x, \theta_y)$ with its complex conjugate:

$$\frac{f(\theta_x, \theta_y) \cdot f^*(\theta_x, \theta_y)}{|F|^2} \sim I(\theta_x, \theta_y). \tag{11.48}$$

Thus $\gamma(k_0\mathbf{r})$ and $I(\boldsymbol{\theta})$ are a Fourier transform pair (up to a normalization prefactor):

$$\gamma(k_0\mathbf{r}) = \frac{\int\int_{-\alpha/2}^{\alpha/2} I(\theta_x, \theta_y) \exp[\mathrm{i}k_0(x\theta_x + y\theta_y)] \, \mathrm{d}\theta_x \, \mathrm{d}\theta_y}{\int\int_{-\alpha/2}^{\alpha/2} I(\theta_x, \theta_y) \, \mathrm{d}\theta_x \, \mathrm{d}\theta_y}. \tag{11.49}$$

This relationship is called the **van Cittert–Zernike theorem**. Although we assumed above that the source was small, this was only because angles θ are only vectors when they are small. In fact, as should be obvious from Fraunhofer diffraction theory, the true variables in the source are the direction cosines $(\ell, m) = (\sin\theta_x, \sin\theta_y)$.

We shall apply it to a circular star as an example. The source has unit intensity within a circle of small angular *diameter* α and zero outside it, i.e. $I(\theta) = \mathrm{circ}\left(\theta / \frac{1}{2}\alpha\right)$. The correlation function is therefore the Fourier transform of $I(\theta)$ which is (§8.3.4)

$$\gamma(k_0r) = \frac{2J_1(k_0\alpha r/2)}{k_0\alpha r/2}, \tag{11.50}$$

it has its first zero when $r = 1.22\lambda/\alpha$.

For example, Betelgeuse has angular diameter 0.07 arcsec, $= 3.4 \times 10^{-7}$ radians, and coherence in green light extends throughout a circle of radius about 1.9 m around a given point (Fig. 11.13). After the first zero, (11.50) predicts there to be further regions of correlation, both negative and positive which result from the sharp cut-off assumed at the edges of the star, but are suppressed if the star is less intense around its edges; this phenomenon is called 'limb-darkening'. Some experimental results for such measurements will be shown in §11.8.

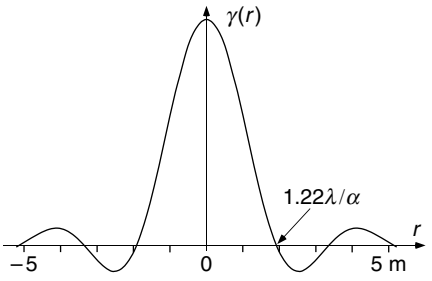

Figure 11.13
Coherence function $\gamma(r)$ for a circular star of angular diameter α. The abscissa also shows actual distances for Betelgeuse, with angular diameter 0.07 arcsec, at $\lambda = 550$ nm.

11.6.4 Partial coherence from an extended source

A particular case in which θ is not small is that of **microscope illumination** (§12.2.7) where the specimen receives light from all directions within a strongly focused cone whose semi-angle $\alpha/2$ can approach $\pi/2$. Continuing from (11.49), and using $u = k_0 \sin\theta$, $\mathrm{d}u = k_0 \cos\theta \, \mathrm{d}\theta$, we write for a one-dimensional source

$$\gamma(x) = \frac{\int_{-k_m}^{k_m} [I(\theta)/\cos\theta] \exp(-\mathrm{i}ux) \, \mathrm{d}u}{\int_{-k_m}^{k_m} [I(\theta)/\cos\theta] \, \mathrm{d}u}, \tag{11.51}$$

where $k_m = k_0 \sin(\alpha/2)$. For a Lambertian source (a black body, §14.1.2 for example) $I(\theta) \sim \cos\theta$, whence (11.51) gives $\gamma(x) = \mathrm{sinc}(k_m x)$. For the limiting case of an infinite source, $\alpha = \pi$ and $\gamma(x) = \mathrm{sinc}(k_0 x)$. The coherence distance x_c is the first x for which $\gamma(x)$ becomes zero, i.e. $x_\mathrm{c} = \lambda/2$. The same calculation for a source infinitely extended in *x and y* follows from the equivalent result for a circular source, $\gamma(r) = 2J_1(k_0 r)/k_0 r$, and gives $r_\mathrm{c} = 0.61\lambda$.

11.6.5 Two laboratory demonstrations of spatial coherence

The van Cittert–Zernike theorem can be illustrated by the experiment of §11.6.1 in which the pair of pinholes P_1 and P_2 with a distance x between them is illuminated by an incoherent source (Fig. 11.11). The visibility (§11.3.2) of the interference fringes then measures the coherence between the fields at the two pinholes. In a simple one-dimensional experiment, the source is a slit S of width a, aligned perpendicularly to the line P_1P_2. The function describing the coherence between P_1 and P_2 is therefore

$$\gamma(x) = \mathrm{sinc}[k_0 x \sin(a/2L)] \approx \mathrm{sinc}\left[\frac{\pi a x}{\lambda L}\right], \tag{11.52}$$

this function being the Fourier transform in (11.51). As a is increased from zero, the coherence between pinholes P_1 and P_2 begins at unity, becomes zero when $a = \lambda L/x$ and has the usual series of weaker maxima and minima as a is increased beyond this value. The interference patterns observed for several

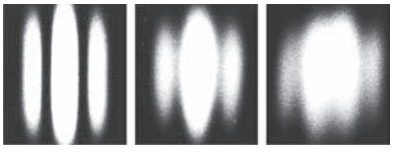

Figure 11.14

Young's fringes with different degrees of spatial coherence: (*a*) $\gamma = 0.97$; (*b*) $\gamma = 0.50$; (*c*) $\gamma = -0.07$. Note particularly the minimum at the middle of (*c*), indicating the negative value of the coherence function.

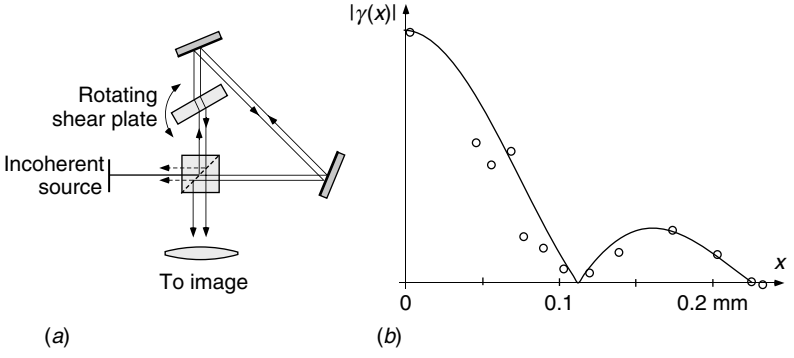

Figure 11.15

Experimental results for measurement of the coherence function for an incoherent rectangular source imaged through a shearing interferometer (*a*), compared with the calculated result (11.51), (*b*). (We are grateful to Yuval Shapira for performing this experiment.)

values of a are illustrated in Fig. 11.14, in which the visibility clearly follows the same pattern. Notice that the effect of negative values of γ is to shift the pattern by half a fringe ($\phi = \pi$).

This experiment is the basis of several fundamentally important interferometers that are used to determine the angular dimensions of inaccessible sources such as stars. These will be described in §11.8.

A second laboratory experiment uses a shearing interferometer (§9.4) to measure the coherence function directly. A shearing interferometer displays the interference pattern between a field centred at $\mathbf{r} = 0$ and the same field centred at $\mathbf{r}$. The contrast of the interference fringes is therefore a direct measure of $\gamma(\mathbf{r})$. Following the discussion in §11.6.4, some results are shown in Fig. 11.15 for an incoherent rectangular source.

11.7 Fluctuations in light beams, classical photon statistics and their relationship to coherence

In §11.1.2 we showed that, however intense a light beam might be, its intensity still appears to fluctuate when investigated with a fast enough detector. The argument was completely classical, and the invention of the laser prompted a

re-examination of the analysis. In particular, it was hoped to discover basic differences in the statistics of light emitted by lasers and conventional sources, a subject that we shall return to in Chapter 14. In this section we shall present a simplified account of the classical theory, which has important applications; the quantum theory of fluctuations will be discussed briefly in Chapter 14. A remarkable feature of the classical results is in fact their similarity to the quantum ones; it has only been since about 1977 that significant differences between the two have been discovered experimentally (§14.3.1).

Before studying the light beam itself, we shall ask what exactly one measures in an experiment to detect fluctuations. The answer, of course, is the electric current from a photo-detector. Any treatment of the subject must take into account the fact that we actually observe discrete electrons emitted by, say, a photo-cathode (other methods of detection, such as semiconductor devices, can be described similarly). In this experiment there are two uncorrelated sources of fluctuation. The first arises because we are observing **discrete electron emissions whose *average* rate is proportional to the instantaneous intensity**; the second because **the instantaneous intensity itself is fluctuating about its long-term mean value**. Recall from §11.1.2 that the term 'instantaneous intensity' implies an average during a period $T_1 < \tau_c$.

The *mean* number of electrons emitted during a given interval $\delta t \ll \tau_c$ is $\bar{n} \equiv \langle n \rangle = \langle I(t) \rangle \eta \, \delta t / \hbar\omega$. Here $\langle I(t) \rangle$ is the mean intensity during δt and η is the **quantum efficiency**, which is the probability of an electron being emitted if a photon of energy $\hbar\omega$ falls on the cathode. However, the *exact* number of electrons emitted is statistical, being given by a Poisson distribution with the above mean. The probability of n electrons being emitted in δt is then

$$p(n) = \bar{n}^n \exp(-\bar{n}) / n!. \tag{11.53}$$

The variance or mean-square fluctuation for the Poisson distribution is well known to be equal to its mean value:

$$\langle (\Delta n)^2 \rangle_{T_1} \equiv \langle n^2 \rangle - \bar{n}^2 = \bar{n}. \tag{11.54}$$

This is one source of fluctuation in the current. Since $\bar{n}$ depends on the mean intensity during the interval, which is itself a fluctuating variable, we can also define $\bar{\bar{n}} = \langle I(t) \rangle_{T_0} \eta \, \delta t / \hbar\omega$, the average of $\bar{n}$ over a very long time $T_0 \gg \tau_c$, and then the expectation value of $\langle (\Delta n)^2 \rangle_{T_1}$ will equal $\bar{\bar{n}}$.

The second source of fluctuation is that of $\langle I(t) \rangle$ itself, which we have already treated in §11.1.2. There we saw in (11.9) that the mean-square difference

$$\langle (\langle I(t) \rangle_{T_1} - \langle I(t) \rangle_{T_0})^2 \rangle_{T_0} = a^4 N^2 = [\langle I(t) \rangle_{T_0}]^2 . \tag{11.55}$$

In terms of electrons emitted in time δt this can be written

$$\langle (\Delta \bar{n})^2 \rangle_{T_0} \equiv \langle (\bar{n} - \bar{\bar{n}})^2 \rangle_{T_0} = \bar{\bar{n}}^2. \tag{11.56}$$

Since $\Delta\bar{n}$ and Δn are not correlated we find that the total variance in photo-electron counts during T_1 is the sum of the individual variances:

$$\langle (n-\bar{\bar{n}})^2\rangle_{T_0} = \langle (\Delta\bar{n})^2\rangle_{T_0} + \langle\langle (\Delta n)^2\rangle_{T_1}\rangle_{T_0} = \bar{\bar{n}}^2 + \bar{\bar{n}}. \tag{11.57}$$

What is remarkable about this equation is that it is identical to the variance in the number of photons in a given state when they are considered as massless Bose–Einstein particles (see, e.g., Landau and Lifshitz (1980)), which is surely a quantum description. Some inklings of an explanation will be given in Chapter 14.

The above argument, which is completely classical, shows that when a photo-detector is illuminated by a quasi-monochromatic wave, the emission of electrons is not a purely random process, governed by Poisson statistics. Photo-emission events are therefore correlated in some way, this is called **photon bunching**. For a high light intensity $\bar{\bar{n}} \ll \bar{\bar{n}}^2$, so that n fluctuates in the range 0 to $2\bar{\bar{n}}$.

The concept of photon bunching, given by the $\bar{\bar{n}}^2$ term, can be understood via the optical stethoscope. We now place two detectors at the exits B_1 and B_2 and correlate their output currents i_1 and i_2 electronically instead of observing the interference pattern. As we have pointed out, these currents are proportional to the mean intensities, $\langle I_1(t)\rangle_{T_1}$ and $\langle I_2(t)\rangle_{T_1}$. Using the model of §11.1.2 we can calculate the correlation between these intensities. Recognizing that the elementary wave j will arrive at A_1 with phase ϕ_j and at A_2 at a different time and therefore with phase ψ_j related to its direction of propagation we can write from (11.3)

$$\begin{aligned}\langle I_1(t)I_2(t)\rangle = a^4 \Bigg\langle &\sum_{j=1}^{N} \exp[\mathrm{i}(\omega_j t+\phi_j)] \sum_{j=1}^{N} \exp[-\mathrm{i}(\omega_j t+\phi_j)] \\ &\times \sum_{j=1}^{N} \exp[\mathrm{i}(\omega_j t+\psi_j)] \sum_{j=1}^{N} \exp[-\mathrm{i}(\omega_j t+\psi_j)] \Bigg\rangle \\ = a^4 \Bigg\langle &\sum_{j,k,l,m=1}^{N} \exp\{\mathrm{i}[(\omega_j-\omega_k+\omega_l-\omega_m)t \\ &+(\phi_j-\phi_k+\psi_l-\psi_m)]\} \Bigg\rangle. \end{aligned} \tag{11.58}$$

When the average is taken over a long time $T_0 \gg 1/\epsilon$, the only non-zero terms arise from $j=k$ and $l=m$, whence the average $\langle I_1(t)I_2(t)\rangle_{T_0} = a^4N^2$. However, if $|\ \phi_j-\psi_m\ |_{\max}$, and $|\ \phi_k-\psi_l\ |_{\max}$ are $\ll \pi/2$, there is an additional contribution $a^4N(N-1) \approx a^4N^2$ from terms with $j=m$ and $k=l$. This condition is a function of the relative positions of A_1 and A_2.

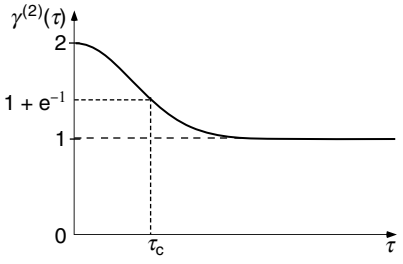

Figure 11.16
Temporal intensity coherence function $\gamma^{(2)}(\tau)$, showing excess correlation of fluctuations when $\tau < \tau_c$.

One can see immediately that if, for example, A_1 and A_2 are one behind the other, so that the phase difference is caused by a time delay τ, then $\phi_j = \omega_j \tau$ and the second contribution to the average of (11.58) comes in only if $\tau \ll \pi/[2|\omega_l - \omega_m|_{\max}] = \pi/2\epsilon \approx \tau_c$, the coherence time. Then let $I_1 \equiv I(t)$, $I_2 \equiv I(t+\tau)$ and we can define the **intensity coherence function** or **second-order coherence function**

$$\gamma^{(2)}(\tau) = \frac{\langle I(t)I(t+\tau)\rangle_{T_0}}{\langle I(t)\rangle^2_{T_0}}. \tag{11.59}$$

The function $\gamma^{(2)}(\tau)$ has the typical form shown in Fig. 11.16, with $\gamma^{(2)}(0) = 2$ and $\gamma^{(2)} \to 1$ as $t \to \infty$. Photon bunching appears as an *excess correlation* for $\tau < \tau_c$. Interpreted in terms of photo-electron counts, this means that if one observes an electron emission event, there is a higher probability of another one within τ_c than would be expected if the events were completely random (see Fig. 14.7(*c* and *d*)). We shall return to the subject in Chapter 14 as a quantum phenomenon.

Photon bunching is similar to traffic on a single-lane road. Cars do not arrive statistically, but tend to arrive in groups, each being led by a slower-than-average car.

A similar calculation can be made for spatial coherence. In this case, $\phi_j - \psi_j$ represents the difference in phase between the waves from a given point on the source on their arrival at A_1 and A_2, so that the enhanced correlation now arises when A_1 and A_2 are within a coherence region. Using this model to express γ in terms of the phase differences, one can demonstrate (Problem 11.11) the general relationship that

$$\gamma^{(2)}(\mathbf{r}, \tau) = 1 + |\gamma(\mathbf{r}, \tau)|^2. \tag{11.60}$$

It follows that the degree of coherence, whether temporal or spatial, can be measured by studying the correlation coefficient $\gamma^{(2)}(\tau)$ or $\gamma^{(2)}(\mathbf{r})$, respectively.

Brown and Twiss developed these ideas in 1955–7 and confirmed them experimentally. It is important to appreciate that the frequency spectrum of the fluctuations is essentially flat from 0 to $1/\tau_c$, so that if the experimental apparatus is capable of measuring only a limited bandwidth of, say, δf, the observed fluctuations will be reduced by a factor of $\delta f \tau_c$. For broad-band (white) light, this factor is dismally small, and electronic detection in the 1950s was limited to maybe $\delta f \approx 50$ MHz. In their laboratory experiments, Brown and

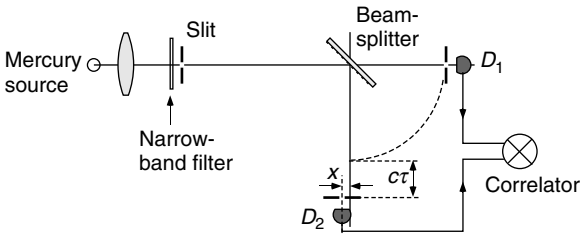

Figure 11.17
Measurement of temporal and spatial coherence by correlation of intensity fluctuations. (Brown and Twiss (1956))

Twiss (1956) therefore used a monochromatic source with narrow bandwidth, having a relatively long τ_c which maximized the fluctuation amplitude. They recorded electronic correlation of the signals from two photocells (Fig. 11.17), which agreed with the theory and paved the way to the astronomical technique of **intensity interferometry** (§11.8.3).

It is clear from (11.60) that $\gamma^{(2)}(\tau) \geq 1$ for any classical wave. We shall show in Chapter 14 that there also exist **quantum forms of light for which $\gamma^{(2)}(0) < 1$, and which therefore have no classical equivalents**.

11.8 The application of coherence theory to astronomy: Aperture synthesis

Coherence studies have made a major contribution to astronomy, since measurement of the spatial coherence function at the Earth's surface in principle allows the intensity distribution in a distance source to be deduced. The scenario that we outlined above, where the source has small angular size and is situated in a surrounding dark field is of course ideal for astronomy, but typical coherence distances are of the order of metres, so that large-scale equipment is needed.

The idea was proposed long before coherence theory was formalized, and can be illustrated primitively by taking a photograph of a scene with many isolated light sources through a pair of slits with separation $d \approx 1.5$ mm (Fig. 11.18). Each source produces Young's fringes around its image, and the contrast of the fringes depends on the size of the source via the spatial coherence function $\gamma(d)$. The photograph in the figure shows many sodium ($\lambda = 600$ nm) street lights at different distances from the observer (indicated roughly in the margin); the lights themselves have a size of about 20 cm, so that their angular diameter is about (20 cm/distance). It is easy to see that the most distant lights (about 2.5 km away) give the highest contrast fringes. The coherence distance is about 1.5 mm when such a lamp is at a distance of about 450 m. Essentially, stellar interferometry involves making such observations quantitative. For Betelgeuse, which is one of the largest stars visible, we saw that the coherence distance at $\lambda = 500$ nm is about 2 m, and this indicates a minimum scale for astronomical observatories carrying out such measurements; but more distant sources have

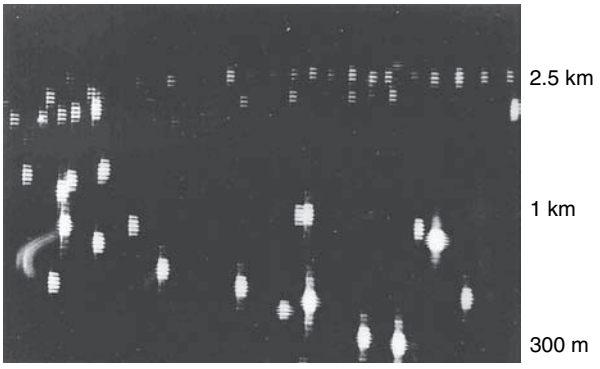

Figure 11.18
A night-time urban scene with several sodium street lights at different distances, photographed through a pair of horizontal slits separated by about 1.5 mm. The fringe visibility improves with distance.

much smaller angular diameters, and so the scale needed may be tens or hundreds of metres (see Fig. 11.1).

Because of the presence of atmospheric turbulence, which is discussed more fully in §12.7, no astronomical telescope can achieve even approximately the Rayleigh limit of resolution (§12.2.1). The turbulence only causes the fringes to move around, but does not affect their visibility.

11.8.1 The Michelson stellar interferometer

The first successful attempt to measure a stellar diameter was made by Michelson, who designed in 1890 a stellar interferometer that enabled dimensional measurements on several large stars. This instrument can be regarded as a practical realization of the optical stethoscope for the case discussed in §11.6.1. In this interferometer (Fig. 11.19) the sizes of the exit apertures M_2 and M_3 are of the order of the distance M_2M_3, therefore only a few fringes form and the time difference τ_p in (11.29) is small. This obviates the need for a narrow bandwidth of the illumination. We saw in the experiment described in §11.6.5 that the visibility of the fringes, measured as a function of the pinhole separation $x = M_1M_4$, was related quantitatively to the size of the source; the van Cittert–Zernike theorem (§11.6.3) shows that $\gamma(x)$, related to the fringe visibility, can be Fourier transformed to yield the stellar intensity distribution in the direction of P_1P_2. But really the fringe visibility measures only $|\gamma(x)|$ and the phase is not known, and so the Fourier transform cannot be performed completely. However, Michelson assumed that the star has a centre of symmetry to make the problem soluble. This point is discussed more fully in another connection in §12.7.1.

Michelson's first 'proof of concept' stellar interferometer was constructed by putting a screen over the objective of a telescope and making two holes in it in such a way that their separation is variable. He used it to measure the diameter of one of Jupiter's moons. The point spread function of the telescope, modified by the mask, is now a circular ring pattern crossed by interference fringes (like the inset to Fig. 11.19). When a source of finite diameter α replaces the point source the visibility of the fringes depends upon the coherence between the illumination of the two circular holes. As the separation of the holes is increased, the fringes become less and less clear, disappearing completely when the separation is $1.22\lambda/\alpha$. Michelson used this property to measure the diameter.

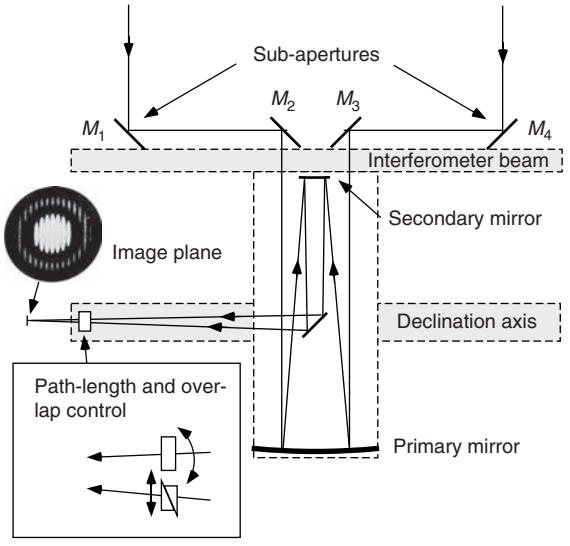

Figure 11.19

Layout of the Michelson stellar interferometer. Small corrections to the relative path lengths could be made while observing the fringes by using a pair of sliding prisms, and overlap of the images by rotating the compensator plate. The circle shows a simulation of the type of fringes seen.

If the angular diameter α of the star is very small, the separation of the holes will need to be very large before the fringes disappear. We saw earlier that to measure the diameter of Betelgeuse, the two apertures must be separated by distances up to at least 2 m. Michelson solved this problem in an ingenious manner by a mirror system (analogous to the optical stethoscope) mounted on the Mount Wilson telescope in Pasadena, CA, as illustrated in Fig. 11.19. The coherence measured is clearly that between the light at mirrors M_1 and M_4, which were mounted on racks to vary their separation. The interference pattern observed is that arising from the two apertures M_2 and M_3, and the scale of the fringes can therefore be made conveniently large by putting the holes M_2 and M_3 close together. Since the starlight is not monochromatic, it is very important to ensure that the path lengths from the star to the image plane are equal to an accuracy of about a wavelength, otherwise measurements of the visibility will not be accurate. This was done by first pointing the telescope at the star (by Fermat's principle, the paths should then be equal), and then correcting small residual path differences by tilted glass plates in the optical paths of the two beams. Then only fringe jitter caused by atmospheric path differences had to be overcome by the experimenter's expertise.

The length of the interferometer beam was chosen so as to be sufficient to confirm a theoretical estimate of the diameter of Betelgeuse, made by Eddington. See Box 11.2.

The most successful Michelson stellar interferometer was built on a beam 6 m long mounted on the 2.5 m Mount Wilson telescope (Michelson (1927)). The input mirrors M_1 and M_4 had diameters about 10 cm. Unfortunately, the inefficient use of light by this instrument and the need to detect the fringes dancing with the atmospheric scintillation limited its use as a visual instrument to stars of exceptional brilliance; some 20 stars within its measurement capability were measured by Michelson and his colleagues. But it proved that, using coherence measurements, the atmospheric limitations to stellar resolution can be overcome, and planted several seeds which later sprouted.

Box 11.1 Stellar images by phase closure and aperture masking

In order to use the measured values of $\gamma(\mathbf{r}) = |\gamma(\mathbf{r})| \exp[i\phi(\mathbf{r})]$ to create an image of the star, one needs to know ϕ as well as $|\gamma|$. If there were no atmospheric jitter to the fringes, the phase could in principle be determined by observing where the central fringe is situated with respect to the optical axis. However, in practice this is not possible. What can be done, however, is to compare the phases of different fringes when observed simultaneously, and therefore suffering from the same atmospheric jitter. Suppose that in Michelson's 'proof of concept' experiment there are *three* entrance apertures, A_1, A_2 and A_3. Then there will be three simultaneous sets of interference fringes, and if the vector distances A_1A_2, A_2A_3 and A_3A_1 are all different these sets can be distinguished because they have different periods. Now if the atmospherically induced phase shift at A_i is ψ_i ($i = 1, 2, 3$), the fringes due to A_iA_j will be shifted from their correct positions by phase $\psi_i - \psi_j$. Therefore, the measured phase of the fringes will be $\phi(A_iA_j) + \psi_i - \psi_j$. Now if all three sets of fringes are measured simultaneously, the *sum* of the measured fringe phases is

$$\begin{aligned}\Phi_{ijk} &= [\phi(A_iA_j) + \psi_i - \psi_j] + [\phi(A_jA_k) + \psi_j - \psi_k] + [\phi(A_kA_i) + \psi_k - \psi_i] \\ &= \phi(A_iA_j) + \phi(A_jA_k) + \phi(A_kA_i),\end{aligned} \tag{11.61}$$

which is **independent of the atmospheric phases** (or, for that matter, of any telescope figuring or other localized phase errors, too). Using this formula, called **phase closure**, with three or more apertures A_i, the phase of γ can be determined and real stellar images formed. It is somewhat reminiscent of the direct method of phase determination in X-ray diffraction patterns (§8.8).

Michelson's 'aperture-masking' experiment has been revived, using phase closure and an array of apertures with distinctly different separations, called a 'non-redundant array'. This has led to many beautiful images of larger stars (Tuthill *et al.* (2000)). For convenience, the mask is situated on the secondary mirror of a Cassegrain telescope, and not on the aperture.

11.8.2 Aperture synthesis in radio astronomy

Following Michelson's pioneering experiments at optical frequencies, the subject of astronomical interferometry lay dormant till the discovery of radio emission from stars by Jansky in 1932. This led to the field of **radio astronomy**. An important difference between radio and optical detection is that at radio frequencies it is possible to record the actual value (amplitude and phase) of the electric field of the waves received from stellar objects, and not just their intensity. One does this by mixing (heterodyning) the current from an antenna with that from a very stable local oscillator of frequency close to that of interest, thereby creating a low-frequency beat signal which can be recorded. The bandwidth of the beat signal is limited by the frequency response of the recording electronics. The beat signals from different antennae can either interfere in real

time, or interference between the recorded signals can be performed at a later time. This facilitates interferometry using well-separated antennae, and large antenna arrays were constructed to simulate telescopes of a similar size, thus obtaining high-resolution images of stellar sources at radio frequencies.

A breakthrough in radio astronomy occurred when it was realized by M. Ryle that Michelson's idea of measuring stellar images by using a pair of apertures with adjustable separation $\mathbf{r}$ could be applied to radio antennae too, the interference signals from the various aperture pairs being correlated *post factum* to generate $\gamma(\mathbf{r})$. The technique is a direct application of the van Cittert–Zernike theorem (§11.6.3) and is called **aperture synthesis**. This name arises because essentially it allows us to build up the equivalent of a large aperture telescope by sampling its area with point measurements at as many vectors $\mathbf{r}$ as possible. The geographical locations of the individual antennae are chosen so as to sample the synthetic aperture area as uniformly as possible, and of course the spatial resolution is determined by its outer dimension, which corresponds to the largest value of the separation between the two antennae. Ryle received the Nobel prize in 1974 for implementing aperture synthesis.

It is important to realise that the mixing technique makes the radiation received essentially quasi-monochromatic, since the bandwidth of the low-frequency signal is much smaller than the frequency of the local oscillator. For example, if the wavelength chosen is 10 cm, and the bandwidth 100 MHz, the ratio ϵ/ω_0 is 0.03 (cf. Fig. 11.4). The techniques of aperture synthesis in radio astronomy are described in detail by Rohlfs (1996) and by Thompson (2001). More recently, the same techniques have been extended to the infra-red region, using a stabilized laser as a local oscillator (Hale *et al.* (2000)).

The basis of the synthetic aperture method is as follows. Consider a Michelson stellar interferometer, in which we observe the interference pattern between the signals received at two apertures. At radio frequencies we use two sensitive point-like receivers[7] at positions $\mathbf{r}_0$ and $\mathbf{r}_0 + \mathbf{r}$, separated by vector $\mathbf{r}$, the length of which can be changed by the observer. We record the values of the two signals, $E(\mathbf{r}_0, t)$ and $E(\mathbf{r}_0 + \mathbf{r}, t)$, for a period of time and calculate $\gamma(\mathbf{r})$ from them using (11.62).

Two geometrical considerations regarding the size and sampling of the synthetic aperture are as follows.

1. As the Earth rotates, during one day the vector $\mathbf{r}$ traces out a cone in inertial space (Fig. 11.20). When this trace is projected onto the (x, y) plane normal to the direction of the star $\hat{\mathbf{s}}$, we have the effective aperture associated with this baseline in one day, which is shown in the figure for NS and EW baselines.
2. When we introduced the spatial coherence function $\gamma_{A_1A_2}(\tau = 0)$ in §11.6.2 and showed that its Fourier transform is the source image, we required for simplicity that A_1 and A_2 be within a coherence length of the same wavefront. This

[7] They are usually parabolic dishes focusing the radiation from the source onto the antennae, so as to achieve maximum sensitivity in the direction of interest. The idea is analogous to the blazed grating, §9.2.5.

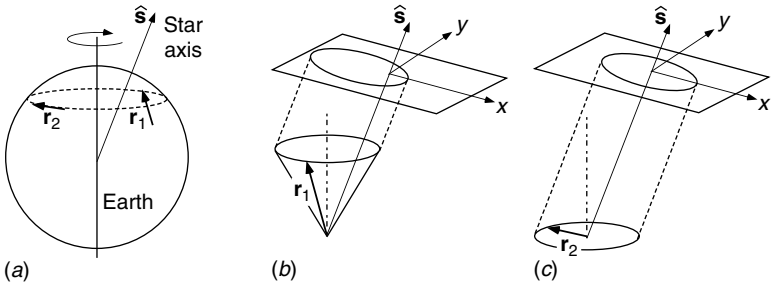

Figure 11.20

Aperture synthesis in radio astronomy: (*a*) shows two baseline vectors $\mathbf{r}_1$ (NS) and $\mathbf{r}_2$ (EW) on the Earth; (*b*) and (*c*) show diurnal traces of $\mathbf{r}_1$ and $\mathbf{r}_2$ and their projections on the (x, y) plane normal to the star axis.

is clearly not the case in an aperture-synthesis system, because both antennae are constrained to be on the Earth's surface. However, we can relate the signal at A_2 to that at the equivalent point in the wavefront through A_1 by introducing a time delay $\mathbf{r} \cdot \hat{\mathbf{s}}/c$ (Fig. 11.20(*b*)). Thus the coherence function is

$$\gamma(\mathbf{r}) = \frac{\langle E(\mathbf{r}_0, t) E^*(\mathbf{r}_0 + \mathbf{r},\, t - \mathbf{r} \cdot \hat{\mathbf{s}}/c)\rangle}{[\langle |E(\mathbf{r}_0, t)|^2\rangle \langle |E(\mathbf{r}_0 + \mathbf{r}, t)|^2\rangle]^{\frac{1}{2}}}, \tag{11.62}$$

where the complex conjugate E^* is derived from E using a Hilbert transform. Since $\gamma(\mathbf{r})$ is the Fourier transform of the source intensity, which is a real function and therefore $\gamma(\mathbf{r}) = \gamma^*(-\mathbf{r})$, collection of data for a given $|\mathbf{r}|$ is complete in 12 hours, although for part of the day a given source might be obscured by the Earth. In successive half-days the spacing between the antennae can be progressively changed up to some maximum depending on the length of the observatory (which may be kilometres) and the astronomers' patience. Clearly, although the outer dimensions of the synthetic aperture are defined by the longest baseline, values of $\gamma(\mathbf{r})$ are not measured for every intermediate value of $\mathbf{r}$. One then uses the van Cittert–Zernike theorem to compute, from the values of $\gamma(\mathbf{r})$, the intensity picture of the stable radio universe at the wavelength chosen. The point spread function of the synthetic telescope is the diffraction pattern of an 'aperture mask' which has holes at those values of $\mathbf{r}$ for which $\gamma(\mathbf{r})$ has been measured, and the resulting raw image has to be processed by deconvolution to achieve the best experimental picture.

Only stellar sources that do not change significantly within the time of the experiment can be investigated by aperture synthesis.

The resolution is determined by the maximum dimension of the array. For example, if this is 4 km, at 2 cm wavelength an angular resolution of 5×10^{-6} rad, approximately 1 arcsec, is achieved, which is about the same as the seeing limit of of an optical telescope. Practical aperture synthesis observatories use more than two antennae simultaneously, but the same principle is involved.

Taking this to its extreme, observatories the world over now cooperate in taking simultaneous measurements of the same sources synchronized to very accurate atomic clocks. The results are then processed together at a central laboratory. This is called **very long baseline interferometry** (Kellerman and Thompson (1988)). With aperture synthesis, the radio universe can be investigated to a resolution determined by a baseline of intercontinental dimensions. Of course, in this case the aperture mask is quite dilute, because both observatories have to observe the same source at the same time.

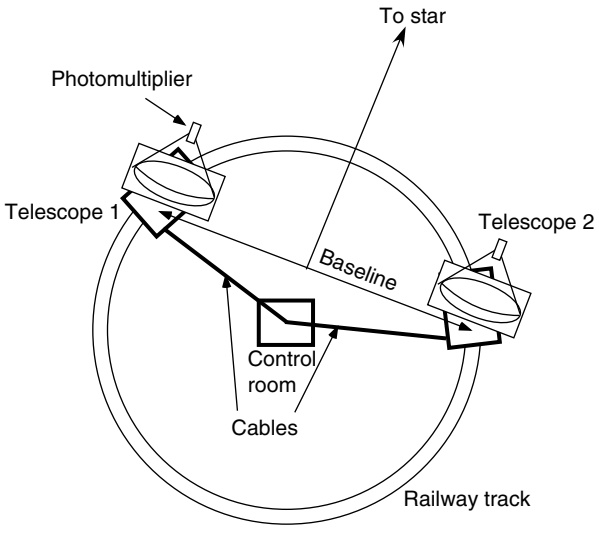

Figure 11.21
Layout of the intensity interferometric observatory at Narrabri, Australia. Notice that the telescopes can be moved round the track so that any baseline up to the track diameter can be achieved, with zero path difference between the star and the telescopes.

11.8.3 Brown and Twiss's intensity interferometer

The next major development in optical stellar interferometry was the work of Brown and Twiss in 1956–72. They realized that the correlation of intensity fluctuations (§11.7) could be used to measure $|\gamma(\mathbf{r})|$ and that the frequency band of the observation δf could be chosen so as to avoid the low frequencies (<200 Hz) typical of atmospheric turbulence. Moreover, since no real wave interferometry was involved, stability of path length differences was not critical. The story of this development is described delightfully by Brown (1974). Brown and Twiss's 'proof of concept' instrument consisted of two searchlight mirrors with variable separation $\mathbf{r}$ and a photo-cell at the focus of each. The two were focused on the star Sirius and the correlation between fluctuations in the photo-currents was measured as a function of $\mathbf{r}$. From the data, $\gamma^{(2)}(\mathbf{r})$ in (11.60), the dimensions of the coherence region, and thus the stellar dimensions, could be deduced. To improve the factor $\delta f \tau_c$, it was necessary to use an optical filter to increase τ_c as much as possible. Thus a lot of light was thrown away, but this allowed large collectors to be used without saturating the photo-cells.[8]

Following the success of the initial experiments, an observatory dedicated to astrophysical measurements by fluctuation correlation, called **intensity interferometry**, was set up at Narrabri, Australia (Fig. 11.21), using collectors with diameter 6.5 m and a maximum baseline of 188 m. These gave a resolution limit at 0.4 μm of 5×10^{-4} arcsec. Many important measurements

[8] It therefore turns out that τ_c cancels out when the *signal-to-noise* of the signal is calculated.

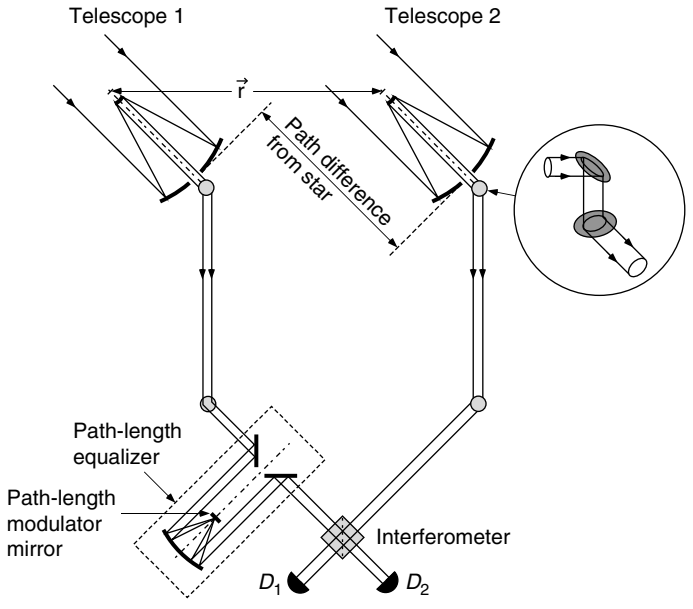

Figure 11.22
Schematic diagram of an optical stellar interferometric observatory.

were made with this system, and it was used to investigate some 200 stars, which essentially exhausted the stellar objects of sufficient brilliance for its application (Brown *et al.* (1974)). In 1972 the observatory was closed, and the baton handed to the newly reborn technique of amplitude interferometry, which would later be shown experimentally (Davis and Tango (1986)) to be some hundreds of times more sensitive, provided that the technical problems associated with baseline stability and atmospheric fluctuations could be overcome.

11.8.4 Modern stellar interferometry

Since the 1970s the optical stellar interferometer based on Michelson's instrument has been revived as an astronomical instrument. Modern versions, of which more than 12 have been built (see Labeyrie *et al.* (2006)) are constructed with two or more telescopes, having apertures up to 10 m diameter, separated by distances reaching as far as 600 m. They allow investigation of stars up to about 9th magnitude. When an interferometer has three or more telescopes, phase closure (Box 11.1) can be used to create stellar images. Figure 11.22 shows a schematic optical diagram indicating most of the important components, and Fig. 11.1 shows an aerial view of one of the interferometric observatories.

The stellar interferometers that are currently operating at wavelengths shorter than 5 μm have the following features:[9]

- They are based on several telescopes with entrance pupils ranging from 14 cm to 10 m, which are pointed simultaneously to the star of interest. The smaller telescopes are often moveable from site to site, so that different baselines can be employed on different nights. The longest baseline built is 640 m.
- The light leaving each telescope goes through a tip-tilt mirror system operating with about 1 ms response time to ensure that the telescope stays exactly focused on the star, despite atmospheric effects.
- The larger telescopes use adaptive optics systems to correct the aperture phase for atmospheric turbulence (Hardy (1998)).
- The telescopes are afocal (§3.5.2) and project the starlight as a parallel beam to the beam-combining centre. Usually, these long paths are enclosed in vacuum pipes to prevent further atmospheric turbulence since their routes are close to the ground, where turbulence would be greatest. Where the paths change direction, mirror groups are used rather than single mirrors in order to preserve polarization.
- In contrast to the Michelson stellar interferometer, where the whole interferometer was pointed at the star and the path difference between the two interfering waves was always close to zero, the telescopes are now fixed at ground level, resulting in large path differences which change with time. These have to be compensated by 'path length equalizers', which are long optical benches with a moving retro-reflector that add a controlled and continuously changing path length to the beam from each telescope, so that the total paths from star to interferometer via each telescope are equal. These path-length equalizers need to be almost as long as the maximum baseline (see Fig. 11.23).
- Interference between the beams from the telescopes is carried out by a system that allows each beam to interfere with each other beam. This is either built on an optical table, using conventional beamsplitters and mirrors, or uses integrated-optics devices built on a chip (Fig. 11.24). The interference fringes are measured either by sensitive point detectors or by imaging CCDs. The optics may include filters or dispersive units which limit the bandwidth in order to improve fringe contrast and to make simultaneous measurements in different wavelength regions. When there are three or more telescopes operating simultaneously, the phase of γ can be measured using phase closure.
- Each optical path includes a length-modulating mirror which is used to stabilize the fringe phase via a feed-back circuit, so that the fringes are stable

[9] One interferometer, ISI, which works at 11 μm, uses heterodyning with a CO_2 laser and is more similar in concept to a radio interferometer; see Box 11.2.

Figure 11.23
Photograph of the path-length equalizer at CHARA (Georgia Institute of Technology).

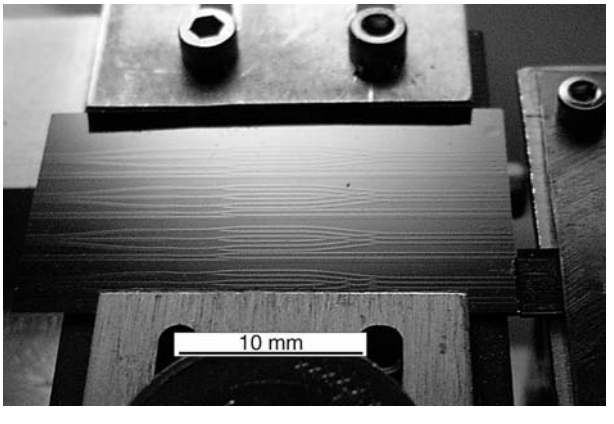

Figure 11.24
An integrated-optics beam combiner for three telescope inputs (IONIC). Contrast the size of this item with the path-length equalizer! (Photograph courtesy of Alain Delboulbe)

over long times and their contrast and phase can be accurately determined. The modulator is often a component of the retro-reflector in the path-length corrector. When the fringes are measured by point detectors, the modulating mirror is used to sweep the path length through a few wavelengths in order to measure the fringe profile.

The achievements of high-resolution stellar interferometry include accurate measurements of stellar dimensions, images of the faces of distant stars and measurements of their atmospheres, and studies of the dynamics of double and triple star systems. The future hopes include visualization of extra-solar planetary systems.

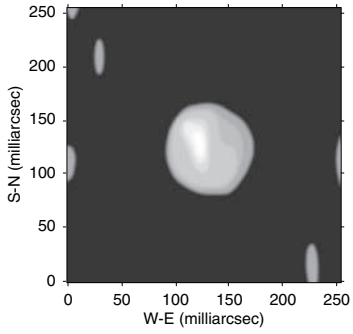

Figure 11.25
Image of Betelgeuse made by the Cambridge Optical Aperture Synthesis Telescope (COAST) at 782 nm. (Haniff *et al.* (2004))

Box 11.2 The diameter and face of Betelgeuse

The supergiant star Betelgeuse (α-Ori), the reddish left shoulder and brightest star in the Orion constellation, has been used as a 'test case' for stellar interferometry of many types at several wavelengths. We only mention the optics here, avoiding a discussion of the astrophysical consequences of the observations! Betelgeuse is sufficiently close to us for its distance to be determined by parallax as 430 light-years, so that angular coordinates can be converted to linear coordinates on the star. The diameter of Betelgeuse was originally measured by Michelson in 1921 as 0.047 arcsec at about 550 nm wavelength to confirm a theoretical estimate by Eddington, which was 0.051 arcsec. Since that time, the star has been measured and imaged by many instruments, at wavelengths from 7 mm down to 370 nm. There are determinations made by five different interferometers, lunar occultation (the time taken for the star to disappear when intersected by the Moon's edge) and aperture masking (Box 11.1). Moreover, images of its surface have been created and indicate the existence of varying hot spots that would bias the apparent diameter downwards (Fig. 11.25).

The measured diameters vary with wavelength in a fairly smooth manner, as would be expected of a star with an atmosphere, where different wavelengths sample different atomic or molecular components. What is more surprising is that the diameter at a constant infra-red wavelength appears to be falling monotonically at quite a large rate amounting to 15% in the last 15 years. Detailed measurements were made by the Berkeley Infra-red Spatial Interferometer (ISI) which works by combining the signals from three 1.65 m telescopes, whose positions can be changed, after their light has been heterodyned with light from a stabilized carbon dioxide laser at 11.15 μm. The diameter measured in 1993 at 11.15 μm was 0.0560 ± 0.0010 arcsec, which had fallen significantly to 0.0530 ± 0.0003 arcsec in 2000 and to 0.0480 ± 0.0008 arcsec in 2009 (Townes *et al.* (2009)).

Chapter summary

In this chapter we studied the classical theory of coherence, and saw some of its applications to spectroscopy and astronomy. We learnt:

- About the difference between real waves and the ideal monochromatic wave from a point source;
- How the spectral width of a quasi-monochromatic source results in phase and intensity fluctuations in the emitted wave-form;
- How the angular size of the source results in phase and intensity fluctuations in the wavefront;
- How to express these fluctuations in terms of a complex coherence function which relates the signals at two points that are separated in time or space;
- How to measure the coherence function by using interferometry;
- That the spectrum of the source is the Fourier transform of the temporal coherence function (Wiener–Khinchin theorem), leading to the technique of Fourier spectroscopy;
- That the source irradiance distribution is the Fourier transform of the spatial coherence function (van Cittert–Zernike theorem);
- How this relationship is used in radio and optical aperture synthesis to create very highly resolved astronomical images, using a small number of widely distributed moveable telescopes.

Problems

11.1. Estimate the Doppler and collision linewidths of emission from H_2O molecules at $\lambda = 0.5\,\mu m$, at 300 K and atmospheric pressure. Assume the collision cross-section to be the same as the geometrical size of the molecule.

11.2. Monochromatic light is scattered at 90° from a cell containing 10^{-16} g particles in suspension at 300 K. Estimate the coherence time and linewidth of the scattered light.

11.3. A laser beam is spatially filtered by focusing it through a pinhole, to give it a smooth intensity profile across the wavefront (spatial filter).

Figure 11.26
Fourier interferogram.

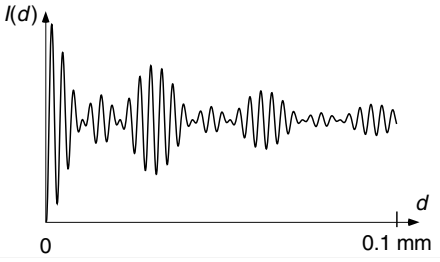

The laser beam has a Gaussian profile (with the addition of noise) with $\sigma = 1$ mm, and is focused by a $\times 50$ microscope objective having focal length 5 mm. What size of pinhole would be suitable to transmit a homogeneous beam? What focal length lens will then convert it to a parallel beam with diameter 10 mm? What would be the effect of using too large or too small a pinhole?

11.4. A Fourier transform spectrometer gives an interferogram, the positive half of which is shown in Fig. 11.26. What qualitative deduction can you make about the source spectrum?

11.5. In asymmetric Fourier transform spectroscopy, one light beam alone travels through a transparent dispersive medium, before returning to the beamsplitter. From the full interferogram (both negative and positive d), both the absorption spectrum and the dispersion can be deduced. Write a general formula for the interferogram in such a case. Consider the following examples, by deducing the interferogram and then showing how its properties are related to those of the sample. Assume quasi-monochromatic light with centre wavenumber k_0.
(a) A transparent slab of material with thickness D and refractive index $n(k) = n_0 + \beta(k - k_0)$.
(b) A similar slab with refractive index $n(k) = n_0 + \gamma(k - k_0)^2$.

11.6. The spectrum of a light source is $J(\omega) = \delta(\omega - \omega_1) + \delta(\omega - \omega_2)$. Discuss the output spectra obtained from a Fourier spectrometer as a function of $d_{\max}$, and the improvement obtained when the observed interferogram $I - I_M(d/c)$ is multiplied by an 'apodizing function' of the form $\cos(d\pi/2d_{\max})$ before being transformed. How is the resolution limit affected by the apodization?

11.7. When two light waves of equal intensity interfere, the visibility of the interference fringes is equal to the degree of coherence (11.31). Derive an equivalent relationship when the two interfering waves have differing intensities I_1 and I_2.

Figure 11.27

Lloyd's mirror with two incoherent sources.

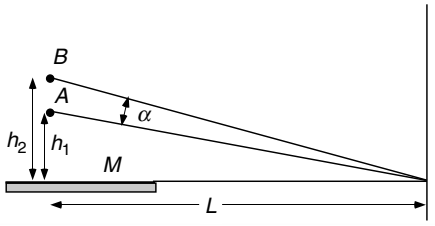

11.8. Calculate the spatial coherence function in the plane of a table illuminated by a standard fluorescent tube at a height of 10 m. Assume monochromatic light.

11.9. Two incoherently illuminated points sources A and B of the same wavelength are situated on a vertical line at heights h_1 and h_2 above the plane surface of a metal mirror M (Fig. 11.27). The interference pattern is observed on a screen at distance L. What is seen? Use this as a model to explain the idea of the coherence area resulting from an extended source AB, which has an angular size α. (Assume all angles to be small.)

11.10. A strange star consists of a laser with a long coherence time of the order of seconds. Why would it not be possible to measure its diameter with a Brown–Twiss interferometer, but only with a Michelson stellar interferometer?

11.11. Prove (11.60), that the intensity correlation coefficient $c(\tau) = 1 + |\gamma(\tau)|^2$, by evaluating $\gamma(\tau)$ in terms of the model of §11.1.2. (Take care how you calculate averages!)

11.12. Show that the real quasi-monochromatic field $E(t)$ of frequency ω_0 can be represented, for the purpose of calculating γ, by the associated complex field $E(t) + \mathrm{i}E(t - \pi/2\omega_0)$.

11.13. An aperture-synthesis array consists of three telescopes at the corners of a triangle of sides 30, 40 and 50 m, where the 40 m arm is N–S. It works at a wavelength 1 μm. It is situated at 60° latitude and observes a star 30° from the Earth's axis. Find the point spread function for this system. Assume observations can be made for 24 hours each day.

11.14. A double star consists of two component stars with angular diameters α and β, separated by angle θ. The stars have the same temperature. Determine $\gamma(k_0 x)$ along an axis in the plane containing the two stars. What information would be necessary in order to determine the

orientation of the doublet, i.e. which star is at greater x, and how can this information be obtained?

11.15. Show that the field of view of an aperture-synthesis system is determined by the *shortest* baseline used in the array. To do this, consider the signal received from two point sources, when the angular distance between them becomes large. (This is essentially the reason that aperture synthesis is not an effective tool for extended sources.)

References

Bell, R. J. (1972), *Introductory Fourier Transform Spectroscopy*, New York: Academic Press.

Brown, R. H. (1974), *The Intensity Interferometer*, London: Taylor and Francis.

Brown, R. H. and Twiss, J. Q. (1956), Correlations between photons in two beams of light, *Nature* **177**, 27.

Brown, R. H., Davis, J. and Allen, L. R. (1974), The angular diameters of 32 stars, *Mon. Not. R. Astron. Soc*. **167**, 121.

Connes, J. and Connes, P. (1966), Near-infrared planetary spectra by Fourier spectroscopy, *J. Opt. Soc. Am*. **56**, 896.

Davis, J. and Tango, W. (1986), New determination of the angular diameter of Sirius, *Nature* **323**, 234.

Foot, J. C. (1991), Laser cooling and trapping of atoms, *Contemp. Phys*. **32**, 369.

Hale, D. D. S., Bester, M., Danchi, W. C. *et al*. (2000), The Berkeley infra-red spatial interferometer, *Astrophys. J*. **537**, 998.

Haniff, C. A. *et al*. (2004), COAST: recent technology and developments, in *New Frontiers in Stellar Interferometry*, ed. W. A. Traub, Proc. SPIE **5491**, 511.

Hardy, J. W. (1998), *Adaptive Optics for Astronomical Telescopes*, New York: Oxford University Press.

Haroche, S. and Kleppner, D. (1989), Cavity quantum electrodynamics, *Physics Today* **42**, 24.

Jeans, J. H. (1982), *An Introduction to the Kinetic Theory of Gases*, Cambridge: Cambridge University Press.

Kellerman, K. I. and Thompson, A. R. (1988), Very Long Baseline Array, *Sci. Am*., January, 44.

Labeyrie, A., Lipson, S. G. and Nisenson, P. (2006), *An Introduction to Optical Stellar Interferometry*, Cambridge: Cambridge University Press.

Landau, L. D. and Lifshitz, E. M. (1980), *Statistical Physics*, Oxford: Pergamon.

Michelson, A. A. (1927, 1995), *Studies in Optics*, University of Chicago Press, reprinted by Dover Publications, New York.

Parker, T. J. (1990), Dispersive Fourier transform spectroscopy, *Contemp. Phys*. **31**, 335.

Rohlfs, K. (1996), *Tools of Radio Astronomy*, 2nd edn., Berlin: Springer.

Thompson, A. R. (2001), *Interferometry and Synthesis in Radio Astronomy*, 2nd edn., New York: Wiley.

Townes, C. H., Wishnow, E. H., Hale, D. D. S. and Walp, B. (2009), A systematic change with time in the size of Betelgeuse, *Astrophys. J. Lett*. **697**, L127.

Tuthill, P. G., Monnier, J. D., Danchi, W. C. and Lopez, B. (2000), Smoke signals from IRC+10216, *Astrophys. J*. **543**, 284.

12 Image formation

Most optical systems are used to create images: eyes, cameras, microscopes, telescopes, for example. These image-forming instruments use lenses or mirrors whose properties, in terms of geometrical optics, have already been discussed in Chapter 3. But geometrical optics gives us no idea of any limitations of the capabilities of such instruments and indeed, until the work of Ernst Abbe in 1873, microscopists thought that spatial resolution was only limited by their expertise in grinding and polishing lenses. Abbe showed that the basic scale is the wavelength of light, which now seems obvious. The relationship between geometrical and physical optics is like that between classical and quantum (wave) mechanics; although classical mechanics predicts no basic limitation to measurement accuracy, it arises in quantum mechanics in the form of the Heisenberg uncertainty principle.

This chapter describes the way in which physical optics is used to describe image formation by a single lens (and by extension, any optical system). The theory is based on Fraunhofer diffraction (Chapter 8) and coherence (Chapter 11) and leads naturally both to an understanding of the limits to image quality and to ways of extending them. We shall learn:

- how Abbe described optical imaging in terms of wave interference;
- that imaging can be formulated as a double process of diffraction;
- what are the basic limits to spatial resolution;
- how microscopes are constructed to achieve these limits;
- how the resolution properties of an imaging system can be described quantitatively;
- methods by which microscopes can be designed to show information, such as phase changes, which are normally invisible;
- about holography, in which the two diffraction processes implicit in imaging are separated in time, thereby allowing the storage and reconstruction of three-dimensional images;
- how, today, Abbe's resolution limit can be surpassed, and what is the price that has to be paid for such 'super-resolution';
- how diffraction ideas have also been used to overcome the resolution limit of astronomical telescopes imposed by the Earth's atmosphere.

The statement of unlimited resolution cannot yet be extended to non-fluorescent, externally illuminated objects.

You can see from this summary that there are two main directions to the chapter, which we shall now briefly illustrate, before going on to the details. The

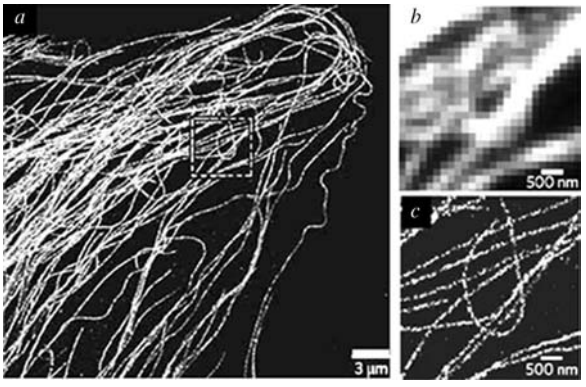

Figure 12.1

A STORM image of microtubules (§12.6.5): (*a*) full-field (scale bar 3 μm), (*b*) bright-field image of the region of (*a*) denoted by the square and (*c*) STORM image of the same region, scale bar 500 nm. (Images courtesy of X. Zhuang; Zhuang (2009))

Figure 12.2

Comparison of images of a live cell taken by (*a*) bright-field, (*b*) Zernike phase-contrast and (*c*) Nomarski DIC techniques, in a Zeiss Axio-observer microscope. (Images courtesy of Kinneret Keren)

first consideration is **resolution**; what is the smallest entity that we can see in a microscope or telescope? The diffraction theory of imaging gives clear answers to these questions; in the case of the microscope, half a wavelength of light – about 200 nm – is the limit. So, naturally, the challenge is to do better than this! In recent years several imaging methods have been devised that achieve a resolution of a small fraction of the wavelength, because of new ideas that have sprung from our understanding of the physical optics of imaging. Today we can show that, **given sufficient light, images of fluorescent objects can now be made with almost unlimited spatial resolution**, and a recent example is shown in Fig. 12.1. The second question raised in the chapter is how to visualize transparent objects in which optical phase retardation, rather than absorption, is dominant, as in many biological objects. This question has been answered elegantly by several methods, each emphasizing a different aspect of the phase structure, and two examples are shown in Fig. 12.2.

12.1 The diffraction theory of image formation

In 1873 Abbe proposed a rather intuitive method of describing the image of a periodic object, which brought out clearly the limit to resolution and its relationship to the wavelength. We shall first describe his physically intuitive method, and later formalize it in terms of a double Fourier transform.

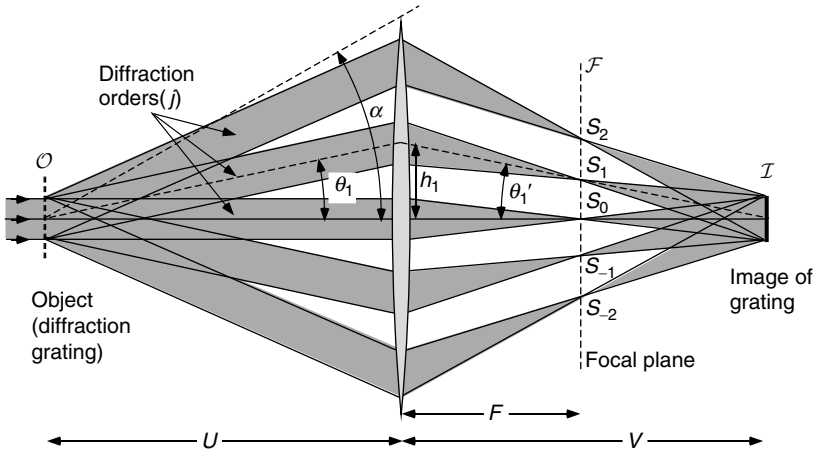

Figure 12.3

Formation of the image of a diffraction grating. Five orders of diffraction j are shown, producing five foci S_j in the plane $\mathcal{F}$. The angular semi-aperture of the lens is α.

One outcome of this theory is to suggest various methods of improving images, in particular to create contrast from phase variations that are normally invisible.

12.1.1 Abbe theory: the image of an infinite periodic object

We have seen in §8.5.4 that if parallel light falls normally upon a diffraction grating several orders of diffraction are produced (Fig. 12.3). Let us place the grating in plane $\mathcal{O}$ and form its image using the diffracted light. Each order m is a plane wave, and the set of plane waves can be refracted by a lens so that they converge individually to a set of points S_j in the focal plane $\mathcal{F}$ of the lens and then continue so that they all overlap again in the plane $\mathcal{I}$. Here they form a complicated interference pattern; this pattern is the image.

The process of image formation can be described as two Fraunhofer diffraction processes occurring sequentially.

The advantage of taking a diffraction grating as an object is that the process of image formation can easily be seen to consist of two distinct stages. First, we have the stage between $\mathcal{O}$ and $\mathcal{F}$. In the latter plane we have produced the Fraunhofer diffraction pattern of the object. Second, we have the stage between $\mathcal{F}$ and $\mathcal{I}$. The orders S_2, S_1,..., S_{-2} behave like a set of equally spaced point sources and the image is their interference pattern. Thus the process of image formation appears to consist of two diffraction processes, applied sequentially.

Figure 12.5 shows an imaging system where the description as a double diffraction process is very clear.

The second diffraction process in this example can also be analyzed without difficulty. Each pair of orders S_j and S_{-j} produces Young's fringes in the plane $\mathcal{I}$. If the object grating has spacing d, the order S_j appears at angle θ_j given, for small angles, by

$$\theta_j \approx \sin\theta_j = j\lambda/d. \tag{12.1}$$

The small-angle approximation will be seen in §12.1.2 to be unnecessary. By simple geometry one can see from Fig. 12.3 that

$$\theta_j \approx \tan\theta_j = h_j/U, \tag{12.2}$$

$$\theta_j' \approx \tan\theta_j' = h_j/V, \tag{12.3}$$

and so

$$\theta'_j \approx U\theta_j/V. \tag{12.4}$$

The waves from the first orders, S_1 and S_{-1}, converge on the image at angles $\pm\theta'_1$ and thus form periodic fringes with spacing

$$d' = \lambda/\sin\theta'_1 \approx \lambda V/\theta_1 U = Vd/U. \tag{12.5}$$

The greater the extent of the Fraunhofer diffraction accessed by the imaging lens, the better the resolution. This is achieved by using as large an angular aperture as possible.

Thus a magnified image has been produced; the magnification is $M = V/U$. Fringes from the higher orders produce harmonics of this periodic pattern, with spacings d'/j, and contribute to determining the detailed structure of the image. **The finest detail observable in the image is determined by the highest order of diffraction that is actually transmitted by the lens.**

But if even the first order is outside the cone of angles α transmitted by the lens, i.e. $\theta_1 > \alpha$, only the zero order contributes to the image and the periodicity is absent. Thus the spacing d is not resolved if $\sin\theta_1 = \lambda/d < \sin\alpha$, or, for resolution,

$$d_{\min} = \frac{\lambda}{\sin\alpha}. \tag{12.6}$$

The zero order contributes a constant amplitude. This zero-order term is of crucial importance. Without it, the interference pattern of the first orders would appear to have half the period of the image, because we observe intensity, and not amplitude; the function $\sin^2 x$ has half the period of $\sin x$ (see Fig. 12.6(f)). However, the addition of the constant restores the correct periodicity to the intensity, since $(c + \sin x)^2 = c^2 + 2c\sin x + \sin^2 x$, which has the period of $\sin x$.

Abbe's argument applies to an infinite periodic object, and may not be exact if the object is finite in extent: see §12.6.7.

The use of an infinite grating as an object has, of course, oversimplified the problem. If we had used a finite grating, there would be subsidiary orders (§8.5.3) which also transmit information. The simple result above therefore needs some modification if the object is more complicated, but it expresses the essence of the resolution limit.

12.1.2 The Abbe sine condition

Although the last section might suggest that a faithful image would be built up only if the angles of diffraction were kept small, Abbe realized that larger angles could be employed if the ratio $\sin\theta/\sin\theta'$ rather than θ/θ' were the same for all values of θ. If we had, instead of (12.4), the equation

Figure 12.4

Ray diagram for the demonstration of the image–object relationship. The coordinate $\xi \equiv uF/k_0$.

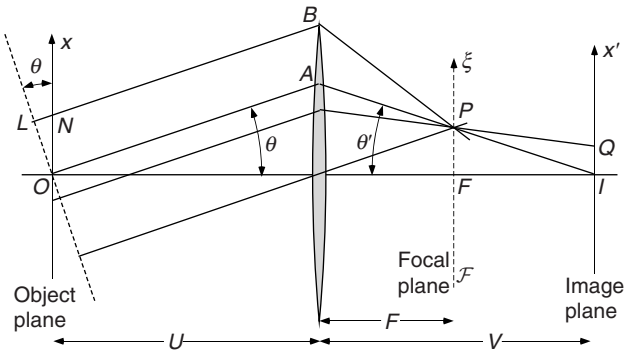

$$\frac{\sin\theta_j}{\sin\theta_j'} = M, \tag{12.7}$$

we should then have the period of the fringes in the image

$$d_j' = \lambda/\sin\theta_j' = M\lambda/\sin\theta_j = Md_j. \tag{12.8}$$

The Abbe sine condition is not satisfied by a symmetrical thin lens, for which the tangents, not the sines, of the angles have a constant ratio.

The harmonics would then have exactly the right periods to fit the fundamental d_1'; and the image would be perfect. The important aplanatic lens obeying (12.7) was described in §3.8, and forms the basis of high-power microscope objectives.[1] The Abbe sine condition does *not* state that $\sin\theta/\sin\theta'$ is a constant in any particular imaging system, but *requires* that this condition be met if the system is not to produce aberrations when large angles θ and θ' are used.

12.1.3 Image formation formally described as a double process of diffraction

In §12.1.1 we introduced, in a qualitative manner, the idea that image formation can be considered as a double process of diffraction, and in §12.1.2 we saw the Abbe sine condition to be necessary for its exact realization. In this section we shall formalize the approach mathematically in one object dimension. There is no particular difficulty in the extension to two dimensions.

In the back focal plane of the imaging lens, the amplitude is given by the Fourier transform of the object, multiplied by a geometrical phase factor.

The analysis is based on the scalar-wave theory of diffraction, and assumes an object uniformly and coherently illuminated by a plane wave. The wave leaving the object is represented by the complex function $f(x)$ (multiplied, of course, by $e^{-i\omega_0 t}$, which is carried unchanged through all the equations, and will be ignored). The object is imaged by a lens, such that the object and image distances are U and V; the object dimensions are small compared with U (Fig. 12.4). The amplitude of the wave reaching point P in the focal plane $\mathcal{F}$

[1] The requirement $\sin\theta/\sin\theta' =$ constant can be deduced from purely geometrical reasoning as a requirement for the absence of spherical aberration and coma (see Kingslake (1978)) but the above argument is more physically intuitive and emphasizes its importance.

In §8.2.1 we said that the phase difference $\overline{OAP}$ is not important in observing Fraunhofer diffraction patterns. But here it is crucial in defining the conjugate planes, through Fermat's principle.

of the lens is, following the treatment and notation of §8.2 in one dimension, the Fourier transform of $f(x)$ with the phase delay appropriate to the path $\overline{OAP}$:

$$\psi(u) = \exp(\mathrm{i}k_0\overline{OAP})F(u) = \exp(\mathrm{i}k_0\overline{OAP})\int_{-\infty}^{\infty} f(x)\exp(-\mathrm{i}ux)\,\mathrm{d}x, \quad (12.9)$$

where $k_0 = 2\pi/\lambda$ and u corresponds to the point P:

$$u = k_0 \sin\theta. \quad (12.10)$$

Now the amplitude $b(x')$ at Q in the image plane can be calculated using Huygens' principle over the plane $\mathcal{F}$.[2] The optical distance from P to Q is

$$\begin{aligned}\overline{PQ} = PQ &= (PI^2 + x'^2 - 2x'PI\sin\theta')^{\frac{1}{2}} \\ &\approx PI - x'\sin\theta', \end{aligned} \quad (12.11)$$

when $x' \ll PI$. If the Abbe sine condition (12.7) is obeyed,

$$\sin\theta = M\sin\theta', \quad (12.12)$$

where M is the magnification. We therefore write, from (12.10),

$$PQ = PI - x'u/Mk_0, \quad (12.13)$$

whence the amplitude at Q is

$$\begin{aligned} b(x') &= \int_{-\infty}^{\infty} \psi(u)\exp(\mathrm{i}k_0 PQ)\,\mathrm{d}u \\ &= \int_{-\infty}^{\infty} \exp(\mathrm{i}k_0 PI)\,\psi(u)\exp(-\mathrm{i}x'u/M)\,\mathrm{d}u. \end{aligned} \quad (12.14)$$

This is the second Fourier transform in the problem. Inserting (12.9) into (12.14) we write the relationship between the image $b(x')$ and the object $f(x)$:

$$\begin{aligned} b(x') = \int_{-\infty}^{\infty} \left\{\exp[\mathrm{i}k_0(\overline{OAP} + PI)]\int_{-\infty}^{\infty} f(x)\exp(-\mathrm{i}ux)\,\mathrm{d}x\right\} \\ \times \exp(-\mathrm{i}ux'/M)\,\mathrm{d}u. \end{aligned} \quad (12.15)$$

Although this proof that imaging is an implementation of the Fourier inversion has been demonstrated for a single-element lens, it is true for any imaging system.

The combined phase factor $\exp[\mathrm{i}k_0(\overline{OAP} + PI)]$ appears at first sight to be a function of the point P, and hence of the parameter u. This is indeed true if the planes $\mathcal{O}$ and $\mathcal{I}$ are chosen arbitrarily. But if they are **conjugate** planes then **by Fermat's principle (§2.6.3) the optical path from O to I is independent of the point** P, and the factor can be written as a constant, equal to $\exp(\mathrm{i}k_0\overline{OI})$, and can be taken outside the integral. We are left with the integral

$$\begin{aligned} b(x') = \exp(\mathrm{i}k_0\overline{OI})\int_{-\infty}^{\infty}\left[\int_{-\infty}^{\infty} f(x)\exp(-\mathrm{i}ux)\,\mathrm{d}x\right] \\ \times \exp(-\mathrm{i}ux'/M)\,\mathrm{d}u. \end{aligned} \quad (12.16)$$

[2] Since this involves interference of spherical waves a factor $1/r$ ought to be included, but this has no effect on the physics.

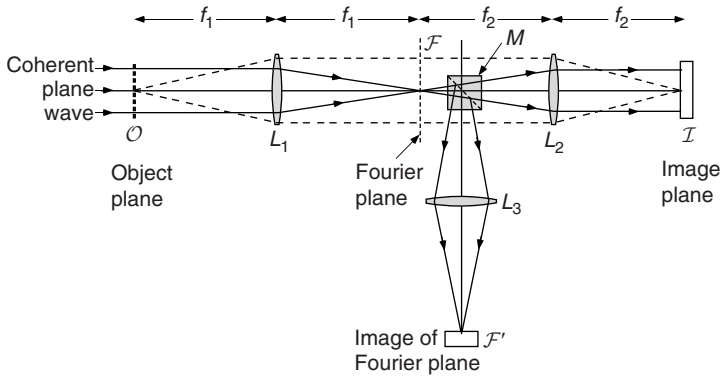

Figure 12.5 **Optical imaging system to illustrate the Abbe theory of image formation. The object $\mathcal{O}$ is illuminated by parallel coherent light from a laser source. It is imaged by the lenses L_1 and L_2 onto a distant screen $\mathcal{I}$. The beamsplitter M and lens L_3 are used to form at $\mathcal{F}'$ a separate image of the Fourier plane $\mathcal{F}$. The various spatial filtering masks are inserted in the plane $\mathcal{F}$, and $\mathcal{F}'$ and $\mathcal{I}$ are observed simultaneously (Fig. 12.6).**

The integrals are the same as those involved in the Fourier inversion theorem. From §4.6 we then have

$$b(x') = \exp(\mathrm{i}k_0\overline{OI})f(-x'/M). \tag{12.17}$$

In the terms of §3.7, a system that obeys Abbe's sine rule has no spherical aberration and coma.

This equation represents the well-known fact that the image is an inverted copy of the object, magnified by the factor M. The above result, first proved by Zernike, can be stated simply: an optical image can be represented as the Fourier transform of the Fourier transform of the object. It applies exactly only if the lens is well corrected; i.e. it obeys the Abbe sine rule and the optical path $\overline{OPI}$ is completely independent of the point P.

12.1.4 Illustrations of the diffraction theory of image formation

The imaging configuration of Fig. 12.5 is often called a '4-f' system, because the object–image distance is $2f_1 + 2f_2$.

In the previous section we have shown theoretically that, when the object is illuminated coherently, the imaging process can be considered as a double Fourier transform. We shall now describe some experiments originally carried out by Porter in 1906 which confirm this result. They are done in an imaging system, shown in Fig. 12.5, which allows the comparison of the intermediate transform in plane $\mathcal{F}$ and the final image (see also Appendix B). A transparent object mask is illuminated with a parallel coherent beam, and is imaged by a pair of converging lenses. We observe the illumination in the focal plane to be the Fraunhofer diffraction pattern of the object, and this is called the 'Fourier plane'. The image is the Fourier transform of that diffraction pattern. The first stage,

that of the formation of the Fraunhofer diffraction pattern, has been adequately illustrated in Chapter 8. To confirm that the second stage is also a Fourier transform, we can modify the transform in the focal plane by additional masks or obstacles and observe the resultant changes in the final image. Such processes are called **spatial filtering** by analogy with the corresponding process in the time domain in electrical circuits. Spatial filtering has some very important applications which will be discussed in detail in later sections.

Figure 12.6 shows experiments with an object consisting of a piece of gauze. It is two-dimensional, and is basically periodic, although there are deviations from exact periodicity as well as defects such as blocked holes. We image it in the system of Fig. 12.5. The diffraction pattern in the Fourier plane is shown in Fig. 12.6(*a*). It contains well-defined spots, corresponding to the periodic component of the gauze, and an additional light distribution surrounding each of the orders which expresses the non-periodic components. The complete image of the gauze is shown in (*b*).

We now insert various masks into the plane $\mathcal{F}$, and thereby cut out parts of the diffraction pattern. For example, if the mask transmits only orders on the horizontal axis (*c*) the image becomes a set of vertical lines (*d*); this is the object that would have given (*c*) as its diffraction pattern. Similarly, a mask that transmits only the orders $(0, \pm 1)$, $(\pm 1, 0)$, (*e*), gives us a different gauze (*f*). But the irregularities are the same, because they contribute to the diffraction pattern at all points. The zero order alone, together with the region half-way out to the next orders, (*g*), gives us an image in which no gauze is visible, but only the irregularities – particularly the blocked holes. Finally, a small region of the diffraction pattern (*i*) remote from the centre emphasizes a different aspect of the deviations from exact periodicity, (*j*).

12.1.5 The phase problem

A question that is always asked at this point refers to the possibility of separating the two stages of the image-forming process. Suppose we were to photograph the diffraction pattern in the focal plane and in a subsequent experiment illuminate the photograph with coherent light and observe its diffraction pattern. Should we not have produced the diffraction pattern of the diffraction pattern and have reconstructed the image? The flaw in the argument concerns **the phases of the diffraction pattern**. The illumination $\psi(u)$ is a complex quantity containing both amplitudes and phases. Photography records only the intensity $|\psi(u)|^2$ and the phase is lost. A second diffraction process as suggested above would be carried out in ignorance of the phases, and therefore would be unlikely to give the right answer. In fact, the second process would assume all the phases to be zero, and would indeed give the correct image if this were so.

The phase of the transform is just as important as its amplitude in representing the characteristics of the object, but cannot be recorded as easily.

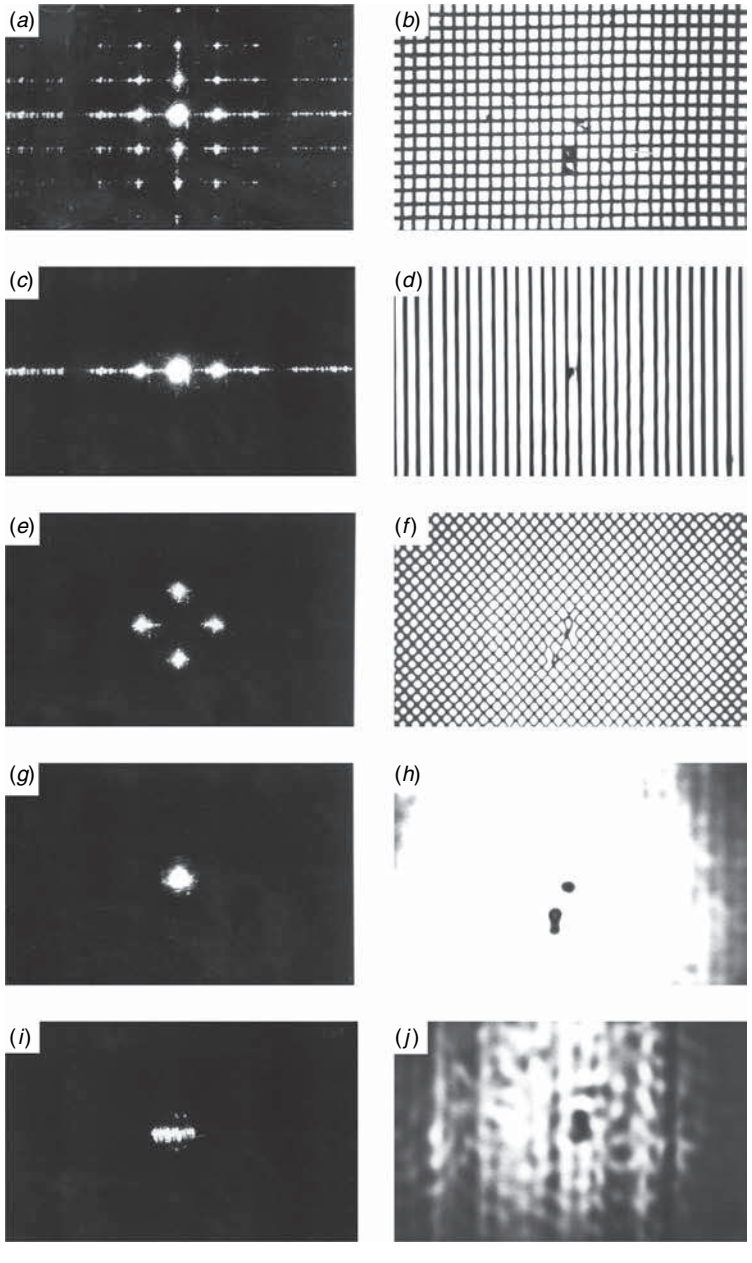

Figure 12.6

Illustrating the Abbe theory of image formation with the aid of the apparatus of Fig. 12.5. On the left are the selected portions of the diffraction pattern of a piece of gauze, and on the right the corresponding images.

Solving the phase problem has been a major goal since the 1930s. No complete solution exists, but solutions now exist in many practical cases.

The above paragraph describes the situation in the crystallographic analysis of materials using X-ray, neutron or electron waves. The diffraction pattern *intensity* can be recorded, but in order to reconstruct the object, the phases of the diffracted waves have to be determined. The problem is called the **phase problem**. Several approaches to its solution are possible. One is to derive the phases intelligently from information in the diffraction pattern, using some prior knowledge of the object. Another, called 'phase retrieval' (§8.8), uses

analytical relationships between the amplitude and phase in the diffraction patterns of objects with well-defined constraints, and is the basis of present-day crystallography.

A third approach is to add an overwhelmingly strong coherent wave to all the diffracted waves. The result is a diffraction pattern in which all the phases are equal to, or very close to, that of the strong wave; then the diffraction pattern can be retransformed to recover the object. Ways of doing this are various. In optics, we add the wave via a beamsplitter, and the resulting technique is called **holography** (§12.5), for which Gabor received the Nobel prize in 1971. In crystallography, a strongly scattering atom is added (or may naturally exist) at the same position in each unit cell of the crystal, which enables the crystal structure to be determined. This **heavy-atom method** has been used to elucidate the structures of many proteins, including haemoglobin and myoglobin by Perutz and Kendrew, for which they received the Nobel prize in 1962, and of vitamin B12 by Hodgkin for which she received the prize in 1964.

12.2 The resolution limit of optical instruments

The light that forms the image in an optical system is limited angularly by the aperture stop (§3.3.2). In this section we shall use the Abbe theory of image formation in order to understand how the size of the aperture stop and the coherence of the illumination affect the characteristics of the image, and in particular how they limit the resolution attainable. It will appear that the limits of perfect coherence and perfect incoherence of the illumination can be treated fairly clearly; the intermediate case of partially coherent illumination is complicated and the results can only be indicated in rather general terms.

12.2.1 Rayleigh's resolution criterion for an incoherent object

The Rayleigh criterion is independent of the relative brightness of the neighbouring points.

The simplest and best-known resolution criterion is that due to Rayleigh and applies to the case of a self-luminous or incoherently illuminated object; it is usually applied to an astronomical telescope, because stars certainly fulfil the requirements of self-luminosity and incoherence; but it applies equally well to a microscope observing, for example, a fluorescent object (§12.2.4).

If we consider a single point on a distant object, we have seen in §7.1.4 that we observe in the image plane the Fraunhofer diffraction pattern of the aperture stop, on a scale determined by the image distance. This diffraction pattern is called the **point spread function**. An extended object can be considered as a collection of such points, and each one produces a similar point spread function

in the image plane; because the sources are incoherent we add *intensities* of the various patterns to get the final image. **The image is therefore the convolution of the object intensity and the point spread function**.

The **Rayleigh resolution criterion** arises when we consider two neighbouring points on the object, separated by a small angle. If the aperture has diameter D, its diffraction pattern, expressed as a function of the angle θ, has normalized intensity (§8.3.4) with $u = k_0 \sin\theta$:

$$I(\theta) = \left[2J_1\left(\frac{1}{2}k_0 D\sin\theta\right) \Big/ \left(\frac{1}{2}k_0 D\sin\theta\right)\right]^2. \tag{12.18}$$

Rayleigh considered two points on the object to be distinguishable if the central maximum of one lies outside the first minimum of the other. Now the function (12.18) has its first zero at that of $J_1(x)$, at $x = 3.83$. Then

$$\frac{1}{2}k_0 D\sin\theta_1 = \pi D\sin\theta_1/\lambda = 3.83. \tag{12.19}$$

The angle θ_1 is the minimum angular separation of resolvable incoherent sources; since $\theta_1 \ll 1$ the resolution limit is thus

$$\theta_{\min} = \theta_1 = 3.83\lambda/\pi D = 1.22\lambda/D \quad \text{(Rayleigh)}. \tag{12.20}$$

Notice that only the *angular* separation of the sources enters the result.[3] When an optical system can indeed resolve two points separated by this angle, it is called **diffraction-limited**.

12.2.2 The Sparrow resolution criterion

The Sparrow condition for resolution does not require the point spread functions to have zeros, but depends on the relative intensity of the points: see Problem 12.20.

Rayleigh's is the best-known resolution criterion, but fails if the diffraction pattern has no well-defined zeros, or these are far from the central maximum. An alternative criterion, which corresponds well with what the human eye can resolve because of its superb sensitivity to intensity *differences*, is the **Sparrow criterion**, which we have already met in the context of spectral resolution in §9.5.2. This considers two point images to be resolved if their joint intensity function has a minimum on the line joining their centres. If the two points have equal intensities, the Sparrow criterion then indicates $\theta_{\min}$ when

$$\left(\frac{\mathrm{d}^2 I}{\mathrm{d}\theta^2}\right)_{\theta\,=\,\theta_{\min}/2} = 0. \tag{12.21}$$

[3] When two equally intense points are separated by this angle, the intensity measured along the line joining them has a minimum half-way between them of value $8/\pi^2 = 0.81$ times the maximum at each point. The Rayleigh criterion is often interpreted under other conditions as the separation that gives a minimum with this value between the two maxima. We shall not use this interpretation here, preferring that of Sparrow as an alternative.

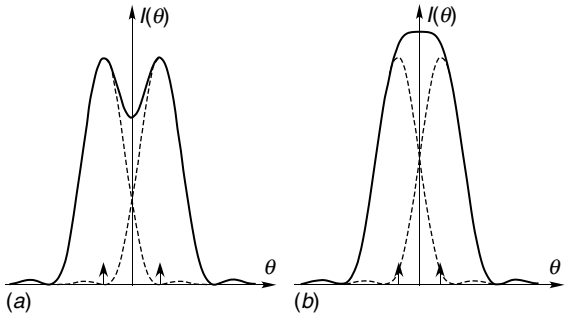

Figure 12.7
Addition of the images of two incoherent point sources. The broken lines show the individual intensity curves and the full line is their sum. The arrows show the positions of the geometrical images: (*a*) Rayleigh and (*b*) Sparrow separations.

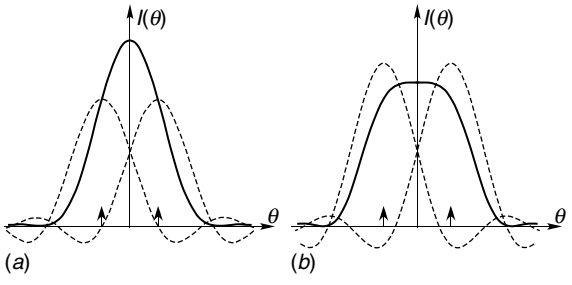

Figure 12.8
Addition of the images of two pinholes coherently illuminated with the same phase. The broken lines show the amplitude curves and the full line the square of their sum. The arrows show the positions of the geometrical images: (*a*) Rayleigh and (*b*) Sparrow separations.

Without entering into details of the differentiation of Bessel functions, this gives

$$\theta_{\min} = 0.95\lambda/D \qquad \text{(Sparrow)}. \tag{12.22}$$

12.2.3 Resolution of a coherently illuminated object

Next we consider the resolution problem when the sources are coherent. If the object consists of two points emitting with the same phase, we must add the *amplitudes* of their point spread functions:

$$A(\theta) = J_1\left(\frac{1}{2}k_0 D\sin\theta\right) \Big/ \left(\frac{1}{2}k_0 D\sin\theta\right). \tag{12.23}$$

The Rayleigh criterion gives the same result as (12.20) because the zeros of the point spread functions have not changed; but the points are not resolved. On the other hand, the Sparrow criterion gives $\theta_{\min} = 1.46\lambda/D$. The reason that the Sparrow criterion gives here a larger $\theta_{\min}$ is illustrated by Figs. 12.7 and 12.8. We show first the intensity as a function of position on a line through the images of two *incoherent* sources at $\theta = 0$ and $\theta = \theta_{\min}$ for the two cases (12.20) and (12.22). The function shown is $I(\theta) + I(\theta - \theta_{\min})$. The Rayleigh resolution is clearly more than adequate. We then look at the equivalent situation

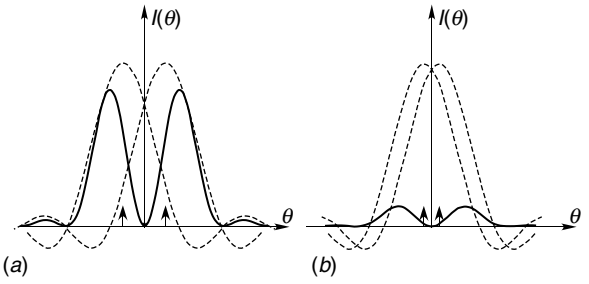

Figure 12.9
Addition of the images of two pinholes coherently illuminated with opposite phases. The broken lines show the amplitude curves and the full line the square of their *difference*. The arrows show the positions of the geometrical images; (*a*) and (*b*) show two different separations, both of which appear to be resolved, but the peaks have little relation to the geometrical positions of the images, shown by arrows.

when the sources are coherent; we add amplitudes *before* squaring to find the intensity, $[A(\theta) + A(\theta - \theta_{\min})]^2$, which is illustrated in Fig. 12.8 for the two criteria. Clearly the Rayleigh separation is inadequate.

12.2.4 Imaging resolution and coherence

The argument in the previous section would indicate that incoherent illumination results in better resolution. But this is not always true; we assumed a particular phase relation between the sources in order to demonstrate the result. If the two sources had phases differing by π, we should have written the joint intensity as $[A(\theta)$ *minus* $A(\theta - \theta_{\min})]^2$, which always has minimum intensity at the mid-point, *however close the sources*, as shown in Fig. 12.9. One should notice in particular in this figure that the separation of the two coherent antiphase images is quite different from their true separation; it is actually determined by the aperture diameter! See Problem 12.6. Moreover, as the sources become closer, the image gets weaker because of destructive interference. An application of antiphase imaging is the use of **phase-shift masks** in photo-lithography of microelectronic devices to improve the density of closely separated units on a complex mask. Alternate units are covered with a transparent film which introduces the necessary π phase change to ensure that a dark line appears between their images (Levenson (1993)). However, *in general* it can indeed be said that incoherent illumination results in the better resolution. Figure 12.10, in which images of a pair of pinholes have been formed under various coherence conditions, demonstrates the above argument.

Coherent illumination of an object may introduce serious artifacts into the image. In most cases a 'speckled' image is obtained because of interference between neighbouring parts.

An important example of incoherent imaging is **fluorescence microscopy**. In such a microscope, a laser or other narrow-band light source serves to excite atomic transitions in the atoms of the object, and the excited atom first decays to a metastable state, from which it subsequently decays back to the ground state with incoherent emission of light at a wavelength longer than that of the excitation. Fluorescence microscopy is very important in analytical biological imaging, because the fluorescing material (tag) can be attached selectively to specific chemically defined parts of a complex body and thus provide a

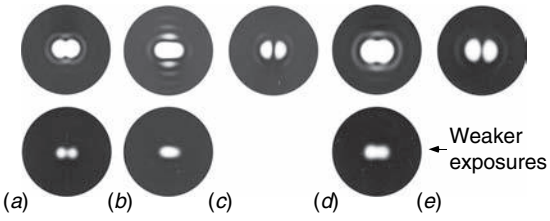

Figure 12.10

Comparison between coherent and incoherent imaging of a pair of pinholes. In (*a*)–(*c*) the aperture is chosen so that the pinhole separation corresponds to the Rayleigh limit, with illumination (*a*) incoherent, (*b*) coherent (same phase), (*c*) coherent (antiphase). In (*d*) and (*e*) the same pair of pinholes is imaged through an aperture for which they are at the Sparrow limit: (*d*) incoherent and (*e*) coherent (antiphase) illumination. The lower row shows weaker exposures of corresponding images in the upper row.

functional image. For developing and understanding the most important of these tags, green fluorescent protein, Shimomura, Chalfie and Tsien were awarded the Nobel prize in 2008. Many fluorescent tags with specific binding chemistry are now commercially available. The mechanism of fluorescence is discussed in more detail in §14.8, but for the present discussion we emphasize that the imaging mechanism is completely incoherent. As remarked earlier, in this case we find that the concept of point spread function is the better way of understanding the imaging properties of such systems. We shall discuss this approach in §12.3. In addition, incoherent emission imaging allows the limits of resolution to be extended significantly (§12.6).

12.2.5 Application of the Abbe theory to coherent resolution

Most conventional transmission or reflection microscopes work with partially coherent illumination, because of the small dimensions of the object and the practical difficulties (§12.2.7) of producing truly spatially-incoherent light. The Abbe theory discussed in §12.1.1 applies to coherent illumination and is therefore fairly appropriate to a discussion of resolution by a conventional microscope.

Abbe theory applies also to transmission electron microscopes. Electron lenses use electric and magnetic fields for focusing, and the largest NA is about 0.04.

We therefore return to transmission or reflection microscopes and to the model of a periodic coherently illuminated object. The resolution that can be obtained with a given lens or imaging system is, as discussed in §12.1.1, limited by the highest order of diffraction that the finite aperture of the lens will admit. If the object has period d, the first order appears at angle θ given by

$$\sin\theta_1 = \lambda/d. \tag{12.24}$$

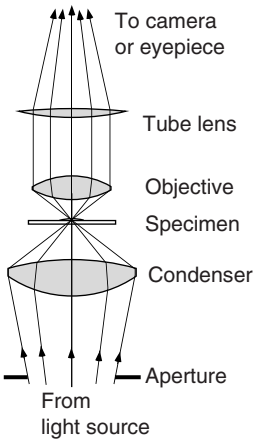

Figure 12.11

Conical illumination of a specimen to get the highest microscopic resolution.

In order to image an object with such a period, the angular semi-aperture α of the lens must be greater than θ_1. Thus the smallest period that can be imaged is given by (12.6)

$$d_{\min} = \lambda / \sin\alpha. \tag{12.25}$$

We now recall from §3.8 the possible immersion of the object in a medium of refractive index n, where the wavelength is λ/n, and to write $d_{\min}$ in terms of the **numerical aperture** $\mathrm{NA} \equiv n\sin\alpha$;

$$d_{\min} = \lambda/n\sin\alpha = \lambda/\mathrm{NA} \tag{12.26}$$

is the coherent imaging resolution in this case.[4]

We have assumed in the above discussion that the illumination is parallel to the axis, and acceptance of the zero and two first orders is necessary to form an image with the correct period. In fact, the correct period will be imaged if the zero order and one first order alone pass through the lens. So we can improve the resolution by illuminating the object with light travelling at angle α to the axis, so that the zero order just passes through; then the condition for the first order on one side to pass through as well is that

$$d_{\min} = \frac{\lambda}{2n\sin\alpha} = \frac{\lambda}{2\,\mathrm{NA}}, \tag{12.27}$$

where we have used the result for Fraunhofer diffraction in oblique illumination from §8.2.2. **This result, called the 'Abbe resolution limit', represents the best that can be achieved with a given lens, and is the best resolution that can be achieved by conventional microscopy.** In order to implement it one needs to illuminate the object incoherently with a cone of light having semi-angle at least α, as shown in Fig. 12.11. **The resulting illumination is then an incoherent superposition of plane waves inclined at the various angles** and the limit (12.27) is achieved in all orientations.

12.2.6 Experimental illustration of coherent resolution

This theory may be illustrated by the apparatus described in Fig. 12.5. This allows us to investigate the changes that occur in an image if the optical transform is limited or modified in some way. For example, suppose that we have a general object as shown in Fig. 12.12(*b*); its transform is shown in (*a*). We then place a series of successively smaller holes over the transform, and we can then see how the image is affected. The succession of images is explained in the caption.

[4] Microscope objectives are usually labelled with two numbers: one is the magnification at a standard image distance of 200 or 250 mm, and the second is the NA. The thickness of cover glass for which aberrations are corrected is also given on high magnification objectives.

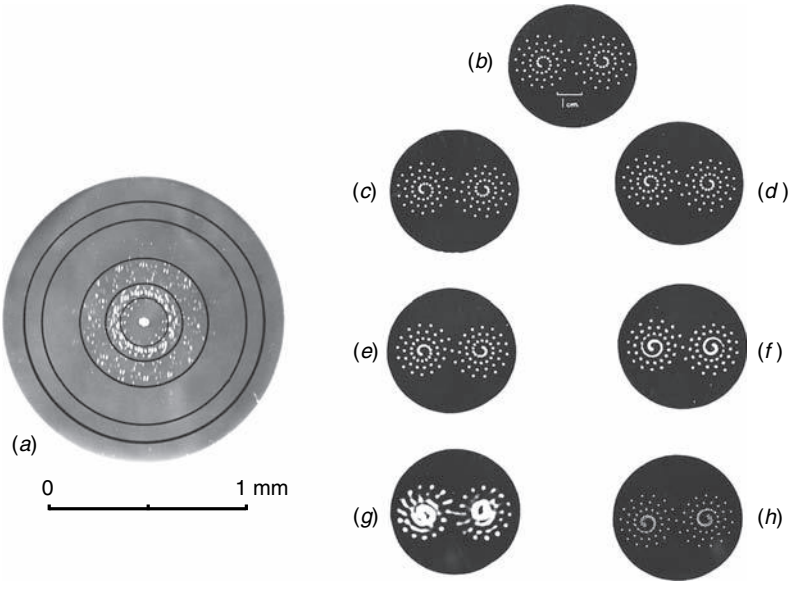

Figure 12.12 **Resolution according to the Abbe theory. (*a*) Diffraction pattern of the set of holes shown in (*b*). The circles indicate the apertures used to limit the transform. (*c*)–(*g*) Images of object shown in (*b*), with different numerical apertures. The apertures used are shown as circles superimposed on the diffraction pattern shown in (*a*). (*h*) The image formed by the part of the diffraction pattern between the second and third circles from the centre. In this case, the image is sharper than the object, but contains false detail.**

The resolution limit imposed by a finite aperture can also be considered as an application of the convolution theorem (§4.7). In a coherently illuminated system, restriction of the optical transform by a finite aperture results in a point spread function in the image plane whose *amplitude* (not intensity as in §12.2.1) must be convolved with that of the object when the image is formed. The result is, once again, a blurring of the image; but because amplitudes are involved, neighbouring parts of the image can interfere. The result is more complicated than in the incoherent case, and false detail or artifacts can be produced.

12.2.7 The importance of the condenser lens and illuminator

As far as geometrical optics is concerned, the condenser in a microscope merely serves to illuminate the specimen strongly. According to the wave theory, however, the coherence of the incident light is important, and the condenser therefore has as much importance as any other part of the optical system. The reason for this can best be expressed in terms of coherence. Ideally, as we shall

In a reflecting microscope, the light enters through the objective, which therefore doubles as condenser.

show below, the object should be illuminated in completely incoherent light, which we could obtain by a general external illumination from a large source such as the sky. But this would be very weak, and we increase the intensity by using a lens to focus a source of light onto the object. An image, however, cannot be perfect, and each point on the source gives an image of finite size on the object. In other words, neighbouring points on the object are illuminated by partially coherent light. The poorer the quality of the condenser, the more false detail is to be expected.

Uniform incoherent illumination, typical of the Köhler system, is most important for quantitative imaging, such as in metrology systems.

In practice, two forms of illumination are widely used. The first is called **critical illumination** and is obtained by forming an image of the source in Fig. 12.13(*a*) directly on the object by means of a condenser. This arrangement, however, has the defect that irregularities of the source can affect the image formed. An arrangement that does not have this defect is called **Köhler illumination** and is shown in Fig. 12.13(*b*). An extended source is used, and although any one point on the source gives parallel coherent illumination at a certain angle, the total illumination from all points on the source is indeed almost incoherent (§11.6.4). This is because the individual coherent plane waves have random phases and various directions of propagation and therefore add up with different relative phases at each point in the field. The position of the object is such that the condenser approximately images the auxiliary lens onto it. One would expect this lens to be reasonably uniformly illuminated if it is not too close to the source, even if the latter is patchy. However, for a given lamp Köhler illumination is much weaker than critical illumination, since the light is spread over a larger area.

For either of the above condensing systems the illumination system results in a field with spatial coherence distance $r_c = 0.61\lambda/\mathrm{NA}_c$ (§11.6.4), where NA_c is the numerical aperture of the condenser. Aberrations in the condenser always increase r_c above this value.

If NA_c is larger than that of the objective, and its optical quality is good, r_c is smaller than the resolution limit, so that neighbouring resolvable points are substantially uncorrelated. As a result, the resolution limit is given by the Rayleigh or Sparrow criteria and false detail is avoided. Reducing NA_c often improves the contrast of an image, but increases false detail.

12.3 The optical transfer function: A quantitative measure of the quality of an imaging system

The **optical transfer function** (OTF) and its absolute value the **modulation transfer function** (MTF) are ways of expressing the quality of an imaging system in a quantitative manner. We already know that the resolution limit is defined by the wavelength and numerical aperture ($\lambda/2\mathrm{NA}$) (12.26), but this

Figure 12.13

Types of incoherent illumination: (*a*) critical; (*b*) Köhler.

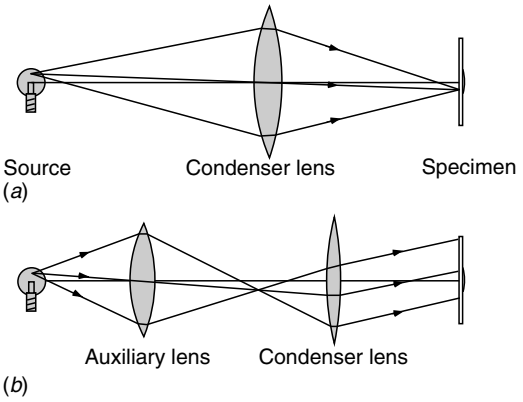

Figure 12.14

False detail produced by imaging with a restricted region of the diffraction pattern, Fig. 12.6(*a*).

Box 12.1 False detail and imaging artifacts

Coherent illumination can result in the production of false detail. In many cases, this may be finer than the limit of resolution (examine Fig. 12.12(*h*) carefully, for example). The use of an optical instrument near to its limit of resolution is always liable to produce effects of this sort; when the Abbe theory was first announced, many microscopists adduced such effects as evidence that the theory was unacceptable (§1.5.3). Even today, when the theory is fully accepted, it is sometimes forgotten in dealing with images produced by, for example, the electron microscope.

The formation of false detail can be conveniently illustrated in the framework of Fig. 12.6. Suppose that the focal plane stop of the instrument limits the transform to the centre five orders only (Fig. 12.14(*a*)). The image is then illustrated by (*b*). Notice the formation of bright spots on the crosses of the gauze wires. One can easily see the origin of these spots by reconstructing a square wave from its zero and first orders only, which is a reasonable model for one dimension of the gauze. Terminating the Fourier series in this way introduces the fine-scale oscillations, which would have been cancelled by the next, omitted, terms in the series (Fig. 4.1).

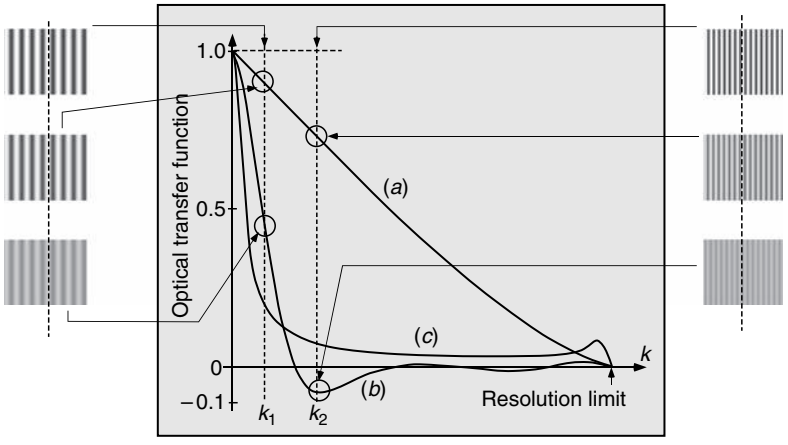

Figure 12.15

Optical transfer functions (OTF) for (*a*) an ideal diffraction-limited lens in the geometrical image plane, (*b*) the same lens defocused by twice the depth of focus (§2.6.4), (*c*) the lens masked by an annular aperture. The images at the sides show how images of sinusoidal object masks of spatial frequencies k_1 and k_2 have different contrasts. Note that when the OTF is < 0, the image phase is reversed.

does not tell us *how well* we can distinguish details in an image even when they are resolved. A key parameter that describes the quality of the system is contrast, since two points are more easily distinguished when their contrast is high. Two systems may have the same numerical aperture and hence a similar resolution limit, but one may have fewer aberrations than the other resulting in higher contrast and a superior image. This is the fundamental difference between a simple lens and a multi-lens objective, the latter enabling us to differentiate better small details near the resolution limit. An MTF graph will tell us the contrast level, 0–100%, by which each spatial frequency (§4.1) in the image is degraded, starting high for well-separated features and dropping towards zero at the resolution limit, not necessarily in a monotonic manner; the faster the drop the poorer the system (Fig. 12.15). Visually we can distinguish a pattern with contrast greater than about 5%.

We generally evaluate an optical system through its point spread function (PSF), which is the Fraunhofer diffraction pattern of the aperture stop in the image plane, as seen around the image of a δ-function source in the object plane. Increasing the size of the aperture decreases the extent of the PSF, which in the case of an ideal lens is the Airy disc pattern (§8.3.4). A full object can be viewed as the convolution of the single point and the object pattern, and therefore its image is a convolution of the PSF and the same pattern, on a scale determined by the magnification of the system. It is important to mention that this linear relationship applies only when the PSF is independent of the position of the point in the field of view, which will be assumed in the present discussion, but is rarely exactly true. Convolution leads to multiplication in the Fourier domain, and the transform of the image is then the transform of the object multiplied by the transform of the PSF. The transform of the PSF is called the **optical transfer function**. When the object is incoherently emitting, the above formulation is carried out using the intensity at each point and the

intensity PSF is the square of the Fourier transform of the aperture stop. This, in turn, is the transform of the spatial auto-correlation of the aperture (§4.9.1).[5]

To understand how the OTF is related to the properties of the imaging system, let us start by considering an incoherent sinusoidal object with spatial frequency $k_1 = 2\pi/\Lambda$ in one dimension.[6] Since the magnification of an optical system depends on the object distance U, which is variable, it is convenient to define k_1 in image space at distance V from the principal plane $\mathcal{H}_2$; this is related to the object frequency by the magnification V/U. An incoherent sinusoidal object with period $2\pi/k_1$ and a unit contrast has an intensity $s(x)$:

$$s_0(x) = \frac{1}{2}(1 + \cos k_1 x). \tag{12.28}$$

The 1 is necessary to ensure that $s_0(x)$ has no negative values. The Fourier transform of the object $S(k)$ is therefore a central δ-function at $k = 0$ and two δ-functions at $\pm k_1$:

$$S_0(k) = \frac{1}{2}\delta(k) + \frac{1}{4}\delta(k - k_1) + \frac{1}{4}\delta(k + k_1). \tag{12.29}$$

The PSF is $p(x)$ and its transform is $P(k)$, therefore in the image plane its transform is the same group of three delta functions multiplied by $P(k)$:

$$S(k) = \frac{P(0)}{2}\delta(k) + \frac{P(k_1)}{4}\delta(k - k_1) + \frac{P(-k_1)}{4}\delta(k + k_1). \tag{12.30}$$

We transform (12.30) back to the image coordinate x:

$$s(x) = \frac{P(0)}{2} + \frac{P(k_1)}{4}\exp[\mathrm{i}k_1 x] + \frac{P(-k_1)}{4}\exp[-\mathrm{i}k_1 x]. \tag{12.31}$$

Since $P(k)$ is the transform of a real function (intensity), $P(-k_1) = P^*(k_1)$ and then (12.31) can be written as

$$s(x) = \frac{P(0)}{2} + \frac{|P(k_1)|}{2}\cos[k_1 x + \Delta(k_1)], \tag{12.32}$$

where Δ is the phase of P. Its visibility, contrast or modulation M, which was defined in (§11.3.2), is

$$M(k_1) \equiv \left[\frac{s_{\max} - s_{\min}}{s_{\max} + s_{\min}}\right] = \frac{|P(k_1)|}{P(0)}. \tag{12.33}$$

We normalize $P(0) = 1$, whence $M(k_1) = |P(k_1)|$. Note that $s_{\min}$ cannot be negative and therefore $P(k_1) \leq P(0)$; convolution can only blur the image and not enhance it. $M(k)$ is called the **modulation transfer function** (MTF) because an object of unit contrast appears in the image as having a contrast $|P(k)|$ (Fig. 12.15). The complex optical transfer function $P(k) = |P(k)|\exp \mathrm{i}\Delta(k)$

[5] Coherent imaging is dealt with using the amplitude of the PSF and results slightly differ. This is a rarely used application.

[6] The dimensions of k are rad/m. A more common notation uses $k/2\pi = 1/\Lambda$, with units of line-pairs/mm, where a line-pair is one period of the sinusoid, of width Λ.

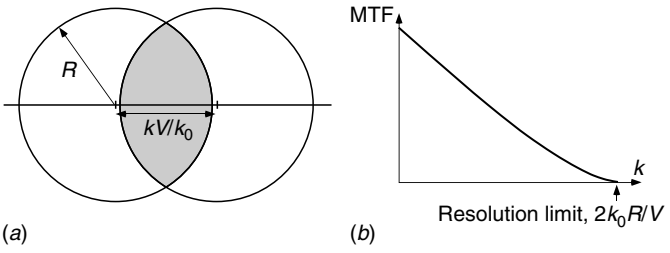

Figure 12.16

(*a*) Construction for calculating the auto-correlation function of a circular aperture. (*b*) The OTF curve is the area shaded in grey in (*a*) as a function of kV/k_0.

also contains the phase information, and you can see from (12.32) that the periodic image is shifted in phase by Δ. For example, in Fig. 12.15 curve (*b*) at k_2 has $\Delta = \pi$. Now any object can be described by a superposition of sines and cosines, and if the PSF is invariant over the field, knowing the OTF will allow the complete image to be simulated.

How do we calculate $P(k)$? We shall do this in one dimension, the extension to two dimensions being straightforward, using X for the position in the aperture stop and x in the image plane. We know that $p(x)$ is the Fraunhofer diffraction pattern of the aperture, whose complex transmission function is defined as $a(X)$. Its Fourier transform is $A(u) = A(k_0 \sin\theta) \approx A(k_0\theta)$ for small angles and the x-coordinate in image space is equal to $V\theta$. Therefore, $p(x)$ is $|A(k_0x/V)|^2$, and $P(k)$ is its transform:

$$P(k) = \int_{-\infty}^{\infty} p(x) \exp(\mathrm{i}kx)\, \mathrm{d}x = \int_{-\infty}^{\infty} \left| A\left(\frac{k_0 x}{V}\right)\right|^2 \exp(\mathrm{i}kx)\, \mathrm{d}x. \quad (12.34)$$

Since we can write the inverse Fourier transform of an auto-correlation (§4.9.1)

$$C(k) \otimes C^*(-k) = \int_{-\infty}^{\infty} |c(x)|^2 \exp(\mathrm{i}kx)\, \mathrm{d}x, \quad (12.35)$$

we can deduce that (12.34) leads to

$$P(k) = a\left(\frac{kV}{k_0}\right) \otimes a^*\left(\frac{-kV}{k_0}\right). \quad (12.36)$$

This provides a method of calculating $M(k)$, given $a(X)$ which describes the shape of the aperture and any phase errors (aberrations) relative to an ideal spherical wavefront emerging from the lens.

The above development was in one dimension but goes directly to two. Let us look at a basic example (Fig. 12.16(*a*)): an ideal circular lens with aperture radius R. The lens aperture is defined by $a(X, Y) = 1$ when $X^2 + Y^2 < R^2$ and zero otherwise. Then, using (12.36), the OTF $P(k)$ is the auto-correlation of $a(X, Y)$, which is described by the overlap of two circles of radius R with their centres separated by kV/k_0. At the resolution limit the image contrast is zero and therefore the OTF drops to zero too. Let us see how this arises from (12.36). From the figure, we see that the overlap reaches zero when $kV/k_0 = 2R$. Since $k = 2\pi/\Lambda$, this limit is reached when $\Lambda = \lambda V/2R$. This is the wavelength times

the f/# (f-number), which emphasizes the importance of the angular aperture of the lens in determining the resolution. The full calculation of the overlap area (Fig. 12.16(*b*)) as a function of the separation describes the **diffraction-limited OTF**, for a lens that has no aberrations (i.e. $a(X, Y)$ is real and has unit value within the aperture stop).

The full OTF of cascaded optical systems is not usually equal to the product of each sub-system's OTF, because one aberration may cancel another, such as in the case of an achromatic doublet lens (§3.7.2); each singlet is worse than their combination. However, there are some situations when the sub-systems are incoherent, such as in the case of cascaded objective lenses and detectors, where the MTFs can be multiplied.

When considering the resolution of a real system, $a(X, Y)$ is a complex function whose absolute value is less than or equal to one, because of aberrations and obscurations. In that case, the MTF can depend not only on k_x and k_y but also on the position x and y in the field of view and therefore on the relationship between the two vectors (x, y) and **k**. For example, in the presence of astigmatism (§3.7.1), which introduces a phase aberration to a proportional to $X^2 - Y^2$, the MTF for vector **k** parallel to (x, y) (sagittal lines) is different than for tangential or meridional lines (vector **k** normal to (x, y)). MTF targets, which are used for measuring the MTF, include patterns that take this type of distinction into account.

12.4 Applications of the Abbe theory: Spatial filtering

Optical instruments can be used without more than a cursory knowledge of how they work, but by understanding their physics we can fully appreciate their limitations, find the conditions under which they can be best used and, most important, find ways of extending their use to problems that cannot be solved by conventional means. The procedures that will be described in this section are known under the general name of **spatial filtering** techniques. They can be expressed in terms of operations carried out by inserting masks affecting the phase and amplitude of the light in the back focal plane $\mathcal{F}_2$ of the lens, which is the plane in which the Fourier transform of a coherently illuminated object would be observed. Because they essentially modify the Fourier transform or spatial frequency spectrum of the image, the name 'spatial filtering' arose by analogy with electronic filtering that is used to modify the temporal frequency spectrum of a signal. When incoherent illumination is used, the Fourier transform in the plane $\mathcal{F}_2$ cannot, of course, be recognized, but the principles to be discussed below still apply. The methods used to achieve them are usually only approximate.

Below we shall discuss the following spatial filtering techniques, which we illustrate by both simulations and laboratory experiments:

1. **Bright-field imaging** is the term used for regular imaging, in which all the transmitted light is used without modification; it shows the relative intensities of all parts of the image, and is insensitive to their phase;
2. **Dark-field imaging**, which can improve the visibility of images with poor contrast, and can also make edges and phase detail visible;
3. **Zernike phase-contrast imaging**, which translates incoherent microscopic phase images into intensity-contrast images;
4. **Schlieren imaging**, which visualizes phase gradients using coherent light;
5. **Diffraction contrast imaging**, which is used in electron microscopy to emphasize inhomogeneities in ordered materials;
6. **Nomarski differential interference contrast**, which visualizes phase or amplitude gradients in microscope images.

12.4.1 Dark-field imaging

Dark-field imaging visualizes mainly discontinuities in the image, such as sharp edges.

Suppose that we wish to observe a very small non-luminous object. If we use bright-field imaging, it is likely that the amount of light scattered by the object will be so small that it will be negligible compared with that contained in the undeviated beam and the object will not be seen. We can avoid this difficulty by arranging that the incident light is directed obliquely at the specimen so that if it is not scattered it does not enter the objective; this method was originally used for observation of Brownian motion, and was called an 'ultramicroscope'. It is adequate if we merely want to know the position of a scattering object, but will not give much information about the nature of the object in general. To create a reasonable image of the object we must use as much as possible of the transform, and this is achieved in practice as shown in Fig. 12.17 by cutting out directly transmitted (*a*) or reflected light (*b*) as completely as possible without affecting the rest. However, if the object has parts that are both brighter and weaker than the average, these can be distinguished by only attenuating the zero order, and not eliminating it completely (Fig. 12.27). Dark-field imaging is also useful for visualizing a phase object which has little absorption, (Fig. 12.18(*d*) and §8.4.1).

A simple analytical model assuming $\phi(x) \ll 1$ illustrates how dark-field imaging makes phase variations visible by eliminating the zero order. Suppose the transmission function of an object is $f(x) = \exp[\mathrm{i}\phi(x)]$, i.e. it only changes the phase of the incident light, but not its amplitude. The incident amplitude A_0 is then transmitted as

$$A(x) = A_0 \exp[\mathrm{i}\phi(x)] \approx A_0 + A_0 \mathrm{i}\phi(x). \tag{12.37}$$

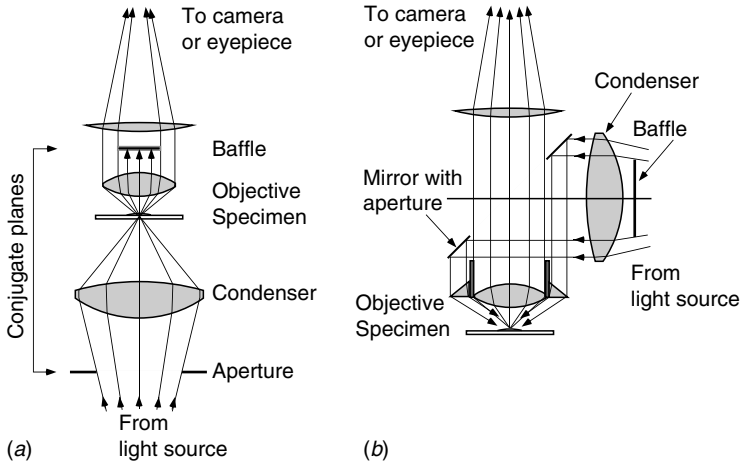

Figure 12.17

Examples of practical systems for dark-field imaging: (*a*) in transmission, where light directly transmitted from the condenser is blocked by a baffle after the objective; (*b*) in reflection, where the specimen is illuminated by a hollow cone of light outside the objective.

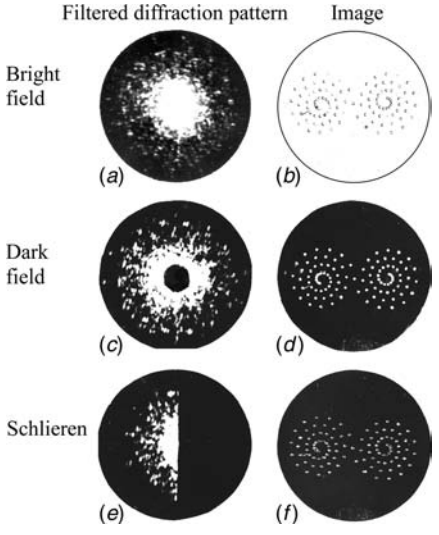

Figure 12.18

Comparison of dark-field and schlieren imaging of a phase object, which are both carried out by obscuring part of the diffraction pattern. (*a*) Diffraction pattern of the pattern of holes in cellophane sheet whose bright-field image is shown in (*b*); (*c*) diffraction pattern with a small opaque spot over its centre; (*d*) dark-field image formed from (*c*); (*e*) diffraction pattern half obscured by a knife-edge; (*f*) schlieren image formed from (*e*).

The term A_0, being independent of x, is represented by the zero order of diffraction. When it is eliminated, we have amplitude and intensity

$$A_{\mathrm{DF}}(x) = A_0 \mathrm{i}\phi(x), \tag{12.38}$$

$$I_{\mathrm{DF}}(x) = |A_{\mathrm{DF}}|^2 = A_0^2 \phi^2(x), \tag{12.39}$$

which visualizes the phase variation, but does not distinguish between positive and negative signs.

The principle of the method can be illustrated quite simply in the apparatus of Fig. 12.5 by placing a small black spot over the central peak of the transform. We have chosen as object a pattern of holes punched in a thin transparent film, whose diffraction pattern is shown in Fig. 12.18(*a*); since the film is not

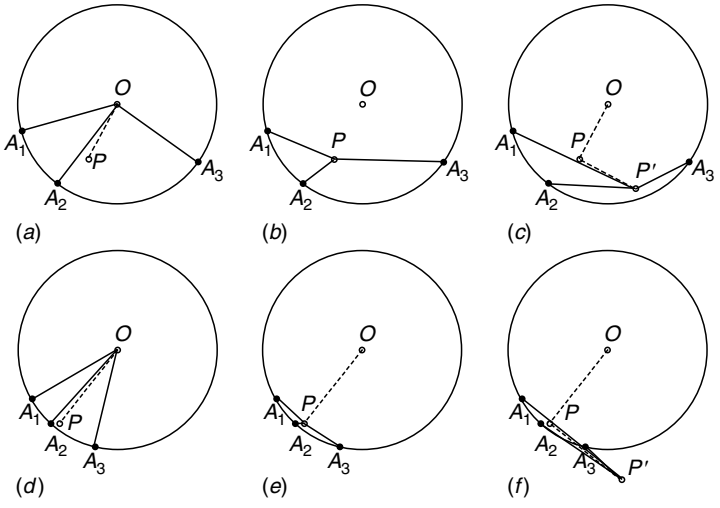

Figure 12.19

Vector diagrams illustrating (*a*) bright-field imaging of a phase object, (*b*) dark-field, and (*c*) phase-contrast. (*d*)–(*f*) show the same for a weak phase object. *OP* is the average of the vectors *OA* and therefore represents the zero order. It can be seen that the phase-contrast technique is sensitive to the *sign* of the phase change relative to the average, whereas dark-field is not.

optically uniform the transform is rather diffuse. The bright-field (unfiltered) image is shown in (*b*). A small black spot on a piece of glass is then placed over its centre, as shown in (*c*), and the final image (*d*) can be compared with (*b*). Although the edges of the holes were visible in the unfiltered image, the contrast is improved considerably by the dark-field filter.

12.4.2 Zernike phase-contrast microscopy

Phase contrast is particularly useful to visualize very small phase variations.

Phase-contrast microscopy is another spatial filtering method to create contrast from a phase object. It was invented by Frits Zernike in 1930 and for the first time allowed live biological entities to be observed in vivo without staining; he was awarded the Nobel prize for this work in 1953. An example is shown in Fig. 12.2(*b*). Large phase gradients at edges are usually visible in bright field, as we saw in Fig. 12.18(*b*), because they result in refraction effects. But Zernike microscopy is sensitive to the *algebraic value* of the phase change. It can be explained as follows, in a way that compares it with the dark-field method.

Suppose that we represent the light amplitude transmitted by an object by a vector in the complex plane. In a phase object (§8.4.1) the vectors representing the complex amplitude at various points on the object are all equal in length, but have different phase angles. In Fig. 12.19(*a*), OA_1, OA_2, OA_3 are typical vectors. In a perfect imaging system, all the corresponding image points have complex amplitudes with the same absolute values, and therefore their intensities are equal; no contrast is observed. Let us picture each vector OA as the sum of a constant OP, which is the mean of the various OAs, and the remainder PA, so that the vector sum of all the PAs is zero. The PAs may now have different lengths. Now **since the vector OP is the mean value, it corresponds**

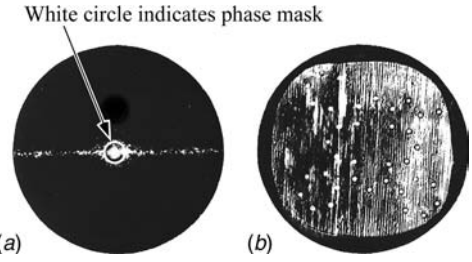

Figure 12.20 **Zernike phase-contrast imaging. (*a*) Fraunhofer diffraction pattern of a phase mask similar to Fig. 12.18(*a*). A spatial filter, consisting of a transparent plate with a small hole whose size is indicated by the white circle, is placed over the zero order, resulting in image (*b*). Notice that because of its linear response to phase changes, the sensitivity of this method to small phase changes is better than dark-field, and non-uniformities in the thickness of the mask material are highlighted as well as the holes. See Fig. 12.2 for an example of this technique in biology.**

to the zero order of diffraction. In the dark-field method, we obstructed the zero order, and therefore subtracted the vector OP from each of the vectors OA. The remaining vectors PA have different lengths and therefore intensity contrast is achieved as shown in Fig. 12.19(*b*). The **Zernike phase-contrast** method involves changing the phase of the vector OP by $\pi/2$, and therefore replacing it by the vector PP'. The new image-point vectors $P'A$ once again have different lengths, as in (*c*). This method has two advantages: all the light transmitted by the object is used in forming the image, and the dependence of intensity on the phase is linear for small phase changes (Fig. 12.19(*f*)), as will be shown analytically in (12.41). It is also clear that the exact value of the phase shift of the zero order is not very important, so that white light can be used.

The phase-contrast method can be described analytically when $\phi(x) \ll 1$ in the same way as dark field. In (12.37) we change the phase of the zero order by $\pi/2$ instead of eliminating it, thereby getting amplitude and intensity of the image

$$f_{\mathrm{PC}}(x) = \mathrm{i}A_0 + \mathrm{i}A_0\phi(x) \approx \mathrm{i}A\exp[\phi(x)], \tag{12.40}$$

$$I_{\mathrm{PC}} = |f_{\mathrm{PC}}(x)|^2 = A_0^2\exp[2\phi(x)] \approx A_0^2[1 + 2\phi(x)], \tag{12.41}$$

which has intensity *linearly dependent* on ϕ (Fig. 12.19(*f*)). In contrast to dark-field microscopy, which has quadratic dependence on ϕ, positive and negative phase changes can therefore be distinguished, and the sensitivity to small values of ϕ is much greater. Figure 12.20 shows a demonstration using the apparatus of Fig. 12.5; the improved sensitivity to small changes in phase is very obvious, when comparing this with Fig. 12.18(*d*).

In practice, the application to an object incoherently illuminated by conical illumination is not so simple, since there is no precise transform whose zero order can be identified. A compromise is necessary, and is effected as follows

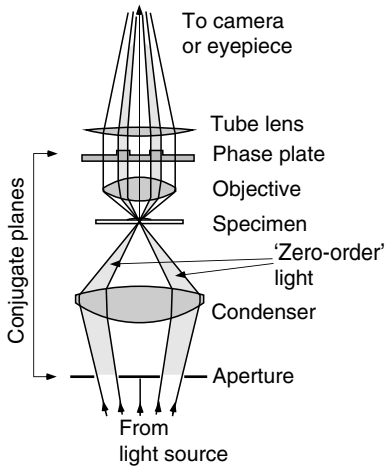

Figure 12.21
Optics of the phase-contrast microscope. The phase plate is coincident with the image of the annular ring formed in the condenser–objective lens system.

(Fig. 12.21). The illuminating beam is limited by an annular opening in the focal plane below the condenser, and a real image of this opening is formed in the back focal plane of the objective, $\mathcal{F}_2$. The phase plate, inserted in $\mathcal{F}_2$, is a thin transparent evaporated ring of optical thickness $\lambda/4$ whose dimensions match those of the image of the annulus. All undeviated light from the specimen must therefore pass through this plate. The final image is formed by interference between the undeviated light passing through the phase plate and the deviated light that passes by the side of it. The ideal conditions are only approximately satisfied, for some of the deviated light will also pass through the phase plate, giving rise to characteristic halos around phase steps. The phase plate is constructed by the vacuum deposition of a dielectric material such as cryolite (Na_3AlF_6) onto a glass support.

When ϕ is small, the zero order of its diffraction pattern is outstandingly strong and changing its phase produces too great a difference in the image. Therefore the phase plate is commonly made to transmit only 10–20% of the light. It looks like a small dark ring on a clear background, and is clearly producing a compromise between dark-field and phase-contrast images.

12.4.3 Schlieren method

Another method of creating contrast from a phase object is to cut off the central peak by a knife-edge, thereby cutting off half the transform as well. In practice the object to be studied is placed in a coherent parallel beam, which is brought to a focus by a lens accurately corrected for spherical aberration. A knife-edge is then translated in the focal plane of the lens until it just overlaps the focus. A clear image of the object can then be seen (Fig. 12.18(f)). But

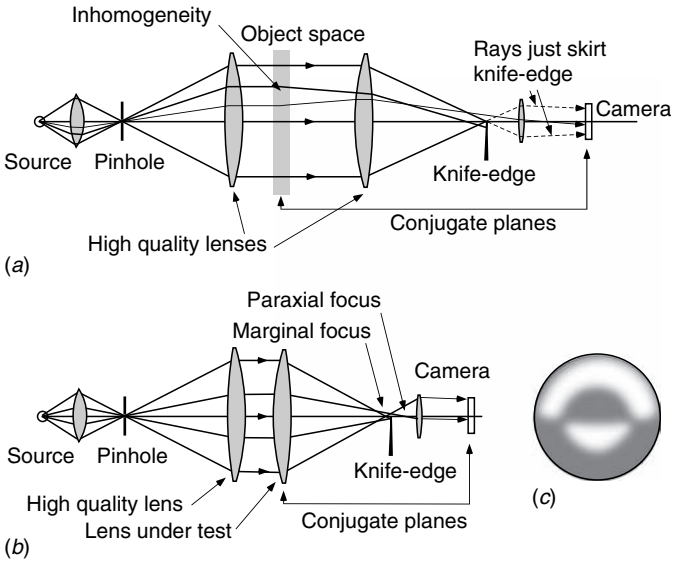

Figure 12.22
(*a*) Schlieren system used for visualizing a region with inhomogeneous refractive index. (*b*) The Foucault knife-edge test, which is an application of the schlieren technique to optical testing. (*c*) Appearance of a lens suffering from spherical aberration when the knife-edge is between the paraxial and marginal focal planes. The effect can easily be understood by geometrical optics.

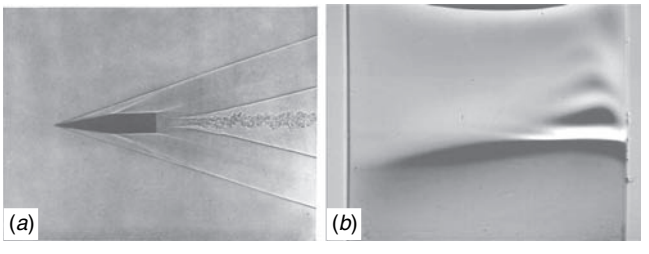

Figure 12.23
(*a*) Schlieren pattern of bullet-shaped object at Mach number 3.62. (From Binder (1985)) (*b*) Schlieren image showing the temperature distribution created in a slightly absorbing fluid when a laser beam is launched through it from right to left. Some convection waves in the fluid above the laser beam are visible on the right. (Courtesy of Elad Greenfield)

removing half of the diffraction pattern introduces some defects that will be discussed later. Moreover, the need for coherent illumination makes this method inappropriate for microscopy and it is mainly used to investigate macroscopic phase objects.

The schlieren method has two important applications. A major use is in fluid dynamics. A wind tunnel in which the density of air is uniform (and hence the refractive index is uniform too) is an object with neither phase nor amplitude variations. Waves or other disturbances in the tunnel will modify the density and refractive index in a non-uniform way, and thus produce a phase object. By using the schlieren technique, the phase variations can be visualized as changes in intensity in the final image (Figs. 12.22(*a*) and 12.23).

Second, it can be used as a critical test of lens quality, for if a lens suffers from aberrations there will not be a sharp focus and it will not be possible to put the knife-edge in a position to cut off only half the light at every point in the field. Thus, if we image the lens aperture itself as the knife-edge traverses the focal plane, the intensity of illumination across the surface will appear

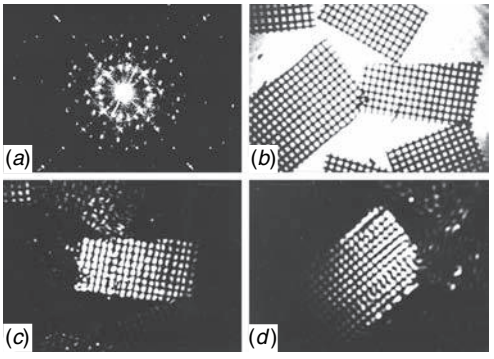

Figure 12.24
Optical demonstration of diffraction contrast, using coherent optics. (*a*) Diffraction pattern of a mask representing a 'polycrystal'; (*b*) image formed using the whole diffraction pattern; (*c*) and (*d*) images formed using selected areas of the diffraction pattern.

Box 12.2 Diffraction contrast in the electron microscope

Spatial-filtering techniques are widely used in the electron microscope as well as the optical microscope. In the former, the numerical aperture is very small, less than 0.04, because of the difficulty of fully correcting electron lens aberrations. When one looks at crystalline matter with an electron microscope it is often possible to use only a very limited region of the Fourier transform, which may contain just one order of diffraction and a limited region around it. As we saw in Fig. 12.6(*h*) and (*j*), this is sufficient to make visible structure on a scale larger than the unit cell. The technique called **diffraction contrast** imaging uses a spatial filter consisting of an aperture that selects the region of a single non-zero order of diffraction only. If, for example, we have a polycrystalline sample, and image it through an off-centre aperture, only those crystallites that have diffraction spots lying within the aperture appear bright in the image; the rest are dark. This can be seen as an optical demonstration in Fig. 12.24. In order to see the periodicity (atomic structure) of the sample one needs to use an aperture that selects several orders of diffraction. An image formed this way is called a **lattice image**; there is great danger of getting misleading structures in such images by an unwise choice of orders.

to change (Fig. 12.22(*b*)). This is called the **Foucault knife-edge test**; for a high quality lens, it can also be used to locate the focal point extremely accurately.

An important difference between phase-contrast and schlieren systems is that the former is isotropic and indicates the value of the phase change, whereas the latter depends on the *phase gradient* and measures its component normal to the knife-edge. Schlieren systems are often adjusted to attenuate but not remove the zero-order light; this practice increases the sensitivity substantially.

12.4.4 An analytical example illustrating dark-field, schlieren and Zernike phase-contrast systems

In this section we shall calculate the intensity distributions in the image of a simple one-dimensional phase object, when the filters discussed in §12.4.1–§12.4.3 are used. Although the examples treat the microscopic methods quantitatively, it should be stressed that their use is mainly qualitative – to visualize phase objects but rarely to analyze them quantitatively. We also show them as computer simulations in Figs. 12.27 and 12.28.

The object we use can be called a *phase slit*; it is a transparent field containing a narrow strip of different optical phase from its surroundings. In one dimension, x, normal to the length of the strip, we describe such an object by

$$f(x) = \exp[\mathrm{i}\phi(x)], \tag{12.42}$$

where $\phi(x) = \beta$ when $|x| \leq a$ and is zero otherwise. This function can be written as the sum of a uniform field and the difference in the region of the strip:

$$f(x) = 1 + (\mathrm{e}^{\mathrm{i}\beta} - 1)g(x), \tag{12.43}$$

where $g(x) = \mathrm{rect}(x/a)$ would represent a normal transmitting slit of width $2a$. The transform of the function written this way is

$$F(u) = \delta(u) + 2a(\mathrm{e}^{\mathrm{i}\beta} - 1)\,\mathrm{sinc}(au). \tag{12.44}$$

First, let us consider the effect of dark-field illumination (§12.4.1). In this technique we eliminate the zero-order component; this is the $\delta(u)$ and a narrow region of negligible width at the centre of the sinc function. After such filtering, the transform is to a good approximation

$$F_1(u) = 0 + 2a(\mathrm{e}^{\mathrm{i}\beta} - 1)\,\mathrm{sinc}(au) \tag{12.45}$$

and the resultant image, the transform of $F_1(u)$, is

$$f_1(x) = (\mathrm{e}^{\mathrm{i}\beta} - 1)\,g(x). \tag{12.46}$$

Recalling the definition of $g(x)$ in (12.43) we see that the slit appears bright on a dark background. In fact, its intensity is dependent on the phase β:

$$I_1(x) = |f_1(x)|^2 = 2(1 - \cos\beta)g(x). \tag{12.47}$$

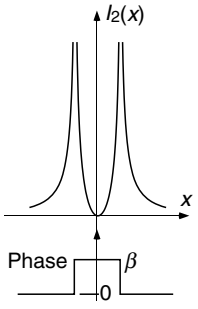

Figure 12.25

Schlieren image of the phase slit. Note that the images of the edges are not sharp.

Using the same example we can illustrate the schlieren method, §12.4.3. In this case the filter cuts out the $\delta(u)$ and all the transform for $u < 0$, leaving us with

$$F_2(u) = 2a(e^{i\beta} - 1)\,\mathrm{sinc}(au)\,D(u), \tag{12.48}$$

where $D(u)$ is the step function: $D(u) = 1$ when $u > 0$, otherwise 0. Using the convolution theorem, the transform of (12.48) is

$$f_2(x) = (e^{i\beta} - 1)g(x) \otimes d(x), \tag{12.49}$$

$$\text{where} \quad d(x) = \int_{-\infty}^{\infty} D(u)e^{-iux}\,du = \frac{1}{ix} \tag{12.50}$$

is the transform of the step function.[7] Evaluating the convolution (12.49) directly for the slit function $g(x)$ gives us

$$\begin{aligned} g(x) \otimes d(x) &= -i\int_{-\infty}^{\infty} \frac{g(x-x')}{x'}\,dx' \\ &= -i\int_{x-a}^{x+a} \frac{dx'}{x'} = -i\,\ln\left|\frac{x+a}{x-a}\right|. \end{aligned} \tag{12.51}$$

The image intensity is then

$$I_2(x) = |f_2(x)|^2 = 2(1 - \cos\beta)\,[\,\ln|(x+a)/(x-a)|\,]^2\,, \tag{12.52}$$

which is illustrated by Fig. 12.25. In this example, the schlieren method clearly emphasizes the edges of the slit, which are discontinuities in object phase. In general it can be shown to highlight phase gradients in the direction normal to the knife-edge; this effect can be seen in the example in Fig. 12.18(*f*) and in the simulation Fig. 12.28.

Finally, this model can be used to illustrate the phase-contrast method (§12.4.2). The transform (12.44)

$$F(u) = \delta(u) + 2a(e^{i\beta} - 1)\,\mathrm{sinc}(au) \tag{12.53}$$

is filtered by the phase plate, which changes the phase of the $u = 0$ component by $\pi/2$ (i.e. multiplication by i):

$$F_3(u) = i\,\delta(u) + 2a(e^{i\beta} - 1)\,\mathrm{sinc}(au). \tag{12.54}$$

The image amplitude is the transform of this:

$$f_3(x) = i + (e^{i\beta} - 1)\,g(x), \tag{12.55}$$

which has value i in the region $|x| > a$ and value

$$i - 1 + e^{i\beta} = (\cos\beta - 1) + i(\sin\beta + 1) \tag{12.56}$$

within the slit. The intensity contrast is maximum when $\beta = 3\pi/4$.

[7] This transform will be discussed in more detail in §13.4.2.

12.4.5 The interference microscope

When we want a quantitative complex analysis of a phase object, we use an **interference microscope**. This form of microscope is constructed around a two-beam interferometer, and if incoherent illumination is to be used, it is clear that the interference fringes will be localized in the object (§9.3.3). Many types of interferometer can be used, and we shall give just one example; others are given in Chapter 9 and in textbooks on interferometry. Interference microscopy is not a spatial-filtering technique, but we include it in this section because of its complementary relationship to the techniques described in §12.4.1–§12.4.2.

The interference microscope that we shall describe here uses a a **shearing interferometer**, a version of which was described in §9.4, which produces an interference pattern between an image field and the same field displaced linearly by a known distance. The image therefore appears double, but the translation may be so small that this does not detract from its sharpness. If, in addition, there is a difference of π between the phases of the two images, destructive interference occurs and the combined field is dark in the absence of phase variations. Regions of the image that have differences of phase within the displacement vector then appear bright on the dark background, and the technique is appropriately called **differential interference contrast** (DIC). It finds many applications ranging from microelectronic wafer inspection to biology (Fig. 12.2(*c*)).

Because DIC empasizes phase gradients along a particular axis, the images look three-dimensional as if they were illuminated from one side.

In the form of the differential interference microscope due to Nomarski, the small displacement is achieved using the differing optical properties of a crystal for light of two orthogonal polarizations. We shall describe it as a transmission microscope, although it is often used in a reflecting form. The illumination at two points on the object corresponds, at the entrance to the condenser, to two plane waves travelling in different directions. These are obtained from a single linearly polarized plane wave by passing it through a thin crystal device (**Wollaston prism**), made from a uniaxial crystal in the form of two opposed thin wedges having orthogonal optic axes *OA*, Fig. 12.26(*a*). The initial plane wave is polarized at 45° to these axes, so that the ordinary and extraordinary waves have equal amplitudes. When the angle α of the wedge is small, the angular deviation of the plane wave is $(n-1)\alpha$, where the appropriate n must be used. The effect of the double wedge is therefore to produce a small angular separation between the two orthogonally polarized waves of $2\alpha(n_\mathrm{e}-n_\mathrm{o})$, which corresponds to a distance $2F\alpha(n_\mathrm{e}-n_\mathrm{o})$ in the object plane where F is the focal length of the condenser.

After transmission through the object and the objective, the two waves are recombined by a second similar Wollaston prism. Since they are mutually coherent (they originated from a single plane-wave component of the illumination), interference between them is produced by an analyzer crossed with

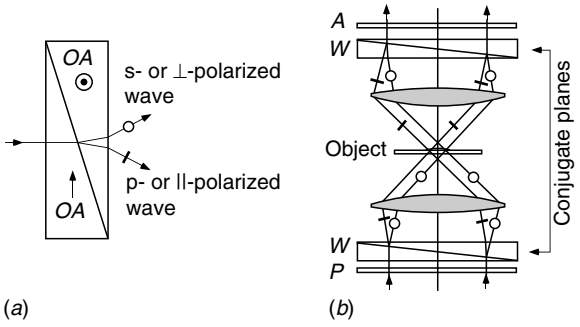

Figure 12.26
Nomarski's differential interference contrast microscope. (*a*) The Wollaston prism with the optic axes *OA*; (*b*) schematic ray diagram of the complete microscope. *W* indicates a Wollaston prism, *P* the polarizer and *A* the analyzer.

the polarizer, thereby also introducing the required π phase shift, independently of the wavelength (Fig. 12.26(*b*)). If the sample introduces no phase difference between the two components, the recombined wave is a plane wave with polarization orthogonal to the analyzer, and the field is dark. Any phase difference introduced will make the light elliptically polarized; likewise, an intensity difference will result in rotation of the plane of polarization. In both cases some light will pass the analyzer.

What does the image represent? If the transmission function of the object is $f(x,y)$, which is assumed to be independent of polarization, the interference image intensity is

$$I(x,y) = |f(x,y) - f(x+\delta x, y)|^2 \otimes p(x,y), \tag{12.57}$$

where δx is the translation vector between the two images and $p(x,y)$ is the point spread function (§12.2.1) of the microscope objective, the illumination being assumed to be incoherent. We can expand (12.57) for small δx and get

$$f(x+\delta x, y) \approx f(x,y) + \delta x \frac{\partial f}{\partial x}, \tag{12.58}$$

$$I(x,y) = \delta x^2 \left| \frac{\partial f}{\partial x} \right|^2 \otimes p(x,y). \tag{12.59}$$

For a phase object, we write $f = |f_0| \exp[\mathrm{i}\phi(x,y)]$, where f_0 is constant. Then

$$\frac{\partial f}{\partial x} = \mathrm{i} f \frac{\partial \phi}{\partial x}, \tag{12.60}$$

$$I(x,y) = |f_0|^2 \delta x^2 \left| \frac{\partial \phi}{\partial x} \right|^2 \otimes p(x,y). \tag{12.61}$$

The image therefore highlights amplitude or phase gradients in the direction of the displacement vector. The phase slit of §12.4.4 would therefore appear as two bright lines along its edges unless δx is parallel to it. If the slit is very narrow, the lines may merge; one is tempted to add their intensities to give a

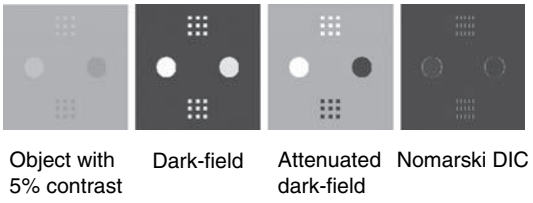

Figure 12.27 Numerical simulation of contrast enhancement by spatial filtering. An object is shown with 5% contrast, both positive and negative with respect to the background field. Dark-field imaging, in which the zero order is removed completely, improves the contrast but ignores its sign. Attenuated dark-field, in which the zero order is only partially removed, is sign-sensitive. Nomarski differential interference contrast (DIC) emphasizes gradients parallel to the image shift (horizontal), independent of their sign.

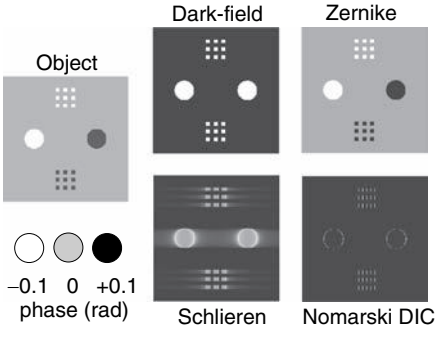

Figure 12.28 Numerical simulations of visualizing a phase object. The object has regions with phase ±0.1 radian with respect to the background. Only the Zernike method is sensitive to the sign of the phase change. Schlieren and DIC are sensitive to gradients; schlieren also spoils the resolution.

Box 12.3 Simulations of spatial filtering

Spatial filtering of an image can be simulated numerically by first calculating its Fourier transform, then multiplying this by the appropriate filter function, and finally performing an inverse transform. We now show some simulations comparing the different methods described in this section. In Fig. 12.27, an object was constructed that has small and large features having amplitude contrast ±0.05. It is shown imaged in dark field, which does not distinguish between the two signs, and attenuated dark field, which does make the distinction. Nomarski DIC shows the edges of the modulated regions in the direction of the image displacement. In Fig. 12.28, the modulated regions have phases ±0.1rad, and one can see that only the Zernike method visualizes the sign of the phase change. Also notice the smearing effect of the convolution in (12.51), which is also observable in the experimental demonstration in Fig. 12.18(*e*).

single line in this case, but one should be wary of doing so because close to the resolution limit the illumination may not be spatially incoherent. As we saw in §12.4.3, the schlieren system also emphasizes phase gradients. However, this microscopic technique uses incoherent illumination, and is therefore more suitable for high-resolution work.

In Fig. 12.2 (at the start of the chapter) we compared images of a live cell taken with three of the techniques described above – bright-field, Zernike phase-contrast and Nomarski DIC. In a modern microscope, it is possible to switch from one technique to the other in one objective by switching the filters.

12.5 Holography

Since all the information concerning the image of an object is contained in its diffraction pattern, it is natural to ask how to record this information on a photographic plate and then use it to reconstruct the image. In other words, can the phase problem (§12.1.5) be circumvented experimentally? The germ of a solution was suggested in 1948 by Gabor and had some limited success at that time; but the invention of the laser subsequently enabled the operation to be carried through completely successfully, and Gabor was awarded the Nobel prize for his work in 1971.

12.5.1 Gabor's method

Gabor's reason for trying to overcome this difficulty was to solve the problem of aberrations in electron-microscope imaging. The resolution obtainable in the electron microscope is not limited by the wavelength ($\sim$0.1 Å) but by the aberrations of the electron lenses. Gabor thought that a better image might be reconstructed if the electron diffraction pattern amplitude could be recorded and the image created optically. To illustrate this idea, he demonstrated his solution optically in both stages. The phase problem was solved by using an object that consisted of a small amount of opaque detail on a large transparent background; the background would produce a strong zero order and the variations in phase of the diffraction pattern would be recorded as variations in intensity. The intensity would be greatest where the phase of the diffraction pattern was the same as that of the background and least where there was a phase difference of π. The idea was only much later applied to electron-microscope images (Tonomura (1999)) but was developed successfully for optical imaging in the 1960s when lasers became available.

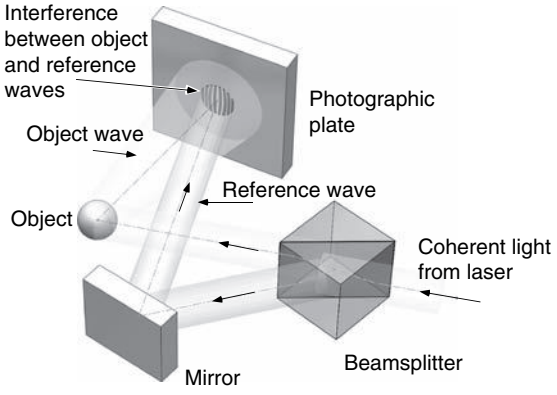

Figure 12.29
Example of a simple holographic recording set-up. The path lengths from the beamsplitter to the plate via the object and via the mirror are approximately equal and the angle between object and reference waves at the plate is fairly small.

12.5.2 Application of the laser

A hologram records both the amplitude and phase of the incident wave-field as the contrast and phase of its interference fringes.

The idea of the hologram was implemented successfully, initially by Leith and Upatnieks in 1960, using a laser.[8] The experimental set-up is quite simple (Fig. 12.29). A spatially coherent laser beam is divided, either in wavefront or amplitude, so that one part falls directly on a photographic plate, and the other falls on the object to be recorded, which scatters light onto the same plate. The two waves, called the **reference wave** and the **object wave** respectively, interfere and the interference pattern is recorded by the plate. It is necessary to reduce relative movements of the various components to amplitudes much less than one wavelength during the exposure to avoid blurring the interference fringes. Reconstruction of the image is carried out by illuminating the developed plate with a light wave that is identical, or at least very similar, to the original reference wave. Two images are usually observed. We shall first give a qualitative interpretation of the recording and reconstruction processes, and afterwards discuss them in a more quantitative manner.

The process can be described in general terms by considering the hologram as analogous to a diffraction grating (§8.5.3 and §9.2). Suppose that we photograph the hologram of a point scatterer – Fig. 12.30(*a*). The point generates a spherical object wave, and this interferes with the plane reference wave. The result is a set of curved fringes (*b*), which look like an off-centre part of a zone plate (§7.2.5), having a sinusoidal profile. The hologram is photographed and the plate developed. To reconstruct the image we illuminate the hologram with a plane wave identical to the original reference wave (Fig. 12.31). We can consider each part of the hologram individually as a diffraction grating with a certain local line spacing. Illumination by the plane reference wave gives

[8] In fact, their first demonstration was with a spatially filtered quasi-monochromatic source of light, but the laser made life much easier.

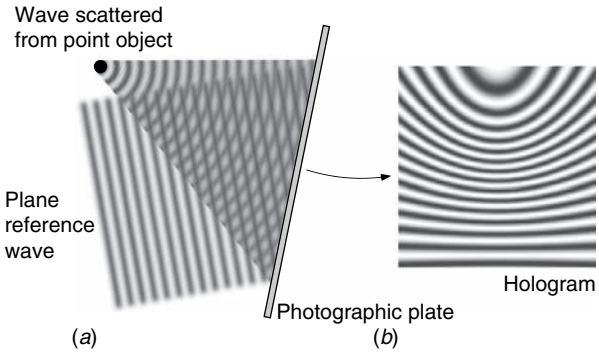

Figure 12.30

Formation and reconstruction of the hologram of a point object: (*a*) spherical wave from the object interferes with plane reference wave; (*b*) fringes recorded on the photographic plate.

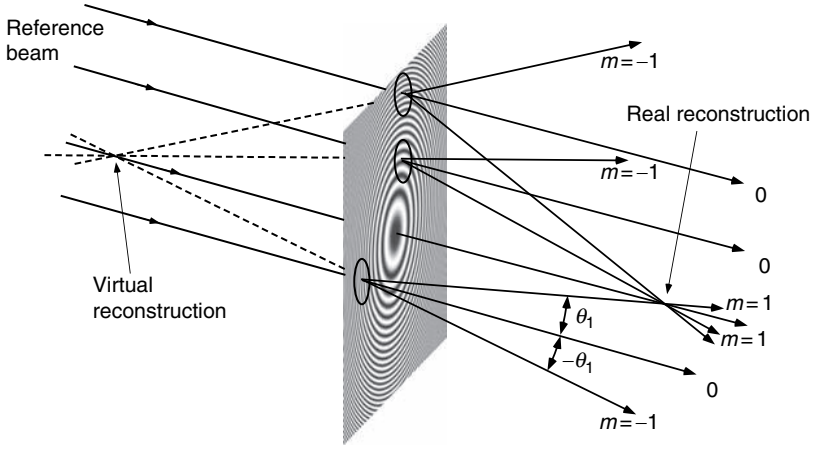

Figure 12.31

Reconstruction of the hologram of a point object: the first orders diffracted from the various regions of the plate intersect to form the real reconstruction, and the −1st orders appear to diverge from the virtual reconstruction.

rise to a zero order and two first orders of diffraction, at angles θ_1, θ_{-1} which depend on the local spacing of the fringes. It is not difficult to see that the -1 orders intersect and form a real image of the point scatterer, and the +1 orders form a virtual image at a position identical to the original point. The images are localized in three dimensions because they are formed by the intersection of waves coming from different directions.

Two other important points are brought out by this model. First, the reconstructed point is more accurately defined in position if a large area of the plate is used, causing the reconstruction orders to meet at a considerable angle; the resolution is therefore a function of the size of the hologram. Second, the fringes are sinusoidal, since only two waves interfere. If the plate records this function faithfully, only zero and first orders will be produced on reconstruction, and only the above two images are produced. This approach is also useful in understanding the effects of altering the angle of incidence, the wavelength or the degree of convergence of the reference wave used for the reconstruction (Problem 12.13).

12.5.3 An analytical model for holography

Now we shall develop an analytical model to show how both the amplitude and the phase of the scattered light are recorded in the hologram and how the reconstruction works. Suppose that at a general point (x,y) in the plate the scattered light has amplitude $a(x,y)$ and phase $\phi(x,y)$. Furthermore, we shall assume that the reference wave is not necessarily a plane wave, but has uniform amplitude A and phase $\phi_0(x,y)$ at the general point. Then the total wave amplitude at (x,y) is

$$\psi(x,y) = A\exp[\mathrm{i}\phi_0(x,y)] + a\exp[\mathrm{i}\phi(x,y)], \tag{12.62}$$

and the corresponding intensity

$$I(x,y) = |\psi(x,y)|^2 = A^2 + a^2 + 2Aa\,\cos[\phi(x,y) - \phi_0(x,y)]. \tag{12.63}$$

To make the holographic process linear, we assume a to be much smaller than A, in which case the term a^2 can be neglected and

$$I(x,y) \approx A^2 + 2Aa\,\cos[\phi(x,y) - \phi_0(x,y)]. \tag{12.64}$$

The photograph of this is the hologram. It consists of a set of interference fringes with sinusoidal profile and phase $\phi - \phi_0$. The visibility of the fringes is $2a/A$. Since A is a constant and ϕ_0 is known, **both** $a(x,y)$ **and** $\phi(x,y)$ **are thus recorded in the hologram**. The need for coherent light to record the hologram should now be clear, since the phase *difference* $\phi - \phi_0$ is recorded in the interference pattern.

To deduce the form of the reconstruction, we assume that the interference pattern (12.64) is photographed on a plate whose amplitude transmission $\mathcal{T}(x,y)$ after development is linearly related to the exposure intensity $I(x,y)$:[9]

$$\mathcal{T}(x,y) = 1 - \alpha I(x,y). \tag{12.65}$$

The hologram is illuminated by a wave identical to the original reference wave $A\exp[\mathrm{i}\phi_0(x,y)]$ and so the transmitted amplitude is

$$\begin{aligned} A\mathcal{T}(x,y)\exp[\mathrm{i}\phi_0(x,y)] &= [1 - \alpha I(x,y)]A\exp[\mathrm{i}\phi_0(x,y)] && (12.66)\\ &= A(1-\alpha A^2)\exp[\mathrm{i}\phi_0(x,y)] && (a)\\ &\quad - \alpha A^2 a(x,y)\exp[\mathrm{i}\phi(x,y)] && (b)\\ &\quad - \alpha A^2 a(x,y)\exp\{\mathrm{i}[2\phi_0(x,y) - \phi(x,y)]\}. && (c) \end{aligned}$$

[9] It is always possible to find a *limited* range of intensities for which this is true. This is another reason for making $a^2 \ll A^2$, so that the range of I is not too large.

The three terms in the above equation are interpreted as follows:

(*a*) The zero order is an attenuated continuation of the reference wave.
(*b*) The first order is the **virtual image**. Apart from the constant multiplier αA^2, the reconstructed wave is *exactly* the same as the object wave and so the light appears to come from a virtual object perfectly reconstructed. Because the complete complex wave $a(x, y)$ has been reconstructed, the reconstruction looks exactly like the object from every direction, and so appears three dimensional.
(*c*) The -1 order is the **phase-conjugate image**. This wave is the complex conjugate of the object wave if ϕ_0 is a constant, and then gives a real (rather than virtual) mirror image of the object. Otherwise it is distorted. An application of the conjugate image will be discussed in §13.6.3.

The ability of a hologram to record both the amplitude and phase of the incident wave-field allows three-dimensional images to be observed.

For practical details on the production of holograms, the reader is referred to texts such as Collier *et al.* (1971) and Hariharan (1989); here, we shall only mention a few points that arise directly from the above discussion.

The intensity ratio between the object beam and the reference beam, a^2/A^2, has been required to be small; in general a ratio of 1:5 is sufficient, although for some purposes even 1:2 can be tolerated. Perfect reconstruction requires the photographic plate to record the light intensity linearly. However, the condition can be relaxed quite considerably for many purposes, since the main effect of non-linearity in the plate is to create second- and higher-order reconstructions which are usually separated in space from the main images. Another obvious requirement is for high spatial resolution of the photographic plate. If the reference beam and the object beam are separated by angle θ, the period of the fringes in the hologram is approximately $\lambda/\sin\theta$. For, say, $\theta = 30°$ this period is only about 1 μm with the common helium–neon laser. To record fringes on this scale, the plate must be capable of resolving less than 0.5 μm, a very stringent requirement which needs special high-resolution photographic plates or film to fulfil it. These plates are usually very insensitive.

12.5.4 Phase, volume and colour holograms

The reader will no doubt remember from the discussion of diffraction gratings in §9.2.4 how poor is the efficiency of an amplitude grating. This is essentially what we have created in a hologram, and the argument in §9.2.4 can be repeated for a sinusoidal grating to show that the diffraction efficiency $\eta \approx a^2/12A^2$, which is very small. For example, if $a^2/A^2 = 1/5$, $\eta \approx 2\%$. The answer, as with the diffraction grating, lies in the use of **phase holograms**. There are several practical methods of replacing the amplitude transmission $\mathcal{T}(x, y)$ by a proportional refractive index field $n(x, y)$. These include bleaching a developed absorption hologram (chemically replacing absorbing silver metal

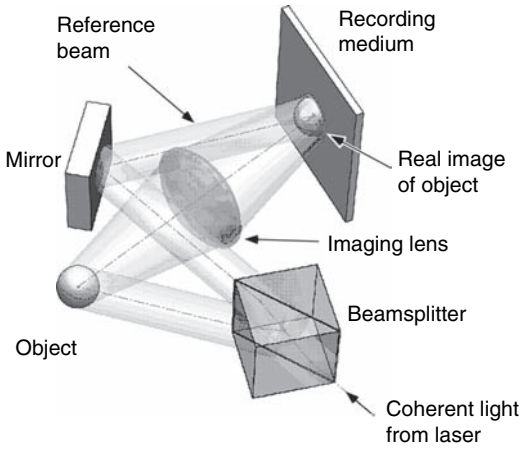

Figure 12.32
Set-up for recording image-plane holograms.

by a transparent complex such as silver chloride whose density locally modifies the refractive index of the emulsion) and the use of gels or polymers in which the degree of cross-linking is modified by exposure to light.

Reflection holograms made by embossing the surface of a metal or metal-coated plastic are very common today, and are widely used for increasing the difficulty of forging devices such as credit cards. Since the surface profile affects the phase of the reflected light, they can be designed to have very high diffraction efficiency. Such holograms are usually made by projecting a real image of the object onto the holographic plate, where it interferes with the reference wave (Fig. 12.32). Reasonably clear reconstructions can be made from such **image plane holograms** using white light, because the images at various wavelengths substantially overlap.

Once we have techniques to make non-absorbing holograms, it is also possible to create **volume holograms**. These are usually polymers or crystals that record the incident light intensity in three dimensions as a local modulation to the refractive index (see §13.6.2, for example). This refractive index distribution is then 'fixed' (i.e. made insensitive to further light exposure). The volume holographic medium replaces the holographic plate in Fig. 12.30 and records the complete spatial fringe pattern, which creates a three-dimensional diffraction grating.

Reconstruction of the image occurs when a plane reference wave is diffracted by this grating. Here we have the same problem as we met in the case of the acousto-optic effect (§8.7) except that in this case the grating is stationary and so the 'acoustic' frequency Ω is zero. We saw there that the volume grating diffracted the wave only if it had exactly the right angle to obey Bragg's law of diffraction, as in Fig. 8.27. Suppose, for simplicity, that we form the hologram of a plane wave such that the angle between it and the reference wave is 2β. Then the fringes in the volume hologram are planar with spacing $\Lambda = \lambda/2 \sin \beta$. Bragg's law then tells us that diffraction occurs when the reference beam is at

angle β, i.e. when it is in the same direction as it was when the hologram was formed. Otherwise *there is no reconstruction at all* and the hologram appears transparent to the wave. Contrast this with the two-dimensional situation, where use of a reconstruction wave differing from the reference wave just gives rise to a distorted image.

The complete absence of reconstruction when the reconstruction wave is not in its original direction allows many holograms (each representing a different image) to be recorded simultaneously in the same medium, each one with a different reference wave, and the possibility of viewing each image separately by choosing the appropriate individual reconstruction wave. This has led to the idea of the **holographic memory** in which a great deal of information (in the form of three-dimensional images) is stored in a crystal, with the possibility of quick access via the appropriate reference beam. Another application of volume holography is to record colour holograms. Three holograms of an object are recorded in the medium with differently coloured lasers, using reference beams in the same direction. When the developed hologram is viewed with white light in that direction, only the same wavelengths reconstruct their corresponding images, and therefore a true-colour reconstruction can be seen.

12.5.5 Holographic interferometry

Holographic reconstructions have two main advantages over ordinary photographs. They are three dimensional, and they contain phase information (§12.4.2). The possibility of recording phase information in a hologram has allowed the development of **holographic interferometry** in which an object can be compared interferometrically with a holographic recording of itself at an earlier time under different conditions. If any changes – of optical density or dimensions, for example – have occurred since the recording was made, the differences will be apparent as interference fringes. There are several ways of doing this, based on the idea that the first hologram is recorded and then its virtual image is reconstructed in the same position as the object, so that changes appear as interference fringes between the two. In particular, details that have not changed should interfere destructively so that they do not appear in the final image. An example is shown in Fig. 12.33 in which the growth of a crystal of transparent material within an optical cell is observed by recording the pattern of changes in optical density. The hologram was recorded before the crystal started to grow, so that the interferogram refers to the crystal alone. The details of the exact shape of the experimental cell are irrelevant to an interpretation of the photograph, since only *changes* in the optical density are observed. Other applications of interferometric holography include vibration analysis and aerodynamic experiments (see the books on holography referenced earlier, and also Jones and Wykes (1989)).

Holographic interferometry between an object and a computer-generated model of itself is a method of testing the accuracy of production of an object.

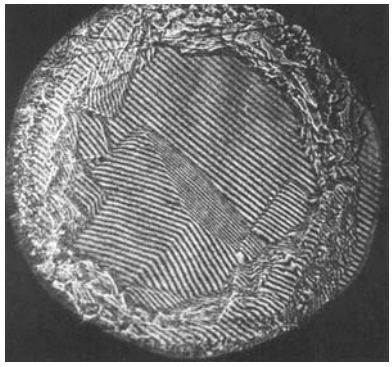

Figure 12.33
Holographic interferogram showing a growing crystal of solid helium at a temperature of 0.5 K.

12.5.6 Computer-generated holograms

Given an object defined by a three-dimensional set of data points, the form of its hologram can be calculated for a given reference wave. Such a hologram can then be printed and recorded photographically on a permanent material, to provide a hologram that can be reconstructed as described above. In recent years programmable media with sufficient spatial resolution for this purpose have also become available, thus allowing direct production of a hologram by the computer. In particular, spatial light modulators with millions of pixels are manufactured from liquid crystals. In these devices, a thin layer of electro-optic liquid crystal is subjected to a spatially addressable electric field, so that its birefringence and its optical thickness for a given polarization of light can be patterned in a predetermined way by a computer. Amongst other things, it can then be used to record a phase hologram and reconstruct an image of the object with high diffraction efficiency. When the hologram is written into the spatial light modulator, illumination by the reference wave reconstructs an optical image of the object. This of course allows dynamic images to be reconstructed, and these can be coloured images too if three holograms related to differently coloured reference beams are superimposed.

12.6 Advanced topic: Surpassing the Abbe resolution limit – super-resolution

None of the spatial filtering techniques described in §12.4 improves the spatial resolution beyond Abbe's $\lambda/2\mathrm{NA}$ limit; in fact some of them, by restricting in some way the region of the Fourier plane used to form the image, actually spoil the resolution (schlieren, for example). The question therefore arises: is the limit of $\lambda/2\mathrm{NA}$ fundamental? We shall see that this is

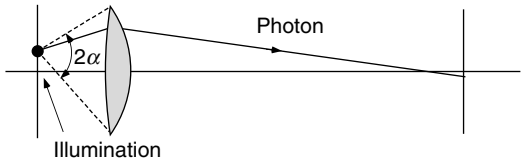

Figure 12.34
The γ-ray microscope thought-experiment. A photon from the source must be within the angle 2α in order to be detected.

not the case for incoherent imaging, and that due to advances made in the last decades, optical resolution is now only limited by the amount of light available.

Nevertheless the Abbe limit indeed has the aura of a fundamental limitation. It was used by Heisenberg to illustrate the quantum-mechanical uncertainty principle in his famous 'γ-ray microscope' thought-experiment as follows. Suppose we wish to determine the position of a point particle in the field of a microscope as accurately as possible. In order to do this, first choose a microscope with a high NA, and use waves with the shortest wavelength available (γ-rays). Then, to make the determination, we must scatter at least one photon off the object, and that photon must enter the lens of the microscope. But there is no way of knowing at which angle the photon entered the lens; all we know is that, after scattering off the point object, the photon had some direction within the cone of semi-angle α which determines the NA of the lens (Fig. 12.34). If the photon has wavenumber k_0, its x-component after scattering must therefore lie in the range $-k_0 \sin\alpha \leq k_x \leq k_0 \sin\alpha$. Thus the uncertainty $\delta k_x = 2k_0 \sin\alpha$. Now from the theory of resolution of the microscope, (12.27) gives an uncertainty in position of the image (the point spread function) $\delta x = \lambda/2\text{NA} = \lambda/2\sin\alpha$. Thus

$$\delta x\, \delta k_x = 2\pi, \tag{12.67}$$

which can be written, using $p = h/\lambda = hk/2\pi$, in the form

$$\delta x\, \delta p_x = h. \tag{12.68}$$

This is the usual form of the uncertainty principle (§14.2.2).

From the above approach, we can immediately see that maximizing δp_x leads to the best resolution, i.e. minimum δx. Since δp_x is an average over the whole lens aperture, it is clear that by using only the edges of the lens we can weight the averaging to the maximum values that δp_x can take. This suggests masking the lens with an annular aperture at its maximum radius, which does indeed give a smaller Airy disc (§8.3.4). Unfortunately this point spread function has stronger diffraction rings than that of the full aperture, and other aberrations are maximized, which often result in imaging artifacts, so it is not a practical option. An example was shown in Fig. 12.12(*h*).

Now we can look for ways of 'circumventing' the uncertainty principle, which might lead us to ways of improving the resolution in microscopy. One obvious idea is to use many photons. Every observed photon must enter the

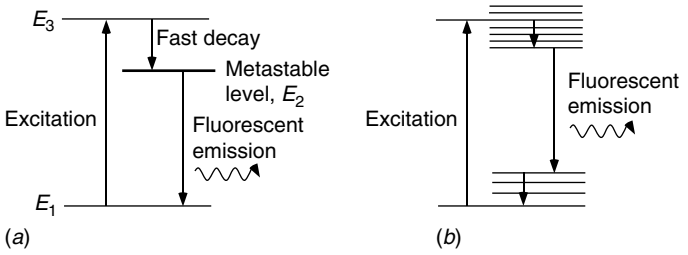

Figure 12.35
Energy level scheme associated with fluorescent emission: (*a*) basic idea involving three levels; (*b*) a commonly encountered scheme involving two multiplets.

lens, so that δk_x is unchanged. But a statistical assembly of N such photons will have a total uncertainty of about $2N^{\frac{1}{2}}k_0 \sin\alpha$, so that we might expect

$$\delta x \approx \lambda / \left(2N^{\frac{1}{2}}\mathrm{NA}\right). \tag{12.69}$$

If N is very large, this can represent a substantial improvement in the resolution of sparse images where the individual points do not overlap or have different wavelengths so that they can be distinguished. This idea is behind one very high resolution method that uses specialized photo-excitable fluorescent tags and will be described in §12.6.5.

During the last 20 years several new super-resolving microscopes have evolved for incoherent imaging, where the emphasis has been on **fluorescent objects** (§12.2.4), because of their importance in biological microscopy. However, unless the object itself is fluorescent (auto-fluorescence), we must always remember that attaching a fluorescent tag can change the way in which a biological entity works. This is akin to staining in conventional microscopy, which was avoided for the first time by the Zernike phase-contrast method (§12.4.2). Fluorescence is a quantum phenomenon and will be discussed in more detail in §14.8. For the purposes of this section, we need to know that fluorescent emission occurs when an atom or molecule ('fluorescent tag') is first excited from its ground state, or from a long-lived metastable state E_1 to an excited state E_3. From there, it decays back to E_1 by means of at least two sequential stages, one of which emits the fluorescent light. This involves an intermediate state E_2, as shown in Fig. 12.35(*a*). Clearly, the excitation wavelength is shorter than the fluorescence wavelength, and therefore there is no constant phase relationship between the two waves, so that **fluorescence can be considered as completely incoherent emission**. Figure 12.35(*b*) shows a more common scheme involving four levels, but the principle is the same.

Another important concept in the field of super-resolution is **scanning microscopy**. In a scanning microscope, a small brightly illuminated spot is moved sequentially across the object, usually in a **raster scan** along a series of closely spaced lines which together cover the field of view. The intensity of the transmitted or reflected light is then measured as a function of time and the image is built up sequentially and displayed on a screen. Scanning microscopy is *ipso facto* incoherent microscopy; since one point is measured at a time,

at a rate far slower than the bandwidth of even the most narrow-band source, there is no opportunity for interference between light from neighbouring points on the object. The question of the resolution limit then boils down to determining the point spread function (§12.2.1) of the scanning system; what is the size of the 'point' that is measured at a given time? And how can we 'tailor' it to be smaller?

In this section we shall discuss five practical techniques for super-resolution, of which 1–3 use raster scanning. Techniques 1, 2 and 5 may employ fluorescent tags, but do not necessarily require them as part of the basic mechanism:

1. The confocal scanning microscope (§12.6.2), which can achieve resolution somewhat better than the diffraction limit in three dimensions and works by multiplying the point spread functions of two optical systems;
2. The near-field scanning optical microscope (NSOM – §12.6.3), which carries out surface imaging using an optical probe in very close physical proximity to the sample;
3. Stimulated emission depletion microscopy (STED – §12.6.4), a scanning technique that uses the fluorescent mechanism itself to create a very small scanning spot;
4. Stochastic optical reconstruction microscopy (STORM – §12.6.5), which achieves very high resolution by using optically switched fluorescent tags;
5. Structured illumination microscopy (SIM – §12.6.6), which uses image multiplication to collect information in an extended region of Fourier space.

12.6.1 A proof that unlimited super-resolution is possible in incoherent imaging

Sixty years ago, Toraldo di Francia (1952) proposed an idea that showed, theoretically at least, that **resolution of an incoherent image is unlimited according to the Rayleigh criterion, provided that enough light is available**. He showed how to create an axially symmetric point spread function with its first zero arbitrarily close to the origin by using a complex non-periodic apodization mask consisting of concentric ring apertures with alternating phases of 0 and π.

The idea is as follows. Consider first an annular ring with zero phase and area a_1 at the maximum aperture radius of the imaging lens, R_1. This creates a point spread function (§12.2.1) with amplitude $a_1 J_0(uR_1)$, which has its first zero at $u = 2.38/R_1$ (Appendix A). Add to this a second ring with phase π, area a_2 and radius $R_2 < R_1$, leading to a combined point spread function $f(u) = a_1 J_0(uR_1) - a_2 J_0(uR_2)$. This has a central maximum of amplitude $a_1 - a_2$ and a_2 is chosen so that the combined function has zero value at some value $u = u_1$, which is smaller than $u = 2.38/R_1$, so that **the Rayleigh limit of the original aperture has been exceeded**. But the central spot is very weak,

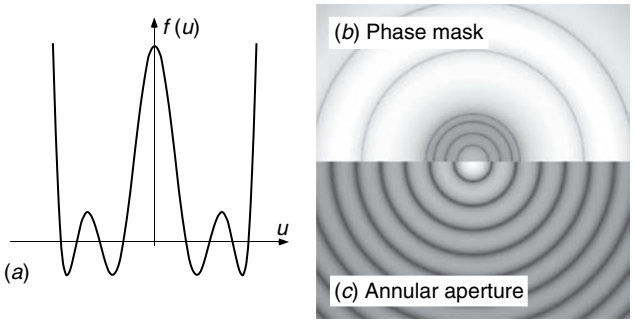

Figure 12.36 **Super-resolution using five annular apertures of alternating phase. (*a*) The amplitude of the point spread function (PSF) $f(u)$, as a function of radius u in the Fourier plane. (*b*) Upper half: the intensity of the PSF shown on an enhanced scale – notice the weak central peak and the very bright peripheral rings. (*c*) Lower half: the intensity of the PSF $J_0^2(uR_1)$ for the outermost annular aperture alone also shown on an enhanced scale. Notice that the first zero in (*b*) is closer to the centre than that in (*c*). (Toraldo di Francia (1952))**

since it is the *difference* between a_1 and a_2, and a calculation shows that outside the first zero, the diffraction patterns of the two rings add to give a bright ring with amplitude proportional to $a_1 + a_2$. One now repeats the process with a second pair of antiphased annuli at radii R_3 and R_4, both smaller than R_2, and amplitudes a_3 and a_4 calculated to give a first zero at the same value u_1 as before and a bright ring in about the same place as before, but of opposite sign so as to cancel the first bright ring. The outcome is the same Rayleigh limit but a weaker central spot surrounded by a relatively dark region and a bright ring at larger u than before. An example of a typical calculated result is shown in Fig. 12.36(a, b); the improvement over the annular aperture is not very great, but the problem of the bright ring is very prominent. This exercise showed for the first time that resolution better than the Rayleigh limit is indeed possible, but very bright illumination is needed and that the field of view, the dark region around the central peak within which a second resolvable incoherent source might be situated, is limited. In principle, the process can be continued with more rings, thereby creating a very weak central peak surrounded by a virtually dark field, and the *choice* of u_1 determines how narrow the central peak is.

Because of its poor light efficiency, this idea was only recently implemented, but illustrates the fact that **with enough photons available, we can circumvent the Abbe criterion**.

12.6.2 Confocal scanning microscopy

The widely used confocal scanning microscope (Wilson and Sheppard (1984)) is based on a conventional microscope and is illustrated schematically in

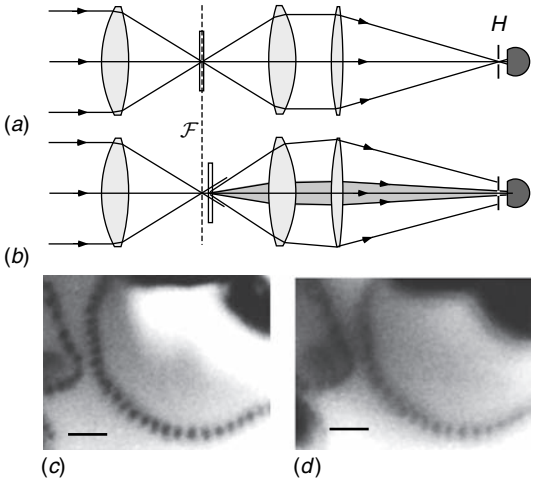

Figure 12.37 **(*a*) Optical layout of a confocal scanning microscope. The object is in the plane $\mathcal{F}$. (*b*) Diagram showing why the confocal image is almost unaffected by scattering from details outside the focal plane, $\mathcal{F}$; only the light from an out-of-focus scatterer within the shaded cone gets through the pinhole *H*. (*c*) Confocal and (*d*) conventional bright-field fluorescence images of a spore of Dawsonia superba. The scale bars show 1 μm. (Photograph courtesy of V. Sarafis and C. Thoni, made at Leica Lasertechnik, Heidelberg)**

Fig. 12.37(*a*). This shows a transmitted light imaging system (it can also be implemented in reflected light) in which the object is illuminated by the diffraction-limited image of a point source. The light transmitted by the object is focused by a second lens onto a small aperture or pinhole H, after which lies a detector that measures the power received. The object is then translated through the system in a raster scan and its image is displayed electronically from the detector output.

The approach to understanding the resolution is to calculate the point spread function, as it appears on the display. We therefore picture a point object having a transmission function $\delta(x)\,\delta(y)$. The illumination system produces an amplitude point spread function $s_1(x)$ in the object plane, so that the amplitude at distance x from the axis is

$$A(x) = A_0 s_1(x). \tag{12.70}$$

As the object point scans through this, it behaves as a point source itself which is situated at x and has amplitude $A_0 s_1(x)$. This is imaged by the objective lens, with magnification M, onto the plane of H so that it appears with its centre at $x' = -Mx$. The objective has amplitude point spread function in the pinhole plane $s_2(x'/M)$. The amplitude in this plane is therefore $A_0 s_1(x) s_2[(x' - Mx)/M]$, and that at H situated at $x' = 0$ is $A_0 s_1(x) s_2(-x)$. If the two lenses are identical, $s_1 = s_2 \equiv s$ and the amplitude point spread function is $s^2(x)$ and that for intensity is $s^4(x)$. Putting in the form for a diffraction-limited lens

of numerical aperture NA, $s(x) = 2J_1(k_0 x\,\mathrm{NA})/(k_0 x\,\mathrm{NA})$, we find a narrower point image than the best the equivalent microscope can do; this is not shown by the Rayleigh criterion (see footnote to §12.2.1) because the zeros are unchanged, but the Sparrow criterion gives

$$d_{\min} = \lambda/3.1\,\mathrm{NA} \tag{12.71}$$

since the second derivative of $[J_1(x)/x]^4$ is zero at $x = 1.08$. Figure 12.37(*c*) and (*d*) show the small improvement in resolution attainable. Note that the aperture H collects only a fraction of the light transmitted by the object, so the improvement of resolution occurs at the price of a reduction in efficiency.

The confocal microscope has exceptional axial (z) resolution as well as improved lateral resolution, and this is in fact a more important feature than the modest improvement in in-plane resolution. If the object is moved axially out of the focal plane of the scanner (Fig. 12.37(*b*)), it becomes illuminated by a patch of light and not a point, and the second imaging stage is no longer conjugate to it. In addition, the only light reaching the detector from the object is that within the bundle shown shaded in the figure, which is limited by the diameter of H. So, for both these reasons, very little light reaches the detector unless the object is very close to the focal plane. This results in very high axial resolution, which is employed to build up images of three-dimensional objects by using three-dimensional scanning.

12.6.3 The near-field scanning optical microscope (NSOM)

The near-field microscope uses a tiny probe in close proximity to the sample surface to create an image as it scans the sample in a raster. The probe can either emit light or collect light emitted from a self-luminous object. We shall consider the former situation, in which we create a very small point spread function by confining light in an aluminium-coated optical fibre which is tapered to sub-wavelength dimensions at its termination (Fig. 12.38(*a*)).

Consider such a light source with very small dimensions $a \ll \lambda$. What does the wave emitted by such a light source look like? If we describe it by a superposition of plane waves of the form $\psi = \psi_0 \exp[\mathrm{i}(\omega t - k_x x - k_y y - k_z z)]$ it is clear that, in order to represent a source that has a non-zero amplitude only within the region $|x|, |y| < a/2$, we must use components with k_x and k_y at least as large as π/a. For such a wave, we have

$$k_0^2 = k_x^2 + k_y^2 + k_z^2 = 2\pi^2/a^2 + k_z^2, \tag{12.72}$$

which, since $a \ll \lambda$, implies that k_z must be imaginary:

$$k_z = 2\pi\mathrm{i}\sqrt{\frac{1}{2a^2} - \frac{1}{\lambda^2}} \approx 2\pi\mathrm{i}\sqrt{\frac{1}{2a^2}}. \tag{12.73}$$

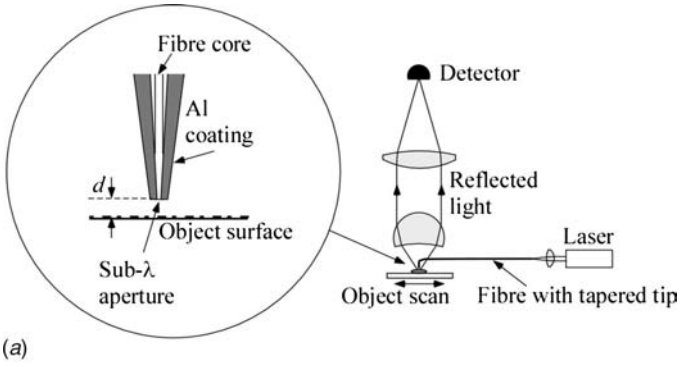

(a)

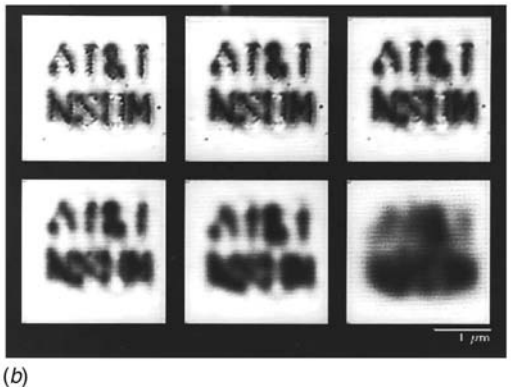

(b)

Figure 12.38

(*a*) Schematic optics of the near-field microscope, showing the extruded fibre tip as inset; and (*b*) images recorded with probe-to-object distances $d < 0.005$, $d = 0.005$, 0.010, 0.025, 0.10, and 0.40 μm. (Photograph courtesy of E. Betzig)

The implication of an imaginary wave-vector k_z is, from §2.3.2, that the wave propagates evanescently in the z-direction, and decays in amplitude like $\exp(-|k_z|z)$. For this reason, the probe has to be extremely close, not much more than distance a, from the sample surface.

High resolution using evanescent propagation was first demonstrated using microwaves, but it was achieved with light waves by Lewis *et al.* (1984) and Pohl *et al.* (1984). Images showing the dependence of resolution on the distance between the probe and object are shown in Fig. 12.38(*b*). The book by Paesler and Moyer (1996) discusses this field in depth, including several different modes by which the probe and light source can be combined.

12.6.4 Stimulated emission depletion microscopy (STED)

Another approach to improving the resolution limit in fluorescence microscopy, STED (Hell and Wichmann (1994)), uses the fluorescence mechanism itself to create a super-resolved scanning spot, with point spread function (PSF) smaller than the diffraction limit $\lambda/2\mathrm{NA}$. In the first stage, a pulse from a laser at the excitation wavelength creates a diffraction-limited PSF, which excites

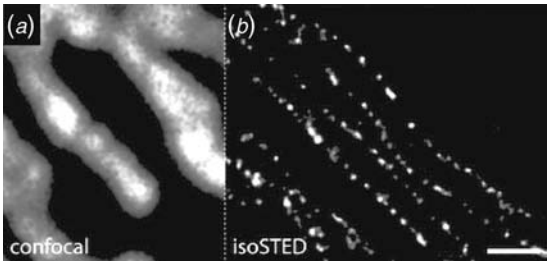

Figure 12.39
Images of fluorescent tags on mitochondria with sub-wavelength detail by (*a*) confocal imaging and (*b*) STED. The scale bar is 500 nm. (Schmidt *et al.* (2009))

any fluorescent atoms within its volume to an excited fluorescing level. Now a second laser pulse at the emission wavelength, with its wavefront phase-modulated so as to produce an annular PSF having a dark centre, de-excites the atoms from this level within the annular region by stimulated emission (§14.4.2). This leaves excited atoms to be detected by their fluorescence only in the dark region at the centre of the annulus, which is necessarily smaller than the diffraction limit. The actual size of the region that remains excited after the two pulses depends on the relative strengths of the two pulses, and requires extremely good co-alignment of the optics and the focal points of the optical trains providing the two spots. One mechanism by which the annular spot is obtained uses a spiral phase plate, which was discussed in §5.9; the depletion PSF is similar to $J_1^2(k_0\theta R)$ which has zero value at $\theta = 0$ (Appendix A). Here the $\sqrt{N}$ factor in (12.69) comes into play in determining the region of the annular PSF that is too weak to stimulate emission (see Problem 12.19). A comparison of images obtained with a confocal microscope and by STED is shown in Fig. 12.39 (Schmidt *et al.* (2009)).

12.6.5 Stochastic optical reconstruction microscopy (STORM)

Earlier in §12.6 we remarked that by using N photons emitted from a point object, its position can be determined to an accuracy $\sqrt{N}$ better than the diffraction limit (12.69). This idea can be used directly for imaging a *sparse* object, consisting of several points separated by distances greater than a few wavelengths, each one emitting randomly a stream of photons by fluorescence. The centre of gravity of each point image is then determined accurately by calculation. By the use of **switchable fluorescent tags**, this has now been extended to dense objects, which are imaged statistically by switching on **a series of sparse random samples of the tags**. The images are then combined, after the position of each tag has been determined accurately. The technique is called STORM (Rust *et al.* (2006)).

The basic concept of a switchable fluorescent molecule is shown in Fig. 12.40(*a*). It has a ground state E_0, which is not fluorescent, and can be switched to the long-lived metastable fluorescent state E_1 of Fig. 12.35 by

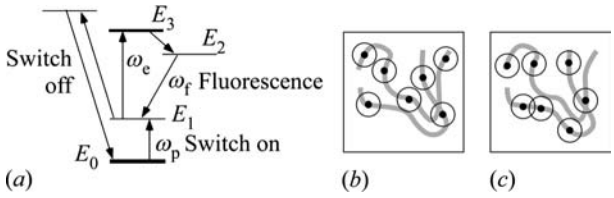

Figure 12.40

STORM: (*a*) An energy-level scheme that allows switchable fluorescence. (*b*, *c*) Stochastically excited fluorescent tags on a dense object. The circle represents the point spread function in the image and the dot at its centre is its centre of gravity. Photons within the two overlapping circles in (*c*) cannot be assigned definitely to a particular tag and will be eliminated in the data processing. An image created by STORM is shown in Fig. 12.1 at the beginning of the chapter.

applying a pump of frequency $\omega_p = (E_1 - E_0)/\hbar$. The return from E_1 to the ground state E_0 (switching off) via an indirect route can be achieved by a wave of another frequency. Several fluorescent tags have been developed that have these properties.

In the fluorescence microscope, the object is illuminated by a weak pump wave at ω_p, which excites a sparse sample of the tags to the metastable level. These tags are then observed fluorescently, using a series of N excitation pulses from a laser at ω_e, and the N fluorescent images are individually recorded (Fig. 12.40(*b*)). Then the level E_1 is switched off, and the process repeated to excite a new sparse sample of tags. Each series of N images is processed so that the position of each tag is determined with accuracy $\lambda/(2\mathrm{NA}\sqrt{N})$, and any suspicious events are eliminated (for example, the two close tags in Fig. 12.40(*c*) that were both excited, and therefore give rise to a queerly shaped distribution of photon images). The images obtained after each excitation by ω_p are then combined to give a complete image of the dense object; an example is shown in Fig. 12.1 at the beginning of the chapter. The resolution is determined by the value of N, which can be several thousands, but is eventually limited by the size of the fluorescent tag itself.

12.6.6 Structured illumination microscopy (SIM)

Structured illumination microscopy provides wide-field super-resolution by manipulations in Fourier space. For this reason we shall discuss it in greater detail because of its close affinity to other topics in this chapter. The basic idea is to illuminate the object with a non-uniform field of light which multiplies the image information and is designed to move high spatial frequencies to lower ones by convolution in the Fourier plane. Since the highest spatial frequency that can be imaged is $2\mathrm{NA}k_0$, the method can therefore make frequencies higher than this visible. The idea was first discussed by Lukosz (1966), but it has only

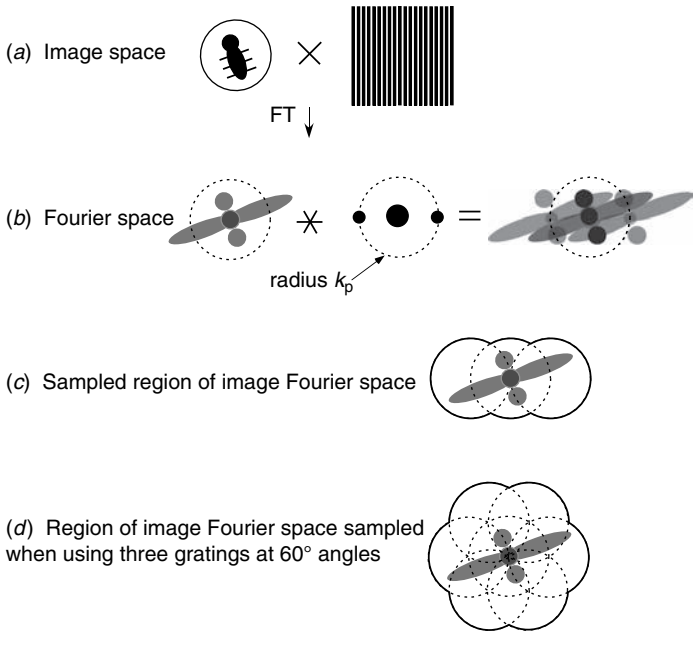

Figure 12.41

(*a*) Image multiplied by a sinusoidal illumination pattern and (*b*) the resulting Fourier spectrum. (*c*) The region of the object Fourier spectrum recorded within the imaging circle. (*d*) The region of the spectrum recorded when three grating orientations, at 0, ±60° are used.

recently been developed into a practical technique for super-resolved biological imaging by Gustafsson (2000).

In this method, the excitation laser field illuminating a fluorescent specimen is patterned in a sinusoidal manner. The result is that the fluorescent emission image of the specimen is multiplied by an all-positive sinusoid $\frac{1}{2}[1+\cos(k_{\mathrm{p}}x)]$. The incoherent image is recorded and its Fourier transform calculated. This is clearly the transform of the required image, convolved with the transform of the illumination, the three δ-functions at $-k_{\mathrm{p}}$, 0 and k_{p}. The result of the convolution is to superimpose, on the transform of the image, repeats of itself shifted by both $\pm k_{\mathrm{p}}$. Now, according to the Abbe theory, the incoherent image is built up from Fourier components with spatial frequencies out to $\pm 2\mathrm{NA}k_0 \equiv \pm k_m$. In that case, because of the convolution, the image will now include information about the spectrum of the image including frequencies in the range between $\pm(k_m + k_{\mathrm{p}})$. The idea is illustrated in Fig. 12.41 for $k_{\mathrm{p}} = 2k_0$.

What has been done here is well known to us in the form of the **moiré pattern**, the optical analogue of beats in acoustics (Fig. 12.42(*a*)). When we put two gratings with similar frequencies on top of one another, we see coarse fringes that correspond to the *vector difference* in spatial frequency between the two gratings. To determine which grating has the higher frequency, it is necessary to translate one of them; the moiré pattern moves in the same direction as the lower-frequency grating. Then, if one frequency is known, the other can be deduced, even if both are out of the range of resolution, Fig. 12.42(*b*). The translation is also required for another reason; clearly image information that falls on zeros of the illumination pattern is lost, and

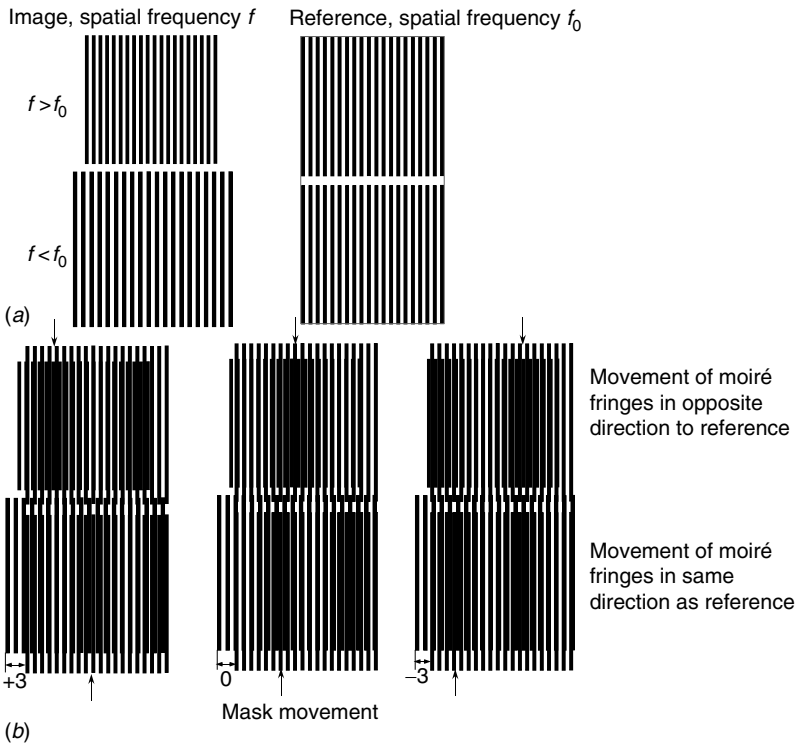

Figure 12.42

(*a*) A periodic object with two spatial frequencies is multiplied by a reference grating having an intermediate spatial frequency f_0. The moiré frequency equals the difference between the object and reference frequencies. (*b*) When the reference grating is translated, the moiré pattern moves the *same* way if the object frequency is *lower* than the reference, and the opposite way if it is higher.

so to include full information, at least three different pattern positions are required.

The processing steps needed to reconstruct the high-resolution image are now clear. The excitation pattern is projected onto the object and the image recorded. The recording must then be repeated with linear shifts of the pattern. For full two-dimensional imaging, the process must also be repeated with fringes in different directions. All the images are Fourier transformed and the resultant sampling of the Fourier plane as used in practice is shown in Fig. 12.41(*d*).

The resolution attainable depends on the value of k_p, which should therefore be as large as possible. Illumination is provided by interfering the first orders from a diffraction grating so as to produce interference fringes on the specimen (Fig. 12.43). The grating period and condenser lens are chosen so that the first orders of diffraction are at the edges of the angular aperture of the objective, which leads to a fringe pattern with spatial frequency $\mathrm{NA_c}k_{0\mathrm{e}}$ (12.26), where $\mathrm{NA_c}$ is the NA of the condenser, and $k_{0\mathrm{e}}$ is the wavenumber of the excitation laser. The zero order is then blocked so as to double the spatial frequency of the illumination pattern to $k_\mathrm{p} = 2\mathrm{NA_c}k_{0\mathrm{e}}$ (§12.1.1). Linear translation of the grating allows the phase ϕ of the fringe pattern to be controlled. In practice, $k_\mathrm{p} \approx k_m$.

An immediate problem arises: how do we separate the spatial frequency components that have been transposed by the convolution from those that were

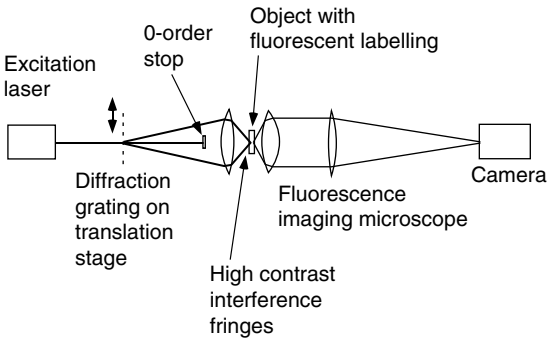

Figure 12.43
The optics of the structured illumination microscope.

there in the first place? This is done by comparing the transforms of the images with various illumination pattern phases ϕ. In one dimension, the structured illumination has the form $s(x) = \frac{1}{2}[1 + \cos(k_p x + \phi)]$. The object's fluorescent strength has form $f(x)$. The emitted intensity $s \times f$ can be represented by its Fourier transform

$$F^{(s)}(k) = F(k) \otimes \frac{1}{2}\left[\frac{1}{2}e^{-i\phi}\delta(k - k_p) + \delta(k) + \frac{1}{2}e^{i\phi}\delta(k + k_p)\right]$$
$$= \frac{1}{4}e^{-i\phi}F(k - k_p) + \frac{1}{2}F(k) + \frac{1}{4}e^{i\phi}F(k + k_p). \quad (12.74)$$

In order to exploit the fact that (12.74) contains information in the range $|k| \geq 4k_0N$, we have to separate the individual terms. There are three unknowns on the right of (12.74) and so we have to generate three independent equations with different values of ϕ by shifting the grating in Fig. 12.43. Then, the equations can be solved to find $F(k)$ in the full range $|k| \leq 4k_0N$.[10] We then have, for $j = 1, 2, 3$,

$$F^{(s)}(\phi_j, k) = \frac{1}{2}e^{-i\phi_j}F(k - k_p) + F(k) + \frac{1}{2}e^{i\phi_j}F(k + k_p). \quad (12.75)$$

Practical application of this method for two-dimensional images requires at least three orientations of the grating and at least three phases ϕ for each orientation. The sampling of the larger region of **k**-space is then shown in Fig. 12.41(*c*). Figure 12.44(*c*) shows an image reconstructed using this method, compared to the same image obtained with a bright-field fluorescence microscope and a confocal microscope.

Recently, the resolution of structured illumination microscopy has been increased three-fold by using a non-linear fluorescent response (Gustafsson (2005)). Under conditions of very bright illumination, which saturates the fluorescence at the peaks of the sinusoid, the function $s(x)$ becomes closer to a square wave whose Fourier transform also includes δ-functions at $\pm 3k_p$, $\pm 5k_p$,

[10] In calculating the image, the OTF(k) of the imaging lens should really multiply the values of $F(k)$, but we omit this to simplify the analysis.

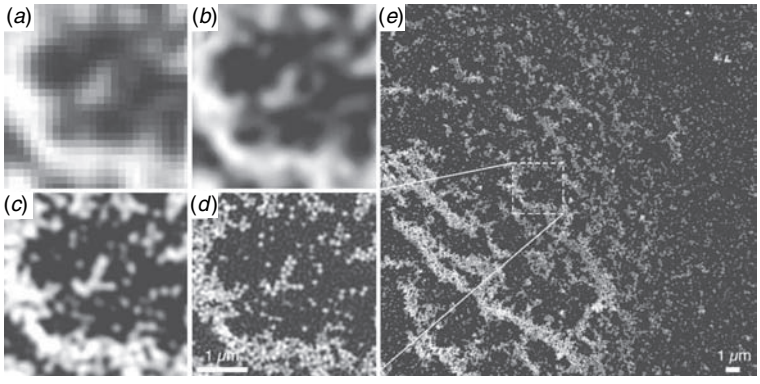

Figure 12.44
Image reconstructed by structured illumination. (*a*) Conventional bright-field, (*b*) confocal, (*c*) linear structured illumination and (*d*) non-linear structured illumination images of the part of the image (*e*) of a two-dimensional array of 100 nm fluorescent glass balls. (Gustafsson (2005))

etc. Under these circumstances a resolution of $\lambda/12\text{NA}$ has been demonstrated (Fig. 12.44(*d*)).

12.6.7 Can super-resolution be reconciled with Abbe's theory, and at what cost?

Now that we have seen several methods of high-resolution imaging that have been demonstrated to exceed the diffraction limit by significant factors, can we understand the limitations of Abbe's theory? The answer is really in the assumption of an infinite periodic object (§12.1.1). Then, the orders of diffraction of a coherent component of the illumination wave were exactly defined and we could determine whether they were, or were not, accepted by the aperture of the imaging lens. If the order was accepted by the aperture, then all its energy would contribute to the image; otherwise none. The optical transfer function (OTF: §12.3) tells us, in fact, for what fraction of the possible coherent illumination components this is true for any particular object period.

But if the instantaneous field of view is modulated, as in SIM (§12.6.6), the diffraction orders have side-bands. Likewise, if it is limited, as in complex phase masking (§12.6.1) and all forms of scanning microscopy, they are diffuse. Then, even if the first order is centred outside the imaging lens aperture, a side-band or part of the diffuse spread may be within the aperture, and the information in this part can be used to reconstruct the image.

Obviously, in such cases only part of the diffracted light contributes to the image, and much of it misses the aperture, so that inefficient use of the illuminating light is inevitable. In fact, only when imaging an object whose diffraction pattern is completely within the aperture of the lens can full use be made of the incident light. A general way of looking at the efficiency problem has been formulated in terms of **information entropy** (Mendlovic *et al.* (2001)). 'Turning on' a super-resolution process increases the amount

of information in the image and therefore decreases its information entropy. However, we know from thermodynamics that any process applied to a closed system can only *increase its total entropy*, so this entropy decrease must be accompanied by an increase somewhere else in the system; it must be the result of destructive interference or reflection or some other process in which photons are extracted randomly from the system. This approach also explains why it is often possible to use image processing to find small changes in an image, well below the diffraction limit, when there is considerable prior information about what the object is likely to be, because then the initial entropy is much smaller.

12.7 Advanced topic: Astronomical imaging by speckle interferometry

The theoretical resolution limit of a telescope, $\theta_{\min} = 1.22\lambda/D$ (§12.2.1), cannot be achieved by any Earth-based instrument because of the presence of non-uniformities in the atmosphere. Local pressure and temperature variations result in the atmosphere having a rather poor optical quality and its properties vary widely as a function of the weather, the time and the azimuth angle. Just to get some idea of the parameters involved, we can quote some typical deviations from the mean optical thickness of the whole atmosphere. The r.m.s. fluctuation amplitude is between two and three wavelengths of visible light, and it changes randomly in a time of the order of 10 ms. In the spatial dimension, fluctuations are correlated within transverse distances of about 0.1 m and are responsible for the twinkling of small stars. The general smearing effect of atmospheric fluctuations on a stellar image is called by the astronomer the **seeing**, and might be 3 arcsec on a poor night and 0.5 arcsec on an exceptionally good, still night. The telescope therefore acts as if it were a collection of small independent telescopes, each of which has diameter (of order 0.1 m) such that $\theta_{\min}$ is the seeing. This should be compared with the Rayleigh resolution limit for, say, a 2 m telescope, which is about 0.05 arcsec. The resolution that can be achieved with a very large telescope therefore seems to be no better than that from a telescope of diameter 10 cm; only the brightness of the image is greater with the larger telescope.

Two major inventions attempted to overcome the resolution limit set by the atmosphere by using multiple telescopes: the Michelson stellar interferometer (§11.8.1) and the Brown–Twiss interferometer (§11.8.3). Recently two new techniques have been introduced in an attempt to overcome the problem of atmospheric degradation of single-telescope images – speckle interferometry, described below, and adaptive optics (wavefront correction by a flexible mirror: see Hardy (1998); Tyson (1998)).

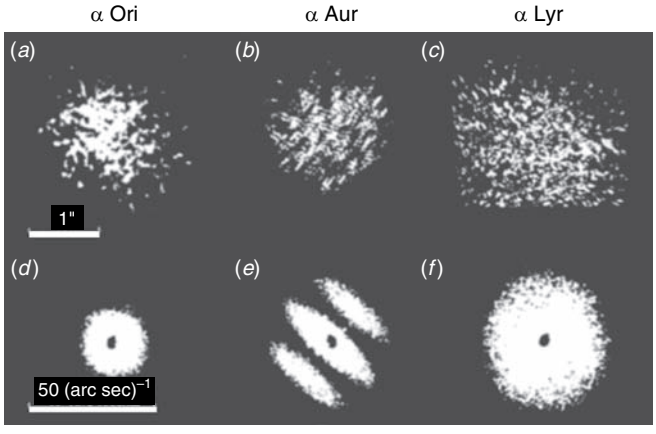

Figure 12.45
Speckle images (above) and corresponding spatial power spectra (12.80) (below). From left to right: (*a*, *d*) Betelgeuse (resolved disc), (*b*, *e*) Capella (resolved binary) and (*c*, *f*) an unresolved reference star. (Labeyrie (1976))

12.7.1 Speckle interferometry

The idea of speckle interferometry (Labeyrie (1976); Labeyrie *et al.* (2006)) arose from careful observation of 'instantaneous' photographs of stellar images. With the introduction of image-intensifier tubes it had become possible to photograph images through a narrow-band filter at a high magnification using an exposure time less than the 10 ms stability time of the atmospheric fluctuations. This is sufficient to see detail at the Rayleigh resolution limit including instantaneous atmospheric fluctuations without further blurring by atmospheric motion. Such images have an overall size of the order of the seeing, but contain a wealth of fine detail. Three examples of 'instantaneous' photographs are shown in Fig. 12.45. There are obvious differences in their detailed structure and these differences represent real differences in the objects. The method of speckle interferometry separates the atmospheric and object contributions to these images by using a series of exposures during which the atmosphere changes from exposure to exposure, but the star remains invariant.

Suppose, first, that the telescope was used to observe an ideal point star at time t. The image, photographed through the atmosphere, has an intensity distribution $p(\mathbf{r}, t)$, (where $\mathbf{r} \equiv (x, y)$), which is the instantaneous atmospherically degraded point spread function of the telescope. This is actually illustrated by Fig. 12.45(c), in which one can see that it is like a random collection of sharp spots. If the atmosphere had been homogeneous, the extended star would have given an ideal image of intensity $o(\mathbf{r})$ with resolution limited only by the finite aperture of the telescope. In the presence of the real atmosphere, the composite image is the convolution of $o(\mathbf{r})$ with the point spread function $p(\mathbf{r})$:

$$i(\mathbf{r}, t) = o(\mathbf{r}) \otimes p(\mathbf{r}, t). \tag{12.76}$$

In the basic technique, this image is photographed at time t_j under conditions such that the photographic film has amplitude transmission proportional to

the exposure intensity (as in holography, §12.5). Subsequently the developed photograph is used as a mask in a diffractometer (§8.1.1). One records on a second film the intensity of its Fraunhofer diffraction pattern, the Fourier transform of $i(\mathbf{r}, t_j)$. The process is repeated for a series of exposures at times t_j, the transforms being superimposed on one another on the second film. Today, video-recording and digital analysis have replaced the photography and the diffraction, but the result is the same.

Now the transform of $i(\mathbf{r}, t_j)$, (12.76), is

$$I(\mathbf{u}, t_j) = O(\mathbf{u})P(\mathbf{u}, t_j), \tag{12.77}$$

where $\mathbf{u}$ is the vector (u, v), and its intensity is

$$|I(\mathbf{u}, t_j)|^2 = |O(\mathbf{u})|^2 |P(\mathbf{u}, t_j)|^2. \tag{12.78}$$

The summation for a long series of t_js gives

$$\sum_j |I(\mathbf{u}, t_j)|^2 = |O(\mathbf{u})|^2 \sum_j |P(\mathbf{u}, t_j)|^2. \tag{12.79}$$

Since $|P(\mathbf{u}, t_j)|^2$ is a random function of $\mathbf{u}$ in which the detail changes significantly from t_j to t_{j+1}, the summation becomes smoother and smoother as more terms are added (§8.5.7). Finally, we have, when enough terms have been added to make $\sum |P(\mathbf{u}, t_j)|^2$ smooth enough,

$$\sum_j |I(\mathbf{u}, t_j)|^2 = |O(\mathbf{u})|^2 \times (\text{a smooth function}). \tag{12.80}$$

The smooth function can be determined by observing an unresolvable star. In this way the intensity of the Fourier transform $|O(\mathbf{u})|^2$ can be measured. If this function is retransformed, we get the spatial auto-correlation function of the stellar image, which reveals simple structural features (such as stellar diameters or separation of binary components); but a true stellar image cannot be deduced.

In Fig. 12.45 we show three examples of speckle transforms obtained by this technique. The upper row shows examples of single exposures from the series of some hundred speckle patterns, and the lower row the summed spatial transforms (12.80). The 'smooth function' is shown in (f), which corresponds to an unresolvable point star with angular diameter less than 0.02 arcsec, the Rayleigh limit of the telescope. The other examples are resolvable stars; transform (e) in particular exhibits Young's fringes which reveal the star to be a binary.

The basic technique of speckle interferometry suffers from the phase problem, but the loss of phase information occurred in this case *after* the speckle images were recorded and it can therefore be retrieved. Several techniques have

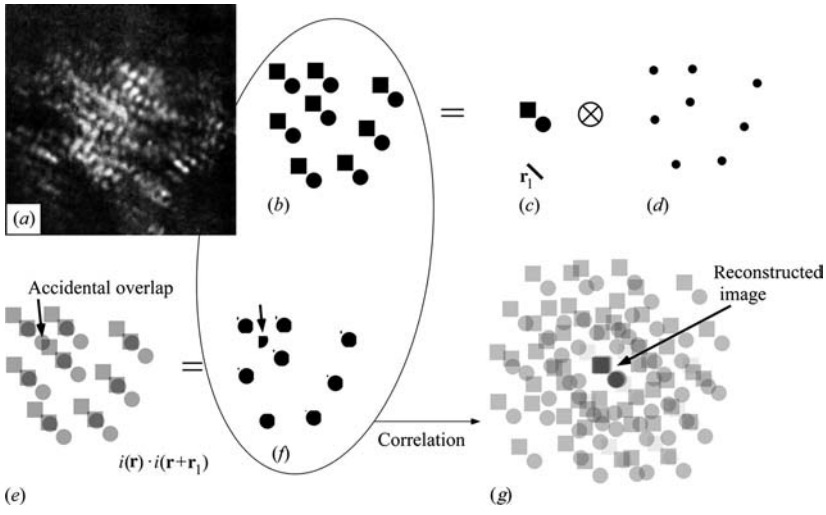

Figure 12.46 Illustrating the principle of speckle masking. (*a*) A single speckle image of Capella (see Fig. 12.45(*b*)), which is drawn schematically as (*b*). This is represented as a convolution of the star image (*c*) with the atmospheric speckle pattern (*d*). (*e*) and (*f*) show that the product of the speckle pattern $I(\mathbf{r})$ with itself shifted by the vector $\mathbf{r}_1$ retrieves the atmospheric speckle pattern (*d*). Note that $\mathbf{r}_1$ can be derived using speckle interferometry on the same data. Finally, (*g*) shows the correlation between (*f*) and the speckle image (*b*) to have an image of the star (*c*) at the origin, surrounded by noise, which averages to a smooth background when many samples are taken.

been devised for this purpose and today are highly developed. We shall briefly describe one method that creates outstanding images.

12.7.2 Speckle masking

Images can be created from a series of speckle patterns by a technique called **speckle masking** (Weigelt (1991)). First we note that, if there were another single isolated and unresolvable star in the field of view, one contribution to the spatial auto-correlation would be an *image* of the original star field (convolved with the unresolvable star, which is essentially a δ-function). Speckle masking creates such a 'reference star' artificially by the process illustrated in Fig. 12.46.

Suppose, as an example, the object $o(\mathbf{r})$ is a binary star (*a*) whose separation $\mathbf{r}_1$ has been determined by speckle interferometry (Fig. 12.46(*b*)–(*d*)). Then the product $i(\mathbf{r}) \cdot i(\mathbf{r}+\mathbf{r}_1)$ contains one overlapping point for each speckle and therefore corresponds to $p(\mathbf{r})$ (Fig. 12.46(*e*), (*f*)). There will be other accidental overlaps in a complex speckle field, which introduce an error that can be corrected statistically. This is treated in the further development of the technique, but we shall ignore it in this discussion. It is now easy to see

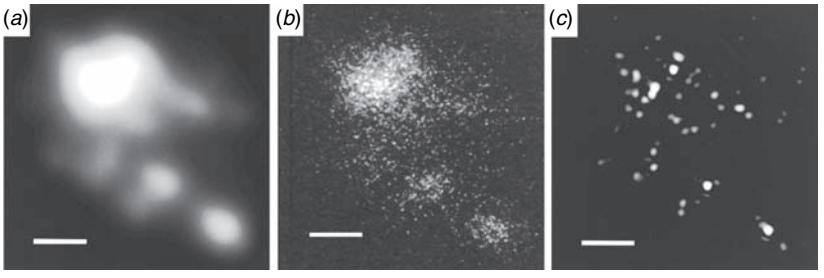

Figure 12.47
An example of a diffraction-limited image retrieved by speckle masking: (*a*) the long-exposure image of R136 in the 30 Doradus Nebula; (*b*) a single speckle image; (*c*) high-resolution reconstruction of the source. The scale bars show 1 arcsec. (Courtesy of G. Weigelt; Pehlemann *et al.* (1992))

that, statistically, the correlation between the point spread function (f) and its speckle image (b) is the object function; one sample is shown in (g). Using (12.76) we write this as $c_3(\mathbf{r})$:

$$\begin{aligned} c_3(\mathbf{r}, t_j) &= i(\mathbf{r}, t_j) \otimes p(-\mathbf{r}, t) \\ &= [o(\mathbf{r}) \otimes p(\mathbf{r}, t_j)] \otimes p(-\mathbf{r}, t_j) \\ &= o(\mathbf{r}) \otimes [p(\mathbf{r}, t_j) \otimes p(-\mathbf{r}, t_j)]. \end{aligned} \tag{12.81}$$

When the term in square brackets (the auto-correlation of p) is averaged over many frames at times t_j, the sharp peak at the origin dominates (see §8.5.7, and Fig. 8.25(c)); this is essentially a δ-function, so that

$$\sum_j c_3(\mathbf{r}, t_j) = C\, o(\mathbf{r}), \tag{12.82}$$

where C is a constant. Thus speckle masking retrieves the image. The tricky point in the technique is the choice of $\mathbf{r}_1$ to get the best approximation to p when we are dealing with an object more complicated than a double star, and often several possibilities are used, the results being averaged. Examples of recent results using this and other techniques can be found in Labeyrie *et al.* (2006), and one is illustrated by Fig. 12.47.

Chapter summary

In this chapter we saw how the imaging process is described by physical optics, and how this leads naturally to an understanding of the limitations and capabilities of imaging systems. We learnt:

- **That the image of a coherently illuminated object is the diffraction pattern of its diffraction pattern;**
- **That this is equivalent to a repeated Fourier transform, which is why the image is basically similar to the object but inverted;**

- That resolution is limited because the extent of the Fourier integrals involved is limited by the wavelength, which leads to the Abbe resolution limit;
- About the Rayleigh and Sparrow resolution limits of imaging instruments;
- How modification of the second Fourier transform by spatial filters can emphasize features of the image, leading to the techniques of dark-field, phase-contrast, schlieren and differential interference contrast imaging;
- How the imaging properties of a system are described in Fourier space by the optical transfer function;
- About holography and interferometric holography;
- How spatial resolution in incoherent imaging has recently been improved well past the Abbe limit by several super-resolution techniques;
- How Fourier image processing is used to achieve diffraction-limited astronomical images with ground-based telescopes, despite atmospheric aberrations.

Problems

12.1. A diffraction-limited astronomical telescope is used in conjunction with a camera to produce a highly magnified image. The imaging sensor used has pixels with dimension 25 μm. If the primary mirror has diameter 1 m and focal length 12 m, what extra magnification should be provided by the camera optics?

12.2. An object consists of two white points on a dark background. Their separation is 3λ. Describe the image that is obtained when the object is viewed in a microscope under the following illumination conditions:
(a) axial coherent illumination, objective with NA = 0.5;
(b) axial coherent illumination, objective with NA = 0.2;
(c) incoherent illumination, objective with NA = 0.2.
Treat the problem as one-dimensional.

12.3. A telescope has a square aperture of side $2a$, with edges horizontal and vertical. Qualitatively, would you expect better resolution along the horizontal/vertical axes, or along the diagonals?
Calculate the Rayleigh and Sparrow resolutions for these axes, and see

if your expectations are justified. Finally, calculate the optical transfer function for these axes. Discuss the significance of your results.

12.4. A photographic transparency shows a monkey behind a fence consisting of equally spaced narrow vertical bars. How would you use a spatial filtering technique to remove the fence, hurting the monkey's image as little as possible?

12.5. For certain types of grey-scale object (with no phase structure) the dark-field image is the negative of the normal image, in the photographic sense. What condition is necessary for this to be true?

12.6. Two close point objects are illuminated coherently in antiphase, so that they are resolved by a microscope however close they may be. What is the apparent separation between them, as a function of the NA of the microscope, when the separation is less than the Abbe limit?

12.7. The Sparrow limit for resolving two point images depends on their relative brightness, but the Rayleigh limit does not. For what value of the brightness ratio are the two limits equal? (To solve this problem analytically, assume the aperture to be square.)

12.8. A phase object consists of many identical small transparent discs on a uniformly illuminated field. The discs are randomly arranged without overlapping, and together they cover half the field of view. The discs change the phase of the transmitted light by angle ϕ. What spatial filter will give maximum contrast between the discs and their surroundings?

12.9. A black-and-white slide has transmitting regions where its value is unity, and opaque regions where it is zero. Suggest a spatial filter that will outline the edges of the transmitting regions with sharp bright lines, whichever way they are oriented.

12.10. Calculate the dimensions of a Wollaston prism from calcite for use in a Nomarski DIC microscope, with objective of focal length 5 mm, NA $= 0.6$. It should be designed so that doubling of the image is not observable. The birefringent properties of calcite are given in §6.6.

12.11. A popular form of phase-contrast imaging consists of simply defocusing the microscope a little. Express this in terms of a complex spatial filter, and apply it to the phase slit of §12.4.4.

12.12. A telescope lens is apodized in order to reduce the prominence of the diffraction rings in the point spread function. If the radius of the

objective is R and the amplitude transmission is reduced by a mask having Gaussian transmission function with parameter σ, find the value of σ that reduces the intensity of the first diffraction ring to 1% of its original value. How is the resolving power affected, according to Rayleigh and Sparrow?

12.13. A hologram of a certain object is made using light of wavelength λ_1. The reconstruction is made using a similar reference beam having wavelength λ_2. How is the reconstruction distorted, and where is it observed? (Assume all angles involved in the problem to be small.)

12.14. Calculate the longitudinal and transverse resolution of a holographic reconstruction, in terms of the wavelength, the dimensions of the illuminated part of the hologram and the image position. (Use Fermat's principle.)

12.15. What is the relationship between the reconstructions produced by an amplitude hologram and its negative?

12.16. Write a computer program using (12.36) to calculate the optical transfer function of a circular optical imaging system with aberrations. Investigate, for example, spherical aberration, coma and astigmatism of various degrees (the forms of the phase errors are given in §3.7). Show that, theoretically, the resolution limit is unaffected by aberrations. However, assuming that detail at spatial frequencies where the MTF $< 5\%$ is not observable, find the relationship between resolution and degree of aberration (in waves at the edge of the aperture stop) for these three aberrations.

12.17. Calculate the resolution limit of a confocal microscope whose two lenses are masked by annular apertures, of radii equal to those of the lenses.

12.18. Write a computer code to describe in two dimensions a monochromatic wave exiting a sub-wavelength aperture, using superposition of plane waves with complex wavenumbers. Use it to show how the resolution of a near-field scanning microscope depends on the distance between the aperture and the sample.

12.19. Formulate a model for a STED microscope with Gaussian point spread function $I_\mathrm{e} = I_m \exp(-r^2/2\sigma^2)$ for excitation of the fluorescent tags, where $\sigma \approx \lambda/2$. The depletion beam can be modelled as having intensity profile $I_\mathrm{d} = I_0 r^2 \sigma^{-2} \exp(-r^2/2\sigma^2)$. If the fluorescent excitation

is quenched by factor $\exp(-I_d/I_m)$, find the r.m.s. width of the point spread function after depletion, as a function of σ and I_0/I_m, and thus deduce the improvement in resolution.

12.20. In a structured-illumination microscope, an object consisting of two points separated by π/k_m is observed. What is the image observed without structured illumination? Three images are recorded using structured illumination with period $2\pi/k_m$, the illumination fringes having phases $\phi_1 = -\pi/2$, in which the right-hand point is obscured by a dark fringe, $\phi_2 = 0$ and $\phi_3 = +\pi/2$, in which the left-hand point is obscured. Describe the images recorded in each stage, and show how they are processed so as to create a single image in which the points are resolved.

References

Binder, R. C. (1973), Fluid Mechanics, 5th edn., Upper Saddle River, NJ: Prentice-Hall.

Collier, R. J., Burkhardt, C. B. and Lin, L. H. (1971), *Optical Holography*, New York: Academic Press.

Gustafsson, M. G. L. (2000), Surpassing the lateral resolution limit by a factor of two using structured illumination microscopy, *J. Microscopy* **198**, 82.

Gustafsson, M. G. L. (2005), Non-linear structured illumination microscopy, *PNAS* **37**, 102.

Hardy, J. W. (1998), *Adaptive Optics for Astronomical Telescopes*, New York: Oxford University Press.

Hariharan, P. (1989), *Optical Holography* Cambridge: Cambridge University Press.

Hell, S. W. and Wichmann, J. (1994), Breaking the diffraction resolution limit by stimulated emission: stimulated-emission-depletion fluorescence microscopy, *Opt. Lett*. **19**, 780.

Jones, H. and Wykes, C. (1989), *Holographic and Speckle Interferometry*, Cambridge: Cambridge University Press.

Kingslake, R. (1978), *Lens Design Fundamentals*, New York: Academic Press.

Labeyrie, A. (1976), High resolution techniques in optical astronomy, in *Progress in Optics XIV*, p. 47, ed. E. Wolf, Amsterdam: North Holland.

Labeyrie, A., Lipson, S. G. and Nisenson, P. (2006), *An Introduction to Optical Stellar Interferometry*, Cambridge: Cambridge University Press.

Levenson, M. D. (1993), Wavefront engineering for microelectronics, *Physics Today*, July, 26.

Lewis, A., Isaacson, M., Harootunian, A. and Murray, A. (1984), Development of a 500 Å resolution light microscope, *Ultramicroscopy* **13**, 227.

Lukosz, W. J. (1966), Optical systems with resolving powers exceeding the classical limit, *J. Opt. Soc. Am*. **56**, 1463.

Mendlovic, D., Zalevsky, Z. and Lipson, S. G. (2001), The optimal system for sub-wavelength point source localization, *Opt. Comm*. **198**, 311.

Paesler, M. and Moyer, P. (1996), *Near Field Optics*, New York: Wiley-Interscience.

Pehlemann, E., Hoffman, K.-H. and Weigelt, G. (1992), Photon-bias compensation in triple-correlation imaging, and observation of R136, *Astron. Astrophys*. **256**, 701.

Pohl, D. W., Denk, W. and Lanz, M. (1984), Optical stethoscopy: image recording with resolution $\lambda/20$, *Appl. Phys. Lett*. **44**, 651.

Rust, M. J., Bates, M. and Zhuang, X. (2006), Sub-diffraction-limit imaging by stochastic optical reconstruction microscopy (STORM), *Nature Methods* **3**, 793.

Schmidt, R., Wurm, C. A., Punge, A. *et al*. (2009), Mitochondrial cristae revealed with focused light, *Nano Lett*. **9**, 2508.

Tonomura, A. (1999), *Electron Holography*, 2nd edn., New York: Springer.

Toraldo di Francia, G. (1952), Super-gain antennae and optical resolving power, *Suppl. Nuovo Cimento* **9**, 426.

Tyson, R. K. (1998), *Principles of Adaptive Optics*, Boston: Academic Press.

Weigelt, K. (1991), Triple correlation imaging in optical astronomy, in *Progress in Optics XXIX*, p. 295, ed. E. Wolf, Amsterdam: North Holland.

Wilson, T. and Sheppard, C. J. R. (1984), *Theory and Practice of Scanning Optical Microscopy*, London: Academic Press.

Zhuang, X. (2009), Nano-imaging with STORM, *Nature Photonics* **3**, 365.

13 The classical theory of dispersion

Many aspects of the interaction between radiation and matter can be described quite accurately by a classical theory in which the medium is represented by model atoms consisting of positive and negative parts bound by an attraction that depends linearly on their separation. Although quantum theory is necessary to calculate from first principles the magnitude of the parameters involved, in this chapter we shall show that many optical effects can be interpreted physically in terms of this model by the use of classical mechanics. Some of the quantum-mechanical ideas behind dispersion will be discussed later in Chapter 14, but most are outside the scope of this book.

In this chapter we shall learn:

- about the way in which a classical dipole atom responds to an oscillating electromagnetic field;
- about Rayleigh scattering, and why sky light is blue and polarized;
- how refractive index, absorption and scattering are related;
- that dispersion, the dependence of refractive properties on frequency, results from atomic resonances;
- about anomalous dispersion near to absorption lines;
- analytical relationships between refractive index and absorption;
- about plasma absorption and magneto-optical effects;
- whether signals can be propagated faster than the speed of light in anomalous-dispersion regions;
- a little about non-linear optical properties, which arise when the wave-fields are very intense;
- about harmonic generation, the photo-refractive effect and soliton propagation;
- about optics at interfaces between conventional dielectrics and materials with negative permittivity;
- about surface plasmon resonance.

Figure 13.1
The classical atom.

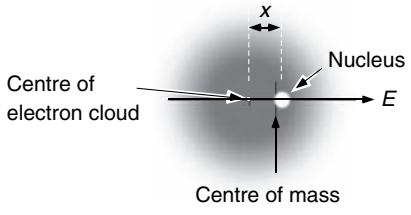

13.1 Classical dispersion theory

The term **dispersion** means the dependence of dielectric response (dielectric constant, refractive index and absorption) on the frequency of the wave-field. This will be the topic of the present section. We can get a surprisingly accurate picture of many dispersive effects simply by postulating a model classical atom, and asking how it responds to an applied wave-field and radiates as a dipole, exactly as we learnt in Chapter 5. We then put many atoms together to discover the properties of bulk optical materials.

13.1.1 The classical atom

The basic description of an atom as an electron cloud oscillating about a massive nucleus is a starting point for understanding many optical phenomena.

Our classical picture of an atom consists of a massive positive nucleus surrounded by a light spherically symmetrical cloud of electrons with an equal negative charge. We imagine the two as bound together as in Fig. 13.1, so that in equilibrium the centres of mass and charge of the core and electron charge coincide. As a result the static atom has zero dipole moment. When it is disturbed, the electron cloud oscillates about the centre of mass with frequency η determined by the reduced mass m of the atom and the spring constant defined as $m\eta^2$.

This model can be applied to individual atoms and simple molecules; more complicated molecules may have internal dynamics and static dipole moments, but still the model gives considerable physical understanding. In addition it can be used for very small particles. But it only predicts a single resonant frequency, whereas atoms really respond resonantly to a number of discrete frequencies; this fact is usually introduced phenomenologically, as in §13.3.2. However, our main concern is with the interaction between the atom and a wave-field having a well-defined frequency ω, and the interaction is strong only if $\omega \approx \eta$; so usually one resonance alone is dominant and the others can be ignored.

We shall show the atom to behave as an oscillating dipole, which therefore loses energy by electromagnetic radiation. In this chapter, we introduce energy loss phenomenologically into the equation of motion of the atom through a

damping constant $m\kappa$. This is one of the parameters whose microscopic origin has to be explained by quantum theory.

Having said all of this, we can write down the equation of motion for the displacement x between the centres of mass of the positive nucleus and the electron charge, when F is a force acting equally and oppositely on each of them:

$$m\frac{\mathrm{d}^2x}{\mathrm{d}t^2} + m\kappa\frac{\mathrm{d}x}{\mathrm{d}t} + m\eta^2 x = F. \tag{13.1}$$

If $F = qE$ is the force due to a constant electric field, (13.1) has the solution $x = F/m\eta^2$. Remembering that x is the separation between positive and negative charges, this corresponds to an induced dipole moment

$$p = qx = q^2E/m\eta^2. \tag{13.2}$$

As a result the electrical polarizability of the atom at zero frequency is

$$\alpha(0) = \frac{p}{\epsilon_0 E} = \frac{q^2}{\epsilon_0 m\eta^2}. \tag{13.3}$$

In the same way, we can calculate the effect of an electric field $E = E_0\exp(-\mathrm{i}\omega t)$, using $\mathrm{d}/\mathrm{d}t \equiv -\mathrm{i}\omega$, to be

$$\alpha(\omega) = \frac{q^2}{\epsilon_0 m(\eta^2 - \omega^2 - \mathrm{i}\kappa\omega)}. \tag{13.4}$$

Notice that α is complex. This indicates that there is a phase difference between the applied field and the induced dipole moment, which is particularly prominent in the frequency interval of about 2κ around η.

We shall now look at some of the applications of this model. We start with a discussion of the scattering by particles sufficiently well separated that there is no interference between the waves they scatter (§13.2). Following this, we shall see the application of the model to dense matter (§13.3) where considerations of interference are crucial.

13.2 Rayleigh scattering

When an electromagnetic wave falls on an isolated particle, it is either absorbed or scattered. If the wave frequency ω is well removed from any resonant frequency η, the absorption of the wave is negligible, and only scattering need be considered. **Rayleigh scattering** occurs when the particle size is much smaller than the wavelength, so the wave-field it experiences is essentially uniform. The result will be seen to be particularly useful for scattering by isolated atoms or molecules, although it is also applicable to very fine particulate matter and density fluctuations. We write the instantaneous dipole moment (13.2)

$$p(t) = \alpha\epsilon_0 E(t). \tag{13.5}$$

If $E(t) = E_0 \exp(-\mathrm{i}\omega t)$, $p(t)$ behaves as an oscillating dipole. This, we know, radiates energy at a rate given by (5.33):

$$W = \frac{\omega^4 p_0^2}{12\pi\epsilon_0 c^3} = \frac{\omega^4 E_0^2 \alpha^2 \epsilon_0}{12\pi c^3}. \tag{13.6}$$

If there are N *independent* scattering particles in a cube of unit volume, the total power scattered is just N times the result (13.6). Now the radiant power incident on a face of the cube is the Poynting vector $\mathbf{S}$ (§5.2.1) which has average magnitude $\frac{1}{2}E_0^2\epsilon_0 c$. Therefore the loss of power per unit distance of propagation is

$$\frac{\mathrm{d}S}{\mathrm{d}z} = -NW = \frac{-N\omega^4\alpha^2 S}{6\pi c^4}. \tag{13.7}$$

This equation has the solution

$$S = S_0 \exp\left(\frac{-N\omega^4\alpha^2 z}{6\pi c^4}\right) = \pi_0 \exp(-z/z_0), \tag{13.8}$$

where $z_0 = 6\pi c^4/N\omega^4\alpha^2$ is a decay distance, telling us that the intensity of light travelling through the scattering region falls to e^{-1} of its initial value in a distance z_0. Before proceeding with an estimate of z_0 for systems such as gases, where N and α are known, it is important to recall that the calculation has assumed the scattering from the individual particles to be independent, so that the scattered waves are incoherent and the intensities of the scattered waves are simply added. This assumption is very often untrue, and will be examined in more detail in §13.2.3.

13.2.1 Wavelength dependence of scattered radiation

Scattering by air molecules and dust particles is very wavelength dependent and is responsible for many atmospheric effects, such as the blue sky and red sunset.

A most striking part of equation (13.8) is the fourth-power dependence on frequency; blue light is scattered about ten times more intensely than red light. This is the reason for the common observation that the sky is blue (weather permitting) during most of the day, but can appear red when one looks directly towards the Sun at dawn or sunset. The sky is blue because we see sunlight scattered by air molecules at all heights and the spectrum is therefore biased strongly to short wavelengths. The redness occurs at daybreak and sundown because at those times the Sun's light, and that reflected from clouds near the horizon, passes horizontally through the atmosphere, and the very long air passage results in the scattering away of a much greater fraction of the blue light than the red. Rayleigh scattering is also responsible for other everyday effects, such as the colours of diluted milk and cigarette smoke, and the glorious sunsets induced by air pollution.

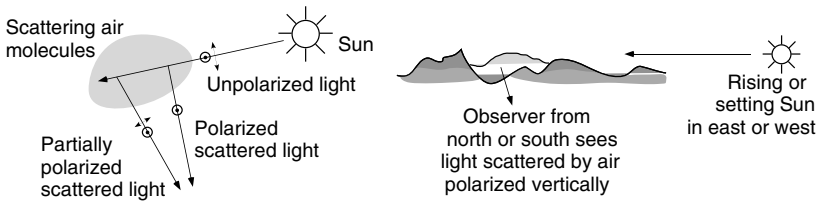

Figure 13.2
Polarization of atmospherically scattered sunlight.

13.2.2 Polarization of scattered radiation

The dipole moment produced in the atom is parallel to the electric vector of the incident light and will reradiate with a radiation polar diagram as described in §5.3.2 (Fig. 5.2(*b*)). The intensity radiated along the axis of the dipole is zero. It therefore follows that scattered radiation along a line perpendicular to the incident light is linearly polarized normal to the plane containing the incident and scattered light. In other directions the light will appear partially polarized. With the aid of a single polaroid sheet (§6.2.2), these conclusions can easily be tested using ordinary sunlight (Fig. 13.2), although polarization is far from complete because of multiple scattering. This effect is commonly used in photography to reduce the effects of haze (Problem 13.1).

13.2.3 Incoherent and coherent scattering

Fluctuations in the density of the atmosphere are responsible for incoherent scattering.

Next we should like to use (13.8) to calculate the decay distance for clean air at atmospheric pressure, but first we should check whether the assumption of independent scattering by individual molecules applies. It turns out that the mean distance between air molecules under atmospheric conditions is two orders of magnitude *less* than a wavelength of light, so that almost completely **coherent** scattering would be expected. If the medium has uniform density, we shall see in §13.3 that there is no net scattering at all. It is only the **deviations from uniform density that give rise to scattering**. The subject of scattering by density fluctuations can be treated fully by thermodynamics (see, e.g., Landau and Lifshitz (1980)) but we can get an idea of the results by a simple argument. One would expect incoherent Rayleigh scattering to result from independent 'blocks' of material of dimensions of order λ, each one therefore having volume $V \approx \lambda^3$. Larger blocks are not small compared with the wavelength, and smaller ones will not scatter incoherently. Now, in such a volume there are on average NV molecules. In a perfect gas the molecules do not interact with one another and the exact number of molecules in the volume V will be governed by Poisson statistics (§11.7). For such statistics, the r.m.s. fluctuation in this number is $(NV)^{\frac{1}{2}}$, and it is these fluctuations that should be considered as the scattering 'particles'. We should therefore consider Rayleigh scattering

by 'particles' containing $(NV)^{\frac{1}{2}}$ molecules, which would have polarizability $\alpha(NV)^{\frac{1}{2}}$ and number density $1/V$. Returning to (13.8) we find

$$z_0 = \frac{6\pi c^4}{V^{-1}\omega^4\left[\alpha(NV)^{\frac{1}{2}}\right]^2} = \frac{6\pi c^4}{N\omega^4\alpha^2}, \tag{13.9}$$

which is exactly the same result as we obtained for incoherent scattering, (13.8)! Thus the scattering by density fluctuations in a perfect gas is just **the same as if all the molecules were to scatter incoherently**.

To estimate the value of z_0 for scattering by a clean atmosphere we relate the atomic polarizability α to the dielectric constant ϵ of the gas and thus to its refractive index (§5.1.2):

$$n = \epsilon^{\frac{1}{2}} = (1 + N\alpha)^{\frac{1}{2}} \approx 1 + N\alpha/2. \tag{13.10}$$

Thus z_0 can be written, substituting the wavelength $\lambda = 2\pi c/\omega$ into (13.8),

$$z_0 = \frac{3N\lambda^4}{32\pi^3(n-1)^2}. \tag{13.11}$$

Using the values at atmospheric pressure $n - 1 = 3 \times 10^{-4}$ and $N = 3 \times 10^{25}\,\mathrm{m}^{-3}$ we find for green light $z_0 \approx 65\,\mathrm{km}$. At first sight this figure seems surprisingly low, particularly as molecular scattering is often not the only factor that limits visibility through the atmosphere. One indeed frequently finds situations where the meteorological visibility exceeds 100 km and even reaches 200 km. However, one should remember that z_0 corresponds to an attenuation factor of $\mathrm{e}^{-1} = 0.37$, and factors of e^{-2} (at $2z_0$) or even $\mathrm{e}^{-3} = 0.05$ (at $3z_0$) can be tolerated before a distant view of snow-capped mountains against an azure sky merges into the haze.

Under what conditions might we expect scattering to differ from the incoherent case? We look for situations where Poisson statistics do not describe the fluctuations satisfactorily. If the medium is relatively incompressible, as is a liquid, the motions of the particles are correlated in such a way that they avoid one another. Density fluctuations are then suppressed and the scattering is less than in the incoherent case, approaching zero in the uniform density limit (§13.3). On the other hand, near the critical point in a fluid, for example, the compressibility diverges and there is a tendency towards local condensation which enhances density fluctuations. We then see excess scattering and the phenomenon of **critical opalescence** (Fig. 13.3).

13.3 Coherent scattering and dispersion

We shall now consider the problem of scattering by a uniformly dense incompressible medium, where the molecules are much closer than one wavelength

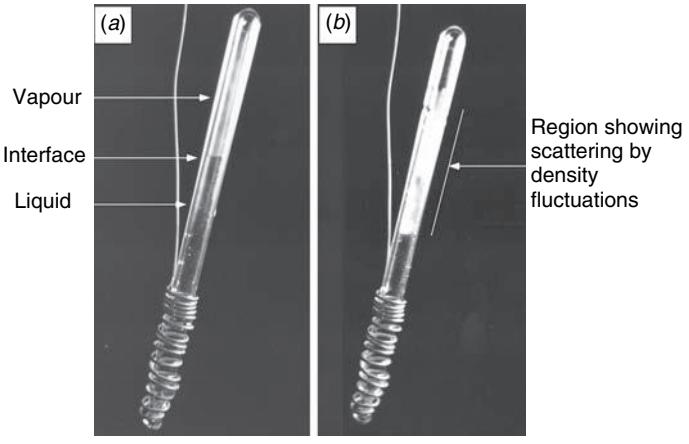

Figure 13.3

Critical opalescence of carbon dioxide near its liquid–vapour critical point. (*a*) $T < T_c$; (*b*) $T \approx T_c$.

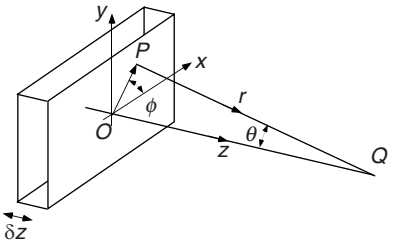

Figure 13.4

Coherent scattering by a dense medium.

There is a strong relationship between molecular scattering and refractive index.

and therefore the scattered waves are correlated in phase. In this problem we have to sum the **amplitudes** of the scattered waves. It turns out that **a real polarizability α results in no net scattering whatsoever**; the material simply refracts the incident wave. But when α is complex, absorption of the incident light occurs.

13.3.1 Refraction as a problem in coherent scattering

Consider scattering by a thin slab of thickness $\delta z \ll \lambda$ in the plane $z = 0$, where z is the axis of propagation of the radiation (Fig. 13.4). In this slab there are N molecules per unit volume, each having polarizability α. Now the oscillating dipoles in the slab will all be excited with the same phase by an incident plane wave $E = E_0 \exp[\mathrm{i}(kz - \omega t)]$ and we can calculate their combined radiation at the point $Q \equiv (0, 0, z)$. A molecule in the slab at point P, $(x, y, 0)$, responds to the incident wave with an oscillating dipole moment of magnitude

$$p(t) = \alpha \epsilon_0 E_0 \exp(-\mathrm{i}\omega t). \tag{13.12}$$

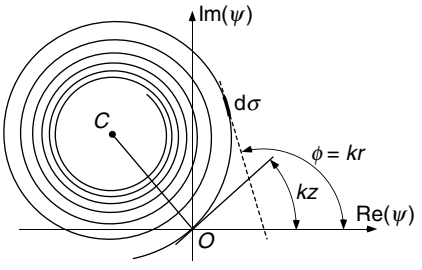

Figure 13.5
Amplitude–phase diagram for the integral (13.16).

From (5.30) its transverse radiation field at Q, $(0, 0, z)$, is

$$e(t) = \frac{\alpha\epsilon_0\omega^2 E_0 \exp[\mathrm{i}(kr - \omega t)]\cos\theta}{4\pi\epsilon_0 c^2 r}, \tag{13.13}$$

where $r^2 = x^2 + y^2 + z^2 \equiv \rho^2 + z^2$ and θ is the angle between the vector $\mathbf{r}$ and the z-axis. The total field from all the molecules in an elementary volume $\mathrm{d}x\,\mathrm{d}y\,\delta z$ at this point is (13.13) multiplied by $N\mathrm{d}x\,\mathrm{d}y\,\delta z$. We can therefore write down the total scattered field δE_Q at Q as the integral of (13.13) over the whole slab:

$$\delta E_Q = \frac{N\alpha\omega^2 E_0\,\delta z\,\exp(-\mathrm{i}\omega t)}{4\pi c^2}\int\!\!\int_{-\infty}^{\infty}\frac{z\exp(\mathrm{i}kr)}{r^2}\mathrm{d}x\,\mathrm{d}y, \tag{13.14}$$

where $\cos\theta$ has been replaced by z/r. In terms of ρ,

$$\delta E_Q = 2\pi z\frac{N\alpha\omega^2 E_0\,\delta z\,\exp(-\mathrm{i}\omega t)}{4\pi c^2}\int_0^{\infty}\frac{\exp\left[\mathrm{i}k(z^2+\rho^2)^{\frac{1}{2}}\right]}{\rho^2+z^2}\rho\,\mathrm{d}\rho. \tag{13.15}$$

The integral in (13.15) can be rewritten simply as

$$\int_z^{\infty}\frac{\exp(\mathrm{i}kr)}{r}\mathrm{d}r, \tag{13.16}$$

which can easily be evaluated by parts or by the amplitude–phase diagram shown in Fig. 13.5 (see §7.2.1 for details of a similar integral) to be $-\mathrm{i}/kz$. Thus

$$\begin{aligned}\delta E_Q &= \frac{N\alpha\omega^2 E_0\delta z}{2c^2k}\exp[\mathrm{i}(kz - \omega t + \pi/2)]\\ &= \frac{1}{2}\mathrm{i}kN\alpha E_0\delta z\,\exp[\mathrm{i}(kz-\omega t)].\end{aligned} \tag{13.17}$$

This scattered wave must be added to the unscattered wave that has reached Q; since δz is small, the unscattered wave is negligibly different from the incident wave $E_{Q0} = E_0\exp[\mathrm{i}(kz - \omega t)]$ whence

$$\delta E_Q = \frac{1}{2}\mathrm{i}kN\alpha\delta z\,E_{Q0}. \tag{13.18}$$

If α is real, the scattered amplitude is in phase quadrature with the direct wave and therefore does not alter its magnitude, but only its phase; in other words,

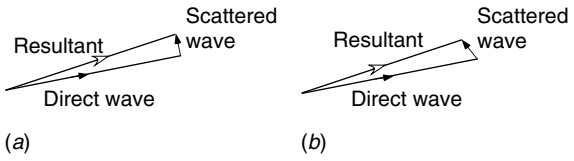

Figure 13.6
Addition of transmitted and scattered wave amplitudes (*a*) when they are in quadrature, and there is no absorption, (*b*) when there is a phase lag and absorption occurs.

the velocity of the wave is modified, but there is no attenuation (Fig. 13.6(*a*)). Then

$$E_Q = E_{Q0} + \delta E_Q = \left(1 + \frac{1}{2}\mathrm{i}kN\alpha\delta z\right) E_{Q0}$$
$$\approx \exp\left(\frac{1}{2}\mathrm{i}kN\alpha\delta z\right) E_{Q0}. \tag{13.19}$$

If we had inserted a transparent plate with refractive index n and thickness δz into the beam, we should have increased the optical path by $(n-1)\delta z$ and modified the wave E_{Q0} to

$$E_Q = E_{Q0} \exp[\mathrm{i}k\delta z(n-1)]. \tag{13.20}$$

So coherent scattering by the slab has resulted in an effective refractive index

$$n = 1 + \frac{1}{2}N\alpha. \tag{13.21}$$

This is just the refractive index we have used, for example in (13.10). Thus, **coherent scattering results in refraction, but not absorption**. It might seem that we have discovered nothing new. The importance of this calculation is that it links refraction and scattering, and can be used to derive an effective refractive index for other types of wave, whose scattering behaviour is known – for example, neutrons or atomic vapours.

If the medium is dense, so that n is not close to unity, we must consider the field that polarizes the molecules as the local field, and not simply the applied field. This makes the treatment more complicated but does not introduce absorption.

13.3.2 Resonance and anomalous dispersion

At frequencies near the resonance η, (13.4) shows α to be complex, and as a result the statement that the scattered wave is in quadrature with the direct wave is no longer correct. The refractive index is still modified, but absorption may also occur as can be seen from Fig. 13.6(*b*). In (13.4) we had polarizability $\alpha(\omega) = q^2/[\epsilon_0 m(\eta^2 - \omega^2 - \mathrm{i}\kappa\omega)]$ and thus the refractive index (13.21) is approximately

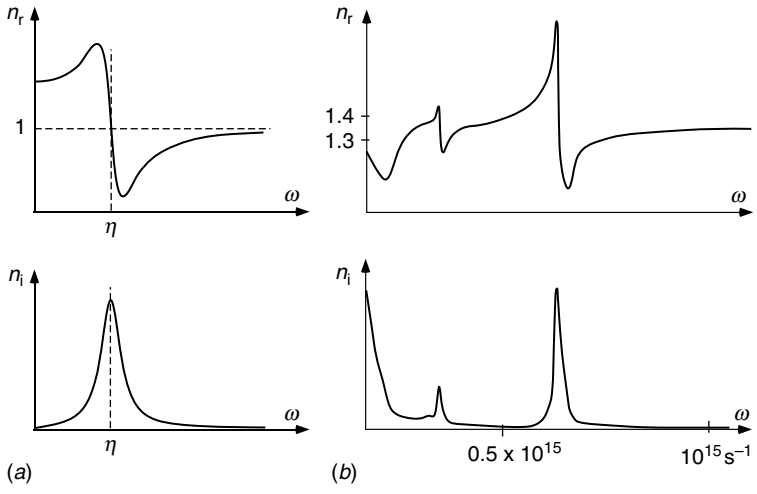

Figure 13.7

Anomalous dispersion near resonances. Real and imaginary parts of the refractive index as a function of frequency: (*a*) theoretical result for a single resonance (13.23) and (13.24); (*b*) experimental data for sea-water in the infra-red, showing several resonances.

$$n = 1 + \frac{1}{2}N\alpha = 1 + \frac{1}{2}\Omega^2(\eta^2 - \omega^2 - \mathrm{i}\kappa\omega)^{-1} \tag{13.22}$$

when $N\alpha \ll 1$. Ω is called the **plasma frequency** $(Nq^2/\epsilon_0 m)^{\frac{1}{2}}$, whose significance will be discussed in §13.7. Then the real and imaginary parts of n are

The typical shape of the curve $n_r(\omega)$ around an absorption line (Fig. 13.7(*a*)) is reversed if the absorption line becomes a transmission line; this is the origin of 'slow light' (Box 13.1).

$$n_r = 1 + \frac{\Omega^2(\eta^2 - \omega^2)}{2[(\eta^2 - \omega^2)^2 + \kappa^2\omega^2]}, \tag{13.23}$$

$$n_i = \frac{\Omega^2\kappa\omega}{2[(\eta^2 - \omega^2)^2 + \kappa^2\omega^2]}. \tag{13.24}$$

Figure 13.7 shows the two quantities, $n_r(\omega)$ and $n_i(\omega)$ schematically. The curves show several important features.

1. Outside the frequency region $\eta \pm \kappa$, $\mathrm{d}n_r/\mathrm{d}\omega$ is positive and $n_i \ll 1$. This is called **normal dispersion** and is typical of all transparent media.
2. The refractive index becomes large at frequencies just below resonance, and sharply drops to a value less than unity just above the resonance. In the region of sharp change, $\mathrm{d}n_r/\mathrm{d}\omega$ is negative; this is called **anomalous dispersion**.
3. In the anomalous dispersion region n_i cannot be neglected and there is absorption. We shall show in §13.4 that this is necessary from very general considerations. This is, of course, the absorption corresponding to an emission line in the atomic spectrum.

A real atom or molecule has a series of spectral lines at various frequencies, and anomalous dispersion takes place in the region of each one of them. As we presented it here, the model atom has only a single resonance; the multiplicity is taken into account by assuming that it has several resonant states, the

jth state having frequency η_j and relative strength N_j. Then, writing the complex dielectric constant index as a superposition of the effects of all of them,

$$\epsilon = 1 + \frac{q^2}{\epsilon_0 m} \sum_j \frac{N_j}{(\eta_j^2 - \omega^2) + \mathrm{i}\kappa_j \omega}. \tag{13.25}$$

The N_js are called **oscillator strengths** and are related to the matrix elements that appear in the quantum-mechanical description (§14.4). Figure 13.7(*b*) shows a typical refractive index curve for sea-water in the infra-red region, where there are several resonances.

13.3.3 Dispersion remote from an absorption band: X-ray refractive index

In the normal dispersion region, remote from a resonance frequency η, we can neglect the absorption and (13.23) becomes

$$n \approx 1 + \frac{\Omega^2}{2(\eta^2 - \omega^2)}. \tag{13.26}$$

In particular, if ω is well above that of the highest resonance in (13.25) we have

$$n \approx 1 - \frac{\Omega^2}{2\omega^2}, \tag{13.27}$$

which shows that the refractive index in the X-ray region is less than unity, but only just so. Substitution of typical values gives $n - 1 \approx -10^{-7}$. This allows the use of **total external reflection** as a method of handling X-rays. Although $v = c/n$ is greater than c, the theory of relativity is not contradicted because it is the group velocity, not the phase velocity, at which information and energy are transported (Problem 2.3).

13.3.4 Plasma absorption edge in a free-electron gas

The model for a free-electron gas gives a good approximation for the complex refractive index of a metal in the infra-red region.

If the electrons in a medium are unbound, for example as a plasma in the ionosphere or as conduction electrons in a simple metal, we can calculate the dispersion by substituting $\eta = 0$. We obtain from (13.22):

$$\epsilon = n^2 = 1 + N\alpha = 1 - \frac{\Omega^2}{\mathrm{i}\kappa\omega + \omega^2}. \tag{13.28}$$

When the electrons are free, $\kappa \ll \omega$, and

$$n \approx (1 - \Omega^2/\omega^2)^{\frac{1}{2}}, \tag{13.29}$$

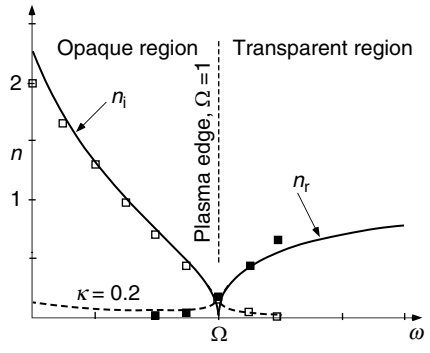

Figure 13.8
Refractive indices near the plasma edge, for a metal. Solid lines show real and imaginary parts of the complex refractive index for a free-electron gas with zero damping. Experimental data points for sodium are shown, and the broken lines show the corrections to the theory resulting from adding an appropriate relaxation time.

which shows that for $\omega < \Omega$ the wave is evanescent and the medium is therefore opaque. At frequency Ω there is a transition to a transparent state. This is called the **plasma absorption edge** and is shown in Fig. 13.8. It is particularly sharp in the alkali metals, where it occurs in the near ultra-violet. At the plasma edge, $n = 0$ and the wavelength is infinite; the whole plasma oscillates in phase, creating a **collective oscillation**.

13.3.5 Refractive index of a free-electron gas in a magnetic field

The refractive index of a free-electron gas is modified by a magnetic field, which is the origin of the Faraday magneto-optic effect (see §6.9.3).

A similar calculation to the above can be made in the presence of a constant magnetic field $\mathbf{B}_0$ and shows one origin of the magneto-optic effect discussed in §6.9.3. Returning to the basic mechanical equation (13.1) we can add a term $q\mathbf{B} \times \mathbf{v}$ representing the Lorentz force, but it is now necessary to work in three dimensions because of the vector product. With $\mathbf{B}_0$ and the incident wave-vector in the z-direction, the dynamic equation for the displacement (x, y) of the charge is

$$m\frac{\mathrm{d}^2(x,y)}{\mathrm{d}t^2} + m\kappa\frac{\mathrm{d}(x,y)}{\mathrm{d}t} + m\eta^2(x,y) + qB_0\frac{\mathrm{d}(y,-x)}{\mathrm{d}t} = q\mathbf{E}_0\exp(-\mathrm{i}\omega t). \tag{13.30}$$

We shall illustrate the effects in the high-frequency region $\omega \gg \kappa, \eta$ only. Clearly the steady-state solution is $(x, y) = (x_0, y_0)\exp(-\mathrm{i}\omega t)$, and so we can replace $\mathrm{d}/\mathrm{d}t$ by $-\mathrm{i}\omega$ whence

$$-m\omega^2(x_0, y_0) - \mathrm{i}q\omega B_0(y_0, -x_0) = q\mathbf{E}_0. \tag{13.31}$$

These equations are analogous to those for the Foucault pendulum in classical mechanics. The result is particularly simple for circularly polarized radiation (§6.1.2) for which $E_{0y} = \pm\mathrm{i}E_{0x}$, the upper and lower signs representing left- and right-handed senses. Eliminating y_0 we have

$$-\left(\omega^2 m - \frac{q^2 B_0^2}{m}\right) x_0 = E_0 q \left(1 \pm \frac{qB_0}{m\omega}\right). \tag{13.32}$$

Then

$$x_0 = \pm \mathrm{i} y_0 = \frac{-E_0 q}{\omega^2 m(1 \mp \omega_\mathrm{c}/\omega)}, \tag{13.33}$$

where $\omega_\mathrm{c} = qB_0/m$ is the **electron cyclotron frequency**. From the charge displacement we calculate the polarization of the medium, $\mathbf{P}_0 = Nq(x_0, y_0)$, and hence the dielectric constant $\epsilon = 1 + \mathbf{P}_0/\epsilon_0 \mathbf{E}_0$:

$$\epsilon = n^2 = 1 - \frac{\Omega^2}{\omega^2(1 \mp \omega_\mathrm{c}/\omega)} \tag{13.34}$$

for the two circularly polarized waves, in which the effect of the magnetic field is represented by ω_c. When ω is large the corresponding refractive indices are real and the medium therefore shows a magnetically induced optical activity, which is the Faraday effect.

We can also represent (13.30) by a matrix equation, which will bring us into line with the formalism of Chapter 6. From (13.31), we calculate in the above manner the dielectric tensor $\boldsymbol{\epsilon}$:

$$\boldsymbol{\epsilon} = \mathsf{I} - \frac{\Omega^2}{\omega^2 - \omega_\mathrm{c}^2} \begin{pmatrix} 1 & \mathrm{i}\omega_\mathrm{c}/\omega & 0 \\ -\mathrm{i}\omega_\mathrm{c}/\omega & 1 & 0 \\ 0 & 0 & 1 - \omega_\mathrm{c}^2/\omega^2 \end{pmatrix}, \tag{13.35}$$

where I is the unit tensor. This can be compared directly to (6.39) for a uniaxial optically active medium, and its principal values can easily be shown to be given by (13.34).

13.4 Dispersion relations

This section will discuss some very general relationships between the real and imaginary parts of response functions such as $\epsilon(\omega)$ that arise because of **causality**, which expresses the self-evident fact that no event can cause observable consequences that precede it in time.

The idea of the impulse response is by no means modern; Newton used it in his analysis of the Moon's motion in the Earth's gravitational field.

13.4.1 Relationship between the impulse and frequency responses

A convenient way to understand the dynamic response of a system to an external field is to start by investigating the effect of a single impulse of the field.

Provided the response of the system is linear, the effect of a more complicated time-varying field can then be built up by superposing the response to impulses.

Suppose we apply an electric field E to a dielectric for a short time $\mathrm{d}t$. The field impulse is then $E\,\mathrm{d}t$, and it causes a polarization $EX(t)\mathrm{d}t$, which is initiated by the field impulse but may die away more slowly. $X(t)$ is called the **impulse response**, and is the temporal polarization response to a unit field impulse applied at $t = 0$. Causality requires that $X(t)$ be zero at negative t. Now let us calculate the polarization caused by a field $E(t)$ by linear superposition of the effects of pulses $E(t')\mathrm{d}t'$ at time t':

$$P(t) = \int_{-\infty}^{t} E(t')X(t-t')\mathrm{d}t'. \tag{13.36}$$

Since $X(t)$ is zero for negative t, the upper limit of the integral can be replaced by ∞. In the particular case of the oscillatory field $E = E_0 \exp(\mathrm{i}\omega t)$, (13.36) becomes, with $t'' \equiv t - t'$,

$$P(t) = E_0 \int_{-\infty}^{\infty} \exp(\mathrm{i}\omega t')\, X(t-t')\mathrm{d}t' \tag{13.37}$$

$$= E_0 \exp(\mathrm{i}\omega t) \int_{-\infty}^{\infty} \exp(-\mathrm{i}\omega t'')\, X(t'')\mathrm{d}t'' = E\,\chi(\omega), \tag{13.38}$$

where $\chi(\omega)$ is the Fourier transform of $X(t)$ and, being the relationship between P and E, is the polarizability ($\equiv N\alpha(\omega)$). The dielectric constant at ω is then

$$\epsilon_0 \epsilon(\omega) E = \epsilon_0 E + P, \tag{13.39}$$

$$\text{whence} \quad \epsilon_0[\epsilon(\omega) - 1] = \chi(\omega). \tag{13.40}$$

This relationship shows that the **frequency response is the Fourier transform of the impulse response** in the dielectric case.

13.4.2 The Kramers–Kronig relations

The refractive index is a complex function of frequency, and its real and imaginary parts are related by the theory of complex functions. The relationship can also be found using complex-plane integrals.

By introducing the requirement that the response of any system must be causal, we can now deduce relationships between the real and imaginary frequency response functions, of which (13.23) and (13.24) are examples. We shall define a unit step function $d(t)$ as follows:

$$d(t) = \begin{cases} \lim_{s\to 0} \exp(st)\ (\sim 1), & \text{when } t < 0; \\ 0, & \text{when } t \geq 0. \end{cases} \tag{13.41}$$

As pointed out in §12.4.4, the step function obtained by putting $s = 0$ does not really have a Fourier transform, but this problem is avoided by letting s be infinitesimal but not zero. Then the transform is

$$D(\omega) = \lim_{s\to 0} (s - \mathrm{i}\omega)^{-1}. \tag{13.42}$$

Now since $X(t)$ only starts at $t = 0$, and $d(t)$ finishes at the same time, we can write[1]

$$X(t)\, d(t) = 0. \tag{13.43}$$

Taking the Fourier transform of this equation

$$\begin{aligned} 0 = \chi(\omega) \otimes D(\omega) &= \lim_{s\to 0} \int_{-\infty}^{\infty} \frac{\chi(\omega')}{s - \mathrm{i}(\omega - \omega')}\, \mathrm{d}\omega' \\ &= \epsilon_0 \lim_{s\to 0} \int_{-\infty}^{\infty} \frac{\epsilon(\omega') - 1}{s - \mathrm{i}(\omega - \omega')}\, \mathrm{d}\omega'. \end{aligned} \tag{13.44}$$

As $s \to 0$ there is a singularity at $\omega' = \omega$. We therefore divide the integral into two parts, that from $\omega - s$ to $\omega + s$ and the rest. The first integral can be evaluated straightforwardly since when s is small enough $\epsilon(\omega')$ is constant throughout the range of integration:

$$\begin{aligned} \lim_{s\to 0} \int_{\omega-s}^{\omega+s} \frac{\epsilon(\omega') - 1}{s - \mathrm{i}(\omega - \omega')} \mathrm{d}\omega' &= [\epsilon(\omega) - 1] \int_{\omega-s}^{\omega+s} \frac{\mathrm{d}\omega'}{s - \mathrm{i}(\omega - \omega')} \\ &= \pi[\epsilon(\omega) - 1]; \end{aligned} \tag{13.45}$$

the integral is independent of s. The rest is called the **principal part** of the integral and is denoted by $\mathcal{P}\int$:

$$\lim_{s\to 0} \left(\int_{-\infty}^{\omega-s} + \int_{\omega+s}^{\infty} \right) \frac{\epsilon(\omega') - 1}{s - \mathrm{i}(\omega - \omega')}\, \mathrm{d}\omega' \equiv \mathcal{P} \int_{-\infty}^{\infty} \frac{\epsilon(\omega') - 1}{-\mathrm{i}(\omega - \omega')}\, \mathrm{d}\omega'. \tag{13.46}$$

Since (13.44) is the sum of (13.45) and (13.46),

$$\epsilon(\omega) = 1 + \frac{1}{\pi} \mathcal{P} \int_{-\infty}^{\infty} \frac{\epsilon(\omega') - 1}{\mathrm{i}(\omega - \omega')} \mathrm{d}\omega'. \tag{13.47}$$

We can equate real and imaginary parts of (13.47) separately and obtain two integral relationships between $\epsilon_\mathrm{r}(\omega)$ and $\epsilon_\mathrm{i}(\omega)$:

$$\begin{aligned} \epsilon_\mathrm{r}(\omega) &= 1 + \frac{1}{\pi} \mathcal{P} \int_{-\infty}^{\infty} \frac{\epsilon_\mathrm{i}(\omega')}{(\omega - \omega')}\, \mathrm{d}\omega' \\ &\left[= 1 + \frac{2}{\pi} \mathcal{P} \int_{0}^{\infty} \frac{\omega' \epsilon_\mathrm{i}(\omega')}{(\omega^2 - \omega'^2)}\, \mathrm{d}\omega' \right]; \end{aligned} \tag{13.48}$$

$$\begin{aligned} \epsilon_\mathrm{i}(\omega) &= -\frac{1}{\pi} \mathcal{P} \int_{-\infty}^{\infty} \frac{\epsilon_\mathrm{r}(\omega') - 1}{(\omega - \omega')}\, \mathrm{d}\omega' \\ &\left[= -\frac{2}{\pi} \mathcal{P} \int_{0}^{\infty} \frac{\omega[\epsilon_\mathrm{r}(\omega') - 1]}{(\omega^2 - \omega'^2)}\, \mathrm{d}\omega' \right]. \end{aligned} \tag{13.49}$$

[1] We ignore a possible δ-function response as part of $X(t)$ which might not give 0 when multiplied by $d(t)$ at $t > 0$.

In the bracketed forms of (13.48) and (13.49) we have used the property $\epsilon(\omega) = \epsilon^*(-\omega)$ of the Fourier transform of a real response to an applied electric field. Equations (13.48) and (13.49) (in either form) are known as the **Kramers–Kronig relations**.

13.5 Group velocity in dispersive media: Superluminal velocities and slow light

It appears that signals cannot propagate faster than light because, when the group velocity exceeds c, there is always absorption.

Although the theory of relativity precludes transmission of information at velocities greater than c, the speed of light in vacuum, in this chapter we have come across some situations where the refractive index is less than unity and therefore 'superluminal' velocities greater than c might be implied. We have to show that this is not really the case in any practical sense.

First, we emphasize again the difference between phase velocity and group velocity. Information is transmitted by modulating a continuous wave, for example shaping it as a pulse or a series of pulses. As we saw in §2.4, the relevant velocity is that at which the envelope of a wave-group propagates, and that is the **group velocity**, $v_g = d\omega/dk$.

In general, the group velocity for a pulse centred at ω_0 can be expressed in terms of the refractive index as

$$v_g = \frac{c}{n + \omega \frac{dn}{d\omega}} \tag{13.50}$$

evaluated at ω_0. One interesting situation, which we shall meet in §13.7, where the refractive index of a plasma at $\omega > \Omega$ is smaller than unity might seem to indicate superluminal propagation; but the dispersion relationship (13.24) for this case is

$$n(\omega) = (1 - \Omega^2/\omega^2) < 1, \tag{13.51}$$

and the group velocity is then easily shown to be $c(1 - \Omega^2/\omega^2)$, which is less than c in that region of frequency. However, when $\omega < \Omega$, which should result in $v_g > c$ according to this result, electromagnetic waves in a plasma are strongly attenuated; and this, it turns out, is not a coincidence.

13.5.1 Superluminal propagation in the anomalous dispersion region?

Clearly, we should be looking for superluminal velocities in a region where $dn/d\omega < 0$. This characterizes the anomalous dispersion region. However, here we have to take into account the inevitable presence of absorption which, as we saw in §13.3.2, is an analytical consequence of anomalous dispersion.

The order-of-magnitude calculation below will show that, if a wave-group is constructed entirely from frequencies in the anomalous dispersion band, it must be sufficiently long that its superluminal velocity is not evident within the decay distance resulting from the absorption. From (13.23) and (13.24), around the resonance frequency $\omega = \eta$, where the anomalous dispersion curve is steepest, we have

$$n_{\mathrm{r}} = 1 + \frac{\Omega^2(\eta^2 - \omega^2)}{2\kappa^2\eta^2}, \tag{13.52}$$

$$n_{\mathrm{i}} = \frac{\Omega^2}{2\kappa\eta}. \tag{13.53}$$

The anomalous dispersion region as described by these equations occurs in a band of frequencies with the half-width defined by

$$|\eta^2 - \omega^2| < \kappa\eta \Rightarrow |\eta - \omega| < \kappa/2. \tag{13.54}$$

Differentiating (13.52), we find the group velocity at $\omega = \eta$ to be

$$v_{\mathrm{g}} = c\left(1 - \frac{\Omega^2}{\kappa^2}\right)^{-1}. \tag{13.55}$$

Now let a pulse of waves at frequency around η propagate for distance D. The time it takes is D/v_{g}. This pulse will arrive ahead of the same pulse travelling in vacuum by time

$$\Delta t = D\left(\frac{1}{c} - \frac{1}{v_{\mathrm{g}}}\right) = \frac{D\Omega^2}{c\kappa^2}. \tag{13.56}$$

Now as a result of the absorption resulting from n_{i} (13.53), this pulse is also attenuated by factor 1/e in distance $D_0 = 1/(n_{\mathrm{i}}k_0) = c/(n_{\mathrm{i}}\eta)$ and the pulse advance within D_0 is

$$\Delta t = \frac{D_0\Omega^2}{c\kappa^2} = \frac{\Omega^2}{\kappa^2\eta n_{\mathrm{i}}} = \frac{2}{\kappa}. \tag{13.57}$$

On the other hand, a pulse built from a spectrum of half-width $\kappa/2$ (13.54) has duration at least $2/\kappa$,[2] so that the superluminal advance of the pulse is never more than the length of the pulse itself!

This approximate argument was made rigorous by Brillouin (1960) who used an analytical method to show that, based on the concept of causality alone (§13.4), the **signal** velocity of a sharp-edged pulse could under no circumstances exceed the phase velocity at infinite frequency, i.e. $c/[\lim_{\omega\to\infty} n(\omega)]$. Since an electromagnetic wave of infinite frequency cannot influence the motion of charged particles, $\lim_{\omega\to\infty} n(\omega) = 1$ and the signal velocity is always equal to c.

[2] The minimum duration occurs if the spectrum is Gaussian. Otherwise it is longer.

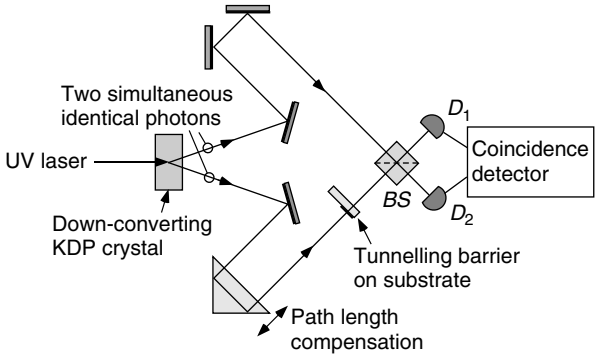

Figure 13.9
Experiment using entangled photons to investigate possible superluminal propagation velocity in a quarter-wave stack. If the photons arrive at *BS* simultaneously, either both go to D_1 or both go to D_2; otherwise they arrive randomly at either detector. This effect is used to detect tiny differences in arrival times at *BS*. (After Chaio and Steinberg (1997))

13.5.2 Superluminal propagation in a resonant quarter-wave stack?

The experiments show that the photons do arrive earlier than in free space, but not by as much as the length of the pulse itself.

Another scenario that has been tested experimentally for superluminal propagation is propagation in the stop band of a multilayer reflector (§10.3.4). In this case, the wave-form in the multilayer is evanescent (§2.3.2); there is no absorption mechanism, but the wave propagates with an exponential decay in its amplitude without a phase change (see Fig. 2.5). The phase and group velocities are therefore both infinite, and a signal entering one side of the stack should appear instantaneously at the other side! Evidence for this behaviour was found using the time delay between pairs of simultaneously emitted entangled photons (§14.3.3) travelling different routes, one through the stack and one outside it (Fig. 13.9) (Chaio and Steinberg (1997)). Once again, the solution to the information propagation paradox lies in the minimum duration of a wave-group made up from frequencies entirely within the stop band.

In §10.3.4, we found that a quarter-wave stack with alternating layers of effective refractive indices u_{H} and u_{L} had a stop band with half-width (10.73) $\delta k = k_0 \sin^{-1}[(u-1)/(u+1)]$, where $u \equiv u_{\mathrm{H}}/u_{\mathrm{L}}$. On the other hand, at the centre of the stop band ($g = \pi$) the transmitted wave decays by factor u^{-1} per half-wavelength period of the stack. The former leads to a minimal half-length $1/\delta k$ for a pulse consisting only of evanescently decaying waves, while the latter gives a decay distance of $1/\ln u$ periods of the stack, i.e. $1/(2\ln u)$ wavelengths. Maybe now not so surprisingly, these two distances are about equal! In other words, the propagation of information at superluminal velocity is again not practical because the wave-group has decayed before the time advance has become longer than the duration of the pulse.

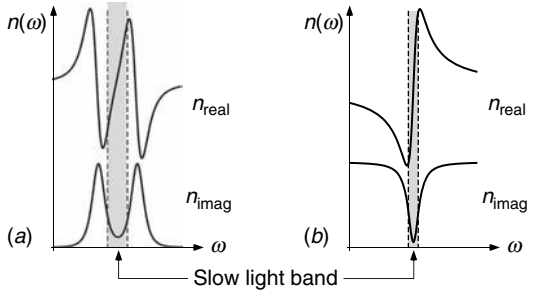

Figure 13.10

Slow light: (*a*) dispersion in the region between the absorption lines of a very close spectroscopic doublet, calculated from (13.23) and (13.24); (*b*) dispersion in the region of a narrow transmission line in an opaque band.

Box 13.1 Slow light

At the other end of the scale, when the dispersion curve is normal and very steep, the group velocity can be very small. This would not be very surprising, except that recently systems have been created with such large dispersions (see §14.9) that group velocities of the order of metres per second have been attained, and light has even been stopped completely.

The general idea can be appreciated if we look first at a pair of closely spaced absorption lines such as the D-lines in alkali metals. The lines in sodium at 589.0 and 589.6 nm are well known; a closer pair of lines is found in rubidium, which has two D_2 hyperfine resonances at about 780 nm separated by 3 GHz in frequency (0.006 nm in wavelength). If the Doppler broadening of the lines is reduced to less than their separation, the transparent region between them, where dispersion is normal, has a very large positive gradient $\mathrm{d}n/\mathrm{d}\omega$, leading to a very small group velocity (Fig. 13.10(*a*)). However, this 'slow light region' is a naturally occurring spectral phenomenon and is not susceptible to control.

Really low group velocities for light pulses have been achieved by using **electromagnetically induced transparency** (EIT) in atomic gases such as strontium, calcium and sodium. The idea of EIT is described in more detail in §14.9. Briefly, in a three-level atomic system (Fig. 14.23), in which the intermediate level and a particular energy sub-level in the rather broad upper band are coupled by a very stable laser, absorption of a probe laser linking the lowest level to the upper band is suppressed when its frequency links it exactly to the same sub-level. This results in a very sharp transmission line, whose width is determined by the strength of the coupling laser. Now we have the opposite situation to an absorption line: a narrow *transmission* line in the midst of an absorbing region (Fig. 13.10(*b*)). The resulting gradient $\mathrm{d}n/\mathrm{d}\omega$ is large and positive, and $v_g = c/[n + \omega \cdot \mathrm{d}n/\mathrm{d}\omega]$ is very small. Since the width of the transmission line is controlled by the strength of the coupling laser, this group velocity can be made almost as slow as one desires, and values of the order of $20\ \mathrm{m\ s^{-1}}$ have been measured (Hau *et al.* (1999)).

13.6 Advanced topic: Non-linear optics

Up to this stage, we have only regarded the polarization of a material by an external field as a linear process. For small enough fields this can be seen as the leading term in the Taylor expansion of $P(E)$:

$$P(E) = P(0) + E\left(\frac{\mathrm{d}P}{\mathrm{d}E}\right)_0 + \frac{1}{2}E^2\left(\frac{\mathrm{d}^2P}{\mathrm{d}E^2}\right)_0 + \frac{1}{6}E^3\left(\frac{\mathrm{d}^3P}{\mathrm{d}E^3}\right)_0 + \cdots. \tag{13.58}$$

For a material with no static dipole moment $P(0) = 0$; and we write (13.58) as

$$P(E) \approx \chi E + \chi_2 E^2 + \chi_3 E^3 + \cdots, \tag{13.59}$$

in which χ_n is the nth-order non-linear polarizability or susceptibility. Since the invention of the laser, a wealth of fascinating phenomena have been discovered which use light beams intense enough to require the expansion (13.59) to be carried beyond the linear term (Yariv (1991)). In the following sections we shall briefly describe two of them: harmonic generation, which involves expansion up to the second order, and four-wave mixing, which involves the next order.

13.6.1 Harmonic generation

We now consider the effect of a wave with time-dependent field $E = E_0 \cos \omega t$ on the medium.[3] From (13.59), expanding as far as the second-order term,

$$P(E) = \chi E_0 \cos \omega t + \frac{1}{4}E_0^2 \chi_2 (\cos 2\omega t + 1) + \cdots. \tag{13.60}$$

One can see that the harmonic frequency 2ω has been induced, and this will be radiated by the oscillating dipole. This is called **second harmonic generation**. In terms of photons, two photons of frequency ω have combined to form one of frequency 2ω, and so the process belongs to the wider category of **three-wave mixing**. In general, higher terms in the expansion will also occur, giving frequencies $n\omega$, but the principle of harmonic generation can be adequately illustrated by considering the case $n = 2$ alone.

What governs the intensity of the observed harmonic waves? First of all the amplitude of the 2ω component in P is proportional to E_0^2 so that the high intensity is necessary to produce observable effects. Second, since the value of χ_2 is identically zero in materials whose molecular structure has a centre

[3] It is not appropriate to use the complex exponential representation here because E will be squared and cubed in what follows.

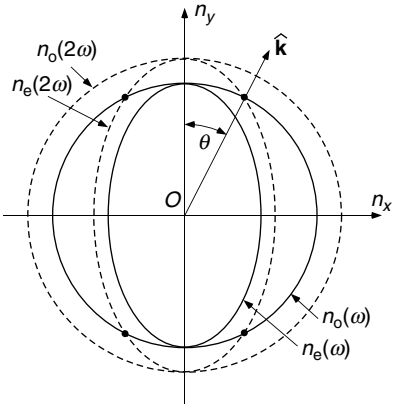

Figure 13.11

Matching refractive indices at ω and 2ω in a uniaxial crystal. The outer branch at ω intersects the inner branch at 2ω in the directions shown, so that phase-velocity matching is achieved at angles θ to the optic axis.

of symmetry, for the same reasons as discussed in §6.9.1, a medium with sufficiently low crystal symmetry must be chosen.

Given large enough E_0 and non-zero χ_2, second harmonic generation will occur in a small volume of the dielectric. For the effect to increase in proportion to the volume of a sample, we also require the harmonic waves generated in different volume elements to add coherently. Now at its point of origin, the 2ω wave is created with a well-defined phase relation to the ω wave that generated it. To maintain this relationship at all other points, which is a requirement for constructive interference, the two waves must propagate in the same direction at the same phase velocity, i.e. $v(\omega) = v(2\omega)$. This is called **phase matching**, and when it is satisfied it becomes quite easy to observe harmonic generation. Commonly available green laser-pointers usually contain frequency-doubled infra-red laser diode sources. Most of the crystals used for second harmonic generation are anisotropic, and the anisotropy of $\mathbf{n}$ (§6.5.4) can then be used to find directions of propagation in which the refractive indices, and hence velocities, for orthogonal polarizations at the two frequencies are equal, i.e. $n_1(\omega) = n_2(2\omega)$. This is shown geometrically in Fig. 13.11 for a uniaxial crystal. The same mechanism can be used to mix light waves of different frequencies (Problem 13.6).

Phase matching can best be appreciated by representing the condition of equal velocities as a requirement for conservation of both energy and linear momentum when the two photons combine in the crystal to create a single one. Clearly, energy is conserved because $2\hbar\omega = \hbar\omega + \hbar\omega$. Conservation of momentum for two photons travelling in the same direction then requires $k(2\omega) = 2k(\omega)$, which implies equal refractive indices at the two frequencies. We could possibly consider the interaction of two waves of the same frequency but different directions, with wave-vectors $\mathbf{k}_1(\omega)$ and $\mathbf{k}_2(\omega)$, and combine the vectors as in Fig. 13.12(a) so that the resultant has the right magnitude $k(2\omega)$. However, this does not work in transparent media having normal dispersion since $n(2\omega) > n(\omega)$ implies that $k(2\omega) \geq 2k(\omega)$. On the other hand, if we

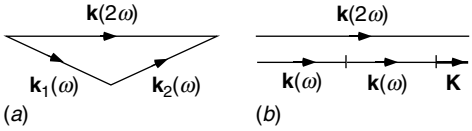

Figure 13.12 **Vector diagrams for conservation of wave-vector in second harmonic generation. (*a*) Hypothetical situation with two input waves in different directions, when dispersion is anomalous; (*b*) interaction of two parallel waves in a medium periodically modulated with wave-vector K.**

can look for a way of adding a fixed vector **K**, it is possible to satisfy the vector equation as shown in Fig. 13.12(*b*). This can be done by modulating the medium periodically, with wave-vector $K = (k(2\omega) - 2k(\omega))$, and provides a commonly used method of phase matching; it is called **quasi phase-matching** (Bloembergen (1996)).

13.6.2 The photo-refractive effect

One result of the third-order term in (13.59) is to make the refractive index of the medium depend on the intensity of the light. We can write the displacement field D in terms of the electric field as

$$D = \epsilon_0 E + P = (\epsilon_0 + \chi)E + \chi_2 E^2 + \chi_3 E^3 + \cdots \tag{13.61}$$

and the instantaneous dielectric constant is

$$\tilde{\epsilon} = D/\epsilon_0 E = (1 + \chi/\epsilon_0) + \chi_2 E + \chi_3 E^2. \tag{13.62}$$

The actual refractive index $n_{\rm nl}$ sensed by a wave is the square root of the average of this instantaneous $\tilde{\epsilon}$ over many wave periods, and so the term linear in E averages to zero and we have

$$n_{\rm nl}^2 = \langle\tilde{\epsilon}\rangle = 1 + \chi/\epsilon_0 + \chi_3 I\,, \tag{13.63}$$

$$n_{\rm nl} = n_0 + \alpha I, \tag{13.64}$$

where $I = \langle E^2 \rangle$ is the intensity of the wave. The sign of α reflects the sign of χ_3, and a typical magnitude is 10^{-2} (watt/cm^2)$^{-1}$. This is called the **photo-refractive effect** (Pepper *et al.* (1990)). Now suppose that a powerful light beam has been used to modulate the refractive index in a photo-refractive crystal. The effect can be measured (or 'read out') by a weak **probe beam**, but the relevant dielectric constant is now $\epsilon_{\rm probe}$ given by $\partial D/\partial E$. The refractive index $n_{\rm probe}$ is then easily shown to be $n_0 + 3\alpha I$. Some experiments on photonic crystals created using the photo-refractive effect were discussed in Box 10.2.

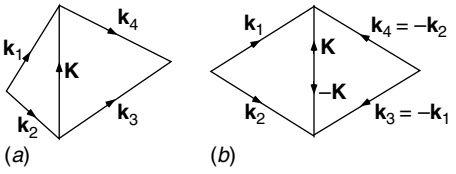

Figure 13.13
Vector diagrams for wave interactions in four-wave mixing: (*a*) the general case; (*b*) the situation for a phase-conjugate mirror.

13.6.3 Four-wave mixing and phase-conjugate mirrors

When a non-linear material is illuminated by a pair of coherent waves travelling in different directions, their combined fields result in a phase grating within the material, which in turn can diffract a third wave (not necessarily coherent with the first two) into a fourth one. This process is called **four-wave mixing** and has been demonstrated in several crystals, notably barium titanate ($BaTiO_3$). The effect can be understood in terms of the photo-refractive effect.

Consider the case where two coherent **pump beams**, with wave-vectors $\mathbf{k}_1$ and $\mathbf{k}_2$, and amplitudes $\frac{1}{2}E_0$, are incident on a non-linear crystal. The total field is $E = E_0 \exp[\mathrm{i}(\omega t - \bar{\mathbf{k}} \cdot \mathbf{r})] \cos\left[\frac{1}{2}(\mathbf{k}_1 - \mathbf{k}_2) \cdot \mathbf{r}\right]$. The intensity is $I = E_0^2 \cos^2\left[\frac{1}{2}(\mathbf{k}_1 - \mathbf{k}_2) \cdot \mathbf{r}\right] = E_0^2(1 - \cos \mathbf{K} \cdot \mathbf{r})$, where $\mathbf{K} = \mathbf{k}_1 - \mathbf{k}_2$. This intensity distribution modulates the refractive index in a sinusoidal manner through the photo-refractive effect. It therefore makes the crystal behave as a three-dimensional grating with wave-vector $\pm\mathbf{K}$ (because $\cos(\mathbf{K} \cdot \mathbf{r}) = \frac{1}{2}[\exp(\mathrm{i}\mathbf{K} \cdot \mathbf{r}) + \exp(-\mathrm{i}\mathbf{K} \cdot \mathbf{r})]$). Clearly, the geometry of Bragg reflection by this grating is identical to the case of the acousto-optic effect (§8.7), where we saw that an incident weaker **probe beam** with wave-vector k_3 undergoes reflection at the Bragg angle. This effect allows direct modulation of one light beam by another, but the time that is often taken for the photo-refractive effect to build up makes it slow compared to other modulation methods. The result can be described simply by a vector diagram (Fig. 13.13(*a*)) showing that the reflected wave $\mathbf{k}_4$ is related to $\mathbf{k}_3$ by $\mathbf{k}_3 - \mathbf{k}_4 = \pm\mathbf{K} = \pm[\mathbf{k}_1 - \mathbf{k}_2]$.

A more interesting situation arises when $\mathbf{k}_3$ is *coherent* with $\mathbf{k}_1$ and $\mathbf{k}_2$. Then, other interference terms can also give rise to gratings within the crystal. We consider a particular case called a **phase-conjugate mirror**, in which $\mathbf{k}_1 = -\mathbf{k}_3$ (Fig. 13.13(*b*)), i.e. two pump beams are counter-propagating so that each is the complex conjugate of the other (their phases are $\mathbf{k}_1 \cdot \mathbf{r}$ and $\mathbf{k}_3 \cdot \mathbf{r} = -\mathbf{k}_1 \cdot \mathbf{r}$). Now suppose that the wavefront of $\mathbf{k}_2$, which we shall call the 'object beam' contains phase and amplitude information $a(x, y)$, so that we write its spatial variation as $a_2(x, y) \exp(\mathrm{i}\mathbf{k}_2 \cdot \mathbf{r})$. Then, the interference between the object beam $\mathbf{k}_2$ and the pump beam $\mathbf{k}_1$ forms a three-dimensional hologram of the object beam (§12.5.4), written into the crystal refractive index.

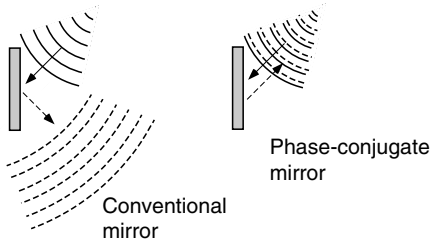

Figure 13.14

Comparison between phase-conjugate and conventional mirrors. In both figures, the incident wavefronts are indicated by continuous arcs, the reflected wavefronts by broken arcs.

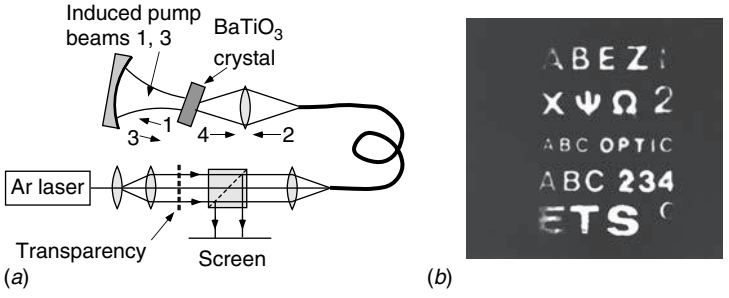

Figure 13.15

(*a*) Experiment to show compensation of distorting optics by a phase-conjugate mirror. The object is a transparency, and the light transmitted by it enters one end of a multi-mode fibre. At the far end of the fibre the light (2) is concentrated onto the phase-conjugate mirror crystal from which it is returned (4) to the fibre. The concentric mirror forms an optical cavity with the crystal, in which the counter-propagating pump waves (1 and 3) build up. The image on the screen, observed with the aid of the beamsplitter, is shown in (*b*). (From Fischer and Sternklar (1985), courtesy of B. Fischer)

What happens when this hologram is reconstructed by the second pump beam $\mathbf{k}_3$? In §12.5.3 we considered the case of reconstruction of a hologram by a wave *identical* to the original reference wave, which resulted in reconstruction of a wavefront $a(x,y)$ identical to that from the original object. Now, replacing $A\exp[\mathrm{i}\phi_0(x,y)]$ in (12.66) by its *conjugate* $A\exp[-\mathrm{i}\phi_0(x,y)]$, we find that the reconstruction $\mathbf{k}_4$ becomes the *conjugate* of the original wavefront, i.e. $a_4(x,y)\exp(\mathrm{i}k_4\cdot\mathbf{r}) = a_2^*(x,y)\exp(-\mathrm{i}k_2\cdot\mathbf{r})$. This **phase-conjugate wave** propagates exactly back to the source of the probe beam (Pepper (1986)). For example, if the object beam $\mathbf{k}_2$ is a *diverging* spherical wave, the system reflects the wave back as a spherical wave *converging* onto the source. This is quite different from a regular mirror where the wave would continue to diverge after reflection, and the comparison is made in Fig. 13.14. These ideas can be applied to imaging through distorting media, where the effect of the distortion can be cancelled out by a phase-conjugate mirror. An example is shown in Box 13.2.

Box 13.2 Demonstration of a phase-conjugate mirror

A phase-conjugate mirror produced in barium titanate was used by Fischer and Sternklar (1985) to show that a complete image could be transmitted through a single multi-mode optical fibre. A plane wave was modulated by a transparency with image information (Fig. 13.15) and the transmitted light focused on the end of a fibre 0.75 m long. At the far end of the fibre the crystal was situated, and the light returned to the input end of the fibre was projected onto a screen. The crystal was made to behave as a phase-conjugate mirror by refocusing the light it transmitted back on to it by means of a concentric spherical mirror. This mirror, together with a Bragg grating which is set up in the crystal, form an optical resonator in which the two counter-propagating modes play the roles of $\mathbf{k}_1$ and $\mathbf{k}_2$. After a time, a good quality image of the original transparency was formed (Fig. 13.15(*b*)). Clearly, when the light passes through the fibre all spatial information in the wavefront becomes completely scrambled, since it is carried on many different modes. However, the phase-conjugate mirror, by exactly reversing the phase at each point on the returning wavefront, could compensate the distortions.

13.6.4 Solitons in a non-linear medium

Suppose that an intense beam of light impinges on a non-linear medium with a positive constant χ_3 (a Kerr medium). In the centre of the beam, where it is most intense, the refractive index of the medium becomes a little larger. We saw earlier that a region of higher refractive index behaves like a GRIN lens (Box 3.4) or an optical waveguide (§10.1) and focuses or confines the incident wave. The optical beam therefore induces such a waveguide and when it is also a guided mode of that waveguide, it no longer becomes broader by diffraction (Fig. 13.16). Such a wave is called a **spatial soliton** (Stegeman and Segev (1999)).

If we look a little closer, we can see that a beam with an approximately Gaussian profile (§7.3) can create a self-consistent scenario. First of all, wave amplitude at the tip of a Gaussian, where it is most intense, can be approximated by an inverted parabola, $\exp(-r^2/2\sigma^2) \approx 1-r^2/2\sigma^2+\cdots$. In a medium with a positive Kerr non-linearity, this results in an inverted parabolic refractive index profile (Fig. 13.17(*a*)). Then, the analysis in §10.2.2 showed that the basic propagation mode in such a waveguide has a Gaussian-shaped amplitude. So all we have to do is to determine under what conditions the parameters match. But there is a catch; even without doing a detailed calculation it is easy to see that the solution is unstable. Suppose that for some reason (absorption, scattering) the wave becomes a little less intense as it propagates. Then, the refractive index profile becomes weaker, which leads to a less confined wave.

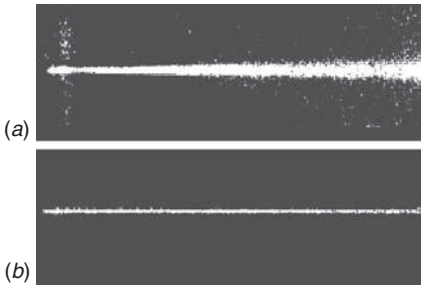

Figure 13.16
Observation of a spatial soliton. (*a*) A laser beam propagates in a linear medium; because the beam is limited in extent, it becomes broader by diffraction. (*b*) The same situation in a Kerr medium. The beam width now remains constant; this is a spatial soliton. (Photographs courtesy of M. Segev; Stegeman and Segev (1999))

Thus the wave will broaden and become even less intense. The opposite would be true if the wave becomes stronger, by focusing for example. Then, the waveguide confines better and the wave intensity increases further, leading to a catastrophic scenario. Actually, what saves the situation is a higher-order non-linearity which would cause the increase in refractive index to saturate at high enough intensity, so that the waveguide does not continue to be more confining as a result of the intensity increase. Then the propagation can be stable.

Quantitatively, we can continue the discussion in §10.2.2 as follows. We saw there that a parabolic profile of the dielectric constant in an axially symmetric system $\epsilon(r) = n^2 = A - \alpha^2 r^2$ leads to a lowest mode with electric field

$$E = E_0 \exp(-r^2/2\sigma^2), \quad \text{where} \quad 1/\sigma^2 = k_0\alpha. \tag{13.65}$$

Since the change in refractive index χE_0^2 is small, we write

$$\epsilon(r) = n^2 = \left[n_0 + \chi_3 E_0^2(1 - r^2/\sigma^2)\right]^2 \approx n_0^2 + 2n_0\chi_3 E_0^2(1 - r^2/\sigma^2), \tag{13.66}$$

from which we see that the coefficients of r^2 in the two expressions for $\epsilon(r)$ are equal if $\alpha^2 = 2n_0\chi_3 E_0^2/\sigma^2$. Since from (13.65) $\alpha^2 = 1/\left(k_0^2\sigma^4\right)$,

$$2n_0\chi_3 E_0^2\sigma^{-2}k_0^2 = \sigma^{-4}, \tag{13.67}$$

$$\sigma^2 = \left[2n_0 E_0^2\chi_3 k_0^2\right]^{-1}. \tag{13.68}$$

This is the unstable equilibrium condition, at which the wave is just intense enough to create a waveguide that supports itself, and confirms that the beam width σ is inversely proportional to $\sqrt{\chi_3}E_0$. Then, saturation of the non-linearity, represented by a reduction of χ_3 as E_0^2 increases, stabilizes the soliton intensity and width.

This is the basic soliton, which is a self-trapped wave whose propagation is quite different from the normal diverging Gaussian beam (§7.3). Soliton interactions can also be very interesting. Consider two solitons that are *mutually incoherent*, such as those produced by two different laser beams with relative phase that fluctuates faster than the response time of the non-linearity. When they come close enough to one another, their intensity fields can overlap, producing a coupled refractive index profile with two peaks slightly closer than

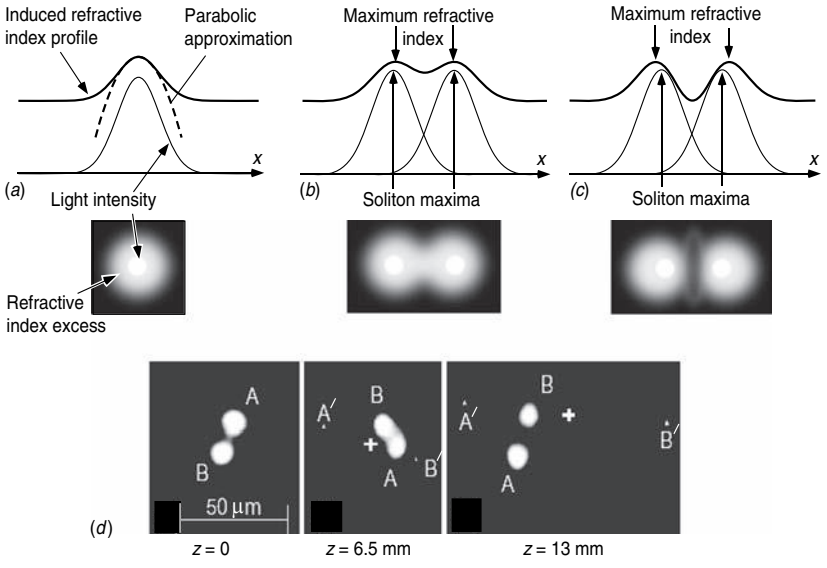

Figure 13.17 **Solitons and soliton interactions. (*a*) The light intensity causes a maximum in the refractive index through the photo-refractive effect, and this maximum acts as a waveguide which traps the light. (*b*) Two neighbouring incoherent solitons produce an overlapping intensity field which guides the solitons closer to one another. (*c*) Two mutually coherent solitons of opposite phases result in an intensity field that is weak in the region between them, and causes them to repel. (*d*) Interaction of two incoherent solitons *A* and *B* travelling along initial paths that are slightly skew. If there were no interaction between them, the solitons would diverge to *A*′ and *B*′ as shown at $z = 6.5$ and 13 mm. However the solitons attract and rotate around one another. (Stegeman and Segev (1999))**

the centres of the beams. This encourages the beams to attract one another, and if they are skew (not lying in the same plane) they may spiral around one another (Fig. 13.17(*b*, *d*)). On the other hand, if the two solitons are *mutually coherent*, and have opposite phases, the field between them is weaker because of destructive interference and the peaks in refractive index move away from the centres of the beams, which are then seen to repel one another (Fig. 13.17(*c*)).

13.7 Advanced topic: Surface plasmons

In §10.1.2 we saw the solution of the electromagnetic wave equation for a planar waveguide constructed from a slab of material with a higher refractive index immersed in a lower index material on both sides. In that case, the wave was confined to the high-index region and decayed evanescently in the lower-index regions. Is it possible to reach such confinement on the interface between two layers alone? It turns out that when one of the media has a *negative*

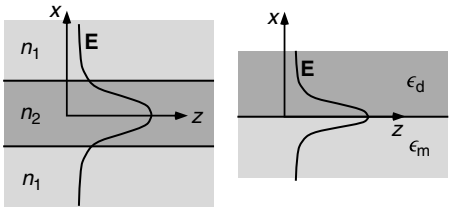

Figure 13.18
(*a*) An electromagnetic wave is confined in a slab of high refractive index n_2 immersed in a surrounding lower index n_1. (*b*) A wave confined to the interface between slabs with dielectric constants ϵ_d and ϵ_m.

dielectric constant, it is indeed possible for a wave to be confined evanescently on both sides of the interface, thus propagating as a surface wave. Such a wave is called a **surface plasmon polariton**, or **surface plasmon**. The names are suggestive of a quantum phenomenon, although in fact the waves are purely classical in origin, as we shall see below. The first evidence of such waves was found by Wood (1902), although they were only understood half a century later (Raether (1988)). The propagation properties of surface plasmons will clearly be influenced strongly by changes in the properties of the materials within the evanescent regions, while being largely unaffected by more distant changes, and the phenomenon has thus found many applications as an optical sensor of surface interactions, particularly as a means of studying biological interactions (Box 13.3). An up-to-date discussion of surface plasmons and their applications is given by Maier (2007).

In Fig. 13.18, we define the propagation geometry when the waves propagate in the z-direction and the variation in ϵ is only in the x-direction. On the left, for comparison, is the waveguide structure discussed in Chapter 10, where ϵ is real and positive in each layer and was written as n^2. On the right is an alternative structure made of two layers only, which will be discussed below.

The master equation remains the same as (10.10), though to make it more general we replace n^2 by ϵ:

$$\frac{\partial^2 E}{\partial x^2} = \left(k_z^2 - \epsilon k_0^2\right) E. \tag{13.69}$$

One layer has dielectric constant ϵ_d and the other ϵ_m. We shall assume that ϵ_d is real and positive, as for all common dielectric materials. We now recall the boundary conditions at the interface, discussed in §10.1.2, where we showed that E_y and $\partial E_y/\partial x$ were continuous (10.18). In like manner, we can show that H_y and $1/\epsilon \cdot \partial H_y/\partial x$ are continuous.

The solution in the dielectric layer remains the same as with the waveguide, (10.16),

$$\begin{aligned} &\frac{\partial^2 \mathbf{E}}{\partial x^2} = k_{x1}^2 \mathbf{E} \\ &\rightarrow \mathbf{E} = \mathbf{E}_0 \exp(-k_{x1} x), \end{aligned} \tag{13.70}$$

where

$$k_{x1}^2 \equiv k_x^2 - \epsilon_\mathrm{d} k_0^2. \tag{13.71}$$

A similar equation can also be written for the magnetic field **H**. We consider the two cases, the ∥, p- or TM polarization, where the field is $\mathbf{H} = (0, H_y, 0)$, and the ⊥, s- or TE polarization where $\mathbf{E} = (0, E_y, 0)$. We take the former case first, because it leads to a practical solution. In the first dielectric medium we have, analogously to (13.70),

$$H_y = H_0 \exp(-k_{x1} x), \tag{13.72}$$

$$\frac{\partial H_y}{\partial x} = -k_{x1} \exp(-k_{x1} x); \tag{13.73}$$

in the second medium ($x < 0$) we have $k_{x2}^2 \equiv k_x^2 - \epsilon_2 k_0^2$ as in (13.70), and

$$H_y = H_0 \exp(+k_{x2} x), \tag{13.74}$$

$$\frac{\partial H_y}{\partial x} = +k_{x2} \exp(+k_{x2} x). \tag{13.75}$$

Here, k_{x1} and k_{x2} are both defined as positive, and we emphasized the signs in the equations. The boundary condition for H_y is already included, in that the amplitudes of both waves at $x = 0$ are H_0. Now the second boundary condition on $\partial H_y/\partial x$ at $x = 0$ implies that on the two sides of the boundary

$$\frac{1}{\epsilon_\mathrm{d}} \frac{\partial H_y}{\partial x} = -\frac{k_{x1}}{\epsilon_\mathrm{d}} H_0, \tag{13.76}$$

$$\frac{1}{\epsilon_\mathrm{m}} \frac{\partial H_y}{\partial x} = +\frac{k_{x2}}{\epsilon_\mathrm{m}} H_0, \tag{13.77}$$

which can only be equal if $\epsilon_\mathrm{m} < 0$ because k_{x1} and k_{x2} were both defined to be positive. Since some metals have complex dielectric constants with negative real parts (§5.6), the surface plasmon waves can indeed propagate on a metal–dielectric interface under suitable conditions.

Repeating the same argument for the ⊥ polarization, comparing the field gradients for $\partial E_y/\partial x$ on the two sides of the boundary gives us

$$\frac{\partial E_y}{\partial x} = -k_{x1} E_0, \tag{13.78}$$

$$\frac{\partial E_y}{\partial x} = +k_{x2} E_0, \tag{13.79}$$

which can never be equal because k_{x1} and k_{x2} have the same sign. The surface plasmon waves therefore have to be polarized with their electric field in the (x, z) plane of incidence.

To find the dispersion relation for the propagating waves we have to solve consistently the three equations

$$\frac{k_{x1}}{\epsilon_\mathrm{d}} = -\frac{k_{x2}}{\epsilon_\mathrm{m}}, \tag{13.80}$$

$$k_{x1}^2 = k_z^2 - k_0^2\epsilon_\mathrm{d}, \tag{13.81}$$

$$k_{x2}^2 = k_z^2 - k_0^2\epsilon_\mathrm{m}, \tag{13.82}$$

which leads directly to

$$k_z = k_0\sqrt{\frac{\epsilon_\mathrm{d}\epsilon_\mathrm{m}}{\epsilon_\mathrm{d}+\epsilon_\mathrm{m}}}. \tag{13.83}$$

Since ϵ_d and ϵ_m have opposite signs, it follows that for k_z to be real, $\epsilon_\mathrm{m} < -\epsilon_\mathrm{d}$. A value of ϵ_m less than zero means that one side of the interface must be a conductor (§5.6) and the requirement that $\epsilon_\mathrm{m} < -\epsilon_\mathrm{d}$ in practice further limits the conductors on which surface plasmons propagate. For example, at $\lambda = 632\,\mathrm{nm}$, gold has $\epsilon_\mathrm{m} = -8.9 + 1.2\mathrm{i}$, but molybdenum has $\epsilon_\mathrm{m} = 1.17 + 27\mathrm{i}$. We also notice that for values of ϵ_m and ϵ_d that have opposite signs, it follows that $k_z > k_0$, so that surface plasmons have wavelengths shorter than free-space waves of the same frequency.

In general, ϵ_m is complex, and complex k_z results. The imaginary part of k_z indicates that surface plasmons are attenuated waves. This is really not surprising, since the finite conductivity of a metal inevitably results in energy dissipation (§5.6). As a practical example, we can consider the interface between gold and water ($\epsilon_\mathrm{d} = 1.33^2 = 1.77$) at $\lambda = 632\,\mathrm{nm}$. We find that $k_z = k_0(1.48 + 0.024\mathrm{i})$. This corresponds to a surface plasmon wavelength 426 nm and decay distance 26 μm.

13.7.1 Excitation of surface plasmons and surface plasmon resonance

Now that we know that a surface plasmon exists when the index of refraction is negative, such as in simple metals, we recall the free-electron gas model, described in §13.3.4, where for simple metals the frequency-dependent dielectric constant, as equation (13.29), is

$$\epsilon(\omega) = 1 - \frac{\Omega^2}{\omega^2}, \tag{13.84}$$

where Ω is the plasma frequency defined in §13.3.2.

Substituting this into (13.83) gives the result shown in Fig. 13.19. As ω approaches zero, the curve is tangent to the 'light line' in the dielectric, $\omega/k_z = c/n_\mathrm{d}$. This may be shown by inserting (13.84) for ϵ_m in (13.83) and examining

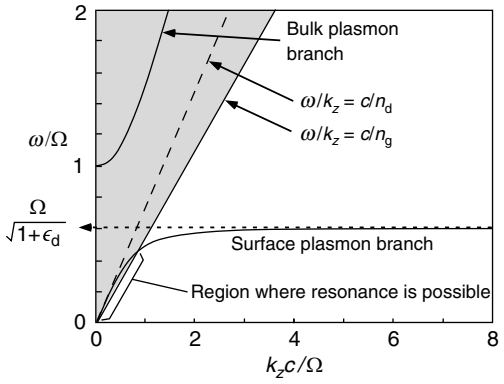

Figure 13.19 **Dispersion of surface plasmons at the interface between a dielectric ($\epsilon_d = n_d^2$) and an ideal metal with dielectric constant given by (13.29). The shaded region, left of the light line $k_z < k_0/n_g$, corresponds to travelling waves in glass, refractive index n_g, at incident angle $\theta = \sin^{-1}(k_z/k_0)$. Between the broken line and the full line, these waves are totally reflected at a glass–dielectric interface. In this region, surface plasmons can resonate (same ω and k_z) with travelling waves incident in the glass.**

the result as $\omega \to 0$, yielding $k = k_0 n_d$. There is also a band gap between the surface plasmon region and the bulk plasmon region ($\omega > \Omega$). Surface plasmon **resonance** (SPR) occurs when an electromagnetic wave is incident on the interface with both k_z and ω equal to those of the plasmon. Clearly this cannot happen by simply illuminating from air since, as we pointed out above, the surface plasmon wavelength is always less than that of a wave in air having the same frequency. This means that there is no intersection between the light line in air and the SPR dispersion curve. The 'Kretschmann' method (Fig. 13.20(a)), probably the most widely used, gets round this problem by introducing the light through a glass prism with higher $n_g > n_d$, which allows large enough values of k_z to be achieved. A thin metal film is deposited on the prism surface, thin enough to transmit the incident wave with relatively little absorption. The surface plasmon is excited on its far surface, where it is in contact with the dielectric medium. Another way to achieve larger values of k_z uses evanescent waves (§2.3.2 and §5.5); by making k_x imaginary, $k_z = \sqrt{k_0^2 - k_x^2}$ can be made larger than k_0. This technique, actually the first to be tried, was invented by Otto in 1958 (Fig. 13.20(b)). A third method uses a grating structure, period Λ, which adds an additional $2\pi/\Lambda$ to the k_z by diffraction and is the equivalent of quasi phase-matching (§13.6.1).

The reflected intensity as a function of angle or wavelength can be calculated using the technique developed in Chapter 10 for thin films. We consider the Kretschmann case, glass–metal–dielectric, where the metal film has a complex refractive index. A typical result, as a function of incident angle is shown in Fig. 13.21.

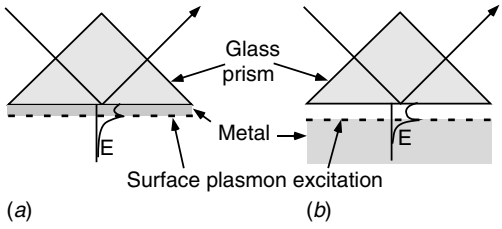

Figure 13.20

Two methods of exciting surface plasmons by using waves incident from a glass prism at angles above the critical angle: (*a*) the Kretschmann configuration where a film of metal is deposited on the prism surface; (*b*) the Otto configuration, where the surface of a bulk metal sample is situated within the evanescent wave outside the hypotenuse of the prism. The form of the evanescent wave is shown schematically in both cases.

Box 13.3 An application of SPR to detecting interactions between biomolecules

The resonance frequency θ_p is a strong function of the dielectric constant $\epsilon_d = n_d^2$ of the dielectric medium within the region sampled by the evanescent wave, which is of the order of $\lambda/2$ deep. This has been developed as a very sensitive method of detecting either small changes of n_d or the thickness of a dielectric film of known properties deposited on the metal surface, which perturbs the measured value of n_d. Sensitivity of the order of 10^{-6} in refractive index has been achieved, which requires optimization of the sharpness of the resonance curve (Fig. 13.21(*a*)), both with respect to the material (gold, silver) and its thickness. Although silver has a sharper dip in the reflectivity curve, gold is favoured due to its superior film quality and chemical resistance. In biodetection, the dielectric medium is usually a water-based solution containing adsorbent molecules. The angle of incidence is scanned to create the resonant reflectivity curve, which has a minimum at an angle related to the amount of material adsorbed on the gold surface. Based on a typical refractive index of about 1.5 for polymers, which replace water ($n = 1.33$) in the adsorbed layer, one can estimate that a change of 10^{-5} in the average n_d within the $\lambda/2$ evanescent layer corresponds to a layer of average thickness 0.015 nm, which is much less than one monolayer coverage. As further molecules are adsorbed on the surface, the resonance frequency changes and the observed dip at θ_p shifts sideways. Monitoring the position of the minimum over time allows a thorough understanding of the biomolecular interactions. Figure 13.22 shows a typical experimental result demonstrating both attachment and detachment of molecules to a substrate film adsorbed on gold.

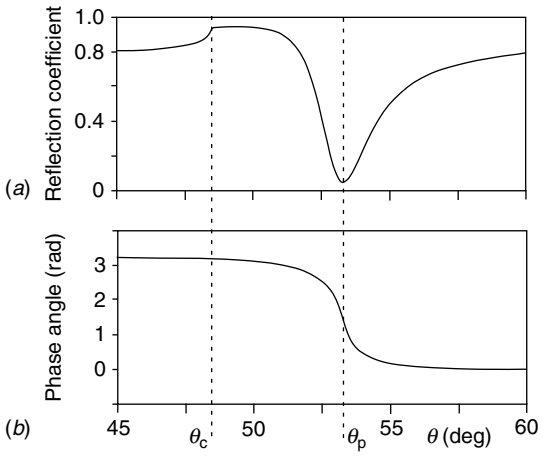

Figure 13.21

The calculated intensity reflection coefficient (*a*) and phase (*b*) for a 45 nm thick gold film between the glass prism and water, as a function of the angle of incidence θ in a Kretschmann device. The critical angle is θ_c. A dip in the intensity is observed at the resonance angle θ_p, which coincides with the maximum gradient in the phase change. (After Ran and Lipson (2006))

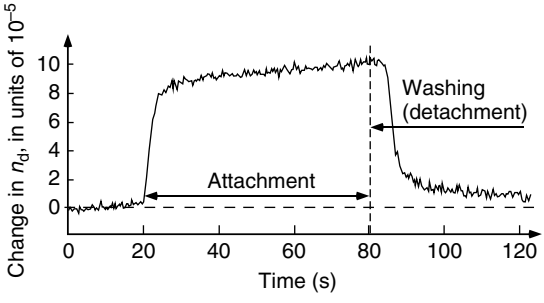

Figure 13.22

A typical SPR biosensor response curve showing the attachment of a biochemical layer to a substrate on a gold film and its subsequent detachment when it is washed off. The ordinate shows changes of equivalent refractive index in units of 10^{-5}, as a function of time. The equilibrium signal reached after about one minute corresponds to less than one monolayer of adsorbate. (Data courtesy of Bio-rad (Haifa) Inc.)

Chapter summary

In this chapter we discussed how the refraction and dispersion of waves are related to the properties of optical materials. We saw that:

1. Many refractive and dispersive properties can be understood in terms of the response of a classical induced dipole atom to an applied oscillating wave-field;
2. Scattering by individual atoms preserves the polarization of the light and has a λ^{-4} wavelength dependence;
3. Refraction can be described in terms of coherent scattering by many atoms;
4. Refraction has anomalous behaviour near a resonance frequency, where the atom absorbs light;

5. **Dispersion and absorption are related analytically as a result of causality;**
6. **Anomalous and evanescent propagation of light suggest scenarios where signals might propagate faster than light, but these do not stand up to detailed scrutiny;**
7. **When the electric wave-field becomes comparable to internal atomic fields, refraction becomes non-linear, and we studied some examples of applications of non-linear optics;**
8. **When the dielectric constant of a material becomes negative, surface plasmon propagation on its surface becomes possible.**

Problems

13.1. In what direction, relative to the Sun, should a photograph be taken so that a polarizing filter will be most effective in reducing scattering by dust in the atmosphere?

13.2. The refractive index of a medium as a function of frequency increases smoothly and monotonically from n_1 to n_2 in a small frequency range of $\Delta\omega$. What can you deduce qualitatively about the absorption of the medium in this frequency region?

13.3. A material has a spectral absorption line at wavelength ω_0, which can be represented as a δ-function of strength a_0. Use the Kramers–Kronig relations to deduce $n(\omega)$.

13.4. A uniaxial non-linear crystal has $n_o = 1.40$ and $n_e = 1.45$. Its dispersion in both polarizations is $\lambda dn/d\lambda = -2.5 \times 10^{-2}$. At what angle to the optic axis would phase matching be observed for second harmonic generation? If the crystal is 1 mm thick, how accurately must the incident beam be aligned to this direction for the second harmonic wave to be observed?

13.5. Explain why a polycrystalline non-linear material can be used for second harmonic generation. Compare the efficiency of such a polycrystal to that of a single crystal at the optimum orientation? Under what conditions might the polycrystal be better?

13.6. Derive the phase-matching condition required for mixing two frequencies ω_1 and ω_2 to obtain their sum $\omega_1 + \omega_2$.

13.7. What interference pattern would you expect to see when one mirror in a Michelson interferometer is replaced by a phase-conjugate mirror?

13.8. You look at yourself in a phase-conjugate mirror. What do you see?

13.9. What properties would be required for a material to support propagation of a *dark* soliton, which is a black spot on a bright background? The dark spot could be created by a spiral phase plate with $m = 1$ (§5.9), so that the wave amplitude is antisymmetric about the dark origin (changes sign from (x, y) to $(-x, -y)$).

References

Bloembergen, N. (1996), *Non-Linear Optics*, Singapore: World Scientific.

Brillouin, L. (1960), *Wave Propagation and Group Velocity*, New York: Academic Press.

Chaio, R. Y. and Steinberg, A. M. (1997), Tunneling times and superluminality, in *Progress in Optics*, ed. E. Wolf, **37**, 347.

Fischer, B. and Sternklar, S. (1985), Image transmission and interferometry with multimode fibers using self-pumped optical phase conjugation, *Appl. Phys. Lett*. **46**, 113.

Hau, L. V., Harris, S. E., Dutton, Z. and Behroozi, C. H. (1999), Light speed reduction to 17m/s in an ultra-cold atomic gas, *Nature* **397**, 594.

Landau, L. D. and Lifshitz, E. M. (1980), *Statistical Physics*, Oxford: Pergamon.

Maier, S. (2007), *Plasmonics: Fundamentals and Applications*, New York: Springer.

Pepper, D. M. (1986), Applications of optical phase conjugation, *Sci. Am*., January, 56.

Pepper, D. M., Feinberg, J. and Kukhtarev, N. V. (1990), The photorefractive effect, *Sci. Am*., October, 34.

Raether, H. (1988), *Surface Plasmons on Smooth and Rough Surfaces and Gratings*, Berlin: Springer.

Ran, B. and Lipson, S. G. (2006), Comparison between sensitivities of phase and intensity detection in surface plasmon resonance, *Optics Express* **14**, 5641.

Stegeman, G. I. and Segev, M. (1999), Optical spatial solitons and their interactions: universality and diversity, *Science* **286**, 1518.

Wood, R. W. (1902), On a remarkable case of uneven distribution of light in a diffraction grating spectrum, *Proc. Phys. Soc. (London)* **18**, 269.

Yariv, A. (1991), *Optical Electronics*, 4th edn., Philadelphia: Holt, Reinhard and Winston.

14 Quantum optics and lasers

This book is intended to explain the physical basis of classical optics and to introduce the reader to a variety of wave phenomena and their applications. However, it was discovered at the end of the nineteenth century that the description of light in terms of Maxwell's classical electromagnetic waves was incomplete, and the notion of quantization had to be added. Since then, in parallel to the development of wave optics, there has been an explosive growth of quantum optics, much of it fuelled by the invention of the laser at the end of the 1950s, which also provided a great incentive to reconsider many topics of classical optics, such as interference and coherence theory. It would be inappropriate that this book should ignore these developments; on the other hand, the subject of quantum optics is now so wide that a single chapter can do no justice to the field. In this chapter, we therefore set out modestly to explain the way in which quantum optics is different from classical optics, and give a qualitative introduction to lasers, followed by a taste of some of the new phenomena that have developed in recent years and are currently at the forefront of optics research.

In this chapter we shall discuss:

- how the electromagnetic field can be quantized, by creating an analogy between an electromagnetic wave and a simple harmonic oscillator;
- the concept of the photon, and some of its properties;
- uncertainty or fluctuations in the electromagnetic field, and how they lead to zero-point field energy;
- some of the statistical properties of non-classical light;
- interaction of light with matter, and stimulated and spontaneous emission of light;
- how lasers work, with some representative examples using different physical principles;
- fluorescent emission and its properties, which we have seen to be particularly important in high-resolution microscopy;
- some recent experiments on electromagnetically induced transparency and their implications.

14.1 Quantization of the electromagnetic field

At the end of the nineteenth century it began to be clear that classical ideas could not explain all physical phenomena (§1.4). Two of the most notable problems were the **ultra-violet catastrophe** and the **photo-electric effect**, whose analysis and understanding by Planck and Einstein led to the foundation of quantum theory.

14.1.1 The 'ultra-violet catastrophe'

We begin by considering the electromagnetic wave spectrum in an ideal cavity according to classical statistical mechanics. Suppose that we have a cubic reflecting cavity, with side L, made out of a highly conducting metal. (The cubic shape is chosen for simplicity only; it is not critical.) Any electromagnetic wave that satisfies the boundary conditions $\mathbf{E}_{\|} = 0$ on the inner surface of the cavity is one of its normal modes. We can find such normal modes easily; for example, the standing wave

$$E_y = \cos zk_z \ \cos xk_x \, \mathrm{e}^{-\mathrm{i}\omega t} \tag{14.1}$$

has zero value on the planes $x = \pm L/2$, $z = \pm L/2$ provided that $Lk_x = l\pi$, $Lk_z = n\pi$, where l and n are odd integers. There are also sine solutions leading to even integers. Since the field is in the y-direction, its component parallel to the planes $y = \pm L/2$ is always zero. Now (14.1) is the superposition of four plane waves; it can be written

$$\begin{aligned} E_y &= \frac{1}{2}\mathrm{e}^{-\mathrm{i}\omega t}[\cos(xk_x + zk_z) + \cos(xk_x - zk_z)] \\ &= \frac{1}{4}\{\exp[\mathrm{i}(xk_x + zk_z - \omega t)] + \exp[\mathrm{i}(-xk_x - zk_z - \omega t)] \\ &\quad + \exp[\mathrm{i}(xk_x - zk_z - \omega t)] + \exp[\mathrm{i}(-xk_x + zk_z - \omega t)]\}, \end{aligned} \tag{14.2}$$

which all have dispersion relations $\omega^2 = k^2c^2$, i.e.

$$\omega^2 = \left(k_x^2 + k_z^2\right)c^2 = \pi^2c^2L^{-2}(l^2 + n^2). \tag{14.3}$$

The allowed frequencies of electromagnetic waves in this cavity, when polarizations E_x and E_z are added, are

$$\omega^2 = \pi^2c^2L^{-2}(l^2 + m^2 + n^2), \tag{14.4}$$

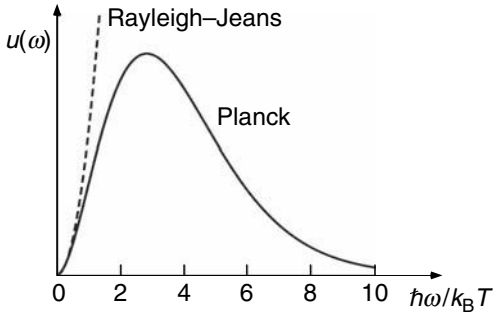

Figure 14.1

Black-body spectrum, compared to the classical Rayleigh–Jeans approximation.

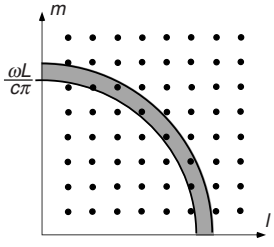

Figure 14.2

Distribution of modes in the (*l*, *m*) plane for a cubical cavity.

in which l, m and n are positive integers,[1] at least two of which must be non-zero. There are two independent polarizations that give the same values of l, m and n. **There is no upper limit to l, m and n.** The number of modes is infinite, and their density (number of modes possible in a given interval of ω) *increases* with ω. Now, according to the classical equipartition theorem of Boltzmann, every normal mode in thermal equilibrium has energy $k_B T$ ($\frac{1}{2}k_B T$ for each degree of freedom, of which an oscillator mode has two; see §14.2) and so the total energy inside the cavity must be infinite, its density increasing without limit at higher frequencies, towards the ultra-violet. This was an absurd conclusion, and was called the **ultra-violet catastrophe**. Rayleigh and Jeans, amongst others, tried hard to find a solution. Experimental data (Fig. 14.1) on the spectrum of a black body (a cavity with a small inspection hole in it) showed a radiation density increasing with frequency at the red end of the spectrum, in accordance with (14.4), which leads to a density that increases like ω^2 as we shall see in (14.6). But then the energy density peaked at a certain frequency (the 'red' of a red-hot body) and fell off rapidly at higher frequencies. Planck found the solution, empirically at first, in terms of the quantization of the radiation modes, and his discovery heralded quantum theory, which has since been applied so successfully to a description of matter through atomic scales and down, at least, to the size of the nucleus.

14.1.2 Quantization of the electromagnetic modes in a cavity

The Rayleigh–Jeans argument, modified by Planck, continues as follows. The numbers (l, m, n) can be represented as integer points in a phase space in which l is counted in the x-direction, m in y and n in z (Fig. 14.2). From (14.4), the frequency ω corresponding to (l, m, n) is $\pi c/L$ times the distance of (l, m, n) from the origin. So the number of states with frequencies between ω and $\omega + \Delta\omega$

[1] Negative integers do not give us new states, but just interchange terms in (14.2).

is the number within the positive quadrant of an onion-layer of radius $\omega L/c\pi$, thickness $\Delta\omega L/c\pi$, which has volume

$$\frac{1}{8}\cdot 4\pi\left(\frac{\omega L}{c\pi}\right)^2\cdot\frac{\Delta\omega L}{c\pi} \tag{14.5}$$

and contains on average the same number of states, since there is one integer point per unit volume. This number, times two for the two independent polarizations, gives the **density of states** per unit interval $\Delta\omega$:

$$D(\omega)=\frac{L^3\omega^2}{c^3\pi^2}. \tag{14.6}$$

Planck's idea was that the electromagnetic energy was **quantized** in units of $\hbar\omega$. Each mode could then have any whole number of quanta of energy. The average number of such quanta would then be given by Boltzmann statistics, and he showed this average number to be

$$\langle n\rangle=\left[\exp\left(\frac{\hbar\omega}{k_{\mathrm{B}}T}\right)-1\right]^{-1} \tag{14.7}$$

at temperature T.[2] If the quantum $\hbar\omega$ is small compared with the classical average energy of a mode, $k_{\mathrm{B}}T$, a large number of quanta is probable, and the classical result $\langle n\rangle\approx\hbar\omega/k_{\mathrm{B}}T$ holds. But if the quantum is large compared with $k_{\mathrm{B}}T$, there is little probability of there being even *one* quantum per mode in a cavity in thermal equilibrium. This is how we understand $\langle n\rangle$ in (14.7). For example, when we are in the region of the maximum of the black-body spectrum, where $\hbar\omega\approx k_{\mathrm{B}}T$, the probable number of photons per mode is $(\mathrm{e}-1)^{-1}\approx 0.6$. Only at frequencies much lower than $k_{\mathrm{B}}T/\hbar$ is there a reasonable probability of finding more than one photon in a mode. From (14.7), the total energy in the cavity between frequencies ω and $\omega+\mathrm{d}\omega$ is $u(\omega)\,\mathrm{d}\omega$ where

$$u(\omega)=\langle n\rangle\hbar\omega D(\omega)=\frac{\hbar L^3}{c^3\pi^2}\cdot\frac{\omega^3}{\mathrm{e}^{\hbar\omega/k_{\mathrm{B}}T}-1}. \tag{14.8}$$

This fits the observed black-body spectrum very well (Fig. 14.1), and can be integrated to find the total black-body radiation energy density in the cavity at temperature T (Stefan's law):

$$U(T)=\int_0^\infty u(\omega)\,\mathrm{d}\omega=\frac{L^3\pi^2k_{\mathrm{B}}^4T^4}{15\hbar^3c^3}. \tag{14.9}$$

The quanta of radiation have been given the name **photons**, and can be considered in many ways like particles. This is because the distribution (14.7) is the same as that obtained for identical particles, which have integer spin and zero

[2] See any text on statistical mechanics for the details.

chemical potential, so it is tempting to consider photons as having these properties. But it is also dangerous, because photons cannot be localized in the way that massive particles can. We shall discuss some of the consequences in §14.1.3.

Another oscillator that has the same statistics is the **quantum-mechanical simple-harmonic oscillator**, and it turns out very fruitful to establish the analogy between this and the electromagnetic wave, because we can then lift the solutions directly from quantum mechanics. In particular, it is usual nowadays to express the concepts of quantum electromagnetic fields in the language of second quantization, i.e. in terms of operators that create and annihilate photons and change the wave-functions appropriately. We shall not develop this approach to the mathematical formulation of the theory (see, for example, Loudon (2000); Mandel and Wolf (1995)); we shall only describe enough of it to see the physical basis of some of the newest ideas which lead to experimental results that cannot be explained on the basis of classical electromagnetic theory. But first we shall go back to one of the oldest and still most puzzling phenomena in photon optics.

14.1.3 Interference in the limit of very weak light

Can we observe interference in the limit of very weak intensity when, statistically, there may occasionally be a single photon within an interferometer, but very rarely more than one? Experiments done by G. I. Taylor in 1909 showed that an interference pattern *could* be recorded under such circumstances, given a long enough photographic exposure. Naively, we might expect that two photons must travel simultaneously through the system, one along each of the alternative paths in order to interfere when they are recombined. But from the experiment it is clear that one photon is sufficient. In fact **the photon is not a localized particle**, and any attempt to discover along which of the routes the photon travelled **destroys the interference pattern**. This apparently paradoxical situation has many implications in basic quantum theory, and has been discussed exhaustively, without any generally accepted understanding having emerged. Because of the controversiality of the subject it is difficult to summarize it here without ending up with more questions than answers!

In general, the electromagnetic wave approach that characterizes this book gives the right average light intensity distribution in any given situation when large numbers of photons are involved. When the numbers are small, the average expectation is still correct, but the result in any particular experiment is modified by the statistics of arrival of the photons, whether the detector is a single unit or an array such as a photographic film. The statistics may be Poisson if the photons are uncorrelated, but may be modified by various techniques to be discussed below (§14.3.1). In many cases the statistics can be adequately

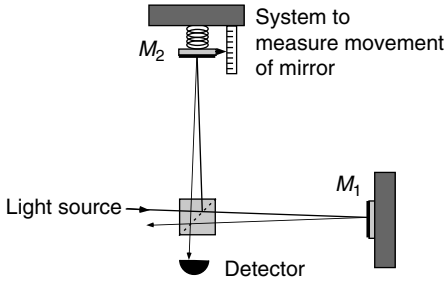

Figure 14.3

Thought-experiment to determine which mirror in a Michelson interferometer reflected the photon.

described by analysis of the detector itself, for example §14.4.1. It is as if the classical electromagnetic field *guides* the individual photons, in the same way as Schrödinger's wave-field gives the probability density for matter particles, without telling us exactly what happens to each one.

A non-mathematical discussion that covers several different approaches to 'which way?' experiments is given in the book by Rae (1986).

To show what happens if we try to trace a photon (as if it were a localized particle) through an interferometer, we shall consider the following thought-experiment as an example on which many variations are possible. The apparatus is a Michelson interferometer (Fig. 14.3), and we shall show that an attempt to find out *which* of the two mirrors reflected a single photon traversing the instrument must result in destruction of the interference pattern. Imagine that all the components of the interferometer are infinitely massive, apart from the mirror M_2, which has finite mass. According to de Broglie's hypothesis, a photon with wavenumber k_0 has momentum $p = \hbar k_0$. When the photon is reflected, the mirror will recoil with momentum $2\hbar k_0$, which can be measured *after* the reflection has occurred, and the measurement can therefore not affect the interference pattern. But in order to detect the recoil, we must know the initial momentum of M_2 to an accuracy δp considerably better than $2\hbar k_0$, which is the quantity we want to measure. So, *before* the reflection, δp must be smaller than $\hbar k_0$. Now the Heisenberg uncertainty principle relates the uncertainties of momentum and position in the form $\delta p\, \delta x \geq h$; this means that the positional uncertainty δx of M_2 is at least $2\pi/k_0 = \lambda$. This much uncertainty in the mirror position makes the fringes unobservable!

Although this is only an example, *any* attempt to determine a photon's route through an interferometer is doomed to destroy the interference pattern that could be observed. We reach the inevitable conclusion that the photon must travel both routes at once, and interferes with itself. In particular, as food for thought, we suggest consideration of two experiments among the many that have been instrumental in focusing the conceptual problems. One involves interference between photons from independent lasers (Pfleegor and Mandel (1968)), and the second, interference between photons emitted by down-converting crystals, in which a single input photon causes ejection of two coherently related photons (Zou *et al.* (1991)), a technique that has already been mentioned in §13.5.3.

14.2 Plane wave modes in a linear cavity

We shall now return to the analogy between the photon and a simple-harmonic oscillator (§14.1.2). It will be sufficient to consider a one-dimensional cavity of length L, in which the plane wave mode has an electric field

$$E = E_0 \cos(kx - \omega t - \phi), \tag{14.10}$$

where the values of k and therefore ω are defined by L. The magnetic field is not independent, and is always related to E by the impedance. Note that k and E will now be written as scalars, since the choice of a particular mode (including its polarization) allows us to consider a single component of the field only. It is the *magnitude* of E_0 that will be shown to be quantized.

First we define two new quantities:

$$q(t) = \frac{E_0}{\omega} \cos(\omega t + \phi), \tag{14.11}$$

$$p(t) = -E_0 \sin(\omega t + \phi), \tag{14.12}$$

noting that $\mathrm{d}q(t)/\mathrm{d}t = p(t)$, and write the field

$$\begin{aligned} E &= E_0[\cos(\omega t + \phi)\cos kx + \sin(\omega t + \phi)\sin kx] \\ &= \omega q(t)\cos kx - p(t)\sin kx. \end{aligned} \tag{14.13}$$

The total energy per unit cross-sectional area of the cavity (including both E and B fields) is then

$$\begin{aligned} U &= \int_0^L \epsilon_0 E^2 \,\mathrm{d}x \\ &= \int_0^L \epsilon_0 (\omega q \cos kx - p \sin kx)^2 \,\mathrm{d}x \\ &= \frac{1}{2}\epsilon_0 L(\omega^2 q^2 + p^2). \end{aligned} \tag{14.14}$$

Using new variables

$$Q(t) = (\epsilon_0 L)^{\frac{1}{2}} q, \tag{14.15}$$

$$P(t) = (\epsilon_0 L)^{\frac{1}{2}} p\,, \tag{14.16}$$

$$U = \frac{1}{2}(\omega^2 Q^2 + P^2). \tag{14.17}$$

This has the same form as the energy of a mechanical simple-harmonic oscillator, for which

$$U = \frac{1}{2}(Kx^2 + mv^2), \tag{14.18}$$

where K is the force constant and m the mass. This can also be written in the same way as (14.17), in which $\omega = (K/m)^{\frac{1}{2}}$ is the classical vibration frequency, $m^{\frac{1}{2}}x = Q$ and $m^{\frac{1}{2}}v = \mathrm{d}Q/\mathrm{d}t = P$.

14.2.1 Energy quantization and zero-point energy

The quantized energy of a simple-harmonic oscillator is well known to be $U_n = \hbar\omega\left(n + \frac{1}{2}\right)$ where n can be any non-negative integer. **We thus deduce that the energy of a given mode of the electromagnetic field is quantized in the same way.** An important non-classical feature is the existence of **zero-point energy**

$$U_0 = \tfrac{1}{2}\hbar\omega, \tag{14.19}$$

When all modes are taken into account this adds up to an infinite total amount of energy since the cavity has an infinite number of possible modes; however this energy is inaccessible because it corresponds to the lowest possible energy state.

which is the lowest allowed energy level for that mode; it is not possible to eliminate field oscillations in any mode completely. Even the **vacuum field** (lowest energy in every mode of a cavity) contains this much energy in every mode. The actual electric field resulting from the zero-point contributions of all the modes is their superposition. Since their phase relations are unspecified, they can be assumed for the moment to be random and give rise to an **inevitable fluctuating background field that adds noise to any physical measurement**, which we shall presently study in more detail. However, the last decade has seen development of methods to order the phases of these zero-point fluctuations, with the consequent possibility of noise reduction. This is called **squeezed light** and will be discussed in more detail in §14.3.1.

14.2.2 Uncertainty relation

The uncertainty principle is one feature of quantum mechanics that can directly be applied to the electromagnetic field through the analogy with the harmonic oscillator. As we saw in §14.1.3, it can be written $\delta p\,\delta x \geq \hbar$. Now the conjugate variables we used in the harmonic oscillator above are $Q = m^{\frac{1}{2}}x$ and $P = m^{\frac{1}{2}}v = p/m^{\frac{1}{2}}$, so

$$\delta P\,\delta Q \geq \hbar, \tag{14.20}$$

which relates, by analogy, the degree of accuracy with which we can specify the amplitudes of the $\cos kx$ and $\sin kx$ parts of the electromagnetic field.

It is illustrative to express the uncertainties on a $(P, \omega Q)$ diagram. In quantum mechanics, this is called a **Wigner diagram**. We plot P horizontally and ωQ vertically, as in Fig. 14.4. The energy (14.17) is then proportional to the square of the radius vector A from the origin to $(P, \omega Q)$. Moreover, from (14.11) and

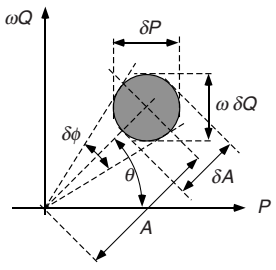

Figure 14.4

Wigner diagram showing $(P, \omega Q)$ for light with minimum uncertainty (chaotic light).

(14.15), $(\epsilon_0 L)^{-\frac{1}{2}}\omega Q$ is the instantaneous amplitude of the $\cos kx$ term, and likewise $(\epsilon_0 L)^{-\frac{1}{2}}P$ is the amplitude of $\sin kx$. Thus the phase $(\omega t + \phi)$ of the field (14.13) is given by the angle θ, and the amplitude by the radius vector. However, we know that the point $(P, \omega Q)$ cannot be defined exactly because of the uncertainty principle. All we know is the average position of the point, and the product of the uncertainty $\delta P\, \delta Q$. From here on we shall ignore the ωt in the phase, so that the $(P, \omega Q)$ diagrams will be drawn as if in a frame of reference rotating at angular velocity $-\omega$. Then the angle θ represents ϕ directly.

Since P and ωQ appear symmetrically in (14.17), we expect the values of δP and $\omega\, \delta Q$ to be equal, so that the defined region in Fig. 14.4 is a circle. This is the situation that would normally be found, and to which any other situation will naturally revert; light in a single mode with this property is called **chaotic light**, to be discussed further in §14.2.3. But all that quantum theory limits is the *area* of the region of uncertainty, and any experiment we propose that distorts its shape while retaining the area is allowed from the theoretical point of view. Let us look at some examples.

When we define an uncertainty region in the $(P, \omega Q)$ plane, the construction of a wave is quite elementary. We choose, randomly, a number of points within the uncertainty region and draw, one on top of the other, the waves that they represent. Each wave has amplitude and phase (A, ϕ), which are the polar coordinates of $(P, \omega Q)$ as in Fig. 14.4, in which $A^2 = P^2 + \omega^2 Q^2 = 2U$. The width covered by the resulting lines represents the uncertainty in the wave-field. Figure 14.5(a) shows what we get for five randomly chosen waves in the equilibrium form $\delta P = \omega\, \delta Q = \sqrt{\hbar\omega}$.

Various techniques have been designed to manipulate the shape of the uncertainty region (§14.3.1). For example, it has been shown to be possible to control the amplitude of a wave emitted by a diode laser (§14.5.5) by very careful stabilization of the excitation current. Then δA is very small, and the uncertainty region is distorted as in Fig. 14.5(b). This gives rise to a wave whose phase is very unstable, which means that it has a large frequency spread. In fact, one can see an alternative form of the uncertainty principle here; the uncertainty areas in Fig. 14.5 are

$$\omega\, \delta P\, \delta Q = A\, \delta A\, \delta\phi = \frac{1}{2}\delta(A^2)\, \delta\phi \geq \hbar\omega. \tag{14.21}$$

But $\frac{1}{2}\delta(A^2)$ is the uncertainty $\delta U = \delta n\, \hbar\omega$ in the energy per unit area (intensity $\times$ time), where n is the number of photons observed in an experiment. Thus

$$\delta n\, \delta\phi \geq 1. \tag{14.22}$$

A second example is just the opposite to the above. We stabilize the phase of the light by making $\delta\phi$ very small, in which case the amplitude fluctuates wildly (Fig. 14.5(c)). This form of squeezed light has applications to accurate interferometry, because the points of zero amplitude are very well defined.

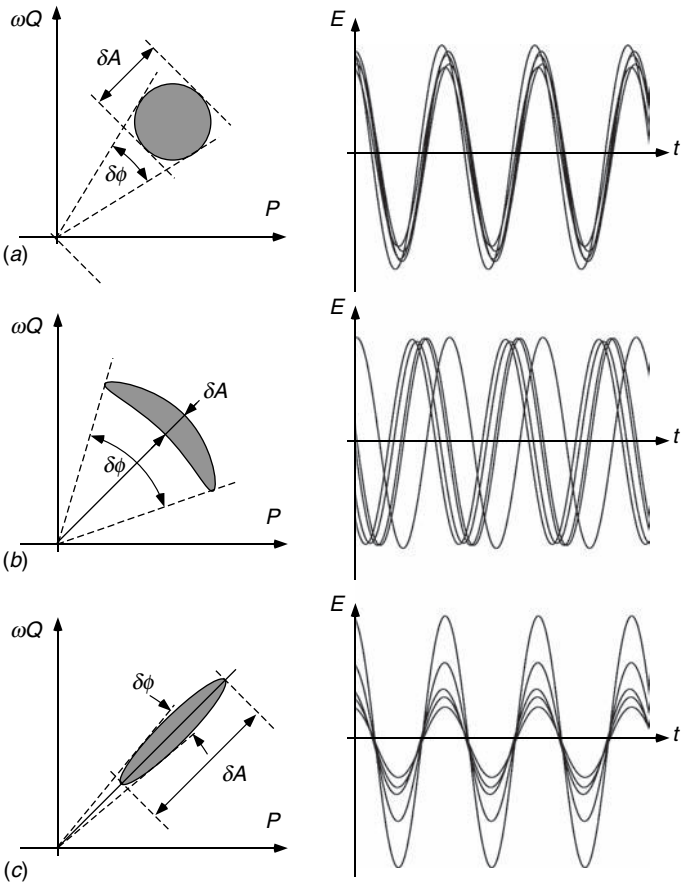

Figure 14.5

Waves represented by various Wigner diagrams. Their uncertainty is illustrated by the range of the five superimposed wave-forms in each case: (*a*) chaotic light, (*b*) amplitude-squeezed light, (*c*) phase-squeezed light.

14.2.3 Fluctuations in chaotic light

Chaotic light has the equilibrium form $\delta P = \omega\,\delta Q = \sqrt{\hbar\omega}$. Then, from (14.17), putting $\phi = 0$ to simplify things,

$$\begin{aligned}\delta U &= \omega^2 Q\,\delta Q + P\,\delta P \\ &= (\epsilon_0 L)^{\frac{1}{2}}\left[\omega^2\frac{E_0}{\omega}\cos\omega t(\hbar/\omega)^{\frac{1}{2}} + E_0\sin\omega t(\hbar\omega)^{\frac{1}{2}}\right] \\ &= (\epsilon_0 L\hbar\omega)^{\frac{1}{2}}(E_0\cos\omega t + E_0\sin\omega t). \end{aligned} \tag{14.23}$$

This shows that the contributions to δU from the $\cos\omega t$ and $\sin\omega t$ phases are equal. The root-mean-square fluctuation ΔU in each phase is

$$\Delta U = \langle\delta U^2\rangle^{\frac{1}{2}} = (\epsilon_0 L\hbar\omega)^{\frac{1}{2}}E_0\langle\cos^2\omega t\rangle^{\frac{1}{2}} = E_0\left(\frac{\epsilon_0 L\hbar\omega}{2}\right)^{\frac{1}{2}}. \tag{14.24}$$

It is most illustrative to compare this fluctuation with the mean intensity, when both are measured as numbers n of photons per unit area in a given time. Then we have

$$\delta n = \frac{\Delta U}{\hbar\omega} = E_0\left(\frac{\epsilon_0 L}{2\hbar\omega}\right)^{\frac{1}{2}}; \tag{14.25}$$

$$\begin{aligned}\langle n\rangle = \frac{U}{\hbar\omega} &= \frac{1}{2}\langle\omega^2 Q^2 + P^2\rangle\frac{1}{\hbar\omega}\\ &= \frac{1}{2}\left\langle\omega^2\frac{E_0^2}{\omega^2}\cos^2\omega t + E_0^2\sin^2\omega t\right\rangle\frac{\epsilon_0 L}{\hbar\omega}\\ &= E_0^2\frac{\epsilon_0 L}{2\hbar\omega}.\end{aligned} \tag{14.26}$$

So for each phase $\quad (\delta n)^2 = \langle n\rangle.$ (14.27)

In §11.8 we used the same result for the detection probability of photoelectrons when observing a source of constant intensity, as a consequence of the Poisson statistics of uncorrelated events; the present result therefore indicates that **Poisson statistics apply to chaotic light**. In that discussion, we continued by adding the resultant classical intensity fluctuations arising from the partially coherent nature of a thermal source, and showed that the result was photon bunching, which can be described loosely as **super-Poisson** in that there is a positive correlation between the times of detection of photons. The fluctuations result eventually in a limitation of the accuracy with which measurements can be made optically. On the other hand, any means of distributing them unequally between the $\sin\omega t$ and $\cos\omega t$ terms, and using the quieter one for measurement, acquire practical implications; this is called **squeezing** the light and we have **sub-Poisson** statistics.

The 'darkest' state, which has the minimum number of photons, has $\langle n\rangle = 0$ in each mode, and is called the **vacuum field**. It still has energy $\frac{1}{2}\hbar\omega$, which is evident as a fluctuating wave-field. Then the picture looks like Fig. 14.6(a, b), in which phase is completely indeterminate. The vacuum field is important in understanding spontaneous emission (§14.4.2).

An example of an optical phase-sensitive amplifier: a Fabry–Perot cavity whose optical length oscillates synchronously with the reference, using non-linear optics, so that it is $m\lambda/2$ long at certain points in each cycle.

However, the vacuum state can be squeezed, which means distorting the shape of the uncertainty region on the Wigner diagram, as in Fig. 14.6(c, d). This essentially decreases the uncertainty in one phase at the expense of the other phase. This can be employed in interferometry to improve measurement signal-to-noise, since in interferometry measurements are made in one phase, that of the reference wave, and that phase can be chosen to be the one where the fluctuations are sub-Poisson (the Q phase in Fig. 14.6(d)). To distort the shape of the uncertainty region, one uses a phase-sensitive amplifier, which amplifies signals that are in phase with a reference, and attenuates by the same factor waves that are in quadrature with it.

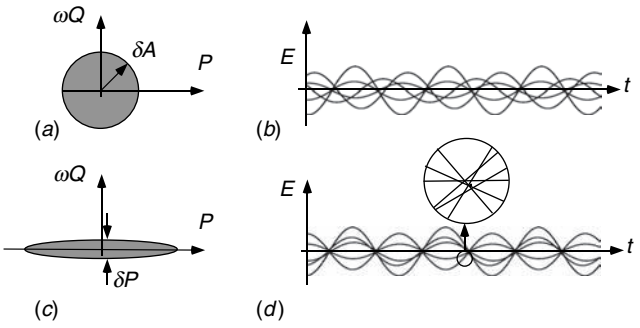

Figure 14.6 Representation of the vacuum field. (*a*) and (*b*) The natural chaotic vacuum state where fluctuations are equally distributed between the *P* and *Q* phases: (*a*) Wigner diagram in *P*, *Q* space and (*b*) typical samples of $E(t)$; (*c*) and (*d*) show the squeezed vacuum state where most fluctuations are in the *P* phase. Notice from the magnified zero-crossing region in (*d*) that all the samples of $E(t)$ have approximately the same phase.

14.3 Are photons real?

The theory behind these experiments is usually treated in terms of quantum operators, but since these have not been discussed in this book, the discussion will avoid their use. After all, they are only a mathematical tool.

Although the picture of particle-like excitations of light with quantized energy produced a simple and appealing explanation of the photo-electric effect, for which Einstein was awarded the Nobel prize in 1921, that effect can, in retrospect, be explained by a semi-classical theory in which the light is described as a classical electromagnetic wave that interacts with a quantized photo-cathode. On the other hand, later experiments produced results that cannot be explained without the concept of a photon as a non-localized entity with zero mass, energy $\hbar\omega$ and unit spin, travelling in free space at velocity c. In this section we shall discuss some of these experiments at an elementary level, to give a taste of what has become a very active area of optics research during the last few decades.

14.3.1 Sub-Poisson light

We have already met two illustrations of fluctuations in light intensities. In §14.2.3 we showed that chaotic light, which is best exemplified by a monochromatic laser beam, obeys **Poisson statistics**. This means that the root-mean-square fluctuations in the intensity are proportional to the square root of the intensity itself. In addition, we saw in §11.8.3 that the experiments of Brown and Twiss (1956) demonstrated increased fluctuations in quasi-monochromatic light resulting from beats between neighbouring frequencies. These are known as 'super-Poisson' fluctuations. Both of these phenomena can be explained by the semi-classical theory in terms of the statistics of interactions between

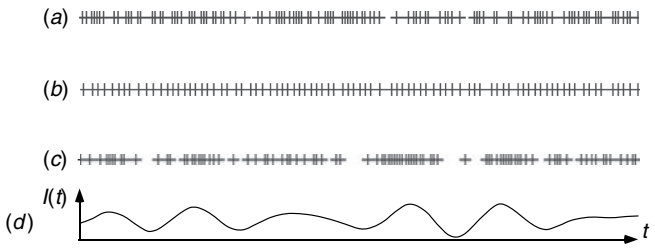

Figure 14.7

Simulation of (*a*) Poisson, (*b*) sub-Poisson and (*c*) super-Poisson events along a time axis. (*c*) corresponds to the fluctuating intensity *I*(*t*) shown in (*d*), typical of incoherent light.

classical light waves and a photo-detector. In that approach, an electromagnetic wave of given intensity provides a perturbation to the electrons in the photo-detector, which are thereby excited statistically to a higher level which is then detected. However, there is no way that such a semi-classical model can explain 'sub-Poisson' fluctuations – light that has smaller fluctuations than Poisson statistics predict. In fact, the Poisson statistics derive from §14.2.3 where we assumed that $\delta P = \omega\,\delta Q$. Figure 14.5(*b*) shows an example where the shape of the uncertainty region has been distorted so as to reduce amplitude fluctuations, at the expense of phase fluctuations. This can only be carried out if the statistical emission of electrons from a photo-cathode is moderated by a regularized stream of photons.

Several ways of doing this have been invented, for example:

1. The operation of a semiconductor laser or light emitting diode (§14.5.5) from a stabilized constant current (pumping) source (Machida *et al.* (1987); Tapster *et al.* (1987)). The electrons, being fermions, tend to anti-bunch and result in a more ordered flow of electrons which, because of the very short lifetime T_2 of electron–hole pairs in the junction, regulates the photon output.
2. The emission of resonance fluorescence (§14.8) from a single atom or ion, which has to be re-excited after every emission. The re-excitation creates a 'dead-time' after each emission, which smooths the flow of photons by creating a dependence of each on the previous one (Kimble *et al.* (1977); Teich and Saleh (1985)).

These methods are only possible when light is emitted as individual quanta, and therefore cannot be described classically. Figure 14.7 shows a *simulation* of Poisson, sub-Poisson and super-Poisson light. In (*a*) we see a series of uncorrelated photon events at rate r. In (*b*) we have taken the sequence (*a*), doubled the rate to $2r$ and then introduced after every registered event a detection dead-time with average value equal to $1/r$, during which any event occurring is erased, so that the mean rate is once again r. It is easy to see that a steadier sub-Poisson stream of photons has been achieved, and is equivalent to method (2) above. In (*c*), we first generated a classical chaotic wave (shown in (*d*)) by the method described in §11.1, and then used Poisson statistics to generate the appropriate super-Poisson photon sequence.

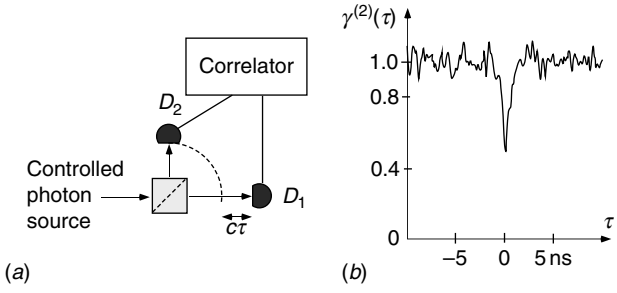

Figure 14.8
(*a*) Experiment to measure correlation between photon arrivals at two detectors, when the source is sub-Poisson. (*b*) The second-order coherence function between photon arrivals at the two detectors separated by time τ, showing anti-correlation. (Courtesy of D. Gershoni)

14.3.2 Photon anti-correlations

The experiment of Brown and Twiss (1956) investigated intensity correlations between the two light beams created by dividing a quasi-monochromatic beam into two by a beamsplitter. In §11.8.3 we saw that the correlations can be described by a second-order coherence function $\gamma^{(2)}(\tau)$, which is a function of the delay τ between the detection times; for the classical wave model $\gamma^{(2)}(\tau)$ was related to the temporal coherence function $\gamma(\tau)$ by

$$\gamma^{(2)}(\tau) = 1 + |\gamma(\tau)|^2. \tag{14.28}$$

Therefore, **classically, the value of $\gamma^{(2)}(\tau)$ can never be less than unity and experimental proof of $\gamma^{(2)}(\tau) < 1$ indicates the need for a quantum description**. Replacing Brown and Twiss's intensity correlation method by photo-electron coincidence counting is a technical improvement (which, historically, had many interpretational problems; Brown (1974)); here one measures the probability of receiving a photo-electron at detector D_2 in the window between $t = \tau$ and $t = \tau + \delta\tau$ after receiving one at $t = 0$. When normalized correctly, this is a measure of $\gamma^{(2)}(\tau)$. For sources of the types listed above, experiments have shown conclusively that $\gamma^{(2)}(\tau) < 1$ is possible; this essentially establishes the reality of the photon as a quantum particle (Fig. 14.8).

It is quite easy to see why this happens. Consider first a beam with Poisson statistics (Fig. 14.7(*a*)), which has a constant probability $p\,\delta\tau$ of a photon arriving in any interval of time $\delta\tau$. If the beam is divided into two, as in Fig. 14.8(*a*), and the photons go randomly to each of D_1 and D_2, each detector now has probability $p\delta\tau/2$ of a photon arrival, but the distribution of events at D_1 is not dependent on those at D_2, and so $\gamma^{(2)}(\tau) = 1$ at all τ. If the beam is classically super-Poisson (Fig. 14.7(*c*)), the probability of arrival of a photon at D_1 in a given window of time is larger when at the peak of a fluctuation, and then the probability of a photon detection at D_2 is also greater if $\tau < \tau_c$; hence $\gamma^{(2)}(|\tau| < \tau_c) > 1$. However, if the photons are sub-Poisson, and therefore more ordered, the fact that a photon arrived at D_1 means that another is *less*

likely to arrive at D_2 within a short time. In case (2) $\gamma^{(2)}(\tau) = 0$ if τ is within the dead-time (Fig. 14.7(*b*)).

The earliest demonstrations of these anti-correlations (i.e. $\gamma^{(2)}(\tau) < 1$) in 1977 were essentially the first unequivocal confirmation of the photon concept. These were followed by exceptionally clear results from resonance fluorescence (§14.8) of single and small clusters of atoms and more recently from quantum dots (Fig. 14.8). The latter are tiny quantum wells which essentially behave like single designer atoms that can supply not only 'photons on demand', but also groups of correlated or 'entangled' photons, which are our next topic.

14.3.3 Entangled photons and the Bell inequality

In 1935 Einstein, Podolsky and Rosen (EPR) described a 'gedankenexperiment' (thought-experiment) that they considered to result in counter-intuitive results and therefore raised the question of whether quantum mechanics could provide a complete description of a system in terms of measurable quantities. In a quantum system, a parameter only has a certain value when it is actually measured. For example, the weak wave in Taylor's experiment (§14.1.3) will probably cause an event on the photographic film at one point in a certain time interval, but it is not possible in advance to say where that point is going to be. The experiment EPR described consisted of the emission of two particles from a source as the result of a spontaneous decay. Then the sums of the momenta and of the positions of the two particles must remain zero at all times ($p_2 = -p_1, x_2 = -x_1$) since the centre of gravity remains stationary. As a result, by measuring x_1 and p_2 it is possible to determine both x_2 and p_1; thus both the positions and momenta of both particles are known simultaneously. Heisenberg's uncertainty principle does not allow this! In addition, the parameters are measured when the distance between the two particles is very great, so that they cannot influence one another. This is known as the **EPR paradox**.

Discussions of this question usually employ a model in which two spontaneously emitted particles have opposite spins, $\pm\frac{1}{2}$, whose components in the direction of a measurement axis have also to be $\pm\frac{1}{2}$. However, experiments done on such systems have proved very difficult to perform.

In the optical regime, such experiments have been carried out with pairs of photons, created by a single event and therefore having correlated polarizations. They show the surprising result that measurement of the polarization of one photon does indeed predict correctly the polarization of the other, even when they are a long way apart. There are two possible explanations for this. The first, implying a 'hidden variable', is that the photons were imbued with intrinsic polarizations at the time of the emission, but we only learnt what they are when the measurement was performed. The second reason could be that one photon's polarization was created by its measurement, and the second then had to fulfil the correlation. But how did it know what the first measurement was, because the first measurement was made when the photons were too far apart to communicate? Such questions have played a great role in studies of

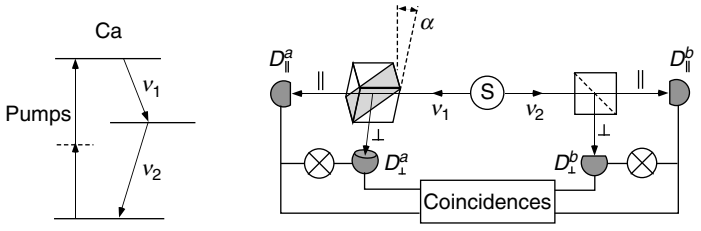

Figure 14.9 **Experimental set-up for investigating polarization correlations in entangled photon pairs. The level scheme on the left shows two simultaneously emitted photons with correlated polarizations. In the experimental system, the polarization correlations are recorded as a function of α and β; the configuration is shown for $\beta = 0$. The elements $\otimes$ reject multiple photon events. (After Aspect *et al.* (1982))**

fundamental quantum mechanics and their implications are discussed at length in books such as Peres (1993). The first explanation assumes that there is a hidden variable whose value we do not know until the first measurement is made. The second explanation requires that the two photons share a common wave-function, which cannot be factorized into the product of two independent functions, and the parameters of which are only chosen when measured for one particle; but the result then applies to both particles! Such particles are called **entangled**. The question is, can we distinguish experimentally between the two explanations, and which is correct?

We shall discuss the paradox in terms that have been discussed earlier in this book, i.e. as direct polarization measurements on photons, for which there are clear and decisive experimental results (Aspect *et al.* (1982)). In these experiments (Fig. 14.9) a ^{40}Ca source emits pairs of photons with correlated polarizations in a single decay event, and we shall assume that the atomic wave-functions require the polarization directions to be parallel.[3] Pairs of photons ($i = a, b$) emitted in opposite directions enter two polarization-measuring devices each consisting of a polarizing beamsplitter which reflects the $\perp$-polarized wave to detector $D^i_\perp$ and transmits the $\parallel$ one to detector $D^i_\parallel$. The planes of incidence of the two devices are fixed at angles α and β respectively to the vertical. Here, we assume the detectors to have 100% efficiency; in the experiments, of course, corrections were made to take account of the real values.

Let us first consider the classical 'hidden variable' explanation. Suppose first that $\alpha = \beta = 0$ and the photons are emitted with polarizations at angle θ to the vertical. Then the probabilities of detection at the four detectors are

$$P^a_\perp = P^b_\perp = \cos^2\theta, \qquad P^a_\parallel = P^b_\parallel = \sin^2\theta. \tag{14.29}$$

Even if a photon is detected at $D^a_\perp$ this only means that its polarization is not exactly $\parallel$, and therefore there is a non-zero probability that its twin be detected

[3] It would make no difference to the argument if the two photons were required to have orthogonal polarizations.

by $D^b_\parallel$, i.e. two photons might be detected simultaneously at orthogonally oriented detectors on the two sides; this would be most likely if $\theta = 45°$.

Now consider the same conditions for the quantum explanation. When the first photon (say a) reaches its device, it might appear at $D^a_\perp$, in which case the two photons acquire $\perp$ polarization ($\theta = 0$). Then there is *zero probability* that photon b will have $\parallel$ polarization, and it cannot appear at $D^b_\parallel$. If, on the other hand, a appears at $D^a_\parallel$, then $P^b_\perp = 0$. The correlations between the signals at the different detectors are much higher in this case.

It seems therefore that there is a basis for experimental determination of which explanation is correct, but the experiment must be analyzed quantitatively. For the classical model, with general α, β, the detection probabilities are

$$P^a_\perp = \cos^2(\theta - \alpha), \qquad P^a_\parallel = \sin^2(\theta - \alpha), \tag{14.30}$$

$$P^b_\perp = \cos^2(\theta - \beta), \qquad P^b_\parallel = \sin^2(\theta - \beta). \tag{14.31}$$

Now we look at correlations between the various detectors, and get joint probabilities

$$\begin{aligned}
P_{\perp,\perp} &= \cos^2(\theta-\alpha)\cos^2(\theta-\beta) = \frac{1}{4}[\cos(\alpha+\beta-2\theta)+\cos(\alpha-\beta)]^2,\\
P_{\parallel,\parallel} &= \sin^2(\theta-\alpha)\sin^2(\theta-\beta) = \frac{1}{4}[\cos(\alpha+\beta-2\theta)-\cos(\alpha-\beta)]^2,\\
P_{\perp,\parallel} &= \cos^2(\theta-\alpha)\sin^2(\theta-\beta) = \frac{1}{4}[\cos(\alpha+\beta-2\theta)-\sin(\alpha-\beta)]^2,\\
P_{\parallel,\perp} &= \sin^2(\theta-\alpha)\cos^2(\theta-\beta) = \frac{1}{4}[\cos(\alpha+\beta-2\theta)+\sin(\alpha-\beta)]^2.
\end{aligned} \tag{14.32}$$

In a long experiment, θ might be uniformly distributed in $(0, 2\pi)$ and the average values observed will be

$$\langle P_{\perp,\perp}\rangle = \frac{1}{4}\left[\frac{1}{2} + \cos^2(\alpha-\beta)\right] = \langle P_{\parallel,\parallel}\rangle, \tag{14.33}$$

$$\langle P_{\perp,\parallel}\rangle = \frac{1}{4}\left[\frac{1}{2} + \sin^2(\alpha-\beta)\right] = \langle P_{\parallel,\perp}\rangle. \tag{14.34}$$

The correlation function is analogous in structure to the visibility of interference fringes, §11.3.2, except that it can also take on negative values.

Finally we construct a normalized correlation function for the whole experiment which can lie in the range from $+1$ (perfect correlation) to -1 (perfect anti-correlation):

$$E(\alpha,\beta) \equiv \frac{P_{\perp,\perp} + P_{\parallel,\parallel} - P_{\perp,\parallel} - P_{\parallel,\perp}}{P_{\perp,\perp} + P_{\parallel,\parallel} + P_{\perp,\parallel} + P_{\parallel,\perp}} = \frac{1}{2}\cos[2(\alpha-\beta)]. \tag{14.35}$$

This never has absolute value greater than $\frac{1}{2}$, and so **in the classical case the correlation is never perfect**.

According to the quantum theory, the calculation is much simpler. If photon a reaches $D_\perp^a$, then photon b has the same polarization. Then the probability of its detection at $D_\perp^b$ is $P_{\perp,\perp} = \cos^2(\alpha-\beta)$ and that at $D_\parallel^a$ is $P_{\perp,\parallel} = \sin^2(\alpha-\beta)$. Similarly, $P_{\parallel,\parallel} = \cos^2(\alpha-\beta)$ and $P_{\parallel,\perp} = \sin^2(\alpha-\beta)$. Whence the correlation function $E(\alpha,\beta) = \cos[2(\alpha-\beta)]$. This is **twice as large as the classical case**, and leads to perfect correlation when $\alpha = \beta$.

However, before deciding how to carry out the decisive experiment, we should take into account the fact that we assumed the value of θ to be a uniform random variable in (14.33) and (14.34); could it be possible that the actual distribution of θ is non-uniform in some way, so as to mimic the quantum case? Maybe this could be the result of crystalline anisotropy or local magnetic fields in the source. A very clever and elegant way round this obstacle was invented by Bell (1966). Every individual observation is described by a binary number q^i, where $q^i = 1$ if the photon is received at $D_\perp^i$, or $q = -1$ if at $D_\parallel^i$. For a given event, the correlation $E(\alpha,\beta) = q^a.q^b$ then has the value ±1, since one photon is detected in each channel on each side. Consider four measurement angles, α, β, α' and β'. Four experiments can be done, each using one α and one β, giving $q^\alpha, q^\beta, q^{\alpha'}$ and $q^{\beta'}$. The results of these four experiments are combined as

Bell's inequality applies in general to any system with hidden variables. Experiments that violate Bell's inequality show that there are no hidden variables, and the two particles have a common wave-function.

$$S = E(\alpha,\beta) + E(\alpha',\beta') - E(\alpha,\beta') + E(\alpha',\beta). \tag{14.36}$$

It is easy to confirm by considering each of the 16 combinations of $+1$'s and -1's for the q's, S always has a value 2 or -2, and so **when S is averaged for a large number of events, the mean must be between -2 and 2**.[4] The result that $|S| \le 2$ is known as **Bell's inequality**.

However, for the quantum case we have $E(\alpha,\beta) = \cos[2(\alpha-\beta)]$. One can easily find a set of values for the angles such that $S > 2$; for example $\alpha = 0, \beta = 22.5°, \alpha' = 45°$ and $\beta' = 67.5°$. Then, $S = 2\sqrt{2}$. A series of experiments (Aspect *et al.* (1982)), which took more than six years to develop and complete, justified the quantum interpretation by showing $S = 2.70 \pm 0.05$. This result justifies our contention that **the value of a parameter of a physical system only exists when it has been measured**.

Aspect *et al.* (1982) even verified that their result was not changed if the polarization of one photon was changed electronically by a random amount after it had been emitted.

14.4 Interaction of light with matter

A detailed discussion of the interaction of light with matter is quite outside the scope of this book, but we must understand some of the essentials in order to

[4] If you consider this development to smack of mathematical juggling, you can use (14.32) directly to show that $E(\alpha,\beta) = \cos[2(\alpha-\theta)]\cos[2(\beta-\theta)]$. Then, you can check numerically that for *any* given α and β in $(0, 2\pi)$, S as defined in (14.36) lies between -2 and 2. It follows that this will also be true for any statistically weighted combination of θ's.

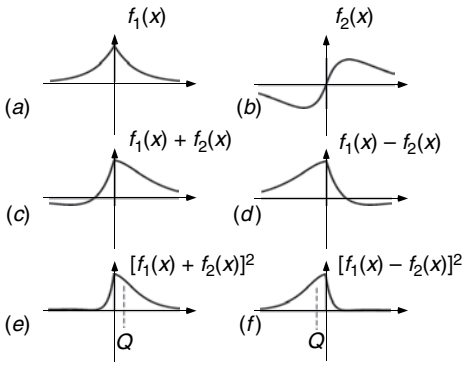

Figure 14.10

Sketches of the x-dependencies of a symmetric function $f_1(\mathbf{r})$ and an antisymmetric function $f_2(\mathbf{r})$ for electron density in an atom. The functions $\psi_1 = f_1(\mathbf{r}) + f_2(\mathbf{r})$ and $\psi_2 = f_1(\mathbf{r}) - f_2(\mathbf{r})$ represent the combined wave-functions at a time interval of $\pi/(\omega_2 - \omega_1)$. The electron densities of the latter functions have centres of gravity at off-centre points on the x-axis labelled Q, showing that the atom in the mixed state acquires an oscillating dipole moment.

appreciate the principle of the laser, which is a necessity for every student of optics. For a much deeper discussion of this subject see, for example, Loudon (2000).

We shall restrict our discussion to a pictorial description of the effect of an oscillating electromagnetic field on a single isolated one-electron atom with just two levels L_1 and L_2. This is about the simplest relevant problem we can imagine. The atom in state $j\,(=1,2)$ is described by an electronic eigenfunction

$$\psi_j(\mathbf{r},t) = f_j(\mathbf{r})\mathrm{e}^{-\mathrm{i}\omega_j t} \tag{14.37}$$

in which the spatial wave-functions $f(\mathbf{r})$ are separated from the temporal oscillations. These functions are assumed to be real and are shown in Fig. 14.10(a) and (b). The eigenvalues of the two wave-functions are $\hbar\omega_1$ and $\hbar\omega_2$ ($\omega_2 > \omega_1$), and ψ is in each case a solution of the Schrödinger equation for the atomic potential $V(\mathbf{r})$. Each wave-function corresponds to an *exact* solution of the Schrödinger equation and therefore an electron in either of the states will **stay there for ever**. All the time-dependence is in the $\exp(-\mathrm{i}\omega t)$. Any other possible electron wave-function can always be written as a superposition of the eigenfunctions $\psi_j(\mathbf{r},t)$, since these form a complete set (like the sine and cosine functions in Fourier theory).

When an atom is in a state described by the superposition of two atomic eigenfunctions, its charge density oscillates as a result of beats between the two eigenfunctions. The oscillating charge can couple to an electromagnetic wave at the beat frequency.

Now suppose an oscillating electric field is applied to the atom. The potential field is modified from $V(\mathbf{r})$ to $V(\mathbf{r}) + e\Phi(\mathbf{r},t)$ where $\Phi(\mathbf{r},t)$ is the electric potential of the oscillating field. The stationary-state wave-functions $\psi(\mathbf{r},t)$, corresponding to the new potential, are no longer the same solutions $\psi_j(\mathbf{r},t)$ of Schrödinger's equation. But we can express $\psi(\mathbf{r},t)$ as a linear superposition of the eigenfunctions $\psi_j(\mathbf{r},t)$. What does the resulting electron probability distribution look like? We write the superposition as

$$\psi(\mathbf{r},t) = a\psi_1(\mathbf{r},t) + b\psi_2(\mathbf{r},t), \tag{14.38}$$

where $a^2 + b^2 = 1$. Remember that $\psi_j(\mathbf{r}, t)$ contains the factor $\mathrm{e}^{-\mathrm{i}\omega_j t}$. When we now calculate the electron density $|\psi(\mathbf{r}, t)|^2$, we find a cross term (underlined) which oscillates with frequency $(\omega_2 - \omega_1)$:

$$\begin{aligned} |\psi(\mathbf{r}, t)|^2 &= |af_1(\mathbf{r})\mathrm{e}^{-\mathrm{i}\omega_1 t} + bf_2(\mathbf{r})\mathrm{e}^{-\mathrm{i}\omega_2 t}|^2 \\ &= a^2 f_1^2(\mathbf{r}) + \underline{2abf_1(\mathbf{r})f_2(\mathbf{r})\cos[(\omega_2 - \omega_1)t]} + b^2 f_2^2(\mathbf{r}). \end{aligned} \quad (14.39)$$

Pictorially, the situation is shown in Fig. 14.10(*c*)–(*f*). At times $t = 0$ or $2m\pi/(\omega_2 - \omega_1)$, where m is an integer, $\psi = af_1 + bf_2$ as shown in (*c*) for $a = b$. The corresponding electron density function (*e*) is asymmetric with respect to the origin: on the right side, where f_1 and f_2 have the same sign, the charge density $|\psi|^2$ is larger than on the left, where f_1 and f_2 have opposite signs. Now, at times $t = \pi(2m + 1)/(\omega_2 - \omega_1)$ we have $\psi = af_1 - bf_2$, (*d*), and the charge density shown in (*f*) is larger on the left. In other words, the charge alternates between the two halves: we have an **oscillating dipole**. We know, from §5.3.2, that an oscillating dipole is a good radiator or absorber, so the atom absorbs or radiates at frequency $\omega = (\omega_2 - \omega_1)$; in general the **atom couples to a radiation field tuned to the frequency difference between energy levels**.

The strength of the oscillating dipole represented by (*e*) and (*f*) corresponds to the underlined term in (14.39), which leads to a dipole moment of amplitude

$$2ab \int\int\int_{\text{all space}} e\mathbf{r} f_1(\mathbf{r}) f_2(\mathbf{r})\, \mathrm{d}^3 r \equiv 2ab\, eM_{12}. \quad (14.40)$$

M_{12} is called the interaction **matrix element**, or the **oscillator strength**, which was introduced empirically in §13.3.2. Because of the antisymmetric factor $\mathbf{r}$ in the integrand, the functions shown in (*a*) and (*b*) must have opposite symmetry for M to be large; this corresponds to a selection rule $\Delta l = \pm 1$ in quantum mechanics (where l is defined in the same way as in §10.2).

The above description might suggest that emission and absorption only occur when $\omega = (\omega_2 - \omega_1)$ exactly. But this is not quite true. The result of energy transfer from the field is that a and b change with time, and so the interaction continues only for a time T during which both a and b are non-zero. So ω only needs to lie within $\omega_2 - \omega_1 \pm \pi/T$; $2\pi/T$ is the natural linewidth (§11.2.1). The larger the values of the matrix element and Φ, the faster a and b change and the wider the frequency range.

Although we have not carried out any detailed mathematics and have used an oversimplified model, the physics should be clear. Now we can make several very important observations:

1. The situation is quite symmetric between the two levels. If the atom starts in level 1, initially $a = 1$ and $b = 0$, and the electromagnetic field causes a transition from the lower level to the upper. If the atom were initially in the upper level, with $a = 0$ and $b = 1$, the same electromagnetic field would cause a transition to the lower level.

2. Because the interaction is essentially that between an oscillating dipole and an electromagnetic field at the same frequency, the direction of energy transfer is determined by the phase relation between the two. In the first case in (1), energy $\hbar(\omega_2 - \omega_1)$ is absorbed from the field by the atom. In the second case, the dipole radiates the same energy coherently into the field.
3. We have seen in §14.2 that the electromagnetic field is never zero. There are always the vacuum fluctuations at least. So an atom cannot stay in the upper level for ever. One might be tempted to say the same about the lower level, but the atom has to absorb energy to ascend to the upper level. The field cannot provide this energy because it is already in its lowest energy state, so there is no available source for an upward transition.

14.4.1 The photo-electric effect

Quantization of energy in a light wave was demonstrated by Einstein in his interpretation of the photo-electric effect, which applies to almost any sensitive photo-detector. The argument in terms of quantized photons should be familiar to the reader, but here we shall describe it in terms of the above interaction picture, in which the electromagnetic field is classical.

Detection of light requires an interaction between the incident wave field and the electrons in a sensitive element, the photo-cathode, in which the electrons have many states. The lowest-lying ones refer to electrons bound within the cathode, but above a certain energy ε_w, called the **work function**, the states refer to free electrons having some amount of kinetic energy. The light wave with frequency ω causes a mixing, like (14.38), between the ground state ω_1 and a certain upper state ω_2 which satisfies $\omega = \omega_2 - \omega_1$. If $\hbar\omega_2 < \varepsilon_w$, the final state is bound and no free electrons are observed. When $\hbar\omega_2 > \varepsilon_w$, the final state is a free electron with kinetic energy $\hbar\omega_2 - \varepsilon_w$. The rate of transition to unbound states, and thus the rate of creation of free electrons, is proportional to the size of the perturbation, the intensity of the light wave. This, in a nutshell, is a description of the photo-electric effect; notice that the quantization has been introduced through the electron states in the photo-cathode, and not through the wave-field. In fact, the photo-electric effect does not really prove that light energy is quantized!

14.4.2 Spontaneous and stimulated emission

The description earlier in §14.4 leads us directly to the most important concepts involved in the laser. We have seen that in the presence of an electromagnetic wave, no atomic-electron wave-function is completely stationary, except for the ground state in the presence of the vacuum field only. Otherwise, transitions

occur in which energy is transferred backwards and forwards between the atom and the electromagnetic field. We emphasize that the atom behaves like an oscillating dipole antenna during a transition and the phase relation between this dipole and the electromagnetic field determines whether the atom absorbs or emits.

Spontaneous emission occurs when an atom is in the upper state L_2 and is influenced by the vacuum field. As we saw in §14.2.3, this generally has random phase and therefore the emitted waves have random phase. However, in principle the random vacuum field fluctuations can be ordered, and this possibility was shown in Fig. 14.6(*c*) and (*d*). The dependence of spontaneous emission on the presence of a vacuum field has been beautifully demonstrated by experiments on radiation from atoms in microcavities. If the cavity dimensions are reduced until its first mode has frequency above that of the transition from level L_2 to the ground state, there are no vacuum fluctuations at the right frequency to stimulate that transition, and the lifetime of L_2 becomes infinite. The experiments are described in more detail by Haroche and Raimond (1993).

Stimulated emission occurs when an atom is in the same state L_2, but is influenced by an electromagnetic field larger than the vacuum field. The atom, perturbed at frequency ω, transits to state L_1 and the phase of the emitted wave is that of the oscillating dipole, which itself is that of the perturbing wave. Thus a second wave, **coherent with the first**, is emitted.

Stimulated absorption occurs when the atom is initially in state L_1. Then, the same description as the previous paragraph applies, but the phase is reversed and the atom absorbs the radiation.

14.4.3 Einstein's *A* and *B* coefficients for spontaneous and stimulated emission

Einstein's work, which predicted the possibility of stimulated emission, was done in 1917, but was only realized experimentally 40 years later.

The relationship between the stimulated and spontaneous emission rates can be compared by a simple argument due to Einstein. He considered the equilibrium of a large ensemble of atoms in the presence of equilibrium isotropic blackbody radiation $u(\omega)$ at temperature T (14.8). From Boltzmann statistics we know the equilibrium ratio between the numbers of atoms n_1 in L_1 and n_2 in L_2 to be

$$\frac{n_2}{n_1} = \exp\left(-\frac{\hbar(\omega_2 - \omega_1)}{k_B T}\right). \tag{14.41}$$

The spontaneous transitions from L_2 to L_1 are dependent on the vacuum field, which is not included in $u(\omega)$. The stimulated transition rate is proportional to $u(\omega)$. Thus the rate of transition from L_2 to L_1 is

$$r_{21} = An_2 + Bu(\omega)n_2, \tag{14.42}$$

where A and B are constants. For transitions from L_1 to L_2, the spontaneous contribution is absent:

$$r_{12} = Bu(\omega)n_1. \tag{14.43}$$

Putting (14.42) and (14.43) equal at equilibrium, and substituting (14.8) for $u(\omega)$, we find

$$\frac{A}{B} = \frac{\hbar\omega^3 L^3}{c^3\pi^2}. \tag{14.44}$$

For the stimulated component to be dominant, we require the energy density $u(\omega)$ to satisfy

$$Bu(\omega) \gg A, \tag{14.45}$$

which, on substituting (14.44) for A/B, gives

$$u(\omega) \gg \hbar\omega^3 L^3/\pi^2 c^3. \tag{14.46}$$

On referring to (14.8), this implies that the mean number of photons in the mode of frequency ω, $\langle n\rangle \gg 1$.

The key to attaining sufficient energy density to cross the lasing threshold in the optical region is the use of a resonator, which concentrates the available radiation and restricts it to a very small solid angle.

It is of interest to see the order of magnitude of the threshold energy density (14.46), which is related to the intensity by $I = cu(\omega)$. At a microwave frequency, $\omega = 10^{11}\,\mathrm{s}^{-1}$ ($\lambda = 2$ cm), the threshold is $3 \times 10^{-20}\,\mathrm{J\,m^{-3}}$, corresponding to about $10^{-11}\,\mathrm{W\,m^{-2}}$, an extremely small intensity. At microwave frequencies, it therefore appears that spontaneous emission is quite negligible. At an optical frequency, $\omega = 3 \times 10^{15}\,\mathrm{s}^{-1}$ ($\lambda = 0.5\,\mu$m), the threshold is $7 \times 10^{-7}\,\mathrm{J\,m^{-3}}$, corresponding to $20\,\mathrm{W\,m^{-2}}$. This is very intense, and led to considerable problems in constructing the first optical lasers (§14.5.3). Those facing the designer of an X-ray laser are even more formidable.

14.5 Lasers

The acronym 'LASER' means 'Light Amplification by Stimulated Emission of Radiation'. Today it is understood to refer to a light source from which the stimulated emission is dominant, although the initial stimulus that triggers the emission is usually spontaneous.

The important difference between stimulated and spontaneously emitted waves is in their phase coherence. Each stimulated photon is exactly in phase with the photon that provided the stimulation, and so the wave grows as a continuous wave with complete temporal coherence; if we know the phase at one time we can, in principle, predict the phase of the wave at any later

A system with population inversion, corresponding to a negative thermodynamic temperature, is needed for laser action.

time because all its components are exactly in phase. This idyll is spoilt by the spontaneous emission, which is caused by the randomly phased vacuum fluctuations. These provide a noisy background which results in a degradation of the complete phase coherence. It will be convenient in what follows to ignore spontaneous emission; to create the large energy density $u(\omega)$ that this demands, one must usually put the lasing material in a cavity that is resonant at the frequency ω (§9.5.4).

Returning to equations (14.42) and (14.43), without the spontaneous term, we have the rate of stimulated emission of light from (14.42):

$$I_{\mathrm{e}} = \hbar\omega r_{21} = Bu(\omega)n_2 \tag{14.47}$$

and that for absorption of the same frequency (14.43):

$$I_{\mathrm{a}} = \hbar\omega r_{12} = Bu(\omega)n_1. \tag{14.48}$$

For (14.47) to be larger than (14.48) it is necessary for n_2 to be larger than n_1, which from (14.41) is clearly impossible in an assembly of atoms in equilibrium at any (positive) temperature. The laser therefore requires that the atoms be excited to a non-equilibrium distribution, in which there are **more atoms in the upper level L_2 than in the lower one L_1**. This is called **population inversion**. As long as this situation is maintained, stimulated emission dominates over absorption.

14.5.1 Population inversion in a chemical laser

Conceptually, the simplest process to achieve population inversion is probably the chemical laser. A chemical reaction takes place that generates large amounts of energy and the resultant molecules are formed in an excited state (signified by a star after the molecular formula). Then at the time of formation, there are no molecules in the ground state, only the new ones in the excited state, and so population inversion is achieved. The reaction takes place within a cavity that resonates at the frequency of the transition from the excited state to the ground state. For example, fluorine and hydrogen react in the required manner:

$$\mathrm{H_2} + \mathrm{F_2} \rightarrow 2\mathrm{HF}^\star. \tag{14.49}$$

Stimulated emission occurs when a photon of frequency ω in the cavity excites the transition from $\mathrm{HF}^\star$ to HF, with the emission of a second photon of the same frequency and phase as the first one:

$$\hbar\omega + \mathrm{HF}^\star \rightarrow 2\hbar\omega + \mathrm{HF}. \tag{14.50}$$

Laser action continues as long as $\mathrm{H_2}$ and $\mathrm{F_2}$ are burnt to provide the excited molecules and the ground-state HF is swept out of the cavity. However, this type of laser is not convenient or safe for everyday use!

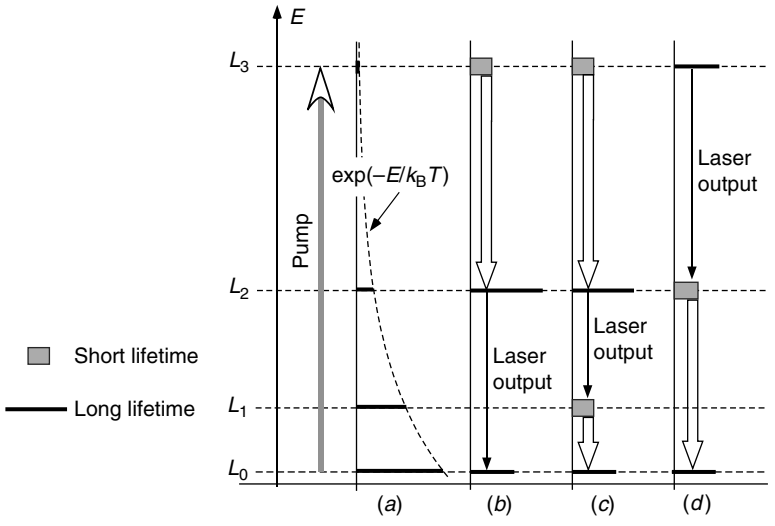

Figure 14.11
Level schemes typical of lasing materials. (*a*) Thermal equilibrium occupation of energy levels; (*b*) and (*d*) show three-level lasers, and (*c*) a four-level laser based on the same levels. Optical pumping is indicated by the upward arrow on the left. The lengths of the level lines represent their relative populations during lasing; their thicknesses indicate their decay rates, $1/T_i$. Fast transitions are indicated by broad arrows.

14.5.2 Population inversion based on atomic fluorescence

Suppose that we flash a short burst of light onto an atom with a number of levels, and the light is absorbed. This means that we have induced transitions from the ground state to an excited state. If the atom subsequently reradiates radiation at a longer wavelength, it is clear that there must exist a radiative route back to the ground state via at least one intermediate level. Such a **fluorescent system** provides us with a means of achieving population inversion. A more detailed discussion of fluorescence under resonant conditions will be given later in §14.8.

Suppose that just one intermediate level is involved. We call the ground state L_0, the uppermost state L_3 (to which we excite the atoms by the flash), and the intermediate one L_2, as in Fig. 14.11(*a*). Denote the lifetime of the atom in level L_i by T_i; this is the average time for which it stays excited before spontaneously emitting (T_0 is of course infinite). If the system is fluorescent as described above, a fraction of the atoms in L_2 decay to L_0 via L_1.

First suppose that $T_3 < T_2$. The short lifetime T_3 indicates that the matrix element M_{03} is large and means that the pump radiation can be absorbed efficiently by the atom. Then L_0 can be substantially emptied by atoms being excited to L_3, from where they rapidly decay to L_2. In L_2 they remain for the longer T_2, and population inversion between L_2 and L_0 arises, provided that the occupation of L_0 is at least half depleted by the pumping, as in Fig. 14.11(b). The ruby and erbium-doped fibre lasers (§14.5.3) operate essentially with this scheme.

Of course real life is never quite so simple. Usually, more levels are involved, but some cases are close to the ideal. For example, using a fourth level L_1 as in Fig. 14.11(*c*) makes it much easier to maintain the inverted population since the ground state does not have to be substantially depopulated; the

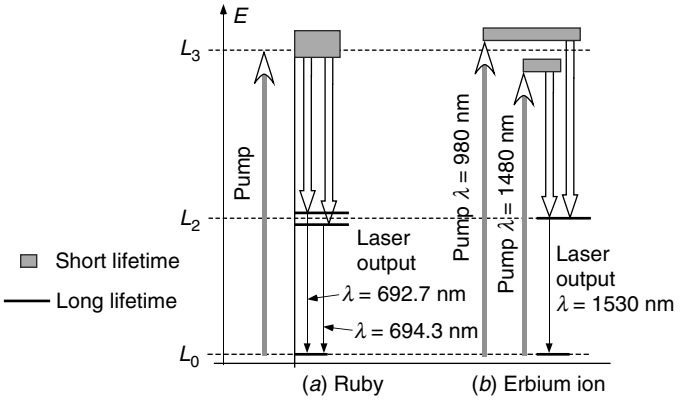

Figure 14.12
Schematic ruby and erbium laser level schemes.

neodymium-YAG laser is an important example. In addition, the lifetime of an atom in the upper state of the lasing pair is shortened once stimulated emission begins, and the balance may be upset. This can lead to pulsed behaviour.

Another possible situation is $T_3 > T_2$, as in Fig. 14.11(*d*). In this case, level L_2 empties faster than L_3 can fill it, so that there are always more atoms in L_3 than L_2 and population inversion occurs between them. Laser action between L_3 and L_2 is then possible while 'pumping' atoms from L_0 to L_3. Because T_3 is long in this scheme, M_{03} is small and optical pumping is inefficient; the argon ion, carbon dioxide and helium-neon lasers (§14.5.4) use this idea, but are pumped by electrical discharge.

14.5.3 Optically pumped ruby and erbium lasers

Ruby is an aluminium oxide (Al_2O_3) crystal with a small amount of Cr^{3+} impurity, which gives it its red colour. The ruby laser constructed by Maiman in 1960 was the first laser working at an optical frequency and employed the energy levels of dilute Cr^{3+} shown schematically in Fig. 14.12(*a*). This is similar to the three-level laser in Fig. 14.11(*b*). Because the three-level scheme requires depopulation of the ground state by at least one-half, this laser is relatively inefficient and needs a very intense pump, provided by a xenon flash tube whose output is focused onto the ruby crystal.

The erbium-doped silica (SiO_2) laser and amplifier, which are now widely used in optical communication systems at 1.5 μm, are also examples of optically pumped three-level lasers, Fig. 14.11(*b*). They are constructed from silica glass fibres containing about 35 ppm of Er^{3+} ions and are pumped by light from diode laser sources (§14.5.5) at either 1.48 μm or 0.98 μm. The level scheme of Er^{3+} is shown in Fig. 14.12(*b*), which includes the two pumping possibilities. Because the wavelengths involved are relatively long and the fibre construction concentrates both the pumping light and the emitted radiation in the core region, a high degree of population inversion can easily be achieved and the emission

Figure 14.13
Level scheme in a helium-neon laser.

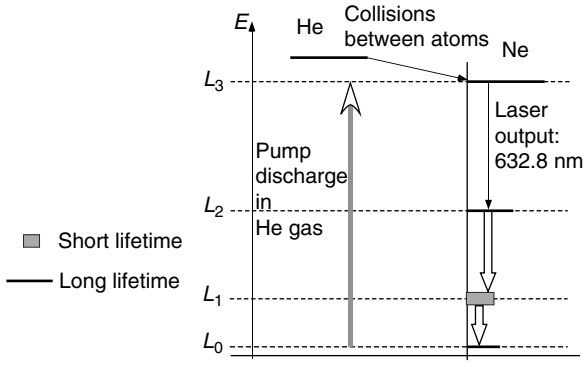

is stimulated very efficiently. As a result, in the absence of a resonator (§14.6.1) the system behaves as an **optical amplifier**, while the addition of a resonator makes it into a laser.

14.5.4 Discharge pumped gas lasers

These lasers employ mixed gases to create the population inversion. In the helium-neon (He-Ne) laser, He is electrically excited by a discharge to an excited state, $He^{\star}$. During collision between He and Ne atoms, the excitation energy can be transferred to the Ne, some of whose energy levels are shown in Fig. 14.13. Thus population inversion is achieved between L_3 and L_2. The figure shows the levels involved in only one of the many possible transitions of Ne, that at 632.8 nm.

The carbon dioxide (CO_2) laser has a generally similar scheme, with nitrogen as the excitation gas instead of helium. Several wavelengths between 9.6 and 10.6 μm can be radiated, depending on the resonator tuning.

14.5.5 Population inversion in semiconductor p-n junctions

Semiconductor lasers based on a reverse-biased p-n junction are of great importance in everyday life – in optical communication, bar-code scanners and CD players, just to give a few examples. The energy levels involved here are not those of individual atoms or ions, but those of free carriers in a heavily doped semiconductor crystal: electrons at the bottom of the conduction band and holes at the top of the valence band. The concepts are described in any book on solid-state or semiconductor physics. Their exact energy values are a function of the position in the junction because of its structure (p-type on one side and n-type on the other). As a result of heavy doping, there are free electrons in the conduction band of the n-type side, and free holes in the valence

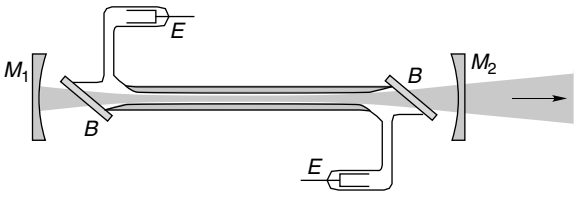

Figure 14.14
Diagram of a helium-neon laser: *E*, electrodes to excite discharge in the gas; *B*, Brewster-angle windows; M_1 and M_2 confocal resonator mirrors; M_2 is partially transmitting.

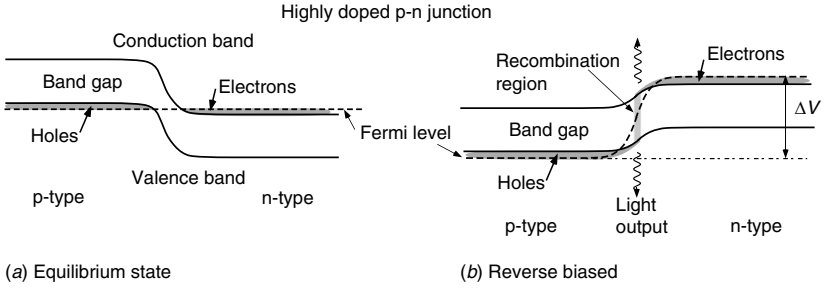

(*a*) Equilibrium state (*b*) Reverse biased

Figure 14.15
Semiconductor diode laser. (*a*) Equilibrium state, with no voltage applied. (*b*) With applied voltage ΔV; recombination of electrons and holes in the junction region results in emission of light.

Box 14.1 Structure of the helium-neon laser

The helium-neon laser is the commonest laser to be found in elementary laboratories, and its structure will be familiar to many students. In §14.5.4 we described the type of level scheme it uses. It is constructed from a sealed discharge tube containing a mixture of helium and neon with about 10:1 ratio in pressure, which is situated within a confocal resonator (§9.5.4), one of whose mirrors transmits a small percentage of the radiation to produce the output beam. The laser transition of choice is encouraged by using multilayer dielectric mirrors, with peak reflectivity at the required wavelength (§10.3.4). The windows used to seal the discharge tube must have the smallest possible reflection losses and may be anti-reflection coated (§10.3.3), uncoated but mounted at the Brewster angle (§5.4.2) as in Fig. 14.14, or may be the confocal resonator reflectors themselves. Since the laser amplification in this system is weak, it is important to reduce the losses to a minimum by these means; if Brewster-angle windows are used, one polarization will have less reflection losses than the other, so the output beam is polarized.

band of the p-type side. In thermal equilibrium, the energies of the bands are as in Fig. 14.15(*a*). There is no point in space where there are *both* free electrons and holes in more than negligible densities. When a reverse bias ΔV is applied, the bands are moved energy-wise as shown in Fig. 14.15(*b*). Now it is energetically favourable for the electrons to drift towards the positive side and the holes towards the negative side, and in doing so, both move into the junction region.

When they reach the same place, we have a population inversion, in that there are substantial densities of free electrons and holes in the same place, which is a higher-energy situation than the recombined one in which the electron has filled the hole and both are annihilated. Laser emission can then occur provided the recombination process results in the emission of a photon alone, which occurs in a class called **direct gap semiconductors** including many III-V materials such as gallium arsenide (GaAs), indium phosphide (InP) and indium antimonide (InSb), but not silicon or germanium. The corresponding fluorescent device is the LED (light emitting diode) which works on the same principle but radiates spontaneous and not stimulated emission. The wavelength of the radiation emitted corresponds closely to the band gap of the semiconductor; for GaAs this is about 870 nm; for a member of the quaternary system InGaAsP it can be designed to be about 1.5 μm, which is most attractive for optical communication because this is about the wavelength of minimum attenuation that has been attained in glass fibres (§10.2.4).

14.6 Laser hardware

Lasers are discussed in detail in many books, such as Yariv and Yeh (2007), Saleh and Teich (1991), Svelto (1989), and in the limited space available to us it is impossible to do justice to the many facets of laser technology that have developed since the 1960s. All we shall do in this section is to point out how some of the physical ideas that we met in this and other chapters of the book have been applied to the design of lasers of various types.

14.6.1 The optical resonator

The gain provided by one of the mechanisms of population inversion exemplified in the previous section must now be harnessed to provide a source of coherent radiation. This can be done by incorporating it in a positive-feedback amplifier system; a familiar acoustic example is a public address system that starts to whistle when the microphone 'hears' the loudspeaker's output (Fig. 14.16(*a*)). Starting from random noise, this creates a coherent sound wave, whose frequency is near that of the amplifier's maximum gain, but is determined exactly by the acoustic delay (distance/sound velocity) between loudspeaker and microphone. The delay must be such that the phase of the input to the amplifier is $2N\pi$ different from the output (N is an integer), so that the two reinforce exactly. When the amplifier gain is sufficiently large to overcome the losses in a single round trip of the wave, a sustained oscillation occurs.

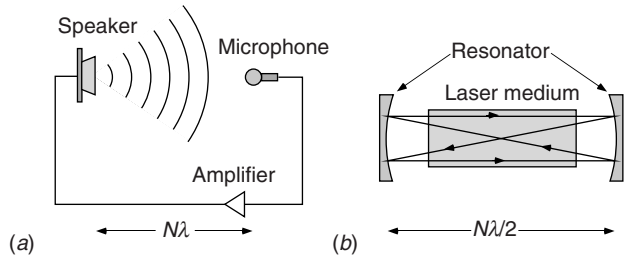

Figure 14.16
Positive feedback in (*a*) a public address system and (*b*) a laser.

It is easy to see the analogy with the laser (Fig. 14.16(*b*)). The laser medium is the amplifier, in which an incident photon creates new photons with the same phase by stimulated emission. Its bandwidth is determined by the linewidth of the emission, which involves the lifetimes of the levels and processes such as Doppler broadening (§11.2.2). Feedback is provided by an optical resonator, often of the type described in §3.9. The actual selection of the frequencies that can be radiated is determined by the optical length of the resonator, and there are sometimes several such frequencies within the linewidth of the transition. These are called the **modes** of the laser. In a semiconductor or fibre laser, the radiation may also be confined laterally by waveguide modes (§10.1.2), which enhance the energy density. Usually the radiation chooses the fundamental mode $m = 0$, and devices are engineered so that the peak of the radiation density in this mode coincides spatially with the peak of the population inversion. When the laser has a slab structure, the radiation is confined in one dimension only; this results in the output beam having a very anisotropic shape, which makes it difficult to focus the output light efficiently.

Quantitatively, the laser gain is determined by the pump power and atomic parameters. It has to overcome the losses occurring in the resonator due to imperfect reflection as well as providing the useful output of the laser (which, from the point of view of the laser itself, is also a loss). Spontaneous emission is also undesirable, as it uses the inverted population to create waves with the wrong phases, although it was necessary as the original stimulus that started the oscillations.

The longitudinal lasing modes correspond to the condition that the optical length $\bar{L}$ of a complete trip back and forth through the resonator is an integral number N of wavelengths: $\bar{L} = 2\bar{n}l = N\lambda$, where $\bar{n}$ is an average refractive index (which may change with intensity). The frequencies of the modes are separated by $2\pi c/\bar{L}$. The length l also depends on the direction the ray takes along the resonator, and sometimes several transverse modes are possible with the same N, but with the rays at different angles to the optical axis. This aspect is best treated as a diffraction problem (§9.5.4).

A frequency analysis of the output from a typical laser is shown in Fig. 14.17, when several longitudinal modes are excited.

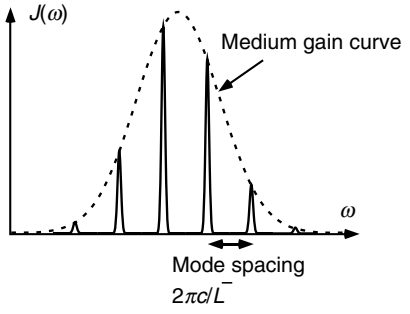

Figure 14.17
Schematic illustration of the frequency spectrum of longitudinal modes in a laser.

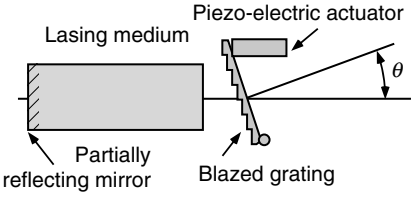

Figure 14.18
Tunable laser resonator using a diffraction grating instead of one mirror.

Many modern experiments require lasers whose output wavelength can be varied. If a small range of variation is required, this can be done by adjusting the properties of the resonator. A method that is commonly used involves replacing one mirror by a reflective blazed diffraction grating (§9.2.5). As shown in Fig. 14.18, the grating is placed at an angle to the axis so that the first order of diffraction returns exactly along its axis of incidence; in terms of the diffraction grating equation for non-normal incidence in reflection,

$$m\lambda = d[\sin\theta - \sin(-\theta)] = 2d\sin\theta \quad (m = 1). \tag{14.51}$$

The grating is of course blazed at angle θ for maximum efficiency in the first order. As the angle is changed, the wavelength at which the resonator peaks varies in accordance to (14.51), since only waves travelling to and fro exactly along the axis are amplified. The exact length of the resonator can be adjusted synchronously by choosing the point about which the grating rotates. All that is left is to assure that the laser gain always peaks at the resonant frequency chosen by the resonator, otherwise there may be mode jumps to a more favoured longitudinal mode (the highest peak in Fig. 14.17); this can be done in diode lasers (§14.5.5) by synchronously adjusting the temperature of the lasing material. This method of scanning was developed for investigating the spectra of lasers such as the CO_2 laser (§14.5.4), as has more recently been applied to diode lasers for very high resolution spectroscopy, such as that involved in electromagnetically induced transparency (§14.9) and Doppler-free saturated absorption spectroscopy.

14.6.2 Continuous-wave versus pulsed lasers

The lifetime T_j of a level depends on the way it can decay. Many lasers can be pumped sufficiently strongly that population inversion is maintained in the presence of stimulated emission and **continuous-wave** emission occurs. On the other hand, an excited level will generally have a shorter lifetime when its emission is stimulated than it had naturally. Then, when laser action starts, it is also possible that the condition for a population inversion ($T_2 > T_3$ in Fig. 14.11(c), for example) is destroyed, and so lasing stops. As a result, we have a **pulsed laser**. Some lasers can be operated in either way.

There are various ways of controlling and ordering pulses, by changing factors coming into the gain. An example is described in Box 14.2. Another situation, which allows regular giant pulses to be created, is called **mode-locking**. When a laser operates in several longitudinal modes, as we saw in §14.6.1, the wave-form obtained is the superposition of the waves corresponding to the individual modes. If these have random phases, the result is similar to the waves we constructed in §11.1.1, except that because the modes are equally spaced in frequency by $2\pi c/\bar{L}$, the wave-form repeats itself at intervals of $\bar{L}/c$. But if the modes have the same phase, their combined wave-form is a series of well-defined wave-groups (Problem 14.8); if more modes are involved, the shorter and more intense are the individual groups. This situation can be forced on the laser by including within the resonator a variable attenuator, which is transparent once in every cycle time of $\bar{L}/c$.

14.7 Laser light

Consider a laser in which only one longitudinal mode of the cavity is excited. Stimulated emission results in a very large number $\langle n \rangle$ of photons in this one mode (14.46). This is what distinguishes laser light from thermal light for which, as we pointed out in §14.1.2, there is on average much less than one photon per mode. The fluctuation δn is given by (14.27) because even laser light has to fulfil the uncertainty relation. Thus $\delta n = \langle n \rangle^{\frac{1}{2}}$ and so, according to (14.22), $\delta\phi = \langle n \rangle^{-\frac{1}{2}}$, which is very small.

Laser light is therefore characterized by having very well-defined phase. This is not necessarily true of *any* bright light. The large number of photons has to be concentrated in a single mode. In addition, when only a few longitudinal modes are excited the light is very well defined in its direction, the angular spread of the beam being determined by diffraction as if it were restricted by an aperture corresponding to its actual physical extent (§7.3). These three properties – phase coherence, high intensity and directionality – are the most characteristic properties of laser light.

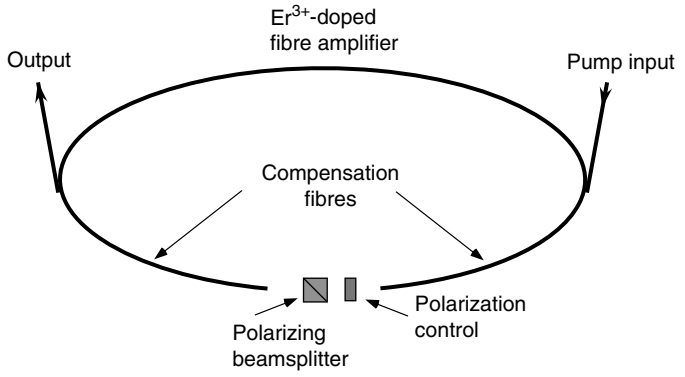

Figure 14.19
Structure of a pulsed laser based on an erbium-doped fibre.

Box 14.2 A fibre-based pulsed laser

In many lasers the resonator is an optical fibre, such as an optically pumped erbium-doped fibre (§14.5.3). In order to get a pulsed output, it is necessary to include a non-linear effect that allows the optical cavity to resonate only when the intensity of the radiation is very large. Then, energy is stored in the excited state until the cavity becomes resonant, and then a large amount of energy is emitted as a very short pulse. One way of creating such a cavity uses the fact that the polarization of a wave in a fibre mode tends to rotate with propagation because of internal stresses (§6.9) and the non-linear photo-refractive effect, which depends on the intensity (§13.6.2).

The laser is constructed from a fibre loop (Fig. 14.19), which consists of three different fibres in series; one is the Er^{3+} laser and the other two are conventional fibres with opposite dispersion so as to prevent pulse broadening (§10.2.4). The loop is closed through an air gap. In the gap there is a polarizing beamsplitter, which transmits one polarization and reflects the other. There is also a mechanism to introduce additional controlled polarization rotation. A pulse, initiated by random noise, will resonate when the losses are minimum, i.e. when it is transmitted by the beamsplitter and the total polarization rotation in the loop is zero (or an integer number of 2π). The rotation mechanism is used to control the power level at which this happens. On the other hand, since a low-power continuous-wave mode does not satisfy the resonance condition, the same consideration prevents amplification of the weak wings of the circulating pulse. This contributes further to shortening the pulse duration (Tamura *et al.* (1993)).

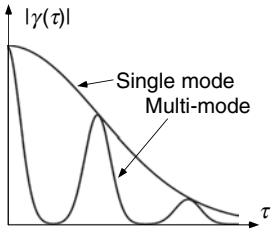

Figure 14.20

Coherence functions for a single-mode laser and a laser emitting a few longitudinal modes.

14.7.1 Coherence function

As described in §11.4.2, the temporal coherence function is the normalized Fourier transform of the spectral intensity. If a laser were to operate in a single longitudinal mode, ideally the spectrum would be a single spike. It is not quite a delta-function because there are phase fluctuations; the time-scale of these fluctuations must be at least the lifetime of the lasing transition, and so the coherence time τ_c is at least equal to this lifetime (for example, 10^{-7} s for T_2 in Fig. 14.13). The corresponding coherence length is $c\tau_c$ (30 m). In practice, the coherence time may be shortened by mechanical fluctuations (due to temperature etc.) in the optical round-trip length $\bar{L}$ of the cavity.

Many lasers operate in more than one longitudinal mode simultaneously (Fig. 14.17). If the modes have random phases, the coherence function, the Fourier transform of a few spectral lines separated by $\delta\omega = 2\pi c/\bar{L}$, has the form of Fig. 14.20, in which the coherence disappears and reappears at intervals of $\bar{L}/c$. There is no simply defined coherence length when the coherence function behaves in this manner, but for many practical purposes, since coherence disappears first after time $\bar{L}/2c$, the effective coherence length is $\bar{L}/2$, the optical length of the cavity. If the laser is pulsed or mode-locked, §14.6.2, the coherence time equals the duration of an individual pulse.

The coherence area of a single or multi-longitudinal mode laser is just the beam area, since the light distribution comes from a single coherent mode or a superposition of such modes.

14.8 Advanced topic: Resonant fluorescence and Rabi oscillations

Continuing our discussion of the interaction between a two-level atom and an electromagnetic wave, we might imagine that an atom starts at time $t = 0$ in the lower state ($a = 1$, $b = 0$) but absorbs radiation and transfers to the upper state ($a = 0$, $b = 1$) during a certain time, which depends on the intensity of the wave. After that, stimulated emission takes place and the atom returns to the lower state in the same time, and so on. Of course, if the electromagnetic wave is not exactly monochromatic, every atom will carry this out a little differently and then the ensemble average will quickly become an equilibrium with about half the atoms in each state. This is what is employed in population inversion in optically pumped lasers (§14.5.2). However, if the wave frequency and phase are very stable, all the atoms synchronize in this periodic behaviour, and oscillations are observed.

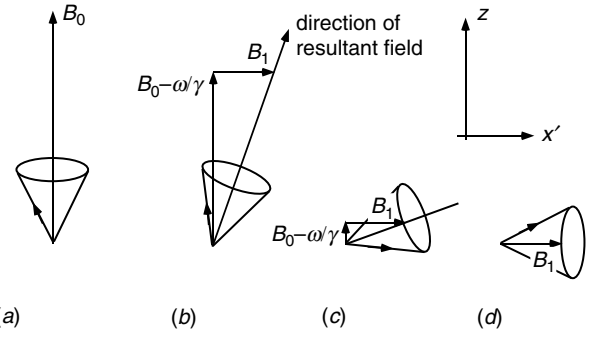

Figure 14.21 **Magnetic spin analogue to explain Rabi oscillations. (*a*) Spin precesses around the applied magnetic field B_0 at the cyclotron frequency ω_c. (*b*) Addition of a circularly polarized wave at ω along $\hat{\mathbf{z}}$, as seen in the frame of reference rotating at ω with the wave-field. (*c*) As (*b*) when ω is almost equal to ω_c. (*d*) As (*b*) when $\omega = \omega_c$. In this case the spin component along $\hat{\mathbf{z}}$ oscillates with the Rabi frequency $\Omega = \gamma B_1$.**

This type of oscillation was initially discovered by Rabi in 1937 in classical magnetic resonance, which in the simplest case is equivalent in quantum language to a two-level system in which the atomic magnetic dipole moment μ_a may be parallel or anti-parallel to an applied uniform magnetic field $B_0\hat{\mathbf{z}}$. Because it describes a two-level system interacting with an oscillatory field, the model applies equally well to a two-level atom in a radiation field. The magnetic model is easy to understand geometrically, so we shall describe it here; the same physical results apply to both cases. It is illustrated by Fig. 14.21.

The two magnetic levels are separated by energy $2\mu_a B_0$. In the classical picture the magnetic dipole, whatever its orientation, precesses around the applied magnetic field at the cyclotron frequency $\omega_c = \gamma B_0$, where γ is the **gyromagnetic ratio** (Fig. 14.21(*a*)). We now add a circularly polarized electromagnetic wave with magnetic field amplitude $B_1 \ll B_0$ at frequency ω, rotating in the same sense as the precession. The wave travels along $\hat{z}$ and therefore B_1 is in the (x, y) plane. Now observe the system in a frame of reference (x', y', z) rotating about z at the wave frequency. In this frame, the dipole precesses at frequency $\omega_c - \omega$ and therefore the value of B_0 appears to be reduced to $B_0' = B_0 - \omega/\gamma = (\omega_c - \omega)/\gamma$. In addition, B_1 is stationary in this frame and is in a direction normal to z, say x'. The resultant magnetic field, which is therefore also fixed in this frame, is thus $\sqrt{\left(B_0'^2 + B_1^2\right)}$ at angle $\tan^{-1}\left(B_1/B_0'\right)$ to z in the (x', z) plane. The magnetic dipole precesses about this resultant field at the appropriate cyclotron frequency $\gamma\sqrt{\left(B_0'^2 + B_1^2\right)}$ (Fig. 14.21(*b*)). As $\omega \to \omega_c$, $B_0' \to 0$ and the resultant field approaches the x'-axis (*c*). Then the precession approaches its minimum frequency which is $\Omega = \gamma B_1$ at $\omega = \omega_c$. This precession about x' results in oscillations of the moment with a component along the z-axis, i.e. between the two states that are parallel and anti-parallel to the

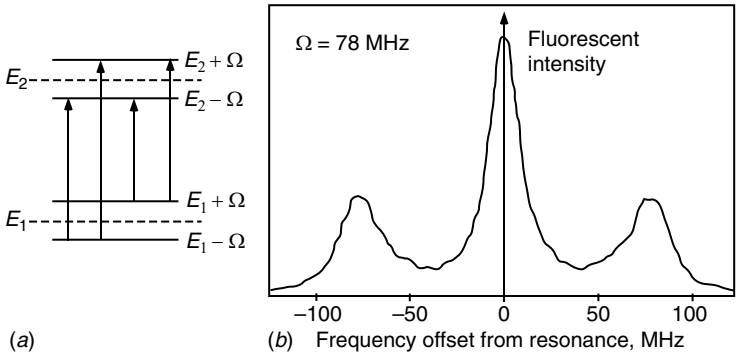

Figure 14.22

Resonance fluorescence in Na. (*a*) The energy levels E_1 and E_2 split by the Rabi frequency; all four transitions shown are allowed. (*b*) High-resolution spectroscopy of the fluorescence spectrum. (After Grove *et al.* (1977))

applied field, the two basic energy states (*d*). Ω is called the **Rabi frequency** and is often used as a measure of the strength of the wave–atom interaction. Finally, we go back to the lab frame of reference. Since the z-axis was unaffected by the rotation, the oscillation between the two states remains, although all other components of the precessing dipole average to zero.

In the optical case, when time-dependent Schrödinger equations are written down for each level of the two-level atom in the presence of the radiation field they are called the 'optical Bloch equations' (see, for example, Mandel and Wolf (1995); Loudon (2000)). The equations are basically identical to those describing the above magnetic problem, and so the solutions are analogous (Problem 14.10).

The model suggests one way of inverting a complete population, by 'adiabatic fast passage' in which the applied frequency ω is swept continuously from a value below resonance to above resonance. The sweep must be completed within the relaxation time of the system. This method was used in some early masers.

In the presence of the monochromatic radiation field at the resonant frequency, it therefore follows that the wave-function for the two-level atom can be written as (14.38) with $a = \cos(\Omega t)$ and $b = \sin(\Omega t)$ (satisfying $a^2 + b^2 = 1$):

$$\psi(\mathbf{r}, t) = \cos(\Omega t)\, \psi_1(\mathbf{r}, t) + \sin(\Omega t)\, \psi_2(\mathbf{r}, t). \tag{14.52}$$

Fourier analysis of this function then shows that the energy levels E_1 and E_2 are now split into doublets at $E_{1,2} \pm \hbar\Omega$. Transitions between the two levels now occur at the three frequencies ω_{12} and $\omega_{12} \pm 2\Omega$, which has been confirmed experimentally by very high resolution spectroscopy (Grove *et al.* (1977)) (Fig. 14.22).

The magnetic model also clarifies some other aspects of fluorescence observed in atomic systems. If the wave is not exactly on resonance, the effective field B_0' is larger than B_1 and the oscillations are faster. In addition, the component of their amplitude along $\hat{\mathbf{z}}$ is smaller, meaning that the resonance is weaker. When the excitation wave is only quasi-monochromatic, and includes a range of frequencies around the resonance, what is seen is a superposition of many Rabi oscillations at different frequencies (all above Ω) which essentially smears out observation of oscillatory behaviour.

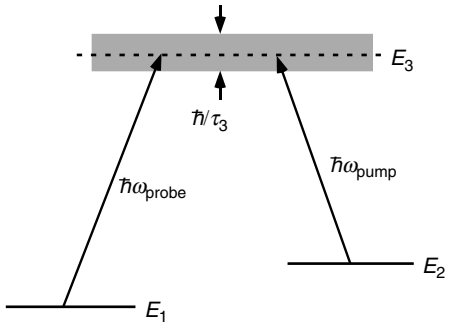

Figure 14.23
Level scheme for an atomic gas showing electromagnetically induced transparency.

14.9 Advanced topic: Electromagnetically induced transparency

The process of stimulated emission can be used to produce artificial and controllable spectral characteristics in materials such as atomic vapours. One such process, discovered by Boller *et al.* (1991), has several interesting applications. In the simplest case we can consider a three-level atomic system (Fig. 14.23) with two closely spaced ground states 1 and 2 at energies E_1 and E_2. The equilibrium population of the lower state E_1 will be greater than that of E_2 by an amount depending on their separation and on the temperature. The system also has a broad excited state 3 with energy E_3; by 'broad' we mean the lifetime τ_3 of an excitation to that state is very short, there being many possible decay paths from it, and so from the uncertainty principle E_3 is not well defined. It is useful to think of this level as being made up from a dense array of sub-levels. In this particular material, the two ground states cannot be coupled directly by an electromagnetic wave because their coupling dipole matrix element (§14.4) $M_{12} = 0$, meaning that their overlap integral has a quadrupole or higher moment. As a result, these levels are very sharply defined.

Suppose we now shine into this material a 'probe' laser beam whose frequency ω_{probe} can be varied in the range of somewhat more than $1/\tau_3$ around $(E_3 - E_1)/\hbar$. This beam is generally *absorbed strongly*, resulting in a wide absorption band (Fig. 14.24(*a*)) resulting from excitation of atoms from E_1 to E_3. In terms of the model discussed in §14.4, the probe beam has interacted with the oscillating dipole moment created by the beats between the wave-functions $\psi_1 \exp(\mathrm{i}E_1 t/\hbar)$ and $\psi_3 \exp(\mathrm{i}E_3 t/\hbar)$. In a second experiment, we now add a 'coupling' beam at a specific frequency in the range $1/\tau_3$ around $(E_3 - E_2)/\hbar$. This is also absorbed (provided there are some atoms in the state E_2), thereby stimulating the superposition dipole between ψ_3 and ψ_2 which oscillates at their beat frequency. Experimentally, it is found (Fig. 14.24(*b*)) that the probe beam is now *transmitted* by the medium when the *difference* between the frequencies of the two waves is equal to $(E_2 - E_1)/\hbar$:

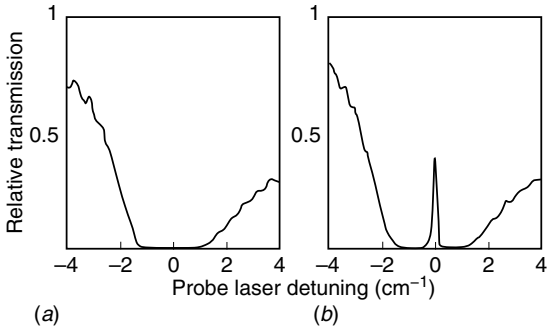

Figure 14.24

Optical absorption in strontium vapour. (*a*) Transmission versus probe laser detuning with the coupling laser absent ($\Omega_{23} = 0$). The minimum transmission in this figure is exp(−20). (*b*) With the coupling laser present ($\Omega_{23} = 1.5\,\text{cm}^{-1}$) the ratio of the transmitted to the incident light at zero detuning is now about 40%. (After Boller *et al.* (1991))

$$\omega_{\text{probe}} - \omega_{\text{coupling}} = (E_2 - E_1)/\hbar. \tag{14.53}$$

Notice that this only involves E_2 and E_1 and therefore the transmission band is extremely narrow. This is called 'electromagnetically induced transparency' (EIT).

Maybe the simplest explanation of the transparency can be given in terms of the Rabi oscillations (§14.8). Let us suppose that the coupling wave excites atoms from level 2 to a particular sub-level in the level 3 defined by its frequency ω_{coupling}. The result is Rabi oscillations between the two states, which splits each of them into a doublet separated by $2\hbar\Omega$, proportional to the amplitude of the coupling wave. In particular, the level at E_3 has become a doublet with components at $E_3 \pm \hbar\Omega$. Now the weak probe wave, which in the absence of the coupling wave excited atoms from E_1 exactly to E_3, is no longer absorbed at the frequency ω_{13} because E_3 has been split, giving rise to the transparency. Its frequency has to be changed by Ω before absorption occurs. In the experiments, this is exactly what is observed; **the width of the transmission line depends directly on the intensity of the coupling laser beam**, and becomes increasingly narrow as the latter is weakened.

In terms of the atomic dipoles, the superposition of the three atomic wavefunctions, with the right phase relation between them, results in a *dipole* moment oscillating at $(E_2 - E_1)/\hbar$. As a result, this oscillating dipole absorbs energy from the coupling and probe beams together at their beat frequency and transfers atoms directly from level 1 to 2, without going through 3. The transfer of atoms from level 1 to 2 results in an increasing population in level 2, so that even if initially its population was negligible, when equilibrium is reached in the presence of the pump and probe beams there is sufficient population in level 2 to maintain the process. This means that the requirement for levels 1 and 2 to be closely separated ground states is not really necessary, and the difference between them can be quite substantial without affecting the phenomenon.

One fascinating application of EIT is that it can be used to create incredibly slow group velocities, of the order of $\text{m}\,\text{s}^{-1}$, for narrow-band pulses lying within the transparency band. This topic was discussed in §13.5. Pulses have even been stopped by reducing the coupling intensity almost to zero, which

means that a signal, or even a picture, written into the medium by means of a spatially modulated pump beam, can be stored there for a relatively long time by reducing the coupling intensity, and then can be released by increasing it again.

Chapter summary

This chapter was intended as an introduction to quantum optics, based on material discussed in earlier chapters. We saw:

- **Why classical optics cannot explain experimental observations such as black-body radiation and interference in very weak light;**
- **How to quantize the electromagnetic field, using an analogy between a cavity mode and a simple-harmonic oscillator, and how this leads to zero-point energy and fluctuations in the field;**
- **The concept of squeezed light, in which fluctuations can be tamed;**
- **Proof that photons exist, based on observations of anti-correlation between detection events at different detectors;**
- **The concept of entangled photons, which share a common wave-function, and how they are recognized by their ability to violate Bell's inequality;**
- **The basic ideas behind the quantum theory of interaction between light and matter, using a two-state model;**
- **The difference between spontaneous and stimulated emission, and how they are related by Einstein's *A* and *B* coefficients;**
- **How lasers work, with examples using several different physical mechanisms;**
- **Some properties of laser light;**
- **How resonance fluorescence can be described by a simple model, resulting in Rabi-type oscillations between two states;**
- **That interaction of two lasers simultaneously with a three-level medium can lead to electromagnetically induced transparency (EIT) and the phenomenon of slow light.**

Problems

14.1. A weak source emits N photons per second. The light goes to an ideal beamsplitter so that half goes to each of two fast, ideal ($\eta = 1$) detectors. The correlation between the outputs from the detectors is

recorded, a positive correlation meaning that both detectors emitted an electron within a given period $T \ll N^{-1}$. Analyze this experiment classically (i.e. each detector sees a wave of half the incident intensity) and from a quantum point of view (the incident photon goes to one detector *or* the other), taking into account the Poisson statistics of the source. Show that the results in the two cases are identical; but not so if the source is not Poisson.

14.2. A Young's slit experiment working with individual photons is constructed with a very light transparent plate of thickness d and refractive index n suspended in front of one slit. The position of the plate is monitored. If a photon goes through the plate it temporarily exchanges momentum with it, and the motion can be detected. Show that this experiment destroys the interference pattern if it is used to determine through which slit the photon passed.

14.3. An atomic nucleus contains an approximately uniform charge distribution throughout a sphere of radius of order 10^{-14} m. It undergoes a transition in which it emits a γ-ray of energy about 1000 keV. Explain why the selection rule $\Delta l = \pm 1$ may not be obeyed in this transition.

14.4. In a semiconductor laser, the energy of the photons emitted is approximately equal to the band gap of the semiconductor. Would you expect the photon energy to be slightly larger or slightly smaller than the band gap?

14.5. Several output modes of a laser, indicated by the small integer m that lies between, say, +5 and –5, are represented by the waves

$$E_m = a \exp\{-\mathrm{i}[(\omega_0 + m\omega_1)t + \phi_m]\}, \tag{14.54}$$

where ω_1 is the mode-spacing frequency. To illustrate mode-locking, calculate the wave resulting from superposition of these modes when (*a*) ϕ_m is a random variable and (*b*) all $\phi_m = 0$.

14.6. An atom has a transition from its first excited state to the ground state with wavelength λ. It is situated in a cubical metal cavity with side l. How would you expect the lifetime of the excited state to depend on the *exact* value of l within the range $0 < l < 3\lambda/2$?

14.7. A material has six energy levels A to F at 2, 1.9, 1.7, 1.6, 1.1 and 0.4 eV above the ground state, G. The time constants for the various possible transitions in nanoseconds are shown in Fig. 14.25. Suggest

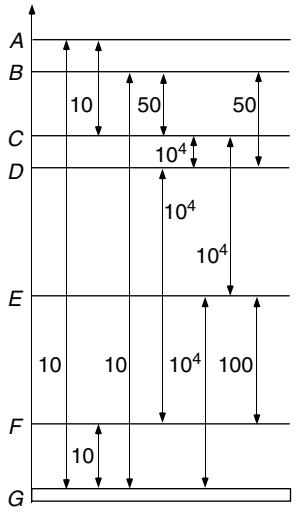

Figure 14.25
Energy scheme for lasing medium. The arrows show the allowed transitions and their decay times in nanoseconds.

possible optically pumped lasers working with this material, and give the pump and output wavelengths of each one.

14.8. Describe some of the problems involved in building an X-ray laser working at $\lambda = 500$ Å. Consider in particular the threshold intensity required and design of the resonator.

14.9. What is the coherence function corresponding to the spectrum of the laser shown in Fig. 14.17? Compare your answer with Fig. 14.20.

14.10. Write down the Schrödinger equations to show the evolution of two states coupled by an oscillating field at the frequency $\omega_1 - \omega_2$, where the wave-function for each state has the form $\psi_j(t) = a_j(t)\exp(\mathrm{i}\omega_j t)$ and $a_1^2 + a_2^2 = 1$. Show that the equations have the same form as those for a magnetic spin vector (a_1, a_2) precessing in a magnetic field whose value is given by the coupling constant. (If you are not too pedantic, this can be done shortly; the full solution is given by Loudon (2000) or Mandel and Wolf (1995).)

14.11. A possible (but incorrect) explanation for observations of EIT (§14.9) is that the coupling laser causes the sub-level in the upper band to be occupied, and so the probe laser cannot be absorbed by a transition to the same level. What evidence (in the text or elsewhere) indicates that this explanation is incorrect?

References

Aspect, A., Grangier, P. and Roger, G. (1982), Experimental test of Bell's inequalities using time-varying analyzers, *Phys. Rev. Lett*. **47**, 91.

Bell, J. S. (1966), On the problem of hidden variables in quantum mechanics, *Rev. Mod. Phys*. **38**, 447.

Boller, K.-J., Imamoğlu, A. and Harris, S. E. (1991), Observation of electromagnetically induced transparency, *Phys. Rev. Lett*. **66**, 2593.

Brown, R. H. and Twiss, R. Q. (1956), Correlation between photons in two coherent beams of light, *Nature* **177**, 27.

Brown, R. H. (1974), *The Intensity Interferometer*, London: Taylor and Francis.

Einstein, A., Podolsky, B. and Rosen, N. (1935), Can a quantum-mechanical description of physical reality be considered complete?, *Phys. Rev*. **47**, 777.

Grove, R. E., Yu, F. Y. and Ezekiel, S. (1977), Measurement of the spectrum of resonance fluorescence from a two-level atom in an intense monochromatic field, *Phys. Rev*. **A15**, 227.

Haroche, S. and Raimond, J. M. (1993), Cavity quantum electrodynamics, *Sci. Am*. April, 26.

Kimble, H. J., Dagenais, M. and Mandel, L. (1977), Photon anticorrelation in resonance fluorescence, *Phys. Rev. Lett*. **39**, 391.

Loudon, R. (2000), *The Quantum Theory of Light*, 3rd edn., Oxford: Oxford University Press.

Machida, S., Yamamoto, Y. and Itaya, Y. (1987), Observation of amplitude squeezing in a constant current driven semiconductor laser, *Phys. Rev. Lett*. **58**, 1000.

Mandel, L. and Wolf, E. (1995), *Optical Coherence and Quantum Optics*, Cambridge: Cambridge University Press.

Peres, A. (1993), *Quantum Theory: Concepts and Methods*, Dordrecht: Kluwer.

Pfleegor, R. L. and Mandel, L. (1968), Further experiments on interference of independent photon beams at low light levels, *J. Opt. Soc. Am*. **58**, 946.

Rae, A. I. M. (1986), *Quantum Physics: Illusion or Reality?* Cambridge: Cambridge University Press.

Saleh, B. E. A. and Teich, M. C. (1991), *Fundamentals of Photonics*, New York: Wiley.

Svelto, O. (1989), *Principles of Lasers*, 3rd edn., New York: Plenum.

Tamura, K., Ippen, E. P., Haus, H. A. and Nelson, L. E. (1993), 77 fs pulse generation from a stretched-pulse mode-locked all-fiber ring laser, *Opt. Lett*. **18**, 1080.

Tapster, P. R., Rarity, J. G. and Satchell, J. S. (1987), Generation of sub-Poissonian light by high-efficiency light-emitting diodes, *Europhys. Lett*. **4**, 293.

Teich, M. C. and Saleh, B. E. A. (1985), Observation of sub-Poisson antibunched light, *J. Opt. Soc. Am*. **B2**, 275.

Yariv, A. and Yeh, P. (2007), *Photonics*, 6th edn., New York: Oxford University Press.

Zou, X. Y., Wang, I. and Mandel, L. (1991), Induced coherence and indistinguishability in optical interference, *Phys. Rev. Lett*. **67**, 318.

A Appendix A **Bessel functions in wave optics**

Bessel functions come into wave optics because many optical elements – lenses, apertures, mirrors – are circular. We have met Bessel functions in several places (§8.3.4, §8.7, §12.2, §12.6.4 for example), although since most students are not very familiar with them (and probably becoming less so with the ubiquity of computers) we have restricted our use of them as far as possible. The one unavoidable meeting is the Fraunhofer diffraction pattern of a circular aperture, the Airy pattern, which is the diffraction-limited point spread function of an aberration-free optical system (§12.2). Another topic that involves the use of Bessel functions is the Fourier analysis of phase functions, in which the function being transformed contains the phase in an exponent. We met such a situation when we studied the acousto-optic effect, where a sinusoidal pressure wave affects directly the phase of the optical transmission function.

In this appendix we simply intend to acquaint the reader with the results that are necessary for elementary wave optics. The proofs can be found in the treatise by Watson (1958) and other places.

A.1 Mathematical formulations of Bessel functions

It is most convenient to start with Bessel's integral formulation of the function $J_n(x)$:

$$J_n(x) = \frac{1}{2\pi}\int_0^{2\pi} \exp[\mathrm{i}(x\cos\phi + n\phi)]\,\mathrm{d}\phi. \tag{A.1}$$

The functions have the forms shown in Fig. A.1. Typically, $J_n(x)$ starts from $x = 0$ like x^n, but when $x > n\pi/2$ it develops damped oscillations $\sim x^{-\frac{1}{2}}$ $\cos\left[x - \left(n - \frac{1}{2}\right)\pi/2\right]$. Thus alternate functions behave roughly as cosine and sine at large x, with a $\pi/4$ shift.

For proving differential and integral properties of the functions, it is often convenient to express them as power series:

$$J_n(x) = \left(\frac{x}{2}\right)^n \sum_{j=0}^{\infty} \frac{(-1)^j}{j!(j+n)!}\left(\frac{x}{2}\right)^{2j} \tag{A.2}$$

from which it is easy to see the $\sim x^n$ behaviour at $x \ll 1$.

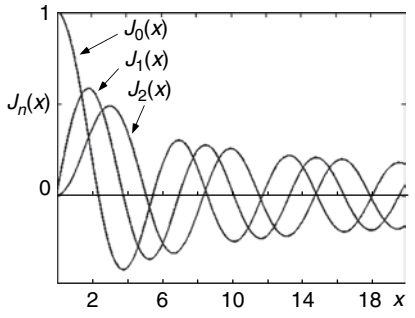

Figure A.1
$J_0(x)$, $J_1(x)$ and $J_2(x)$.

A.2 Fraunhofer diffraction by circular systems

A.2.1 An annular aperture

The zero-order Bessel function arises as the diffraction pattern of an annular aperture. It has radius a and width $\delta a \ll a$. The Fourier transform is, following (8.30),

$$F_0(\zeta, \phi) = \int_a^{a+\delta a} \int_0^{2\pi} \exp[-\mathrm{i}\zeta\rho\cos(\phi - \theta)]\,\rho\,\mathrm{d}\rho\,\mathrm{d}\theta. \tag{A.3}$$

By symmetry, this is not a function of ϕ and so, putting $\phi = 0$,

$$F_0(\zeta) = a\,\delta a \int_0^{2\pi} \exp[\mathrm{i}\zeta a\cos\theta]\,\mathrm{d}\theta = 2\pi a\,\delta a\,J_0(\zeta a). \tag{A.4}$$

This is the diffraction pattern you will find for (c) in Problem 8.7 and can see in the central region of Fig. A.2(b). It is also beautifully illustrated in Harburn *et al.* (1975).

A.2.2 A circular aperture

The diffraction pattern of a circular aperture is obtained by integrating (A.4) from $a = 0$ to $a = R$:

$$F_1(\zeta) = 2\pi \int_0^R J_0(\zeta a) a\,\mathrm{d}a = \frac{2\pi}{\zeta^2} \int_0^{R\zeta} J_0(\zeta a)\zeta a\,\mathrm{d}(\zeta a)\,. \tag{A.5}$$

From (A.2) one can prove easily that

$$\int_0^{\zeta} x^{n+1} J_n(x)\,\mathrm{d}x = \zeta^{n+1} J_{n+1}(\zeta) \tag{A.6}$$

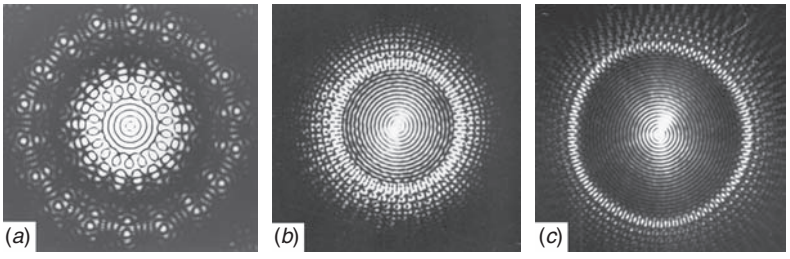

Figure A.2
Fraunhofer diffraction patterns of (*a*) 18, (*b*) 47 and (*c*) 72 pinholes equally spaced around a circle. In (*b*) and (*c*), the contributions of $J_0(\zeta a)$ and $J_m(\zeta a)$ are clearly separated.

from which, putting $n = 0$,

$$F_1(\zeta) = 2\pi \frac{R}{\zeta} J_1(\zeta R) = 2\pi R^2 \frac{J_1(\zeta R)}{\zeta R}\,. \tag{A.7}$$

Let us stress the similarity between the transforms of equivalent linear and circular systems:

- A slit of width $2R$ has transform $2R\ \sin(uR)/uR$.
- A hole of radius R and area $A = \pi R^2$ has transform $2A\,J_1(\zeta R)/\zeta R$.
- Two narrow slits of width w at $x = \pm R$ have transform $2w\cos(uR)$.
- A narrow annular ring of width w and radius R has transform $2\pi wRJ_0(\zeta R)$.

One can see that, roughly, $J_1(x)$ replaces $\sin x$, $J_0(x)$ replaces $\cos x$.

A.2.3 A ring of equally spaced holes

An illustration of the use of higher Bessel functions is worth presenting because of the beauty of the diffraction patterns. A ring of m pinholes can be represented roughly by the function

$$f(\rho, \theta) = [1 + \cos(m\theta/2\pi)]\delta(\rho - a), \tag{A.8}$$

which has m peaks equally spaced around a circle of radius a. The transform is

$$\begin{aligned}
&F_m(\zeta, \phi) \\
&\quad = \int_0^{2\pi} \left[1 + \frac{1}{2}\exp(\mathrm{i}m\,\theta/2\pi) + \frac{1}{2}\exp(-\mathrm{i}m\,\theta/2\pi)\right] \\
&\qquad \times \exp[\mathrm{i}\zeta a\cos(\phi - \theta)]\,\mathrm{d}\theta \\
&\quad = J_0(\zeta a) + \frac{1}{2}\int \exp\{\mathrm{i}[-\zeta a\cos(\phi - \theta) + m\theta/2\pi]\}\,\mathrm{d}\theta \\
&\qquad + \frac{1}{2}\int \exp\{\mathrm{i}[-\zeta a\cos(\phi - \theta) - m\theta/2\pi]\}\,\mathrm{d}\theta \\
&\quad = J_0(\zeta a) + \frac{1}{2}[\mathrm{e}^{\mathrm{i}m\phi/2\pi} + \mathrm{e}^{-\mathrm{i}m\phi/2\pi}]J_m(\zeta a) \\
&\quad = J_0(\zeta a) + \cos(m\phi/2\pi)J_m(\zeta a).
\end{aligned} \tag{A.9}$$

The intensity $|F_m(\zeta,\phi)|^2$ has two contributions which overlap very little when m is large. At the centre ($\zeta a \sim 1$) there is the usual $J_0(\zeta a)$ pattern from the ring at $\rho = a$; the individual holes are not resolved at small ζ. On the other hand, the function $J_m^2(\zeta a)$ is very weak when $\zeta a < m\pi/2$ but develops decaying oscillations at larger ζ. This function is modulated by $\cos^2(m\phi/2\pi)$ which has $2m$ peaks around the full circle. Figure A.2 shows the diffraction patterns for $m = 18, 47$ and 72.

A.3 Fourier transform of a periodic phase function

The examples discussed so far involved Fourier transforms of real functions, where the Bessel function arose from the coordinate transformation necessary to deal with the axial geometry. In this section we shall discuss an example in which the Bessel function arises because the function is complex with periodic phase. A particular feature of such functions is that the zero order may be small or even vanish because parts of the integral with different phase may cancel out. This would apply to a sinusoidal phase grating, such as that induced by a sound wave in the acousto-optic effect (§8.7).

Consider the Fourier transform of the sinusoidal phase function $f(x) = \exp[\mathrm{i}a\cos(qx)]$. This is

$$F(k) = \int_{-\infty}^{\infty} \exp[\mathrm{i}(a\cos(qx) - kx)]\,\mathrm{d}x. \tag{A.10}$$

This is a periodic function, with period $2\pi/q$, so we know that its transform consists of diffraction orders that are δ-function peaks at the values $k = mq$. The mth order has value

$$F(mq) = \int_{-\infty}^{\infty} \exp[\mathrm{i}(a\cos(qx) - mqx)]\,\mathrm{d}x. \tag{A.11}$$

We see that the integrand is periodic, with period $2\pi/q$, and so instead of integrating between $-\infty$ and ∞ we can just integrate over a single period. Then, replacing qx by ϕ, we have, up to a constant multiplier,

$$F(mq) = \frac{1}{q}\int_0^{2\pi} \exp[\mathrm{i}(a\cos(\phi) - m\phi)]\,\mathrm{d}\phi = \frac{1}{2\pi q} J_m(a). \tag{A.12}$$

The mth diffraction order therefore has amplitude proportional to the mth order Bessel function of the phase amplitude a. For example, if we want to find the phase amplitude for which the zero order disappears, we need to solve $J_0(a) = 0$, giving the values of a shown in Table A.1. On the other hand, the first order is maximized at the first value of a where $J_1'(a) = 0$.

Table A.1. Zeros of the first three Bessel functions and their derivatives

Order n	Positions of first three zeros of $J_n(x)$			Positions of first three zeros of $J_n'(x)$		
0	2.40	5.52	8.65	3.83	7.02	10.17
1	3.83	7.02	10.17	1.84	5.33	8.54
2	5.14	8.42	11.62	3.05	6.70	9.97

A.4 Fraunhofer diffraction pattern of a phase spiral

In §5.9 we introduced the idea of a wave with a spiral wavefront, with a screw dislocation along the axis $z = 0$, which transports angular momentum. Amongst other things, such waves are being employed to create a ring-like spot of light, with a zero on the axis, for purposes such as dark solitons (§13.6.4) or stimulated emission depletion microscopy (STED, §12.6.4) where the ring causes fluorescence to be quelled everywhere except for a small spot at the centre. The Fourier transform $F(\zeta, \phi)$ of the wavefront $f(r, \theta) = g(r) \exp(\mathrm{i}m\theta)$, where $g(r)$ is an arbitrary but bounded function, is calculated using a Bessel function, following (A.3):

$$F(\zeta,\phi) = \int_0^\infty \int_0^{2\pi} g(r) \exp(\mathrm{i}m\theta)\ \exp[\mathrm{i}\zeta r \cos(\theta - \phi)]\, r\, \mathrm{d}r\, \mathrm{d}\theta \tag{A.13}$$

$$= \exp(\mathrm{i}m\phi) \int_0^\infty \int_0^{2\pi} g(r) \exp[\mathrm{i}\zeta r \cos(\theta - \phi) + \mathrm{i}m(\theta - \phi)]\, r\, \mathrm{d}r\, \mathrm{d}\theta$$

$$= \exp(\mathrm{i}m\phi) \int_0^\infty J_m(\zeta r) g(r)\, \mathrm{d}r. \tag{A.14}$$

Near the origin $x = 0$ we can expand the Bessel function $J_m(x)$ as $(x/2)^m$ and so the value of $F(\zeta, \phi)$ is given by

$$F(\zeta,\phi) \sim \exp(\mathrm{i}m\phi) \int_0^\infty (\zeta r)^m g(r)\, \mathrm{d}r \sim \zeta^m, \tag{A.15}$$

when the integral converges. If we put, for example, the exponent $g(r) = \exp(-ar)$ or a Gaussian $g(r) = \exp(-ar^2)$, the integrals can easily be performed by parts and be shown to be finite. In STED, where the narrowest central zero is required, one chooses $m = 1$ to get a parabolic form for the intensity $F^2(\zeta) \sim \zeta^2$.

References

Harburn, G., Taylor, C. A. and Welberry, T. R. (1975), *Atlas of Optical Transforms*, London: G. Bell and Sons.

Watson, G. N. (1958), *A Treatise on the Theory of Bessel Functions*, 2nd edn., Cambridge: Cambridge University Press.

B Appendix B Lecture demonstrations in Fourier optics

Optics is the ideal subject for lecture demonstrations. Not only is the output of an optical experiment usually visible (and today, with the aid of closed circuit video, can be projected for the benefit of large audiences), but often the type of idea being put across can be made clear pictorially, without measurement and analysis being required. Recently, several institutes have cashed in on this, and offer for sale video films of optical experiments carried out under ideal conditions, done with equipment considerably better than that available to the average lecturer. Although such films have some place in the lecture room, we firmly believe that students learn far more from seeing real experiments carried out by a live lecturer, with whom they can interact personally, and from whom they can sense the difficulty and limitations of what may otherwise seem to be trivial experiments. Even the lecturer's failure in a demonstration, followed by advice and help from the audience which result in ultimate success, is bound to imprint on the student's memory far more than any video film can do.

The purpose of this appendix is to transmit a few ideas that we have, during the years, found particularly valuable in demonstrating the material covered in this book, and can be prepared with relatively cheap and easily available equipment. Need we say that we also *enjoyed* developing and performing these experiments?

B.1 Correlation and convolution by a pinhole camera

According to geometrical optics, a pinhole camera with a δ-function pinhole produces on a screen an exact image of the object. If the pinhole is not a δ-function, but has a shape, then the point spread function is a projection of the pinhole shape on the screen, and the image is the correlation of this with the exact image. We use this idea to demonstrate correlation and convolution.

The geometrical analysis of this idea is shown schematically for one dimension in Fig. B.1. The apparatus shown in Fig. B.2, which carries this out on the lecture bench, produces an image $h(x, y)$ which is the correlation between two real positive functions, $f(x, y)$ and $g(x, y)$, and was used to create Fig. 4.11. A projector incoherently illuminates a mask $f(x, y)$ in contact with a translucent

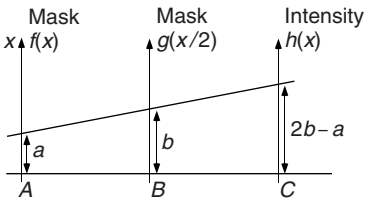

Figure B.1
Geometry of the correlation apparatus. $AB = BC$.

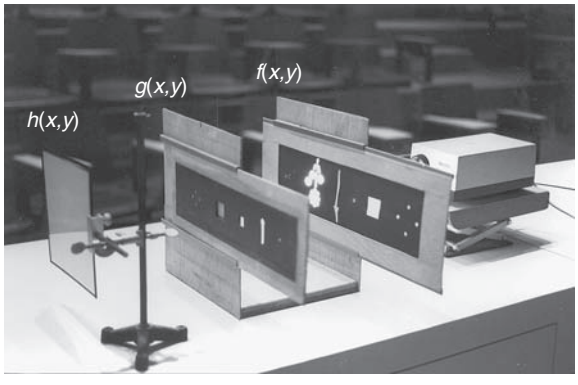

Figure B.2
The correlation apparatus.

screen in plane A. In plane B there is a second screen with cutouts representing the function $g(x,y)$. A third translucent screen is placed in plane C positioned so that the distances AB and BC are equal. We shall show that the illumination $h(x,y)$ on plane C is the **correlation function** of $f(x,y)$ and $g(x/2,y/2)$, or the **convolution** of $f(x,y)$ and $g(-x/2,-y/2)$. It is viewed from its reverse side and can conveniently be projected with the video camera.

In one dimension, it can easily be seen from the figure that if $f(x) = \delta(x-a)$ and $g(x) = \delta(x-b)$ then $h(x) = \delta(x+a-2b)$, i.e. a point on C at $x = 2b-a$ is illuminated. The correlation function of $f(x) = \delta(x-a)$ and $g(x/2) = \delta(x/2-b)$ is indeed $h(x) = \delta(x+a-2b)$. Moreover, the intensity of the point on C is proportional to the product of the source intensity f and the transmission of the point g. Since a general function can be described as a sum of δ-functions and since the operation of correlation is associative, the following equation is then generally valid:

$$h(x) = \int f(x'+x)\, g(x'/2)\, \mathrm{d}x'. \tag{B.1}$$

The function $h(x)$ therefore describes the correlation function of $f(x)$ and $g_1(x)$, where $g_1(x) = g(x/2)$.

Some particular cases can be emphasized. If the masks are similar but $g(x)$ is half the size of $f(x)$, i.e. $g(x/2) = f(x)$, then $h(x)$ describes the **auto-correlation function** of $f(x)$. This can be shown for sets of holes – note the very strong central peak in Fig. 4.11(f) – and for continuous functions such as the square hole – Fig. 4.11(g). Showing the gradation of intensity in the image in the latter case (its section has a roof-top profile) needs careful adjustment of

the video camera. By rotating the second function 180° about its origin, so that the axes of $g(x, y)$ are now down and to the left, we get the **convolution** of the two functions. An important demonstration shows the periodic function to be the convolution of the unit with a periodic lattice of small holes (δ-functions) either in one dimension (diffraction grating) or two (crystal).

In constructing this apparatus it is important to use translucent screens that diffuse as uniformly as possible in all directions, because a convenient-sized apparatus involves quite large angles, otherwise there are angular effects that complicate the analysis. Tracing paper or drafting film work well, although one can see from Fig. 4.11 that the edges of the images are weaker than their centres.

B.2 Fraunhofer diffraction

The demonstration of Fraunhofer diffraction was developed initially for crystallographic analysis (Taylor and Lipson (1964)) using a mercury arc source. The use of a helium-neon laser, $\lambda = 0.633\ \mu\text{m}$, makes the demonstration of diffraction and spatial filtering effects in a classroom quite easy, and with video projection the output is clearly visible.

B.2.1 Optical bench

We describe here an optical bench that was developed for this purpose and is shown schematically in Fig. B.3. A low-power (1 mW) laser is used. This is safe for classroom use; there is almost no danger of damage to the eye at this power, unless one looks for a long time directly into the unexpanded beam. The laser beam is expanded with the help of lenses L_1 ($F \approx -50\,\text{mm}$) and L_2 ($F \approx 250\,\text{mm}$) to about 8 mm diameter; one can then use diffraction masks of a reasonable size. For demonstrations, we found it unnecessary to use a pinhole spatial filter to 'clean up' the laser beam; this makes the apparatus very delicate, and means frequent readjustment. With a typical mask constructed with round 0.5 mm holes, at a mask–screen distance of 5 m, the radius of the first dark ring of the Airy disc of the envelope is only about 7 mm, which is rather small. Two lenses L_3 and L_4 acting as a telephoto combination (§3.6.4) are therefore used to magnify the image by a factor of three or more, depending on the mask and the details one wants to see. This way, the effective focal length is multiplied, but the apparatus can be made even shorter. To focus the system properly, we use a coarse periodic object such as a Ronchi ruling (square-wave grating) for a mask, and focus on one of the δ-function orders.

The video camera makes the diffraction patterns visible to the audience even without turning off the room lights. If the pattern, now about 20 mm in diameter,

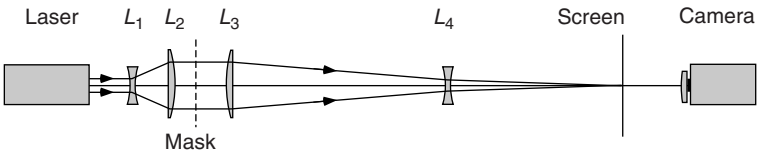

Figure B.3
Demonstration diffractometer using telephoto combinations.

is projected onto a semi-transparent screen shaded from the room lights, it can easily be shown using a video camera with a close-up lens focused on the screen. The latter also minimizes speckle effects.

You may want to show an image of the mask on the same screen as the diffraction pattern. This can be done as shown in Fig. B.5 by inserting a cube beamsplitter after the mask; a simple lens L_5 is then used to generate the required image of the mask. The same set-up will be used in §B.2.3 to show spatial filtering.

B.2.2 Objects for Fraunhofer diffraction

Diffracting masks with outside dimensions up to about 8 mm must be constructed. The best masks are made from unexposed photographic film (X-ray film is ideal – it is somewhat thicker than optical photographic film), thin black cardboard, or phosphor-bronze foil (about 0.1 mm). Taylor and Lipson (1964) described a pantograph for producing the masks, which is easily modified to a simplified form. The rectangular holes in punched computer cards (can you still find any?) are useful for showing single and multiple apertures. Other shapes such as triangle, square, ellipse etc. can be drilled and filed in foil (Fig. B.4(*a*)). The patterns of multiple apertures are very beautiful, particularly if the latter are symmetrical – for example rings of pinholes (Fig. A.2). Note in particular the symmetry relations when the numbers of holes in the ring are odd and even (Figs. 8.20 and B.4(*b*)). However, the drilling has to be quite accurate for the symmetry to be complete.

Dynamic demonstrations are particularly impressive, and some objects are illustrated in Fig. B.4(*c*)–(*h*):

(*c*) The effect of changing the separation of a pair of apertures can be shown with the aid of a double slit having variable separation. This can be constructed from a pair of long narrow slits that are not quite parallel, a region of their length being selected for use by a sliding cursor.

(*d*) Likewise, a pair of parallel wedge slits allows one to show the effect of changing the individual aperture dimension with constant separation.

(*e*) The sequence of diffraction patterns produced by 1, 2 . . . n parallel apertures can be shown by superposition of a coarse periodic square-wave grating (Ronchi ruling) and a slit of variable width, which selects the required number of periods (Fig. 8.17). This demonstration is particularly valuable because the

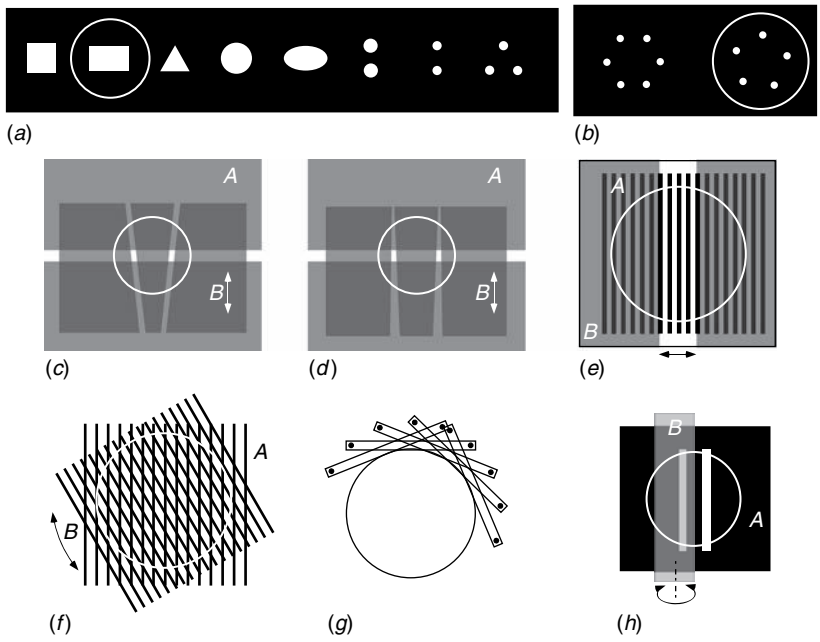

Figure B.4

Some useful diffraction masks. The beam size is indicated approximately by the white circle in each case. (*a*) A set of holes illustrating various examples. (*b*) Masks used in Fig. 8.20 to illustrate even and odd axial symmetries. (*c*) *B* slides across *A* to show the effect of changing the separation between slits of given width. (*d*) *B* slides across *A* to show the effect of changing the width of slits of given separation. (*e*) Changing the width of slit *B* exposes a varying number of slits of the ruling *A*. (*f*) The reciprocal lattice: two crossed gratings provide a two-dimensional array of apertures, and the angle between them can be varied. (*g*) An iris diaphragm is actually a polygon, but this can be used as a round hole to demonstrate scaling between real and reciprocal space. (*h*) A microscope cover slip covers one of a pair of slits, to show the effect of phase changes.

mask is obviously a product, and the two diffraction patterns that are convoluted are clearly visible (particularly when the variable slit is accidentally not quite parallel to the lines of the grating).

(*f*) The reciprocal lattice can be demonstrated by using two superimposed coarse Ronchi rulings with different periods. Since the mask is in a region where the light is parallel, the rulings do not need to be in contact. First, you show the diffraction pattern of one ruling, and then add the second one and show the convolution described in §4.8. The effect of changing the angle between *A* and *B* is easy to show, and you can change the dimension of one grating by tilting it about a transverse axis.

(*g*) A set of holes with different diameters can be used to show the inverse relationship between reciprocal and real space dimensions, but if you use an iris diaphragm the demonstration is more vivid. An iris is actually a polygon, but this is not really noticeable.

(*h*) The effect of changing the phase difference between two slits can be shown by covering one of them with a thin piece of glass (microscope cover slip). If the glass is rotated about a transverse axis, the phase difference can be changed continuously.

A demonstration of Babinet's principle can be done simply by comparing the patterns produced by a thick wire (say 1.5 mm diameter) and a slit of the same width. However, this is not as convincing as a more complicated object such as that used for Fig. 8.11.

Phase masks can be produced in various ways. Of course, photography can be used, together with bleaching, but this is quite time consuming. More simply, cleaved mica and thin glass cover slips can be used to construct phase masks, for which the actual magnitude of the phase differences can be changed by tilting the plane of the mask with respect to the z-axis. Phase objects with much detail (to show phase-contrast imaging, for example) can be made by smearing transparent glue on a microscope slide. Fingerprints are also good phase objects. We should also mention blazed gratings, which are quite easily available. The hot air field around a candle flame gives a dynamical phase object, particularly useful for showing schlieren filtering.

B.2.3 Spatial filtering

We can use a variation of the above apparatus to demonstrate the Abbe theory and effects of spatial filtering in the Fourier plane (Fig. B.5). The laser beam expanded by L_1 and L_2 illuminates the object slide and is focused to point P in the Fourier plane, where the diffraction pattern (optical transform) appears and filters can be inserted. The beamsplitter BS comes directly after P and the lens L_5 in one of its outputs is used to image the filtered optical transform onto the screen. Meanwhile, the other output from the beamsplitter is used to create the filtered image. This has to be formed with a telephoto combination, otherwise it is too small to be visible. There is actually a conflict of requirements here, which only a telephoto combination can solve. On the one hand, a large object would be required to give a large image. But then the diffraction pattern is small, and spatial filtering becomes a delicate operation. On the other hand, a small object with fine detail would solve this problem, but the re-imaging lens cannot be put close enough to it in order to get a highly magnified image because it can only be placed after P. The telephoto combination, with one principal plane close to the object mask, provides the answer.

Figure 12.6 shows Porter's experiments demonstrating spatial filtering of the image of a piece of gauze, carried out with this apparatus. The spatial filters that are inserted into the Fourier plane include first of all a variable iris diaphragm to demonstrate resolution and then a series of wires, slits and other apertures to select the combinations of diffraction spots. Since these need

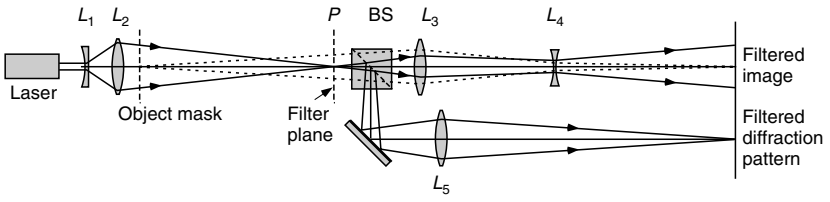

Figure B.5
Diffractometer used to illustrate spatial filtering.

to be positioned quite accurately with respect to the diffraction pattern, it is convenient to mount the filters on frames the size of a standard microscope slide and to use a microscope specimen stage to get fine x–y control of their positions.

Using the same apparatus, we can demonstrate phase-contrast techniques, using a phase object. It is easy to show dark-field imaging using a filter consisting of a black dot on a microscope slide to obstruct the zero order, and schlieren imaging using a razor blade to cut out half of the optical transform. In principle, a filter consisting of a small hole in a transparent celluloid sheet should show phase-contrast filtering but, demonstrated this way, the results never seem very convincing!

B.3 Fresnel diffraction

Fresnel diffraction patterns can be shown just by defocusing the Fraunhofer apparatus (Fig. B.3), although pedagogically it is better to take out the diffraction lenses L_3 and L_4 completely since they are not part of the theory. Then we put the diffraction obstacle in the expanded laser beam and project its shadow on the screen. It is important that the incident wave be a plane wave ($z_1 = \infty$) so that the effect of changing z alone is obtained by sliding the object along the optical bench. To avoid scattering at the edges of the apertures, it is best to make them from film and not from metal foil, and to paint them matt black.

Various simple objects can be used, such as a round hole, a sharp edge, slits and an opaque strip. The last of these was Young's original experiment, and is shown in Fig. 1.2. Particularly impressive is the Fresnel–Arago bright spot at the centre of the shadow of the disc, which is easily shown with the aid of a disc about 5 mm in diameter. It can be glued to a microscope slide or supported on a wire, which affects the spot very little, as can be seen from Fig. 1.3. The use of a video camera is important here, because its non-linear response can be used to boost the intensity of the very small spot by letting the outer parts of the diffraction pattern be saturated.

You can also demonstrate focusing by a Fresnel zone plate with this apparatus. A zone plate can be made by photographing a picture such as Fig. 7.6 on

high-contrast film, with magnification such as to give a focal length of order 20 cm. Usually the first- and third-order foci can be located.

B.4 Interferometry

B.4.1 Thin-film interference and Newton's rings

A simple projection apparatus for thin-film interference effects consists of a strong white-light source (a quartz-halogen bulb) followed by a condenser lens to concentrate it on the object. Light reflected from the object is focused onto a screen using an imaging lens (Fig. B.6(*a*)). According to §3.3.3, to maximize the field of view the condenser lens should focus the light source, after reflection from the object, onto the projection lens. The object can be a soap film in order to demonstrate interference in a thin film (note that the imaging lens creates an inverted image of the film, so that it appears to drain by flowing upwards!). Newton's rings between a glass plate and a long focal length lens can also be shown using the same system. The white source is important here because the colour effects are vivid.

B.4.2 Michelson's interferometer

A simple Michelson interferometer (Fig. B.6(*b*)) can easily be constructed to show the different types of fringes and the complementary patterns at the *A* and *B* outputs. We made this with all the elements, including a 0.5 mW helium-neon laser, screwed rigidly to a thick piece of plywood about 30 cm square. A small diverging lens is mounted directly on the laser output to give a diverging beam. This construction gives stable enough fringes for demonstration. The mirrors need to have angular degrees of freedom and one of then must allow linear translation.

B.5 Aperture synthesis

A lecture demonstration of aperture synthesis, devised by D. Wilson and J. Baldwin of Cambridge University works as follows (Lawson *et al.* (2002)). An incoherent light source (small lamp bulb) illuminates an object mask consisting of, say, two small holes representing a double star. This is projected to infinity by a converging lens at the focal distance (Fig. B.7). It is imaged by

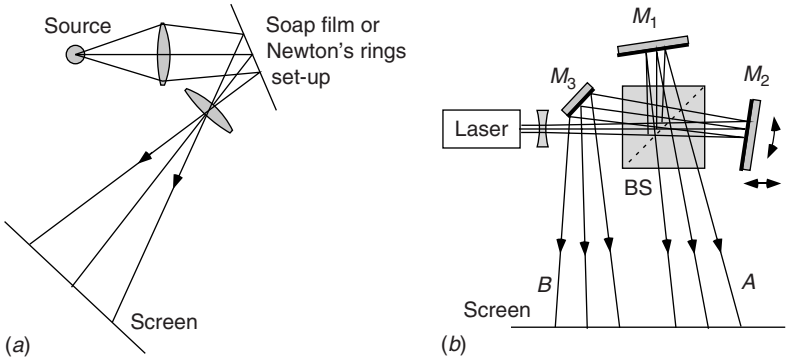

Figure B.6

Interferometry: (*a*) apparatus for demonstrating thin-film interference or Newton's rings; (*b*) Michelson's interferometer, visualizing the complementary outputs at *A* and *B*.

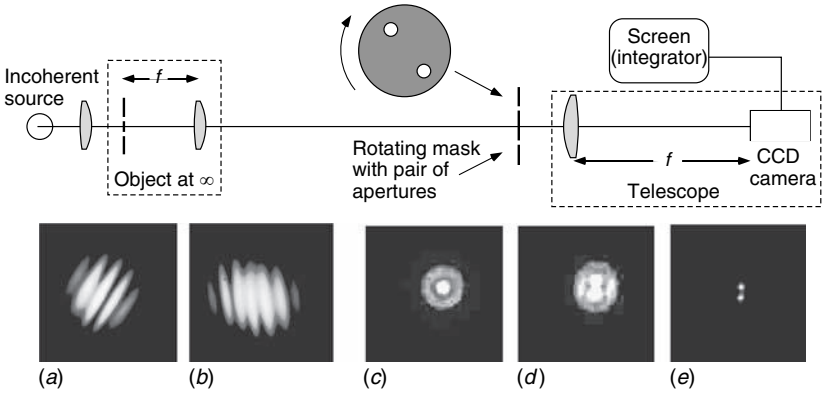

Figure B.7

Demonstration of aperture synthesis. (Top) The mask simulates a pair of receivers whose outputs are combined coherently. Its rotation simulates the Earth's diurnal rotation, and must be fast enough for the screen or observer's eye to integrate the images. The images below from a laboratory experiment show: (*a*) and (*b*) fringes from single and double stars, (*c*) and (*d*) synthesis images of the single and double stars, and (*e*) the deconvolved image of the latter. (Labeyrie *et al.* (2006))

a telescope, consisting of a second lens and a CCD camera, which shows the image on a monitor screen.

Now a mask is placed in front of the telescope lens. The mask has two holes, corresponding to two coherently combined antennae or telescopes separated by a baseline. If the coherence radius r_c of the waves from each of the 'stars' individually is greater than the distance between the mask holes, the image of the source becomes two sets of overlapping Young's fringes (Fig. B.6(*b*)). The mask now rotates in its plane, corresponding to collection of data as the Earth rotates. The monitor screen integrates the fringes, which is approximately the same as Fourier synthesis, and lo and behold!, an image of the double star appears on the screen.

When we first saw this demonstration, it was done without the lenses; it worked because the interference pattern of two sources is still a set of Young's fringes even in the near field. However, without the lenses, the image of the source is obtained *only* if the mask rotates exactly about the centre-point between the two holes, because the near-field fringes are not invariant to translation. With the lenses, the need for accurate alignment is avoided.

If the images are stored electronically as a video-clip, this can be made into a laboratory experiment. Results for various baselines can be accumulated, and

the DC offset of the fringes can be removed; then true aperture synthesis can be demonstrated (Labeyrie *et al.* (2006)) and deconvolution with the image of a point source can also be carried out (Fig. B.7(*c*)–(*e*)).

References

Labeyrie, A., Lipson, S. G. and Nisenson, P. (2006), *An Introduction to Optical Stellar Interferometry*, Cambridge: Cambridge University Press.

Lawson, P. R., Baldwin, J. E. and Wilson, D. (2002), Desktop interferometer for optical synthesis imaging, *Proc SPIE* **4838**, 404.

Taylor, C. A. and Lipson, H. (1964), *Optical Transforms*, London: Bell.

Index